Low-Lying Potential Energy Surfaces

EDITED BY
Mark R. Hoffmann
and Kenneth G. Dyall

Downloaded by 217.66.152.144 on September 14, 2012 | http://pubs.acs.org
Publication Date: August 14, 2002 | doi: 10.1021/bk-2002-0828.fw001

Low-Lying Potential Energy Surfaces

In Low-Lying Potential Energy Surfaces; Hoffmann, M., et al.;
ACS Symposium Series; American Chemical Society: Washington, DC, 2002.

Downloaded by 217.66.152.144 on September 14, 2012 | http://pubs.acs.org
Publication Date: August 14, 2002 | doi: 10.1021/bk-2002-0828.fw001

ACS SYMPOSIUM SERIES **828**

Low-Lying Potential Energy Surfaces

Mark R. Hoffmann, Editor
University of North Dakota

Kenneth G. Dyall, Editor
Eloret Corporation.

American Chemical Society, Washington, DC

Downloaded by 217.66.152.144 on September 14, 2012 | http://pubs.acs.org
Publication Date: August 14, 2002 | doi: 10.1021/bk-2002-0828.fw001

QD 462.6 .P64L68 2002 c. 1

Low-lying potential energy
surfaces

Downloaded by 217.66.152.144 on September 14, 2012 | http://pubs.acs.org
Publication Date: August 14, 2002 | doi: 10.1021/bk-2002-0828.fw001

Library of Congress Cataloging-in-Publication Data

Low-lying potential energy surfaces / Mark R. Hoffmann, editor, Kenneth G. Dyall, editor.

p. cm.—(ACS symposium series ; 828)

Includes bibliographical references and index.

ISBN 0–8412–3792–1

1. Potential energy sources—Congresses.

I. Hoffmann, Mark R., 1958-. II. Dyall, Kenneth G., 1955- III. American Chemical Society. Division of Physical Chemistry. IV. American Chemical Society. Meeting (221st: 2001 : San Diego, Calif.). V. Series.

QD462.6.P64 L68 2002
541.2′8—dc21 2002018582

The paper used in this publication meets the minimum requirements of American National Standard for Information Sciences—Permanence of Paper for Printed Library Materials, ANSI Z39.48–1984.

Copyright © 2002American Chemical Society

Distributed by Oxford University Press

All Rights Reserved. Reprographic copying beyond that permitted by Sections 107 or 108 of the U.S. Copyright Act is allowed for internal use only, provided that a per-chapter fee of $22.50 plus $0.75 per page is paid to the Copyright Clearance Center, Inc., 222 Rosewood Drive, Danvers, MA 01923, USA. Republication or reproduction for sale of pages in this book is permitted only under license from ACS. Direct these and other permission requests to ACS Copyright Office, Publications Division, 1155 16th St., N.W., Washington, DC 20036.

The citation of trade names and/or names of manufacturers in this publication is not to be construed as an endorsement or as approval by ACS of the commercial products or services referenced herein; nor should the mere reference herein to any drawing, specification, chemical process, or other data be regarded as a license or as a conveyance of any right or permission to the holder, reader, or any other person or corporation, to manufacture, reproduce, use, or sell any patented invention or copyrighted work that may in any way be related thereto. Registered names, trademarks, etc., used in this publication, even without specific indication thereof, are not to be considered unprotected by law.

PRINTED IN THE UNITED STATES OF AMERICA

American Chemical Society
Library
1155 16th St., N.W.
Washington, D.C. 20036

Downloaded by 217.66.152.144 on September 14, 2012 | http://pubs.acs.org
Publication Date: August 14, 2002 | doi: 10.1021/bk-2002-0828.fw001

Foreword

The ACS Symposium Series was first published in 1974 to provide a mechanism for publishing symposia quickly in book form. The purpose of the series is to publish timely, comprehensive books developed from ACS sponsored symposia based on current scientific research. Occasion-ally, books are developed from symposia sponsored by other organizations when the topic is of keen interest to the chemistry audience.

Before agreeing to publish a book, the proposed table of contents is reviewed for appropriate and comprehensive coverage and for interest to the audience. Some papers may be excluded to better focus the book; others may be added to provide comprehensiveness. When appropriate, overview or introductory chapters are added. Drafts of chapters are peer-reviewed prior to final acceptance or rejection, and manuscripts are prepared in camera-ready format.

As a rule, only original research papers and original review papers are included in the volumes. Verbatim reproductions of previously published papers are not accepted.

ACS Books Department

In Low-Lying Potential Energy Surfaces; Hoffmann, M., et al.;
ACS Symposium Series; American Chemical Society: Washington, DC, 2002.

Preface

This book is based on the *Accurate Description of Low-Lying Electronic States and Potential Energy Surfaces* symposium at the 221st National Meeting of the American Chemical Society (ACS) in San Diego, California from March 30–April 4, 2001. The symposium was organized because of our own interests in this area and because of the many recent developments in methodology for simultaneous treatment of many electronic states across an extended region at comparable levels of accuracy. The availability of such methods underpins developments in other areas such as dynamics and spectroscopy and provides necessary information for understanding phenomena involving electronic excited states. We felt that it was useful to bring together the producers and the consumers of such potential energy surfaces in the hope that each group would provide stimulus to the others.

Of the 33 invited speakers and the seven who contributed talks, 17 accepted our invitation to contribute a chapter to this book. These chapters are complemented by three additional chapters from individuals to help develop a more cohesive book as well as an overview chapter. Approximately half of the chapters are focused on the development of ab initio electronic structure methods and consideration of specific challenging molecular systems using electronic structure theory. Some of these chapters document the dramatic developments in the range of applicability of the coupled-cluster method, including enhancements to coupled-cluster wavefunctions based on additional small multireference configuration interaction (MR-CISD) calculations, the method of moments, the similarity transformed equation of motion (STEOM) method, a state-specific multireference coupled-cluster method, and a computationally efficient approximation to variational coupled-cluster theory. The concentration on the coupled-cluster approach is balanced by an approximately equal number of chapters discussing other aspects of modern electronic structure theory. In particular, other methods appropriate for the description of excited electronic states, such as multireference

Downloaded by 217.66.152.144 on September 14, 2012 | http://pubs.acs.org
Publication Date: August 14, 2002 | doi: 10.1021/bk-2002-0828.pr001

In Low-Lying Potential Energy Surfaces; Hoffmann, M., et al.;
ACS Symposium Series; American Chemical Society: Washington, DC, 2002.

perturbation theory and time-dependent density functional theory, are not neglected. Although the book has no pretense of being encyclopedic, we intended that the electronic structure sections of the book will provide a poised view of state-of-the-art electronic structure theory.

The complementary half considers either structural or dynamical aspects of the coupling of potential surfaces or of regions of potential energy surfaces far from stationary points, and includes chapters on a diversity of methods and applications that illustrate the breadth of the subject, from photodissociation dynamics and molecular resonances in unimolecular decomposition to collisions of vibrationally excited molecules and comparison of quantum scattering and trajectory hopping results for a model system that investigates intersystem-crossing effects. Symmetry properties of adiabatic-to-diabatic transformation matrices and symmetry properties and strategies for efficient evaluation of the spin–orbit coupling operator are two more of the diverse set of topics that are covered. Although the focus of the volume is on small molecules, a formulation of semiclassical path integral methods appropriate for studying quantum dynamics in large systems and a chapter on bridging ab initio results and thermodynamic properties of collections of molecules are included.

It is our hope that this book will serve as a useful work for advanced graduate students and postdoctoral associates in the field of molecular electronic structure theory and serve as a useful contemporary reference for more established researchers in electronic structure theory, as well as disciplines that directly use potential energy surfaces. In particular, the volume was written with the chemical dynamicist and molecular spectroscopist in mind.

Downloaded by 217.66.152.144 on September 14, 2012 | http://pubs.acs.org
Publication Date: August 14, 2002 | doi: 10.1021/bk-2002-0828.pr001

Acknowledgments

As with all organizational efforts, the support of many individuals and offices was critical to the successful completion of the symposium and ultimately this book. We acknowledge the Petroleum Research Fund as well as the ACS Division of Physical Chemistry and the ACS Red River Valley Section. Within the University of North Dakota, the Office of Research and Program Development, the Chemistry Department, and particularly, John Ettling, the Vice President of Academic Affairs and Provost, are thanked. We are grateful to Tim Lee

(NASA Ames) and Julia Rice (IBM Almaden) for their confidence and encouragement in organizing the symposium. The staff at the ACS Books Department, especially Kelly Dennis and Stacy VanDerWall in acquisitions and Margaret Brown in editing and production, have been more than helpful in assisting in all phases of the preparation of this book. And, lastly, we thank our wives, Cathy and Gillian, for their support and patience.

Mark R. Hoffmann
Chemistry Department
University of North Dakota
Grand Forks, ND 58202-9024
Phone: (701) 777–2742
Fax: (701) 777–2331
Email: mhoffmann@chem.und.edu

Kenneth G. Dyall
Eloret Corporation
690 West Fremont Avenue, Suite 8
Sunnyvale, CA 94087
Email: dyall@pegasus.arc.nasa.gov

Downloaded by 217.66.152.144 on September 14, 2012 | http://pubs.acs.org
Publication Date: August 14, 2002 | doi: 10.1021/bk-2002-0828.pr001

Chapter 1

Overview: Accurate Description of Low-Lying Electronic States and Potential Energy Surfaces

Mark R. Hoffmann[1] and Kenneth G. Dyall[2]

[1]Chemistry Department, University of North Dakota, Grand Forks, ND 58202–9024
[2]Eloret Corporation, 690 West Fremont Avenue, Sunnyvale, CA 94087

Downloaded by 217.66.152.144 on September 14, 2012 | http://pubs.acs.org
Publication Date: August 14, 2002 | doi: 10.1021/bk-2002-0828.ch001

This paper provides an overview of recent trends in the development of electronic structure theory for the accurate characterization of all, or large regions, of ground and excited potential energy surfaces. Topics include the treatment of dynamical and nondynamical correlation and the calculation of nonadiabatic coupling matrix elements, as arising from spin-orbit coupling and from nuclear motion.

The theoretical study of accurate potential energy surfaces (PESs) has seen some essential progress in the last decade. Much of this progress can be attributed, at least in broad terms, to advancements in the ability to include nondynamical electron correlation equitably with dynamical electron correlation. Perhaps this point can be underscored by noting the tremendous response of the greater chemistry community to the CASPT2 *(1)* functionality in the widely

In Low-Lying Potential Energy Surfaces; Hoffmann, M., et al.;
ACS Symposium Series; American Chemical Society: Washington, DC, 2002.

distributed GAUSSIAN *(2)* software package. Moreover, CASPT2 is but one of many such efforts to achieve a useful balance between the different types of electron correlation. There has also been progress in other areas than that of correlation, such as nonadiabatic couplings via the spin-orbit interaction and nuclear motion. In this chapter we give an overview of some of the important theoretical developments. It should be stated at the outset that this overview is not intended to be encyclopedic, and more complete bibliographies are to be found in the individual chapters of this volume. Rather, this overview represents our attempts to indicate important trends in the field and therefore the motivations in organizing the symposium that served as a basis of this book.

Downloaded by 217.66.152.144 on September 14, 2012 | http://pubs.acs.org
Publication Date: August 14, 2002 | doi: 10.1021/bk-2002-0828.ch001

Dynamical vs. Nondynamical Electron Correlation

While the venerable multireference configuration interaction method, including single and double excitations (MR-CISD), remains the approach of choice for some problems, alternatives have been proposed and are showing their usefulness. One can describe MR-CISD as the variational calculation within a specified reference, or model, space, $\mathcal{L}_0$, and the spaces generated by all single excitations relative to the specified model space, $\mathcal{L}_1$, and likewise the double excitations, $\mathcal{L}_2$. Provided that the model space is sufficiently large to describe the nondynamic electron correlation adequately, MR-CISD provides a well-balanced and unbiased description of both nondynamic and dynamic electron correlation. It is precisely in the caveat in which lies the problem with MR-CISD. Since the size of the excitation spaces $\mathcal{L}_1$ and $\mathcal{L}_2$ grow rapidly with the size of the dimension of the model space, $\mathcal{L}_0$, one is often faced with the unpleasant task of restricting $\mathcal{L}_0$ to a size smaller than physically justified. Of course, if such restriction is not required for the problem at hand, MR-CISD is a reliable and robust method and, so, continues to see modern usage. It is also worth noting that MR-CISD suffers from a lack of size-extensivity, and, although this is usually not a serious problem, relative to other sources of error, for the mapping of PESs of small molecular systems, there is need for theoretical advancements.

In situations in which physically well-motivated MR-CISD calculations are not computationally feasible, the need for adequate approximations of nondynamical and dynamical electron correlation must be balanced. One useful way of categorizing alternatives to MR-CISD is to focus on the sequence of treating nondynamical and dynamical correlation. One could address dynamical correlation for all, or part, of the model space first and, then, proceed to address the nondynamical correlation. This approach gives rise to an effective

Hamiltonian. Indeed, this approach, with many variations, finds expression in the current coupled cluster equation of motion (EOM) or similarity transform EOM (STEOM) procedures *(3-5)* and also in the multireference (or quasidegenerate) perturbation theory approaches (MRPT or QDPT) *(6-10)*. In fact, the CCSD(T) method *(11)*, which was recently referred to as the "gold standard" of modern quantum chemistry *(12)*, also addresses dynamic correlation prior to nondynamic correlation. However, since CCSD(T) is generally only applicable to the ground electronic state (or, possibly, the lowest state of a particular symmetry) and the emphasis of this volume is on multiple PESs, this approach is not considered in any detail herein. Alternatively, one could address the nondynamical correlation first and then only consider the dynamical correlation. State selective methods, including "diagonalize-then-perturb" multireference perturbation theories (e.g., CASPT2) and internally-contracted CI methods *(13)*, are of this philosophy. Taking into account that both general approaches are currently being used successfully, and continue to be developed further, it must be clear that both have merit.

Downloaded by 217.66.152.144 on September 14, 2012 | http://pubs.acs.org
Publication Date: August 14, 2002 | doi: 10.1021/bk-2002-0828.ch001

Multiple Potential Energy Surfaces

One criterion for recommending effective Hamiltonian methods over state-selective methods is whether multiple PESs are of simultaneous interest. State-selective methods are in general capable of determining excited PESs, even of the same symmetry as the ground state (or lowest state of a given symmetry), but, by their nature, use essentially different representations of the multiple surfaces. Conversely, precisely because state-selective approaches need consider only one state in a particular calculation, they can often achieve quite high computational efficiencies. In many of the state-selective procedures, a multiconfiguration self-consistent (MCSCF) calculation is performed to determine the nondynamical electron correlation, after which the dynamical electron correlation method of choice is applied. So, for different states, different molecular orbitals will be used. This complicates, but not hopelessly, the calculation of matrix elements that couple surfaces. Such matrix elements arise when considering nonadiabatic effects, i.e., in consideration of spin-orbit coupling or nuclear derivative coupling.

Multiple PESs may be of simultaneous interest based not only on physical reasons, as emphasized in the previous paragraph, but also for mathematical or computational reasons. Consider the basic paradigm of state-selective methods: the nondynamical electron correlation for a specific state is calculated within a model space and then the dynamical electron correlation is calculated. The implicit assumption is that the zero-order model space many-electron basis functions (MEBFs) (e.g., MCSCF functions and MCSCF complementary space functions) are sufficiently close to the correlated (i.e., true) model space MEBFs that the mixing between the correlated space MEBFs can be made on the basis of the zero-order model space MEBFs. In fact, for well-separated states, and a physically realistic model space, this assumption is well founded. However, in cases in which the states are in close proximity the dynamic electron correlation can significantly alter the mixing between zero-order functions of the model space. Avoided crossings represent just such physical conditions. In these cases, state-selective methods are presented with severe mathematical challenges. The reader is directed to the chapter by Mukherjee in this volume in which recent progress on this problem has been made. On the other hand, it is precisely in such situations that multireference or quasidegenerate methods, which form effective Hamiltonians, are most appropriate. The dynamic correlation is considered prior to the nondynamic correlation that mixes the two close lying states.

However, effective hamiltonians can be mathematically unstable in precisely the situations in which state selective methods are most adept: widely separated energy levels. The problem is the appearance of intruder states, whether physical (or infinite order) or zero-order (i.e., many-electron basis functions). Intruder states stymied the development of quasidegenerate perturbation theories for many years and, although there are now known remedies, intruder states continue to require care when formulating new variants of QDPT. In essence, one compromises on the goal of treating the effect of dynamical electron correlation on the entire model space prior to consideration of nondynamical correlation. As pioneered by Malrieu and coworkers and by Kirtman, one contents oneself with describing only part of the model space well. Recent work in the group of Hoffmann has demonstrated that it is feasible to remove the arbitrariness in selecting the part of the model space that will be treated well *(14)*.

In fact, both state-selective methods and effective Hamiltonian methods are faced with the challenge of describing variable quasidegeneracy equitably over entire potential energy surfaces.

Downloaded by 217.66.152.144 on September 14, 2012 | http://pubs.acs.org
Publication Date: August 14, 2002 | doi: 10.1021/bk-2002-0828.ch001

Nonadiabatic Coupling Matrix Elements

Several other issues are relevant to the discussion of multiple PESs. As previously mentioned, multiple PESs are required for the description of any nonadiabatic effects. Such processes arise in considering relativistic effects and nuclear dynamics. The situation here is more complex than with just the calculation of multiple PESs. Indeed, the accuracy and effort of the calculation of nonadiabatic matrix elements must be assessed against the reliability of the PESs themselves. Furthermore, the issue of coupling of adiabatic surfaces places additional emphasis on the criterion of uniform accuracy of PESs. Whereas for individual PES calculations it might not be really essential to maintain uniform accuracy, provided, for example, that each PES had its critical points (e.g., local minima and transition states) calculated at comparable accuracies, for nonadiabatic effects it may be regions of PESs far removed from these relatively benign points which require uniform accuracy. It is precisely for this reason that the majority of studies involving nonadiabatic dynamics and relativistic descriptions of stationary points have utilized MR-CISD wavefunctions. However, as previously noted, computational considerations recommend the development of alternatives to MR-CISD.

The development of methods for inclusion of relativistic effects on PESs is at a much earlier stage than that of electron correlation effects. Granted, scalar relativistic effects can be – and have been – routinely incorporated into nonrelativistic calculations, either using effective core potentials or ab initio model potentials, or one of the scalar all-electron methods such as the Douglas-Kroll-Hess *(15,16)* method. The incorporation of spin-orbit coupling is more difficult because it breaks both the spatial and the spin symmetry of the nonrelativistic wavefunction. But it is precisely this phenomenon that makes it so interesting and important in the consideration of multiple potential energy surfaces. Spin-orbit mediated avoided crossings can radically change reaction dynamics, for example, and change the nature of conical intersections, as shown earlier *(17)*, and addressed further in this symposium, by Yarkony.

Furthermore, one must consider where to include spin-orbit effects in relation to both dynamical and nondynamical correlation. The most widely used approach is to construct an effective Hamiltonian for spin-orbit coupling from MRCI wavefunctions that are built from a common orbital set. The small set of wavefunctions is often sufficient to describe spin-orbit coupling between the nonrelativistic surfaces, and was used to good effect by Werner in the reaction dynamics calculations presented in this symposium. Another approach is to obtain a set of natural orbitals from MRCI calculations and use these in a CI calculation that includes spin-orbit interaction. In this way dynamical correlation, nondynamical correlation and spin-orbit interaction are treated on the same footing, albeit with some compromise on the first of these three.

The more rigorous approaches are still in their infancy due largely to technical difficulties and the magnitude of the calculations resulting from the lowering of the symmetry. These approaches include MRCI methods based on nonrelativistic wave functions such as that of Yabushita and coworkers *(18)* and Rakowitz and Marian *(19)* that include the spin-orbit interaction on an equal footing with the Coulomb (or scalar relativistic) interaction, and methods that start from spin-coupled wavefunctions, either at a 2-component or 4-component level *(20)*. Such methods are necessary to address the challenges like those

Downloaded by 217.66.152.144 on September 14, 2012 | http://pubs.acs.org
Publication Date: August 14, 2002 | doi: 10.1021/bk-2002-0828.ch001

presented by high-accuracy experimental PESs for the halogen monoxides measured by Miller and coworkers *(21)*.

Nondynamical (or Static) Correlation

Another issue which is relevant to the accurate description of PESs is the question of the treatment of nondynamical correlation. Above, we accepted, without comment, the conventional paradigm of description of nondynamical electron correlation by an MCSCF calculation, in the case of antecedent nondynamical electron correlation, or of a variational calculation within the model space in the case of subsequent nondynamical electron correlation. Although this is the modus operandi, which usually takes specific form in a CASSCF calculation and/or a state-averaged variant (SA-MCSCF), this can hardly be considered a wholly resolved issue. Indeed, it has been shown that coupled cluster based alternatives to variational calculations within a model space have merit. Within this volume, Head-Gordon describes some very recent advances. Another related issue concerns the molecular orbitals themselves. Earlier, Freed demonstrated that high-lying valence molecular orbitals obtained from MCSCF calculations are not particularly desirable MOs for describing excited states *(22)*, as required in an effective hamiltonian calculation. Although the situation may be expected to be improved by increasingly large state-averaged calculations, such calculations can of themselves become computationally resource significant. Moreover, such calculations are quite prone to optimization to one of many, and possibly myriad, local minima; thus, seriously raising the question of reproducibility. In this volume, Freed and coworkers give further account of efforts to circumvent the low occupation MO problem by a novel improved virtual orbital scheme.

Downloaded by 217.66.152.144 on September 14, 2012 | http://pubs.acs.org
Publication Date: August 14, 2002 | doi: 10.1021/bk-2002-0828.ch001

Concluding Remarks

One of the driving forces for the development of theoretical methods to describe accurately ground and excited PESs, and their couplings, is the study of chemical reaction dynamics [for a recent overview, with many references, see Ref. *(23)*]. Although many reactions can be reasonably well described as proceeding on a single adiabatic surface, there are at least two regimes in which this conceptualization is wanting. First, near dissociation limits PESs that are well isolated from each other in other geometrical regions can become quasidegenerate or even exactly degenerate. In such situations, couplings, such as spin-orbit, Coriolis and nuclear derivative, can give rise to an effective PES that is different than the adiabatic surface. As mentioned previously, the challenge to electronic structure theory is to describe surfaces equitably under conditions of variable quasidegeneracy. Second, even in the interior, or non-fragment, regions of PESs, it may be the case that two surfaces couple relatively strongly in a small geometrical region. Using a classical description, reaction paths approaching or passing through such regions can lead to qualitatively different results than in the absence of the couplings. Conical intersections are a dramatic example. In this symposium, several speakers were asked to describe advances and challenges in chemical reaction dynamics. Several of the speakers, complemented by contributions from outside the symposium, also contributed to this volume. Although this volume is even less comprehensive with respect to advances in chemical dynamics than it is with respect to the description of PESs, it was our intention that the interplay between electronic structure theory and the study of chemical reactions be represented herein.

Downloaded by 217.66.152.144 on September 14, 2012 | http://pubs.acs.org
Publication Date: August 14, 2002 | doi: 10.1021/bk-2002-0828.ch001

References

1. Andersson, K.; Malmqvist, P.-Å; Roos, B. O. *J. Chem. Phys.* **1992**, *96*, 1218.
2. *Gaussian 98*; Frisch, M. J., et al.; Gaussian, Inc.: Pittsburgh, PA, 1998.
3. Koch, H; Jørgensen, P. *J. Chem. Phys.* **1990**, *93*, 3333.
4. Stanton, J. F.; Bartlett, R. J. *J. Chem. Phys.* **1993**, *98*, 7029.
5. Nooijen, M.; Bartlett, R. J. *J. Chem. Phys.* **1997**, *106*, 6441.
6. Sheppard, M. G; Freed, K. F. *J. Chem. Phys.* **1981**, *75*, 4507.
7. Hirao, K *Chem. Phys. Lett.* **1992**, *190,* 374.
8. Hoffmann, M. R. *Chem. Phys. Lett.* **1992**, *195*, 127.
9. Nakano, H *J. Chem. Phys.* **1993**, *99*, 7983.
10. Kozłowski, P. M.; Davidson, E. R. *J. Chem. Phys.* **1994**, *100,* 3672.
11. Raghavachari, K; Trucks, G. W.; Pople, J. A.; Head-Gordon, M. *Chem. Phys. Lett.* **1989**, *157*, 479.
12. Head-Gordon, M. Presented at the 10th American Conference on Theoretical Chemistry, Boulder, CO, 1999.
13. Werner, H.-J.; Knowles, P. J. *J. Chem. Phys.* **1988**, *89*, 5803.
14. Khait, Y. G.; Hoffmann, M. R. *J. Chem. Phys.* **1998**, 108, 8317.
15. Douglas, M.; Kroll, N. M. *Ann. Phys. (N.Y.)* **1974**, *82*, 89.
16. Hess, B. A. *Phys. Rev. A* **1985**, *32*, 756; **1986**, 33, 3742.
17. Matsika, S.; Yarkony, D. R. *J. Chem. Phys.* **2001**, *115*, 2038–2050, 5066–5075.
18. Yabushita, S.; Zhang, Z. Y.; Pitzer, R. M. *J. Phys. Chem. A* **1999**, 103, 5791.
19. Rakowitz, F, Marian, C. *Chem. Phys.* **1997**, 225, 223.

20. Visscher, L.; Visser, O.; Aerts, P. J. C.; Merenga, H.; Nieuwpoort, W. C. *Comp. Phys. Commun.* **1994**, 81, 120.
21. Miller, C. E.; Drouin, B. J. *J. Mol. Spectrosc.* **2001**, *205*, 128; **2001**, *205*, 312.
22. Finley, J. P; Freed, K. F. *J. Chem. Phys.* **1995**, *102*, 1306.
23. Truhlar, D. G. Molecular-Scale Modeling of Reactions and Solvation. In *First International Conference on Foundations of Molecular Modeling and Simulation;* Cummings, P. T.; Westmoreland, P. R.; Carnahan, B, Eds.; AIChE Symposium Series Vol. 97; American Institute of Chemical Engineers: New York, 2001; pp 71-83.

Downloaded by 217.66.152.144 on September 14, 2012 | http://pubs.acs.org
Publication Date: August 14, 2002 | doi: 10.1021/bk-2002-0828.ch001

Downloaded by NORTH CAROLINA STATE UNIV on September 14, 2012 | http://pubs.acs.org
Publication Date: August 14, 2002 | doi: 10.1021/bk-2002-0828.ch002

Chapter 2

Simultaneous Account of Dynamic and Nondynamic Correlations Based on Complementarity of CI and CC Approaches

Xiangzhu Li[1] and Josef Paldus[1,2]

[1]Department of Applied Mathematics, University of Waterloo, Waterloo, Ontario N2L 3G1, Canada
[2]Department of Chemistry and Guelph-Waterloo Center for Graduate Work in Chemistry, University of Waterloo, Waterloo, Ontario N2L 3GI, Canada

In order to overcome the shortcommings of standard post-Hartree-Fock approaches in their handling of the dynamic and nondynamic correlations, we investigate the possibility of mutual enhancement between variational and perturbative approaches, as represented by various CI and CC methods, respectively. This is achieved either via the amplitude-corrections to the one- and two-body CCSD cluster amplitudes based on some external source, in particular a modest size MR CISD wave function, in the so-called reduced multireference (RMR) CCSD method, or via the energy-corrections to the standard CCSD based on the same MR CISD wave function. The latter corrections are based on the asymmetric energy formula and may be interpreted either as the MR CISD corrections to CCSD or RMR CCSD, or as the CCSD corrections to MR CISD. This reciprocity is pointed out and a new perturbative correction within the MR CISD is also formulated. The earlier results are briefly summarized and compared with those introduced here for the first time using the exactly solvable double-zeta model of the HF and N_2 molecules.

In Low-Lying Potential Energy Surfaces; Hoffmann, M., et al.;
ACS Symposium Series; American Chemical Society: Washington, DC, 2002.

Downloaded by NORTH CAROLINA STATE UNIV on September 14, 2012 | http://pubs.acs.org
Publication Date: August 14, 2002 | doi: 10.1021/bk-2002-0828.ch002

I. Introduction

The variational methods of the configuration interaction (CI) type and the perturbative-type methods relying on the exponential coupled-cluster (CC) Ansatz are the most often used approaches in *ab initio* computations of highly accurate molecular properties, in particular of the potential energy surfaces (PESs) or curves (PECs) for the purposes of molecular dynamics [for recent reviews, see Refs. (*1-4*)]. In this latter case it is essential that the entire surface — or its various one- or multi-dimensional cuts — is available for a wide enough range of molecular geometries.

For nondegenerate states, the single reference (SR) version of either the CI or CC method, truncated at the doubly excited level (i.e., CISD or CCSD, respectively), is capable of producing reasonably accurate results. Unfortunately, the requirement of nondegeneracy is invariably violated when we break genuine chemical bonds, which in turn enhances the importance of higher than doubly-excited configurations or connected cluster components, in particular of the triply (T) and quadruply (Q) excited ones. Since the number of the corresponding parameters dramatically increases with the increasing size of the basis set, such methods become computationally unaffordable, except for smaller benchmark systems. Moreover, when breaking triple bonds, even hexuples play a non-negligible role. Clearly, an appropriate approach in such cases is to use the multireference (MR) formalism that is based on a suitable model space $\mathcal{M}_0$, which is spanned by those quasidegenerate configurations that enable an appropriate description of the relevant dissociation channel(s).

In this regard, it is important to emphasize the multifaceted complementarity of CI and CC approaches (*5*). While the generalization of SR CISD to MR CISD is, at least conceptually, straightforward (even at the spin-adapted level; see e.g. UGA based formalism (*6*)), this is not the case for CC approaches. The stumbling block is the ambiguity in the generalization of the SR CC Ansatz to the MR case. Although two such viable MR Ansätze have been formulated [namely the *valence universal* or Fock space and *state universal* or Hilbert space Ansätze; cf., e.g. Ref.(*7*) for an overview], their complexity and especially various conceptual difficulties (such as the intruder state problem, multiplicity of solutions and their genealogy, etc.) prevented the development of efficient general purpose codes to this very day. Consequently, many of the current developments focus on the so-called *state specific* or *state selective* (SS) approaches, i.e., an essentially SR approaches that are guided, in one way or another, by the MR formalism.

Another aspect of the just mentioned complementarity is the ability with which the CI and CC approaches account for the dynamic and nondynamic correlations. As alluded to above, the CI approaches are very efficient in handling of the latter, already at a low-dimensional level, while the dynamic correlation requires the inclusion of a large number of highly-excited configurations, thus making unrealistic demands on the dimensionality of the CI matrices one has to handle. For this very reason, even at the MR level, the CI results are invariably corrected *ex post* by relying on various semi-empirical Davidson-type corrections.

In contrast to CI, the CC approaches, even at the SR level, very efficiently account for the dynamic correlation thanks to the exponential CC Ansatz for the wave operator. The general form of the CC wave function also automatically guarantees the size-extensivity of the computed energies [as do, in fact, the individual linked diagrams of the many-body perturbation theory (MBPT)]. Unfortunately, this size-extensive property is of a little use when the nondynamic correlation is not properly accounted for. Indeed, the CCSD PECs often display an artificial "hump" in the region of intermediate internuclear separations, as well as grossly erroneous asymptotic behavior in the completely dissociated limit [cf., e.g. the CCSD PECs for N_2 in Refs. (*8,9*)].

Numerous steps have been undertaken in order to overcome these shortcommings of the standard CCSD method. The simplest way to achieve a proper dissociation limit (size-consistency) is to employ the unrestricted Hartree-Fock (UHF) reference. This often works rather well, except that UHF solution(s) exist(s) only in a limited range of internuclear separations and, at the onset of the RHF triplet instability the computed energies display a nonanalytic behavior. Of course, in more general situations, the UHF solution may dissociate to a wrong limit [cf., e.g. Refs. (*4,10*)]. not to mention the multiplicity and often haphazard behavior of various broken-spin-symmetry solutions, spin contamination, etc (*4*). Thus, this approach is usually reserved for computation of dissociation energies rather than for the generation of accurate PESs.

The effect of higher than pair clusters (primarily of triples) is often estimated perturbatively. This is particularly efficient as long as the state considered remains nondegenerate, as is the case for nearly equilibrium geometries. In such cases, the often-employed CCSD(T) method (*11*) yields invariably excellent results (*3,12*). Unfortunately, with the increasing quasidegeneracy, the perturbative treatment of triples breaks down, even in cases

Downloaded by NORTH CAROLINA STATE UNIV on September 14, 2012 | http://pubs.acs.org
Publication Date: August 14, 2002 | doi: 10.1021/bk-2002-0828.ch002

where the standard SR CCSD works well and the CCSD PEC does not show any "hump" [cf., e.g. the case of the HF molecule (*4*)].

Turning our attention to various SS type CCSD approaches, we first mention those based on the SR CCSDTQ method (*13*), in which the T and Q manifolds are severely truncated, yet the full CCSDTQ equations are employed (*14*). The most suitable truncation, leading to the so-called CCSDtq method (*15*), relies on the same choice of the T and Q cluster amplitudes as our RMR CCSD method (see below). These methods do provide a substantial improvement over the standard CCSD yet, in spite of the truncation, become computationally demanding with the increase of the AO basis set, not unlike CCSDTQ itself.

While all the above listed methods rely solely on the CC formalism (and, in some cases, on finite order MBPT), the so-called *externally corrected* (ec) CCSD methods (*4,16,17*) try to simultaneously exploit the information from some independent source, which is capable of handling the nondynamic correlation, is readily available, and requires only modest computational effort. The essence of these ecCCSD methods stems from the fact that the CC energy, at whatever level of truncation, is fully determined by the one- and two-body clusters via the asymmetric energy formula

$$E_{CC} = \langle \Phi_0 | H | \Psi_{CC} \rangle = \langle \Phi_0 | H (1 + T_1 + T_2 + T_1^2/2) | \Phi_0 \rangle. \qquad (1)$$

This implies that one way to improve this energy is to improve the accuracy of the one- and two-body cluster amplitudes. We thus also refer to these approaches as the *amplitude-correcting* methods.

In ecCCSD methods this improvement is achieved by extracting a subset of important three- and four-body cluster amplitudes from the external source wave function and by using them for a physically more meaningful decoupling of the CC chain of equations at the pair cluster level. In practice this means that the external source wave function is first cluster analyzed, and the resulting approximate three- and four-body clusters $T_3^{(0)}$ and $T_4^{(0)}$, respectively, are then used to evaluate the corresponding terms $\Lambda^{(1)}(3)$, $\Lambda^{(2)}(3)$, $\Lambda^{(2)}(4)$, and $\Lambda^{(2)}(1,3)$ in eqs. (2.76) of Ref. (*4*). Finally, the corrected CCSD equations are solved just as in the standard CCSD method (*4,16-19*).

Various wave functions have been employed as the external source, in particular the UHF (*20,21*), VB (*18*), CASSCF or CASCI (*5,19*) wave functions, but the most effective and practical turned out to be a modest size MR CISD

Downloaded by NORTH CAROLINA STATE UNIV on September 14, 2012 | http://pubs.acs.org
Publication Date: August 14, 2002 | doi: 10.1021/bk-2002-0828.ch002

(*5,22-25*), which employs a small reference or model space $\mathcal{M}_0$. This method is referred to as the *reduced multireference* (RMR) CCSD and yields excellent results (*26-30*).

In addition to these amplitude-correcting approaches, it is also possible to formulate the *energy-correcting* methods, which directly compute the energy corrections to various CC energies. This is in fact the case of the CCSD(T) method, which uses a perturbative estimate of triples and calculates the corresponding energy correction (*11*). The above mentioned breakdown of CCSD(T), as one moves away from the equilibrium geometry, has been largely avoided by the design of the so-called *renormalized* versions, referred to as RCCSD(T) and RCCSD(TQ) methods (*31*). These arose as a special case of the recently developed *method of moments* (MM) CC approach by Piecuch and Kowalski (*32*), who also extended it to the equation of motion (EOM) CC and state universal MR CC (*33*). Indeed, the results obtained so far are most encouraging (*31-33*).

We have recently pursued this idea and developed several energy-correcting approximations by relying on the simple asymmetric energy formula (*9,34*). Here we relied again on the low-dimensional MR CISD wave function and, in lieu of projecting onto the SR configuration $|\Phi_0\rangle$, as in the standard CC or RMR CCSD methods, we project onto the zero-order or full MR CISD wave function. This approach can be interpreted either as the MR-CISD-based energy correction to CCSD or RMR CCSD or, conversely, as CCSD- or RMR-CCSD-based correction to MR CISD. The test applications carried out so far are very encouraging (*9,34*).

Let us finally mention two additional SS-type CC approaches that strive for the same goal. First, we mention the *valence optimized orbital* (VOO) CCSD method (*35*) and the variational VCCD method of Van Voorhis and Head-Gordon (*8*). Particularly the latter approach, based on the energy expectation value with the CCD cluster Ansatz, represents the upper bound to (full) FCI or FCC, and thus avoids the fallacious asymptotic behavior of standard CCSD PECs [see, e.g. the case of N_2 (*8,9*)]. Yet, the variational requirement tends to raise the energy [cf. also Ref. (*36*)] and produces a rather significant overestimate in the $R \rightarrow \infty$ limit [e.g., about 45 mhartree for the VDZ model of N_2, cf. Ref. (*8*)], not to mention the complexity of the resulting formalism which depends factorialy on the electron number.

The SS methods, which most closely follow the MR formalism, have been recently pursued by Mukherjee and collaborators (*37*), by Hubač and collaborators (*38*), and by Meißner and Paldus (*39-41*). This last approach relies

Downloaded by NORTH CAROLINA STATE UNIV on September 14, 2012 | http://pubs.acs.org
Publication Date: August 14, 2002 | doi: 10.1021/bk-2002-0828.ch002

Downloaded by NORTH CAROLINA STATE UNIV on September 14, 2012 | http://pubs.acs.org
Publication Date: August 14, 2002 | doi: 10.1021/bk-2002-0828.ch002

on the direct iterative solution of the generalized Bloch equations (referred to as the DGB method). All these methods do avoid the intruder state problem and can handle the excited states of the same symmetry as the reference. Mukherjee's SS version (*37*) of the state universal MR CCSD, in its so-called relaxed and nonrelaxed versions, is conceptually reminiscent of the perturb-first diagonalize-later and diagonalize-first perturb-later MBPT, respectively. For the lowest state, though, this MR CC method (*37*) (at least in its nonrelaxed version) does not perform as well as the RMR CCSD (*22*) or DGB (*40*) methods. Finally, the approach of Hubač *et al.* is based on the Brillouin-Wigner-type MBPT and must take special precautions to achieve size extensivity.

It is hoped that the above listed approaches will eventually provide a rich "toolbox" enabling a proper, yet affordable account of both dynamic and nondynamic correlations, and will enable a routine generation of reliable PESs for the purposes of molecular dynamics and spectroscopy. In this paper we wish to compare the performance of amplitude- and energy-correcting methods, using the exactly solvable DZ model of the HF and N_2 molecules. In addition, we formulate and test the new perturbative-type corrections to MR CISD. We show that both the amplitude- and energy-corrected schemes can provide very good results even in the difficult case of the triple bond breaking.

II. Amplitude-Correcting Methods

We focus here on the RMR CCSD version of ecCCSD, for which numerous applications have been carried out (*22-30*), and leave the comparison with the energy corrected approaches for Sects. III and IV. In order to illustrate the capabilities of RMR CCSD, we only summarize our recent work (*29,30*), which compares the calculated and experimentally directly observed spectroscopic data for the HF and N_2 molecules. In this work we used a low-dimensional (dim $\mathcal{M}_0 =$ 4 or 8; further referred to as 4R and 8R reference spaces) RMR CCSD to generate PECs, which were subsequently used to compute the corresponding rovibrational levels with the LEVEL codes of LeRoy (*42*) and, finally, the frequencies of relevant spectral lines. For the sake of brevity, we focus here on the vibrational levels, since the rotational sublevels depend strongly on the average bondlength and are easier to match. For example, for the experimentally observed frequencies in the fundamental rotational Raman band of N_2 (for J values ranging from 0 to 18) we obtained an excellent agreement with deviations not exceeding 0.6 cm^{-1} using either CCSD or 8R-RMR CCSD (*29*).

For the cc-pVQZ model of HF, the average error for the first 20 vibrational levels amounts to 113.8 cm^{-1} when computed with the 4R-RMR CCSD method,

Downloaded by NORTH CAROLINA STATE UNIV on September 14, 2012 | http://pubs.acs.org
Publication Date: August 14, 2002 | doi: 10.1021/bk-2002-0828.ch002

representing a dramatic improvement over the standard CCSD in which case this average error amounts to 1099 cm^{-1} (*30*). At this point it is important to emphasize the crucial role of the basis set employed. Indeed, one can obtain accidentally a good agreement with the experiment due to the error cancellation. This is illustrated in Table I for the vibrational levels of HF obtained with the standard CCSD and 4R-RMR CCSD methods with cc-pVXZ basis sets, ranging from X=D to X=Q. We only present the average deviations from the experimental values in this table for different ranges of the vibrational quantum number v. We see that the cc-pVDZ CCSD results seem to yield very good result with the average deviation for the first 17 levels (from v=0 to v=16) of 145 cm^{-1}. However, this rather good agreement deteriorates when we employ larger and larger basis sets (to an almost 800 cm^{-1} for cc-pVQZ basis). On the other hand, we observe a systematic improvement, particularly for the high lying levels, when we employ 4R-RMR CCSD method. Indeed, the average error for the first 17 levels decreases from 727, to 141, to 81 cm^{-1} as we proceed from the DZ, to TZ, to QZ basis, respectively.

Table I. Mean absolute deviations of computed from experimentally observed vibrational frequencies for levels from v_1 to v_2, Ave(v_1-v_2), for the HF molecule obtained with CCSD and 4R-RMR CCSD methods and cc-pVXZ (X=D,T,Q) basis sets.

Ave(v_1-v_2)	SR CCSD			4R RMR CCSD		
	X=D	X=T	X=Q	X=D	X=T	X=Q
Ave(0-4)	52.8	191.0	168.0	19.7	78.6	53.8
Ave(5-9)	84.3	608.6	582.4	267.8	160.1	118.9
Ave(10-14)	162.7	1104.2	1191.5	1190.1	90.4	81.1
Ave(0-16)	145.4	748.8	793.5	727.0	141.4	81.3

Turning our attention to the demanding triply bonded case of N_2, we find again a dramatic improvement in the agreement between the experimentally determined and computed vibrational term values as we proceed from standard CCSD to 4R-RMR, and to 8R-RMR CCSD, as illustrated for a few levels (for v=0, 5, 10, 15, 20 and 25) in Table II [actually, the highest experimentally observed level corresponds to v=15 and the values up to v=25 were obtained via the RKR procedure (*43*)]. For example, for the highest available v=25 level, the discrepancies from the experimental value decrease from 2872, to 357, to 93 cm^{-1} as we go from CCSD, to 4R-RMR, to 8R-RMR CCSD (*29*) (see Table II).

Table II. Vibrational term values G(v) for selected levels v of the N_2 molecule, and the deviations from the experimental values, G(v)-G$^{(exp)}$(v), as obtained with the CCSD, 4R- and 8R-RMR CCSD methods and the cc-pVTZ basis set. All values are in cm^{-1}.

v	*G(v)*	*G(v)-G$^{(exp)}$(v)*		
	Exp.	CCSD	4R-RMR	8R-RMR
0	1175.80	33.80	3.40	2.90
5	12538.30	412.60	45.30	39.00
10	23180.20	871.20	100.80	73.20
15	33094.40	1422.70	169.90	93.40
20	42270.80	2083.60	254.70	99.40
25	50696.00	2872.00	356.60	92.90

Table III. Average deviations of calculated from experimental frequencies in the vibrationally excited Raman bands of the N_2 molecule, as obtained with the CCSD, 4R- and 8R-RMR CCSD methods and cc-pVTZ basis set. The last column gives the range of experimentally available rotational J values, J_{min}–J_{max}, and the difference between the maximum and minimum deviations for this range of rotational sublevels is enclosed in parentheses.

	CCSD	4R-RMR	8R-RMR	J_{min}–J_{max}
$\langle \Delta Q_1 \rangle$	72.82 (0.31)	7.91 (0.10)	7.15 (0.08)	0–14
$\langle \Delta Q_2 \rangle$	75.89 (0.63)	8.44 (0.18)	7.37 (0.14)	0–20
$\langle \Delta Q_3 \rangle$	78.92 (0.64)	9.06 (0.18)	7.54 (0.13)	0–20
$\langle \Delta Q_4 \rangle$	81.98 (0.55)	9.55 (0.16)	7.54 (0.11)	0–18
$\langle \Delta Q_5 \rangle$	85.18 (0.49)	10.15 (0.12)	7.54 (0.07)	2–17
$\langle \Delta Q_6 \rangle$	93.21 (0.86)	11.23 (0.20)	7.71 (0.09)	2–22
$\langle \Delta Q_7 \rangle$	91.78 (0.20)	11.07 (0.05)	6.90 (0.02)	6–12

Even more direct comparison is shown in Table III where we present the average deviations from the experimentally measured frequencies in several vibrationally excited Raman bands as obtained with CCSD, 4R- and 8R-RMR CCSD (*29*) (the range of J values is shown in the last row). These deviations systematically increase with the increasing J value and the difference between

Downloaded by NORTH CAROLINA STATE UNIV on September 14, 2012 | http://pubs.acs.org
Publication Date: August 14, 2002 | doi: 10.1021/bk-2002-0828.ch002

the maximum and minimum deviations for the given range of rotational quantum numbers J is given in parentheses. We see that for the standard CCSD, the discrepancies range from about 72 cm^{-1} to 92 cm^{-1}. A significant improvement is found with 4R-RMR CCSD when both the magnitude and the range of these deviations are lowered to 8 and 11 cm^{-1}. With the 8R-RMR CCSD, we get an almost constant shift of about 7.5 cm^{-1} for all the vibrational bands, so that the corresponding spectrum is practically identical with the experimental one except for a small and almost constant shift.

III. Energy-Correcting Methods

We now proceed to the other option of improving on standard CCSD via various energy corrections and focus on the very recently proposed schemes that are based on the asymmetric energy formula of CC theory (*9,34*). We first very briefly present the basic formalism and refer the reader to the original papers for detail (*34*) [see also Refs. (*31-33*)] . At the same time we also present yet another perturbative energy correction, this time for MR CISD. We then compare the performance of these corrections using the same DZ models of HF and N_2 as in Refs. (*9,34*).

Theory

Let $|\chi\rangle$ designate a normalized CI-type wave function associated with some subspace $\mathcal{M}$ = Span$\{|\Phi_i\rangle\}$ of the relevant N-electron space V (say, the SD subspace relative to $|\Phi_0\rangle$ or relative to some model space $\mathcal{M}_0$),

$$|\chi\rangle = \textstyle\sum_i c_i |\Phi_i\rangle, \qquad \langle\chi|\chi\rangle = 1, \tag{2}$$

and $|\Psi\rangle$ an intermediately normalized CC-type wave function given by a SR CC Ansatz relative to the reference configuration $|\Phi_0\rangle$,

$$|\Psi\rangle = e^T |\Phi_0\rangle\,, \qquad \langle\Phi_0|\Psi\rangle = \langle\Phi_0| e^T |\Phi_0\rangle = 1. \tag{3}$$

In principle, T is arbitrary, even though we shall only consider CCSD and RMR CCSD Ansätze. We further assume that both CI and CC wave functions have been obtained in a standard way, i.e., by diagonalizing the Hamiltonian H within the space $\mathcal{M}$ and by solving the appropriate CC equations, respectively, and we associate with them the corresponding energies

Downloaded by NORTH CAROLINA STATE UNIV on September 14, 2012 | http://pubs.acs.org
Publication Date: August 14, 2002 | doi: 10.1021/bk-2002-0828.ch002

$$E_{\mathrm{CI}} = \langle\chi|H|\chi\rangle / \langle\chi|\chi\rangle = \langle\chi|H|\chi\rangle\,, \tag{4}$$

$$E_{\mathrm{CC}} = \langle\Phi_0|H|\Psi\rangle/\langle\Phi_0|\Psi\rangle = \langle\Phi_0|He^{T}|\Phi_0\rangle = E_0 + \langle\Phi_0|H(T_1+T_2+T_1^{2}/2)|\Phi_0\rangle, \tag{5}$$

where $E_0 = \langle\Phi_0|H|\Phi_0\rangle$. Note that in the standard CC theory, the energy depends only on one- and two-body clusters T_1 and T_2, respectively.

We next consider the energy quantity $\mathcal{E}$, given by the asymmetric energy formula

$$\mathcal{E} \equiv \mathcal{E}(\chi,\Psi) = \langle\chi|H|\Psi\rangle / \langle\chi|\Psi\rangle\,, \tag{6}$$

which combines the CI and CC energy formulas: E_{CI} results when we set $|\Psi\rangle = |\chi\rangle$ and E_{CC} is obtained when $\langle\chi| = \langle\Phi_0|$. An interesting fact is that with a properly chosen CI wave function in lieu of $\langle\Phi_0|$, we can obtain a much better result than the standard CC energy, eq 5.

It is not difficult to see that the energy $\mathcal{E}$ can be expressed either as the CI energy E_{CI} plus a correction or as the CC energy E_{CC} plus a correction (*34*). To see the former claim, we note that the action of the Hamiltonian H on the CI wave function gives

$$H|\chi\rangle = E_{\mathrm{CI}}|\chi\rangle + \textstyle\sum_{i\in\mathcal{M}^{\perp}} |\Phi_i\rangle\langle\Phi_i|H|\chi\rangle\,, \tag{7}$$

where the sum extends over all configurations spanning the orthogonal complement $\mathcal{M}^{\perp}$ of $\mathcal{M}$ in V. In order that the matrix element $\langle\Phi_i|H|\chi\rangle$ does not vanish, the configuration $|\Phi_i\rangle$ must belong to the interacting space of $\mathcal{M}$, which we shall designate by $\mathcal{M}^{\mathrm{IS}}$. We can thus replace the sum over $i \in \mathcal{M}^{\perp}$ in eq 7 by $i\in \mathcal{M}^{\mathrm{IS}}$. Using now the hermitian conjugate of eq 7 in eq 6 with $|\Psi\rangle$ given by eq 3, we obtain

$$\mathcal{E} = E_{\mathrm{CI}} + \textstyle\sum_{i\in\mathcal{M}^{\mathrm{IS}}} \langle\chi|H|\Phi_i\rangle\langle\Phi_i|e^{T}|\Phi_0\rangle / \langle\chi|e^{T}|\Phi_0\rangle, \tag{8}$$

We see that the second term on the right hand side of eq 8 describes the interaction between the CI wave function $|\chi\rangle$ and its interacting space, and thus can be expected to improve the CI energy by supplying the missing dynamic correlation part.

We can also interpret the correction to E_{CI}, eq 8, as the second-order perturbation theory (PT) contribution. For this purpose we consider the space $\mathcal{W}$

Downloaded by NORTH CAROLINA STATE UNIV on September 14, 2012 | http://pubs.acs.org
Publication Date: August 14, 2002 | doi: 10.1021/bk-2002-0828.ch002

$= \mathcal{M} \oplus \mathcal{M}^{\mathrm{IS}}$ and regard $|\chi\rangle$ as a zero-order wave function with the unperturbed Hamiltonian $H_0 = PHP$, where P designates the projection operator onto $\mathcal{M}$. The perturbation W is then given by $W = PHQ + QHP + QHQ$, where $Q = I - P = P^{\perp}$ is the projector onto $\mathcal{M}^{\mathrm{IS}}$ and I is the identity on $\mathcal{W}$. The first order wave function $|\chi^{(1)}\rangle$ then takes the general form

$$|\chi^{(1)}\rangle = |\chi\rangle + \Sigma_{i\in\mathcal{M}^{\mathrm{IS}}}\, c_i^{(1)}\, |\Phi_i\rangle, \qquad \langle\chi|\chi^{(1)}\rangle = 1. \tag{9}$$

The corresponding zero-order energy $E(0)$ is given by $E_{\mathrm{CI}} = \langle\chi|H_0|\chi\rangle = \langle\chi|H|\chi\rangle$, the first-order energy $E(1) = \langle\chi|W|\chi\rangle$ vanishes, and the second-order energy $E(2)$ is

$$E(2) = \langle\chi|W|\chi^{(1)}\rangle = \Sigma_{i\in\mathcal{M}^{\mathrm{IS}}}\, \langle\chi|W|\Phi_i\rangle\, c_i^{(1)} = \Sigma_{i\in\mathcal{M}^{\mathrm{IS}}}\, \langle\chi|H|\Phi_i\rangle\, c_i^{(1)}. \tag{10}$$

If we now employ the CC wave function $|\Psi\rangle$, eq 3 — renormalized as $|\Xi\rangle = |\Psi\rangle/\langle\chi|\Psi\rangle$, so that $\langle\chi|\Xi\rangle = 1$ — to estimate $c_i^{(1)}$, we find easily that [cf. also Ref.(*34*)]

$$c_i^{(1)} = \langle\Phi_i|\Psi\rangle \,/\, \langle\chi|\Psi\rangle = \langle\Phi_i|\, e^T |\Phi_0\rangle \,/ \langle\chi|\, e^T |\Phi_0\rangle\,. \tag{11}$$

Substituting this result into eq 10, we recover the correction of eq 8.

In addition to our earlier work (*9,34*), we wish to point out that we can also calculate the first-order coefficients $c_i^{(1)}$ by relying entirely on perturbation theory. Of course, the result will very much depend on the way we partition the Hamiltonian H into the unperturbed part H_0 and the perturbation W, $H = H_0 + W$. Since our zero-order wave function $|\chi\rangle$ is assumed to represent a general multi-configurational CI wave function, it is easier to employ the Epstein-Nesbet (EN) type perturbation theory. For this purpose we choose the unperturbed Hamiltonian H_0 as follow

$$H_0 = E_{\mathrm{CI}}\, |\chi\rangle\langle\chi| + \Sigma_{i\in\mathcal{M}^{\perp}}\, H_{ii}\, |\Phi_i\rangle\langle\Phi_i|, \tag{12}$$

where H_{ii} is the diagonal CI matrix element $\langle\Phi_i|H|\Phi_i\rangle$, implying the perturbation $W = H - H_0$. This partitioning is somewhat reminiscent of that used by Gershgorn and Shavitt in their B_k-approximation (*44*).

We now easily see that

$$H_0|\chi\rangle = E_{\mathrm{CI}}\,|\chi\rangle \qquad \text{and} \qquad H_0|\Phi_i\rangle = H_{ii}\,|\Phi_i\rangle, \tag{13}$$

Downloaded by NORTH CAROLINA STATE UNIV on September 14, 2012 | http://pubs.acs.org
Publication Date: August 14, 2002 | doi: 10.1021/bk-2002-0828.ch002

Downloaded by NORTH CAROLINA STATE UNIV on September 14, 2012 | http://pubs.acs.org
Publication Date: August 14, 2002 | doi: 10.1021/bk-2002-0828.ch002

so that $c_i^{(1)}$, as given by the standard PT, is

$$c_i^{(1)} = \langle \Phi_i | W | \chi \rangle / (E_{\mathrm{CI}} - H_{ii}) = \langle \Phi_i | H | \chi \rangle / (E_{\mathrm{CI}} - H_{ii}). \tag{14}$$

The second-order PT energy is then

$$E(\mathrm{EN},2) = \sum_{i \in \mathcal{M}_{\mathrm{IS}}} |\langle \chi | H | \Phi_i \rangle|^2 / (E_{\mathrm{CI}} - H_{ii}). \tag{15}$$

In the following, we shall compare the energies given by eq 10 and eq 15.

Returning now to our interpretation of the asymmetric energy expression eq 6, we can also write $\mathcal{E}$ as the standard CC energy plus a correction. Considering, without any loss of generality, the CCSD or RMR CCSD Ansatz, we find that in both cases we have

$$\mathcal{E} = E_{\mathrm{CC}} + \langle \chi | e^T | \Phi_0 \rangle^{-1} \sum_{k > (2)} \langle \chi | e^T | \Phi_k \rangle \langle \Phi_k | e^{-T} H e^T | \Phi_0 \rangle, \tag{16}$$

where $k > (2)$ implies that the sum extends over higher than doubly excited configurations. The detailed derivation, as well as an explicit form of eq 16, is given elsewhere (*34*) [cf. also (*31,32*)]. Here we only point out that the excitation order of configurations in the CC wave function $e^T|\Phi_k\rangle$ is either identical or higher than the excitation order of $|\Phi_k\rangle$. This implies that unless the CI wave function $|\chi\rangle$ contains higher than doubly excited configurations, the energy $\mathcal{E}$ is identical to the standard CCSD or RMR CCSD energy. Thus, if we write

$$|\chi\rangle = |\chi(0)\rangle + |\chi(\mathrm{S})\rangle + |\chi(\mathrm{D})\rangle + \sum_i{}' c_i |\Phi_i\rangle, \tag{17}$$

where the first three terms on the right hand side represents the zero-, singly-, and doubly-excited components of $|\chi\rangle$ relative to $|\Phi_0\rangle$, while the primed sum in the last term involves all higher than doubly-excited configurations that are contained in $|\chi\rangle$, eq 16 becomes

$$\mathcal{E} = E_{\mathrm{CC}} + \langle \chi | e^T | \Phi_0 \rangle^{-1} \sum_i{}' c_i^* \sum_{k>(2)} \langle \Phi_i | e^T | \Phi_k \rangle \langle \Phi_k | e^{-T} H e^T | \Phi_0 \rangle. \tag{18}$$

Note that $|\Phi_k\rangle$ is basically fixed by $|\Phi_i\rangle$ (all particle-hole labels of $|\Phi_k\rangle$ must be identical to some of the particle-hole labels of $|\Phi_i\rangle$). Hence, the summation in eq 18 extends only over higher than doubly excited configurations in $|\chi\rangle$. Depending on the choice of $|\chi\rangle$, the number of higher than doubles in $|\chi\rangle$ can be rather small.

Although the energy $\mathcal{E}$, as given by eq 6, may be interpreted as the corrected CI or CC energy, eq 8 or eq 18, respectively, the summations in these expressions extend over two very different domains: In eq 8 the sum extends over the interacting space of $\mathcal{M}$, while in eq 18 it extends over a subspace of $\mathcal{M}$ which contains higher than doubly-excited configurations. The size of the interacting space of $\mathcal{M}$ scales, generally, as the size of the space $\mathcal{M}$ itself, times the factor n^4 (n being the size of basis set). For example, when $|\chi\rangle$ represents a single Hartree-Fock configuration, its interacting space contains all singles and doubles. When $|\chi\rangle$ is an SR CISD wave function, its interacting space contains all triples and quadruples. Thus, when calculating the energy $\mathcal{E}$ as a correction to the CC energy, eq 18, we in fact account for the effect of the interacting space $\mathcal{M}^{\text{IS}}$ of $\mathcal{M}$, which explicitly appears in eq 8, by considering only those configurations that are within the space $\mathcal{M}$ itself.

Obviously, when $|\Psi\rangle$ is the exact FCC or $|\chi\rangle$ the exact FCI wave function, the energy $\mathcal{E}$ is exact. Of course, in practice, both $|\Psi\rangle$ and $|\chi\rangle$ will be approximate. In particular, we restrict $|\Psi\rangle$ to the CCSD or RMR CCSD case. Then the quality of the energy $\mathcal{E}$ depends primarily on the choice of the CI wave function $|\chi\rangle$. For practical reasons, we must try to keep the number of higher than double excitations in $|\chi\rangle$ as small as possible. This suggests that we choose a multireference-type CI wave function for $|\chi\rangle$. In this way we can also account for the nondynamic correlation. In the following, we thus focus our attention on MR CISD wave functions as $|\chi\rangle$. These can be either the zero-order wave functions obtained by diagonalizing the Hamiltonian within the M-configurational reference space $\mathcal{M}_0$, or the MR CISD wave functions using $\mathcal{M}_0$ as the model space.

When $|\chi\rangle$ is an MR-CI-type wave function, the energy expression given by eq 8 has a very simple interpretation. We know that the MR-CI-type wave function can efficiently describe the nondynamic correlation while the CC Ansatz, even at the CCSD level, can very effectively account for the dynamic correlation. Thus, by combining an MR CI and CC Ansätze, we should be able to account for both the dynamic and nondynamic correlations. The energy $\mathcal{E}$, as given by eq 8, precisely reflects this fact, with E_{CI} accounting for the nondynamic correlation and the second term on the right hand side, which involves the CC Ansatz, for the dynamic one.

As already mentioned above, there are several ways in which to exploit the energy expression for $\mathcal{E}$. For example, we can use either the CCSD or RMR CCSD Ansatz, while the CI wave function $|\chi\rangle$ may be of the SR or MR type. In the latter case, it can be either a simple M-configurational CI wave function, or

Downloaded by NORTH CAROLINA STATE UNIV on September 14, 2012 | http://pubs.acs.org
Publication Date: August 14, 2002 | doi: 10.1021/bk-2002-0828.ch002

an MR CISD wave function based on the M-reference space $\mathcal{M}_0$. It is beyond the scope of this article to explore all these possibilities and to assess their performance.

We thus focus here on the case of the CCSD Ansatz for $|\Psi\rangle$ and the MR CISD wave function for $|\chi\rangle$. The reference space $\mathcal{M}_0$= Span$\{|\Phi_i\rangle\}$ is referred to as the zero-order space, and all singles and doubles from $\mathcal{M}_0$ span the first-order interacting space $\mathcal{M}^{IS}$. Hence, when $|\chi\rangle$ is an MR CISD wave function, the summations in eq 8 or eq 18 extend over all configurations in the second-order interacting space of $\mathcal{M}_0$. We will then compare two distinct ways that take into account the second-order interacting space, namely we will compare the energy $\mathcal{E}$, eq 8 or eq 18, which exploits the CCSD Ansatz, with the energy calculated by using eq 15 that is based on the EN PT and the MR CISD wave function $|\chi\rangle$.

We shall employ the following acronyms to designate the methods used: When the reference space $\mathcal{M}_0$ involves M configurations, dim$\{\mathcal{M}_0\}$= M, we designate it by MR (e.g. 2R, 4R, 8R, etc.). When $|\Psi\rangle$ is a CCSD and $|\chi\rangle$ is an MR-CISD wave function, the approach is designated by CCSD-[MR]. When $|\chi\rangle$ is an MR CISD wave function and eq 15 is employed to calculate the second-order EN PT energy, the corresponding total energy is referred to by the acronym MR-CISD+EN(2).

Illustrative Examples

We first consider the standard double-zeta (DZ) model of the HF molecule. Relying on the minimal 2-electron/2-active-orbital space, we employ both the 2R space spanned by $|\Phi_0\rangle = |\sigma\alpha\sigma\beta\rangle$ and $|\Phi_1\rangle = |\sigma^*\alpha\sigma^*\beta\rangle$, and the 4R space spanned by $|\Phi_0\rangle$, $|\Phi_1\rangle$, $|\Phi_2\rangle = |\sigma\alpha\sigma^*\beta\rangle$, and $|\Phi_3\rangle = |\sigma^*\alpha\sigma\beta\rangle$. In Table IV, we list the FCI energies for the five geometries (namely for R=R_e=1.733 bohr, 1.5R_e, 2R_e, 2.5R_e, and 3R_e), and the energy differences relative to the FCI as obtained with the CCSD, 2R-CISD, 2R-CISD+EN(2), CCSD-[2R], and with 4R-CISD, 4R-CISD+EN(2), and CCSD-[4R] methods.

The CCSD error increases from 1.6 millihartree (mhartree) at R_e to 11.6 mhartree at 3R_e, an increase of about 10 mhartree. The 2R-CISD error increases by about the same amount. The 4R-CISD method performs better, and its errors are within the 5.7—7.5 mhartree range. With the second-order EN perturbation corrections to a small MR CISD wave function, we also get good results. For 2R-CISD+EN(2), the deviations are less than 1 mhartree, and for 4R-

Downloaded by NORTH CAROLINA STATE UNIV on September 14, 2012 | http://pubs.acs.org
Publication Date: August 14, 2002 | doi: 10.1021/bk-2002-0828.ch002

Downloaded by NORTH CAROLINA STATE UNIV on September 14, 2012 | http://pubs.acs.org
Publication Date: August 14, 2002 | doi: 10.1021/bk-2002-0828.ch002

CISD+EN(2), the errors range from 0.75 to 1.2 mhartree. In both cases, the *M*R-CISD+EN(2) energy overestimates the FCI energy, as is usual for the EN PT.

When we calculate the CCSD energy by projecting onto the 2R-CISD or 4R-CISD wave function, the resulting CCSD-[2R] and CCSD-[4R] energies differ very little one from the other and their deviations from the FCI are about 1.3—3.1 mhartree. As we have pointed out above, the CCSD-[*M*R] energy can also be viewed as the MR CISD energy corrected by exploiting the CCSD Ansatz and relying on the second-order interacting space, eq 8. Thus, it is not surprising that both the CCSD-[*M*R] and *M*R-CISD+EN(2) energies behave in a similar way.

Table IV. The total FCI energies (in hartree) and the energy differences relative to FCI, E–E(FCI) (in mhartree), for the DZ model of the HF molecule, as obtained with various methods (see the text for the definition of acronyms). All electrons were correlated. R_e = 1.733 bohr.

Method	R_e	$1.5R_e$	$2R_e$	$2.5R_e$	$3R_e$
Total energy E [reported as –(E+99)]					
FCI	1.160307	1.092501	1.021711	0.992698	0.985279
Relative energy E–E (FCI)					
CCSD	1.633	3.046	6.049	9.701	11.597
2R-CISD	5.775	6.694	7.954	11.666	15.026
2R-CISD+EN(2)	–0.814	–0.758	–0.816	–0.597	–0.569
CCSD-[2R]	1.450	1.717	2.023	2.646	3.091
4R-CISD	5.673	6.601	6.859	7.239	7.494
4R-CISD+EN(2)	–0.742	–0.751	–1.078	–1.213	–1.237
CCSD-[4R]	1.316	1.672	2.282	2.820	3.037

As the second example, we consider the N_2 molecule. In all CI and CC calculations, we keep the 1*s* core orbitals frozen and eliminate the corresponding top two virtual orbitals. The results are collected in Table V. As is well known, this example is qualitatively different from the preceding one, since in contrast to HF, the N_2 CCSD PEC has a "hump" between $1.6R_e$ and $2R_e$ (R_e = 2.068 bohr), (cf. Table V).

Considering the direct product of three 2-electron/2-orbital spaces corresponding to the orbital pairs (σ, σ^*), (π_x, π_x^*), and (π_y, π_y^*), we obtain eight configurations: $|\Phi_0\rangle = |\sigma^2\, \pi_x^2\, \pi_y^2\rangle$, $|\Phi_1\rangle = |\sigma^2\, \pi_y^2\, \pi_x^{*2}\rangle$, $|\Phi_2\rangle = |\sigma^2\, \pi_x^2\, \pi_y^{*2}\rangle$, $|\Phi_3\rangle =$

Downloaded by NORTH CAROLINA STATE UNIV on September 14, 2012 | http://pubs.acs.org
Publication Date: August 14, 2002 | doi: 10.1021/bk-2002-0828.ch002

Table V. The total FCI energies (in hartree) and the energy differences relative to FCI, E–E(FCI) (in mhartree), for the DZ model of the N_2 molecule, as obtained with various CI and CC methods (see the text for the definition of acronyms). All electrons except 1*s* were correlated and R_e = 2.068 bohr. The last row is a shifted CCSD-[8R] potential.

Method	R_e	$1.25R_e$	$1.5R_e$	$1.75R_e$	$2R_e$	$2.5R_e$	$3R_e$
Total energy E [reported as −(E+108)]							
FCI	1.10512	1.05463	0.95073	0.88991	0.86824	0.86016	0.85890
Relative energy E–E (FCI)							
CCSD	8.29	19.06	33.55	17.71	−69.92	−142.18	−155.91
SR-CISD	26.64	49.20	90.11	147.55	210.90	304.96	357.38
SR-CISDT	18.17	39.02	74.30	125.42	181.99	267.60	317.27
SR-CISDTQ	1.38	5.12	13.94	26.93	39.36	55.69	63.50
2R-CISD	23.57	48.21	78.66	115.57	150.20	158.11	161.28
4R-CISD	13.24	19.81	27.52	39.40	55.25	76.55	85.56
8R-CISD	13.17	18.99	21.79	25.91	31.11	36.42	37.66
2R-CISD+EN(2)	−3.65	−3.89	−13.03	−19.98	−26.89	−128.32	−170.39
4R-CISD+EN(2)	−1.07	−0.36	2.22	8.41	15.79	23.24	26.10
8R-CISD+EN(2)	−1.07	−0.29	2.05	5.46	8.35	10.77	11.48
CCSD-[2R]	8.26	18.61	29.88	14.71	−40.48	−72.22	−52.19
CCSD-[4R]	4.99	8.61	13.04	14.35	9.04	13.02	16.82
CCSD-[8R]	4.95	8.17	10.29	10.89	12.19	16.52	17.72
CCSD-[8R] −6.026	−1.07	2.15	4.27	4.87	6.17	10.49	11.69

$|\sigma^2 \pi_x^{*2} \pi_y^{*2}\rangle$, $|\Phi_4\rangle = |\pi_x^2 \pi_y^2 \sigma^{*2}\rangle$, $|\Phi_5\rangle = |\pi_y^2 \pi_x^{*2} \sigma^{*2}\rangle$, $|\Phi_6\rangle = |\pi_x^2 \pi_y^{*2} \sigma^{*2}\rangle$, and $|\Phi_7\rangle = |\pi_x^{*2} \pi_y^{*2} \sigma^{*2}\rangle$. The 2R space spanned by $|\Phi_0\rangle$ and $|\Phi_4\rangle$ describes the breaking of the σ bond. The 4R space, Span$\{|\Phi_i\rangle$: i=0,1,2,3$\}$, describes the breaking of two π bonds. Finally, the 8R space that is spanned by all eight determinants $|\Phi_i\rangle$, i = 0–7, represents the minimal model space for the breaking of a triple bond.

While the standard CCSD PEC has a "hump" and grossly underestimates the FCI energy in the $R \rightarrow \infty$ limit, both SR and MR CISD PECs always overestimates the FCI energy in view of their variational character. The quality of the CI PECs can be improved by relying on either SR CI, i.e., by considering SR CISD, SR CISDT, and SR CISDTQ, or via MR CI by considering 2R CISD, 4R CISD, and 8R CISD. The results given in Table V clearly show that the latter approach is much more effective. Moreover, the computational cost for the former sequence of methods scales as n^6, n^8, and n^{10}, while for the latter sequence the cost scales as $2n^6$, $4n^6$, and $8n^6$. Thus, the MR CISD methods yield not only better results, but are also computationally more efficient. In fact, the simple 8R CISD method is clearly preferable to SR CISDTQ, thus supporting the above given reasoning why we should employ the MR-CI-type wave functions for $|\chi\rangle$.

Although the 8R CISD results are reasonably good, they are far from being satisfactory, since the deviations from the FCI increase from 13 mhartree at R_e to 38 mhartree at $3R_e$. However, when we compute the energy $\mathcal{E}$, combining effectively CCSD with 8R CISD, or even 4R CISD, we get much improved results: The CCSD-[8R] errors are within 5—18 mhartree, and the CCSD-[4R] ones are within 5—17 mhartree. Yet, using the smallest 2R CISD, the CCSD-[2R] PEC still shows a hump.

It is interesting to compare the MR-CISD+EN(2) results with the CCSD-[MR] ones for M= 2, 4, and 8. Qualitatively, they are very similar. In both cases the smallest 2R space is not large enough to eliminate the CCSD hump, even though CCSD-[2R] yields a better result than 2R-CISD+EN(2). With 4R and 8R spaces, the MR-CISD+EN(2) absolute errors are smaller for $R \in [R_e, 1.5R_e]$ than CCSD-[MR] ones, but for $R > 1.5R_e$, the 4R-CISD+EN(2) error increases much faster than the corresponding CCSD-[4R] error. Indeed, over the interval $R_e \leq R \leq 3R_e$, the former one increases by 27 mhartree while the latter one by only 12 mhartree. With the 8R space, the 8R-CISD+EN(2) and CCSD-[8R] PECs are almost identical. In particular, when we shift the CCSD-[8R] PEC by −6.026 mhartree, so that the 8R-CISD+EN(2) and CCSD-[8R] PECs coincide at R_e (see the last row of Table V), the two PECs are separated by no more than 2.5 mhartree over the entire range of internuclear separations.

Downloaded by NORTH CAROLINA STATE UNIV on September 14, 2012 | http://pubs.acs.org
Publication Date: August 14, 2002 | doi: 10.1021/bk-2002-0828.ch002

Summarizing the results for the N_2 molecule, we find that the CCSD-[8R] and 8R-CISD+EN(2) methods represent the best approximations amongst those considered (cf. Table V). Both represent a significant improvement over CCSD and even over 8R CISD, showing much smaller errors and no hump on their PECs.

IV. Conclusions

In our earlier work we have examined various ways of accounting for the nondynamic correlation in the SR-type CC approaches. Our main aim was directed towards the improvement of one- and two-body cluster amplitudes by relying on the ecCCSD approach, particularly on RMR CCSD which exploit the MR CISD wave function of a modest size as the source of higher than pair clusters. The capability of this approach to generate highly accurate spectroscopic data was briefly summarized in Sec. II.

In addition to these amplitude-correcting approaches, we also examine what may be referred to as the energy-correcting approaches, not unlike the recently pioneered renormalized perturbative corrections for triples, and triples and quadruples (*31-33*). In this spirit, we formulated (*9,34*) the energy corrections to the standard CI and CC energies, combining both approaches which complement one another in their ability to account for the dynamic and nondynamic correlations. Our approach is based on the standard asymmetric energy expression, which may be shown to take the form of either the standard CI energy plus a correction or of the standard CC energy plus a correction. In the former case, the correction accounts for the interaction between the CI wave function and the interacting space of the CI manifold, and is assessed by relying on the related CC wave function. In the latter case, the correction arises from higher than doubly excited configurations in the CI wave function.

Although the above outlined idea is generally applicable to any CI and CC wave functions, we focus in this paper on a small reference space MR CISD wave function and the CCSD Ansatz, exploiting their complementarity in handling of correlation effects. The CCSD method accounts very effectively for the dynamic correlation, but is rather limited when handling the nondynamic one. On the other hand, a small reference space MR CISD can describe well the nondynamic correlation, while lacking the flexibility in accounting for the dynamic correlation. Hence, by combining both approaches we can benefit from their strong points, while overcoming their shortcommings. Our results for the HF and N_2 molecules support this claim.

Downloaded by NORTH CAROLINA STATE UNIV on September 14, 2012 | http://pubs.acs.org
Publication Date: August 14, 2002 | doi: 10.1021/bk-2002-0828.ch002

By using the asymmetric energy formula that combines the MR CISD and CCSD wave functions, one effectively exploits the CCSD Ansatz to evaluate the coefficients of configurations that span the MR CISD interacting space while dealing only with the SD excited state manifold. These coefficients can also be assessed by relying on perturbation theory. However, the interacting space of a MR CISD wave function is the second-order interacting space of the reference space. For an M-dimensional reference space, the size of the first-order interacting space scales as $M\ n^4$, while the size of the second-order interacting space scales as $M\ n^8$. Thus, using the CCSD Ansatz to assess the effects of the MR CISD interacting space turns out to be a viable alternative, as we have shown in this study. Currently, we are investigating the possibility of combining the CC methods and MR perturbation theory that employs a small model space as an unperturbed problem. The results will be published elsewhere.

Acknowledgements

The continued support by NSERC (J.P.) is gratefully appreciated.

References

1. McWeeny, R. *Methods of Molecular Quantum Mechanics*; Academic Press: London, 1989.
2. Bauschlicher, C. W. Jr.; Langhoff, S. R.; Taylor, P. R. *Adv. Chem. Phys.* **1990**, 77, 103 and *loc. cit.*
3. Bartlett, R. J. In *Modern Electronic Structure Theory, Part I*; Yarkony, D. R., Ed.; World Scientific: Singapore, 1995; pp 1047-1131.
4. Paldus, J.; Li, X. *Adv. Chem. Phys.* **1999**, 110, 1.
5. Paldus, J.; Li, X. In *Correlation and Localization*; Surján, P. R., Ed.; Springer-Verlag: Berlin, 1999; pp1-20.
6. See, e.g., Paldus, J. In *Mathematical Frontiers in Computational Chemical Physics*; Truhlar, D. G., Ed.; IMA Series; Springer-Verlag: Berlin, 1988; Vol. 15, pp 262-299; Shavitt, I. *ibid.* pp 300-349.
7. Paldus, J. In *Methods in Computational Molecular Physics*; Wilson, S.; Diercksen, G. H. F., Eds.; NATO ASI Series B: Physics; Plenum Press: New York, 1992; Vol. 293, pp 99-194; *idem.* In *Relativistic and Correlation Effects in Molecules and Solids*; Malli, G. L., Ed.; NATO ASI Series B: Physics; Plenum Press: New York, 1994; Vol. 318, pp 207-282.
8. Van Voorhis, T.; Head-Gordon, M. *J. Chem. Phys.* **2000**, 113, 8873.
9. Li, X.; Paldus, J. *J. Chem. Phys.* **2001**, 115, (October issue).
10. Li, X.; Paldus, J. *J. Chem. Phys.* **1995**, 103, 6536.

Downloaded by NORTH CAROLINA STATE UNIV on September 14, 2012 | http://pubs.acs.org
Publication Date: August 14, 2002 | doi: 10.1021/bk-2002-0828.ch002

Downloaded by NORTH CAROLINA STATE UNIV on September 14, 2012 | http://pubs.acs.org
Publication Date: August 14, 2002 | doi: 10.1021/bk-2002-0828.ch002

11. Raghavachari, K.; Trucks, G. W.; Pople, J. A.; Head-Gordon, M. *Chem. Phys. Lett.* **1989**, 157, 479.
12. Lee, T. J.; Scuseria, G. E. In *Quantum Mechanical Electronic Structure Calculations With Chemical Accuracy*; Langhoff, S. R., Ed.; Kluver Academic: Dordrecht, The Netherlands, 1995; pp 47-108.
13. Kucharski, S. A.; Bartlett, R. J. *J. Chem. Phys.* **1992**, 97, 4282.
14. Oliphant, N.; Adamowicz, L. *Chem. Phys. Lett.* **1991**, 190, 13; *Int. Rev. Phys. Chem.* **1993**, 12, 339; Piecuch, P.; Adamowicz, L. *J. Chem. Phys.* **1994,** 100, 5792, 5857 and *loc. cit.*
15. Piecuch, P., Kucharski, S. A.; Bartlett, R. J. *J. Chem. Phys.* **1999**, 110, 6103; Piecuch, P.; Kucharski, S. A.; Špirko, V. *J. Chem. Phys.* **1999**, 111, 6679.
16. Paldus, J.; Planelles, J. *Theor. Chim. Acta* **1994**, 89, 13.
17. Stolarczyk, L. Z. *Chem. Phys. Lett.* **1994**, 217, 1.
18. Planelles, J.; Paldus, J.; Li, X. *Theor. Chim. Acta* **1994**, 89, 33; *ibid.* **1994**, 89, 59.
19. Peris, G.; Planelles, J.; Paldus, J. *Int. J. Quantum Chem.* **1997**, 62, 137; Li, X.; Peris, G.; Planelles, J.; Rajadell, F.; Paldus, J. *J. Chem. Phys.* **1997,** 107, 90; Peris, G.; Rajadell, F.; Li, X.; Planelles, J.; Paldus, J. *Mol. Phys.* **1998**, 94, 235; Planelles, J.; Peris, G.; Paldus, J. *Int. J. Quantum Chem.* **2000**, 77, 693.
20. Paldus, J.; Čížek, J.; Takahashi, M. *Phys. Rev. A* **1984,** 30, 2193.
21. Piecuch, P.; Tobоła, R.; Paldus, J. *Phys. Rev. A* **1996**, 54, 1210.
22. Li, X.; Paldus, J. *J. Chem. Phys.* **1997**, 107, 6257.
23. Li, X.; Paldus, J. *J. Chem. Phys.* **1998**, 108, 637.
24. Li, X.; Paldus, J. *Chem. Phys. Lett.* **1998,** 286, 145.
25. Peris, G.; Planelles, J.; Malrieu, J.-P.; Paldus, J. *J. Chem. Phys.* **1999**, 110, 11708; Li, X.; Grabowski, I.; Jankowski, K.; Paldus, J. *Adv. Quantum Chem.* **1999**, 36, 231; Li, X.; Paldus, J. *Int. J. Quantum Chem.* **2000**, 80, 743.
26. Li, X.; Paldus, J. *Coll. Czech. Chem. Commun.* **1998**, 63, 1381.
27. Li, X.; Paldus, J. *J. Chem. Phys.* **1999**, 110, 2844.
28. Li, X.; Paldus, J. *Mol. Phys.* **2000**, 98, 1185.
29. Li, X.; Paldus, J. *J. Chem. Phys.* **2000**, 113, 9966.
30. Li, X. *J. Mol. Struct.: THEOCHEM* **2001**, 547, 69.
31. Kowalski, K.; Piecuch, P. *J. Chem. Phys.* **2000**, 113, 18; *ibid.* **2000**, 113, 5644.
32. Piecuch, P.; Kowalski, K. In *Computational Chemistry: Reviews of Current Trends*; Leszczynski, J., Ed.; World Scientific: Singapore, 2000; Vol. 5, pp 1-104.
33. Piecuch, P.; Kucharski, S. A.; Kowalski, K. *Chem. Phys. Lett.* **2001**, 344, 176; Kowalski, K.; Piecuch, P. *J. Chem. Phys.* **2001**, 115, 2966; *J. Mol. Struct.: THEOCHEM* **2001**, 547, 191.

34. Li, X.; Paldus, J. *J. Chem. Phys.* **2001**, 115, (October issue).
35. Krylov, A. I.; Sherrill, C. D.; Byrd, E. F. C.; Head-Gordon, M. *J. Chem. Phys.* **1998**, 109, 10669.
36. Paldus, J.; Wormer, P. E. S.; Visser, F.; van der Avoird, A. *J. Chem. Phys.* **1982**, 76, 2458.
37. Mahapatra, U. S.; Datta, B.; Mukherjee, D. *J. Chem. Phys.* **1999**, 110, 6171.
38. Mášik, J.; Hubač, I.; Mach, P. *J. Chem. Phys.* **1998**, 108, 6571; Pittner, J.; Nachtigall, P.; Čársky, P.; Mášik, J.; Hubač, I. *ibid.* **1999**, 110, 10275.
39. Meißner, H.; Paldus, J. *J. Chem. Phys.* **2000**, 113, 2594; *ibid.* **2000**, 113, 2622; *idem. Int. J. Quantum Chem.* **2000**, 80, 782 and *loc. cit.*
40. Meißner, H.; Paldus, J. *J. Chem. Phys.* **2000**, 113, 2612.
41. Meißner, H.; Ema, I. *J. Mol. Struct.: THEOCHEM* **2001**, 547, 171.
42. LeRoy, R. J. *LEVEL 6.1, A Computer Program Solving the Radial Schrödinger Equation for Bound and Quasibound Levels, and Calculating Various Expectation Values and Matrix Elements*; University of Waterloo: Waterloo, Canada, 1996; Chemical Physics Research Report CP-555R.
43. Edwards, S.; Roncin, J.-Y.; Launay, F.; Rostas, F. *J. Mol. Spectrosc.* **1993,** 162, 257.
44. Gershgorn, Z.; Shavitt, I. *Int. J. Quantum Chem.* **1968**, 2, 751.

Downloaded by NORTH CAROLINA STATE UNIV on September 14, 2012 | http://pubs.acs.org
Publication Date: August 14, 2002 | doi: 10.1021/bk-2002-0828.ch002

Downloaded by PENNSYLVANIA STATE UNIV on September 14, 2012 | http://pubs.acs.org
Publication Date: August 14, 2002 | doi: 10.1021/bk-2002-0828.ch003

Chapter 3

Method of Moments of Coupled-Cluster Equations: A New Theoretical Framework for Designing "Black-Box" Approaches for Molecular Potential Energy Surfaces

**Piotr Piecuch[1], Karol Kowalski[1], Ian S. O. Pimienta[1],
and Stanislaw A. Kucharski[2]**

**[1]Department of Chemistry, Michigan State University, East Lansing, MI 48824
[2]Institute of Chemistry, Silesian University, Szkolna 9, 40–006 Katowice, Poland**

The recently proposed method of moments of coupled-cluster equations (MMCC) is reviewed. The ground-state MMCC formalism and its excited-state extension via the equation-of-motion coupled-cluster (EOMCC) approach are discussed. The main idea of all MMCC methods is that of the noniterative energy corrections which, when added to the ground- and excited-state energies obtained in approximate CC calculations, recover the exact energies. Approximate MMCC methods, including the renormalized CCSD(T), CCSD(TQ), and CCSDT(Q) approaches and the EOMCC-related MMCC(2,3) method, are described and examples of applications of these new approaches are given. It is demonstrated that the MMCC formalism provides a new framework for designing "black-box" approaches that give excellent description of entire potential energy surfaces at the small fraction of the effort associated with multireference calculations.

In Low-Lying Potential Energy Surfaces; Hoffmann, M., et al.;
ACS Symposium Series; American Chemical Society: Washington, DC, 2002.

Introduction

One of the most important problems in coupled-cluster (CC) theory (*1–7*) is extension of the existing single-reference CC (SRCC) methods to quasidegenerate and excited states. Potential energy surfaces (PESs) of ground and excited states represent a particularly challenging problem. The standard CC "black-boxes" for ground electronic states, such as the CCSD (CC singles and doubles) approach, and their perturbative triples and quadruples extensions, including CCSD[T] (*8–10*), CCSD(T) (*11*), CCSD(TQ$_f$) (*12*), and CCSDT(Q$_f$) (*12*), fail to describe bond dissociation (cf., e.g., refs 6, 7, 13–20). The response CC methods (*21–26*) and their equation-of-motion CC (EOMCC) analogs (*27–30*) are capable of providing very good results for excited states dominated by singles (cf., e.g., refs 27–29, 31–37), but accurate calculations of excited states of quasidegenerate systems (particularly, excited states having large biexcited components) and of entire PESs of excited states with the standard response CC and EOMCC approximations, including the EOMCCSD (*27–29*), EOMCCSD(T) (*31*), EOMCCSD($\tilde{T}$) (*32*), EOMCCSD(T′) (*32*), EOMCCSDT-*n* (*31, 32*), CCSDR(3) (*36, 37*), and CC3 (*34–37*) methods, are not possible (cf., e.g., refs 38–41). The genuine multi-reference CC (MRCC) approaches of the state-universal type (*4, 6, 42–56*) (the SUMRCC methods) have showed some promise in studies of molecular PESs (cf., e.g., refs 45, 47, 48, 51–53, 56), but the SUMRCC calculations are plagued by intruder states (*51, 52*) and by multiple intruder solutions (*51, 54*). The applicability of the valence-universal MRCC methods (*4, 6, 57–60*), which also suffer from intruder states and unphysical multiple solutions (*61, 62*), is limited to vertical excitation energies of atoms and molecules at their equilibrium geometries. Thus, in spite of tremendous progress in CC theory, which is nowadays routinely used in accurate calculations of various equilibrium properties of closed-shell and simple open-shell molecular systems, there is a need for new ideas that would extend the applicability of CC methods to entire molecular PESs.

Several attempts have been made to remove the pervasive failing of the perturbative CC approximations at large internuclear separations. The representative examples include the externally-corrected SRCC methods (*6, 10, 63–74*), the active-space SRCC approaches (*14, 19, 75–86*), the orbital-optimized SRCC methods (*39, 87, 88*), and the perturbative CC approaches based on the partitioning of the similarity-transformed Hamiltonian (*89, 90*) (see ref 91 for the original idea). Of all these approaches, the reduced MRCCSD (RMRCCSD) method (*68–74*), which uses the multi-reference configuration interaction (MRCI) wave functions to extract information about triply and quadruply excited clusters, and the active-space CCSDt and CCSDtq methods (*19, 85, 86*) and their earlier state-selective (SS) CCSD(T) and CCSD(TQ) analogs (*14, 75–84*) are particularly promising. The RMRCCSD approach can be used to success-

Downloaded by PENNSYLVANIA STATE UNIV on September 14, 2012 | http://pubs.acs.org
Publication Date: August 14, 2002 | doi: 10.1021/bk-2002-0828.ch003

fully describe bond breaking and ro-vibrational term values in the ground state (*6*, *68*–*70*, *72*–*74*), and to calculate the lowest-energy excited state of a given symmetry (*71*, *73*). Unfortunately, it is not possible to apply the RMRCCSD method to several electronic states of the same symmetry and the cost of the MRCI calculations that are used to extract the triply and quadruply excited clusters may significantly increase the cost of the RMRCCSD calculations. The CCSDt and CCSDtq methods and their SSCCSD(T) and SSCCSD(TQ) analogs, in which higher–than–doubly excited components of the cluster operator are selected through active orbitals, have fewer limitations. The CCSDt or SSCCSD(T) and CCSDtq or SSCCSD(TQ) approaches are less expensive than the MRCI methods and can easily be extended to excited states of the same or different symmetries via the EOMCC formalism (*40*, *41*). The active-space CC approaches proved to be successful in describing quasidegenerate ground states (*79*, *80*, *85*), ground-state PESs involving bond breaking (*14*, *19*, *81*, *84*–*86*), highly excited vibrational states (*86*), and ground-state property functions (*83*) at the fraction of the computer cost associated with the parent CCSDT (CC singles, doubles, and triples) (*92*, *93*) and CCSDTQ (CC singles, doubles, triples, and quadruples) (*79*, *94*–*96*) approaches. The EOMCC extension of the CCSDt method, termed EOMCCSDt (*40*, *41*), in which relatively small subsets of triexcited components of cluster operator T and EOMCC excitation operator R are selected through active orbitals, proved to be capable of providing excellent description of excited states dominated by doubles and states having large triexcited components (including excited states of molecules whose ground states are quasidegenerate). The EOMCCSDt approach proved to be successful in describing entire excited-state PESs at the fraction of the computer cost associated with MRCI and full EOMCCSDT (EOMCC singles, doubles, and triples) (*41*) calculations (*40*, *41*, *97*).

The active-space SRCC methods and their EOMCC extensions are very promising and we will continue to develop them. They are relatively easy to use, although, in analogy to multireference approaches, they require choosing active orbitals, which in some cases may be a difficult thing to do. From this point of view, the active-space CC methods are not as easy–to–use as the noniterative perturbative methods, such as CCSD(T) or CCSD(TQ_f), or their response CC or EOMCC extensions. Undoubtedly, it would be desirable to have an approach that combines the simplicity of the noniterative CC schemes with the effectiveness with which the iterative active-space CC and EOMCC methods, such as CCSDt and EOMCCSDt, describe ground- and excited-state PESs.

It has recently been demonstrated that the applicability of the ground-state SRCC approaches, including the popular noniterative approximations, such as CCSD(T), can be extended to bond breaking and quasidegenerate states, if we switch to a new type of the SRCC theory, termed the ***method of moments of CC equations*** (MMCC) (*7*, *16*–*18*). It has further been demon-

Downloaded by PENNSYLVANIA STATE UNIV on September 14, 2012 | http://pubs.acs.org
Publication Date: August 14, 2002 | doi: 10.1021/bk-2002-0828.ch003

strated that the MMCC theory can be extended to excited-state PESs, if we combine the MMCC and EOMCC (*98*) or MMCC and SUMRCC (*18*) formalisms. The main idea of the ground-state MMCC formalism (*7*, *16*–*18*) is that of the noniterative energy correction which, when added to the energy obtained in approximate SRCC calculations, such as CCSD or CCSDT, recovers the exact (full CI) energy. The noniterative energy corrections defining the EOMCC-based MMCC theory (*98*), added to the energies obtained in approximate EOMCC (e.g., EOMCCSD) calculations, recover the full CI energies of excited states. It has been demonstrated that the MMCC formalism allows us to *renormalize* the existing noniterative SRCC approximations, such as CCSD[T], CCSD(T), CCSD(TQ$_f$), and CCSDT(Q$_f$), so that they can correctly describe entire ground-state PESs (*7*, *16*–*20*). It has also been demonstrated that the excited-state MMCC theory, based on the EOMCC method, allows us to introduce a new hierarchy of simple noniterative CC approximations that remove the pervasive failing of the EOMCCSD and perturbative EOMCCSDT approximations in describing entire excited-state PESs (*98*).

In our view, the MMCC theory represents an interesting development in the area of new CC methods for molecular PESs. The MMCC-based *renormalized CCSD(T), CCSD(TQ), and CCSDT(Q) methods* and the *noniterative MMCC approaches to excited states* provide highly accurate results for ground and excited-state PESs, while preserving the simplicity and the "black-box" character of the noniterative perturbative CC schemes. In this chapter, we review the MMCC theory and new CC approximations that result from it and show the examples of the MMCC and renormalized CC calculations for ground and excited state PESs of several benchmark molecules, including HF, F_2, N_2, and CH^+. The review of the previously published numerical results (*7*, *16*–*20*) is combined with the presentation of new results for the C_2, N_2, and H_2O molecules.

The Method of Moments of Coupled-Cluster Equations: The General Formalism

We begin our review of the MMCC theory with the ground-state formalism. The extension of the MMCC formalism to the EOMCC case is discussed in the next subsection.

The Ground-State Theory

In the SRCC theory, we represent the ground-state wave function of an N-electron system, described by the Hamiltonian H, in the following way:

$$|\Psi_0\rangle = e^T|\Phi\rangle, \tag{1}$$

Downloaded by PENNSYLVANIA STATE UNIV on September 14, 2012 | http://pubs.acs.org
Publication Date: August 14, 2002 | doi: 10.1021/bk-2002-0828.ch003

Downloaded by PENNSYLVANIA STATE UNIV on September 14, 2012 | http://pubs.acs.org
Publication Date: August 14, 2002 | doi: 10.1021/bk-2002-0828.ch003

where T is the cluster operator and $|\Phi\rangle$ is an independent-particle-model (IPM) reference configuration (usually, the Hartree-Fock determinant). In the exact theory, T is a sum of all of its many-body components, including the N-body one. In the standard SRCC approximations, the many-body expansion of T is truncated at some excitation level.

Let us consider the standard SRCC approximation (hereafter referred to as method A), in which T is approximated as follows:

$$T \approx T^{(A)} = \sum_{n=1}^{m_A} T_n , \tag{2}$$

where T_n, $n = 1, \ldots, m_A$, are the many-body components of T included in the calculations and $m_A < N$ ($m_A = 2$ defines the CCSD method, $m_A = 3$ defines the CCSDT method, etc.). The system of equations for the cluster amplitudes defining the T_n components has the following form:

$$Q^{(A)} \bar{H}^{(A)} |\Phi\rangle = 0, \tag{3}$$

where

$$\bar{H}^{(A)} = e^{-T^{(A)}} H e^{T^{(A)}} = (H e^{T^{(A)}})_C \tag{4}$$

is the similarity-transformed Hamiltonian of the CC theory, subscript C designates the connected part of the corresponding operator expression, and $Q^{(A)}$ is the projection operator onto the subspace of all excited configurations described by $T^{(A)}$, i.e.,

$$Q^{(A)} = \sum_{n=1}^{m_A} Q_n , \tag{5}$$

where Q_n represents the projection operator onto the n-tuply excited configurations relative to $|\Phi\rangle$. Once the system of equations, eq (3), is solved for $T^{(A)}$, the energy is calculated using the formula

$$E_0^{(A)} = \langle \Phi | \bar{H}^{(A)} | \Phi \rangle . \tag{6}$$

The main idea of the MMCC theory is as follows: After analyzing the relationships between multiple solutions of the nonlinear equations representing different levels of the CC theory (CCSD, CCSDT, etc.), Piecuch and Kowalski have recently derived a formula for the noniterative correction $\delta_0^{(A)}$ which, when added to the energy obtained in approximate SRCC calculation, $E^{(A)}$, eq (6), recovers the full CI energy E_0. We obtain (*7*, *16*–*18*),

$$\begin{aligned}\delta_0^{(A)} \equiv E_0 - E_0^{(A)} = & \sum_{n=m_A+1}^{N} \sum_{j=m_A+1}^{n} \langle \Psi_0 | Q_n C_{n-j}(m_A) M_j^{\mathrm{CC}}(m_A) | \Phi \rangle / \\ & \langle \Psi_0 | e^{T^{(A)}} | \Phi \rangle , \end{aligned} \tag{7}$$

where

$$C_{n-j}(m_A) = (e^{T^{(A)}})_{n-j} \tag{8}$$

represents the $(n-j)$-body component of the wave operator $e^{T^{(A)}}$, defining the SRCC approximation A, and

$$M_j^{\mathrm{CC}}(m_A)|\Phi\rangle = (\bar{H}^{(A)})_j|\Phi\rangle = Q_j(\bar{H}^{(A)})|\Phi\rangle \tag{9}$$

are the SRCC equations, in which $T = T^{(A)}$, projected onto the j-tuply excited configurations relative to $|\Phi\rangle$. Here and elsewhere in the present chapter, we use a notation in which O_j represents the j-body component of operator O. The original proof of formula (7) has been based on the ***Fundamental Theorem of the Formalism of β-Nested Equations*** (*7*), which describes relationships between multiple solutions of the SRCC equations representing different levels of theory (CCSD, CCSDT, etc.). An alternative (and more elementary) derivation of eq (7), based on the MMCC functional

$$\Lambda[\Psi] = \langle\Psi|(H - E_0^{(A)})e^{T^{(A)}}|\Phi\rangle/\langle\Psi|e^{T^{(A)}}|\Phi\rangle, \tag{10}$$

introduced in ref 16, has been given in Appendix A of ref 16.

Equation (7) is the basic equation of the ground-state MMCC formalism. The main element of eq. (7) are the SRCC equations, in which $T = T^{(A)}$, projected on the j-tuply excited configurations with $j > m_A$, i.e., the ***SRCC equations projected onto the excited configurations not included in approximate method A***. These readily available quantities represent the ***generalized moments of coupled-cluster equations*** (for a discussion of the relationship between the method of moments of Krylov (*99*) and the CC theory, see ref 100). Indeed, if $|\Phi_J^{(j)}\rangle$ designate the j-tuply excited configurations relative to $|\Phi\rangle$, then

$$M_j^{\mathrm{CC}}(m_A)|\Phi\rangle = \sum_J \mathcal{M}_J^{\mathrm{CC},(j)}(m_A)\,|\Phi_J^{(j)}\rangle, \tag{11}$$

where

$$\mathcal{M}_J^{\mathrm{CC},(j)}(m_A) = \langle\Phi_J^{(j)}|\bar{H}^{(A)}|\Phi\rangle \tag{12}$$

are the SRCC equations projected on excited configurations $|\Phi_J^{(j)}\rangle$. All this means that if we, for example, want to correct the results of CCSD calculations (the $m_A = 2$ case) and recover the full CI energy by adding the noniterative correction $\delta_0^{(A)}$ to the CCSD energy, we need to calculate the generalized moments of the CCSD equations, i.e., the CCSD equations projected on triples, quadruples, pentuples, and hextuples, or

$$M_j^{\mathrm{CC}}(2)|\Phi\rangle = Q_j(He^{T_1+T_2})_C|\Phi\rangle, \tag{13}$$

Downloaded by PENNSYLVANIA STATE UNIV on September 14, 2012 | http://pubs.acs.org
Publication Date: August 14, 2002 | doi: 10.1021/bk-2002-0828.ch003

where T_1 and T_2 are the singly and doubly excited clusters resulting from the CCSD calculations and $j = 3 - 6$ ($M_j^{\mathrm{CC}}(2)|\Phi\rangle = 0$ for $j > 6$).

The correction $\delta_0^{(A)}$ also depends on the exact wave function $|\Psi_0\rangle$, which we do not know. We can use, however, very simple guesses for $|\Psi_0\rangle$, obtained in inexpensive many-body perturbation theory (MBPT) or CI calculations, and calculate approximate values of $\delta_0^{(A)}$. The renormalized CCSD(T), CCSD(TQ), and CCSDT(Q) methods, mentioned in the Introduction, are based on the MBPT(2)-like guesses for $|\Psi_0\rangle$ (*7*, *16*, *17*). The difference between a new hierarchy of approximations that is obtained in this way and the standard approaches to electron correlation is in that in computing $\delta_0^{(A)}$, we focus on the leading correction to the energy obtained in an approximate CC calculation, such as CCSD; in all conventional approaches, we are only trying to correct the results of the Hartree-Fock (or some other IPM) calculations without having any non-trivial relationship with full CI. Thus, the MMCC energy formula, eq (7), gives us a new way of controlling the quality of CC results. In MMCC calculations, we are not interested in improving the Hartree-Fock (or other IPM) description by simply adding corrections due to correlation, with the hope that the more we add the better. We are rather dealing with the remanent error that occurs in approximate CC calculations by directly considering the quantity of interest, i.e., $E - E^{(A)}$ (e.g., $E - E^{\mathrm{CCSD}}$, where E^{CCSD} is the CCSD energy; cf. ref 91 for very useful remarks). This is particularly important in situations, where standard arguments originating from MBPT fail due to divergent behavior of the MBPT series (as is the case in studies of quasidegenerate states and bond breaking). Interestingly enough, all approximate approaches resulting from eq (7) *correctly describe a separation of a given* N*-electron system into fragments consisting of no more than* m_A *electrons each, independent of a particular approximation used to define* $|\Psi_0\rangle$ (*7*, *16*). This means, for example, that each MMCC approximation, in which we correct the CCSD results, provides a correct description of a separation of a given N-electron system into non-interacting electron pairs, independent of the form of $|\Psi_0\rangle$.

The Excited-State Theory

The MMCC theory can be extended to excited states. Kowalski and Piecuch have proposed two such extensions. In the first one, the MMCC theory is combined with the genuine MRCC formalism of the state-universal type. The main idea of the resulting MM-SUMRCC approach (*18*) is that of the noniterative energy corrections which, when added to the eigenvalues of the effective Hamiltonian defining the approximate SUMRCC method, such as SUMRCCSD (*46*, *49*, *53*, *55*), recover the exact energies of the electronic states of interest. In complete analogy to the single-reference

Downloaded by PENNSYLVANIA STATE UNIV on September 14, 2012 | http://pubs.acs.org
Publication Date: August 14, 2002 | doi: 10.1021/bk-2002-0828.ch003

case, the noniterative corrections to the SUMRCC energies are expressed in terms of the generalized moments of the SUMRCC equations (*18*). In the second extension of the MMCC formalism to excited states, introduced in ref 98 and overviewed here, we correct the results of approximate EOMCC (e.g., EOMCCSD) calculations.

In the EOMCC theory, the excited states $|\Psi_K\rangle$ of a given N-electron system are represented in the following way:

$$|\Psi_K\rangle = R_K|\Psi_0\rangle, \quad |\Psi_0\rangle = e^T|\Phi\rangle, \tag{14}$$

where R_K is the excitation operator generating excited state $|\Psi_K\rangle$ from the SRCC ground state $|\Psi_0\rangle$. For the consistency of our presentation, the excitation operator R_K is defined as a unit operator for $K = 0$. The excited-state energies E_K and the corresponding operators R_K are obtained by diagonalizing the similarity-transformed Hamiltonian $\bar{H} = e^{-T}He^T$, where T is the cluster operator determined by solving the SRCC equations. In the exact EOMCC formalism, the cluster operator T and the excitation operators R_K are sums of all relevant many-body components. In the standard EOMCC approximations, the many-body expansions of T and R_K are truncated at some excitation level.

In analogy to the ground-state case, let A represent the standard EOMCC approximation, in which the many-body expansions of T and R_K are truncated at the m_A-body components ($m_A < N$), so that

$$T \simeq T^{(A)} = \sum_{n=1}^{m_A} T_n, \tag{15}$$

$$R_K \simeq R_K^{(A)} = R_{K,0}^{(A)} + R_{K,\mathrm{open}}^{(A)}, \tag{16}$$

with the "open" part of $R_K^{(A)}$ defined as

$$R_{K,\mathrm{open}}^{(A)} = \sum_{n=1}^{m_A} R_{K,n}. \tag{17}$$

As usual, T_n and $R_{K,n}$ are the n-body components of $T^{(A)}$ and $R_K^{(A)}$, respectively. In the EOMCCSD method, $m_A = 2$; in the EOMCCSDT approach, $m_A = 3$, etc. The cluster operator $T^{(A)}$ is obtained by solving the system of energy-independent equations represented by eq (3), whereas the excitation operators $R_K^{(A)}$ are obtained by diagonalizing the similarity-transformed Hamiltonian $\bar{H}^{(A)}$, eq (4), in a space spanned by reference $|\Phi\rangle$ and excited configurations included in $T^{(A)}$ and $R_K^{(A)}$. We obtain,

$$(P + Q^{(A)})(\bar{H}^{(A)} - E_K^{(A)})R_K^{(A)}|\Phi\rangle = 0, \tag{18}$$

Downloaded by PENNSYLVANIA STATE UNIV on September 14, 2012 | http://pubs.acs.org
Publication Date: August 14, 2002 | doi: 10.1021/bk-2002-0828.ch003

Downloaded by PENNSYLVANIA STATE UNIV on September 14, 2012 | http://pubs.acs.org
Publication Date: August 14, 2002 | doi: 10.1021/bk-2002-0828.ch003

where $P = |\Phi\rangle\langle\Phi|$, $Q^{(A)}$ is defined by eq (5), and $E_K^{(A)}$ is the energy of state $|\Psi_K\rangle$ obtained in the calculations with the EOMCC approximation A. Notice that eq (18) reduces to the ground-state SRCC equations, eqs (3) and (6), when $K = 0$ (recall that $R_0^{(A)} = 1$).

The main idea of the excited-state MMCC theory (*98*) is that of the noniterative energy corrections

$$\delta_K^{(A)} \equiv E_K - E_K^{(A)}, \tag{19}$$

which, when added to the energies of excited states, $E_K^{(A)}$, obtained in approximate EOMCC (method A) calculations, recover the corresponding exact energies E_K. By considering the excited-state extension of functional $\Lambda[\Psi]$, eq (10), i.e., the expression

$$\Lambda[\Psi] = \langle\Psi|(H - E_K^{(A)})R_K^{(A)}e^{T^{(A)}}|\Phi\rangle / \langle\Psi|R_K^{(A)}e^{T^{(A)}}|\Phi\rangle, \tag{20}$$

which satisfies the property

$$\Lambda[\Psi_K] = E_K - E_K^{(A)} \equiv \delta_K^{(A)}, \tag{21}$$

we can derive the following formula for the energy corrections $\delta_K^{(A)}$ (*98*):

$$\begin{aligned}\delta_K^{(A)} \;=\; & \sum_{n=m_A+1}^{N}\;\sum_{j=m_A+1}^{n} \langle\Psi_K|Q_n\, C_{n-j}(m_A)\, M_{K,j}^{\mathrm{EOMCC}}(m_A)|\Phi\rangle / \\ & \langle\Psi_K|R_K^{(A)}e^{T^{(A)}}|\Phi\rangle,\end{aligned} \tag{22}$$

where $C_{n-j}(m_A)$ is defined by eq (8) and

$$M_{K,j}^{\mathrm{EOMCC}}(m_A)|\Phi\rangle = (\bar{H}^{(A)}R_K^{(A)})_j|\Phi\rangle = Q_j(\bar{H}^{(A)}R_K^{(A)})|\Phi\rangle. \tag{23}$$

In analogy to the ground-state case, the $M_{K,j}^{\mathrm{EOMCC}}(m_A)|\Phi\rangle$ quantities appearing in eq (22) are related to the generalized moments of the EOMCC equations defining method A, i.e., to the *left-hand side of the EOMCC eigenvalue problem* involving $\bar{H}^{(A)}$ (the $\bar{H}^{(A)}R_K^{(A)}|\Phi\rangle$ term), *projected on the* j*-tuply excited configurations with* $j > m_A$. We can immediately write,

$$M_{K,j}^{\mathrm{EOMCC}}(m_A)|\Phi\rangle = \sum_J \mathcal{M}_{K,J}^{\mathrm{EOMCC},(j)}(m_A)\,|\Phi_J^{(j)}\rangle, \tag{24}$$

where

$$\mathcal{M}_{K,J}^{\mathrm{EOMCC},(j)}(m_A) = \langle\Phi_J^{(j)}|(\bar{H}^{(A)}R_K^{(A)})|\Phi\rangle \tag{25}$$

are the generalized moments of the EOMCC equations defining method A. It can be shown (*98*) that the generalized moments $\mathcal{M}_{K,J}^{\mathrm{EOMCC},(j)}(m_A)$ with

$j > m_A$ that define $M^{\text{EOMCC}}_{K,j}(m_A)|\Phi\rangle$ through eq (24) and that are needed to calculate correction $\delta^{(A)}_K$, eq (22), are given by the following expression:

$$\mathcal{M}^{\text{EOMCC},(j)}_{K,J}(m_A) = r^{(A)}_{K,0}\,\langle\Phi^{(j)}_J|\bar{H}^{(A)}|\Phi\rangle + \langle\Phi^{(j)}_J|\left(\bar{H}^{(A)}_{\text{open}}R^{(A)}_{K,\text{open}}\right)_{C,j}|\Phi\rangle + \sum_{p=m_A+1}^{j-1}\langle\Phi^{(j)}_J|\left(\bar{H}^{(A)}_{p}R^{(A)}_{K,j-p}\right)_{DC}|\Phi\rangle, \tag{26}$$

where $r^{(A)}_{K,0}$ is the coefficient at reference $|\Phi\rangle$ in the many-body expansion of the K-th right eigenvector of $\bar{H}^{(A)}$, $R^{(A)}_K|\Phi\rangle$. Here, subscripts "open," C, and DC refer to the open (i.e., having external lines), connected, and disconnected parts of a given operator expression. In particular,

$$\bar{H}^{(A)}_{\text{open}} = (He^{T^{(A)}})_{C,\text{open}} = e^{-T^{(A)}}He^{T^{(A)}} - E^{(A)}_0, \tag{27}$$

where $E^{(A)}_0$ is the ground-state energy obtained with method A. Equation (26) becomes very useful in obtaining the explicit formulas for the $\mathcal{M}^{\text{EOMCC},(j)}_{K,J}(m_A)$ moments in terms of matrix elements of the similarity-transformed Hamiltonian $\bar{H}^{(A)}$, which can be used in computer implementations of approximate MMCC methods discussed in the next section.

Equation (22), with $C_{n-j}(m_A)$ defined by eq (8) and $M^{\text{EOMCC}}_{K,j}(m_A)|\Phi\rangle$ defined by eqs (24) and (26), defines the excited-state MMCC theory. In analogy to the ground-state case, the main elements of eq (22) are the generalized moments of the EOMCC equations defining approximate method A, i.e., the EOMCC equations, in which T is approximated by $T^{(A)}$ and R_K is approximated by $R^{(A)}_K$, *projected onto the excited configurations not included in method A*. For example, if we want to correct the excited-state energies obtained in EOMCCSD calculations (the $m_A = 2$ case) and recover the full CI energies E_K, we must calculate the EOMCCSD equations projected on triples, quadruples, etc., or

$$M^{\text{EOMCC}}_{K,j}(2)|\Phi\rangle = Q_j(\bar{H}^{\text{CCSD}}R^{\text{CCSD}}_K)|\Phi\rangle, \tag{28}$$

with $j > 2$, where

$$\bar{H}^{\text{CCSD}} = e^{-(T_1+T_2)}He^{T_1+T_2} \tag{29}$$

is the similarity-transformed Hamiltonian of the EOMCCSD approach, T_1 and T_2 are the singly and doubly excited clusters resulting from the CCSD calculations, and

$$R^{\text{CCSD}}_K = R_{K,0} + R_{K,1} + R_{K,2} = R_{K,0} + R^{\text{CCSD}}_{K,\text{open}} \tag{30}$$

is the EOMCCSD excitation operator R_K. The corrections $\delta^{(A)}_K$ also depend on the exact wave functions $|\Psi_K\rangle$, which we do not know. However,

Downloaded by PENNSYLVANIA STATE UNIV on September 14, 2012 | http://pubs.acs.org
Publication Date: August 14, 2002 | doi: 10.1021/bk-2002-0828.ch003

Downloaded by PENNSYLVANIA STATE UNIV on September 14, 2012 | http://pubs.acs.org
Publication Date: August 14, 2002 | doi: 10.1021/bk-2002-0828.ch003

as in the ground-state MMCC theory (*7, 16–18*), we can use simple guesses for $|\Psi_K\rangle$, provided, for example, by inexpensive CI calculations, and obtain excited-state energies that are much closer to the full CI energies than the approximate EOMCC energies $E_K^{(A)}$. The only requirement that eq (22) imposes on the approximate form of $|\Psi_K\rangle$, to make it usable for the calculation of $\delta_K^{(A)}$, is the presence of higher–than–m_A-tuply excited configurations in $|\Psi_K\rangle$ (e.g., triples in the $m_A = 2$ case). The state-selective character of the MMCC formula for the energy corrections $\delta_K^{(A)}$, eq. (22), must be emphasized, too. By having some approximate form of $|\Psi_K\rangle$, we can calculate a given correction $\delta_K^{(A)}$ without considering other states.

Finally, it should be noticed that eq (22) represents a natural generalization of the ground-state MMCC formula, eq (7), to excited states. Indeed, in the ground-state ($K = 0$) case, R_K is a unit operator, so that $r_{K,0} = 1$ and $R_{K,j} = 0$ for $j > 0$ or $R_{K,\text{open}} = 0$. In consequence (see eq (26)),

$$\mathcal{M}_{0,J}^{\text{EOMCC},(j)}(m_A) = \langle \Phi_J^{(j)} | \bar{H}^{(A)} | \Phi \rangle \equiv \mathcal{M}_J^{\text{CC},(j)}(m_A), \tag{31}$$

where $\mathcal{M}_J^{\text{CC},(j)}(m_A)$ are the generalized moments of the SRCC equations defining method A (see eq (12)).

Approximate MMCC Methods: The MMCC(m_A, m_B) and Renormalized CC Schemes

The hierarchy of the MMCC(m_A,m_B) approximations is obtained, when we restrict the wave functions $|\Psi_K\rangle$ in eqs (7) and (22) to functions that do not contain higher–than–m_B-tuply excited configurations in the corresponding CI expansions. The nonzero values of corrections $\delta_K^{(A)}$ are obtained only when $m_B > m_A$. The energy expressions describing the resulting MMCC(m_A,m_B) approximations are as follows (*7, 16, 17, 98*):

$$E_K(m_A, m_B) = E_K^{(A)} + \delta_K(m_A, m_B), \tag{32}$$

where the formula for the ground-state ($K = 0$) correction $\delta_0(m_A, m_B)$ is

$$\begin{aligned}\delta_0(m_A, m_B) \;=\; & \sum_{n=m_A+1}^{m_B} \sum_{j=m_A+1}^{n} \langle \Psi_0 | Q_n \, C_{n-j}(m_A) \, M_j^{\text{CC}}(m_A) | \Phi \rangle / \\ & \langle \Psi_0 | e^{T^{(A)}} | \Phi \rangle,\end{aligned} \tag{33}$$

and

$$\begin{aligned}\delta_K(m_A, m_B) \;=\; & \sum_{n=m_A+1}^{m_B} \sum_{j=m_A+1}^{n} \langle \Psi_K | Q_n \, C_{n-j}(m_A) \, M_{K,j}^{\text{EOMCC}}(m_A) | \Phi \rangle / \\ & \langle \Psi_K | R_K^{(A)} e^{T^{(A)}} | \Phi \rangle,\end{aligned} \tag{34}$$

for excited states (the $K > 0$ case). As explained earlier, the $M_j^{\rm CC}(m_A)|\Phi\rangle$ and $M_{K,j}^{\rm EOMCC}(m_A)|\Phi\rangle$ quantities, $j = m_A + 1, \ldots, m_B$, entering eqs (33) and (34), respectively, can be expressed in terms of the higher generalized moments of the approximate CC and EOMCC methods, commonly labeled as method A. When $m_B = N$ and when wave functions $|\Psi_K\rangle$ are exact, we obtain the exact MMCC theory described in the previous section.

The Ground-State MMCC(m_A, m_B) Methods and the Renormalized CCSD(T), CCSD(TQ), and CCSDT(Q) Schemes

Three choices of (m_A, m_B) are particularly useful in the ground-state case, namely, $(m_A, m_B) = (2,3)$, $(2,4)$, and $(3,4)$. These three choices lead to the MMCC(2,3), MMCC(2,4), and MMCC(3,4) schemes. In the MMCC(2,3) and MMCC(2,4) ground-state methods, we add correction δ_0 to the CCSD energy, $E^{\rm CCSD}$, whereas in the MMCC(3,4) approach we correct the CCSDT energy, $E^{\rm CCSDT}$. We obtain (*7*, *16*, *17*),

$$E_0(2,3) = E^{\rm CCSD} + \langle \Psi_0 | Q_3 \, M_3(2) | \Phi \rangle / \langle \Psi_0 | e^{T_1+T_2} | \Phi \rangle \,, \tag{35}$$

$$\begin{aligned} E_0(2,4) \;=\; & E^{\rm CCSD} + \langle \Psi_0 | \{ Q_3 \, M_3(2) \\ & + Q_4 \, [M_4(2) + T_1 M_3(2)] \} | \Phi \rangle / \langle \Psi_0 | e^{T_1+T_2} | \Phi \rangle \,, \end{aligned} \tag{36}$$

$$E_0(3,4) = E^{\rm CCSDT} + \langle \Psi_0 | Q_4 \, M_4(3) | \Phi \rangle / \langle \Psi_0 | e^{T_1+T_2+T_3} | \Phi \rangle , \tag{37}$$

where

$$M_3(2)|\Phi\rangle = \sum_{\substack{i<j<k \\ a<b<c}} \mathcal{M}_{ijk}^{abc}(2) |\Phi_{ijk}^{abc}\rangle \,, \tag{38}$$

$$M_4(2)|\Phi\rangle = \sum_{\substack{i<j<k<l \\ a<b<c<d}} \mathcal{M}_{ijkl}^{abcd}(2) |\Phi_{ijkl}^{abcd}\rangle \,, \tag{39}$$

and

$$M_4(3)|\Phi\rangle = \sum_{\substack{i<j<k<l \\ a<b<c<d}} \mathcal{M}_{ijkl}^{abcd}(3) |\Phi_{ijkl}^{abcd}\rangle , \tag{40}$$

with

$$\mathcal{M}_{ijk}^{abc}(2) = \langle \Phi_{ijk}^{abc} | \left(H e^{T_1+T_2} \right)_C | \Phi \rangle \tag{41}$$

and

$$\mathcal{M}_{ijkl}^{abcd}(2) = \langle \Phi_{ijkl}^{abcd} | \left(H e^{T_1+T_2} \right)_C | \Phi \rangle \tag{42}$$

Downloaded by PENNSYLVANIA STATE UNIV on September 14, 2012 | http://pubs.acs.org
Publication Date: August 14, 2002 | doi: 10.1021/bk-2002-0828.ch003

representing the projections of the CCSD equations on triply and quadruply excited configurations, respectively, and with

$$\mathcal{M}_{ijkl}^{abcd}(3) = \langle\Phi_{ijkl}^{abcd}|\left(He^{T_1+T_2+T_3}\right)_C|\Phi\rangle \tag{43}$$

representing the projections of the CCSDT equations on quadruply excited configurations. Here and elsewhere in the present chapter, we use the standard notation in which $i, j, k, l, \ldots$ represent the spin-orbitals occupied in $|\Phi\rangle$ and $a, b, c, d, \ldots$ are the unoccupied spin-orbitals.

Different types of the MMCC(2,3), MMCC(2,4), and MMCC(3,4) approximations are obtained by making different choices for $|\Psi_0\rangle$ in eqs (35)–(37) (*7, 16–18*). The most intriguing results are obtained when wave functions $|\Psi_0\rangle$ are defined by the low-order MBPT. The MBPT-like forms of $|\Psi_0\rangle$ lead to the *renormalized and completely renormalized CCSD[T], CCSD(T), CCSD(TQ), and CCSDT(Q) schemes* (*7, 16–18*). As demonstrated below, these new methods represent powerful computational tools that remove the failing of the standard CCSD[T], CCSD(T), CCSD(TQ), and CCSDT(Q) approximations at large internuclear separations, while preserving the simplicity and "black-box" character of the noniterative perturbative CC approaches.

The *completely renormalized CCSD[T] and CCSD(T) methods* (the CR-CCSD[T] and CR-CCSD(T) approaches) are examples of the MMCC(2,3) scheme. If T_1 and T_2 are cluster operators obtained by solving the CCSD equations and if $R_0^{(3)}$ designates the three-body component of the MBPT reduced resolvent, then the energy formulas defining the CR-CCSD[T] and CR-CCSD(T) methods are (*7, 16–18*)

$$E^{\text{CR-CCSD[T]}} = E^{\text{CCSD}} + \langle\Psi^{\text{CCSD[T]}}|M_3(2)|\Phi\rangle / \langle\Psi^{\text{CCSD[T]}}|e^{T_1+T_2}|\Phi\rangle \tag{44}$$

and

$$E^{\text{CR-CCSD(T)}} = E^{\text{CCSD}} + \langle\Psi^{\text{CCSD(T)}}|M_3(2)|\Phi\rangle / \langle\Psi^{\text{CCSD(T)}}|e^{T_1+T_2}|\Phi\rangle, \tag{45}$$

respectively, where functions $|\Psi^{\text{CCSD[T]}}\rangle$ and $|\Psi^{\text{CCSD(T)}}\rangle$, entering eqs (44) and (45), are defined as follows:

$$|\Psi^{\text{CCSD[T]}}\rangle = [1 + T_1 + T_2 + R_0^{(3)}(V_N T_2)_C]|\Phi\rangle, \tag{46}$$

$$|\Psi^{\text{CCSD(T)}}\rangle = [1 + T_1 + T_2 + R_0^{(3)}(V_N T_2)_C + R_0^{(3)} V_N T_1]|\Phi\rangle. \tag{47}$$

We use the usual notation, in which operator V_N is the two-body part of the Hamiltonian in the normal-product form. Clearly, the

$$R_0^{(3)}(V_N T_2)_C|\Phi\rangle \equiv T_3^{[2]}|\Phi\rangle \tag{48}$$

term in eqs (46) and (47) is a CCSD analog of the MBPT(2) wave function contribution due to triples. Thus, the $|\Psi^{\text{CCSD[T]}}\rangle$ wave function,

Downloaded by PENNSYLVANIA STATE UNIV on September 14, 2012 | http://pubs.acs.org
Publication Date: August 14, 2002 | doi: 10.1021/bk-2002-0828.ch003

Downloaded by PENNSYLVANIA STATE UNIV on September 14, 2012 | http://pubs.acs.org
Publication Date: August 14, 2002 | doi: 10.1021/bk-2002-0828.ch003

defining the CR-CCSD[T] approximation, represents a CC analog of the MBPT(2)[SDT] wave function. The $|\Psi^{\mathrm{CCSD(T)}}\rangle$ wave function uses the additional $R_0^{(3)} V_N T_1 |\Phi\rangle$ term, which is reminiscent of the extra term that distinguishes the CCSD(T) approach from its CCSD[T] analog. If we further approximate the $\mathcal{M}_{ijk}^{abc}(2)$ CCSD moments in eqs (44) and (45) by their lowest-order estimates, i.e., $\langle\Phi_{ijk}^{abc}|(V_N T_2)_C|\Phi\rangle$, we obtain the renormalized CCSD[T] and CCSD(T) methods, respectively, or the R-CCSD[T] and R-CCSD(T) approaches. The energy expressions defining the R-CCSD[T] and R-CCSD(T) methods can be given the following form (*7*, *16*, *17*):

$$E^{\mathrm{R\text{-}CCSD[T]}} = E^{\mathrm{CCSD}} + \langle\Psi^{\mathrm{CCSD[T]}}|Q_3\,(V_N T_2)_C|\Phi\rangle / \langle\Psi^{\mathrm{CCSD[T]}}|e^{T_1+T_2}|\Phi\rangle\,, \tag{49}$$

$$E^{\mathrm{R\text{-}CCSD(T)}} = E^{\mathrm{CCSD}} + \langle\Psi^{\mathrm{CCSD(T)}}|Q_3\,(V_N T_2)_C|\Phi\rangle / \langle\Psi^{\mathrm{CCSD(T)}}|e^{T_1+T_2}|\Phi\rangle\,. \tag{50}$$

The R-CCSD[T] and R-CCSD(T) approaches reduce to the standard CCSD[T] and CCSD(T) methods, when the corresponding $\langle\Psi^{\mathrm{CCSD[T]}}|e^{T_1+T_2}|\Phi\rangle$ and $\langle\Psi^{\mathrm{CCSD(T)}}|e^{T_1+T_2}|\Phi\rangle$ denominators in the R-CCSD[T] and R-CCSD(T) energy formulas are replaced by 1 (*7*, *16*, *17*) (as shown in refs 7, 16, both denominators equal 1 plus terms which are at least of the second order). The presence of the $\langle\Psi|e^{T^{(A)}}|\Phi\rangle$ denominators in eqs (44), (45), (49), and (50), and in their analogs describing the renormalized and completely renormalized CCSD(TQ) and CCSDT(Q) methods is essential for improving poor description of bond breaking by the standard noniterative approximations (*7*, *16*–*20*).

The idea of renormalizing the CCSD[T] and CCSD(T) methods can be extended to the CCSD(TQ) and CCSDT(Q) cases. The *completely renormalized CCSD(TQ) methods*, termed CR-CCSD(TQ),a and CR-CCSD(TQ),b, are examples of the MMCC(2,4) scheme, in which we correct the CCSD results by considering the projections of the CCSD equations on triply and quadruply excited configurations. The CR-CCSD(TQ),a and CR-CCSD(TQ),b energies are calculated as follows (*7*, *16*, *17*):

$$\begin{aligned} E^{\mathrm{CR\text{-}CCSD(TQ),x}} = {} & E^{\mathrm{CCSD}} + \langle\Psi^{\mathrm{CCSD(TQ),x}}|[M_3(2) + T_1 M_3(2) \\ & + M_4(2)]|\Phi\rangle / \langle\Psi^{\mathrm{CCSD(TQ),x}}|e^{T_1+T_2}|\Phi\rangle \quad (\mathrm{x} = \mathrm{a,b}), \end{aligned} \tag{51}$$

where

$$|\Psi^{\mathrm{CCSD(TQ),a}}\rangle = |\Psi^{\mathrm{CCSD(T)}}\rangle + \tfrac{1}{2} T_2 T_2^{(1)} |\Phi\rangle \tag{52}$$

and

$$|\Psi^{\mathrm{CCSD(TQ),b}}\rangle = |\Psi^{\mathrm{CCSD(T)}}\rangle + \tfrac{1}{2} T_2^2 |\Phi\rangle, \tag{53}$$

with $T_2^{(1)}$ representing the first-order MBPT estimate of T_2. As in the case of the CR-CCSD[T] and CR-CCSD(T) methods, we can simplify the CR-CCSD(TQ) energy expressions by considering the lowest-order approximations to the $\mathcal{M}_{ijk}^{abc}(2)$ and $\mathcal{M}_{ijkl}^{abcd}(2)$ moments, which enter eq (51) via eqs

(38) and (39), and by dropping the $T_1 M_3(2)$ term in eq (51). This leads to the renormalized CCSD(TQ) methods, referred to as the R-CCSD(TQ)-1,x and R-CCSD(TQ)-2,x (x = a, b) schemes. We refer the reader to the original papers (*7*, *16*, *17*) for further details. In analogy to the relationship between the MMCC-based R-CCSD(T) method and the standard CCSD(T) approach, we can demonstrate that the R-CCSD(TQ)-1,a scheme reduces to the factorized CCSD(TQ$_\mathrm{f}$) approach of ref 12, when the $\langle\Psi^{\mathrm{CCSD(TQ),a}}|e^{T_1+T_2}|\Phi\rangle$ denominator is replaced by 1 in the R-CCSD(TQ)-1,a energy formula. Thus, the R-CCSD(TQ) and CR-CCSD(TQ) approaches can be viewed as extensions of the standard CCSD(TQ$_\mathrm{f}$) method.

Finally, in two variants of the *completely renormalized CCSDT(Q) approach*, referred to as the CR-CCSDT(Q),a and CR-CCSDT(Q),b schemes, which are examples of the MMCC(3,4) approximation, we add the renormalized energy corrections due to T_4 to the CCSDT energy. Thus, if T_1, T_2, and T_3 are cluster operators obtained by solving the CCSDT equations, then the energy expressions defining the CR-CCSDT(Q),a and CR-CCSDT(Q),b approaches are (*7*, *16*, *20*)

$$\begin{aligned} E^{\mathrm{CR\text{-}CCSDT(Q),x}} &= E^{\mathrm{CCSDT}} + \langle\Psi^{\mathrm{CCSDT(Q),x}}|M_4(3)|\Phi\rangle / \\ &\quad \langle\Psi^{\mathrm{CCSDT(Q),x}}|e^{T_1+T_2+T_3}|\Phi\rangle \quad (\mathrm{x} = \mathrm{a}, \mathrm{b}), \end{aligned} \tag{54}$$

where E^{CCSDT} is the CCSDT energy and

$$|\Psi^{\mathrm{CCSDT(Q),a}}\rangle = (1 + T_1 + T_2 + T_3 + T_1T_2 + \tfrac{1}{2}T_2T_2^{(1)})|\Phi\rangle, \tag{55}$$

$$|\Psi^{\mathrm{CCSDT(Q),b}}\rangle = (1 + T_1 + T_2 + T_3 + T_1T_2 + \tfrac{1}{2}T_2^2)|\Phi\rangle. \tag{56}$$

The simpler R-CCSDT(Q),a and R-CCSDT(Q),b (renormalized CCSDT(Q)) methods are obtained by replacing the $\mathcal{M}_{ijkl}^{abcd}(3)$ moments of the CCSDT equations, which enter eq (54) via the relationship between $M_4(3)|\Phi\rangle$ and $\mathcal{M}_{ijkl}^{abcd}(3)$ given by eq (40), by their lowest-order (i.e., third-order-like) estimates that are used to construct the (Q$_\mathrm{f}$) correction of the standard CCSDT(Q$_\mathrm{f}$) method (cf. refs 7, 16, 20 for further details). As in the CCSD(T) and CCSD(TQ) cases, the R-CCSDT(Q),a method reduces to the CCSDT(Q$_\mathrm{f}$) approach of ref 12, when $\langle\Psi^{\mathrm{CCSDT(Q),a}}|e^{T_1+T_2+T_3}|\Phi\rangle$ is replaced by 1 in the R-CCSDT(Q),a energy formula.

The general nature of the MMCC theory, on which all renormalized and completely renormalized CC methods described here are based, allows us to proposed many other potentially useful approximations. We can, for example, introduce the MMCC(2,6) method, in which the CCSD results are corrected by considering all nonzero moments of the CCSD equations, including those corresponding to projections on pentuply and hextuply excited configurations. We can also introduce the active-space variants of the renormalized and completely renormalized CC approaches, in which we consider small subsets of the generalized moments of CC equations defined

Downloaded by PENNSYLVANIA STATE UNIV on September 14, 2012 | http://pubs.acs.org
Publication Date: August 14, 2002 | doi: 10.1021/bk-2002-0828.ch003

via active orbitals. Finally, we can use various non-perturbative choices for the wave function $|\Psi\rangle$ that enters the MMCC(m_A, m_B) energy formula, eq (32). Simple CI wave functions $|\Psi\rangle$ are particularly useful in excited-state MMCC calculations, which we discuss next.

The Excited-State MMCC(m_A, m_B) Methods: MMCC(2,3)

The MMCC(m_A, m_B) energy formula, eq (32), can be used in calculations of excited states, if instead of the generalized moments of the ground-state SRCC equations, $M_j^{\mathrm{CC}}(m_A)|\Phi\rangle$ or $\mathcal{M}_J^{\mathrm{CC},(j)}(m_A)$ (cf. eqs (11) and (12)), we use the generalized moments of the EOMCC equations, i.e., $M_{K,j}^{\mathrm{EOMCC}}(m_A)|\Phi\rangle$ or $\mathcal{M}_{K,J}^{\mathrm{EOMCC},(j)}(m_A)$ (cf. eqs (24) and (25)). The simplest choice of (m_A, m_B), which is particularly useful in calculations for excited states dominated by doubles and excited-state PESs, is obtained by setting m_A at 2 and m_B at 3. In the resulting MMCC(2,3) approximation, we use corrections $\delta_K(m_A, m_B)$, eq (34), to correct the EOMCCSD energies (the $m_A = 2$ case) and assume that wave functions $|\Psi_K\rangle$ do not contain higher–than–triexcited contributions in the corresponding CI expansions (the $m_B = 3$ case). The MMCC(2,3) energy expression is (*98*)

$$E_K(2,3) = E_K^{\mathrm{EOMCCSD}} + \delta_K(2,3), \tag{57}$$

where E_K^{EOMCCSD} is the energy of the K-th state obtained in the EOMCCSD calculations and

$$\delta_K(2,3) = \langle\Psi_K|M_{K,3}^{\mathrm{EOMCC}}(2)|\Phi\rangle / \langle\Psi_K|R_K^{\mathrm{CCSD}} e^{T^{\mathrm{CCSD}}}|\Phi\rangle. \tag{58}$$

The R_K^{CCSD} operator is the EOMCCSD excitation operator (cf. eq (30)) and T^{CCSD} is the CCSD cluster operator ($T^{\mathrm{CCSD}} = T_1 + T_2$). The formula for $M_{K,3}^{\mathrm{EOMCC}}(2)|\Phi\rangle$ can be given the following form (cf. eq (24)):

$$M_{K,3}^{\mathrm{EOMCC}}(2)|\Phi\rangle = \sum_{\substack{i<j<k \\ a<b<c}} \mathcal{M}_{K,ijk}^{abc}(2)|\Phi_{ijk}^{abc}\rangle, \tag{59}$$

where $\mathcal{M}_{K,ijk}^{abc}(2)$ are the EOMCCSD moments corresponding to projections of the EOMCCSD equations on triexcited configurations,

$$\mathcal{M}_{K,ijk}^{abc}(2) = \langle\Phi_{ijk}^{abc}|(\bar{H}^{\mathrm{CCSD}} R_K^{\mathrm{CCSD}})|\Phi\rangle, \tag{60}$$

with $\bar{H}^{\mathrm{CCSD}}$ representing the similarity-transformed Hamiltonian of the EOMCCSD approach, eq. (29). According to eq (26),

$$\mathcal{M}_{K,ijk}^{abc}(2) = r_{K,0}^{\mathrm{CCSD}} \langle\Phi_{ijk}^{abc}|\bar{H}^{\mathrm{CCSD}}|\Phi\rangle + \langle\Phi_{ijk}^{abc}|\left(\bar{H}_{\mathrm{open}}^{\mathrm{CCSD}} R_{K,\mathrm{open}}^{\mathrm{CCSD}}\right)_C|\Phi\rangle, \tag{61}$$

Downloaded by PENNSYLVANIA STATE UNIV on September 14, 2012 | http://pubs.acs.org
Publication Date: August 14, 2002 | doi: 10.1021/bk-2002-0828.ch003

Downloaded by PENNSYLVANIA STATE UNIV on September 14, 2012 | http://pubs.acs.org
Publication Date: August 14, 2002 | doi: 10.1021/bk-2002-0828.ch003

where $r_{K,0}^{\mathrm{CCSD}}$ is the coefficient at reference $|\Phi\rangle$ in the many-body expansion of $R_K^{\mathrm{CCSD}}|\Phi\rangle$. It can be shown (*98*) that

$$\mathcal{M}_{K,ijk}^{abc}(2) = \langle\Phi_{ijk}^{abc}|(\bar{H}_2^{\mathrm{CCSD}} R_{K,2})_C|\Phi\rangle + \langle\Phi_{ijk}^{abc}|[\bar{H}_3^{\mathrm{CCSD}}(R_{K,1} + R_{K,2})]_C|\Phi\rangle \\ +\langle\Phi_{ijk}^{abc}|(\bar{H}_4^{\mathrm{CCSD}} R_{K,1})_C|\Phi\rangle + r_{K,0}^{\mathrm{CCSD}}\langle\Phi_{ijk}^{abc}|\bar{H}^{\mathrm{CCSD}}|\Phi\rangle, \qquad (62)$$

where $\bar{H}_j^{\mathrm{CCSD}}$ is the j-body component of $\bar{H}^{\mathrm{CCSD}}$ and $R_{K,1}$ and $R_{K,2}$ are the singly and doubly excited components of R_K^{CCSD}. It immediately follows from eq (62) that corrections $\delta_K(2,3)$ are expressed in terms of matrix elements of the EOMCCSD similarity-transformed Hamiltonian that enter the triples-reference (T0), triples-singles (TS), and triples-doubles (TD) blocks of $\bar{H}^{\mathrm{CCSD}}$. *The triples-triples (TT) block of $\bar{H}^{\mathrm{CCSD}}$ does not enter the MMCC(2,3) energy formula.* This characteristic of the MMCC(2,3) approximation makes this approach particularly appealing to us. Very similar arguments can be used to demonstrate that the MMCC(2,4) approximation, in which the EOMCCSD energies are corrected by considering projections of the EOMCCSD equations on triply and quadruply excited configurations, requires a consideration of the T0, TS, TD, Q0, QS, and QD blocks of $\bar{H}^{\mathrm{CCSD}}$ in calculating the corresponding corrections $\delta_K(2,4)$.

In analogy to the ground-state case, different variants of the MMCC(2,3) approximation are obtained by choosing different forms of $|\Psi_K\rangle$ in eq (58). An interesting possibility is offered by the active-space CISDt approach (*7, 98*). In order to calculate the CISDt wave functions, we divide the available spin-orbitals into core spin-orbitals (**i**, **j**, **k**, ...), active spin-orbitals occupied in $|\Phi\rangle$ (**I**, **J**, **K**, ...), active spin-orbitals unoccupied in $|\Phi\rangle$ (**A**, **B**, **C**, ...), and virtual spin-orbitals (**a**, **b**, **c**, ...). Once active orbitals are selected, we define the CISDt wave functions as follows (*7, 98*):

$$|\Psi_K^{\mathrm{CISDt}}\rangle = (C_{K,0} + C_{K,1} + C_{K,2} + c_{K,3})|\Phi\rangle, \qquad (63)$$

where $C_{K,0}|\Phi\rangle$, $C_{K,1}|\Phi\rangle$, and $C_{K,2}|\Phi\rangle$ are the reference, singly excited, and doubly excited components of $|\Psi_K^{\mathrm{CISDt}}\rangle$ and

$$c_{K,3} = \sum_{\substack{\mathbf{I}>j>k \\ a>b>\mathbf{C}}} c_{\mathbf{I}jk}^{ab\mathbf{C}}(K)\,|\Phi_{\mathbf{I}jk}^{ab\mathbf{C}}\rangle. \qquad (64)$$

Thus, in the CISDt method, we construct wave functions $|\Psi_K\rangle$ by including all singles and doubles from $|\Phi\rangle$ and a small set of triples containing at least one active occupied and one active unoccupied spin-orbital indices. The CI expansion coefficients defining wave functions $|\Psi_K^{\mathrm{CISDt}}\rangle$ are determined variationally. If N_o (N_u) is the number of active orbitals occupied (unoccupied) in $|\Phi\rangle$ and if n_o (n_u) is the number of all occupied (unoccupied) orbitals, then the number of triples included in the CISDt calculations is $N_oN_un_o^2n_u^2$,

American Chemical Society
Library
1155 16th St., N.W.
Washington, D.C. 20036

which is a relatively small prefactor times the number of doubles. Thus, the CISDt approach provides us with an inexpensive source of wave functions $|\Psi_K\rangle$ for calculating corrections $\delta_K(2,3)$.

The CISDt approach, used to generate wave functions $|\Psi_K\rangle$ for the MMCC(2,3) calculations, can be regarded as a CI analog of the recently developed EOMCCSDt method (*40*, *41*). The noniterative character of the MMCC(2,3) method and the fact that the CISDt calculations are less expensive than the EOMCCSDt calculations means that the CISDt-based MMCC(2,3) approximation represents a useful and inexpensive alternative to the already relatively inexpensive EOMCCSDt method. The MMCC(2,3) approach is an alternative to the perturbative triples approaches, such as EOMCCSD(T) (*31*), EOMCCSD($\tilde{T}$) (*32*), EOMCCSD(T′) (*32*), and CCSDR(3) (*36*, *37*), and their iterative EOMCCSDT-*n* (*31*, *32*) and CC3 (*34*–*37*) analogs. The perturbative triples EOMCC or response CC approximations provide erroneous description of excited-state PESs (*38*) and fail to describe more complicated excited states, such as the lowest $^1\Delta$ state of the C_2 molecule (*37*). As demonstrated below, the CISDt-based MMCC(2,3) method has no such problems.

Downloaded by PENNSYLVANIA STATE UNIV on September 14, 2012 | http://pubs.acs.org
Publication Date: August 14, 2002 | doi: 10.1021/bk-2002-0828.ch003

Representative MMCC Calculations for Ground- and Excited-State PESs

In this section, we discuss the performance of the MMCC and renormalized CC methods in calculations of molecular PESs.

Ground-State PESs Involving Bond Breaking

We have performed a series of test MMCC calculations for ground-state PESs of several small molecules, including HF (*7*, *16*), H_2O (*16*), BH (*19*), F_2 (*19*), N_2 (*17*, *20*), and C_2 (this work). The representative results are shown in Figure 1. We have also calculated the entire vibrational spectrum of the HF molecule, based on the PESs obtained in the renormalized CC calculations (*101*) (see Table I). In all calculations, we used the ground-state RHF configuration as a reference. The most intriguing result is the fact that unlike the standard CCSD[T], CCSD(T), CCSD(TQ$_f$), and CCSDT(Q$_f$) methods, their MMCC-based CR-CCSD[T], CR-CCSD(T), CR-CCSD(TQ), and CR-CCSDT(Q) counterparts are capable of describing bond breaking, in spite of the presence of the MBPT-like terms in the CR-CCSD[T], CR-CCSD(T), CR-CCSD(TQ), and CR-CCSDT(Q) expressions (cf. eqs. (44), (45), (51), and (54)). The presence of similar terms in the conventional CCSD[T], CCSD(T), CCSD(TQ$_f$), and CCSDT(Q$_f$) expressions leads to erroneous description of PESs due to divergent behavior of the MBPT series at large internuclear separations (cf., e.g., refs 6, 7, 13–20, and references therein).

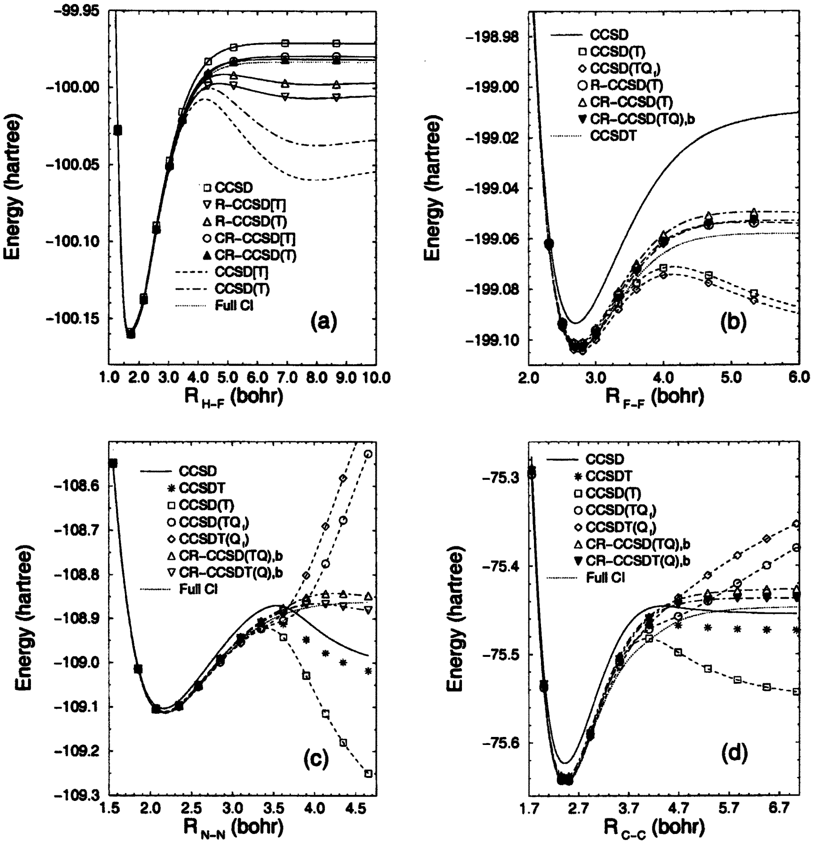

Figure 1. Potential energy curves for the double-zeta (DZ) HF (a), N_2 (c), and C_2 (d) molecules, and the cc-pVDZ F_2 molecule (b) (see refs 7, 16, 17, 19, 20 for the numerical data for HF, N_2, and F_2, and see the text for further details).

As shown in Figure 1 (a), the simple CR-CCSD(T) method eliminates the unphysical hump on the PES for the HF molecule, produced by the CCSD(T) approach at intermediate internuclear distances *R*. The CR-CCSD(T) potential energy curve is located above the exact (full CI) curve. For the double zeta (DZ) (*102*) basis set, the errors in the CR-CCSD(T) energies, relative to full CI, do not exceed 2 milihartree over

Downloaded by PENNSYLVANIA STATE UNIV on September 14, 2012 | http://pubs.acs.org
Publication Date: August 14, 2002 | doi: 10.1021/bk-2002-0828.ch003

the entire range of R values (*7*, *16*). For the considerably larger aug-cc-pVTZ basis set (*103*, *104*), the errors in the CR-CCSD(T) energies, relative to full CCSDT (the full CCSDT approach is almost exact for single bond breaking (*14*, *85*)), do not exceed 3.9 milihartree (*101*). The CR-CCSD(T) results for geometries near the equilibrium ($R \approx R_e$), where the CCSD(T) method works great, are virtually identical to those obtained with the CCSD(T) approach (at $R = R_e$ and for the DZ basis set, the CCSD(T) method gives a 0.325 milihartree error, which should be compared to a 0.500 milihartree error obtained with CR-CCSD(T) (*7*, *16*)). Even the simplest R-CCSD[T] and R-CCSD(T) approaches, which differ from the standard CCSD[T] and CCSD(T) methods only by the presence of the $\langle\Psi^{\text{CCSD[T]}}|e^{T_1+T_2}|\Phi\rangle$ and $\langle\Psi^{\text{CCSD(T)}}|e^{T_1+T_2}|\Phi\rangle$ denominators in the corresponding energy expressions, provide considerable improvements in the calculated PESs (see Figure 1 (a)).

Similar remarks apply to the CR-CCSD(T), CR-CCSD(TQ), and CR-CCSDT(Q) results for other benchmark systems (H_2O, BH, F_2, N_2). For example, when both O–H bonds in H_2O are simultaneously stretched to $R = 2R_e$, so that the T_3 and T_4 effects become large and difficult to describe, the CCSD(T) and CCSD(TQ$_\text{f}$) approaches completely fail. For a DZ basis set, errors in the CCSD(T) and CCSD(TQ$_\text{f}$) results, relative to full CI, are 7.699 and 5.914 milihartree, respectively. The CR-CCSD(T) and CR-CCSD(TQ) methods reduce these large errors to 1.830 and 1.461 milihartree, respectively, with almost no extra effort (*16*). At the same time, the CR-CCSD(T) and CR-CCSD(TQ) results are virtually identical to their CCSD(T) and CCSD(TQ$_\text{f}$) analogs at $R = R_e$. For another challenging case of the F_2 molecule, the CCSD method produces a minimum, which is nearly twice as deep as the minimum on the practically exact CCSDT curve, whereas the CCSD(T) and CCSD(TQ$_\text{f}$) methods give completely erroneous PESs, with well-pronounced humps for intermediate values of R and with energies at large R values that are almost identical to the energy at the equilibrium geometry (*19*). The CR-CCSD(T) and CR-CCSD(TQ) methods provide potential energy curves, which are very close to the CCSDT curve (see Figure 1 (b)). For the cc-pVDZ basis set, used in the benchmark study of F_2, the reference CCSDT value of the dissociation energy D_e is 28.19 kcal/mol. The CCSD calculation gives 53.13 kcal/mol. Our R-CCSD(T), CR-CCSD(T), and CR-CCSD(TQ) methods using RHF orbitals give 28.46, 30.92, and 28.60 kcal/mol, respectively, in excellent agreement with the CCSDT value of D_e (*19*). The recently proposed VOD(2) and OD(2) approximations (*89*, *90*), which include the effects of both T_3 and T_4 clusters through the perturbative expansion for the similarity-transformed Hamiltonian and which require orbital optimization at the CC level, give 33.3 and 33.0 kcal/mol, respectively (*90*). These results are considerably worse than our results obtained with the much simpler R-CCSD(T) and CR-CCSD(T) approaches, which use only T_3 corrections and do not require

Downloaded by PENNSYLVANIA STATE UNIV on September 14, 2012 | http://pubs.acs.org
Publication Date: August 14, 2002 | doi: 10.1021/bk-2002-0828.ch003

orbital optimization. Similar remarks apply to the equilibrium bond lengths for F_2, which for the cc-pVDZ basis set are 2.73, 2.74, and 2.74 bohr for the (C)R-CCSD(T), (C)R-CCSD(TQ), and CCSDT methods, respectively (*19*), and ~ 2.8 bohr for the OD(2) and VOD(2) approaches (*90*).

The next example is a dissociation of the triple bond in the N_2 molecule (*17*, *20*) (see Figure 1 (c)). The N_2 molecule is characterized by large T_3 and T_4 effects, even at $R = R_e$. For the stretched N–N distances R, the CCSD potential energy curve has an unphysical hump and is located significantly below the exact (full CI) curve. The orbital optimization at the CC doubles level via the so-called VOO-CCD approach does not help at all: The VOO-CCD potential energy curve for N_2 is as bad as the CCSD curve (*88*). Even the full CCSDT method fails to provide a realistic description of the PES of N_2. The CCSDT curve has a hump for the intermediate values of R, and for larger values of R is located significantly below the exact and CCSD curves (see Figure 1 (c)). This implies the need for T_4 (perhaps, even T_5 and T_6) clusters in this case. The inclusion of T_3 and T_4 clusters via perturbative CCSD(T), CCSD(TQ_f), and CCSDT(Q_f) approximations leads to disastrous results at large internuclear separations. The CCSD(T) curve has a huge hump for the intermediate values of R, and for larger values of R is located significantly below the exact and CCSD curves. The CCSD(TQ_f) and CCSDT(Q_f) curves are located significantly above the exact curve for larger R values (see Figure 1 (c)). In view of the failure of all standard CC methods for N_2, it is remarkable to observe the great improvement of the results, when the noniterative CC methods are renormalized according to the MMCC theory. As shown in Figure 1 (c), the CR-CCSD(TQ),b method, which is a simple modification of the CCSD(TQ_f) approach and which, as the latter method, uses elements of MBPT to estimate higher-order effects, provides the potential energy curve which is almost identical to the exact curve. A large 334.985 milihartree error relative to full CI, obtained with the CCSD(TQ_f) approach for a DZ basis set at $R = 2.25R_e$, reduces to 14.796 milihartree, when the CR-CCSD(TQ),b method is employed (*17*). The 177.641 milihartree error relative to full CI, obtained at $R = 2R_e$ with the CCSDT(Q_f) method, reduces to 1.161 milihartree, when the CR-CCSDT(Q),b approach is used (*20*). The CR-CCSDT(Q),b PES of N_2 is very close to and above the full CI curve in the entire $R \leq 2R_e$ region (see Figure 1 (c)). In this region, the differences between the CR-CCSDT(Q),b and full CI energies do not exceed 7.6 milihartree and are as small as 0.719 milihartree at $R = R_e$ and 1.161 milihartree at $R = 2R_e$ (*20*).

An interesting example is provided by the C_2 molecule, which is characterized by the large T_n, $n > 2$, effects already at the equilibrium geometry. The effect of T_3 clusters at $R = R_e$, as measured by the difference between the CCSDT and CCSD energies, is 18.593 milihartree, when the DZ basis set is employed. The difference between the CCSDT and full CI energies at $R = R_e$ is 2.091 milihartree, which indicates that T_4 clusters play a nonnegligible role, too. As in the case of N_2, all standard CC approaches, including

Downloaded by PENNSYLVANIA STATE UNIV on September 14, 2012 | http://pubs.acs.org
Publication Date: August 14, 2002 | doi: 10.1021/bk-2002-0828.ch003

the iterative CCSD and CCSDT methods and their perturbative CCSD(T), CCSD(TQ$_f$), and CCSDT(Q$_f$) extensions, fail to provide a correct description of the PES of C_2 (see Figure 1 (d)). The CCSD, CCSD(T), and full CCSDT PESs have well-pronounced humps for the intermediate values of R. At $R = 3R_e$, the errors in the CCSD(T), CCSD(TQ$_f$), and CCSDT(Q$_f$) energies, relative to full CI, are 96.055, 67.237, and 94.229 milihartree, respectively, when a DZ basis set is employed. The CR-CCSD(TQ),b and CR-CCSDT(Q),b approaches reduce these errors to 20.282 and 10.052 milihartree, respectively. Even the simple R-CCSDT(Q),b method, which differs from the standard CCSDT(Q$_f$) approach only by the presence of the $\langle\Psi^{\mathrm{CCSDT(Q)}}|e^{T_1+T_2+T_3}|\Phi\rangle$ denominator in the corresponding energy expression, provides excellent results (the 8.834 milihartree error at $R = 3R_e$). The CR-CCSD(TQ),b and CR-CCSDT(Q),b potential energy curves of C_2 are considerably better than curves provided by all standard CC methods. The R-CCSDT(Q),b curve is virtually identical to the CR-CCSDT(Q),b curve and for this reason is not shown in Figure 1 (d).

Table I. Selected vibrational term values and dissociation energies of the HF molecule[a]

v	*RKR*[b]	*CCSD*	*CCSDT*	*CCSD(T)*	*R-CCSD(T)*	*CR-CCSD(T)*
0	2051	15	-7	-7	-4	-3
1	6012	52	-19	-18	-9	-4
2	9802	96	-28	-25	-9	-2
3	13424	144	-36	-32	-9	2
5	20182	252	-54	-47	-6	12
10	34363	623	-116	-136	1	49
11	36738	728	-131	-175	1	60
12	38955	850	-148	-232	-2	72
13	41007	993	-166		-9	87
15	44576	1370	-207		-55	123
19	49027	2881	-325			227
D_e	49362	5847	-453			207

[a] Units are cm^{-1}, v is the vibrational quantum number, and D_e is the dissociation energy. All CC values represent errors in the calculated energies relative to the RKR data. All CC calculations were performed with the aug-cc-pVTZ basis set (103, 104). The spherical components of the d orbitals were employed and the lowest orbital was kept frozen. The complete description of these CC calculations has been reported elsewhere (101).

[b] Vibrational term values from ref 105. The D_e value from refs 106, 107.

Encouraged by the results of the above benchmark calculations, we have recently performed more realistic calculations for the potential energy curve

Downloaded by PENNSYLVANIA STATE UNIV on September 14, 2012 | http://pubs.acs.org
Publication Date: August 14, 2002 | doi: 10.1021/bk-2002-0828.ch003

and vibrational term values of the HF molecule using the aug-cc-pVTZ basis set (*103*, *104*) (see Table I). As we can see, the simple, noniterative CR-CCSD(T) method reduces the 5847 cm^{-1} (0.72 eV) error in the dissociation energy D_e obtained with the CCSD approach, to 0.03 eV (the experimental value of D_e is 6.12 eV). The expensive and fully iterative CCSDT method gives the 453 cm^{-1} or 0.06 eV error. The standard noniterative approximations, such as CCSD(T), do not support bound vibrational states with $v > 12$ and errors in the CCSD(T) vibrational term values rapidly increase, from a few cm^{-1} for $v = 0$ to more than 230 cm^{-1} for $v = 12$. The simplest way of renormalizing CCSD(T) via the R-CCSD(T) approach provides excellent vibrational term values, which differ from the RKR values (*105*) by as little as 1-9 cm^{-1} for $v \leq 13$ (the energy of the $v = 13$ level is $\sim 41,000$ cm^{-1} !). The noniterative CR-CCSD(T) method reduces the 2881 cm^{-1} and 325 cm^{-1} errors in the CCSD and full CCSDT results, respectively, for the $v = 19$ state of HF (energy of this highest observed state is 49,027 cm^{-1}) to 227 cm^{-1}. *None of the existing methods can provide the results of similar quality with such a small effort. In fact, it would be difficult to obtain the results of this high quality with a lot more demanding multireference approaches.* The analogous R-CCSD(TQ) and CR-CCSD(TQ) results for HF have been discussed in our recent paper (*101*). For example, the CR-CCSD(TQ),a and CR-CCSD(TQ),b approaches give the 135 and 159 cm^{-1} errors, respectively, for the $v = 19$ state. Moreover, the CR-CCSD(TQ),b method predicts the existence of the $v = 20$ energy level to be located 28 cm^{-1} below the corresponding dissociation limit. The most accurate potential function for HF to date, obtained using the hybrid RKR-based theoretical approach (RKR plus improved long-range plus very accurate and expensive *ab initio* calculations), produces the $v = 20$ level with the energy of 23 cm^{-1} below the dissociation limit (*106*, *107*).

Although we have focused in this section on the ground-state MMCC methods employing the MBPT-like guesses for $|\Psi_0\rangle$, we can also use inexpensive CI approximations, such as the aforementioned CISDt approach (cf. eq (63)), to generate $|\Psi_0\rangle$. For example, when the CISDt ground-state wave function is inserted into the MMCC(2,3) energy expression (cf. eq (35)) and the resulting MMCC(2,3)/CISDt approach is applied to a DZ HF molecule, the 12.291 and 33.642 milihartree errors, relative to full CI, produced by the CCSD and CISDt methods, respectively, at $R = 5R_e$, reduce to 3.264 milihartree (*7*). As demonstrated in the next subsection, this new way of grafting CI onto the CC method is particularly successful when we apply the MMCC formalism to excited states.

Excited-State PESs

We have performed a series of MMCC(2,3)/CISDt calculations for vertical excitation energies of H_2O, N_2, and C_2 (this work), and for the entire

Downloaded by PENNSYLVANIA STATE UNIV on September 14, 2012 | http://pubs.acs.org
Publication Date: August 14, 2002 | doi: 10.1021/bk-2002-0828.ch003

Downloaded by PENNSYLVANIA STATE UNIV on September 14, 2012 | http://pubs.acs.org
Publication Date: August 14, 2002 | doi: 10.1021/bk-2002-0828.ch003

PESs of ground and excited states of the CH^+ ion (*98*). The results are summarized in Table II and Figure 2.

Table II. Vertical excitation energies[a] of H_2O, N_2, and C_2

Molecule	*State*	*Full CI*[b]	*EOMCCSD*[b]	*CC3*[b]	*EOMCCSDt*[c,d]	*MMCC(2,3)*[d]
H_2O	$2\,^1A_1$	362.87	360.362	362.27	361.078	362.151
	$1\,^1B_1$	273.68	271.027	272.95	271.790	272.828
	$1\,^1B_2$	426.72	423.523	425.97	424.206	425.464
	$1\,^1A_2$	338.49	335.243	337.62	335.862	337.121
N_2	$^1\Pi_g$	352.22	355.179	353.44	353.271	356.281
	$^1\Sigma_u^-$	379.57	384.567	379.84	379.406	379.723
	$^1\Delta_u$	393.89	400.508	394.21	393.919	394.610
	$^1\Pi_u$	500.10	514.824	506.62	503.413	510.315
C_2	$^1\Pi_u$	50.89	54.183	48.38	48.598	47.474
	$^1\Delta_g$	84.26	159.741	115.82	94.134	88.406
	$^1\Sigma_u^+$	205.88	213.105	204.14	208.992	204.621
	$^1\Pi_g$	165.15	227.912	183.39	167.936	164.176

[a] Units are milihartree. The basis set and nuclear geometries were taken from ref 37. The lowest-energy core orbitals (the $1a_1$ orbital in H_2O, the $1\sigma_g$ and $1\sigma_u$ orbitals in N_2 and C_2) were kept frozen.

[b] From ref 37 (see, also, ref 41 for the EOMCCSD results). The spherical components of the *d* orbitals were employed.

[c] From ref 41.

[d] The Cartesian *d* orbitals were employed. The active space used in the calculations for H_2O consisted of the $1b_1$, $3a_1$, $1b_2$, $4a_1$, and $2b_1$ orbitals. The active space used in the calculations for N_2 consisted of the $3\sigma_g$, $1\pi_u$, $2\pi_u$, $1\pi_g$, $2\pi_g$, and $3\sigma_u$ orbitals. The active space used in the calculations for C_2 consisted of the $1\pi_u$, $2\pi_u$, $3\sigma_g$, $3\sigma_u$, $1\pi_g$, and $2\pi_g$ orbitals.

The H_2O, N_2, and C_2 molecules provide us with examples of several important types of excited states, including states that are dominated by single excitations in a situation where the CCSD method gives accurate description of the ground state (H_2O), states that are dominated by singles in a situation where the CCSD method gives a poorer representation of the ground state (N_2 and C_2), and complicated excited states dominated by doubles in a situation where the T_3 and T_4 clusters are large and CCSD provides poor description of the ground state (C_2). We used our MMCC(2,3)/CISDt approach to calculate the lowest excited $^1A_1$ ($2\,^1A_1$) state and the lowest $^1B_1$, $^1B_2$, and $^1A_2$ states of H_2O, the lowest $^1\Pi_g$, $^1\Sigma_u^-$, $^1\Delta_u$, and $^1\Pi_u$ states of N_2, and the lowest $^1\Pi_u$, $^1\Delta_g$, $^1\Sigma_u^+$, and $^1\Pi_g$ states of C_2. The corresponding full CI excitation energies were calculated by

Christiansen *et al.* (*37*), who used the modified aug-cc-pVDZ basis sets (*103*, *104*) for H_2O and C_2, and the cc-pVDZ basis set (*103*) for N_2 (for further details about basis sets and equilibrium nuclear geometries used in these full CI calculations, see ref 37). In our MMCC(2,3) calculations, we used the same basis sets, although we had to use the Cartesian components of the *d* orbitals, instead of the spherical components used in ref 37; as explained in ref 41, the effect of using the Cartesian *d*'s on the calculated excitation energies is minor (0.05–0.34 milihartree for H_2O, 0.26–1.06 milihartree for N_2, and 0.11–0.70 milihartree for C_2). As in ref 37, the lowest-energy core orbitals were kept frozen (see Table II).

In Table II, our MMCC(2,3) results are compared with the EOMCCSD and CC3 excitation energies reported in ref 37 and with the EOMCCSDt excitation energies reported in ref 41. The EOMCCSDt approach is the EOMCC method, in which relatively small subsets of triexcited components of cluster operator T and excitation operator R are selected through active orbitals (*40*, *41*). The manifold of triexcited configurations used in the EOMCCSDt method is identical to that used in the CISDt calculations. This remark is important, since the CISDt wave functions $|\Psi_K^{\rm CISDt}\rangle$, eq (63), are used to calculate the MMCC(2,3) corrections $\delta_K(2,3)$, eq (58). The active orbitals used in MMCC(2,3)/CISDt and EOMCCSDt calculations for H_2O, N_2, and C_2 are listed in footnote *d* of Table II. They were chosen on the basis of their importance in describing the valence excited states of H_2O, N_2, and C_2. The number of triples used in MMCC(2,3)/CISDt and EOMCCSDt calculations reported here is a small fraction of all triples ($\sim$ 20 % in the H_2O case, one third in the N_2 case, and $\sim$ 30 % in the C_2 case). This means that the cost of calculating the MMCC(2,3) correction $\delta_K(2,3)$ is small compared to EOMCC and other schemes that use all triples.

The results in Table II show that the valence excitations in H_2O are rather easy to describe by all EOMCC methods. This is a consequence of the fact that all these states are dominated by singles. The errors in the EOMCCSD excitation energies, relative to full CI, for the lowest excited state of the $^1A_1$ symmetry and the lowest $^1B_1$, $^1B_2$, and $^1A_2$ states range between 2.5 and 3.2 milihartree (0.07–0.09 eV), which is a very good result. The iterative CC3 approximation, in which triples effects are estimated using perturbation theory, reduces these small errors to 0.6–0.9 milihartree ($\sim$ 0.02 eV). The full EOMCCSDt method, which uses a small subset of all triples defined through active orbitals, gives the 1.8–2.6 milihartree (0.05–0.07 eV) errors. Our noniterative MMCC(2,3) approach, which uses inexpensive CISDt wave functions to calculate corrections $\delta_K(2,3)$, which are in turn added to EOMCCSD energies, reduces the 2.5–3.2 milihartree errors in the EOMCCSD results to 0.7–1.4 milihartree (0.02–0.04 eV).

The N_2 molecule represents a more challenging case than H_2O. The ground state of N_2 is characterized by relatively large T_3 contributions (for the cc-pVDZ basis set used here, the difference between the CCSD and full CI ground-state energies is 13.465 milihartree (*37*); for comparison, the

Downloaded by PENNSYLVANIA STATE UNIV on September 14, 2012 | http://pubs.acs.org
Publication Date: August 14, 2002 | doi: 10.1021/bk-2002-0828.ch003

difference between the CCSDT and full CI ground-state energies is as little as 1.627 milihartree (*41*)). In addition, the lowest $^1\Pi_u$ state of N_2 has a partially doubly excited character (*37*). In consequence, the errors in the EOMCCSD excitation energies, relative to full CI, are considerably larger than in the case of H_2O (they range between 3.0 and 14.7 milihartree; cf. Table II). For the lowest $^1\Pi_u$ state, the EOMCCSD and full CI energies differ by 14.7 milihartree (0.40 eV). The CC3 and MMCC(2,3) methods reduce this large error to 6.5 and 10.2 milihartree, respectively (0.18 and 0.28 eV, respectively). The EOMCCSDt approach is in this case the only method that is capable of reducing the large error in the EOMCCSD result for the lowest $^1\Pi_u$ state of N_2 to < 0.1 eV. It is encouraging to see, though, that the MMCC(2,3) approach is capable of improving the EOMCCSD result for the $^1\Pi_u$ state of N_2. The improvements in the results for the remaining three states listed in Table II are worth noticing here, too. The MMCC(2,3) method reduces the 3.0–6.6 milihartree errors in the EOMCCSD results for the $^1\Pi_g$, $^1\Sigma_u^-$, and $^1\Delta_u$ states to 0.2–4.1 milihartree. The MMCC(2,3) results for the $^1\Sigma_u^-$ and $^1\Delta_u$ states, which are dominated by singles, are virtually identical to the CC3 and EOMCCSDt results.

The most spectacular improvements in the EOMCCSD results and in the results of the calculations with the perturbative triples models, such as CC3, are obtained for the excited states of C_2. In this case, the lowest $^1\Delta_g$ and $^1\Pi_g$ states are dominated by doubles. In addition, the correlation effects characterizing the ground state of C_2 are largely nondynamic, which is reflected in the large T_3 and T_4 contributions to the ground-state energy (26.3 and 2.7 milihartree, respectively (*85*)). This leads to a complete failure of the EOMCCSD and CC3 approximations. For the vertical excitation energy corresponding to the transition from the ground state ($X\ ^1\Sigma_g^+$) to the lowest $^1\Delta_g$ state, the error in the EOMCCSD result, relative to full CI, is 75.5 milihartree ($>$ 2 eV; see Table II). This error is almost as big as the full CI value of the $X\ ^1\Sigma_g^+ \rightarrow 1\ ^1\Delta_g$ excitation energy, which is 2.293 eV. The otherwise successful CC3 method gives a large, 31.6 milihartree (0.86 eV), error. The $X\ ^1\Sigma_g^+ \rightarrow 1\ ^1\Pi_g$ transition is also difficult to describe by the EOMCC and response CC methods. The EOMCCSD approach gives a large, $>$ 1.7 eV error, relative to a full CI value of the corresponding excitation energy of 4.494 eV. The CC3 method reduces this error to still large 0.50 eV. The active-space EOMCCSDt approach greatly improves these poor results by reducing the large errors in the EOMCCSD and CC3 results to 9.9 milihartree (0.27 eV), for the lowest $^1\Delta_g$ state, and 2.8 milihartree (0.08 eV) for the lowest $^1\Pi_g$ state. It is remarkable to observe that our new MMCC(2,3)/CISDt approximation, employing a small ($\sim$ 30 %) fraction of all triples in constructing noniterative corrections $\delta_K(2,3)$, gives a small, 4.1 milihartree (0.11 eV), error in the excitation energy for the lowest $^1\Delta_g$ state and even smaller, 1.0 (0.03 eV), error in the excitation energy for the lowest $^1\Pi_g$ state. We should keep in mind that we do not even have

Downloaded by PENNSYLVANIA STATE UNIV on September 14, 2012 | http://pubs.acs.org
Publication Date: August 14, 2002 | doi: 10.1021/bk-2002-0828.ch003

to consider the TT block of the EOMCCSD similarity-transformed Hamiltonian to obtain these accurate MMCC(2,3) results. For the remaining two states of C_2, which are dominated by singles, the MMCC(2,3) results are as good as those obtained with the CC3 method.

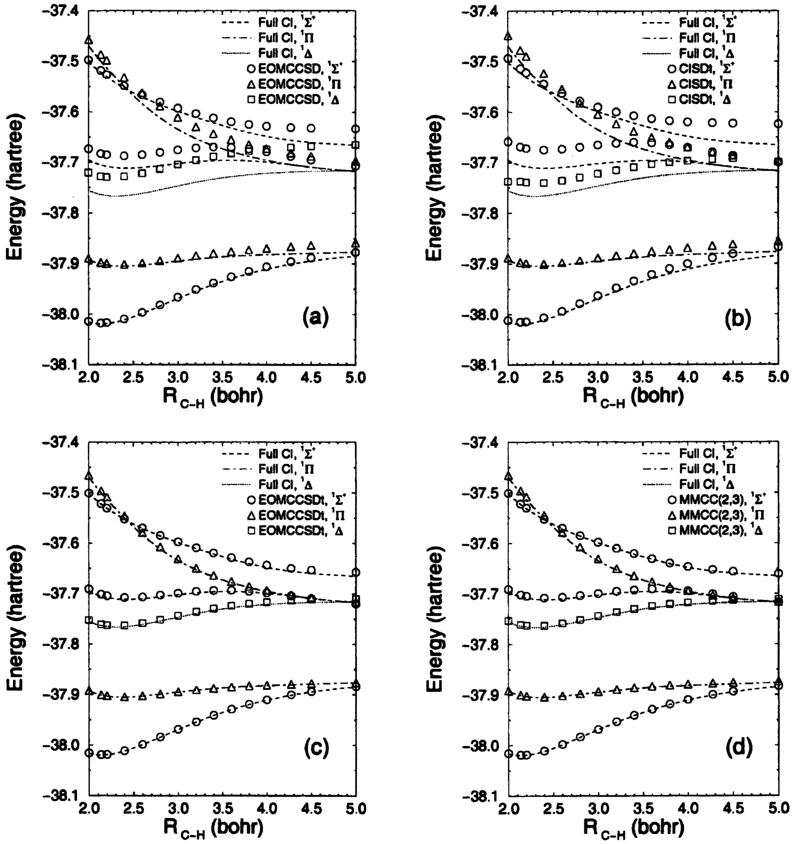

Figure 2. Potential energy curves for the CH^+ ion. (a) A comparison of the EOMCCSD and full CI results. (b) A comparison of the CISDt and full CI results. (c) A comparison of the EOMCCSDt and full CI results. (d) A comparison of the MMCC(2,3) and full CI results (see refs 41, 97, 98 for the numerical data and see the text for further details).

The final example is provided by the CH^+ ion (see Figure 2). The results of the full CI calculations for the ground state and for a few excited states of the $^1\Sigma^+$, $^1\Pi$, and $^1\Delta$ symmetries can be found in refs 108 (the equilibrium geometry, $R_{C-H} = R_e$) and 39 (other values of R_{C-H}, including $1.5R_e$

Downloaded by PENNSYLVANIA STATE UNIV on September 14, 2012 | http://pubs.acs.org
Publication Date: August 14, 2002 | doi: 10.1021/bk-2002-0828.ch003

and $2R_e$). These authors used the [$5s3p1d/3s1p$] basis set described in ref 108. The same basis set was used in the MMCC(2,3)/CISDt calculations reported in ref 98 and overviewed here. In calculating the CISDt wave functions, used to generate the $|\Psi_K\rangle$ states for the MMCC(2,3) calculations, we employed a small active space consisting of the highest-energy occupied orbital, 3σ, and the three lowest-energy unoccupied orbitals, $1\pi_x$, $1\pi_y$, and 4σ. This choice of active space reflects the nature of the orbital excitations that define the valence excited states of CH^+ (*40*, *41*).

As explained in ref 98, the only other EOMCC-related approach that can compete with the noniterative MMCC(2,3) method is the iterative EOMCCSDt method (the EOMCCSDT approach is competitive, too (*41*, *97*), but we must keep in mind that the cost of the full EOMCCSDT calculations is considerably higher). Thus, in our discussion we focus on a comparison of the MMCC(2,3) results with those obtained with the EOMCCSD approach, which the MMCC(2,3) method should correct (see Figure 2 (a)), with those obtained with the CISDt method, which is used to generate the $|\Psi_K\rangle$ wave functions for calculating corrections $\delta_K(2,3)$ (see Figure 2 (b)), and with those obtained in the full EOMCCSDt calculations (*41*, *97*), in which we used the same active space as used in the MMCC(2,3) calculations (see Figure 2 (c)). The MMCC(2,3) results for the PESs of the three lowest $^1\Sigma^+$ states, two lowest $^1\Pi$ states, and the lowest $^1\Delta$ state are shown in Figure 2 (d). The more complete set of the EOMCCSD, EOMCCSDt, and MMCC(2,3)/CISDt results for the four lowest $^1\Sigma^+$ states, two lowest $^1\Pi$ states, and two lowest $^1\Delta$ states and several nuclear geometries can be found in refs 41, 97, 98. The results for $R_{\mathrm{C-H}} = R_e$ obtained by other authors with the perturbative triples methods, including the noniterative EOMCCSD(T), EOMCCSD($\tilde{\mathrm{T}}$), and EOMCCSD(T′) approaches and the iterative EOMCCSDT-*n* and CC3 models, which are worse than those obtained with MMCC(2,3) and EOMCCSDt, can be found elsewhere (*31*, *32*, *35*, *36*). The full EOMCCSDT results for $R_{\mathrm{C-H}} = R_e$, $1.5R_e$, and $2R_e$ will be reported in the future publication (*97*).

We begin our discussion with the results for $R_{\mathrm{C-H}} = R_e$. For transitions to states that have a predominantly biexcited nature (the first-excited $^1\Sigma^+$ state and the lowest two $^1\Delta$ states) and for the second $^1\Pi$ state that has a significant biexcited component, the errors in the vertical excitation energies at the equilibrium value of $R_{\mathrm{C-H}}$, obtained with the noniterative MMCC(2,3) approach, are 0.01–0.10 eV (*98*). This should be compared to the 0.33–0.92 eV errors in the EOMCCSD results, the 0.2–0.3 eV errors obtained with various perturbative triples approaches, and the 0.50–0.88 eV errors in the results obtained with the CISDt approach (see refs 40, 41, 97, 98, and references therein). For other states studied in refs 40, 41, 97, 98 and elsewhere (*31*, *32*, *35*, *36*) (the third and fourth $^1\Sigma^+$ states and the lowest $^1\Pi$ state), the errors in the MMCC(2,3) results, relative to full CI, are 0.00–0.01 eV (*98*). The MMCC(2,3) results at $R_{\mathrm{C-H}} = R_e$ are as good as or even better than the results provided by the EOMCCSDt method,

Downloaded by PENNSYLVANIA STATE UNIV on September 14, 2012 | http://pubs.acs.org
Publication Date: August 14, 2002 | doi: 10.1021/bk-2002-0828.ch003

which gives the 0.02–0.09 eV errors for the first-excited $^1\Sigma^+$ state, the lowest two $^1\Delta$ states, and the second $^1\Pi$ state, and 0.00–0.01 eV errors for the third and fourth $^1\Sigma^+$ states and the lowest $^1\Pi$ state (*41*).

This spectacular performance of the noniterative MMCC(2,3) approximation is not limited to vertical excitation energies at $R_{\mathrm{C-H}} = R_e$. As shown in Figure 2 (d), the MMCC(2,3) method is capable of providing excellent description of entire excited-state PESs. The huge (often > 1 eV) errors in the EOMCCSD and CISDt results for the entire excited-state PESs of CH^+ (cf. Figures 2 (a) and (b)) reduce in our MMCC(2,3) calculations to 0.00–0.10 eV. For example, the errors in the EOMCCSD excitation energies, relative to full CI, for the three lowest excited states of the $^1\Sigma^+$ symmetry, the two lowest $^1\Pi$ states, and the two lowest $^1\Delta$ states are 0.668, 0.124, 0.256, 0.109, 0.564, 1.114, and 2.095 eV, respectively, at $R_{\mathrm{C-H}} = 1.5R_e$, and 0.299, 0.532, 0.771, 0.234, 0.467, 1.178, and 3.950 eV, respectively, at $R_{\mathrm{C-H}} = 2R_e$ (*41*). Our MMCC(2,3) method reduces these large errors to 0.072, 0.005, 0.025, 0.024, 0.059, 0.065, and 0.086 eV, respectively, at $R_{\mathrm{C-H}} = 1.5R_e$, and 0.074, 0.048, 0.046, 0.045, 0.007, 0.079, and 0.029 eV, respectively, at $R_{\mathrm{C-H}} = 2R_e$ (*98*). As in the $R_{\mathrm{C-H}} = R_e$ case, the only other EOMCC approaches that can provide the results of this high quality are the full EOMCCSDt and EOMCCSDT approaches (*41*, *97*). Interestingly enough, the MMCC(2,3) approximation is capable of providing the correct asymptotic behavior of the potential energy curves of CH^+, restoring, for example, the degeneracy of the second $^1\Sigma^+$ state, the second $^1\Pi$ state, and the lowest $^1\Delta$ state in the $R_{\mathrm{C-H}} = \infty$ limit, which is broken by all doubles models, including the EOMCCSD approach (see Figure 2 (a) and ref 98) and the VOO-CCD method advocated by Head-Gordon and coworkers (*39*). Clearly, ***the MMCC theory provides us with the least expensive ab initio methods of obtaining high quality PESs of excited states.*** There is no need to reoptimize orbitals to obtain excellent excited-state PESs in MMCC calculations; the ordinary RHF orbitals are sufficient. The required computer effort is small. For example, the fraction of all triples used in the MMCC(2,3)/CISDt calculations discussed here was, depending of state's symmetry, 26–29 %.

Summary and Concluding Remarks

We have overviewed the new approach to the many-electron correlation problem in atoms and molecules, termed the method of moments of coupled-cluster equations (MMCC). The main idea of the MMCC theory is that of the noniterative energy corrections which, when added to the ground- and excited-state energies obtained in approximate CC calculations, recover the exact energies. We have demonstrated that the MMCC formalism leads to a number of useful approximations, including the renormalized and completely renormalized CCSD(T), CCSD(TQ), and CCSDT(Q) methods for

Downloaded by PENNSYLVANIA STATE UNIV on September 14, 2012 | http://pubs.acs.org
Publication Date: August 14, 2002 | doi: 10.1021/bk-2002-0828.ch003

ground states, and the MMCC(m_A, m_B) approaches for calculating excited states. The main theoretical concepts have been illustrated by the examples of applications of approximate MMCC methods to ground- and excited-state PESs of small molecular systems. We have demonstrated that the MMCC theory provides us with the framework for designing "black-box" approaches that can be used in accurate calculations of molecular PESs at the fraction of the effort associated with multireference calculations.

Clearly, the new formalism needs further development and testing. Among interesting formal problems are studies of the open-shell extensions of the (C)R-CCSD(T), (C)R-CCSD(TQ), (C)R-CCSDT(Q), and MMCC(m_A, m_B) methods, development of the excited-state extensions of the renormalized CC approaches, and investigation of the role of higher moments of CC equations, which were heuristically neglected in the MMCC(2,3), MMCC(2,4), and MMCC(3,4) approximations discussed in this chapter. Analytical derivatives for the (C)R-CCSD(T), (C)R-CCSD(TQ), and (C)R-CCSDT(Q) methods and other MMCC(m_A, m_B) schemes represent another important problem. All these issues are under intense investigation by our group and the results will be reported as soon as they become available.

Acknowledgements

One of us (P.P.) would like to thank Professor Mark R. Hoffmann and Dr. Ken G. Dyall for inviting him to write a chapter in this ACS Book. This work has been supported by funds provided to P.P. by Michigan State University and, in part, by the Chemical Sciences, Geosciences and Biosciences Division, Office of Basic Energy Sciences, Office of Science, U.S. Department of Energy (Grant No. DE-FG02-01ER15228; P.P.).

References

1. Čížek, J. *J. Chem. Phys.* **1966**, *45*, 4256.
2. Čížek, J. *Adv. Chem. Phys.* **1969**, *14*, 35.
3. Čížek, J.; Paldus, J. *Int. J. Quantum Chem.* **1971**, *5*, 359.
4. Paldus, J. In *Methods in Computational Molecular Physics*; Wilson, S.; Diercksen, G.H.F., Eds.; NATO Advanced Study Institute, Series B: Physics, Vol. 293; Plenum: New York, 1992; pp. 99-194.
5. Bartlett, R.J. In *Modern Electronic Structure Theory*; Yarkony, D.R., Ed.; World Scientific: Singapore, 1995; Part I, pp. 1047-1131.
6. Paldus, J.; Li, X. *Adv. Chem. Phys.* **1999**, *110*, 1.
7. Piecuch, P.; Kowalski, K. In *Computational Chemistry: Reviews of Current Trends*; Leszczyński, J., Ed.; World Scientific: Singapore, 2000; Vol. 5, pp. 1-104.

Downloaded by PENNSYLVANIA STATE UNIV on September 14, 2012 | http://pubs.acs.org
Publication Date: August 14, 2002 | doi: 10.1021/bk-2002-0828.ch003

8. Urban, M.; Noga, J.; Cole, S.J.; Bartlett, R.J. *J. Chem. Phys.* **1985**, *83*, 4041.
9. Cole, S.J.; Bartlett, R.J. *J. Chem. Phys.* **1987**, *86*, 873.
10. Piecuch, P.; Paldus, J. *Theor. Chim. Acta* **1990**, *78*, 65.
11. Raghavachari, K.; Trucks, G.W.; Pople, J.A.; Head-Gordon, M. *Chem. Phys. Lett.* **1989**, *157*, 479.
12. Kucharski, S.A.; Bartlett, R.J. *J. Chem. Phys.* **1998**, *108*, 9221.
13. Laidig, W.D.; Saxe, P.; Bartlett, R.J. *J. Chem. Phys.* **1987**, *86*, 887.
14. Ghose, K.B.; Piecuch, P.; Adamowicz, L. *J. Chem. Phys.* **1995**, *103*, 9331.
15. Piecuch, P.; Špírko, V.; Kondo, A.E.; Paldus, J. *J. Chem. Phys.* **1996**, *104*, 4699.
16. Kowalski, K.; Piecuch, P. *J. Chem. Phys.* **2000**, *113*, 18.
17. Kowalski, K.; Piecuch, P. *J. Chem. Phys.* **2000**, *113*, 5644.
18. Kowalski, K.; Piecuch, P. *J. Mol. Struct.: THEOCHEM* **2001**, *547*, 191.
19. Kowalski, K.; Piecuch, P. *Chem. Phys. Lett.* **2001**, *344*, 165.
20. Piecuch, P.; Kucharski, S.A.; Kowalski, K. *Chem. Phys. Lett.* **2001**, *344*, 176.
21. Monkhorst, H. *Int. J. Quantum Chem. Symp.* **1977**, *11*, 421.
22. Sekino, H.; Bartlett, R.J. *Int. J. Quantum Chem. Symp.* **1984**, *18*, 255.
23. Daalgard, E.; Monkhorst, H. *Phys. Rev. A* **1983**, *28*, 1217.
24. Takahashi, M.; Paldus, J. *J. Chem. Phys.* **1986**, *85*, 1486.
25. Koch, H.; Jørgensen, P. *J. Chem. Phys.* **1990**, *93*, 3333.
26. Koch, H.; Jensen, H.J.Aa.; Jørgensen, P.; Helgaker, T. *J. Chem. Phys.* **1990**, *93*, 3345.
27. Geertsen, J.; Rittby, M.; Bartlett, R.J. *Chem. Phys. Lett.* **1989**, *164*, 57.
28. Comeau, D.C.; Bartlett, R.J. *Chem. Phys. Lett.* **1993**, *207*, 414.
29. Stanton, J.F.; Bartlett, R.J. *J. Chem. Phys.* **1993**, *98*, 7029.
30. Piecuch, P.; Bartlett, R.J. *Adv. Quantum Chem.* **1999**, *34*, 295.
31. Watts, J.D.; Bartlett, R.J. *Chem. Phys. Lett.* **1995**, *233*, 81.
32. Watts, J.D.; Bartlett, R.J. *Chem. Phys. Lett.* **1996**, *258*, 581.
33. Watts, J.D.; Bartlett, R.J. *J. Chem. Phys.* **1994**, *101*, 3073.
34. Koch, H.; Christiansen, O.; Jørgensen, P.; Olsen, J. *Chem. Phys. Lett.* **1995**, *244*, 75.
35. Christiansen, O.; Koch, H.; Jørgensen, P. *J. Chem. Phys.* **1995**, *103*, 7429.
36. Christiansen, O.; Koch, H.; Jørgensen, P. *J. Chem. Phys.* **1996**, *105*, 1451.
37. Christiansen, O.; Koch, H.; Jørgensen, P.; Olsen, J. *Chem. Phys. Lett.* **1996**, *256*, 185.

Downloaded by PENNSYLVANIA STATE UNIV on September 14, 2012 | http://pubs.acs.org
Publication Date: August 14, 2002 | doi: 10.1021/bk-2002-0828.ch003

38. Larsen, H.; Olsen, J.; Jørgensen, P.; Christiansen, O. *J. Chem. Phys.* **2000**, *113*, 6677.
39. Krylov, A.I.; Sherrill, C.D.; Head-Gordon, M. *J. Chem. Phys.* **2000**, *113*, 6509.
40. Kowalski, K.; Piecuch, P. *J. Chem. Phys.* **2000**, *113*, 8490.
41. Kowalski, K.; Piecuch, P. *J. Chem. Phys.* **2001**, *115*, 643.
42. Jeziorski, B.; Monkhorst, H.J. *Phys. Rev. A* **1981**, *24*, 1668.
43. Jeziorski, B.; Paldus, J. *J. Chem. Phys.* **1988**, *88*, 5673.
44. Meissner, L.; Jankowski, K.; Wasilewski, J. *Int. J. Quantum Chem.* **1988**, *34*, 535.
45. Paldus, J.; Pylypow, L.; Jeziorski, B. In *Many-Body Methods in Quantum Chemistry*; Kaldor, U., Ed.; Lecture Notes in Chemistry, Vol. 52; Springer: Berlin, 1989; pp. 151-170.
46. Kucharski, S.A.; Bartlett, R.J. *J. Chem. Phys.* **1991**, *95*, 8227.
47. Balková, A.; Kucharski, S.A.; Meissner, L.; Bartlett, R.J. *Theor. Chim. Acta* **1991**, *80*, 335.
48. Balková, A.; Kucharski, S.A.; Bartlett, R.J. *Chem. Phys. Lett.* **1991**, *182*, 511.
49. Piecuch, P.; Paldus, J. *Theor. Chim. Acta* **1992**, *83*, 69.
50. Paldus, J.; Piecuch, P.; Jeziorski, B.; Pylypow, L. In *Recent Progress in Many-Body Theories*; Ainsworthy, T.L.; Campbell, C.E.; Clements, B.E.; Krotschek, E., Eds.; Plenum: New York, 1992; Vol. 3, pp. 287-303.
51. Paldus, J.; Piecuch, P.; Pylypow, L.; Jeziorski, B. *Phys. Rev. A* **1993**, *47*, 2738.
52. Piecuch, P.; Paldus, J. *Phys. Rev. A* **1994**, *49*, 3479.
53. Piecuch, P.; Paldus, J. *J. Chem. Phys.* **1994**, *101*, 5875.
54. Kowalski, K.; Piecuch, P. *Phys. Rev. A* **2000**, *61*, 052506.
55. Piecuch, P.; Landman, J.I. *Parallel Comp.* **2000**, *26*, 913.
56. Kowalski, K.; Piecuch, P. *Chem. Phys. Lett.* **2001**, *334*, 89.
57. Lindgren, I.; Mukherjee, D. *Phys. Rep.* **1987**, *151*, 93.
58. Mukherjee, D.; Pal, S. *Adv. Quantum Chem.* **1989**, *20*, 291.
59. Jeziorski, B.; Paldus, J. *J. Chem. Phys.* **1989**, *90*, 2714.
60. Bernholdt, D.E.; Bartlett, R.J. *Adv. Quantum Chem.* **1999**, *34*, 271.
61. Jankowski, K.; Paldus, J.; Grabowski, I.; Kowalski, K. *J. Chem. Phys.* **1992**, *97*, 7600; **1994**, *101*, 1759, Erratum.
62. Jankowski, K.; Paldus, J.; Grabowski, I.; Kowalski, K. *J. Chem. Phys.* **1994**, *101*, 3085.
63. Paldus, J.; Čížek, J.; Takahashi, M. *Phys. Rev. A* **1984**, *30*, 2193.
64. Piecuch, P.; Toboła, R.; Paldus, J. *Phys. Rev. A* **1996**, *54*, 1210.
65. Paldus, J.; Planelles, J. *Theor. Chim. Acta* **1994**, *89*, 13.
66. Stolarczyk, L. *Chem. Phys. Lett.* **1994**, *217*, 1.
67. Peris, G.; Planelles, J.; Paldus, J. *Int. J. Quantum Chem.* **1997**, *62*, 137.

Downloaded by PENNSYLVANIA STATE UNIV on September 14, 2012 | http://pubs.acs.org
Publication Date: August 14, 2002 | doi: 10.1021/bk-2002-0828.ch003

68. Li, X.; Paldus, J. *J. Chem. Phys.* **1997**, *107*, 6257.
69. Li, X.; Paldus, J. *J. Chem. Phys.* **1998**, *108*, 637.
70. Li, X.; Paldus, J. *Chem. Phys. Lett.* **1998**, *286*, 145.
71. Li, X.; Paldus, J. *Collect. Czech. Chem. Commun.* **1998**, *63*, 1381.
72. Li, X.; Paldus, J. *J. Chem. Phys.* **1999**, *110*, 2844.
73. Li, X.; Paldus, J. *Mol. Phys.* **2000**, *98*, 1185.
74. Li, X.; Paldus, J. *J. Chem. Phys.* **2000**, *113*, 9966.
75. Oliphant, N.; Adamowicz, L. *J. Chem. Phys.* **1991**, *94*, 1229.
76. Oliphant, N.; Adamowicz, L. *J. Chem. Phys.* **1992**, *96*, 3739.
77. Oliphant, N.; Adamowicz, L. *Int. Rev. Phys. Chem.* **1993**, *12*, 339.
78. Piecuch, P.; Oliphant, N.; Adamowicz, L. *J. Chem. Phys.* **1993**, *99*, 1875.
79. Piecuch, P.; Adamowicz, L. *J. Chem. Phys.* **1994**, *100*, 5792.
80. Piecuch, P.; Adamowicz, L. *Chem. Phys. Lett.* **1994**, *221*, 121.
81. Piecuch, P.; Adamowicz, L. *J. Chem. Phys.* **1995**, *102*, 898.
82. Ghose, K.B.; Adamowicz, L. *J. Chem. Phys.* **1995**, *103*, 9324.
83. Ghose, K.B.; Piecuch, P.; Pal, S.; Adamowicz, L. *J. Chem. Phys.* **1996**, *104*, 6582.
84. Adamowicz, L.; Piecuch, P.; Ghose, K.B. *Mol. Phys.* **1998**, *94*, 225.
85. Piecuch, P.; Kucharski, S.A.; Bartlett, R.J. *J. Chem. Phys.* **1999**, *110*, 6103.
86. Piecuch, P.; Kucharski, S.A.; Špirko, V. *J. Chem. Phys.* **1999**, *111*, 6679.
87. Sherrill, C.D.; Krylov, A.I.; Byrd, E.F.C.; Head-Gordon, M. *J. Chem. Phys.* **1998**, *109*, 4171.
88. Krylov, A.I.; Sherrill, C.D.; Byrd, E.F.C.; Head-Gordon, M. *J. Chem. Phys.* **1998**, *109*, 10669.
89. Gwaltney, S.R.; Head-Gordon, M. *Chem. Phys. Lett.* **2000**, *323*, 21.
90. Gwaltney, S.R.; Sherrill, C.D.; Head-Gordon, M. *J. Chem. Phys.* **2000**, *113*, 3548.
91. Stanton, J.F. *Chem. Phys. Lett.* **1997**, *281*, 130.
92. Noga, J.; Bartlett, R.J. *J. Chem. Phys.* **1987**, *86*, 7041; **1988**, *89*, 3401, Erratum.
93. Scuseria, G.E.; Schaefer III, H.F. *Chem. Phys. Lett.* **1988**, *152*, 382.
94. Kucharski, S.A.; Bartlett, R.J. *Theor. Chim. Acta* **1991**, *80*, 387.
95. Kucharski, S.A.; Bartlett, R.J. *J. Chem. Phys.* **1992**, *97*, 4282.
96. Oliphant, N.; Adamowicz, L. *J. Chem. Phys.* **1991**, *95*, 6645.
97. Kowalski, K.; Piecuch, P. *Chem. Phys. Lett.*, in press, 2001.
98. Kowalski, K.; Piecuch, P. *J. Chem. Phys.* **2001**, *115*, 2966.
99. Kantorovich, L.V.; Krylov, V.I. *Approximate Methods of Higher Analysis*; Interscience: New York, 1958; p. 150.
100. Jankowski, K.; Paldus, J.; Piecuch, P. *Theor. Chim. Acta* **1991**, *80*, 223.

Downloaded by PENNSYLVANIA STATE UNIV on September 14, 2012 | http://pubs.acs.org
Publication Date: August 14, 2002 | doi: 10.1021/bk-2002-0828.ch003

101. Piecuch, P.; Kucharski, S.A.; Špírko, V.; Kowalski, K. *J. Chem. Phys.* **2001**, *115*, 5796.
102. Dunning, T.H. *J. Chem. Phys.* **1970**, *53*, 2823.
103. Dunning, Jr., T.H. *J. Chem. Phys.* **1989**, *90*, 1007.
104. Kendall, R.A.; Dunning, Jr., T.H.; Harrison, R.J. *J. Chem. Phys.* **1992**, *96*, 6769.
105. Coxon, J.A.; Hajigeorgiou, P.G. *J. Mol. Spectr.* **1990**, *142*, 254.
106. Zemke, W.T.; Stwalley, W.C.; Coxon, J.A.; Hajigeorgiou, P.G. *Chem. Phys. Lett.* **1991**, *177*, 412.
107. Zemke, W.T.; Stwalley, W.C.; Langhoff, S.R.; Valderrama, G.L.; Berry, M.J. *J. Chem. Phys.* **1991**, *95*, 7846.
108. Olsen, J.; Sánchez de Merás, A.M.; Jensen, H.J.Aa.; Jørgensen, P. *Chem. Phys. Lett.* **1989**, *154*, 380.

Downloaded by PENNSYLVANIA STATE UNIV on September 14, 2012 | http://pubs.acs.org
Publication Date: August 14, 2002 | doi: 10.1021/bk-2002-0828.ch003

Downloaded by OHIO STATE UNIV LIBRARIES on September 14, 2012 | http://pubs.acs.org
Publication Date: August 14, 2002 | doi: 10.1021/bk-2002-0828.ch004

Chapter 4

The Photoelectron Spectrum of the NO_3 Radical Revisited: A Theoretical Investigation of Potential Energy Surfaces and Conical Intersections

Mark Wladyslawski[1,2] and Marcel Nooijen[1,*]

[1]Department of Chemistry, Princeton University, Princeton, NJ 08544
[2]National Science Foundation Graduate Research Fellow

The vertical ionization spectrum of the nitrogen trioxide radical (NO_3) has been examined by the DIP-STEOM-CCSD and DIP-EOM-CCSD methods (double ionization potential [similarity transformed] equation-of-motion coupled-cluster singles and doubles). The DIP-STEOM and DIP-EOM approaches avoid artifactual symmetry breaking of the reference wavefunction by starting from the symmetry-correct nitrate anion (NO_3^-) orbitals and provide a balanced treatment of dynamical and non-dynamical correlation effects. The five lowest singlet and five lowest triplet states of the cation (NO_3^+) are considered. The calculated vertical ionization potentials match well with the band maxima in the photoelectron spectrum obtained by Wang. D. X.; *et al.* (*J. Chem. Phys.* **1997**, *106*, 3003). A broad feature in the spectrum, which has previously been assigned to the $^1E''$ state, is assigned by us to the nominally forbidden $^3A_2'$ state. The $^3A_2'$ state exhibits a conical intersection with the nearby, allowed $^3E'$ state and is thus expected to gain intensity through a vibronic coupling mechanism; the $^1E''$ state is instead found to nearly coincide with the lower-energy $^3E''$ state. Another conical intersection may account for the broad feature associated with the $^3E'$ state.

Introduction

The importance of the nitrogen trioxide radical (NO_3) in atmospheric chemistry is well recognized and has prompted widespread investigation of its chemical and physical properties (*1*). Two recent experimental studies (*2,3*) of the NO_3 ionization spectrum have motivated several new theoretical analyses. In addition to examining the lowest NO_3 ionization potential (IP), much theoretical work has focused on the "symmetry breaking" problem in the neutral and cation (NO_3^+) ground states, namely whether the precise minimum of each ground potential energy surface possesses D_{3h} or C_{2v} symmetry. Very few analyses have considered any excited states of the NO_3^+ system. No study has yet attempted to reproduce the full vibrational features of the NO_3 ionization spectrum. In this work, we begin to examine the elements that may play a critical role in such an explanation.

In the first reported photoionization study of the neutral NO_3 system, Monks *et al.* (*2*) observed a single sharp peak at 12.57 eV and attributed it to the lowest adiabatic ionization, NO_3^+ ($^1A_1'$) ← NO_3 ($^2A_2'$), in D_{3h} symmetry. The sharp onset and absence of vibrational structure suggest that the ground states of the neutral and cation have nearly identical geometries. They concluded that both states are of D_{3h} symmetry, primarily based on their CASSCF calculations and the earlier MP4 single point results for the cation (*4,5*). The MP*n* studies are considered inconclusive, however, as the symmetry of the cation ground state was found to depend on the order of perturbation employed. Recent work by Miller and Francisco (*6*), in which the MP*n* geometries were allowed to relax, also found similar variations and has verified that, through fourth order, the MP*n* series fails to provide an accurate treatment of NO_3^+.

In the second recent experimental study, Wang *et al.* (*3*) measured the HeI photoelectron (PE) spectrum, observing five distinct bands. Again, the lowest ionization was a single sharp peak (12.55 eV), suggesting the similarity of the neutral and cation ground state geometries. The five bands were assigned to the five lowest vertical IPs of NO_3 as computed by DFT calculations in D_{3h} symmetry (*3*). Recent MCSTEP (multi-configurational spin tensor electron propagator) calculations by Heryadi and Yeager (*7*) also found reasonable agreement with the experimental peaks, but they concluded that the radical ground state could have *either* D_{3h} or C_{2v} symmetry. Although their optimizations do slightly favor the C_{2v} geometry, the D_{3h} neutral and cation structures are more consistent with the sharp first ionization peak.

The symmetry breaking problem for the neutral and cation ground states has proven to be a very difficult theoretical question, with results supporting either the D_{3h} (*4,5,7-15*) or C_{2v} (*4-8,12,16-20*) symmetry. A recent study by Eisfeld and Morokuma (*8*) examined in detail the reasons and effects of symmetry breaking on the NO_3 ground state potential energy surface. In particular, they

Downloaded by OHIO STATE UNIV LIBRARIES on September 14, 2012 | http://pubs.acs.org
Publication Date: August 14, 2002 | doi: 10.1021/bk-2002-0828.ch004

considered how the NO_3 *wavefunction* symmetry breaking of the Hartree-Fock (HF) reference is difficult to overcome by dynamic correlation. The symmetry-broken wavefunction persists in the correlated calculation and can lead to artifactual symmetry breaking (*21*) of the *equilibrium geometry.*

Eisfeld and Morokuma (*8*) went on to detail the non-trivial task of obtaining symmetrically correct wavefunctions for the NO_3 ground state in CASSCF and MR-SDCI. They found that a significantly large active space was necessary. Even the reasonable elimination of active orbitals that were almost always doubly occupied or almost always entirely empty resulted in symmetry breaking of the CASSCF wavefunction.

Downloaded by OHIO STATE UNIV LIBRARIES on September 14, 2012 | http://pubs.acs.org
Publication Date: August 14, 2002 | doi: 10.1021/bk-2002-0828.ch004

Another category of approaches that avoids the symmetry breaking problem of the orbitals for the target state is based on using a related, well-behaved HF reference instead. Examples of such techniques include: quasi-restricted Hartree-Fock coupled-cluster (QRHF CC) (*11,19*), symmetry adapted cluster configuration interaction (SAC-CI) (*22,23*), coupled-cluster linear response theory (CCLRT) (*24-26*) or equivalently equation-of-motion coupled-cluster (EOM-CC) (*27-32*), Fock space multi-reference coupled-cluster (FSMRCC) (*33-37*), and similarity transformed equation-of-motion coupled-cluster (STEOM-CC) (*38-40*). In the case of NO_3 and NO_3^+, the restricted Hartree-Fock (RHF) orbitals of the closed-shell NO_3^- *anion* system can be used as the reference. The anion orbitals are stable with respect to symmetry perturbations, and the system does not suffer from the artifactual symmetry breaking of the neutral and cation.

The QRHF CC method has been applied by Stanton and co-workers (*11,19*) and the FSMRCC method has been applied by Kaldor (*9,10*) to consider the ground state of the NO_3 radical system. In these approaches, the RHF orbitals for the nitrate *anion* are first solved, and a valence electron is then deleted to form the reference for the *neutral.* Although such a reference is not variationally optimal, it may be more suitable for the NO_3 correlation problem than the standard UHF (unrestricted HF) reference. In UHF-based approaches, extensive orbital relaxation is involved in correcting for the symmetry-broken reference, while in the anion-based methods, the wavefunction symmetry conditions are satisfied from the start.

The symmetry-correct anion orbitals can also be utilized in calculations of states of the NO_3^+ *cation.* The primary purpose of this work is to examine the NO_3 ionization spectrum and the ground and low excited states of the NO_3^+ cation system by the DIP-STEOM-CCSD method (*40*) (double ionization potential similarity transformed equation-of-motion coupled-cluster singles and doubles). The DIP-STEOM-CCSD method is built upon the IP-EOM-CCSD method (*32*) (ionization potential equation-of-motion coupled-cluster singles and doubles), which in turn, has been shown to be equivalent (*41,42*) to singly ionized FSMRCC, such as the example of Kaldor above. The DIP-STEOM-CCSD method generates ground and excited states of the cation by deletion of *two* electrons from the closed-shell anion reference determinant. Thus, a symmetry-broken wavefunction is automatically avoided by starting from the symmetry-correct anion orbitals. Additionally, the method treats the multi-configurational character of the cation states in a balanced way.

We will begin by considering the IP-EOM-CCSD neutral NO_3 ground state ($^2A_2'$) geometry and harmonic vibrational frequencies. The DIP-STEOM-CCSD method will then be applied to compute the NO_3 vertical ionization spectrum. We also perform the first calculations of a newly developed DIP-EOM-CCSD method (*double* ionization potential EOM-CCSD), which verify the DIP-STEOM-CCSD results. Agreement is very good between the vertical results and the experimental PE band maxima (*3*). However, our calculated vertical ionization potential to the $^1E''$ state does not agree well with previous theoretical results (*3,7*), and this leads to a tentative reassignment of the PE spectrum. The potential energy surfaces of the ground and low excited states of the cation are then examined by the DIP-STEOM-CCSD method. The geometry of the cation ground state ($^1A_1'$) is optimized and some recent contradicting theoretical results are scrutinized. We go on to consider the cation $^1E''$ potential energy surface in detail, particularly in terms of the Jahn-Teller effect. Finally, the geometries of the low-lying triplet states ($^3E''$, $^3E'$, and $^3A_2'$) are optimized and suggest a possible explanation for the broad features and the reassigned peak in the PE spectrum: Conical intersections are found near the $^3E'$ and the $^3A_2'$ equilibrium structures; these are expected to dramatically affect the observed spectrum, altering it from that predicted in the vertical, Franck-Condon approximation (*43*). The broad, reassigned feature may be attributed to vibronic coupling of the nominally forbidden $^3A_2'$ state with the intersecting, allowed $^3E'$ state.

Theoretical and Computational Details

The RHF orbital diagram for the closed-shell NO_3^- anion is presented in Figure 1 and should aid the reader in the discussion to follow. The molecular orbital (MO) configuration of the NO_3^- anion in D_{3h} symmetry is $[Core](4a_1')^2(1a_2'')^2(3e')^4(4e')^4(1e'')^4(1a_2')^2$, where [Core] refers to the seven deepest-lying (filled) MOs. The uppermost [Core] orbital has an energy of −31 eV and is thus well separated from the orbitals shown. The closest-lying virtual orbital ($2a_2''$) has an eigenvalue of +10 eV.

The key element of the EOM and STEOM methods is a similarity transformation (*42*) of the second-quantized Hamiltonian (prior to the diagonalization). A similarity transformation changes the matrix elements and eigenvectors of an operator but leaves the eigenvalues unchanged. A careful choice of transformation can reduce the coupling between excitation levels, thereby reducing the size of the minimum reasonable subspace needed in the

Downloaded by OHIO STATE UNIV LIBRARIES on September 14, 2012 | http://pubs.acs.org
Publication Date: August 14, 2002 | doi: 10.1021/bk-2002-0828.ch004

Downloaded by OHIO STATE UNIV LIBRARIES on September 14, 2012 | http://pubs.acs.org
Publication Date: August 14, 2002 | doi: 10.1021/bk-2002-0828.ch004

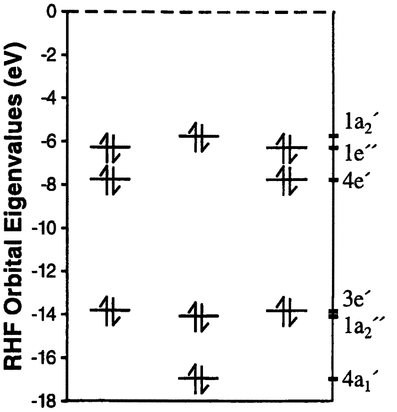

Figure 1. Energy diagram of the uppermost RHF orbitals of NO_3^- (TZ2P basis at D_{3h} R_{NO} = 1.230 Å)

approximate diagonalization. Essentially, the effects of higher levels of excitation can be (approximately) incorporated into the lower level elements of the transformed, effective Hamiltonian.

In the most straightforward diagonalization approach, the familiar configuration interaction (CI) theory, in order to approximate predominantly *singly* excited states of a closed-shell system, one should include in the diagonalization at least up to a selection of *triply* excited determinants. This is a simple consequence of the single and double, pure excitation operators in the Hamiltonian, which couple determinants that are up to two excitation levels apart. In the EOM-CCSD method (*27-29*), however, a similarity transformation is first performed such that the pure single- and double-excitation operators are made to vanish. The double-excitation operators are the primary coupling elements between the singly and triply excited determinants. To a reasonable approximation, therefore, states dominated by single excitations can be obtained in EOM-CCSD by diagonalization of the transformed Hamiltonian over the subspace including only up to *doubly* excited determinants. In addition to excitations, due to the formulation of the theory in second-quantization, states with a different number of electrons than the starting determinant can also be considered, yielding ionized and attached states of the reference system.

The EOM-CCSD method has been shown to be an accurate approach for calculating excitation energies (EE-) (*29,30*), electron affinities (EA-) (*31*), and ionization potentials (IP-) (*32*) of closed-shell systems. For the computations presented here, a coupled-cluster singles and doubles (CCSD) calculation is first performed on the closed-shell NO_3^- *anion* system. The Hamiltonian is similarity transformed using the NO_3^- CCSD amplitudes and then, in IP-EOM-CCSD, is diagonalized over the subspace of one-hole ($1h$) (analogous to "singles") and two-hole one-particle ($2h1p$) (analogous to "doubles") configurations to obtain states of the *neutral* NO_3 system. (*Holes* correspond to deletions of electrons from occupied orbitals in the reference determinant, and *particles* correspond to creation of electrons in virtual orbitals.) In this way, ground and excited, singly ionized states (relative to the closed-shell reference) are obtained. The IP-EOM-CCSD method is similar in spirit to Green's function or electron propagator approaches (*44-48*) and is in fact equivalent to coupled-cluster Green's function (CCGF) theory (*49,50*) for ionizations.

In the STEOM-CCSD method (*38-40*), a *second* similarity transformation is performed such that the primary coupling elements between the singly and *doubly* excited determinants are also made to vanish. Now, states dominated by single excitations can be obtained in STEOM-CCSD by diagonalization over only *singly* excited determinants. This represents an enormous reduction in computational cost compared to that of CI or even EOM. In fact, the STEOM method can be considered a rigorous correlated equivalent (*40*) of the CI singles (CIS or Tamm-Dancoff approximation, TDA) method, but using a fully correlated, effective Hamiltonian.

The STEOM-CCSD method can be applied to excitation energies (EE-) (*38-40,51-54*), double electron attachments (DEA-) (*40*), and double ionization potentials (DIP-) (*40,55,56*) of closed-shell systems. In the DIP-STEOM-CCSD method, applied here, the matrix elements that couple the $2h$ (analogous to "singles") and the $3h1p$ (analogous to "doubles") determinants are primarily *hhph* integrals. A selection of the most important of these is made to vanish through a corresponding selection of IP-EOM-CCSD eigenvectors used to construct the second similarity transformation. States of the NO_3^+ *cation* system are double deletions relative to the closed-shell NO_3^- *anion* reference; with the main coupling to the $3h1p$ determinants included implicitly, the NO_3^+ ground and excited states can be obtained by diagonalization of the NO_3^--based STEOM Hamiltonian over the subspace of $2h$ configurations only. By this simple CI-"singles"-like diagonalization of the (doubly transformed) STEOM Hamiltonian, a large number of electronic states of the twice-ionized system (relative to the closed-shell reference) can be obtained at very little cost.

We have also recently implemented a DIP-EOM-CCSD approach, where states of the NO_3^+ cation can also be obtained by diagonalization of the *singly* transformed EOM Hamiltonian over the larger subspace of $2h$ and $3h1p$ configurations. To our knowledge, the DIP-EOM-CCSD calculations presented here are the first to appear in the literature. The method is akin to $2h$-type propagator approaches (*57,58*), as applied for example by Tarantelli *et al.* to problems in Auger spectroscopy (*59-64*). Although the DIP-EOM-CCSD diagonalization space is significantly larger than that of DIP-STEOM-CCSD

Downloaded by OHIO STATE UNIV LIBRARIES on September 14, 2012 | http://pubs.acs.org
Publication Date: August 14, 2002 | doi: 10.1021/bk-2002-0828.ch004

Downloaded by OHIO STATE UNIV LIBRARIES on September 14, 2012 | http://pubs.acs.org
Publication Date: August 14, 2002 | doi: 10.1021/bk-2002-0828.ch004

(and thus more expensive), the DIP-EOM-CCSD method includes the $3h1p$ ("doubles") configurations *explicitly*. The DIP-STEOM-CCSD method, on the other hand, includes the most important $3h1p$ ("doubles") and $4h2p$ ("triples") contributions *implicitly* through the second similarity transformation. It is therefore interesting to compare the results of the two approaches. Although not presented here, an extended-STEOM-CCSD approach has also recently been developed (*65,66*), where the larger diagonalization over singles and doubles is performed, but of the doubly transformed STEOM Hamiltonian; the method therefore implicitly incorporates some effects up to quadruple excitations.

Through the similarity transformations and diagonalizations described, the EOM and STEOM methods incorporate both dynamic and non-dynamic electron correlation effects. The ground and excited states of a system are obtained in a uniform manner in these methods. Similarly, the singlet and triplet states are treated consistently in the DIP methods, as they are simply deletions of two electrons of appropriate spins.

All calculations were performed with a local version of the ACES II suite of electronic structure programs (*67*). Working calculations were carried out in a DZP basis set (double-zeta plus polarization), while final calculations were performed in a TZ2P basis set (triple-zeta with two polarization functions per atom) (*68,69*). Spherical harmonic *d*-type orbitals were used. The four core 1*s* orbitals were dropped from the post-HF calculations. All IP-EOM-CCSD and DIP-STEOM-CCSD optimizations were performed using analytical energy gradients, while numerical gradients were used for DIP-EOM-CCSD. We recently derived explicit formulas for the analytical STEOM-CCSD gradients (*70*) for all variants (EE-, DEA-, and DIP-), and these will appear in a future work (*71*). The analytical STEOM gradients were implemented into ACES II and have been thoroughly tested against numerical gradients. Harmonic vibrational frequencies were computed through finite differences of the gradients above. In the DIP-STEOM-CCSD method, an active space of occupied orbitals for the second similarity transformation must be chosen. All occupied RHF anion orbitals greater in energy than –20 eV were taken, and precisely these were shown in Figure 1.

We have also recently implemented into ACES II an electronic state-tracking algorithm. Excited electronic states are typically optimized by following the energy-ordered state of a particular symmetry (*e.g.* the 2nd state of $^3A_2$ symmetry). In the course of the optimization, however, it can often happen that the desired diabatic state crosses through another state of the same symmetry (*e.g.* the 2nd state of $^3A_2$ symmetry becomes the 1st state), and the state followed is subsequently incorrect. To overcome this problem, at each geometry step in the optimization, we compute the approximate overlap of the set of *all* nearby states (of the same symmetry) with the set of states from the previous iteration. The mixing and crossing diabatic states can thus be tracked through the different

Downloaded by OHIO STATE UNIV LIBRARIES on September 14, 2012 | http://pubs.acs.org
Publication Date: August 14, 2002 | doi: 10.1021/bk-2002-0828.ch004

geometries. For this procedure to be practical, however, we need to compute a number of excited electronic states in an efficient manner. In this regard, the STEOM method is ideal. In the final simple diagonalization, a sizable number of excited states can be obtained at essentially no additional cost.

Results and Discussion

I. NO_3 Neutral Ground State $^2A_2'$

Table I. Neutral NO_3 ground state $^2A_2'$ equilibrium geometry and vibrational frequencies

NO_3 Ground State, D_{3h} $^2A_2'$		*Exp.*	*IP-EOM-CCSD* *DZP*[a]	 *TZ2P*	*MR-SDCI* *DZP*[b]
D_{3h} Geometry	R_{NO} (Å)	1.240[c]	1.238	1.230	1.246
Vibrational Freqs. (cm^{-1})					
Sym. stretch	a_1'	1060[d]	1148	1133	1141
Umbrella	a_2''	762[e]	794	814	757
Asym. stretch	e'	1480[d], 1492[c,f]	1144	1113	1439
Asym. bend	e'	~250[h], 360[g], 380[d]	251	249	174
Zero-Point Vib. Energy (eV)			0.29	0.29	

[a] See also reference (*13*) [b] Reference (*8*) [c] Reference (*72*) [d] Reference (*73*)
[e] Reference (*74*) [f] Reference (*75*) [g] Reference (*76*)

[h] Reference (*13*) uses a linear vibronic coupling model between the $^2A_2'$ and $^2E''$ states to estimate the asymmetric bend harmonic frequency from experimental data in reference (*76*).

The NO_3 ground state ($^2A_2'$) equilibrium geometry and harmonic vibrational frequencies as computed by the IP-EOM-CCSD method are collected in Table I. The various experimental assignments are given, with appropriate references. Also tabulated is the recent symmetry-correct CASSCF/MR-SDCI analysis of Eisfeld (*8*). (The reported data refers to the largest state averaging used in the study, $^2A_2'$+$^2E''$+$^2E'$.) Very recently, Crawford and Stanton (*13*) published IP-EOM-CCSD/DZP results for the NO_3 ground state, and our DZP data in Table I nearly identically reproduce theirs. The small discrepancies can be attributed to our dropping of the four core 1*s* orbitals.

Downloaded by OHIO STATE UNIV LIBRARIES on September 14, 2012 | http://pubs.acs.org
Publication Date: August 14, 2002 | doi: 10.1021/bk-2002-0828.ch004

As we intuitively expect, the principal component of the IP-EOM-CCSD ground state of the neutral NO_3 system is the single deletion of an electron from the anion $1a_2'$ HOMO (92% in TZ2P). The NO_3 ground state equilibrium structure is found to be of D_{3h} symmetry. Vibrational frequencies are all real and verify the D_{3h} structure to be a true minimum on the potential energy surface. The calculated bond lengths agree fairly well with the experimental and MR-SDCI structures. The IP-EOM-CCSD results are also consistent with the earlier FSMRCC results of Kaldor (*9,10*), as expected, since the methods have been shown to be equivalent (*41,42*). The IP-EOM-CCSD vibrational frequencies agree reasonably with the experimental assignments, with the exception of the *e′* asymmetric stretch.

As is well known, the potential energy surface of the neutral NO_3 ground state is very flat in the region of the minimum (*12*). The harmonic approximation for the vibrational frequencies is thus expected to be rather poor. A better description of the neutral vibrational features was provided by Mayer, Cederbaum, and Köppel (*12*) in terms of a vibronic coupling model of interacting electronic states. As we shall later see, a similar model may be needed to properly describe the NO_3^+ cation vibrational dynamics seen in the Wang (*3*) PE spectrum.

The closest alternative to the IP-EOM-CCSD method is the QRHF CCSD approach, which also starts from the same well-behaved anion orbitals. Despite this symmetry-correct reference, the QRHF CCSD/DZP optimization of Stanton, Gauss, and Bartlett (*19*) found a "one-long-two-short" minimum structure of C_{2v} symmetry (R_1=1.351 Å; R_2=R_3=1.206 Å; A_{12}=A_{13}=114°) that was 2.6 kcal/mol more stable than their D_{3h} stationary point (R_{NO}=1.236 Å). At the QRHF CCSD(T) single point level (*11*), however, these authors found the above D_{3h} structure to become 0.3 kcal/mol *more* stable than the C_{2v} structure above. For comparison, we find IP-EOM-CCSD/DZP single point calculations at these geometries to increase the D_{3h} stability to 2.5 kcal/mol.

Clearly, the potential energy surface is very flat in the region of the minimum, and it is difficult to assert the symmetry of the $^2A_2'$ state definitively. Nevertheless, the optimized IP-EOM-CCSD energetic and harmonic frequency data suggest that the true minimum structure is of D_{3h} symmetry. Even if the minimum might be of C_{2v} symmetry, it may be of sufficiently shallow nature such that the effective geometry still remains D_{3h} (*12*). However, the precise nature of the minimum structure may not be especially relevant to the spectral features observed experimentally. Due to the flatness of the potential energy surface, the full vibrational-electronic wavefunction and energy of the NO_3 ground state are expected *not* to depend sensitively on the true symmetry of the lowest point. Such were the findings of Mayer *et al.* (*12*), for example, in the vibronic analysis of the photoionization of the NO_3^- anion to the ground state of the neutral NO_3.

Downloaded by OHIO STATE UNIV LIBRARIES on September 14, 2012 | http://pubs.acs.org
Publication Date: August 14, 2002 | doi: 10.1021/bk-2002-0828.ch004

II. NO_3 Neutral Vertical Ionization Energies

Table II. NO_3 Vertical Ionization Energies (eV)
(at D_{3h} R_{NO} = 1.230 Å for DIP-STEOM and DIP-EOM)

Cation State	*DIP-STEOM-CCSD*		*DIP-EOM-CCSD*		*MC-STEP*^{a}	*PE Spectrum*^{b}	*Tentative reassignment*
	DZP	*TZ2P*	*DZP*	*TZ2P*	*cc-pVTZ*		
$^1A_1'$	12.04	12.31	12.57	12.93	12.60	12.55	12.55
$^1E''$	+0.69	+0.73	+0.83	+0.85	+1.38	+1.50	+0.63
$^3E''$	+0.71	+0.73	+0.75	+0.76	+0.86	+0.63	
$^3E'$	+1.08	+1.07	+1.08	+1.08	+1.18	+1.07	+1.07
$^3A_2^{\prime f}$	*+1.22*^{f}	*+1.24*^{f}	*+1.23*^{f}	*+1.25*^{f}			+1.50
$^1A_2^{\prime\prime f}$	*+2.25*^{f}	*+2.30*^{f}	*+2.49*^{f}	*+2.51*^{f}			
$^3A_2^{\prime\prime f}$	*+2.29*^{f}	*+2.31*^{f}	*+2.39*^{f}	*+2.40*^{f}			
$^1E^{\prime f}$	*+2.39*^{f}	*+2.47*^{f}	*+2.85*^{f}	*+2.85*^{f}			
$^1E'$	+3.15	+3.13	+3.04	+3.03	+3.05	+2.99	+2.99
$^3A_2^{\prime f}$	*+3.83*^{f}	*+3.80*^{f}	*+3.67*^{f}	*+3.66*^{f}			

[a] Reference (*7*) [b] Reference (*3*)

[f] *Italics* indicates states that are *forbidden* by a one-photon ionization from the neutral ground state.

At the IP-EOM-CCSD/TZ2P optimized geometry, the vertical ionization potentials of the neutral NO_3 ground state were computed by the DIP-STEOM-CCSD and DIP-EOM-CCSD methods. The results are reported in Table II as relative IPs with respect to the absolute first IP. The photoelectron spectrum of Wang *et al.* (*3*) is reproduced in Figure 2. Wang assigned the experimental peak regions by DFT calculations, and the assignments are also given in Table II. The only other theoretical study in reference to the full PE spectrum are the recent MCSTEP calculations of Heryadi and Yeager (*7*), also tabulated.

In the DIP-STEOM and DIP-EOM calculations, we consider the five lowest singlet and five lowest triplet states of the cation. Cation states that are forbidden by ionization from the neutral NO_3 ground state with a single photon are written as *italics*^{f}. To be allowed, a state must have a component involving the deletion of an electron from the *anion* $1a_2'$ HOMO, as this is the main component of the *neutral* system. Table III lists the major components of the lowest DIP-STEOM-CCSD states of the cation, written as double deletions relative to the anion determinant.

We first observe that, for both the DIP-STEOM-CCSD and DIP-EOM-CCSD results, the *relative* ionization potentials are very consistent between the

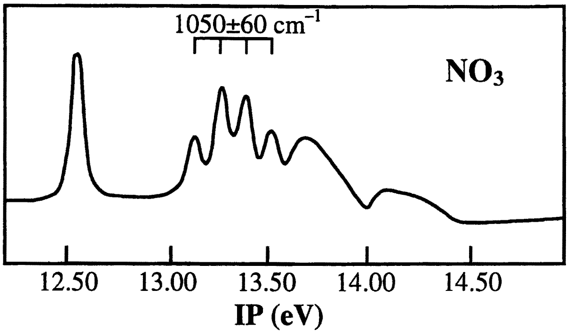

Figure 2. Experimental photoelectron spectrum of Wang et al. (Reproduced with permission from reference (3). Copyright 1997 American Institute of Physics.)

Downloaded by OHIO STATE UNIV LIBRARIES on September 14, 2012 | http://pubs.acs.org
Publication Date: August 14, 2002 | doi: 10.1021/bk-2002-0828.ch004

DZP and TZ2P basis sets. The *absolute* ionization potentials, however, as evidenced by the reported first IP for each method, show a significant dependence on the basis set. The IPs are calculated as the difference between the IP-EOM-CCSD total energy for the neutral ground state in the particular basis and the respective DIP total energy for the various cation states. We think this basis set dependence reflects mainly orbital relaxation effects, which can be assumed larger in the larger basis set. The anion orbitals are expected to describe the neutral system better than the cation system, and hence the neutral system will be more stabilized by the larger basis set than the cation. The absolute IPs, therefore, are expected to increase with the size of the basis (as observed). The constancy with respect to the basis set of the relative excitation energies, however, is striking, and it is these that are appropriate for our subsequent analysis.

The relative IPs are also found to agree very well between the DIP-STEOM-CCSD and DIP-EOM-CCSD methods. The largest deviation is found for the two high-lying states of $^1E'$ symmetry. The lower of the two $^1E'$ states shows appreciable dependence on the basis set and differs by 0.4 eV between the DIP-STEOM and DIP-EOM results. It is likely that the close proximity of two states of the same symmetry causes this higher sensitivity. Nevertheless, for nearly all of the states, the agreement is excellent.

The agreement is also good, for the most part, between the DIP-STEOM and DIP-EOM vertical IP results and the assignments of the experimental PE spectrum by Wang (*3*). A notable exception is the $^1E''$ state. The DIP-STEOM method finds the $^1E''$ state to be very close in energy to the $^3E''$ state. This result is supported by the DIP-EOM calculations as well. These results, however, are in sharp contrast with the DFT calculations of Wang (*3*) and the MCSTEP calculations of Heryadi (*7*), which both find a singlet-triplet splitting

Table III. Character of the lowest DIP-STEOM-CCSD NO_3^+ states

Anion:	$[Core](4a_1')^2(1a_2'')^2(3e')^4(4e')^4(1e'')^4(1a_2')^2$	
Cation State	*Character (in TZ2P)*	
$^1A_1'$	79%	$(1a_2')^{-2}$
	2 x 10%	$(4e')^{-2}$
$^1E''$	68%	$(1e'')^{-1}(1a_2')^{-1}$
	2 x 15%	$(4e')^{-1}(1e'')^{-1}$
$^3E''$	76%	$(1e'')^{-1}(1a_2')^{-1}$
	2 x 11%	$(4e')^{-1}(1e'')^{-1}$
$^3E'$	98%	$(4e')^{-1}(1a_2')^{-1}$
$^3A_2'$	100%	$(1e'')^{-2}$

Downloaded by OHIO STATE UNIV LIBRARIES on September 14, 2012 | http://pubs.acs.org
Publication Date: August 14, 2002 | doi: 10.1021/bk-2002-0828.ch004

of approximately 0.5 eV for these states. The experimental PE spectrum, on the other hand, shows a difference of 0.9 eV between the peaks assigned by Wang to these two states.

There is little reason to think the DIP-STEOM or DIP-EOM methods would treat triplet states more accurately than singlet states, as both arise naturally in the deletion of two electrons from the closed-shell reference. We note the multi-configurational nature of the DIP-STEOM states collected in Table III; this character presents a significant difficulty to the DFT calculations used in assigning the experimental spectrum. The MCSTEP calculations, on the other hand, provide little treatment of dynamic correlation. The DIP-STEOM and DIP-EOM methods, in contrast, offer an extended treatment of dynamic and non-dynamic correlation, and these results should be considered the best treatment of this collection of vertical IPs so far.

Both the DIP-STEOM-CCSD and DIP-EOM-CCSD methods suggest that the cation $^1E''$ state contributes to the sharp lower energy peaks (12.55 + 0.63 = 13.18 eV), rather than to the broad feature (12.55 + 1.50 = 14.05 eV) to which it was assigned by Wang (*3*) (see Figure 2). Although the allowed vertical IP results offer no immediate alternative assignment for the broad features in the region of 14.05 eV, we suggest a possible explanation for these features in a later section in terms of a vibronic coupling model of the nearby intersecting triplet states ($^3E''$, $^3E'$, and $^3A_2'$). It will be shown that the equilibrium structures of the upper triplet states lie in close proximity to regions of conical intersection with the electronic states immediately below. Such regions of intersection can dramatically change the observed spectrum from that expected in the Born-

Oppenheimer / Franck-Condon approximation (*43*). In particular, states that would otherwise be forbidden can borrow intensity from nearby bright states. The broad feature at 14.05 eV might thus be explained by the interaction of the nominally dark $^3A_2'$ state with the nearby, allowed $^3E'$ state.

In order to begin to better understand the vibrational features in the experimental PE spectrum, we now consider the DIP-STEOM-CCSD optimized geometries for the NO_3^+ cation states.

III. NO_3^+ Cation Ground State $^1A_1'$

Table IV. Cation NO_3^+ ground state $^1A_1'$ equilibrium geometry and vibrational frequencies

NO_3^+ Ground State, D_{3h} $^1A_1'$		*DIP-STEOM-CCSD DZP*	*DIP-STEOM-CCSD TZ2P*	*DIP-EOM-CCSD DZP*	*DIP-EOM-CCSD TZ2P*
D_{3h} Geometry	R_{NO} (Å)	1.241	1.233	1.239	1.230
Vibrational Frequencies (cm^{-1})					
Sym. stretch	a_1'	1098	1085	1110	1095
Umbrella	a_2''	711	729	719	740
Asym. stretch	e'	1105	1087	1141	1123
Asym. bend	e'	504	508	506	510
Zero-Point Vib. Energy (eV)		0.31	0.31	0.32	0.32

For the NO_3^+ cation ground state ($^1A_1'$), the DIP-STEOM-CCSD and DIP-EOM-CCSD equilibrium geometries and harmonic vibrational frequencies are reported in Table IV. The frequencies are all real and confirm the true minimum structure to be of D_{3h} symmetry. Both methods find similar geometries and frequencies, as well as similar basis set effects. The equilibrium bond distances elongate only slightly (≤0.003 Å) from their respective IP-EOM-CCSD neutral ground state geometry (see Table I). Likewise, the adiabatic electronic ionization energies decrease by less than 0.003 eV relative to the verticals. We thus expect a sharp feature with no vibrational structure for the lowest NO_3 ionization peak, as was observed experimentally by both Monks (*2*) and Wang (*3*).

Conclusions in the literature about the precise symmetry of the cation ground state are nearly as varied as those of the neutral ground state. The experimental photoionization spectra indirectly support the D_{3h} symmetry; the CASSCF (*2*) and DFT (*3*) calculations used (respectively) in assigning the

Downloaded by OHIO STATE UNIV LIBRARIES on September 14, 2012 | http://pubs.acs.org
Publication Date: August 14, 2002 | doi: 10.1021/bk-2002-0828.ch004

spectra find nearly identical D_{3h} structures for both the neutral and cation ground states. Another very recent DFT study (*14*) by some of the researchers involved in the Wang PE spectrum also calculates a D_{3h} minimum structure, with a bond length (R_{NO} = 1.220 Å) comparable to that found in this work. Some studies (*5,7*) have considered both D_{3h} and C_{2v} structures, ultimately arriving at D_{3h} symmetry, though not conclusively. The C_{2v} structures found were Y-like with angles deviating only slightly from 120°.

Most recently, however, an extensive study by Miller and Francisco (*6*) reported RHF CCSD(T) (as well as B3LYP, QCISD, and CCSD) cation C_{2v} structures that are *highly* distorted, with large angles $A_{12}=A_{13}=\sim141°$. Such nitrosyl ring-like structures are analogous to the isoelectronic CO_3 molecule (*77*). Vibrational frequency calculations demonstrate these structures to be true minima at these levels of theory. The C_{2v} structures in CCSD(T) were more stable than the double-saddle D_{3h} stationary points by a range of 0.7 to 6 kcal/mol, depending on the basis set. Note that these C_{2v} structures are markedly different from other reported C_{2v} neutral and cation geometries.

We have repeated matching RHF CCSD(T) geometry optimizations of the cation ground state in the DZP and TZ2P basis sets and have found C_{2v} structures similar to those of Miller and Francisco. Several factors, however, cast doubt on the reliability of the CCSD(T) results. We note the significant multi-configurational nature of the $^1A_1'$ state as computed by DIP-STEOM-CCSD (see Table III). In addition to the primary (79%) component of the anion HOMO ($1a_2'$) double deletion, there are two sizable symmetry-equivalent components (totaling 20% of the cation ground state) that are double deletions from the lower-lying 4e′ orbitals. These latter contributions are difficult to recover by correlation in the single-reference CCSD(T) method. Indeed, this difficulty is manifest in large T2 amplitudes (greater than 0.2) observed in our CCSD(T) calculations; these large coefficients are precisely those associated with the 20% components above. Additionally, we find the discrepancy between the CCSD(T) and the related CCSD+T (*78*) total energies to be on the order of 0.15 eV. This difference is typically less than 0.05 eV, and this casts further doubt on the reliability of the CCSD(T) results.

For comparison, we have performed DIP-STEOM-CCSD and DIP-EOM-CCSD single point calculations at the RHF CCSD(T)/TZ2P optimized C_{2v} geometry. The C_{2v} structure is less stable by a sizable 17 kcal/mol in DIP-STEOM and by 12 kcal/mol in DIP-EOM. Miller and Francisco (*6*) acknowledge that they can offer no explanation why vibrational structure is not observed in the first peak of either ionization spectrum, given their significantly distorted geometry for the cation ground state. The D_{3h} structures by the IP-EOM-CCSD and the DIP-STEOM-CCSD and DIP-EOM-CCSD methods, on the other hand, are nearly identical and are consistent with the experimental findings of a single sharp peak with no vibrational structure.

Downloaded by OHIO STATE UNIV LIBRARIES on September 14, 2012 | http://pubs.acs.org
Publication Date: August 14, 2002 | doi: 10.1021/bk-2002-0828.ch004

Downloaded by OHIO STATE UNIV LIBRARIES on September 14, 2012 | http://pubs.acs.org
Publication Date: August 14, 2002 | doi: 10.1021/bk-2002-0828.ch004

IV. NO_3^+ Cation Excited State $^1E''$

Table V. DIP-STEOM-CCSD/TZ2P optimized geometries and adiabatic electronic IPs for the $^1E''$ state

State	*Type*	*Sym.*	*Geometry (R/Å)*		*Adiabatic IP (eV)*
$^1E''$	Conical	D_{3h}	$R_{NO}=$	1.256	+0.659
$^1B_2$	Transition State (TS)	C_{2v}	$R_1=$	1.255	+0.638
			$R_2=R_3=$	1.256	
			$A_{12}=A_{13}=$	118°	
$^1A_2$	Min	C_{2v}	$R_1=$	1.268	+0.632
			$R_2=R_3=$	1.250	
			$A_{12}=A_{13}=$	122°	

NOTE: The $^1E''$ vertical electronic IP is 12.308 + 0.726 = 13.034 eV.

NOTE: The adiabatic electronic IPs are reported relative to the lowest vertical IP, 12.308 eV, as in Table II.

As seen previously, the vertical DIP-STEOM-CCSD calculations find the $^1E''$ state to be very close in energy to the $^3E''$ state (see Table II). This result is supported by the DIP-EOM-CCSD calculations as well. We again note the discrepancy with the DFT calculations of Wang (*3*) and the MCSTEP results of Heryadi (*7*). These other results may be questioned, however, as previously discussed. We are left with the suggestion that the $^1E''$ state contributes to the lower-energy peaks in the region of 13.18 eV observed in the PE spectrum (see Figure 2).

We now consider the equilibrium geometry of the $^1E''$ state. The DIP-STEOM-CCSD/TZ2P optimized geometries and adiabatic electronic IPs (relative to the lowest vertical IP, 12.31 eV) are given in Table V. An extra digit is reported to better resolve the energy values. By the adiabatic electronic IPs, we mean the difference in total energies between the IP-EOM-CCSD equilibrium ground state of the neutral NO_3 and the DIP-STEOM-CCSD optimized stationary point of the cation NO_3^+; zero-point vibrational corrections are not included.

Although first optimized under the restriction of D_{3h} symmetry, the doubly degenerate $^1E''$ electronic state will distort by the Jahn-Teller theorem (*79,80*). In symmetric non-linear molecules, there is always at least one non-totally symmetric vibrational coordinate that will split the potential energy surface for a degenerate electronic state such that the minima are *not* at the high-symmetry

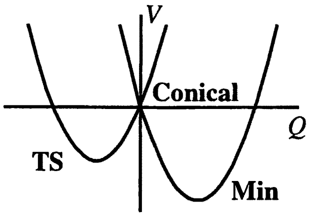

Figure 3. Cross section of a Jahn-Teller distorted potential energy surface (V) for a D_{3h} degenerate electronic state (E′ or E″) in a non-symmetric (e′) vibrational coordinate (Q)

position (*79*). For the case of D_{3h} symmetry, *all* (degenerate) *E′* and *E″* electronic states will split in the directions of the (degenerate) *e′* vibrational coordinates. For an excellent discussion of Jahn-Teller distortion in the specific example of D_{3h} symmetry, see Herzberg (*80*). The relevant points of the discussion will be summarized here. We will focus on the topological features of the electronic potential energy surfaces.

Figure 3 shows a cross section of the potential energy surface for a D_{3h} degenerate electronic state (*E′* or *E″*) in one of the coordinates of a non-totally symmetric, degenerate *e′* vibrational mode. The point labeled **Conical** in the center of the graph is the high-symmetry D_{3h} nuclear configuration. In the non-symmetric coordinate, the two components of the degenerate electronic state cross each other at a non-zero angle (*80*); the resulting stationary points are necessarily, therefore, shifted to configurations of lower symmetry. The magnitude of the distortion increases with the strength of the vibrational-electronic, or *vibronic*, interaction.

Regardless of the strength of the Jahn-Teller distortion, however, the full potential energy surface in terms of all nuclear coordinates retains the full D_{3h} symmetry of the nuclear point group (*80*). The *three*-dimensional potential energy surface as a function of *both* components of an *e′* vibrational mode retains a matching symmetry. There are three equivalent cross sections (through the D_{3h} center point) that are identical to Figure 3; thus, there are three equivalent structures for each Jahn-Teller distorted state. The three cross sections are 120° "apart", and each set of equivalent structures falls on the points of an equilateral triangle (if viewed from above). A contour plot of such a D_{3h} Jahn-Teller surface as a function of the two *e′* vibrational components can be found in Herzberg (*80*) (Fig. 17b, p. 48).

The adiabatic potential energy surface below the intersection point possesses three equivalent minimum regions. One of these surface minima is seen in the cross section in Figure 3 and is labeled as point **Min**. The three minima on the surface are separated by three saddle-point transition states. Point **TS** in the Figure 3 cross section is the transition state between the two *other*

Downloaded by OHIO STATE UNIV LIBRARIES on September 14, 2012 | http://pubs.acs.org
Publication Date: August 14, 2002 | doi: 10.1021/bk-2002-0828.ch004

Downloaded by OHIO STATE UNIV LIBRARIES on September 14, 2012 | http://pubs.acs.org
Publication Date: August 14, 2002 | doi: 10.1021/bk-2002-0828.ch004

Table VI. DIP-STEOM-CCSD/TZ2P vibrational frequencies (cm^{-1}) at the minimum ($^1A_2$) and transition state ($^1B_2$) C_{2v} stationary points, Jahn-Teller split from the $^1E''$ D_{3h} conical intersection

D_{3h} Vibrational Mode		*$^1E''$ Min ($^1A_2$)*		*$^1E''$ TS ($^1B_2$)*	
Sym. stretch	a_1'	a_1	1053	a_1	1050
Umbrella	a_2''	b_2	652	b_1	656
Asym. stretch	e'	a_1	899	a_1	912
		b_1	856	b_2	839
Asym. bend	e'	a_1	503	a_1	578
		b_1	418	b_2	435*i*

surface minima not shown (symmetry-equivalent to point **Min**). Likewise, point **Min** is connected to the other two surface minima by the two transition states (symmetry-equivalent to point **TS**) not shown. The minima and transition states are joined together in the center by a conical peak, and hence the term *conical intersection* is given to the exact crossing region, in this case the point of high symmetry. Note that as a function of *all* nuclear coordinates, the crossing region, rather than being a single point, forms a multi-dimensional surface. Lastly, an inverted conical, upper surface is formed from the "inner walls" of the lower surface. This artificial upper surface has no minimum in the sense of a region with zero gradient, and its lowest point is a point of conical intersection.

Allowing the symmetry of the D_{3h} $^1E''$ conical intersection point to relax, we obtain the transition state ($^1B_2$) and the minimum ($^1A_2$) structures, both of C_{2v} symmetry (Table V). Both C_{2v} Jahn-Teller structures are found to be Y-like, only slightly distorted from the D_{3h} configuration. The relative energies of the states can be seen in the tabulated adiabatic electronic IPs. We note that upon lowering the symmetry from D_{3h} to C_{2v}, the two states comprising the degenerate E'' (or E') state fall into different symmetry groups. Thus, by specifying the proper symmetry at a slight distortion, the diabatic transition state can be optimized without collapsing to a minimum structure.

To verify the nature of the two states, the harmonic vibrational frequencies at the minimum and transition state stationary points are reported in Table VI. For these states, the calculated frequencies in the harmonic approximation may be expected to be similar to those obtained from a full Jahn-Teller description, since the Jahn-Teller distortion in this case is relatively small. The deeper-lying $^1A_2$ state is demonstrated to be a true minimum in all directions. The slightly less stable (0.006 eV) $^1B_2$ state retains a single imaginary frequency in one component of the former e' asymmetric bend mode and is thus a transition state, in this case to pseudorotation between the equivalent minima. On the full potential energy surface, the three equivalent minima and three equivalent transition states correspond to the three possible positions for the unique C_{2v} axis. To verify that the diabatic states do in fact lie on the same adiabatic surface, the transition state structure was slightly distorted in C_s symmetry in either "direction" of the imaginary asymmetric bend mode. Upon optimization, both distortions did indeed converge to a C_{2v} structure equivalent to the minimum in Table V, but with the unique axis on one of the other Oxygen atoms.

The non-degenerate a_1' and a_2'' modes are not subject to the Jahn-Teller instability. The a_1' symmetric stretch frequency agrees well with the 1050 cm^{-1} progression observed the Wang PE spectrum (see Figure 2). The differences between the geometries in Table V and the neutral ground state geometry (D_{3h} R_{NO} = 1.230 Å) are sufficiently large such that vibrational structure may be expected in the photoionization. In the NO_3^- anion photoionization spectrum (*76*), for example, a similar a_1' vibrational progression was simulated in the Franck-Condon approximation with a comparable deviation in bond length of 0.03 ± 0.01 Å.

Finally, we note the near degeneracy of the $^1E''$ and $^3E''$ states, and thus spin-orbit coupling is also expected to play some role in the vibrational dynamics.

Downloaded by OHIO STATE UNIV LIBRARIES on September 14, 2012 | http://pubs.acs.org
Publication Date: August 14, 2002 | doi: 10.1021/bk-2002-0828.ch004

V. NO_3^+ Cation Excited States $^3E''$, $^3E'$, and $^3A_2'$

The three lowest triplet states of the cation, $^3E''$, $^3E'$, and $^3A_2'$, lie rather close to one another in energy and will be examined together. As we saw previously, the $^3E''$ and $^3E'$ vertical IPs as computed by both the DIP-STEOM-CCSD and DIP-EOM-CCSD methods (see Table II) agree fairly well with the peak regions in the PE spectrum. The broad feature near 14.05 eV (see Figure 2), assigned by Wang to $^1E''$, however, could not be explained in terms of the allowed vertical states. The nominally dark $^3A_2'$ state, although falling near this region, does not contain any character of a deletion of an electron from the anion $1a_2'$ HOMO (see Table III) and should therefore not be accessible by a single photon ionization from the neutral. As we shall suggest below, however, vibronic coupling through a very nearby conical intersection with the allowed $^3E'$ state may cause the appearance of substantial intensity borrowing lines associated with the $^3A_2'$ state. Likewise, a conical intersection of the $^3E'$ with the $^3E''$ state may affect the $^3E'$ vibrational structure, altering it significantly from that expected in the Franck-Condon approximation.

The DIP-STEOM-CCSD/TZ2P optimized geometries of all components of the three states are collected in Table VII. Vibrational frequency calculations verify the $^3A_2'$ state to be a true minimum in D_{3h} symmetry. The doubly degenerate $^3E''$ and $^3E'$ electronic states, on the other hand, will undergo Jahn-Teller distortion in the non-symmetric e' vibrational coordinates. The D_{3h}

conical intersection structures are found to split into minimum and transition state stationary points of C_{2v} symmetry. The minimum structures were verified to exhibit real frequencies in all directions, while the transition states retained a single imaginary frequency in a former e' coordinate.

The $^3E''$ state splits into a "one-long-two-short" (1L2S) true minimum and a "one-short-two-long" (1S2L) transition state. The magnitude of the distortion is somewhat larger than seen previously in the $^1E''$ state. In contrast, the $^3E'$ state shows a reversal of the ordering of the two C_{2v} configurations; it is the 1L2S configuration that is the transition state between the equivalent 1S2L minima. The magnitude of the $^3E'$ Jahn-Teller distortion is also significantly larger than for the $^3E''$ state.

In contrast to the $^3E''$ 1L2S minimum in DIP-STEOM-CCSD, a recent DFT study (*14*) reported a significantly distorted 1S2L structure for the $^3E''$ state (R_1=1.152 Å; R_2=R_3=1.315 Å; A_{12}=A_{13}=132°). It is unclear if the stationary point was verified to be a true minimum by vibrational frequency calculations. As an additional confirmation of the DIP-STEOM-CCSD results, we also performed DIP-EOM-CCSD geometry optimizations and vibrational frequency calculations on the $^3E''$ state. The DIP-EOM method finds C_{2v} minimum and transition state structures nearly identical to the DIP-STEOM results in Table VII.

The proximity in energy of the $^3E''$, $^3E'$, and $^3A_2'$ states suggests the possibility that these electronic surfaces may approach one another in the nuclear coordinates or even cross in conical intersections. The approach of the surfaces leads to a breakdown of the Born-Oppenheimer approximation (*81,82*), and the adiabatic potential energy surfaces can couple residually through the nuclear kinetic energy operator. Vibrational motion need no longer be confined to a single adiabatic electronic surface, but rather, can proceed on a number of surfaces simultaneously (*43*). The resulting spectra can exhibit a multitude of intensity borrowing lines that were nominally forbidden, and the Franck-Condon and adiabatic lines themselves can be significantly altered in position and intensity.

For an extensive study of the effects of vibronic coupling on optical spectra, we refer the reader to the beautiful work by Köppel, Domcke, and Cederbaum (*43*). A vibronic coupling model has been applied with success (*12*) to the NO_3 $^2A_2'$ band of the anion photoionization (*76*). A detailed treatment of these effects in the NO_3^+ system is beyond the scope of this work, but we shall substantiate the suggestion that conical intersections may play a critical role in explaining the broad features in the NO_3 PE spectrum. We expect to present a more detailed analysis in a future study.

Here we wish to examine the extent to which the $^3E''$, $^3E'$, and $^3A_2'$ electronic potential energy surfaces approach one another in the nuclear coordinates. Table VII presents the relative energies of the five components

Downloaded by OHIO STATE UNIV LIBRARIES on September 14, 2012 | http://pubs.acs.org
Publication Date: August 14, 2002 | doi: 10.1021/bk-2002-0828.ch004

Downloaded by OHIO STATE UNIV LIBRARIES on September 14, 2012 | http://pubs.acs.org
Publication Date: August 14, 2002 | doi: 10.1021/bk-2002-0828.ch004

Table VII. DIP-STEOM-CCSD/TZ2P optimized geometries and energies of the components of the NO_3^+ $^3E''$, $^3E'$, and $^3A_2'$ states

			Geometry			Relative Energies (kcal/mol)				
						$^3E''$		$^3E'$		$^3A_2'$
Optimized State	Sym.	Type	R_1 (Å)	$R_2=R_3$ (Å)	$A_{12}=A_{13}$	$^3A_2$	$^3B_{1\text{ or }2}$	$^3B_{1\text{ or }2}$	$^3A_1$	
$^2A_2'$	D_{3h}	Min	1.230		≡120°	0.00	0.00	7.97	7.97	11.89
$^3A_2$	C_{2v}	Min	1.282	1.238	121°	$\boxed{-1.60}$	0.46⁽¹⁾	12.11⁽²⁾	3.38	9.73
$^3B_2$	C_{2v}	TS	1.226	1.266	119°	-0.25	$\boxed{-1.46^{(2)}}$	3.99⁽¹⁾	10.81	9.32
$^3E''$	D_{3h}	Conical	1.252		≡120°	$\boxed{-1.13}$	$\boxed{-1.13}$	6.93	6.93	8.98
$^3B_1$	C_{2v}	Min	1.161	1.321	120°	3.46	0.32⁽²⁾	$\boxed{0.64^{(1)}}$	25.60	12.18
$^3A_1$	C_{2v}	TS	1.339	1.219	123°	-0.31	5.86⁽¹⁾	23.91⁽²⁾	$\boxed{1.12}$	13.82
$^3E'$	D_{3h}	Conical	1.251		≡120°	-1.13	-1.13	$\boxed{6.93}$	$\boxed{6.93}$	9.06
$^3A_2'$	D_{3h}	Min	1.269		≡120°	-0.55	-0.55	7.58	7.58	$\boxed{8.35}$

(1) and (2) The number indicates the symmetry group B_1 and B_2, respectively.

NOTE: The IP-EOM-CCSD/TZ2P neutral NO_3 ground state $^2A_2'$ and vertical IPs are included for comparison.

NOTE: All energies are given relative to the $^3E''$ vertical IP (12.31 + 0.73 = 13.04 eV).

NOTE: Boxed energies in each row indicate the state for which the geometry was optimized.

In Low-Lying Potential Energy Surfaces; Hoffmann, M., et al.;
ACS Symposium Series; American Chemical Society: Washington, DC, 2002.

Downloaded by OHIO STATE UNIV LIBRARIES on September 14, 2012 | http://pubs.acs.org
Publication Date: August 14, 2002 | doi: 10.1021/bk-2002-0828.ch004

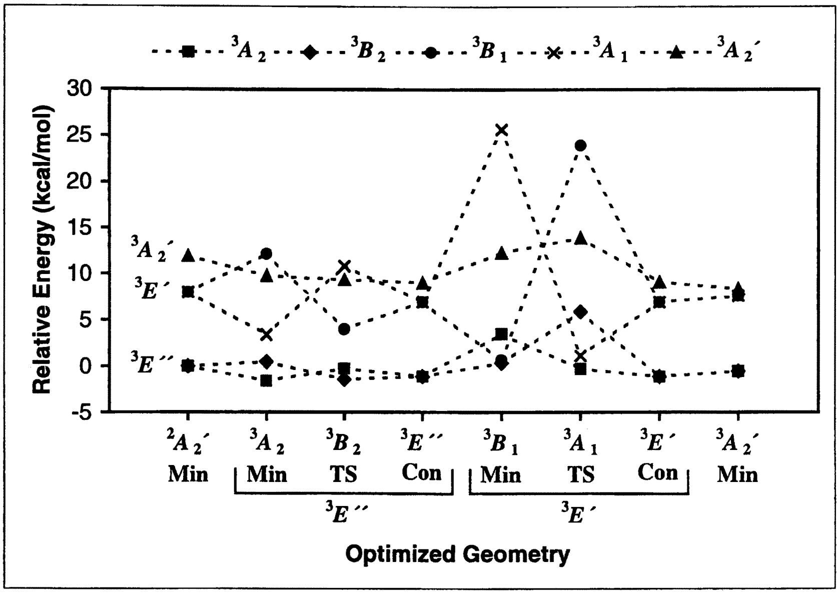

Figure 4. Graph of Table VII, the DIP-STEOM-CCSD/TZ2P relative energies of the components of the $^3E''$, $^3E'$, and $^3A_2'$ states at each optimized geometry

of these states at each of the optimized geometries. The state for which the geometry was optimized is indicated by the boxed energy in each row. The geometries are written in order of increasing energy of the optimized state. For comparison, we have also included the IP-EOM-CCSD/TZ2P equilibrium geometry of the *neutral* NO_3 ground state and the vertical IPs (referenced relative the $^3E''$ state). Note that for the E'' and E' states, the high-symmetry conical intersection stationary point is tabulated in addition to the Jahn-Teller minimum and transition state structures.

The proximity of the electronic states in Table VII is perhaps better visualized by the plot in Figure 4. Each "column" of points in the graph indicates the five energy levels at a particular optimized geometry. Note that the horizontal axis does not represent some continuous deformation in geometry but rather is simply the optimized stationary points written serially in order of increasing energy of the optimized state, as in Table VII. Dashed lines follow the state of a particular orbital character rather than follow the adiabatic potential energy surface. Table VII and Figure 4 thus correspond to a diabatic representation of the surfaces. The major orbital components of each state remain fairly well preserved at the different geometries and thereby make this type of following viable.

Readily visible in Figure 4 is the difference in magnitude of the Jahn-Teller effect for the $^3E''$ and $^3E'$ states. At the optimized $^3E'$ minimum ($^3B_1$), for example, the splitting between the lower ($^3B_1$; ●) and upper ($^3A_1$; ×) Jahn-Teller surfaces is relatively large (~25 kcal/mol). At the $^3E''$ minimum ($^3A_2$), on the other hand, the splitting between the lower ($^3A_2$; ■) and upper ($^3B_2$; ◆) surfaces is substantially smaller (~2 kcal/mol). The barrier to pseudorotation for the $^3E'$ state (0.48 kcal/mol) is also larger than for the $^3E''$ state (0.14 kcal/mol).

We next observe that near its stationary points ($^3A_2$, $^3B_2$, $^3E''$), the ground triplet electronic surface remains fairly well separated from the other, higher-lying triplet surfaces. It can thus be expected that the lower-energy vibrational features associated with this state might be relatively well represented under the adiabatic approximation (*43*) and treating this surface independently of the other triplet surfaces. (Note, however, that due to the near degeneracy of the $^3E''$ and $^1E''$ surfaces, spin-orbital coupling with this state may become important.) The relative simplicity of the vibrational structure in this region of the PE spectrum is consistent with $^3E''$ state being vibronically independent of the other triplet states.

The same cannot be said for the higher-lying $^3E'$ and $^3A_2'$ surfaces. At its minimum structure ($^3B_1$), the $^3E'$ surface is *extremely* close in energy (0.3 kcal/mol) to the lower component of the $^3E''$ surface (see Figure 4). The upper component of the (nominally lower) $^3E''$ surface has already in fact crossed through and lies 2.8 kcal/mol *above* the $^3E'$ minimum. Similarly, at its minimum structure, the $^3A_2'$ surface approaches very closely the lower-lying $^3E'$ surfaces (0.8 kcal/mol separation). Conical intersections are thus expected in close proximity to the $^3E'$ and $^3A_2'$ equilibrium structures.

We went about calculating these expected regions of intersection by minimizing the energy functional $E_1 + E_2 + \lambda(E_1 - E_2)^2$. Optimization of this functional approximates the lowest point on the intersection surface. The penalty parameter λ is chosen as some suitably large value, typically 10^4 to 10^6. The results for the ($^3E'$ with $^3E''$) and the ($^3A_2'$ with $^3E'$) intersections in C_{2v} symmetry are presented in Table VIII. Four intersection regions were calculated for the two components of the $^3E'$ state with the two components of the (nominally lower) $^3E''$ state. Likewise, two intersection regions were calculated for the crossing of the $^3A_2'$ state with the two components of the (nominally lower) $^3E'$ state.

Near both the minimum and transition state stationary points of the $^3E'$ surface, there are conical intersections with the upper and lower portions of the $^3E''$ surface. (By upper and lower, we mean the portions above and below the center D_{3h} region as in the cross section in Figure 3.) As predicted, an intersection region with the lower component of the $^3E''$ surface is found in very close proximity to the $^3E'$ minimum structure. A second intersection is found at a nearby geometry with the upper $^3E''$ component. Two more intersection

Downloaded by OHIO STATE UNIV LIBRARIES on September 14, 2012 | http://pubs.acs.org
Publication Date: August 14, 2002 | doi: 10.1021/bk-2002-0828.ch004

Downloaded by OHIO STATE UNIV LIBRARIES on September 14, 2012 | http://pubs.acs.org
Publication Date: August 14, 2002 | doi: 10.1021/bk-2002-0828.ch004

Table VIII. DIP-STEOM-CCSD/TZ2P conical intersections of the ($^3E'$ with $^3E''$) and ($^3A_2'$ with $^3E'$) surfaces in C_{2v} symmetry

	"Upper" State[a]	*Intersecting State*	*Intersecting State*
	$^3E'$ Min ($^3B_1$)	$^3E''$ ($^3B_2$)	$^3E''$ ($^3A_2$)
$E_{intersection}$[b] (kcal/mol)	+0.636[a]	+0.653	+1.378
Geometry (R/Å)	R_1= 1.161 R_2=R_3= 1.321 A_{12}=A_{13}= 119.6°	ΔR_1= -0.002 ΔR_2=ΔR_3= +0.003 ΔA_{12}=ΔA_{13}= -0.2°	ΔR_1= +0.024 ΔR_2=ΔR_3= -0.023 ΔA_{12}=ΔA_{13}= +0.6°
	$^3E'$ TS ($^3A_1$)	$^3E''$ ($^3A_2$)	$^3E''$ ($^3B_1$)
$E_{intersection}$[b] (kcal/mol)	+1.117[a]	+1.812	+1.939
Geometry (R/Å)	R_1= 1.339 R_2=R_3= 1.219 A_{12}=A_{13}= 123.0°	ΔR_1= +0.025 ΔR_2=ΔR_3= -0.007 ΔA_{12}=ΔA_{13}= +1.5°	ΔR_1= -0.024 ΔR_2=ΔR_3= +0.008 ΔA_{12}=ΔA_{13}= -1.7°
	$^3A_2'$ Min	$^3E'$ ($^3A_1$)	$^3E'$ ($^3B_1$)
$E_{intersection}$[b] (kcal/mol)	+8.350[a]	+8.366	+8.368
Geometry (R/Å)	R_{NO}= 1.269 A= 120°	ΔR_1= -0.006 ΔR_2=ΔR_3= +0.004 ΔA_{12}=ΔA_{13}= -0.02°	ΔR_1= +0.006 ΔR_2=ΔR_3= -0.002 ΔA_{12}=ΔA_{13}= +0.1°

[a] Energy and geometry of $^3E'$ and $^3A_2'$ stationary points from Table VII.

[b] The same zero reference is used as in Table VII ($^3E''$ vertical IP).

regions are found near the $^3E'$ transition state structure. Clearly the vibrational dynamics of the $^3E'$ state can sample these nearby conical intersection regions. We thus expect a profound impact on the spectral vibrational structure associated with the $^3E'$ state. This suggestion is consistent with the broad feature at 13.62 eV in the experimental PE spectrum (see Figure 2), which may be composed of a multitude of vibronic lines.

The intersections of the $^3A_2'$ state with the two $^3E'$ components immediately below are also in astonishingly close proximity to the $^3A_2'$ equilibrium structure. The intersection regions in Table VIII are raised in energy relative to the minimum by less than 0.02 kcal/mol, and the minimum and intersection structures are nearly indistinguishable. This concurrence of the minimum and conical intersection regions can again have great impact on the observed vibrational structure.

In particular, this nominally dark $^3A_2'$ state is expected to gain intensity through vibronic interaction with the bright $^3E'$ state. The weak, broad feature near 14.05 eV (see Figure 2) that could not be accounted for in terms of the DIP-STEOM-CCSD and DIP-EOM-CCSD allowed vertical IPs might thus be attributable to the vibronically coupled $^3A_2'$ state. A tentative reassignment of the PE spectrum is made in Table II. Here we make these suggestions, based on the proximity of the conical intersections near the $^3E'$ and $^3A_2'$ equilibrium structures; we reserve a full detailed analysis for a future study.

Downloaded by OHIO STATE UNIV LIBRARIES on September 14, 2012 | http://pubs.acs.org
Publication Date: August 14, 2002 | doi: 10.1021/bk-2002-0828.ch004

Summary and Conclusions

The NO_3 vertical ionization spectrum was calculated by the DIP-STEOM-CCSD and DIP-EOM-CCSD methods. These methods avoid artifactual symmetry breaking of the reference wavefunction by starting from the symmetry-correct nitrate anion orbitals and provide a balanced treatment of dynamical and non-dynamical correlation effects. In general, the DIP-STEOM and DIP-EOM results agree well with the experiment of Wang (*3*) and with previous theoretical assignments (*3,7*). However, in our calculations, the vertical transition to the $^1E''$ state nearly coincides with that of the $^3E''$ state, in contrast to previous studies. Our calculations therefore do not support the assignment of the broad experimental feature near 14.05 eV to the $^1E''$ state.

Optimization of the cation ground state $^1A_1'$ geometry by the DIP-STEOM-CCSD and DIP-EOM-CCSD methods yields a D_{3h} true minimum structure that is nearly identical to that of the D_{3h} IP-EOM-CCSD neutral ground state $^2A_2'$. These matching geometries are consistent with the spectra of both Monks (*2*) and Wang (*3*), which observed a single sharp peak for the lowest ionization of NO_3. We have considered the mechanism of Jahn-Teller distortion for the D_{3h} states of E'' and E' symmetry. In agreement with Herzberg (*80*), the D_{3h} conical intersection stationary point distorts into three equivalent C_{2v} minimum structures, connected by three equivalent C_{2v} transition states to pseudorotation.

Optimization of the $^3E''$, $^3E'$, and $^3A_2'$ states in DIP-STEOM-CCSD yields some very interesting results. While the $^3E''$ surface remains fairly well separated from the other triplet surfaces near its stationary points, the $^3E'$ and $^3A_2'$ states exhibit conical intersections at geometries nearly *identical* to their equilibrium structures. Strong non-adiabatic effects are expected in the vibrational spectra associated with these states. These effects may explain the broad envelope of the $^3E'$ state observed in the PE spectrum, as this may be a collection of a multitude of vibronic lines. In addition, the nominally dark $^3A_2'$ state is expected to gain intensity by vibronic interaction with the intersecting, bright $^3E'$ state. This coupling would explain the weak, broad feature near 14.05 eV that is missing from the allowed vertical ionization results. A tentative reassignment of the PE spectrum of Wang (*3*) is proposed. A full vibronic analysis of the low triplet surfaces is warranted in order to verify these suggestions.

We also suggest more refined experimental studies of the NO_3^+ cation states. The Wang PE spectrum (*3*) is of modest resolution and involved "stripping" of a strong NO_2 signal. (The combined NO_3-NO_2 spectrum was recorded from pyrolysis of N_2O_5.) This stripping may introduce inaccuracies, particularly in the peak intensities. The cation $^3E'$ and $^3A_2'$ states may prove especially attractive for experimental study due to the remarkable concurrence of their equilibrium structures and conical intersections with the electronic surfaces immediately below.

Downloaded by OHIO STATE UNIV LIBRARIES on September 14, 2012 | http://pubs.acs.org
Publication Date: August 14, 2002 | doi: 10.1021/bk-2002-0828.ch004

Acknowledgements

The authors would like to thank Dr. John F. Stanton for fruitful discussions regarding this work. M.W. gratefully acknowledges support from the National Science Foundation Graduate Research Fellowship Program.

References

1. Wayne, R. P.; Barnes, I.; Biggs, P.; Burrows, J. P.; Canosamas, C. E.; Hjorth, J.; Lebras, G.; Moortgat, G. K.; Perner, D.; Poulet, G.; Restelli, G.; Sidebottom, H. *Atmos. Environ. A-Gen.* **1991**, *25*, 1.
2. Monks, P. S.; Stief, L. J.; Krauss, M.; Kuo, S. C.; Zhang, Z.; Klemm, R. B. *J. Phys. Chem.* **1994**, *98*, 10017-10022.
3. Wang, D. X.; Jiang, P.; Qian, X. M.; Hong, G. Y. *J. Chem. Phys.* **1997**, *106*, 3003-3006.
4. Boehm, R. C.; Lohr, L. L. *J. Phys. Chem.* **1989**, *93*, 3430-3433.
5. Boehm, R. C.; Lohr, L. L. *J. Comput. Chem.* **1991**, *12*, 119-125.
6. Miller, C. E.; Francisco, J. S. *J. Phys. Chem. A* **2001**, *105*, 1662-1668.
7. Heryadi, D.; Yeager, D. L. *J. Chem. Phys.* **2000**, *112*, 4572-4578.
8. Eisfeld, W.; Morokuma, K. *J. Chem. Phys.* **2000**, *113*, 5587-5597.
9. Kaldor, U. *Chem. Phys. Lett.* **1990**, *166*, 599-601.
10. Kaldor, U. *Chem. Phys. Lett.* **1991**, *185*, 131-135.
11. Stanton, J. F.; Gauss, J.; Bartlett, R. J. *J. Chem. Phys.* **1992**, *97*, 5554-5559.
12. Mayer, M.; Cederbaum, L. S.; Köppel, H. *J. Chem. Phys.* **1994**, *100*, 899-911.
13. Crawford, T. D.; Stanton, J. F. *J. Chem. Phys.* **2000**, *112*, 7873-7879.
14. Cao, X. Y.; Hong, G. Y.; Wang, D. X.; Li, L. M.; Xu, G. X. *Chin. J. Chem.* **2000**, *18*, 267-270.

15. Cohen, R. D.; Sherrill, C. D. *J. Chem. Phys.* **2001**, *114*, 8257-8269.
16. Olsen, J. F.; Burnelle, L. *J. Am. Chem. Soc.* **1970**, *92*, 3659-3664.
17. Davy, R. D.; Schaefer, H. F. *J. Chem. Phys.* **1989**, *91*, 4410-4411.
18. Morris, V. R.; Bhatia, S. C.; Hall, J. H. *J. Phys. Chem.* **1990**, *94*, 7414-7418.
19. Stanton, J. F.; Gauss, J.; Bartlett, R. J. *J. Chem. Phys.* **1991**, *94*, 4084-4087.
20. Crawford, T. D.; Lee, T. J.; Handy, N. C.; Schaefer, H. F. *J. Chem. Phys.* **1997**, *107*, 9980-9984.
21. Davidson, E. R.; Borden, W. T. *J. Phys. Chem.* **1983**, *87*, 4783-4790.
22. Nakatsuji, H.; Hirao, K. *J. Chem. Phys.* **1978**, *68*, 2053-2065.
23. Hirao, K.; Nakatsuji, H. *J. Chem. Phys.* **1978**, *69*, 4535-4547.
24. Monkhorst, H. J. *Int. J. Quantum Chem. Symp.* **1977**, *11*, 421-432.
25. Mukherjee, D.; Mukherjee, P. K. *Chem. Phys.* **1979**, *39*, 325-335.
26. Koch, H.; Jørgensen, P. *J. Chem. Phys.* **1990**, *93*, 3333-3344.
27. Sekino, H.; Bartlett, R. J. *Int. J. Quantum Chem. Symp.* **1984**, *18*, 255-265.
28. Geertsen, J.; Rittby, M.; Bartlett, R. J. *Chem. Phys. Lett.* **1989**, *164*, 57-62.
29. Stanton, J. F.; Bartlett, R. J. *J. Chem. Phys.* **1993**, *98*, 7029-7039.
30. Comeau, D. C.; Bartlett, R. J. *Chem. Phys. Lett.* **1993**, *207*, 414-423.
31. Nooijen, M.; Bartlett, R. J. *J. Chem. Phys.* **1995**, *102*, 3629-3647.
32. Stanton, J. F.; Gauss, J. *J. Chem. Phys.* **1994**, *101*, 8938-8944.
33. Lindgren, I. *Int. J. Quantum Chem. Symp.* **1978**, *12*, 33-58.
34. Lindgren, I.; Morrison, J. *Atomic Many-Body Theory*; Springer: Berlin, 1982.
35. Haque, M. A.; Mukherjee, D. *J. Chem. Phys.* **1984**, *80*, 5058-5069.
36. Stolarczyk, L. Z.; Monkhorst, H. J. *Phys. Rev. A* **1985**, *32*, 725-742.
37. Mukherjee, D.; Pal, S. *Adv. Quantum Chem.* **1989**, *20*, 291-373.
38. Nooijen, M.; Bartlett, R. J. *J. Chem. Phys.* **1997**, *106*, 6441-6448.
39. Nooijen, M.; Bartlett, R. J. *J. Chem. Phys.* **1997**, *106*, 6449-6455.
40. Nooijen, M.; Bartlett, R. J. *J. Chem. Phys.* **1997**, *107*, 6812-6830.
41. Sinha, D.; Mukhopadhyay, S. K.; Chaudhuri, R.; Mukherjee, D. *Chem. Phys. Lett.* **1989**, *154*, 544-549.
42. Nooijen, M. *J. Chem. Phys.* **1996**, *104*, 2638-2651.
43. Köppel, H.; Domcke, W.; Cederbaum, L. S. *Adv. Chem. Phys.* **1984**, *57*, 59-246.
44. Linderberg, J.; Öhrn, Y. *Propagators in Quantum Chemistry*; Academic: London, 1973.
45. Cederbaum, L. S.; Domcke, W. *Adv. Chem. Phys.* **1977**, *36*, 205.
46. Öhrn, Y.; Born, G. *Adv. Quantum Chem.* **1981**, *13*, 1-88.
47. von Niessen, W.; Schirmer, J.; Cederbaum, L. S. *Comp. Phys. Rep.* **1984**, *1*, 57-125.
48. Ortiz, J. V. *Adv. Quantum Chem.* **1999**, *35*, 33-52.
49. Nooijen, M.; Snijders, J. G. *Int. J. Quantum Chem. Symp.* **1992**, *26*, 55-83.

Downloaded by OHIO STATE UNIV LIBRARIES on September 14, 2012 | http://pubs.acs.org
Publication Date: August 14, 2002 | doi: 10.1021/bk-2002-0828.ch004

50. Nooijen, M.; Snijders, J. G. *Int. J. Quantum Chem.* **1993**, *48*, 15-48.
51. Gwaltney, S. R.; Bartlett, R. J. *J. Chem. Phys.* **1998**, *108*, 6790-6798.
52. Nooijen, M. *Spectroc. Acta Pt. A-Molec. Biomolec. Spectr.* **1999**, *55*, 539-559.
53. Parusel, A. B. J.; Kohler, G.; Nooijen, H. *J. Phys. Chem. A* **1999**, *103*, 4056-4064.
54. Nooijen, M. *J. Chem. Phys.* **1999**, *111*, 10815-10826.
55. Korkin, A. A.; Nooijen, M.; Bartlett, R. J.; Christe, K. O. *J. Phys. Chem. A* **1998**, *102*, 1837-1842.
56. Fau, S.; Bartlett, R. J. *J. Phys. Chem. A* **2001**, *105*, 4096-4106.
57. Schirmer, J.; Barth, A. *Z. Phys. A.-Hadrons Nuclei* **1984**, *317*, 267-279.
58. Tarantelli, A.; Cederbaum, L. S. *Phys. Rev. A* **1989**, *39*, 1639-1655.
59. Tarantelli, F.; Sgamellotti, A.; Cederbaum, L. S. In *Applied Many-Body Methods in Spectroscopy and Electronic Structure*; Mukherjee, D., Ed.; Plenum: New York, 1992.
60. Tarantelli, F.; Sgamellotti, A.; Cederbaum, L. S. *J. Chem. Phys.* **1991**, *94*, 523-532.
61. Tarantelli, F.; Cederbaum, L. S.; Sgamellotti, A. *J. Electron Spectrosc. Relat. Phenom.* **1995**, *76*, 47-54.
62. Gottfried, F. O.; Cederbaum, L. S.; Tarantelli, F. *J. Chem. Phys.* **1996**, *104*, 9754-9767.
63. Schulte, H. D.; Cederbaum, L. S.; Tarantelli, F. *J. Chem. Phys.* **1996**, *105*, 11108-11133.
64. Schulte, H. D.; Cederbaum, L. S.; Tarantelli, F. *Phys. Rev. A* **1999**, *60*, 2047-2062.
65. Nooijen, M.; Lotrich, V. *J. Chem. Phys.* **2000**, *113*, 494-507.
66. Nooijen, M. *J. Phys. Chem. A* **2000**, *104*, 4553-4561.
67. Stanton, J. F.; Gauss, J.; Watts, J. D.; Nooijen, M.; Oliphant, N.; Perera, S. A.; Szalay, P. G.; Lauderdale, W. J.; Kucharski, S. A.; Gwaltney, S. R.; Beck, S.; Balková, A.; Bernholdt, D. E.; Baeck, K. K.; Rozyczko, P.; Sekino, H.; Huber, C.; Bartlett, R. J., ACES II is a program product of the Quantum Theory Project, University of Florida. Integral packages included are VMOL (J. Almlöf, P. R. Taylor); VPROPS (P. R. Taylor); ABACUS (T. Helgaker, H. J. Aa. Jensen, P. Jørgensen, P. R. Taylor).
68. Dunning, T. H. *J. Chem. Phys.* **1970**, *53*, 2823-2833.
69. Redmon, L. T.; Purvis, G. D.; Bartlett, R. J. *J. Am. Chem. Soc.* **1979**, *101*, 2856-2862.
70. Gwaltney, S. R.; Bartlett, R. J.; Nooijen, M. *J. Chem. Phys.* **1999**, *111*, 58-64.
71. Wladyslawski, M.; Nooijen, M. *to be published.*
72. Ishiwata, T.; Tanaka, I.; Kawaguchi, K.; Hirota, E. *J. Chem. Phys.* **1985**, *82*, 2196-2205.

Downloaded by OHIO STATE UNIV LIBRARIES on September 14, 2012 | http://pubs.acs.org
Publication Date: August 14, 2002 | doi: 10.1021/bk-2002-0828.ch004

73. Ishiwata, T.; Fujiwara, I.; Naruge, Y.; Obi, K.; Tanaka, I. *J. Phys. Chem.* **1983**, *87*, 1349-1352.
74. Friedl, R. R.; Sander, S. P. *J. Phys. Chem.* **1987**, *91*, 2721-2726.
75. Kawaguchi, K.; Hirota, E.; Ishiwata, T.; Tanaka, I. *J. Chem. Phys.* **1990**, *93*, 951-956.
76. Weaver, A.; Arnold, D. W.; Bradforth, S. E.; Neumark, D. M. *J. Chem. Phys.* **1991**, *94*, 1740-1751.
77. Froese, R. D. J.; Goddard, J. D. *J. Phys. Chem.* **1993**, *97*, 7484-7490.
78. Urban, M.; Noga, J.; Cole, S. J.; Bartlett, R. J. *J. Chem. Phys.* **1985**, *83*, 4041-4046.
79. Jahn, H. A.; Teller, E. *Proc. Roy. Soc.* **1938**, *161A*, 220.
80. Herzberg, G. *Electronic Spectra and Electronic Structure of Polyatomic Molecules*; Van Nostrand: Princeton, N.J., 1966; Vol. 3.
81. Born, M.; Oppenheimer, R. *Ann. Physik* **1927**, *84*, 457.
82. see also Ballhausen, C. J.; Hansen, A. E. *Annu. Rev. Phys. Chem.* **1972**, *23*, 15-38.

Downloaded by OHIO STATE UNIV LIBRARIES on September 14, 2012 | http://pubs.acs.org
Publication Date: August 14, 2002 | doi: 10.1021/bk-2002-0828.ch004

Downloaded by UNIV MASSACHUSETTS AMHERST on September 14, 2012 | http://pubs.acs.org
Publication Date: August 14, 2002 | doi: 10.1021/bk-2002-0828.ch005

Chapter 5

Coupled Cluster Methods for Bond-Breaking

Martin Head-Gordon, Troy Van Voorhis, Steven R. Gwaltney, and Edward F. C. Byrd

Department of Chemistry, University of California Berkeley, and Chemical Sciences Division, Lawrence Berkeley National Laboratory, Berkeley, CA 94720

A class of coupled cluster methods designed to describe bond-breaking processes are described. The approach taken involves first approximating the complete valence space Schrödinger equation to account for static electron correlations. For simplicity and tractability, the coupled cluster wave functions are restricted to double substitutions within this active space. Such reference functions are capable of correctly breaking only a single chemical bond, when developed within conventional coupled cluster theory. There are, however, at least two modifications to the theory that allow this limitation to be largely overcome. These modifications are described and discussed. A perturbative approach to correct active space coupled cluster methods for dynamical correlations is then described. The performance of these theories is tested on some model problems to illustrate their current capabilities and limitations.

In Low-Lying Potential Energy Surfaces; Hoffmann, M., et al.;
ACS Symposium Series; American Chemical Society: Washington, DC, 2002.

Downloaded by UNIV MASSACHUSETTS AMHERST on September 14, 2012 | http://pubs.acs.org
Publication Date: August 14, 2002 | doi: 10.1021/bk-2002-0828.ch005

Introduction

Single reference electronic structure methods are most widely used in quantum chemistry today. This is because of their ease of application; they require no molecule-specific customization unlike multireference methods where either reference configurations or an active space must be chosen for each problem at hand. However, computationally tractable single reference methods, ranging from simple mean-field Hartree-Fock theory to quite sophisticated methods such as CCSD(T) fail to correctly describe potential energy surfaces for bond-breaking. This is manifestly true for calculations based on restricted orbitals where incorrect dissociation products are obtained. The point is perhaps more debatable for unrestricted (spin symmetry-broken) orbitals where potential curves are qualitatively correct using single reference methods. However beginning at equilibrium with a pure spin state and finishing at dissociation with a statistical mixture is also unsatisfactory. By contrast, multireference electronic structure methods are well-suited to the description of global potential energy surfaces, apart from their inherent difficulty of application.

There is hence much incentive to develop electronic structure methods that retain the simplicity of use of existing single reference theories, but address their deficiencies for the description of bond-breaking processes. This chapter reports our recent progress towards this objective. Due to its short length, we make no pretense of reviewing the work of others, but instead seek to provide an overview of our recent work with some selected results. Our general strategy is as follows. We seek to partition electron correlation effects into nondynamical correlations associated with (relatively few) low-lying electron configurations, and dynamical correlations associated with the collective effect of (relatively many) high-energy configurations. We define the nondynamical correlation as being the difference between the mean field Hartree-Fock energy, and the energy obtained by solving the Schrödinger equation in the space of valence orbitals only. This could be the valence minimum basis, or the perfect pairing active space that supplies one correlating virtual orbital for each occupied valence orbital. The dynamical correlation is then the difference between the valence space Schrödinger energy, and the energy associated with solving the Schrödinger equation in the full orbital basis.

While the general strategy of dividing electron correlations into nondynamical and dynamical effects is similar to that of multireference methods (*1*) such as complete active space (CAS) methods (*2,3*), there is a crucial difference. Specifically, our insistence on the use of the full valence or perfect pairing active space means that there is no need to customize the number of active orbitals for each problem. In other words, techniques based on this procedure will meet the requirements of a theoretical model chemistry. Of course this means that much larger active spaces will be generated for a given molecule than would typically be employed in a standard CAS calculation. As a result, exact solution of the valence space Schrödinger equation (which scales approximately exponentially with the number of valence space electrons) is intractable with our approach. Instead, we must approximate the valence space Schrödinger equation as the initial step, and then subsequently approximate the correction for dynamical correlations. Our approaches to each of these two steps are described in each of the following main sections, and are performed within the framework of coupled cluster theory. This ensures proper extensivity of the approximations with respect to the number of electrons in the system.

Downloaded by UNIV MASSACHUSETTS AMHERST on September 14, 2012 | http://pubs.acs.org
Publication Date: August 14, 2002 | doi: 10.1021/bk-2002-0828.ch005

How good can a CCD wave function be?

The trial function that we have chosen to focus on is of the coupled cluster doubles (CCD) type (*4-6*):

$$\left|\Psi_{\text{CCD}}\right\rangle = e^{\hat{T}_2}\left|\Phi\right\rangle \tag{1}$$

Here the excitation operator promotes pairs of electrons from filled to empty orbitals. We note in passing that a generalized T_2 operator, which includes creation operators for filled orbitals, and destruction operators for empty orbitals is exact (*7-9*): however this form cannot yet be used tractably, so we do not consider it in this work.

We anticipate that the orbitals in the reference single determinant $\left|\Phi\right\rangle$ will be optimized to minimize the trial energy (*10,11*), so we shall neglect single substitutions. This also makes optimization within an active space possible (*12*). While the CCD wave function is well-known, and has desirable properties such as recovery of a substantial fraction of electron correlation at equilibrium geometries and proper extensivity with size, it has not traditionally been viewed as a suitable candidate for bond-breaking. This is because failures of conventional coupled cluster theory are well-known for bond-breaking (*13*).

To investigate whether this is due to limitations of the CCD wave function, or the way in which the CCD energy and amplitudes are conventionally obtained, we have recently performed variational CCD calculations (*14*). Variational CCD calculations are a restricted form of full configuration interaction (with factorial cost), because the energy expectation value includes contributions from all orbital replacements as high as the number of electrons:

$$E_{\text{var-CCD}} = \left\langle\Psi_{\text{CCD}}\middle|\hat{H}\middle|\Psi_{\text{CCD}}\right\rangle \Big/ \left\langle\Psi_{\text{CCD}}\middle|\Psi_{\text{CCD}}\right\rangle \tag{2}$$

As an example of the results that are obtained in this way, Figures 1 and 2 illustrate the potential curves obtained for homolytically dissociating the two single bonds in the water molecule by full CI, conventional CCD, and variational CCD, in two basis sets.

Downloaded by UNIV MASSACHUSETTS AMHERST on September 14, 2012 | http://pubs.acs.org
Publication Date: August 14, 2002 | doi: 10.1021/bk-2002-0828.ch005

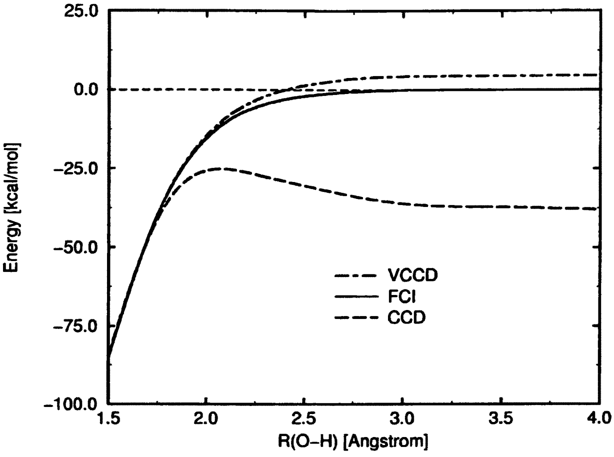

Figure 1. Variational CCD (VCCD), conventional CCD, and full CI (FCI) calculations on the double dissociation of H_2O, in the STO-3G basis. The experimental bond angle (104.5°) and FCI Brueckner orbitals were used.

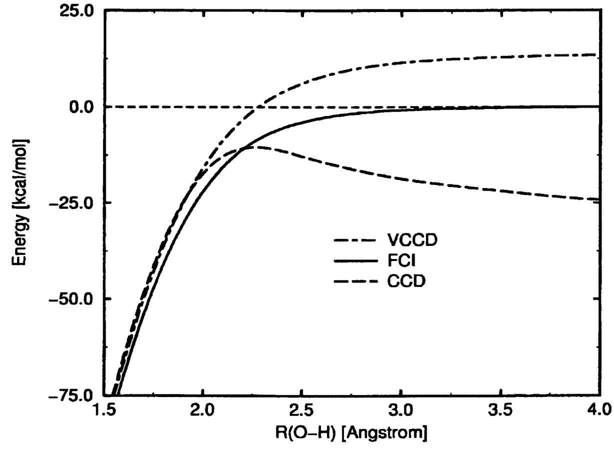

Figure 2: Same calculations as Figure 1, but in a double zeta (DZ) basis.

There are two principal conclusions that can be drawn from these results:

- While conventional CCD fails dramatically, the variational CCD calculations are well-behaved at long bond-lengths. The difficulties with conventional CCD for this 4 active electron problem are clearly a result of solving for the energy in a nonvariational fashion. Note that conventional CCD is qualitatively correct for a 2 active electron process such as a single bond-breaking, while it fails even more dramatically in a 6 active electron process such as a triple bond-breaking.

- The errors associated with variational CCD are significantly larger in the double zeta basis (Fig. 2) than in the minimal basis (Fig. 1). This simple trial wave function can do a near quantitatively accurate job of approximating the valence space (static) correlation (which is all that is present in the STO-3G basis), but is less successful in reproducing both static and dynamic correlation in the larger DZ basis.

These results and conclusions suggest a possible path towards practical coupled cluster methods for bond-breaking. The simple CCD trial function is potentially useful, if we are able to better approximate the variational CCD solution (conventional CCD is inadequate beyond single bond-breaking). Furthermore, the CCD trial function should be applied within a valence active space, because it performs far better in the minimal basis than the DZ basis. From the point of view of approximating the Schrödinger equation, we are being led to first approximate the valence space (CASSCF) equation, and then subsequently the remaining dynamical correlation. We turn to the first of these tasks below.

Downloaded by UNIV MASSACHUSETTS AMHERST on September 14, 2012 | http://pubs.acs.org
Publication Date: August 14, 2002 | doi: 10.1021/bk-2002-0828.ch005

How difficult must a CCD energy functional be?

How might we approximate the variational CCD approach discussed above, without incurring its factorial computational cost? Let us briefly re-examine the conventional CCD energy ansatz as a prelude to discussing how we have chosen to go beyond it. In conventional CC theory the equations that determine the doubles amplitudes can be obtained by minimizing the following functional:

$$L_{\mathrm{CCD}} = \left\langle \left(1+\hat{\Lambda}_2\right)\Phi \middle| \bar{\hat{H}} \middle| \Phi \right\rangle \tag{3}$$

In this expression, the variables to be minimized are the usual doubles amplitudes (T_2), the corresponding bra amplitudes (Λ_2), and the reference orbitals. In Eq. (3), the T_2 amplitudes are used to define a similarity transformed Hamiltonian:

$$\bar{\hat{H}} = \left(\hat{H}e^{\hat{T}_2}\right)_C = e^{-\hat{T}_2}\hat{H}e^{\hat{T}_2} \tag{4}$$

Since the bra amplitudes occur only as linear terms, the resulting CCD equations for the ket amplitudes (T_2) are independent of Λ_2:

$$\left\langle \Phi_d \middle| \bar{\hat{H}} \middle| \Phi \right\rangle = 0 \tag{5}$$

Indeed, the Λ_2 amplitudes are not required to determine the CCD energy. They arise in analytical derivatives of the energy as the so-called Z-vector (*15*).

Extended coupled cluster (ECC) theory (*16,17*) is a powerful existing framework for going beyond the standard coupled cluster energy ansatz, (3) In ECC theory (limited to double excitations, here), the energy is obtained by minimizing the following functional with respect to the bra (Λ_2) and ket (T_2) amplitudes:

$$L_{\text{ECCD}} = \left\langle e^{\hat{\Lambda}_2}\Phi \middle| \hat{\bar{H}} \middle| \Phi \right\rangle \tag{6}$$

Comparing Equations (3) and (6), it is evident that the usual CCD expression is the leading term in the ECCD energy, when $\exp(\Lambda_2)$ is expanded as a Maclaurin series. Therefore ECCD and CCD will be similar when the amplitudes are small (when CCD works well). For strongly correlated problems such as bond-breaking, it is likely that the more even-handed treatment of bra and ket degrees of freedom would permit the ECCD energy to much better approximate the variational CCD energy than CCD. To our knowledge, molecular calculations at the ECCD level have not yet been reported. This is presumably because of the large increase in both algebraic and computational complexity that is inherent in the minimization of Eq. (6) Indeed, analysis of the ECCD functional (*18*) suggests that computational cost will scale as N^{10}, far worse than the N^6 scaling of CCD in a straightforward implementation.

However, there is an interesting intermediate step between standard CCD and ECCD. This is a model that includes terms quadratic in Λ_2 in the bra function. We term this energy functional the quadratic coupled cluster doubles (QCCD) method (*19*):

$$L_{\text{QCCD}} = \left\langle \left(1+\hat{\Lambda}_2+\tfrac{1}{2}\hat{\Lambda}_2^2\right)\Phi \middle| \hat{\bar{H}} \middle| \Phi \right\rangle \tag{7}$$

The QCCD energy is to be made stationary with respect to both the ket (T_2) and bra (Λ_2) degrees of freedom, as well as the orbitals. In this respect it is a generalization of the conventional optimized orbital CCD method (*11*). However, the extra term relative to CCD introduces new physics, such as the coupling of the Λ_2 and T_2 amplitudes. For example, the equations for the T_2 amplitudes can be symbolically written as:

$$\left\langle \left(1+\hat{\Lambda}_2\right)\Phi_d \middle| \hat{\bar{H}} \middle| \Phi \right\rangle = 0 \tag{8}$$

This coupling will be weak when the Λ_2 amplitudes are small (CCD will be recovered with only minor differences), but when the amplitudes are large as in bond-breaking, this may lead to energies that are not as prone to nonvariational collapse.

It is beyond our present scope to discuss the QCCD equations or their computational implementation in any further detail. This task is addressed in

Downloaded by UNIV MASSACHUSETTS AMHERST on September 14, 2012 | http://pubs.acs.org
Publication Date: August 14, 2002 | doi: 10.1021/bk-2002-0828.ch005

Downloaded by UNIV MASSACHUSETTS AMHERST on September 14, 2012 | http://pubs.acs.org
Publication Date: August 14, 2002 | doi: 10.1021/bk-2002-0828.ch005

both published (*19*) and pending (*20*) publications. However, let us note some general features. The QCCD energy and associated amplitudes can be obtained in computational effort that scales with the 6th power of molecular size, and storage that scales as the 4th power of molecular size. These are the same scalings that conventional CCD exhibits, and therefore QCCD calculations will generally be feasible on molecules for which CCD is feasible. With a valence active space, the cost ratio is a small factor that is independent of basis set size. In the full space, the extra computation increases as the basis set size increases because one additional step in QCCD scales as V^6 where V is the number of (active) unoccupied orbitals. By contrast the rate-determining step in CCD scales as O^2V^4. Still, QCCD is dramatically less expensive than ECCD!

The question then is whether QCCD is robust enough to be faithful to variational CCD in bond-breaking problems. For double bond-breaking in water (see Fig. 1), the calculated energy differences between QCCD and VCCD do not exceed 5 microHartrees (*19*)! On a plot like Fig. 1 such differences are not even visible, and QCCD is thus an unqualified success. A second and more challenging test is triple bond-breaking in the nitrogen molecule, as shown in Fig. 3. These are also minimal basis calculations, because we know from the previous section that the performance of the CCD wave function for bond-breaking degrades when used out of the valence space.

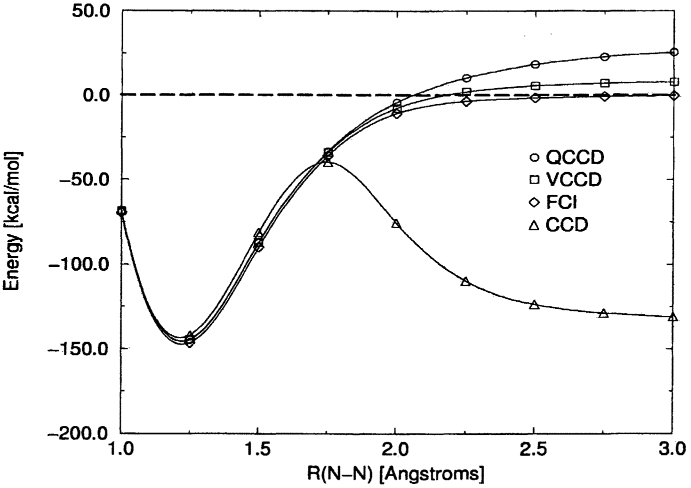

Figure 3. Calculations of the triple bond dissociation of N_2 in the STO-3G basis, using full CI, conventional CCD, variational CCD, and quadratic CCD.

Downloaded by UNIV MASSACHUSETTS AMHERST on September 14, 2012 | http://pubs.acs.org
Publication Date: August 14, 2002 | doi: 10.1021/bk-2002-0828.ch005

The results contained in Figures 3 are also quite encouraging. For N_2 dissociation, the QCCD results are qualitatively excellent, but there are noticeable differences between variational CCD and QCCD, which amount to roughly 15 kcal/mol as dissociation is approached. The difference between this test case, and the water double dissociation discussed above reflects the role of Λ_2^3 terms (which are neglected in QCCD) in the N_2 problem (corresponding to 6-electron contributions), while they are insignificant in the double bond-breaking problem.

Our conclusion at this stage is that QCCD represents a very significant and yet tractable improvement upon CCD, when used with orbital optimization in the valence space. In this sense, our first generation valence optimized orbital CCD method (*12*) is clearly superceded by QCCD in the valence space. We have implemented QCCD (both in active spaces and in the full space) within the correlation module of the Q-Chem program (*21*). Both energies and gradients are available, as the latter can be immediately computed from the 1- and 2-particle density matrices (and an energy-weighted density matrix) once the optimum orbitals and amplitudes have been determined.

How simple can a CCD wave function be?

To this stage our cluster wave function has been left in the general form of Eq. (1), with the restriction that double substitutions are confined to an active space. Within the active space, the double substitution operator couples together all pairs of occupied orbitals with all pairs of virtual orbitals. Physically we expect this description to be more complicated than is essential for a qualitatively correct description of the main correlations in bond-breaking. As is evident in minimal basis dissociation of H_2, they are surely the alpha-beta bond-antibond correlations necessary to permit homolytic bond separation.

So, restricting ourselves to the 1:1 perfect pairing active space, the simplest possible version of a CCD wave function would be to retain only the linear number of excitations needed to provide alpha-beta bond-antibond correlations:

$$\hat{T}_2^{PP} = \sum_{i}^{\substack{\textit{valence} \\ \textit{pairs}}} t_i a_{i^*}^{\dagger} a_{\bar{i}^*}^{\dagger} a_{\bar{i}} a_i \qquad (9)$$

This defines the CCD perfect pairing (PP) operator (*22,23*). Mathematically it converts the coupled cluster equations into the "uncoupled cluster equations", because the amplitude equations for the valence pairs are no longer coupled to each other. The only coupling is indirect through the orbital optimization procedure. As a result of this decoupling, we anticipate (and it is true) that the nonvariational catastrophes of conventional CCD will be eliminated. Of course CCD itself is exact for a single pair.

Perhaps the next simplest form of trial CCD wave function would be to retain the 1:1 active space, but reintroduce some coupling between valence electron that are associated with different pairs. The simplest way to do this defines what we have termed the imperfect pairing (IP) operator (*24*):

$$\hat{T}_2^{IP} = \hat{T}_2^{PP} + \sum_{i \neq j}^{\substack{valence \\ pairs}} \left(t_{ij}^{i^* j^*} \hat{E}_{ii^*} \hat{E}_{jj^*} + t_{ij}^{j^* i^*} \hat{E}_{ij^*} \hat{E}_{ji^*} \right) \tag{10}$$

We have used the unitary group generators, $\hat{E}_{ij^*} = a_{j^*}^{\dagger} a_i + a_{\bar{j}^*}^{\dagger} a_{\bar{i}}$ for conciseness. The IP form of the CCD operator is somewhat analogous to the GVB-RCI wave function, although there are important distinctions. For example, the cluster equations for this simplified CCD operator directly couple the different pairs (unlike PP), and accordingly the nonvariational failures associated with full CCD remain in the IP model (*24*).

Given the much simpler form of Eq. (10), which involves only a quadratic number of amplitudes, relative to Eq. (1), it is also more straightforward to understand how and why conventional CCD exhibits difficulties for multiple bond-breaking. The simplest model problem to examine is a double bond-breaking, as in the separation of ethylene into 2 triplet methylene fragments, in a 2:2 active space comprising the 2 bond orbitals. For this problem, it is possible to show that the trial CCD operator, Eq. (10), does not yield a physically correct solution at dissociation. In particular, because there is a forced relation between double and quadruple excitations through the exp(T_2) form of the wave function, we find a spurious ionic contribution at dissociation (*25*). This is a result of the restricted form of the cluster wave function, and is, in a practical sense, a fundamental problem with limited cluster wave functions for bond-breaking.

While a detailed presentation of both the analysis of the model problem, and the design of a solution is beyond our scope here, we shall summarize the central result (*25*). Within the IP form of the CCD operator, we must modify the quadruples term to ensure that no ionic contribution is obtained at dissociation in the model 2:2 double bond dissociation problem. For this purpose, it is sufficient to eliminate terms in the quadruples which involve a repeated index split between different amplitudes (for example the $t_{12}^{1^*2^*} t_{12}^{1^*2^*}$ terms, as opposed to $t_{11}^{1^*1^*} t_{22}^{2^*2^*}$ terms). This procedure defines a modification of the IP model that we term the GVB-RCC model, by analogy with the GVB-RCI approach.

Whether deleting these terms that prevent correct dissociation in the model double bond-breaking also helps to avoid the nonvariational catastrophes that occur in CCD and IP is unclear: it must be answered by numerical tests. However the answer appears to be affirmative. To illustrate the performance of

Downloaded by UNIV MASSACHUSETTS AMHERST on September 14, 2012 | http://pubs.acs.org
Publication Date: August 14, 2002 | doi: 10.1021/bk-2002-0828.ch005

the 3 models discussed in this section, Figure 4 shows potential curves for the PP method, the IP method and the GVB-RCC method for double bond-breaking in water relative to CASSCF in the same perfect pairing active space. The results are clearly quite encouraging. PP is qualitatively correct, and GVB-RCC successfully overcomes the limitations of the IP model to obtain nearly quantitative agreement with CASSCF for this problem. Other examples are presented elsewhere (*25*), and also support the likely value of GVB-RCC as a very inexpensive approximation to CASSCF. The development of somewhat more complete pair approximations than Eq. (10) is underway, and promises to still further improve these results. With additional difficulty, it is also possible to apply these simplified T_2 models to the QCCD energy functional, which will be of considerable interest.

Downloaded by UNIV MASSACHUSETTS AMHERST on September 14, 2012 | http://pubs.acs.org
Publication Date: August 14, 2002 | doi: 10.1021/bk-2002-0828.ch005

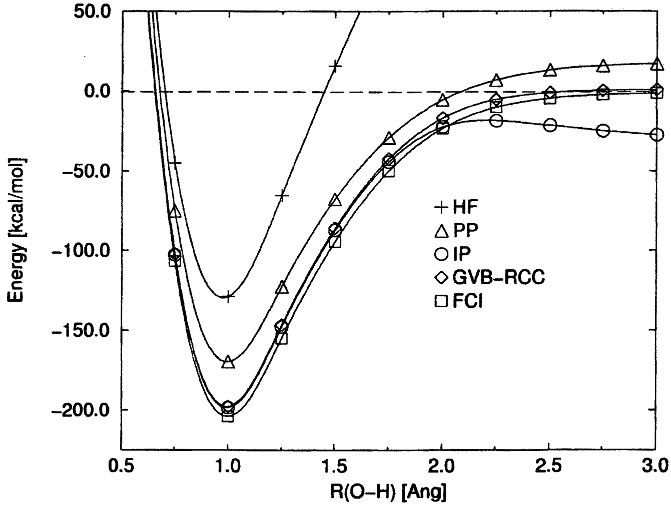

Figure 4. Double bond dissociation of the water molecule using the perfect pairing (PP), imperfect pairing (IP) and restricted pairing (GVB-RCC) local correlation models, compared to full configuration interaction (FCI) and Hartree-Fock theory in a minimal (STO-3G) basis.

How can a reference CCD energy be improved?

To this stage we have established that the simple CCD wave function is capable of yielding good accuracy when applied in a valence space, with an

Downloaded by UNIV MASSACHUSETTS AMHERST on September 14, 2012 | http://pubs.acs.org
Publication Date: August 14, 2002 | doi: 10.1021/bk-2002-0828.ch005

appropriately modified energy functional. However for quantitative accuracy it will be essential to also account for the neglected correlation effects associated with fluctuations of electrons into orbitals that are not in the valence space. This correlation is of the dynamical type. As it involves primarily high energy fluctuations, we expect that it should be reasonably well accounted for by perturbation theory. Our problem therefore is to develop such a correction given a reference solution of the CCD type. Piecuch and co-workers (*26-28*) have recently considered an approach to this problem in which the denominators of perturbative corrections are stabilized by a renormalization term. Our approach, which we summarize below, has been described in a series of recent papers (*29-31*).

We begin by recalling (*32*) that the initially solved CCD problem can be written as a linear eigenvalue problem with the similarity transformed Hamiltonian, Eq. (4), right eigenvector $\left|R^{(0)}\right\rangle = |0\rangle$, and left eigenvector $\left\langle L^{(0)}\right| = \langle 0|\left(1+\hat{\Lambda}_2^{\dagger}\right)$. This is true within the space defined by the reference plus active double substitutions, which we shall term the primary space, $|\mathbf{p}\rangle$. The remaining substitutions (singles, inactive doubles, triples, etc) comprise the secondary space, $|\mathbf{q}\rangle$. Our objective is to perturbatively correct this initial solution towards exact solution of the similarity transformed Schrödinger equation, $\hat{\bar{H}}|R\rangle = E|R\rangle$, where, formally the exact right eigenfunction would be related to the full configuration interaction (FCI) wave function by $|\Psi_{\mathrm{FCI}}\rangle = \exp\left(\hat{T}_2\right)|R\rangle$.

The similarity-transformed Hamiltonian is partitioned for perturbation theory, with the zero order part recovering the CCD solution in the primary space, $|\mathbf{p}\rangle$:

$$\hat{\bar{H}} = \hat{\bar{H}}^{(0)} + \hat{\bar{H}}^{(1)}$$

$$\hat{\bar{H}}^{(0)} = |\mathbf{p}\rangle\hat{\bar{H}}_{\mathbf{pp}}\langle\mathbf{p}| + |\mathbf{q}\rangle\hat{\bar{D}}_{\mathbf{qq}}\langle\mathbf{q}| \qquad (11)$$

$$\hat{\bar{H}}^{(1)} = |\mathbf{p}\rangle\hat{\bar{H}}_{\mathbf{pq}}\langle\mathbf{q}| + |\mathbf{q}\rangle\hat{\bar{H}}_{\mathbf{qp}}\langle\mathbf{p}| + |\mathbf{q}\rangle\left(\hat{\bar{H}} - \hat{\bar{D}}\right)_{\mathbf{qq}}\langle\mathbf{q}|$$

The zero-order Hamiltonian in the secondary space (denoted as $\hat{\bar{D}}$, to suggest that it will be diagonal in an appropriate basis) is taken as the one-body part of $\bar{H}$, excluding occupied virtual terms (which would couple the **p** and **q** spaces), plus an energy shift, $\bar{H}_{00} - H_{00}$. This shift ensures that diagonal matrix elements of $\left(\hat{\bar{H}}^{(0)} - E^{(0)}\right)$ in the $\mathbf{q}$ space have the form of intensive excitation energies (as needed for size-consistency). Expanding the energy to second order yields the following contributions:

$$\begin{aligned} E^{(0)} &= \left\langle L^{(0)} \middle| \hat{\bar{H}}^{(0)} \middle| R^{(0)} \right\rangle = E_{\mathrm{CCD}} \\ E^{(1)} &= \left\langle L^{(0)} \middle| \hat{\bar{H}}^{(1)} \middle| R^{(0)} \right\rangle = 0 \\ E^{(2)} &= \left\langle L^{(0)} \middle| \hat{\bar{H}}^{(1)} \middle| R^{(1)} \right\rangle \end{aligned} \tag{12}$$

Formally, the first order correction to the zero order right eigenvector, $\left|R^{(0)}\right\rangle = \left|0\right\rangle$, is given by:

$$\left|R^{(1)}\right\rangle = -\left(\hat{\bar{H}}^{(0)} - E^{(0)}\right)^{-1} \hat{\bar{H}}^{(1)} \left|R^{(0)}\right\rangle \tag{13}$$

To proceed further one must evaluate the matrix elements of $\bar{H}$ required for the first order right eigenvector, Eq. (13), and the second order energy, Eq. (12). We shall not do this explicitly here (for details, see ref. (*30*)), but rather just consider the general form of the result. $\bar{H}$ as defined in Eq. (4) contains from one-body to six-body terms (i.e. up to strings of 6 creation and 6 annihilation operators). Given that $\left|R^{(0)}\right\rangle = \left|0\right\rangle$, this means that the first order eigenvector, (13), is a sum of single, double, triple, quadruple, pentuple and hextuple substitutions!

Fortunately, however the pentuples and hextuples cannot couple with $\left\langle L^{(0)}\right| = \left\langle 0\right|\left(1 + \hat{\Lambda}_2^{\dagger}\right)$, as matrix elements $\bar{H}_{fg} = \left\langle f \middle| \hat{H}e^{\hat{T}_2} \middle| g \right\rangle_C$ are zero when substitution f is more than 2 levels smaller than substitution g. Thus doubles in the zero order left eigenvector (Λ_2) can only couple with up to quadruple substitutions. This leaves our second order energy expression as:

$$\begin{aligned} E^{(2)} = {} & \sum_{s}^{\text{singles}} \left(\bar{H}_{0s}^{(1)} + \sum_{d\in\mathbf{p}} L_d^{(0)} \bar{H}_{ds}^{(1)} \right) R_s^{(1)} + \sum_{d'\in\mathbf{q}}^{\text{doubles}} \left(\bar{H}_{0d'}^{(1)} + \sum_{d\in\mathbf{p}} L_d^{(0)} \bar{H}_{dd'}^{(1)} \right) R_{d'}^{(1)} \\ & + \sum_{t}^{\text{triples}} \left(\sum_{d\in\mathbf{p}} L_d^{(0)} \bar{H}_{dt}^{(1)} \right) R_t^{(1)} + \sum_{q}^{\text{quadruples}} \left(\sum_{d\in\mathbf{p}} L_d^{(0)} \bar{H}_{dq}^{(1)} \right) R_q^{(1)} \end{aligned} \tag{14}$$

To make this expression more tractable, we employ a factorization approximation (*33*) for the energy denominators associated with the quadruple substitutions. Otherwise any explicit evaluation of the $O(N^8)$ quadruple substitutions cannot require less than $O(N^9)$ computation. In 5th order Møller-

Downloaded by UNIV MASSACHUSETTS AMHERST on September 14, 2012 | http://pubs.acs.org
Publication Date: August 14, 2002 | doi: 10.1021/bk-2002-0828.ch005

Plesset theory (*34*), the quadruple substitutions can be exactly factorized, resulting in a significantly lower $O(N^6)$ computational cost. In our application, the factorization is not exact, but the errors introduced appear to be in the microHartree range (*33*). For the explicit spin-orbital equations, see ref. (*30*).

The physical significance of the terms in Eq. (14) is as follows. The two leading terms (singles and inactive doubles) are roughly analogous to the singles and doubles that occur in MP2 theory (the former only when a non-Brillouin reference is used). They provide dynamic correlation for electron pairs that are primarily unexcited from the reference determinant. Note that the explicit presence of Λ_2 in the expressions for singles and doubles contributions renormalizes the MP2-like contributions for the effect of other reference configurations. The triple substitutions are similar in effect to the MP4 triples that occur in CCSD(T) and related theories. They provide dynamical correlation for electron pairs in which one electron comes from an excited configuration in the reference, while the other does not (thus creating a triple excitation). Likewise the quadruple substitutions provide dynamical correlation for unexcited electron pairs in doubly excited configurations, when that correlation effect is different from the correlation of this pair in the reference configuration (either because it involves orbitals outside the active space, or because the amplitude itself differs).

To this stage, the theory we have described is only applicable directly to the CCD-based models that use the conventional energy expression, Eq. (3), (with or without the use of local correlation approximations). To apply this approach to perturbatively correct the QCCD model requires that we modify the second order energy to avoid double counting of correlation effects (*35*). The QCCD energy, (7), contains additional terms relative to CCD that involve quadruple excitations in the left-hand wave function. They are in fact very similar to the last term of the second-order correction, Eq. (14), when all orbitals involved are active. Therefore a simple generalization of the second order correction to QCCD is to delete the quadruples terms where all indices are in the active space. In the limit where all orbitals are active, there is no quadruples correction, while for smaller active spaces, quadruples with indices out of the active space still contribute.

To explore the performance of the second order corrections without use of active spaces, Table 1 shows the performance of OD(2) and QCCD(2) against OD, QCCD and FCI for the problem of N_2 dissociation for small bond stretches. Considering the result at equilibrium, it is very encouraging that QCCD(2) yields a deviation from FCI that is about 1/3 smaller than OD(2). For bond-stretching, it is also evident that the superiority of QCCD(2) relative to OD(2) increases. Since OD(2) (*29*) itself is an improvement on a conventional triples correction, these results are clearly encouraging for the applicability of QCCD(2) to difficult problems. While further studies are clearly necessary to better define the performance of QCCD(2), it appears likely that it will be a useful theory

Downloaded by UNIV MASSACHUSETTS AMHERST on September 14, 2012 | http://pubs.acs.org
Publication Date: August 14, 2002 | doi: 10.1021/bk-2002-0828.ch005

particularly for cases where conventional CCSD(T) is poor. For explorations of the corresponding CCSD(2) correction, see ref. (*31*).

Table I. Energy deviations[a,b] from FCI (in mH) for N_2

R (Ångstroms)	*OD*	*OD(2)*	*QCCD*	*QCCD(2)*
1.0679	12.668	1.242	10.626	0.809
1.1208	14.741	1.499	12.216	0.930
1.1737	17.104	1.799	13.991	1.055
1.2700	22.243	2.520	17.744	1.330
1.4288	33.308	4.491	25.514	2.127

[a] FCI calculations from Larsen, H.; Jørgensen, P; and Christiansen, O. *J. Chem. Phys.* **2000**, *113*, 6677-6686.

[b] Basis set is cc-pVDZ, and no active space is employed for these calculations.

As an example of the performance of the second order corrections when active spaces are employed, Table 2 shows the performance of valence OD, OD(2), QCCD, and QCCD(2) relative to FCI for the double dissociation of water (again!). The perfect pairing active space is employed. It is evident that the (2) corrections are able to reduce the absolute deviations against FCI by a factor of approximately 8 at equilibium. As the bonds are stretched this factor gradually decreases for QCCD(2) towards about a factor of 4. VOD (and therefore VOD(2)), on the other hand, exhibit the nonvariational collapse characteristic of conventional coupled cluster methods. These results indicate that VQCCD(2) is an effective correction to VQCCD, although the level of agreement with FCI is qualitative rather than quantitative.

Table II. Deviations from FCI[a] (in mH) for water double dissociation[b].

bondlength/R_e	*VOD*	*VOD(2)*	*VQCCD*	*VQCCD(2)*
1.0	96.550	12.472	96.061	12.466
1.5	97.788	14.140	96.256	13.986
2.0	93.740	15.104	96.725	15.757
2.5	63.907	2.880	98.883	22.000
3.0	47.645	-8.760	100.933	26.488

[a] FCI results from Olsen, J.; Jørgensen, P.; Koch, H.; Balkova, A.; Bartlett, R .J. *J. Chem. Phys.* **1996**, *104*, 8007-8015.

[b] Basis set is cc-pVDZ, valence active space is perfect pairing (1:1).

Downloaded by UNIV MASSACHUSETTS AMHERST on September 14, 2012 | http://pubs.acs.org
Publication Date: August 14, 2002 | doi: 10.1021/bk-2002-0828.ch005

Conclusions

The work described here is a useful extension of the traditional capabilities of single reference coupled cluster theories, in our opinion. We have shown that tractable approximations to the valence space Schrödinger equation can be obtained in at least two complementary ways. The first approach is by making the form of the trial energy "more variational", in the quadratic coupled cluster doubles method. The second approach is to eliminate terms in the conventional CCD equations that are responsible for its breakdown in bond-breaking processes, which leads to the perfect pairing and restricted pairing models. For any of these approaches, perturbation theory in terms of the similarity-transformed Hamiltonian defined by a valence space coupled cluster calculation is developed to account for the remaining dynamical correlations. We hope for future advances that will improve the present level of qualitative agreement with full configuration interaction calculations towards quantitative agreement. However, the theories described here are already accurate enough to be useful for many purposes, without the need to select the active space size on an ad-hoc molecule-by-molecule basis that has plagued traditional multireference methods.

Acknowledgements

This work was supported by the Director, Office of Energy Research, Office of Basic Energy Sciences, Chemical Sciences Division of the US Department of Energy under Contract DE-AC03-76SF00098, by NSF Grant CHE-9981997, a SUR equipment grant from IBM, and supercomputer time from NERSC.

References

(1) Shepard, R. In *Ab Initio Methods in Quantum Chemistry II*; Lawley, K. P., Ed.; John Wiley and Sons, Ltd.: Chichester, 1987; Vol. 69, pp 64-200.
(2) Roos, B. O.; Taylor, P. R. *Chem. Phys.* **1980**, *48*, 157-173.
(3) Ruedenberg, K.; Schmidt, M. W.; Gilbert, M. M.; Elbert, S. T. *Chem. Phys.* **1982**, *71*, 41-49.
(4) Cizek, J. *J. Chem. Phys.* **1966**, *45*, 4256-.
(5) Pople, J. A.; Krishnan, R.; Schlegel, H. B.; Binkley, J. S. *Int. J. Quantum Chem.* **1978**, *14*, 545-560.
(6) Bartlett, R. J.; Purvis, G. D. *Int. J. Quantum Chem.* **1978**, *14*, 561-581.
(7) Nooijen, M. *Phys. Rev. Lett.* **2000**, *84*, 2108-2111.
(8) Nakatsuji, H. *J. Chem. Phys.* **2000**, *113*, 2949-2956.
(9) Van Voorhis, T.; Head-Gordon, M. *J. Chem. Phys.* **2001**, *115*, 5033-5040.

Downloaded by UNIV MASSACHUSETTS AMHERST on September 14, 2012 | http://pubs.acs.org
Publication Date: August 14, 2002 | doi: 10.1021/bk-2002-0828.ch005

(10) Scuseria, G. E.; Schaefer, H. F. *Chem. Phys. Lett.* **1987**, *142*, 354-358.

(11) Sherrill, C. D.; Krylov, A. I.; Byrd, E. F. C.; HeadGordon, M. *J. Chem. Phys.* **1998**, *109*, 4171-4181.

(12) Krylov, A. I.; Sherrill, C. D.; Byrd, E. F. C.; Head-Gordon, M. *J. Chem. Phys.* **1998**, *109*, 10669-10678.

(13) Bartlett, R. J.; Stanton, J. F. In *Reviews in Computational Chemistry, Volume V*; Lipkowitz, K. B., Boyd, D. B., Eds.; VCH Publishers, Inc.: New York, 1994; pp 65-169.

(14) Van Voorhis, T.; Head-Gordon, M. *J. Chem. Phys.* **2000**, *113*, 8873-8879.

(15) Handy, N. C.; Schaefer, H. F. *J. Chem. Phys.* **1984**, *81*, 5031-5033.

(16) Arponen, J. *Ann. Phys.* **1983**, *151*, 311-382.

(17) Arponen, J. S.; Bishop, R. F.; Pajanne, E. *Phys. Rev. A* **1987**, *36*, 2519-2538.

(18) Szalay, P. G.; Nooijen, M.; Bartlett, R. J. *J. Chem. Phys.* **1995**, *103*, 281-298.

(19) Van Voorhis, T.; Head-Gordon, M. *Chem. Phys. Lett.* **2000**, *330*, 585-594.

(20) Byrd, E. F. C.; Van Voorhis, T.; Head-Gordon, M. *in preparation* **2001**.

(21) Kong, J.; White, C. A.; Krylov, A. I.; Sherrill, D.; Adamson, R. D.; Furlani, T. R.; Lee, M. S.; Lee, A. M.; Gwaltney, S. R.; Adams, T. R.; Ochsenfeld, C.; Gilbert, A. T. B.; Kedziora, G. S.; Rassolov, V. A.; Maurice, D. R.; Nair, N.; Shao, Y. H.; Besley, N. A.; Maslen, P. E.; Dombroski, J. P.; Daschel, H.; Zhang, W. M.; Korambath, P. P.; Baker, J.; Byrd, E. F. C.; Van Voorhis, T.; Oumi, M.; Hirata, S.; Hsu, C. P.; Ishikawa, N.; Florian, J.; Warshel, A.; Johnson, B. G.; Gill, P. M. W.; Head-Gordon, M.; Pople, J. A. *J. Comput. Chem.* **2000**, *21*, 1532-1548.

(22) Cullen, J. *Chem. Phys.* **1996**, *202*, 217-229.

(23) Van Voorhis, T.; Head-Gordon, M. *J. Chem. Phys.* **2000**, *112*, 5633-5638.

(24) Van Voorhis, T.; Head-Gordon, M. *Chem. Phys. Lett.* **2000**, *317*, 575-580.

(25) Van Voorhis, T.; Head-Gordon, M. *J. Chem. Phys.* **2001**, *in press*.

(26) Kowalski, K.; Piecuch, P. *J. Chem. Phys.* **2000**, *113*, 18-35.

(27) Kowalski, K.; Piecuch, P. *J. Chem. Phys.* **2000**, *113*, 5644-5652.

(28) Piecuch, P.; Kucharski, S. A.; Kowalski, K. *Chem. Phys. Lett.* **2001**, *344*, 176-184.

(29) Gwaltney, S. R.; Head-Gordon, M. *Chem. Phys. Lett.* **2000**, *323*, 21-28.

(30) Gwaltney, S. R.; Sherrill, C. D.; Head-Gordon, M.; Krylov, A. I. *J. Chem. Phys.* **2000**, *113*, 3548-3560.

(31) Gwaltney, S. R.; Head-Gordon, M. *J. Chem. Phys.* **2001**, *115*, 2014-2021.

(32) Stanton, J. F. *Chem. Phys. Lett.* **1997**, *281*, 130-134.

(33) Kucharski, S. A.; Bartlett, R. J. *J. Chem. Phys.* **1998**, *108*, 9221-9226.

(34) Kucharski, S. A.; Bartlett, R. J. *Adv. Quantum Chem.* **1986**, *18*, 281-344.

(35) Gwaltney, S. R.; Van Voorhis, T.; Byrd, E. F. C.; Head-Gordon, M. *Chem. Phys. Lett.* **2001**, *submitted*.

Downloaded by UNIV MASSACHUSETTS AMHERST on September 14, 2012 | http://pubs.acs.org
Publication Date: August 14, 2002 | doi: 10.1021/bk-2002-0828.ch005

Downloaded by PENNSYLVANIA STATE UNIV on September 14, 2012 | http://pubs.acs.org
Publication Date: August 14, 2002 | doi: 10.1021/bk-2002-0828.ch006

Chapter 6

State-Specific Multireference Coupled Cluster-Based Methods for Potential Energy Surfaces and Their Approximate Variants

Sudip Chattopadhyay[1], Uttam Sinha Mahapatra[1], Pradipta Ghosh[1], and Debashis Mukherjee[2]

[1]Department of Physical Chemistry, Indian Association for the Cultivation of Science, Calcutta 700 032, India
[2]Jawaharlal Nehru Centre for Advanced Scientific Research, Bangalore 560 064, India

Traditional multi-reference (MR) coupled-cluster approaches based on the effective hamiltonian formalism are often plagued with intruder states, and are generally unsuitable for potential energy surface (PES) studies. We present here a concise account of our recently developed state-specific multi-reference coupled-cluster (SS-MRCC) theory and its certain approximate variants, which are size-extensive and size-consistent and are designed to obviate intruders in a natural manner. The approximations include the state-specific perturbative theories (SS-MRPT) and the coupled electron-pair approximation (SS-MRCEPA) versions, which retain the essential physics without losing much of the accuracy of the full-blown SS-MRCC. All these methods are based on a complete active space (CAS), and the target energy is obtained by diagonalizing an effective operator in this space. The methods are free of intruders whenever the target state energy is well separated from the virtual functions and work smoothly over wide range of geometries of various molecular states having pronounced MR character and/or those possessing potential intruders at various points. For low-lying excited states of molecular ground states with varying degrees of quasi-degeneracy, where it may

In Low-Lying Potential Energy Surfaces; Hoffmann, M., et al.;
ACS Symposium Series; American Chemical Society: Washington, DC, 2002.

be difficult to discern a viable intruder-free CAS, a linear response theory (LRT) based on the SS-MRCC (MR-CCLRT) for the ground state and its approximate variants provide a simple but effective description of the associated PES. We provide illustrative numerical applications of the SS-MRCC and SS-MRPT formulations with the ground state PES profile of the square-to-rectangular stretch of the Li_4 model system. The excited states of Li_4 are generated by implementing the MR-CCLRT scheme. We demonstrate the efficacy of the SS-MRCEPA suite of methods by calculating the ground state PES of the trapezoidal H_4 model. The excited states of the same model system are obtained via the LRT based on the MR-CEPA scheme (MR-CEPALRT).

Downloaded by PENNSYLVANIA STATE UNIV on September 14, 2012 | http://pubs.acs.org
Publication Date: August 14, 2002 | doi: 10.1021/bk-2002-0828.ch006

Introduction

The single-reference (SR) coupled-cluster (CC) theory is now well established as a powerful tool for incorporating correlation for states dominated by a single determinant [1, 2, 3]. The truncation schemes such as CCSD [1, 2] and CCSD(T) [4] are now being routinely applied to molecules of small and medium sizes. Accuracy of the SRCC at the SD or SD(T) truncation levels, however, goes down significantly in the presence of quasi-degeneracy, warranting computationally viable appropriate extensions of the SRCC method. While inclusion of the 3- and 4-body cluster operators in the SRCC method (CCSDT [5, 6] and CCSDTQ [7]) improves the performance, they are computationally very demanding. Any minimal stratagem in such a situation, which remains within the framework of the SRCC theory itself, requires an accurate treatment of at least a subset of 3- and 4- body cluster operators involving the active orbitals involved in the active space containing the quasi-degenerate determinants. Such methods have appeared in recent years [8, 9]. Although these extensions are straightforward, the working equations are rather lengthy. Another recent alternative scheme estimates the higher-body cluster amplitudes by augmenting the SR-CCSD equations by inclusion of these cluster amplitudes from a CAS function [10]. We, however, feel that a more natural way to treat quasi-degeneracy is to treat the non-dynamical correlation stemming from quasi-degeneracy by starting from an active space of quasi-degenerate determinants, while the remaining dynamical correlations can be included via a cluster expansion of the wave-function involving virtual determinants. This approach is thus a multi-reference (MR) generalization of the SRCC method. The primary strength of an MR-based method as compared to an SR approach is that one gains the flexibility needed to describe features such as bond-breaking within a few-body truncation scheme that may require accurate treatment of rather large-body cluster operators if described within the SRCC method. For this reason, there has been considerable efforts to formulate MRCC methods for both the ground and excited states for more than two decades. Among these developments are the valence universal (VU) [11] and state-universal (SU) [12, 13] approaches, which are based on effective hamiltonians defined in a model space (MS) chosen to be a CAS. The former method is useful for treating differential correlation effects as encountered in spectroscopic energy differences, while the latter determines state-energies *per se*. Both these methods have been applied with considerable success for quasi-degenerate situations at fixed internuclear separation. There have been other recent interesting attempts to develop CC theories based on a single, but multi-determinantal reference functions for non-singlet states, using the unitary-group adapted spin-free formulations [14].

These traditional MRCC theories, despite their success, face serious problems in their use in studying potential energy surfaces (PES). All of them are often plagued with the emergence of instability of the CC equations stemming from the near degeneracy of some MS functions with those of some virtual functions at some geometry or the other. This is the notorious problem of intruders [15, 16]. Although the intruders can be avoided to a large extent at some specific geometries by working with incomplete model space (IMS) [17, 18, 19], the situation is far less satisfactory, however, for generating PES since different IMS are needed in the different regions over the wide range of geometry [20]. One way out of this problem is to develop theories based on MR approach but to partition the model space into two subspaces – primary and secondary, where the latter may have energetic overlap with the virtual space. The idea is to define a pseudo-wave

Downloaded by PENNSYLVANIA STATE UNIV on September 14, 2012 | http://pubs.acs.org
Publication Date: August 14, 2002 | doi: 10.1021/bk-2002-0828.ch006

operator which acts on the entire model space, but generates exact states which are equal in number to the dimension of the primary model subspace and are dominated by the model functions spanning this subspace. This approach was advocated by Kirtman [21], and developed fully by Malrieu *et al.* [22] in the perturbative context, who termed this the intermediate hamiltonian approach (IH). There have been important innovations by Hoffmann [23], and Khait and Hoffmann [24]. The latter method generates the optimal primary subspace in an iterative manner, which improves the performance of the IH considerably. Coupled-cluster IH formalisms [25], which are size-extensive, were also developed. Another approach to circumvent the difficulty is to abandon the partitioning of the MS into primary and secondary subspace, and define a wave operator which acts on just one reference function, which is a linear combination of all the functions of the MS. In other words, the emphasis in this approach is on developing a theory which targets only one state – rather than several states at the same time. This is thus a state-specific approach. In this strategy, it is not necessary that the exact function is dominated by only certain model functions (which are taken to form the primary subspace in the IH methods). There have been two distinct courses of development of this approach. In one, the coefficients of the model functions forming the initial reference function are fixed by a prior diagonalization in the model space, and they are not revised as a consequence of mixing with the virtual functions. There have been both perturbative [26, 27, 28, 29] and non-perturbative [30, 31] formulations, mostly using CAS. Among these, the non-perturbative method has been explicitly proven to be size-extensive. In the other, the combining coefficients are updated as a result of the inclusion of the virtual functions via the wave operator. There have been three formalisms [31, 32, 33, 34], based on this idea, one of which is our recent state-specific multi-reference coupled-cluster (SS-MRCC) formalism [31, 32, 35]. The SS-MRCC method is non-perturbative, works in a CAS, is explicitly size-extensive and size-consistent, and allows systematic size-extensive approximations by either truncation in the rank of the cluster operators or in approximate ways of evaluating them. The method is intruder-free whenever the target state

Downloaded by PENNSYLVANIA STATE UNIV on September 14, 2012 | http://pubs.acs.org
Publication Date: August 14, 2002 | doi: 10.1021/bk-2002-0828.ch006

energy is well-separated from the energies of the virtual functions. While this situation is often encountered for the ground state PES, even in the regions of avoided crossings, the low-lying excited states whose ground states are pronouncedly MR in character, may not display this behavior. An appropriate generalization of the CC based linear response theory (LRT), starting from the SS-MRCC, offers a simple and viable access to the excited PES in such cases [36].

In this article we will focus on some of the latest developments using the SS-MRCC based formulations. In particular, we shall explore the efficacy of some physically sensible approximations of the parent theory, viz. the second order perturbation theories (SS-MRPT) [37] derived from the first order approximations of the cluster operators and the non-perturbative schemes in the spirit of coupled electron pair approximations (CEPA), SS-MRCEPA, for the PES of ground states. We shall also present a brief account of the LRT based on the parent SS-MRCC [31, 32] and SS-MRCEPA, termed by us as MR-CCLRT and MR-CEPALRT respectively, for studying the PES of the low-lying excited states from a knowledge of the multi-reference ground state PES. The most important advantage of the LRT based methods is to naturally circumvent intruder problem in the excited states. Moreover, the MR-CCLRT and MR-CEPALRT are size-intensive [36, 38, 39] in the sense of providing excitation energies for fragments in the asymptotic limit of separation into non-interacting fragments.

State-specific Multi-reference Coupled-cluster Theory and its Approximate Versions

We begin this section with a succinct summary of the essential ingredients and the theoretical underpinnings leading to the development of the SS-MRCC formalism. This will form the starting point for the perturbative and the CEPA-like approximations to follow.

Downloaded by PENNSYLVANIA STATE UNIV on September 14, 2012 | http://pubs.acs.org
Publication Date: August 14, 2002 | doi: 10.1021/bk-2002-0828.ch006

A natural choice to develop a size-extensive and size-consistent correlation theory for states with strong MR character is to work with a set of reference determinants spanning a CAS. We write the reference function $|\psi_0\rangle$ as a combination of the reference determinants $|\phi_\mu\rangle$ spanning the CAS:

$$|\psi_0\rangle = \sum_\mu |\phi_\mu\rangle c_\mu \tag{1}$$

The exact function $|\psi\rangle$ is written as a cluster expansion involving cluster operators T^μ exciting from corresponding $|\phi_\mu\rangle$'s:

$$|\psi\rangle = \sum_\mu \exp(T^\mu)|\phi_\mu\rangle c_\mu \tag{2}$$

$|\psi\rangle$ is taken to satisfy the Schrödinger equation with the eigenvalue E :

$$H|\psi\rangle = H\sum_\mu \exp(T^\mu)|\phi_\mu\rangle c_\mu = E|\psi\rangle \tag{3}$$

Each T^μ excites to all the virtual functions from ϕ_μ via the various n hole - n particle excitations, where the holes and particles are defined with respect to each ϕ_μ. Such a cluster expansion Ansatz was first used by Jeziorski and Monkhorst in the context of the effective hamiltonian based state-universal multi-reference coupled cluster (SU-MRCC) theory [12] and has recently been exploited in the state-specific formulations too [31, 32, 34]. Since each ϕ_μ has different sets of active orbitals, any specific core-to-particle excitation would lead to a different virtual determinant from each ϕ_μ. This is, however not so, in general for excitations involving active orbitals. Thus, we would encounter *redundancy* of the cluster operators involving active orbitals. To determine all of them, we have to invoke suitable sufficiency conditions. One may imagine that sufficiency conditions introduce a great degree of arbitrariness in a formalism. This is, however, not so if we want to exploit the arbitrariness in our choice to satisfy our twin desirable goals: to ensure that intruders are absent and to guarantee size-extensivity. It has been found that there are only two choices which naturally lead to MRCC equations which generate manifestly connected cluster operators. One

Downloaded by PENNSYLVANIA STATE UNIV on September 14, 2012 | http://pubs.acs.org
Publication Date: August 14, 2002 | doi: 10.1021/bk-2002-0828.ch006

Downloaded by PENNSYLVANIA STATE UNIV on September 14, 2012 | http://pubs.acs.org
Publication Date: August 14, 2002 | doi: 10.1021/bk-2002-0828.ch006

set is precisely the same as the SU-MRCC theory of Jeziorski and Monkhorst [12], which is known to encounter intruders. The other is our SS-MRCC formalism [31, 32]. We present below, without the detailed derivation, the form of the working equations for the cluster amplitudes:

$$\langle\chi_l|\overline{H}_\mu|\phi_\mu\rangle c_\mu + \sum_\nu \langle\chi_l|\exp(-T^\mu)\exp(T^\nu)|\phi_\mu\rangle\tilde{H}_{\mu\nu}c_\nu = 0 \;\; \forall\, l,\mu \qquad (4)$$

where

$$\overline{H}_\mu = \overline{H\exp(T^\mu)} \qquad (5)$$

and

$$\tilde{H}_{\mu\nu} = \langle\phi_\mu|\overline{H}_\nu|\phi_\nu\rangle \qquad (6)$$

The model space coefficients $\{c_\mu\}$ are determined from

$$\sum_\nu \tilde{H}_{\mu\nu}c_\nu = Ec_\mu \qquad (7)$$

We note that eq (4) involves the coefficients c_μ and c_ν explicitly, indicating that the cluster amplitudes depend on them, as is expected of a state-specific theory. We also note that the sets $\{T_\mu\}$ and $\{c_\mu\}$ are coupled through eq (4) and eq (7). Solving these coupled set of equation we obtain both the cluster amplitudes and the converged coefficients from the diagonalization. The number of unknowns in this formalism is exactly the same as in the effective hamiltonian based SU-MRCC theory [12].

The detailed derivation and the proof of the extensivity of the SS-MRCC theory have been discussed at length in our recent papers [31, 32]. What is pertinent for us here is the identification of one of the essential arguments leading to extensivity, since this will form the guideline of the approximations to be discussed below. Dividing eq (4) through by c_μ, we have

$$\langle\chi_l|\overline{H}_\mu|\phi_\mu\rangle + \sum_\nu \langle\chi_l|\exp(-T^\mu)\exp(T^\nu)|\phi_\mu\rangle\tilde{H}_{\mu\nu}(c_\nu/c_\mu)$$
$$= 0 \;\; \forall\, l,\mu \qquad (8)$$

The first term of eq (8) above is manifestly extensive, while the connectivity property of the second term requires a careful treatment, since this involves a product of two matrix-elements and may not have terms with common orbital labels in the two factors. Using the Baker-Campbell-Hausdorff formula for the product of exponentials, the second term can be written as

$$\sum_{\nu}\langle\chi_l|\exp(-T^{\mu})\exp(T^{\nu})|\phi_\mu\rangle\tilde{H}_{\mu\nu}(c_\nu/c_\mu) =$$
$$\sum_{\nu}\langle\chi_l|(T^{\nu}-T^{\mu}+\frac{1}{2}[T^{\nu},T^{\mu}]$$
$$+\frac{1}{12}[[T^{\nu},T^{\mu}],T^{\mu}]-\frac{1}{12}[[T^{\nu},T^{\mu}],T^{\nu}]$$
$$+\cdots)|\phi_\mu\rangle\tilde{H}_{\mu\nu}(c_\nu/c_\mu) \qquad (9)$$

Now, the second factor in eq (9), $\tilde{H}_{\mu\nu}(c_\nu/c_\mu)$ is labeled by all the active orbitals which distinguish the determinants ϕ_μ and ϕ_ν, and the first factor $\langle\chi_l|(T^{\nu}-T^{\mu}+\frac{1}{2}[T^{\nu},T^{\mu}]+\frac{1}{12}[[T^{\nu},T^{\mu}],T^{\mu}]-\frac{1}{12}[[T^{\nu},T^{\mu}],T^{\nu}]+\cdots)|\phi_\mu\rangle$ should contain terms with some of these distinguishing active orbitals in $\tilde{H}_{\mu\nu}(c_\nu/c_\mu)$ for extensivity. While it is straightforward to show that the commutators and the multiple commutators generated by the Baker-Campbell-Hausdorff formula do have active orbital labels with this property, the individual terms linear in T^{μ} and T^{ν} do not. In fact there are excitation operators involving orbitals different from those active orbitals distinguishing ϕ_μ and ϕ_ν. Interestingly enough, it has been proved [31, 32] that the term $\langle\chi_l|(T^{\nu}-T^{\mu})|\phi_\mu\rangle$ containing *the difference* $(T^{\nu}-T^{\mu})$ is, however, labeled by some or all the active orbitals distinguishing ϕ_μ and ϕ_ν, and thus the two factors in the term in eq (9) above have indeed some orbital labels in common. For any approximation of the SS-MRCC equations preserving the extensivity, it is mandatory to treat all the cluster amplitudes on an equal footing; otherwise the difference $(T^{\nu}-T^{\mu})$ will not be labeled by the active orbitals distinguishing ϕ_μ and ϕ_ν. This aspect would be one guiding principle in our development of the perturbative and CEPA approximations.

We now present a brief critique of the other two SS formalisms [33, 34] which bear kinship with the SSMR formulation being dis-

Downloaded by PENNSYLVANIA STATE UNIV on September 14, 2012 | http://pubs.acs.org
Publication Date: August 14, 2002 | doi: 10.1021/bk-2002-0828.ch006

Downloaded by PENNSYLVANIA STATE UNIV on September 14, 2012 | http://pubs.acs.org
Publication Date: August 14, 2002 | doi: 10.1021/bk-2002-0828.ch006

cussed above. Malrieu and his group developed non-perturbative SS theories based on the same Ansatz, using a dressed-CI approach [33]. They eliminated the redundancy of their working equation in favor of some fractional parentage coefficients, and suggested expressions for determining them. The method is size-consistent with respect to fragment separations using localized orbitals. The SS-MRCC theory, however, is invariant with respect to rotations with the active and virtual orbitals separately, and thus is size-consistent in either localized or delocalized orbitals. A SS Brillouin-Wigner approach, proposed very recently by Hubač and co-workers [34], is also related to ours. Although their method has a much simpler structure compared to the more elaborate expression of our SS-MRCC theory, it is plagued by size-extensivity and size-consistency errors in energy in the limit of separation.

We now focus on the development of a suite of quasi-linearized approximations of the SS-MRCC theory, viz. SS-MRPT and SS-MRCEPA. We would deal with the perturbative formulations first, and development of the SS-MRCEPA methods next.

State-specific multi-reference perturbation theories: SS-MRPT

We rewrite our SS-MRCC eq (4) in the following quasi-linearized form to obtain the cluster amplitude finding equations:

$$\begin{aligned}
&[\langle\chi_l|H|\phi_\mu\rangle + \sum_m(\langle\chi_l|H|\chi_m\rangle - \langle\phi_\mu|\overline{H}_\mu|\phi_\mu\rangle\delta_{lm})\langle\chi_m|T^\mu|\phi_\mu\rangle \\
&+\cdots]c_\mu + \sum_\nu\langle\chi_l|(T^\nu - T^\mu + \cdots)|\phi_\mu\rangle\tilde{H}_{\mu\nu}c_\nu \equiv [\langle\chi_l|H|\phi_\mu\rangle \\
&+(\sum_m\langle\chi_l|H|\chi_m\rangle - \langle\phi_\mu|\overline{H}_\mu|\phi_\mu\rangle\delta_{lm})\langle\chi_m|T^\mu|\phi_\mu\rangle + \cdots]c_\mu + \\
&\sum_\nu\langle\chi_l|(T^\nu + \cdots)|\phi_\mu\rangle\tilde{H}_{\mu\nu}c_\nu - E\langle\chi_l|T^\mu|\phi_\mu\rangle c_\mu = 0 \;\forall\; l,\mu \qquad (10)
\end{aligned}$$

To develop the state-specific perturbation theories, we first partition our hamiltonian, H, into an unperturbed part, H_0, and a perturbation, V, and use the above equation to systematically generate the proper Rayleigh-Schrödinger (RS) and Brillouin-Wigner (BW) versions of the perturbative expansion. While the RS version uses E as a power series expansion, in the BW the E is kept unexpanded. We expand each cluster operator T^{μ} that appear in the above equation as a power series in V. The terms $\langle\phi_{\mu}|\overline{H}_{\mu}|\phi_{\mu}\rangle$ in eq (10) are expanded as power series in the RS theory, while we leave them unexpanded in the BW version.

The formal expressions for the RS- or BW-based SS-MRPT of order n are obtained by expanding the cluster operator T^{μ} in power series, followed by collecting all terms of order n. In particular, the cluster amplitudes at the first order for the RS expansion are obtained from

$$\begin{aligned}
&[\langle\chi_l|H|\phi_{\mu}\rangle + \sum_{m}(\langle\chi_l|H_{0_{\mu}}|\chi_m\rangle - \langle\phi_{\mu}|H_{0_{\mu}}|\phi_{\mu}\rangle\delta_{lm}) \\
&\qquad \langle\chi_m|T^{\mu(1)}|\phi_{\mu}\rangle]c_{\mu} + \sum_{\nu}\langle\chi_l|T^{\nu(1)}|\phi_{\mu}\rangle H_{0_{\mu\nu}}c_{\nu} \\
&\qquad\qquad -E_0\langle\chi_l|T^{\mu(1)}|\phi_{\mu}\rangle c_{\mu} = 0 \ \ \forall\, l,\mu
\end{aligned} \tag{11}$$

The corresponding BW version takes the following form:

$$\begin{aligned}
&[\langle\chi_l|H|\phi_{\mu}\rangle + \sum_{m}(\langle\chi_l|H_{0_{\mu}}|\chi_m\rangle - \langle\phi_{\mu}|\overline{H}_{\mu}|\phi_{\mu}\rangle\delta_{lm}) \\
&\qquad \langle\chi_m|T^{\mu(1)}|\phi_{\mu}\rangle]c_{\mu} + \sum_{\nu}\langle\chi_l|T^{\nu(1)}|\phi_{\mu}\rangle \tilde{H}_{\mu\nu}c_{\nu} \\
&\qquad\qquad -E\langle\chi_l|T^{\mu(1)}|\phi_{\mu}\rangle c_{\mu} = 0 \ \ \forall\, l,\mu
\end{aligned} \tag{12}$$

One of the most crucial features of our perturbation theories lie in the coupling of various T^{μ} operators for different μ's through the term $\sum_{\nu}\langle\chi_l|(T^{\nu(1)} - T^{\mu(1)})|\phi_{\mu}\rangle H_{0_{\mu\nu}}c_{\nu}$, where $H_{0_{\mu\nu}}$ is the zeroth order matrix. The coupling essentially originates from the off-diagonal terms $H_{0_{\mu\nu}}c_{\nu}$ with $\mu \neq \nu$, and is of paramount importance for our purpose, as this ensures size-extensivity of our perturbative formalisms. There are two interrelated issues here: (a) we need an efficient partitioning of H into H_0 and V, such that a good amount of coupling via $\tilde{H}_{\mu\nu}$ is

Downloaded by PENNSYLVANIA STATE UNIV on September 14, 2012 | http://pubs.acs.org
Publication Date: August 14, 2002 | doi: 10.1021/bk-2002-0828.ch006

incorporated and (b) the treatment of $T^{\mu(1)}$ and $T^{\nu(1)}$ in the coupling term $\langle \chi_l | (T^{\nu(1)} - T^{\mu(1)}) | \phi_\mu \rangle$ should be on equal footing.

For the point (a), at least the portion of the two-body terms in H_0 which can couple the ϕ_μ's which are at least doubly excited with respect to one another, since a substantial portion of the non-dynamical correlation effects emerge from the off-diagonal coupling between determinants which are at least doubly excited with respect to one another. Use of two-body terms in H_0 has previously been considered by others as well [40, 41]. Thus, our H_0 consists of all the two-body terms that scatter electrons from all pairs of active orbitals, same or different. Hence to have our H_0 precisely defined, we rewrite H in normal order with respect to the core as the vacuum:

$$H = E_c + \sum_{ij} \langle i | f_c | j \rangle \{a_i^\dagger a_j\}_c + \frac{1}{2} \sum_{ijkl} \langle ij | kl \rangle \{a_i^\dagger a_j^\dagger a_l a_k\}_c \tag{13}$$

in which the labels i, j, etc. span the one particle basis and E_c is the core energy, the expectation value, $\langle 0 | H | 0 \rangle$, is with respect to the core function, $|0\rangle$, and f_c is the core Fock-like one-body operator. Invoking a multi-partitioning of the hamiltonian, and taking each model function ϕ_μ, on which the perturbation acts, as the vacuum, we obtain,

$$H_\mu = < H >_\mu + \sum_{ij} \langle i | f_\mu | j \rangle \{a_i^\dagger a_j\}_\mu + \frac{1}{2} \sum_{ijkl} \langle ij | kl \rangle \{a_i^\dagger a_j^\dagger a_l a_k\}_\mu \tag{14}$$

where

$$< H >_\mu = E_c + \frac{1}{2} \sum_{uv \in \phi_\mu} (\langle uv | uv \rangle - \langle uv | vu \rangle) \tag{15}$$

and

$$f_{\mu ij} = f_{cij} + \sum_{u \in \phi_\mu} (\langle iu | ju \rangle - \langle iu | uj \rangle) \tag{16}$$

where f_μ is the Fock operator with respect to ϕ_μ.

We advocate a particular choice of H_0 which is akin to the Epstein-Nesbet (EN) partitioning for all the determinants which have at least

Downloaded by PENNSYLVANIA STATE UNIV on September 14, 2012 | http://pubs.acs.org
Publication Date: August 14, 2002 | doi: 10.1021/bk-2002-0828.ch006

one inactive orbital, but it differs from EN in that $H_{0\mu\nu}$, which happens to coincide with just the matrix-element $H_{\mu\nu}$. We define our H_0 as a sum of $\langle H\rangle_\mu$, the diagonal part of the Fock operator, f_μ, with respect to ϕ_μ as vacuum, when there is at least one inactive orbital, the whole active block of f_μ, plus all the ladder operators of the two-body term in eq (14) which contains at least one inactive orbital and the entire active portion of the two-body term. Though this resembles the choice of Dyall [40] in the context of CASPT2, but is appropriately generalized in the context of multi-partitioning.

For the point (b), let us recall at this point the observation noted earlier (after eq (9)) that the term $\langle\chi_l|(T^\nu - T^\mu)|\phi_\mu\rangle\tilde{H}_{\mu\nu}(c_\nu/c_\mu)$ is connected provided T^ν and T^μ are treated on the same footing. This aspect would have a direct bearing on the structure of the RS and BW form of the working equations, bearing in mind that size-extensivity has to be rigorously maintained.

We note carefully that we want the unperturbed energy E_0 to appear in the denominator in the RS version. To achieve this, we approximate $\tilde{H}_{\mu\nu}$ by $H_{\mu\nu}$ in $\sum_\nu\langle\chi_l|(T^{\nu(1)} - T^{\mu(1)})|\phi_\mu\rangle\tilde{H}_{\mu\nu}c_\nu$, since this leads to :

$$\begin{aligned}\sum_\nu\langle\chi_l|(T^{\nu(1)} - T^{\mu(1)})|\phi_\mu\rangle H_{\mu\nu}c_\nu &= \sum_\nu\langle\chi_l|T^{\nu(1)}|\phi_\mu\rangle H_{\mu\nu}c_\nu \\ &\quad -E_0\langle\chi_l|T^{\mu(1)}|\phi_\mu\rangle c_\mu \qquad (17)\end{aligned}$$

Thus we note that the term containing $\langle\chi_l|T^{\nu(1)}|\phi_\mu\rangle$ should appear multiplied by $H_{\mu\nu}c_\nu$ in the RS version.

Similarly, for the BW theory, the perturbed energy $E^{(2)}$ should appear in the denominator of the working equation. This will follow if we would approximate $\tilde{H}_{\mu\nu}$ by its second order counterpart $\tilde{H}^{(2)}_{\mu\nu}$. The corresponding coupling term then takes the form:

$$\begin{aligned}\sum_\nu\langle\chi_l|(T^{\nu(1)} - T^{\mu(1)})|\phi_\mu\rangle\tilde{H}_{\mu\nu}c_\nu &= \sum_\nu\langle\chi_l|T^{\nu(1)}|\phi_\mu\rangle\tilde{H}^{(2)}_{\mu\nu}c_\nu \\ &\quad -E^{(2)}\langle\chi_l|T^{\mu(1)}|\phi_\mu\rangle c_\mu \qquad (18)\end{aligned}$$

This implies that the term containing $\langle\chi_l|T^{\nu(1)}|\phi_\mu\rangle$ should appear multiplied by $\tilde{H}^{(2)}_{\mu\nu}c_\nu$ for the BW version.

Downloaded by PENNSYLVANIA STATE UNIV on September 14, 2012 | http://pubs.acs.org
Publication Date: August 14, 2002 | doi: 10.1021/bk-2002-0828.ch006

Downloaded by PENNSYLVANIA STATE UNIV on September 14, 2012 | http://pubs.acs.org
Publication Date: August 14, 2002 | doi: 10.1021/bk-2002-0828.ch006

Thus our working equation for $T^{\mu(1)}$ in the RS expansion may be written as

$$t_\mu^{l(1)} = \frac{H_{l\mu} + \sum_\nu^{\nu\neq\mu}\langle\chi_l|T^{\nu(1)}|\phi_\mu\rangle H_{\mu\nu}(c_\nu/c_\mu) + \sum'_{m,l\neq m} H_{lm} t_\mu^{m(1)}}{E_0 - H_{ll}} \tag{19}$$

where $\langle\chi_l|T^{\mu(1)}|\phi_\mu\rangle$ is abbreviated as $t_\mu^{l(1)}$. The prime in the sum above restricts the sum to χ_m's differing from χ_l only in the active orbitals. This is a consequence of our choice of H_0. E_0 and c_μ's (zeroth order) are obtained by diagonalizing the matrix of $H_{\mu\nu}$ (matrix of hamiltonian in the model space).

The corresponding BW expression is given by

$$t_\mu^{l(1)} = \frac{H_{l\mu} + \sum_\nu^{\nu\neq\mu}\langle\chi_l|T^{\nu(1)}|\phi_\mu\rangle \tilde{H}_{\mu\nu}(c_\nu/c_\mu) + \sum'_{m,l\neq m} H_{lm} t_\mu^{m(1)}}{E - H_{ll}} \tag{20}$$

It is straightforward to discern that the energy denominators $[E_0 - H_{ll}]$ and $[E - H_{ll}]$ in the RS and the BW versions respectively are robust as long as the unperturbed or the perturbed energy is well-separated from the energies of the virtual functions. Both the perturbation theories are thus intruder-free, and both are explicitly size-extensive. They are also size-consistent when we use orbitals localized on the separated fragments.

The pseudo-effective operator $\tilde{H}_{\mu\nu}^{(2)}$ up to second order in both cases is given by

$$\tilde{H}_{\mu\nu}^{(2)} = H_{\mu\nu} + \sum_l H_{\mu l} t_\nu^{l(1)} \tag{21}$$

$\tilde{H}^{(2)}$ on diagonalization provides us the respective second order energy $E^{(2)}$:

$$\sum_\nu \tilde{H}_{\mu\nu}^{(2)} c_\nu^{(2)} = E^{(2)} c_\mu^{(2)} \tag{22}$$

Eqs (19-22) are our final working expressions for the evaluation of cluster operators and energy in the perturbative framework. It is noteworthy that in the SS-MRPT(RS) formalism the zeroth order coefficients, c_μ^0's are used to evaluate the cluster operators in eq (19), but the coefficients are relaxed during the computation of $E^{(2)}$, since this is obtained by diagonalization via eq (21). On the other hand, in the BW context, the coefficients are iteratively updated. It is pertinent to mention that in our applications in this article the term $\sum'_{m,l\neq m} H_{lm} t_{\mu}^{m(1)}$ is zero by symmetry. For more details, we refer to our earlier papers [37].

Downloaded by PENNSYLVANIA STATE UNIV on September 14, 2012 | http://pubs.acs.org
Publication Date: August 14, 2002 | doi: 10.1021/bk-2002-0828.ch006

State-specific multi-reference CEPA-like formalisms: SS-MRCEPA

Starting with the parent SS-MRCC equations, we can derive CEPA-like approximations leading to the SS-MRCEPA methods by imposing a set of approximations.

We recall the approximation that leads to the single-reference CEPA (SR-CEPA) [42]. CEPA(0) emerges when the SRCC equations are totally linearized, and the virtual space is restricted to functions reached via the hamiltonian. In the same spirit, we can generate the analogous SS-MRCEPA(0), if we linearize our SS-MRCC equations and retain only the one- and the two-body cluster operators in $\{T^{\mu}\}$. In the SR-CEPA(2), the diagonal exclusion principle violating (EPV) terms are additionally retained, and we propose a similar scheme, SS-MRCEPA(2), where analogous terms in $\tilde{H}$ are retained in the SS-MRCC theory.

Thus, in SS-MRCEPA(0), we approximate the $\overline{H}_{\mu}$ originating from SS-MRCC theory as follows:

$$\overline{H}_{\mu} \cong H_{\mu} + \overline{H_{\mu} T^{\mu}} \equiv \overline{H}'_{\mu} \tag{23}$$

Using this approximation, the model space equation becomes

$$\sum_{\nu} \langle \phi_{\mu} | \overline{H}'_{\nu} | \phi_{\nu} \rangle c_{\nu} = E c_{\mu} \tag{24}$$

and the corresponding cluster finding equations take the form

$$\langle \chi_l | \overline{H}'_{\mu} | \phi_{\mu} \rangle c_{\mu} + \sum_{\nu} \langle \chi_l | (T^{\nu} - T^{\mu}) | \phi_{\mu} \rangle H_{\mu\nu} c_{\nu} \quad = \quad 0 \;\forall\, \mu, l \tag{25}$$

or, equivalently,

$$\langle\chi_l|\overline{H}'_\mu|\phi_\mu\rangle c_\mu + \sum_\nu \langle\chi_l|T^\nu|\phi_\mu\rangle H_{\mu\nu} c_\nu = E_0\langle\chi_l|T^\mu|\phi_\mu\rangle c_\mu \qquad (26)$$

where E_0 is the zeroth order energy, and c_μ's are the zeroth order coefficients, obtained by diagonalizing the zeroth order matrix $H_{\mu\nu}$. Eqs.(24) and (26) are our working equations for the SS-MRCEPA(0) theory. Let us note here that the structure of the SS-MRCEPA(0) equations bear close resemblance with our SS-MRPT(RS). The presence of E_0 and c^0_μ, rather than E and c_μ respectively, underlines this kinship.

To derive the SS-MRCEPA(2), we selectively consider the diagonal EPV terms. This implies that we retain terms of the type: *powers of* $T_{l\mu}$ acting on ϕ_μ where $T_{l\mu}$ excites to a χ_l from ϕ_μ. Thus, this could be termed as a quasi-linearized version of SS-MRCC theory. This approximation closely resembles Meyer's single-reference based CEPA(2) method [42]. The $\overline{H}_\mu$ in this method is taken as

$$\overline{H}_\mu \cong H_\mu + \overline{H_\mu T^\mu} + \frac{1}{2}(\overline{(\overline{H_\mu T^\mu})T^\mu})_{\text{diag}} \equiv \overline{H}''_\mu \qquad (27)$$

Then, the energy and cluster amplitude finding equations are as follows:

$$\sum_\nu \langle\phi_\mu|\overline{H}''_\mu|\phi_\nu\rangle c_\nu = E c_\mu \qquad (28)$$

$$\langle\chi_l|\overline{H}''_\mu|\phi_\mu\rangle c_\mu + \sum_\nu \langle\chi_l|(T^\nu - T^\mu)|\phi_\mu\rangle \tilde{H}''_{\mu\nu} c_\nu = 0 \;\; \forall\, \mu, l \qquad (29)$$

Using eq (28) we get,

$$\langle\chi_l|\overline{H}''_\mu|\phi_\mu\rangle c_\mu + \sum_\nu \langle\chi_l|T^\nu|\phi_\mu\rangle \tilde{H}''_{\mu\nu} c_\nu = E\langle\chi_l|T^\mu|\phi_\mu\rangle c_\mu \qquad (30)$$

where

$$\langle\phi_\mu|\overline{H}''_\nu|\phi_\nu\rangle = \tilde{H}''_{\mu\nu}$$

Downloaded by PENNSYLVANIA STATE UNIV on September 14, 2012 | http://pubs.acs.org
Publication Date: August 14, 2002 | doi: 10.1021/bk-2002-0828.ch006

Eqs.(28) and (30) are the required equations for SS-MRCEPA(2). Structurally the SS-MRCEPA(2) closely resembles the SS-MRPT(BW), since E, rather E_0, appears in eq (30). Our SS-MRCEPA(2) theory can also be cast as an eigen-problem form of certain kind of dressed multi-reference configuration interaction (MRCI) equation.

$$\begin{aligned}\sum_{\mu}\langle\chi_l|H_\mu|\phi_\mu\rangle c_\mu + \sum_{\mu m}\langle\chi_l|\overline{H_\mu|\chi_m}\rangle c_\mu^m \\ + \sum_{\mu}\frac{1}{2}\langle\chi_l|(\overline{(\overline{H_\mu T^\mu})T^\mu})_{\mathrm{diag}}|\phi_\mu\rangle c_\mu \\ + \sum_{\mu\nu}\tilde{H}''_{\mu\nu}c_\nu^l = E\sum_{\mu}c_\mu^l\end{aligned} \qquad (31)$$

where $c_\mu^l = t_\mu^l c_\mu$, with t_μ^l, the amplitude of $T_{l\mu}$ and $\langle\chi_l|\overline{H_\mu|\chi_m}\rangle$ indicates the quantity to be connected. Eq (31) indicates that the SS-MRCEPA(2) equations may be viewed as *extensivity corrected* MRCI equations.

Just as in SS-MRPT(RS), a typical feature in our SS-MRCEPA(0) formalism is the use of the zeroth-order coefficients c_μ^0 to compute the cluster operators and $\tilde{H}$, but allow the coefficients to relax while computing energy, since this is obtained by diagonalization. For the SS-MRCEPA(2) case, however, the coefficients also get updated iteratively.

The main advantage of approximating the SS-MRCC theory in the SS-MRCEPA form lies in the fact that we save a lot of computing time since we neglect a host of nonlinear terms. They would thus be very attractive approximate schemes if there is no significant loss of accuracy in the computed energy. The theories are explicitly size-extensive, size-consistent and are also intruder free.

For completeness, we want to quote here the earlier MR-based CEPA-like formulations which appeared in the literature [43].

Downloaded by PENNSYLVANIA STATE UNIV on September 14, 2012 | http://pubs.acs.org
Publication Date: August 14, 2002 | doi: 10.1021/bk-2002-0828.ch006

Theories of Excited State PES via Linear Response Approach

As discussed earlier, one of the important thrusts in this article is the development and study of linear response theories based on the SS-MRCC method and its CEPA-like approximations. For the excited states whose ground states are multi-reference in nature, this is a very convenient and compact approach.

Linear Response Theory Based on the State-specific Multi-reference CC Formalism: MR-CCLRT

In the CC based linear response theory, the excited functions are written in terms of the ground state function via the action of a suitable excitation operator. In the spirit of the single-reference coupled-cluster based linear response theory (SR-CCLRT) [38, 44, 45] (or SAC-CI [46]) we posit on our excited state, $|\psi_k\rangle$, the following Ansatz:

$$|\psi_k\rangle = \sum_{\mu} \exp(T^{\mu}) \hat{S}_k^{\mu} |\phi_{\mu}\rangle c_{\mu} \tag{32}$$

$|\psi_k\rangle$ satisfies the Schrödinger equation

$$H|\psi_k\rangle = E_k|\psi_k\rangle \tag{33}$$

In close analogy with the SR-CCLRT, we include in each excitation operator $\hat{S}_k^{\mu}$ all the virtual excitations from $|\phi_{\mu}\rangle$, and retain the cluster components T^{μ} of the multi-reference ground state (eq (2)) in our Ansatz for $|\psi_k\rangle$. In addition, we also want to change the relative weights of the various $|\phi_{\mu}\rangle$'s in the function $|\psi_k\rangle$. With this choice, we can represent $\hat{S}_k^{\mu}$ as

$$\hat{S}_k^{\mu} = s_k^{\mu 0} I + S_k^{\mu} \qquad \text{with} \quad S_k^{\mu} = \sum_{m} s_{\mu k}^{m} Y_{\mu}^{m\dagger} \tag{34}$$

Downloaded by PENNSYLVANIA STATE UNIV on September 14, 2012 | http://pubs.acs.org
Publication Date: August 14, 2002 | doi: 10.1021/bk-2002-0828.ch006

where $Y_\mu^{m\dagger}$ creates a virtual function $|\chi_m\rangle$ from $|\phi_\mu\rangle$. It is evident that there are several S_k^μ's which excite to the same $|\chi_m\rangle$ from several $|\phi_\mu\rangle$'s. Thus, we have to invoke a set of sufficiency conditions to determine them. We have

$$\begin{aligned}\sum_{\mu\nu}[&\exp(T^\mu)|\phi_\nu\rangle\langle\phi_\nu|\overline{\overline{H}_\mu S_k^\mu}|\phi_\mu\rangle + \exp(T^\mu)S_k^\mu|\phi_\nu\rangle\langle\phi_\nu|\overline{H}_\mu|\phi_\mu\rangle \\ &+\exp(T^\mu)s_k^{\mu 0}|\phi_\nu\rangle\langle\phi_\nu|\overline{H}_\mu|\phi_\mu\rangle + \sum_\mu \exp(T^\mu)Q\overline{\overline{H}_\mu S_k^\mu}|\phi_\mu\rangle \\ &+\exp(T^\mu)S_k^\mu Q\overline{H}_\mu|\phi_\mu\rangle + \exp(T^\mu)s_k^{\mu 0}Q\overline{H}_\mu|\phi_\mu\rangle]c_\mu \\ &= E_k\sum_\mu \exp(T^\mu)\hat{S}_k^\mu|\phi_\mu\rangle c_\mu \end{aligned} \tag{35}$$

Following the same manipulations leading to the SS-MRCC equations [31, 32] we interchange the labels μ and ν in the above equation in the first three terms and equate terms with same μ. For each virtual space projection onto $\langle\chi_l|\exp(-T^\mu)$ we have

$$\begin{aligned}&\langle\chi_l|\overline{\overline{H}_\mu S_k^\mu}|\phi_\mu\rangle c_\mu + \langle\chi_l|S_k^\mu Q\overline{H}_\mu|\phi_\mu\rangle c_\mu + \langle\chi_l|\overline{H}_\mu|\phi_\mu\rangle s_k^{\mu 0}c_\mu \\ &+\sum_\nu\langle\chi_l|\exp(-T^\mu)\exp(T^\nu)S_k^\nu|\phi_\mu\rangle\langle\phi_\mu|\overline{H}_\nu|\phi_\nu\rangle c_\nu \\ &+\langle\chi_l|\exp(-T^\mu)\exp(T^\nu)|\phi_\mu\rangle\langle\phi_\mu|\overline{\overline{H}_\nu S_k^\nu}|\phi_\nu\rangle c_\nu \\ &+\langle\chi_l|\exp(-T^\mu)\exp(T^\nu)|\phi_\mu\rangle\langle\phi_\mu|\overline{H}_\nu|\phi_\nu\rangle s_k^{\nu 0}c_\nu \\ &= E_k\langle\chi_l|S_k^\mu|\phi_\mu\rangle c_\mu\end{aligned} \tag{36}$$

The sufficiency conditions imply that each virtual function $\langle\chi_l|$ can be reached from several ϕ_μ's and the projection for each $\langle\chi_l|$ has to be done for each $|\phi_\mu\rangle$. Also, each ket $|\chi_m\rangle$ appears with a different coefficient, depending on how it is generated via various S_k^μ's acting on the associated $|\phi_\mu\rangle$'s. To keep this information as a mnemonic, we would from now on denote a $\langle\chi_l|$ as $\langle\chi_\mu^l|$ if it is used for projection from the eq (36) for a certain $|\phi_\mu\rangle$ and a functions $|\chi_m\rangle$ as $|\chi_\mu^m\rangle$ if it is obtained by $Y_\mu^{m\dagger}$ acting on $|\phi_\mu\rangle$ From now on, we shall introduce the coefficients $d_{\mu k}$'s and $d_{\mu k}^m$'s defined by

$$d_{\mu k} = s_k^{\mu 0}c_\mu \tag{37}$$

Downloaded by PENNSYLVANIA STATE UNIV on September 14, 2012 | http://pubs.acs.org
Publication Date: August 14, 2002 | doi: 10.1021/bk-2002-0828.ch006

$$d^m_{\mu k} = s^m_{\mu k} c_\mu \tag{38}$$

Using the above equations, we can rewrite eq (36) with the notation $|\chi^m_\mu\rangle$ for $|\chi_m\rangle$ reached from $|\phi_\mu\rangle$:

$$\begin{aligned}
\langle\chi^l_\mu|\overline{H}_\mu|\phi_\mu\rangle d_{\mu k} &+ \sum_m \langle\chi^l_\mu|\overline{\overline{H}_\mu Y^{m\dagger}_\mu}|\phi_\mu\rangle d^m_{\mu k} \\
&+ \sum_m \langle\chi^l_\mu|Y^{m\dagger}_\mu Q\overline{H}_\mu|\phi_\mu\rangle d^m_{\mu k} \\
+ \sum_{\nu m} \langle\chi^l_\mu| \exp(-T^\mu) &\exp(T^\nu) Y^{m\dagger}_\nu |\phi_\mu\rangle\langle\phi_\mu|\overline{H}_\nu|\phi_\nu\rangle d^m_{\nu k} \\
+ \sum_{\nu m} \langle\chi^l_\mu| \exp(-T^\mu) &\exp(T^\nu)|\phi_\mu\rangle\langle\phi_\mu|\overline{\overline{H}_\nu Y^{m\dagger}_\nu}|\phi_\nu\rangle d^m_{\nu k} \\
+ \sum_{\nu} \langle\chi^l_\mu| \exp(-T^\mu) &\exp(T^\nu)|\phi_\mu\rangle\langle\phi_\mu|\overline{H}_\nu|\phi_\nu\rangle d_{\nu k} \\
&= E_k d^l_{\mu k}
\end{aligned} \tag{39}$$

The third term in eq (39) involves $Q\overline{H}_\mu$ acting on $|\phi_\mu\rangle$, which implies that $Q\overline{H}_\mu|\phi_\mu\rangle$ is an excited function (henceforth denoted by $\left[\overline{H}_\mu\right]_{\text{ex}}$).

In the same manner we project eq (35) onto the active space manifold $\langle\phi_\lambda|\exp\,(-T^\mu)$ and get

$$\sum_\nu \langle\phi_\lambda|\overline{\overline{H}_\nu S^{\nu\dagger}_k}|\phi_\nu\rangle c_\nu + \sum_\nu \langle\phi_\lambda|\overline{H}_\nu|\phi_\nu\rangle s^{\mu 0}_k c_\nu = E_k c_\lambda s^{\lambda 0}_k \tag{40}$$

which on simplification generates,

$$\sum_{\nu m} \langle\phi_\lambda|\overline{\overline{H}_\nu Y^{m\dagger}_\nu}|\phi_\nu\rangle d^m_{\nu k} + \sum_\nu \langle\phi_\lambda|\overline{H}_\nu|\phi_\nu\rangle d_{\nu k} = E_k d_{\lambda k} \tag{41}$$

Thus, the use of the sufficiency conditions in the linear response equations based on SS-MRCC theory leads naturally to a set of eigenvalue equations. Thus, once the cluster amplitudes of T^μ for all μ's have been found out by solving the SS-MRCC equations, we can get the associated excited state energies relative to the state $|\psi\rangle$ by solving the MR-CCLRT equations. An attractive feature of our MR-CCLRT is that the computed excitation energies are size-intensive

Downloaded by PENNSYLVANIA STATE UNIV on September 14, 2012 | http://pubs.acs.org
Publication Date: August 14, 2002 | doi: 10.1021/bk-2002-0828.ch006

[38, 39] in the sense that they become asymptotically equal to the sum of the fragment excitation energies in the limit of non-interacting fragments.

Linear Response Theories Based on the State-specific Multi-reference CEPA Formalisms: MR-CEPALRT

We will now develop the corresponding MR-CEPALRT using exactly the same approximations on MR-CCLRT as has been used in the SS-MRCC theory to arrive at the SS-MRCEPA theories. To derive the working equations for the SS-MRCEPA based response theories, we start with the parent MR-CCLRT equations (39) and (41) for the excited states and make approximations akin to what have been used to arrive at the SS-MRCEPA(0) and SS-MRCEPA(2) theories from the SS-MRCC theory for the ground state. Both the MR-CEPALRT schemes can be subsumed in the same type of working equations, with appropriate definitions of certain dressed operators.

Since in CEPA-like methods, we ignore multiple excitations out of the model functions leading to χ^l_μ and linearize the terms in $[\exp(-T^\mu)\exp(T^\nu)]$, the working equations of the virtual space projections of the CEPA-based MR-CCLRT eq (39) for both the CEPA-based schemes can be simplified as follows

$$\begin{aligned}
&\sum_m \langle\chi^l_\mu|\overline{\overline{H}_\mu Y^{m\dagger}_\mu}|\phi_\mu\rangle d^m_{\mu k} + \sum_m \langle\chi^l_\mu|Y^{m\dagger}_\mu \left[\overline{H}_\mu\right]_{\mathrm{ex}}|\phi_\mu\rangle d^m_{\mu k} \\
&+\langle\chi^l_\mu|\overline{H}_\mu|\phi_\mu\rangle d_{\mu k} + \sum_{\nu m}\langle\chi^l_\mu|(T^\nu - T^\mu)Y^{m\dagger}_\nu|\phi_\mu\rangle \tilde{H}'_{\mu\nu} d^m_{\nu k} \\
&\quad +\sum_{\nu m}\langle\chi^l_\mu|(T^\nu - T^\mu)|\phi_\mu\rangle\langle\phi_\mu|\overline{\overline{H''}_\nu Y^{m\dagger}_\nu}|\phi_\nu\rangle d^m_{\nu k} \\
&\qquad +\sum_\nu \langle\chi^l_\mu|(T^\nu - T^\mu)|\phi_\mu\rangle \tilde{H}'_{\mu\nu} d_{\nu k} = E_k d^l_{\mu k}
\end{aligned} \tag{42}$$

Downloaded by PENNSYLVANIA STATE UNIV on September 14, 2012 | http://pubs.acs.org
Publication Date: August 14, 2002 | doi: 10.1021/bk-2002-0828.ch006

Downloaded by PENNSYLVANIA STATE UNIV on September 14, 2012 | http://pubs.acs.org
Publication Date: August 14, 2002 | doi: 10.1021/bk-2002-0828.ch006

The corresponding model space equation

$$\sum_{\nu m}\langle\phi_\lambda|\overline{\overline{H}_\nu Y_\nu^{m\dagger}}|\phi_\nu\rangle d_{\nu k}^m + \sum_{\nu}\langle\phi_\lambda|\overline{H}_\nu|\phi_\nu\rangle d_{\nu k} = E_k d_{\lambda k} \tag{43}$$

In the above working equations of the MR-CEPALRT, some appropriate approximant to the operator $\overline{H}_\mu$ figures, whose actual form depends on whether we are considering SS-MRCEPA(0) or SS-MRCEPA(2). We shall give the explicit forms in the article later (in eqs (51) and (53)). Similarly, the dressed operators $\overline{H}'_\mu$ and $\overline{H}''_\mu$ are defined later through the eqs (51) and (53).

The above MR-CEPALRT equations can be cast as a set of eigenvalue equations of the general form:

$$\sum_{\nu}\langle\phi_\mu|\mathcal{H}|\phi_\nu\rangle d_{\nu k} + \sum_{\nu m}\langle\phi_\mu|\mathcal{H}|\chi_\nu^m\rangle d_{\nu k}^m = E_k d_{\mu k} \tag{44}$$

$$\sum_{\nu}\langle\chi_\mu^l|\mathcal{H}|\phi_\nu\rangle d_{\nu k} + \sum_{\nu m}\langle\chi_\mu^l|\mathcal{H}|\chi_\nu^m\rangle d_{\nu k}^m = E_k d_{\mu k}^l \tag{45}$$

In the matrix notation the above two equations can be represented as

$$\begin{pmatrix} \mathcal{H}_{\mu\nu} & \mathcal{H}_{\mu m} \\ \mathcal{H}_{l\nu} & \mathcal{H}_{lm} \end{pmatrix}\begin{pmatrix} d_{\nu k} \\ d_{\nu k}^m \end{pmatrix} = E_k \begin{pmatrix} d_{\mu k} \\ d_{\mu k}^l \end{pmatrix}$$

The parent MR-CCLRT [36] also can be cast in exactly the same form, though in this article we have not shown the details. The elements of the operator $\mathcal{H}$ are given by

$$\langle\phi_\mu|\mathcal{H}|\phi_\nu\rangle = \langle\phi_\mu|\overline{H}_\nu|\phi_\nu\rangle \tag{46}$$

$$\langle\phi_\mu|\mathcal{H}|\chi_\nu^m\rangle = \langle\phi_\mu|\overline{\overline{H}_\nu Y_\nu^{m\dagger}}|\phi_\nu\rangle \tag{47}$$

$$\langle\chi_\mu^l|\mathcal{H}|\phi_\nu\rangle = \langle\chi_\mu^l|\overline{H}_\nu|\phi_\nu\rangle\delta_{\mu\nu} + \langle\chi_\mu^l|(T^\nu - T^\mu)|\phi_\mu\rangle\tilde{H}'_{\mu\nu} \tag{48}$$

$$\begin{aligned}\langle\chi^l_\mu|\mathcal{H}|\chi^m_\nu\rangle &= \langle\chi^l_\mu|(T^\nu - T^\mu)Y^{m\dagger}_\nu|\phi_\mu\rangle\tilde{H}'_{\mu\nu}\\ &+\langle\chi^l_\mu|Y^{m\dagger}_\nu[\overline{H}_\nu]_{ex}|\phi_\nu\rangle\delta_{\mu\nu} + \langle\chi^l_\mu|\overline{\overline{H}_\nu Y^{m\dagger}_\nu}|\phi_\nu\rangle\delta_{\mu\nu}\\ &+\langle\chi^l_\mu|(T^\nu - T^\mu)|\phi_\mu\rangle\langle\phi_\mu|\overline{\overline{H''}_\nu Y^{m\dagger}_\nu}|\phi_\nu\rangle\end{aligned} \qquad (49)$$

For SS-MRCEPA(0) based response equations

$$\begin{aligned}\overline{H}_\mu &= H_\mu + \overline{H_\mu T^\mu} &(50)\\ \tilde{H}'_{\mu\nu} &= \langle\phi_\mu|H_\nu|\phi_\nu\rangle\\ \overline{H}''_\nu &= H_\nu &(51)\end{aligned}$$

However, for the SS-MRCEPA(2) based response equations

$$\begin{aligned}\tilde{H}'_{\mu\nu} &= \langle\phi_\mu|\overline{H}_\nu|\phi_\nu\rangle\\ \overline{H}''_\nu &= \overline{H}_\nu &(52)\\ \text{with } \overline{H}_\mu &= H_\mu + \overline{H_\mu T^\mu} + \frac{1}{2}(\overline{(\overline{H_\mu T^\mu})T^\mu})_{\text{diag}} &(53)\end{aligned}$$

Thus, once the cluster amplitudes of T^μ for all μ's have been found out by solving the SS-MRCEPA equations, we can get the associated excited state energies relative to the state $|\psi\rangle$ by solving the MR-CEPALRT equations by constructing the matrix of $\mathcal{H}$ via eqs.(44-49).

It is evident that if one drops the excitation operator, $Y^{m\dagger}_\mu$ from the working equations of MR-CEPALRT they naturally reduce to the corresponding ground state CEPA theories, SS-MRCEPA. This implies that SS-MRCEPA are the completely unperturbed versions of MR-CEPALRT, which is why we coin the term, MR-CEPALRT, for the linear response theory based on the SS-MRCEPA method. We not only get the excited state energies but also the ground state energy by solving the MR-CEPALRT equations.

We conclude the section with the comment that, just as in the full-blown MR-CCLRT [36], one can prove in the same manner that the underlying operators in the eigenvalue problem of MR-CEPALRT are connected and the possible excitation energies also satisfy the size-intensivity criteria [38, 39].

Downloaded by PENNSYLVANIA STATE UNIV on September 14, 2012 | http://pubs.acs.org
Publication Date: August 14, 2002 | doi: 10.1021/bk-2002-0828.ch006

Numerical Implementations

Algorithmic considerations

Downloaded by PENNSYLVANIA STATE UNIV on September 14, 2012 | http://pubs.acs.org
Publication Date: August 14, 2002 | doi: 10.1021/bk-2002-0828.ch006

In all of our applications, the T_μ amplitudes are confined to single and double excitations with respect to each ϕ_μ. We note that there are coupling between various cluster operators T_μ in the SS-MRCC and the SS-MRCEPA equations. But these are not too numerous: only those components of T_ν's with $\nu \neq \mu$ can couple which can cause excitations to χ_l by their action on ϕ_μ. The couplings are even less in the SS-MRPT methods. The coupling effects can be included in an iterative manner. We start a loop for μ. The cluster finding equations are then solved for T_μ by using the previously computed values for other T_ν's ($\nu \neq \mu$). For SS-MRPT(RS) and SS-MRCEPA(0) theories, the values of the energy E_0 can be obtained by diagonalizing the matrix of $H_{\mu\nu}$. Only after the convergence of cluster amplitudes and the coefficients c_μ are reached we get the energy, using the corresponding energy finding equations. It is important to emphasize here once more that the computation of the cluster operators in the SS-MRPT(RS) and the SS-MRCEPA(0) method hinges upon the use of the zeroth-order coefficients, c^0_μ. For the rest of the methods, the coefficients have to be iteratively updated. We have found that a fast convergence is reached by converging the cluster amplitudes first in an inner loop while keeping the coefficients and E fixed, and update E and the coefficients in an outer loop after the convergence of the cluster amplitudes in the current inner loop is reached.

For the MR-CCLRT and MR-CEPALRT, we restrict ourselves in our applications to only a singles-doubles approximation for the excitation operators $\{S^\mu_k\}$:

$$S^\mu_k = S^\mu_{1k} + S^\mu_{2k} \tag{54}$$

First the ground state problem is solved using the ground state SS-MR methods, and the sets $\{c_\mu\}$, $\{T^\mu\}$ are obtained along with the ground state energy E. The nonhermitian transformed hamiltonians $\overline{H}_\mu$ are constructed once we get the set of cluster operators $\{T^\mu\}$. In the singles-doubles truncation scheme, we need to compute up to three-body components of the transformed hamiltonians $\overline{H}_\mu$. The three-body matrix elements have been found to be very important for the calculation of accurate excited state energies. All the two-body matrix elements are stored in the memory, and the three-body elements are generated on the fly as needed.

We emphasize here that, the equations of our SSMR-based LRT are defined in a space of *overcomplete* basis: each virtual function $|\chi_m\rangle$ appears several times-generated from various $|\phi_\nu\rangle$'s, with attendant coefficients $d^m_{\nu k}$. If the number of linearly independent functions in the Hilbert space is N, then only N roots are meaningful. The rest of the roots are extraneous. They can be identified in a rather straightforward manner by looking at the norm of the full eigenvector for each eigenvalue. The spurious roots show abnormally small values of the associated norms. In all our applications, we could discard the spurious roots unambiguously in a routine manner. For details we refer to our recent article [36].

Results and Discussion

We present now a few illustrative applications, with special attention to difficult situations where degeneracy tends to occur in varying degrees between the various model determinants and also when they are plagued by intruders at various geometries. We provide first the results obtained with the parent SS-MRCC method, and its perturbative variants, by studying the ground state PES of a rectangular Li_4 model system. Both the SS-MRPT(RS) and the SS-MRPT(BW) results are shown. The second order results obtained with the quasi-degenerate perturbation theory (MC-QDPT(2)) [47] are also shown along with our perturbative results for comparison.

Downloaded by PENNSYLVANIA STATE UNIV on September 14, 2012 | http://pubs.acs.org
Publication Date: August 14, 2002 | doi: 10.1021/bk-2002-0828.ch006

Downloaded by PENNSYLVANIA STATE UNIV on September 14, 2012 | http://pubs.acs.org
Publication Date: August 14, 2002 | doi: 10.1021/bk-2002-0828.ch006

The MC-QDPT(2) theory starts with fixed coefficients for the model space functions, unlike in our SS-MRPT theories. It is also not fully extensive. We also present the second order SR-MBPT and the effective hamiltonian based MR-MBPT results, since we want to investigate to what extent the SR-MBPT results behave poorly at the quasi-degenerate regions, and the MR-MBPT results sense the presence of intruders. H_0 in both SR-MBPT and MR-MBPT is taken as in the standard EN partitioning, which is structurally closer to our choice for H_0 in the two SS-MRPT methods.

We also display the PES of some of the low-lying states of this system using our MR-CCLRT. The pair of our newly proposed SS-MRCEPA methods are applied to the trapezoidal H_4 model system [48] to study its ground state. For the same model, we also generate the excited state PES, through our MR-CEPALRT. The performance of the methods discussed in this article is compared with the corresponding full CI (FCI) results.

All the systems chosen above are described well in the reference level by two-determinantal model spaces for the ground states, described generically by the functions $\phi_1 = [\text{core}]a^2$ and $\phi_2 = [\text{core}]b^2$. The two active orbitals a and b belong to two different symmetries. This ensures the completeness of the model space. Since the reference determinants used in the applications in the present work are closed-shell singlets, the spin-adaptation of the working equations is a very simple task in this case.

We employ the Hartree-Fock (HF) orbitals of one of the reference determinants from ϕ_1 and ϕ_2 to generate the orbitals in our calculations. Since our state-specific formulations treat both the determinants democratically, we could have opted for any of the two determinants to generate the orbitals. However, once a decision regarding the determinant is made, we keep this fixed throughout the PES, even if at some geometries it might not be the dominant determinant. The electronic structure programme package GAMESS is used to generate the required molecular integrals and FCI results.

Li_4 Model: Rectangular Geometry

We introduce here the Li_4 model, where we start from a square geometry of four Li atoms, and study the PES of its various states generated by a gradual elongation of the perfectly square form to a rectangular geometry (see Figure 1). This simulates interactions between two Li_2 molecules at certain specific geometries. The Li–Li distance in each Li_2 molecule is kept fixed at the stretched bond length (r) of 7.578 a.u. (approximately 1.5 times of ground state equilibrium distance of Li_2) to enhance the effect of quasi-degeneracy. The lowest energy determinant corresponds to the function $\phi_1 = 1a_2^2 1b_1^2 1b_2^2 1a_1^2 2a_1^2 2b_2^2$ in the C_{2v} point group and this becomes quasi-degenerate with $\phi_2 = 1a_2^2 1b_1^2 1b_2^2 1a_1^2 2a_1^2 2b_1^2$ at R=7.578 a.u. These functions, ϕ_1 and ϕ_2, form the model space for this system. There is a gradual fading off of the quasi-degeneracy as R is increased. Potential intruders are encountered within the region of R=10.04 to R=10.8 a.u. This behavior is different from the analogous rectangular H_4 (the so-called P4) model [48] at the geometries studied so far. We depict this situation by a plot of the CSF energies of Li_4 as a function of R in Figure 2. We employ the DZP [2s 1p] ANO basis [49] for our calculation. In our applications in this article, the Li core orbital is kept frozen. The function ϕ_1 is chosen as the one whose HF orbitals are employed in our calculations.

Figure 3 displays the deviation of the ground state energies computed using our SSMR methods with respect to FCI values. It is observed from Figure 3 that the performance of the SS-MRCC method is excellent. The corresponding SS-MRPT methods are good as well, and are more accurate than the MC-QDPT(2) [47] results, with the same model space. As is expected, the SR-MBPT results are quite inferior as compared to our SS methods around the quasi-degenerate region. The performance of the effective hamiltonian based MR-MBPT method is very poor, sensing intruders right at the beginning. This feature clearly indicates that this model system warrants a truly MR description but a state-specific treatment.

The performance of the MR-CCLRT for the low-lying PES of Li_4

Downloaded by PENNSYLVANIA STATE UNIV on September 14, 2012 | http://pubs.acs.org
Publication Date: August 14, 2002 | doi: 10.1021/bk-2002-0828.ch006

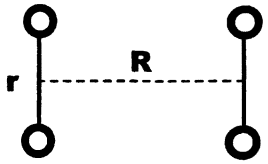

Figure 1. Geometrical arrangement of four Li atoms in rectangular Li_4.

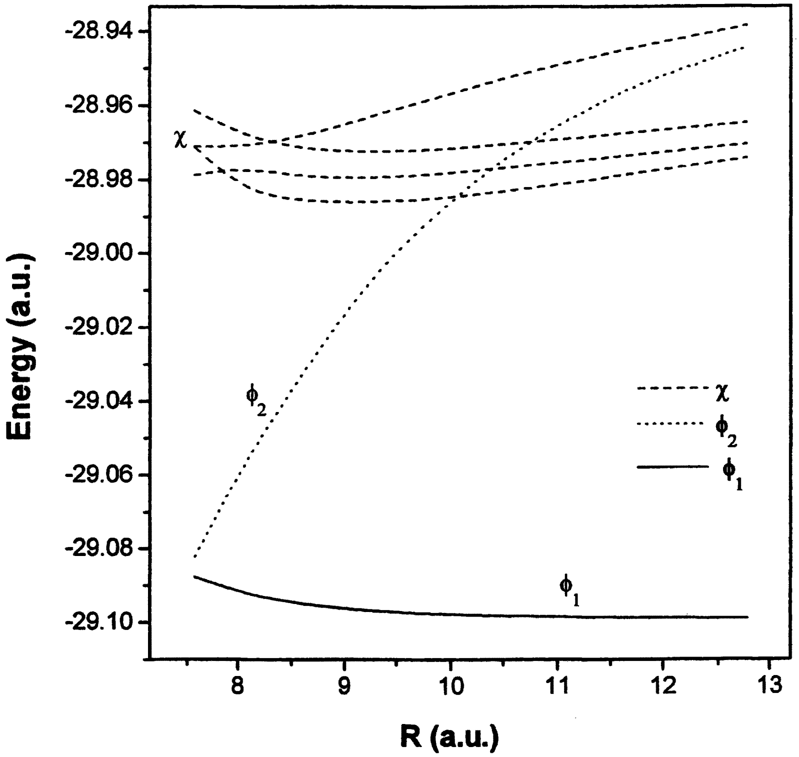

Figure 2. Plot of CSF energies of the rectangular Li_4 model.

Downloaded by PENNSYLVANIA STATE UNIV on September 14, 2012 | http://pubs.acs.org
Publication Date: August 14, 2002 | doi: 10.1021/bk-2002-0828.ch006

Downloaded by PENNSYLVANIA STATE UNIV on September 14, 2012 | http://pubs.acs.org
Publication Date: August 14, 2002 | doi: 10.1021/bk-2002-0828.ch006

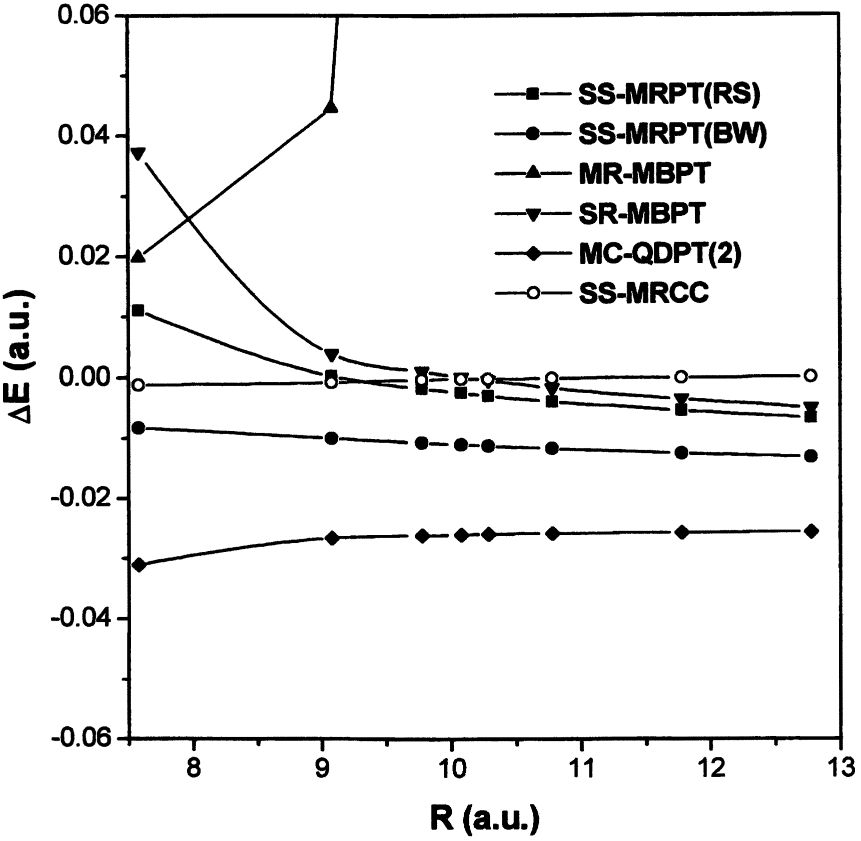

Figure 3. Difference energy plot of the ground state of the rectangular Li_4 model with respect to FCI.

model is presented in Figures 4 – 7, along with the corresponding SR-CCLRT and FCI values. From the figures it is evident that the MR-CCLRT provides more or less uniform description of the PES of the low-lying states of Li_4. The corresponding SR-CCLRT results are vastly inferior for all the excited states shown in the figures.

H_4 model: Trapezoidal geometry

Downloaded by PENNSYLVANIA STATE UNIV on September 14, 2012 | http://pubs.acs.org
Publication Date: August 14, 2002 | doi: 10.1021/bk-2002-0828.ch006

The trapezoidal H_4 model (so called H4) system, originally introduced by Jankowski and Paldus [48] and later studied in detail by a host of workers [32, 50] serves as an excellent benchmark for judging the performance of any multi-reference formulation. For the present we choose the trapezoidal H_4, the so called H4 model, as our working system and employ the DZP basis [51] for all the calculations performed. In its ground state, H4 shows remarkable degree of multi-reference character coupled with the presence of intruders. The degree of quasi-degeneracy of the model functions can be effectively tuned by the opening angle leading to the trapezoidal form. The H4 model could be conceived of as having two H_2 molecules with fixed bond length of 2.0 a.u. and they are kept in an isosceles trapezoidal position with the shorter end-to-end distance fixed at 2.0 a.u. We start out with a geometry wherein the two H_2 molecules are placed parallel to each other, thus constituting a square conformation and corresponding to the situation of maximum degeneracy. This is then continuously deformed by symmetrically widening the angle so that the two H_2 molecules make progressively obtuse angles with the line joining the two fixed end points 2.0 a.u. apart. Each of the functions thus generated correspond uniquely to an angle ϕ, which is the difference between the actual obtuse angle and $\pi/2$. We specify the functions by the parameter $\phi = \alpha\pi$ [51]. Changing α from 0 to 0.5, we go from the square configuration to the linear one, which corresponds to a continuous variation of the degree of quasi-degeneracy among the ground state determinants $\phi_1 = 1a_1^2 1b_2^2$ and $\phi_2 = 1a_1^2 2a_1^2$. ϕ_1 and ϕ_2 are equally important at $\alpha = 0$ (corresponding to the square geometry) and are practically non-degenerate at $\alpha = 0.5$ (corresponding

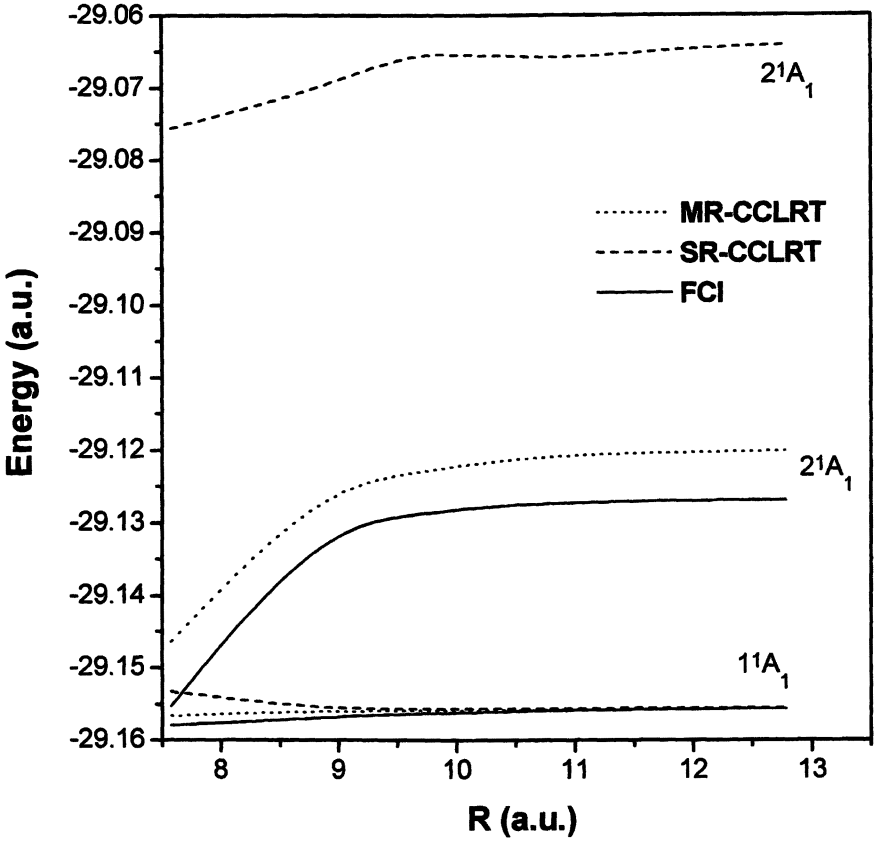

Figure 4. PES of some low-lying $^1A_1$ states of the rectangular Li_4 model.

Downloaded by PENNSYLVANIA STATE UNIV on September 14, 2012 | http://pubs.acs.org
Publication Date: August 14, 2002 | doi: 10.1021/bk-2002-0828.ch006

Downloaded by PENNSYLVANIA STATE UNIV on September 14, 2012 | http://pubs.acs.org
Publication Date: August 14, 2002 | doi: 10.1021/bk-2002-0828.ch006

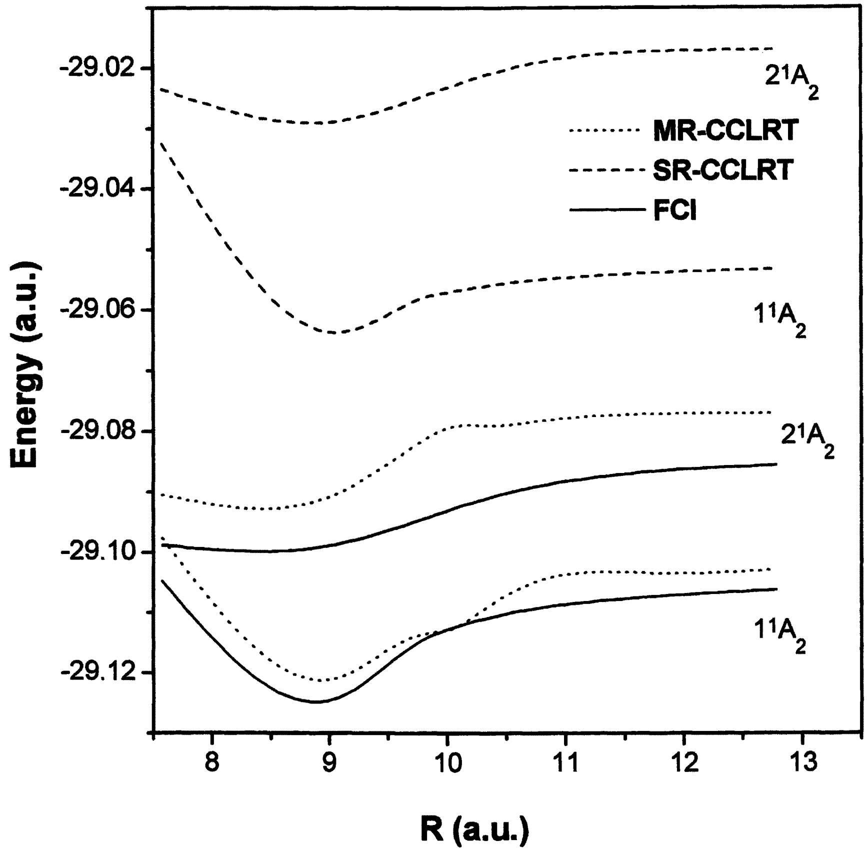

Figure 5. PES of some low-lying $^1A_2$ states of the rectangular Li_4 model.

Downloaded by PENNSYLVANIA STATE UNIV on September 14, 2012 | http://pubs.acs.org
Publication Date: August 14, 2002 | doi: 10.1021/bk-2002-0828.ch006

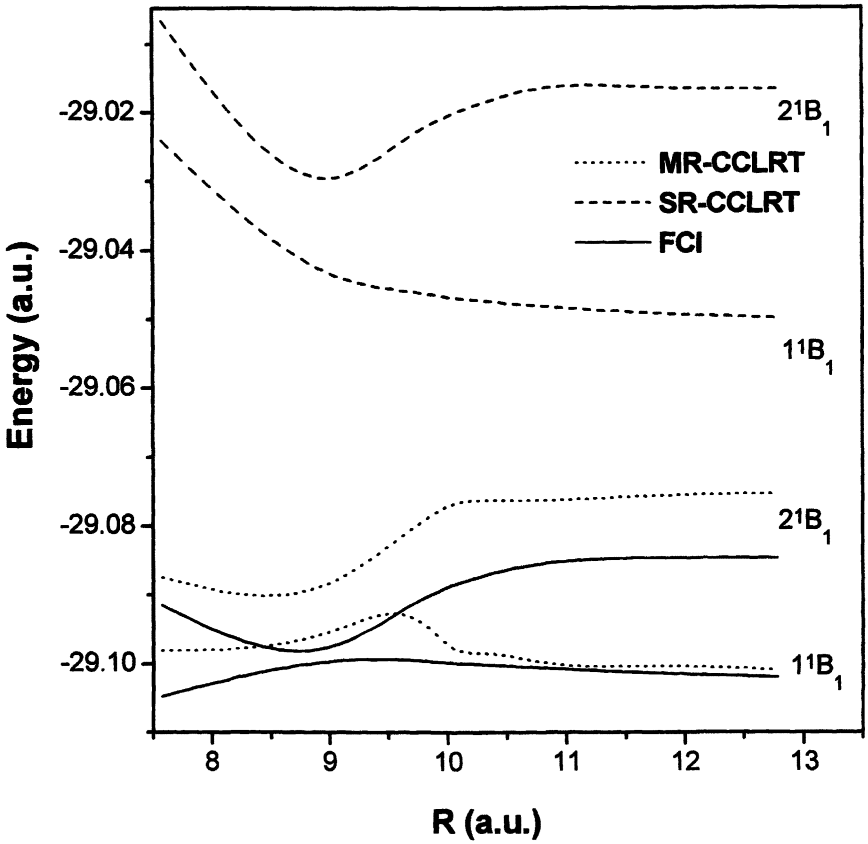

Figure 6. PES of some low-lying $^1B_1$ states of the rectangular Li_4 model.

Downloaded by PENNSYLVANIA STATE UNIV on September 14, 2012 | http://pubs.acs.org
Publication Date: August 14, 2002 | doi: 10.1021/bk-2002-0828.ch006

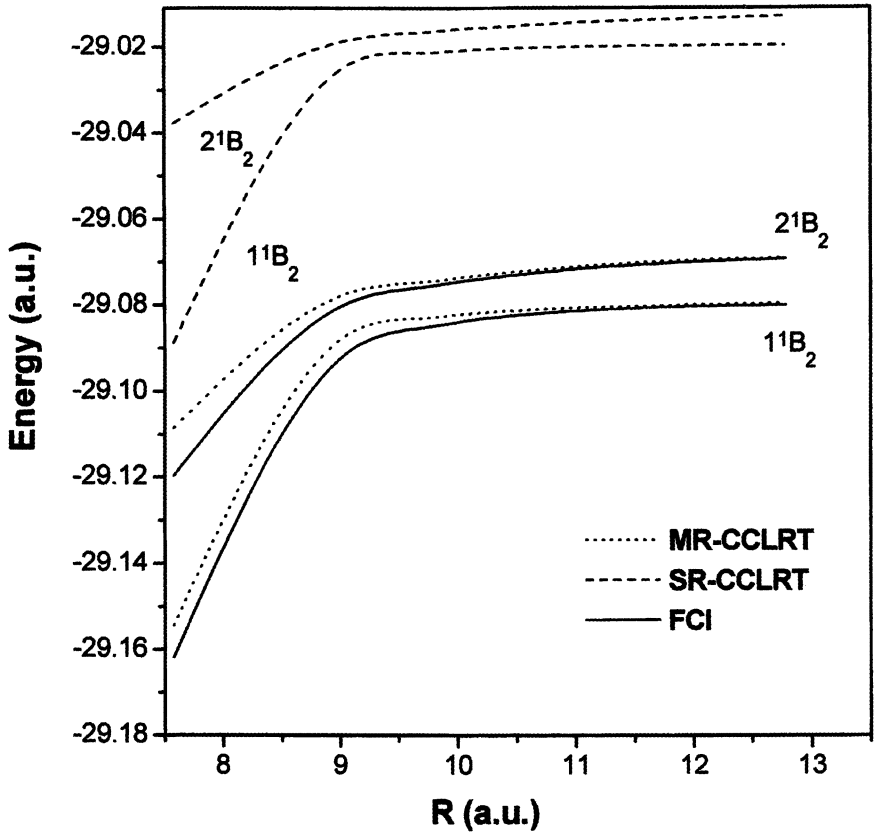

Figure 7. PES of some low-lying $^1B_2$ states of the rectangular Li_4 model.

to the linear situation). We encounter an intruder around $\alpha = 0.3$. We select the function ϕ_1 as the determinant whose HF orbitals are used throughout our calculations.

We have applied the pair of SS-MRCEPA theories to generate the ground state PES. We depict in Figure 8 the ground state PES for the H4 model, and compare them with the FCI results. Throughout the PES, both the SS-MRCEPA methods are in excellent numerical agreement with the FCI values for every α. Moreover, both the SS-MRCEPA methods are seen to be free of the intruder state problem, as is evident from the non-divergence of the PES around $\alpha = 0.3$. To further ascertain the potentiality of the SS-MR methods, we summarize in Table I the correlation energies for the ground state of H4 model along with those of other standard MR techniques. For the ease of comparison, we present only the energy differences from the corresponding FCI values, ΔE = (E_{FCI} - E_{method}). A perusal of the table clearly reflects that all the SS-MR methods and the sr-MRBWCC method are intruder free. In a global manner the performance of the SS-MRCC method is the best. The sr-MRBWCC method is the MR-based state-specific nonsize-extensive formulation of Hubač *et al.* [34]. The MRL-CCSD approximation is the linearized version of the SU-MRCCSD [52], which is intruder-prone. It indeed displays a serious singular behavior around $\alpha = 0.2$, and fails completely in the non-degenerate region. The SS-MRCEPA(0) results are excellent, and the SS-MRCEPA(2) results are also good. The behavior of the effective hamiltonian based linearized version of the MR-BW theory of the Hubač *et al.* [34] is also reasonably good, but consistently inferior to our SS-MRCEPA(0), which is also a linearized theory.

As a further test of the robustness of the formalisms, we have deliberately homed in on to the *excited* root while diagonalizing the effective matrix to generate the first excited state. It is gratifying to note that, although ϕ_1 is no longer dominant in the domain of geometry studied by us for the excited state, the method still provides quite credible results, as a comparison with FCI values depicted in Table II shows. However, in the geometries 0.3, 0.4 and 0.5 we cannot

Downloaded by PENNSYLVANIA STATE UNIV on September 14, 2012 | http://pubs.acs.org
Publication Date: August 14, 2002 | doi: 10.1021/bk-2002-0828.ch006

Downloaded by PENNSYLVANIA STATE UNIV on September 14, 2012 | http://pubs.acs.org
Publication Date: August 14, 2002 | doi: 10.1021/bk-2002-0828.ch006

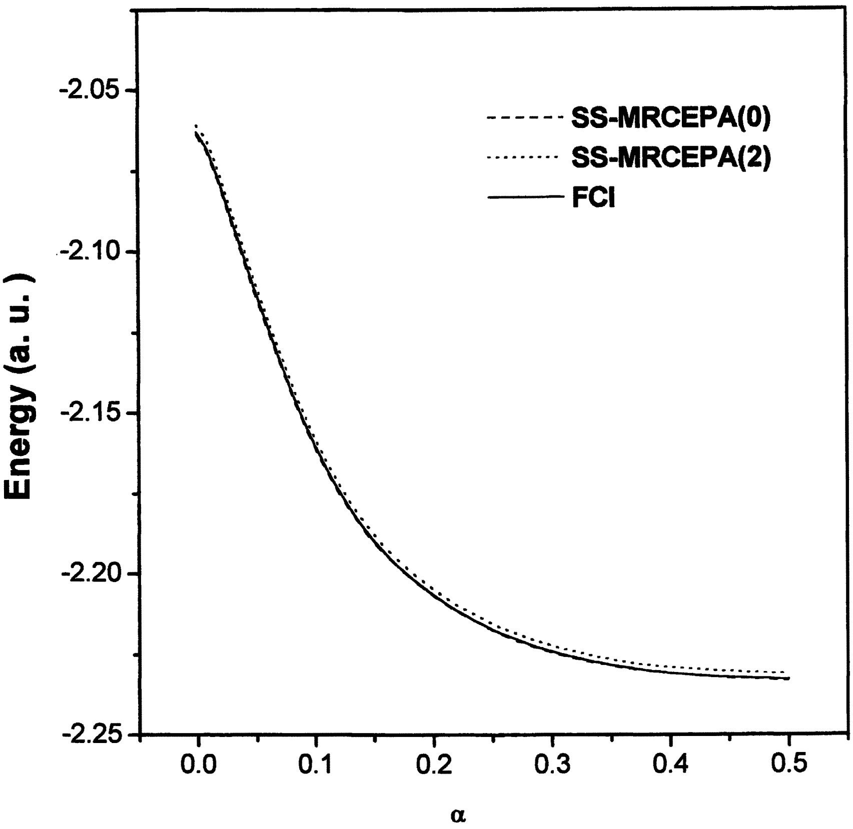

Figure 8. PES of the ground state of H4 model.

evaluate the energies of the 2^1A_1 state because the state itself has intruders in these geometries. This indicates that the SS-MRCEPA theories are applicable for the ground state as well as the excited states with equal ease, but these states must be free from intruders. However, it is important to mention here that the excited states perturbed by intruders can still be tackled with the response approach based on our SS-MRCEPA methods.

Table-I Energy differences (in mH) with respect to the FCI values, ΔE, of the ground state of the H4 model for different values of α.

α	0.0	0.01	0.02	0.1	0.2	0.3	0.5
MRMBPT3^a	-2.172	-2.295	-2.386	-2.155	-2.079	-2.136	-2.166
MR-CISD^a	-	-1.771	-1.706	-1.277	-1.039	-	-0.895
MRL-CCSD^a	3.685	3.610	3.436	5.027	⋆	⋆	⋆
MR-CCSD^a	0.687	0.594	0.408	0.172	1.186	1.995	2.375
MRL-BWCCSD^a	-3.942	-3.961	-3.863	-3.212	-3.071	-3.092	-3.151
SS-MRCEPA(0)	0.849	0.872	0.968	0.855	0.448	0.254	0.154
SS-MRCEPA(2)	-2.323	-2.461	-2.513	-2.183	-1.871	-1.760	-1.719
SS-MRCC	0.279	0.188	0.170	0.442	-0.422	-0.393	0.406
sr-MRBWCCSD^a	0.100	0.012	-0.146	-0.582	-0.579	-0.559	-0.548

Data ^{a} taken from Ref [34].
MRMBPT3 implies third-order MRMBPT calculation.
MR-CISD: missing values were not shown in [34].
⋆ denotes that no convergence is achieved.

We compare our results for the excited states with the corresponding FCI values as shown in Figure 9 where we have plotted the energies of different states as a function of α. For both the ground and excited states of different symmetry with respect to the ground state, both the MR-CEPALRT yield results which are close to the FCI values over a wide range of geometries, including the points of quasi-degeneracy and avoided crossings. The results from the full-blown MR-CCLRT, computed by us earlier [36], are comparable to the SS-MRCEPA(2) values, but the latter is much simpler.

Downloaded by PENNSYLVANIA STATE UNIV on September 14, 2012 | http://pubs.acs.org
Publication Date: August 14, 2002 | doi: 10.1021/bk-2002-0828.ch006

Downloaded by PENNSYLVANIA STATE UNIV on September 14, 2012 | http://pubs.acs.org
Publication Date: August 14, 2002 | doi: 10.1021/bk-2002-0828.ch006

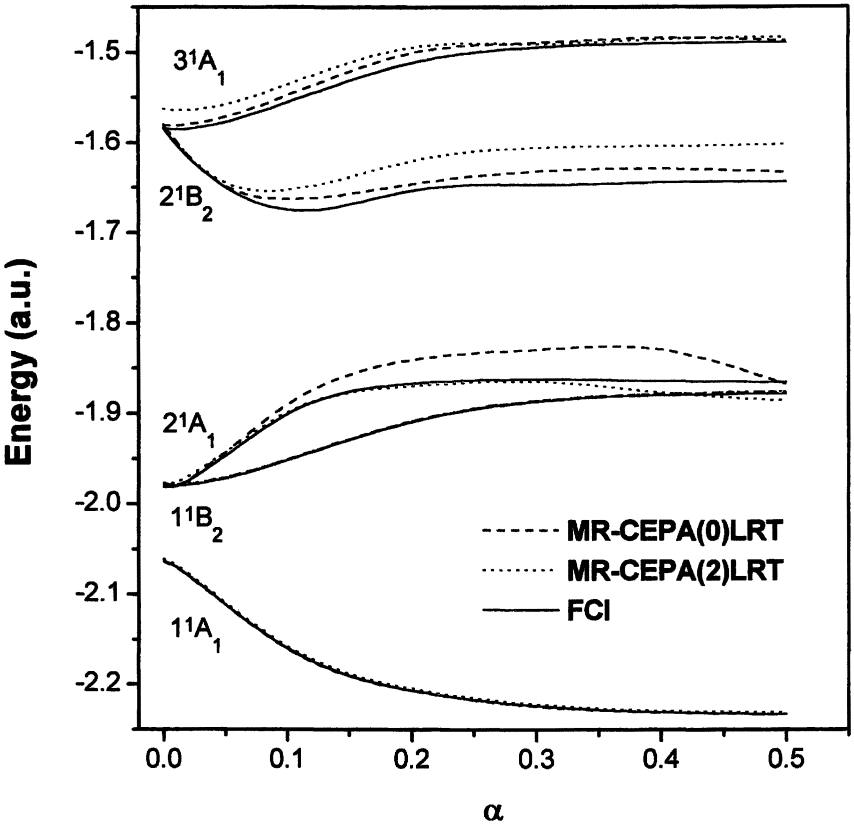

Figure 9. PES of some low-lying states of the H4 model.

Table-II. Energies (a.u.) for the 2^1A_1 state of H4 model. Values (mH) within the parenthesis indicate the deviation from FCI.

α	FCI	SS-MRCEPA(0)	SS-MRCEPA(2)
0.00	-1.981434	-1.986031 (4.597)	-1.978542 (-2.892)
0.01	-1.980637	-1.985741 (5.104)	-1.977680 (-2.957)
0.02	-1.974328	-1.980042 (5.714)	-1.971203 (-3.125)
0.10	-1.900893	-1.955619 (54.726)	-1.892647 (-8.246)
0.20	-1.866764	⋆	-1.849494 (-17.270)

⋆ Divergence

Summary

In this article, we have presented the formulation and numerical applications of a set of size-extensive intruder-free state-specific multi-reference (SSMR) methods based on a CAS designed for the PES of a base state whose energy is well-separated from those of the virtual functions, and linear response methods based on these methods for the PES of other excited states relative to the base state. The parent SSMR method is a non-perturbative CC theory, which we call the SS-MRCC formalism. The approximate variants are the perturbation theories (SS-MRPT) of the RS as well as the BW variety, and the two non-perturbative CEPA-like truncations (SS-MRCEPA). The systems studied by us are the rectangular Li_4 and H4 models, which show strong quasi-degeneracy in certain regions of the PES, while there are potential intruders in some other regions of the ground state. The illustrative applications are given mostly for ground states with varying degrees of multi-reference character, but excited states

Downloaded by PENNSYLVANIA STATE UNIV on September 14, 2012 | http://pubs.acs.org
Publication Date: August 14, 2002 | doi: 10.1021/bk-2002-0828.ch006

at certain selected geometries are also described well with these methods. Starting from our recently formulated SS-MRCC method in the singles and doubles truncation, we have studied the efficacy of certain approximate versions such as the perturbative SS-MRPT in both RS and BW forms, and two SS-MRCEPA schemes vis-a-vis the parent method. All these approximations preserve the extensivity of the parent theory, and perform quite well. Once the ground state is determined by these methods, the excited state PES can be accessed via the linear response approach based on the ground state function. The earlier formulated MR-CCLRT based on the SS-MRCC with singles and doubles for the ground state has also been described briefly. In addition, we have developed and applied in this article a pair of LRT based on SS-MRCEPA methods from the parent MR-CCLRT. We have shown the efficacy of the MR-CEPALRT by comparing the results with those computed by FCI, and have shown that they are quite good, despite the neglect of a host of terms present in the parent MR-CCLRT. Just like the MR-CCLRT, the MR-CEPALRT too yield size-intensive excitation energies.

Downloaded by PENNSYLVANIA STATE UNIV on September 14, 2012 | http://pubs.acs.org
Publication Date: August 14, 2002 | doi: 10.1021/bk-2002-0828.ch006

Acknowledgment

The computations have been carried out using the facility of the Level III computer centre under the ICOSER project of the DST (India) of our Institute. We thank Professor S. Ray of the computer center for help and advice. PG thanks the CSIR, India for a junior research fellowship.

This article is dedicated to the memory of Per-Olov Löwdin, a pioneer in electron correlation theory and an indefatigable champion in propagating the cause of Quantum Chemistry.

References

[1] *Čížek*, J., *J. Chem. Phys.* **1966**, *45*, 4256; *Adv. Chem. Phys.*

1969, *14*, 35; *Čížek*, J.; Paldus, J.; Shavitt, I., *Phys. Rev. A* **1972**, *5*, 50.

[2] Bartlett, R. J., *Modern Electronic Structure Theory*, Yarkony, D. R., Ed.; World Scientific, Singapore, 1995; Part II, pp 1047.

[3] Crawford, T. D.; Schaefer III, H. F., *Reviews in Computational Chemistry*, Lipkowitz, K. B.; Boyd, D. B., Eds.; Wiley-VCH, John Wiley and Sons, Inc., New York, 2000, Vol. 14; pp 33.

[4] Raghavachari, K.; Trucks, G. W., Pople, J. A.; Head-Gordon, M., *Chem. Phys. Lett.* **1989**, *157*, 479; Bartlett, R. J.; Watts, J. D.; Kucharski, S. A.; Noga, J., *Chem. Phys. Lett.* **1990**, *165*, 513.

[5] Noga, J.; Bartlett, R. J., *J. Chem. Phys.* **1987**, *86*, 7041.

[6] Scuseria, G. E.; Schaefer III, H. F., *Chem. Phys. Lett.* **1988**, *152*, 382.

[7] Kucharski, S. A.; Bartlett, R. J., *Theor. Chim. Acta* **1991**, *80*, 387; *J. Chem. Phys.* **1992**, *97*, 4282.

[8] Oliphant, N.; Adamowicz, L., *J. Chem. Phys.* **1991**, *94*, 1229; **1992**, *96*, 3739; Ivanov, V. V.; Adamowicz, L., *J. Chem. Phys.* **2000**, *112*, 9258.

[9] Piecuch, P.; Kucharski, S. A.; Bartlett, R. J., *J. Chem. Phys.* **1999**, *110*, 6103 and references therein.

[10] Paldus, J.; Planelles, J., *Theor. Chim. Acta* **1994**, *89*, 13; Li, X.; Paldus, J., *J. Chem. Phys.* **1997**, *107*, 6257.

[11] Mukherjee, D.; Moitra, R. K.; Mukhopadhyay, A., *Mol. Phys.* **1977**, *33*, 955; Lindgren, I., *Int. J. Quantum Chem.* **1978**, *S12*, 33; Mukherjee, D.; Pal, S., *Adv. Quantum Chem.* **1989**, *20*, 292 and references therein.

[12] Jeziorski, B.; Monkhorst, H. J., *Phys. Rev. A* **1981**, *24*, 1668.

Downloaded by PENNSYLVANIA STATE UNIV on September 14, 2012 | http://pubs.acs.org
Publication Date: August 14, 2002 | doi: 10.1021/bk-2002-0828.ch006

[13] Paldus, J., *Methods in Computational Molecular Physics*, Wilson, S.; Diercksen, G. F. H., Eds.; Plenum Press, New York, 1992, pp 293 and references therein.

[14] Paldus, J.; Li, X., *Symmetries in Science VI*, Gruber, B., Ed.; Plenum Press, New York, 1993, pp 573; Jeziorski, B.; Paldus, J.; Jankowski, K., *Int. J. Quantum Chem.* **1995**, *56*, 129.

[15] Schucan, T. H.; Weidenmüller, H. A., *Ann. Phys.* **1972**, *73*, 108.

[16] Hose, G.; Kaldor, U., *J. Phys. B (At. Mol. Opt. Phys.)* **1979**, *12*, 3827; *Phys. Scripta* **1980**, *21*, 357.

[17] Mukherjee, D., *Chem. Phys. Lett.* **1986**, *125*, 207; *Int. J. Quantum Chem.* **1986**, *S20*, 409; Sinha, D.; Mukhopadhyay, S. K.; Mukherjee, D., *Chem. Phys. Lett.* **1986**, *129*, 369.

[18] Mukhopadhyay, D.; Mukherjee, D., *Chem. Phys. Lett.* **1989**, *163*, 171; **1991**, *177*, 441.

[19] Meissner, L.; Kucharski, S. A.; Bartlett, R. J., *J. Chem. Phys.* **1989**, *91*, 6187; Meissner, L.; Bartlett, R. J., *ibid.* **1990**, *92*, 561.

[20] Kaldor, U., *Chem. Phys. Lett.* **1990**, *140*, 1; *Theor. Chim. Acta* **1991**, *80*, 427.

[21] Kirtman, B., *J. Chem. Phys.* **1981**, *75*, 798.

[22] Malrieu, J. P.; Durand, Ph.; Daudey, J. P., *J. Phys. A Math. Gen.* **1985**, *18*, 809; Durand, Ph.; Malrieu, J. P., *Adv. Chem. Phys.* Lawley, K. P., Ed.; Wiley, New York, 1987; Vol. 67, pp 321 and references therein.

[23] Hoffmann, M. R., *Chem. Phys. Lett.* **1993**, *210*, 193.

[24] Khait, Y. G.; Hoffmann, M. R., *J. Chem. Phys.* **1998**, *108*, 8317.

[25] Mukhopadhyay, D.; Datta, B.; Mukherjee, D. *Chem. Phys. Lett.* **1992**, *197*, 236; Datta, B.; Chaudhuri, R.; Mukherjee, D., *J.*

Downloaded by PENNSYLVANIA STATE UNIV on September 14, 2012 | http://pubs.acs.org
Publication Date: August 14, 2002 | doi: 10.1021/bk-2002-0828.ch006

Mol. Structure (Theochem) **1996**, *361*, 21; Landau, A.; Eliav, E.; Ishikawa, Y.; Kaldor, U., *J. Chem. Phys.* **2000**, *113*, 9905.

[26] Wolinski, K.; Sellers, H. L.; Pulay, P., *Chem. Phys. Lett.* **1987**, *140*, 225; Murray, C. W.; Davidson, E. R., *J. Chem. Phys.* **1991**, *187*, 451.

[27] Andersson, K.; Malmqvist, P. Å.; Roos, B. O., *J. Chem. Phys.* **1992**, *96*, 1218; Roos, B. O.; Andersson, K.; Fulscher, M. P.; Malmqvist, P. Å.; Serrano-Andres, L.; Pierloot, K.; Merchan, M., *Adv. Chem. Phys.* **1996**, Vol. XCIII, pp 219 and references therein.

[28] Hirao, K., *Chem. Phys. Lett.* **1992**, *190*, 374; *Int. J. Quantum Chem.* **1992**, *S26*, 517.

[29] Dyall, K. G., *J. Chem. Phys.* **1995**, *102*, 4909.

[30] Mukherjee, D., *Recent Progress in Many-Body Theories* , Schachinger, E., Mitter, H.; Sormann, H., Eds.; Plenum Press, New York, 1995, Vol. 4, pp 127.

[31] Mahapatra, U. S.; Datta, B.; Bandyopadhyay, B.; Mukherjee, D., *Adv. Quantum Chem.* **1998**, *30*, 163.

[32] Mahapatra, U. S.; Datta, B.; Mukherjee, D., *Mol. Phys.* **1998**, *94*, 157; *J. Chem. Phys.* **1999**, *110*, 6171.

[33] Nebot-Gil, I.; Sanchez-Marin, J.; Malrieu, J. P.; Heully, J. L.; Maynau, D., *J. Chem. Phys.* **1995**, *103*, 2576; Heully, J. L.; Malrieu, J. P.; Zaitsevski, A., *J. Chem. Phys.* **1996**, *105*, 6887; Meller, J.; Malrieu, J. P.; Caballol, R., *J. Chem. Phys.* **1996**, *104*, 4068.

[34] Mášik, J.; Hubač, H., *Quantum Systems in Chemistry and Physics: Trends in Methods and Applications*, McWeeny, R.; Maruani, J.; Smeyers; Y. G.; Wilson, S., Eds.; Kluwer Academic, Dordrecht, 1997; pp 283.

[35] Chattopadhyay, S.; Mahapatra, U. S.; Mukherjee, D., *J. Chem. Phys.* **1999**, *111*, 3820.

Downloaded by PENNSYLVANIA STATE UNIV on September 14, 2012 | http://pubs.acs.org
Publication Date: August 14, 2002 | doi: 10.1021/bk-2002-0828.ch006

[36] Chattopadhyay, S.; Mahapatra, U. S.; Mukherjee, D., *Recent Advances in Computational Chemistry: Recent Advances in Multi-reference Methods*, Hirao, K., Ed.; World Scientific, Singapore, 1999; Vol. 4, pp 65; *J. Chem. Phys.* **2000**, *112*, 7939; *Ind. J. Chem. A: Special Issue on Contemporary Theoretical Chemistry Research in India* **2000**, *39A*, 1.

[37] Mahapatra, U. S.; Datta, B.; Mukherjee, D., *Chem. Phys. Lett.* **1999**, *299*, 42; *J. Phys. Chem. A* **1999**, *103*, 1822.

[38] Koch, H.; Jϕrgensen, P., *J. Chem. Phys.* **1990**, *93*, 3333; Koch, H.; Kobayashi, R.; Sanchez de Mears, A.; Jϕrgensen, P., *ibid.* **1994**, *100*, 4393.

[39] Mukhopadhyay, D.; Mukhopadhyay, S.; Mukherjee, D., *Theor. Chim. Acta.* **1991**, *80*, 441.

[40] Murray, C. W.; Davidson, E. R., *J. Chem. Phys.* **1991**, *187*, 451; Kozlowski, P. M.; Davidson, E. R., *J. Chem. Phys.* **1994**, *100*, 3672.

[41] Dyall, K. G., *J. Chem. Phys.* **1995**, *102*, 4909.

[42] Meyer, W., *J. Chem. Phys.* **1973**, *58*, 1017; *Theor. Chim. Acta* **1989**, *35*, 277.

[43] Ruttink, P. J. A.; van Lenthe, J. H.; Zwaans, R.; Groenenboom, G. C., *J. Chem. Phys.* **1991**, *94*, 7212; Fulde, P.; Stoll, H., *J. Chem. Phys.* **1992**, *97*, 4185; Fink, R.; Staemmler, V., *Theor. Chim. Acta* **1993**, *87*, 129; for a recent review see Szalay, P. G., *Recent Advances in Computational Chemistry: Recent Advances in Coupled-Cluster Methods*, Bartlett, R. J., Ed.; World Scientific, Singapore, 1997; Vol. 3, pp 81.

[44] Monkhorst, H. J., *Int. J. Quantum Chem.* **1977**, *S11*, 421; Piecuch, P.; Bartlett, R. J., *Adv. Quantum Chem.* **1999**, *34*, 295, and references therein.

[45] Mukherjee, D.; Mukherjee, P. K., *Chem. Phys.* **1979**, *39*, 325; Datta, B.; Sen, P.; Mukherjee, D., *J. Phys. Chem.* **1995**, *99*, 6441.

Downloaded by PENNSYLVANIA STATE UNIV on September 14, 2012 | http://pubs.acs.org
Publication Date: August 14, 2002 | doi: 10.1021/bk-2002-0828.ch006

[46] Nakatsuji, H.; Hirao, K., *J. Chem. Phys.* **1978**, *68*, 2053; Nakatsuji, H., *Acta Chim. Hung.* **1992**, *129*, 719 and references therein.

[47] Nakano, H., *J. Chem. Phys.* **1993**, *99*, 7983; *Chem. Phys. Lett.* **1993**, *207*, 372.

[48] Jankowski, K.; Paldus, J., *Int. J. Quantum Chem.* **1980**, *18*, 1243.

[49] Widmark, P. O.; Malmqvist, P. Å.; Roos, B. O., *Theor. Chim. Acta* **1990**, *77*, 291.

[50] Zarrabian, S.; Paldus, J., *Int. J. Quantum Chem.* **1990**, *38*, 761; Jankowski, K.; Paldus, J.; Grabowski, I.; Kowalski, K.; *ibid.* **1991**, *97*, 7600; **1994**, *101*, 3085; Finley, J. P.; Chaudhuri, R. K.; Freed, K. F., *ibid.* **1995**, *103*, 4990.

[51] Piecuch, P.; Paldus, J., *J. Chem. Phys.* **1994**, *101*, 5875.

[52] Balková, A.; Kucharski, S. A.; Meissner, L.; Bartlett, R. J., *Theor. Chim. Acta* **1991**, *80*, 335.

Downloaded by PENNSYLVANIA STATE UNIV on September 14, 2012 | http://pubs.acs.org
Publication Date: August 14, 2002 | doi: 10.1021/bk-2002-0828.ch006

Downloaded by COLUMBIA UNIV on September 14, 2012 | http://pubs.acs.org
Publication Date: August 14, 2002 | doi: 10.1021/bk-2002-0828.ch007

Chapter 7

The Excited and Ion States of Allene

Rajat K. Chaudhuri[1,2], Karl F. Freed[1], and Davin M. Potts[1]

[1]The James Franck Institute and the Department of Chemistry, The University of Chicago, 5640 South Ellis Avenue, Chicago, IL 60637
[2]Indian Institute of Astrophysics, Koramangala, Bangalore 34, India

Large scale ab initio calculations for the excited states of C_3H_4 and $C_3H_4^+$ are reported here for the vertical ionization potentials (VIPs), excitation energies, and oscillator strengths using the IVO-CASCI and third order effective valence shell Hamiltonian (H^v) methods. The results are in excellent agreement with experiment and with those predicted by the MRSDCI and ADC(4) methods. The potential energy surfaces (PES) of $C_3H_4^+$ show the presence of a "conical intersection" between the X^2E and A^2E states near 12.3 eV and a 145° dihedral angle, which strongly suggests that the experimental peak at 12.7 eV is most likely non-vertical in origin and is a "shake-up" type state. A similar conical intersection is also observed in the PES of C_3H_4 but at a relatively small dihedral angle (105°). We provide computations for quartet ion states, triplet neutral states, and potential curves for the twisting of neutral allene, quantities that have not previously been reported.

I. Introduction

The photoelectron and optical spectra of allene (1,2-propadiene) have been of considerable theoretical and experimental interest because a significant portion of these spectra is not only quite complex but also rather peculiar. The molecular point group of allene in the ground state is D_{2d}, with the self-consistent field (SCF) approximation described by the orbital occupation $1a_1^2 1b_2^2 2a_1^2 3a_1^2 2b_2^2 4a_1^2 3b_2^2 1e^4 2e^4$. Removal of an electron from the highest occupied molecular orbital 2π (or 2e) of

In Low-Lying Potential Energy Surfaces; Hoffmann, M., et al.;
ACS Symposium Series; American Chemical Society: Washington, DC, 2002.

allene yields the positive ion ^2E state, which has been suggested to be Jahn-Teller unstable. The photoelectron spectrum (PES) of allene shows two peaks at 10.06 and 10.60 eV in the first ionization band[1]. These peaks are split by ≈ 4500 cm^{-1} and have been assigned to be the Jahn-Teller components of the ^2E molecular ion state. The photoelectron study of Baltzer[2-4] reveals the existence of peaks at 12.7 eV, 18.5 eV, 24.05 eV, and 25.45 eV in addition to the main peaks at 10.06 eV and 10.60 eV. Although the peak at 12.7 eV is clearly visible in the earlier PES study of Kimura *et al.*[1] and Bieri *et al.*[5], no comments have appeared regarding this low intensity peak until the recent reports of Baltzer *et al.*[2] Based on ADC(4)[6] (algebraic diagrammatic construction accurate to 4th order in the electron-electron interaction) theoretical calculations, Baltzer *et al.* assign this low intensity peak as a correlation (also called satellite or shake-up) state of ^2E symmetry with binding energy 14.05 eV. Since it is quite unusual to have satellite states at fairly low binding energies[7], this assignment remains controversial. Furthermore, the difference between the observed (12.7 eV) and the theoretically predicted binding energy (14.05 eV) is too large to be attributed solely to computational uncertainties. Recent high level MRSDCI calculations[8] clearly show that the observed peak at a binding energy of 12.7 eV can not be simply attributed to a satellite state of the allene ion if the ion is assumed to be at the *fixed geometry of neutral allene.* Since the first ionization band in allene already displays clear Jahn-Teller splitting (0.6 eV), it is quite likely that the peak at 12.7 eV arises due to strong vibronic coupling involving two electronic states, and the transition is most likely non-vertical in origin. Note that traditional calculations for the ionization energy spectra of molecules assume a vertical ionization transition, which is valid provided the adiabatic Born-Oppenheimer approximation holds reasonably well.

The first optical spectrum of allene by Sutcliffe and Walsh[9] has been followed by measurements of Rabalais *et al.*[10] that provide the spectrum from 4.78 to 10.2 eV. A moderately high resolution gas phase study from 6.2 to 10.7 eV is described by Iverson and Russell [11]. Fuke *et al.*[12] also report the absorption and MCD spectra in both the gas phase and in perflurohexane solution from 6.2 to 8.0 eV. The absorption spectrum of allene is rather complex. There is weak structureless absorption below 6.45 eV. Four distinct absorption bands are observed between 6.54 and 9 eV of which the first band is weak with a maximum at 6.70 eV, and a strong broad absorption covers the range of 6.95-7.85 eV. Five distinct peaks of roughly the same intensity are present in the 8.02-8.38 eV region, followed by a strong transition around 8.57 eV. The absorption bands beyond 8.57 eV are fairly complicated and remain to be characterized.

According to Fuke *et al.*[12] and Robin[13], the $^1A_1$, $^1A_2$, $^1B_1$ and $^1B_2$ states of allene arise from singlet $\pi \rightarrow \pi^*$ ($e \rightarrow e^*$) transitions. Among these four excited

Downloaded by COLUMBIA UNIV on September 14, 2012 | http://pubs.acs.org
Publication Date: August 14, 2002 | doi: 10.1021/bk-2002-0828.ch007

states, only the $^1B_2$ state is optically allowed in the electric dipole approximation, and the remaining three states are observed as the very weak absorption below 6.45 eV. In the weak band around 6.70 eV, Fuke *et al.* observe an MCD (magnetic circular dichroism) signal with only a B term type behavior. They conclude this is a transition to a non-degenerate Rydberg state and confirm Robin's assignment of the upper state as one component of the $2e \rightarrow 3s$ ($^1A_1 \rightarrow {}^1E$) Rydberg state that converges to the ionization threshold at 10.0 eV, arguing moreover that the other component is 4500cm^{-1} higher, i.e., around 7.30 eV. The strong (f=0.34) transition in the 6.95-7.8v eV band exhibits diffuse structure. Fuke and Schnepp assign two states to this band: the $\pi \rightarrow \pi^*$ ($^1A_1 \rightarrow {}^1B_2$) valence transition and the other component of the $\pi \rightarrow 3s$ ($^1A_1 \rightarrow {}^1E$) Rydberg state converging to the upper ionization threshold at 10.6 eV. Fuke et al. also observe a strong B term type MCD transition at 7.7 eV in the gas phase. They argue this state is of valence character, but Robin assigns this state to the $\pi \rightarrow 3p$ Rydberg series at 7.3 eV that converges to the ionization threshold at 10.0 eV. The absorption spectrum beyond 8.02 eV is rather complex and remains unassigned.

We describe highly correlated *ab initio* calculations for the vertical ionization and excitation energies of allene using the effective valence shell Hamiltonian (H^v) method through third order and our recently developed, more approximate IVO-CASCI approach that is a non-iterative replacement (with no loss of accuracy) for the popular CASSCF method. In addition, we present the ground and excited state potential energy curves of allene and the allene cation as a function of the torsional angle between the two CH_2 groups in order to identify the origin of the mysterious peak at 12.7 eV which is believed to be non-vertical.[8] Several papers document the H^v formalism, the computational algorithms for evaluating atomic and molecular properties,[14-19] and the convergence behavior.[20-22] Some conceptual advantages of these two methods are the following:

(i) The H^v method manifestly maintains the size-extensivity of the computed state energies, a property that is known to be crucial for highly correlated many-particle systems. (ii) A common set of orbitals is used to describe all the state of interest. This choice leads to the cancellation of correlation energy contributions that are common to all states considered, thereby yielding a balanced description of both dynamical and non-dynamical correlation. (iii) A single computation of the effective Hamiltonian simultaneously. provides all the ionization potentials, excitation energies, and associated molecular properties such as transition dipole and oscillator strengths. (iv) While the IVO-CASCI method represents only the first approximation within the H^v scheme, it provides comparable accuracy to CASSCF approaches with greatly reduced computational labor because no iterations are required beyond an initial SCF calculation.

Downloaded by COLUMBIA UNIV on September 14, 2012 | http://pubs.acs.org
Publication Date: August 14, 2002 | doi: 10.1021/bk-2002-0828.ch007

Section II briefly outlines the theory behind the H^v method, while the IVO generation scheme is described in Section III for systems, such as allene, where there is a degenerate highest occupied molecular orbital in the SCF ground state wavefunction. The computations are described in Section IV along with comparisons to experiment and other high level calculations.

II. Theory

Since the basic formalism of the effective valence shell Hamiltonian (H^v) method is presented elsewhere,[23] we only provide a brief overview of the approach. As in conventional many-body perturbation theory, the H^v method begins with the decomposition of the exact Hamiltonian H into the zeroth order Hamiltonian H_0 and the perturbation V,

$$H=H_0+V, \qquad (2.1)$$

where H_0 is constructed as a sum of one-electron Fock operators described below. The full many-electron Hilbert space is then partitioned into an active (also called valence) space with projector P and its orthogonal complement with projector Q=1-P. The active space spans the space of all distinct configuration state functions involving a filled core and the remaining electrons distributed among the valence orbitals in all possible manners to ensure completeness of the active space. Hence, the orthogonal complement space contains all basis functions with at least one vacancy in a core orbital and/or at least one electron in an excited orbitals. Thus, we designate the orbitals as "core", "valence," and "excited", where the doubly filled orbitals in P-space are denoted as core, the partially filled orbitals of P-space are valence, and the orbitals that are unoccupied in all active space functions are the excited orbitals.

With the aid of the projectors P and Q, the H^v method transforms the full Schrõdinger equation[24-25]

$$H\Psi_i = E_i \Psi_i , \qquad (2.2)$$

into the P-space "effective valence shell" Schrõdinger equation

$$H^v\Psi_i^v = E_i \Psi_i^v , \qquad (2.3)$$

where $\Psi_i^v = P\Psi_i$ are the projections of the exact eigenfunctions on the valence space, and the energies E_i are the corresponding exact eigenvalues of the full

Downloaded by COLUMBIA UNIV on September 14, 2012 | http://pubs.acs.org
Publication Date: August 14, 2002 | doi: 10.1021/bk-2002-0828.ch007

Schrõdinger equation. Here, the effective operator H^v through third order is given by

$$H^v_{3rd} = PHP + [\ V_{eff}^{(2)} + V_{eff}^{(3)} + h.c\ ]/2\,, \tag{2.4}$$

in which *h.c.* designates the Hermitian conjugate and E_0^P is the zeroth order energy of the *P*-space state. The operators $V_{eff}^{(2)}$ and $V_{eff}^{(3)}$ are defined as

$$V_{eff}^{(2)} = PVQ\ (E_0^P\text{-}QH_0Q)^{-1}\ QVP \tag{2.5}$$

$$V_{eff}^{(3)} = PVQ\,(E_0^P\text{-}QH_0Q)^{-1}\ V\,(E_0^P\text{-}QH_0Q)^{-1}\,QVP - PVQ(E_0^P - QH_0Q)^{-2}VPVP \tag{2.6}$$

Apart from specifying the reference (*P*) space, the only variability in this and all MR-MBPT methods lies in the choice of orbitals, orbital energies, and the definition of the zeroth order Hamiltonian H_0 since the perturbation approximation is completely determined by these choices. The zeroth order Hamiltonian (i.e., the partitioning of the exact Hamiltonian into H_0 and *V*), may, ***in principle***, be specified at our disposal, but, ***in practice***, this choice strongly affects the perturbative convergence.[20-22,26-27] Generally, the zeroth order Hamiltonian is prescribed as a sum of one-electron operators,

$$H_0(i) = \Sigma_c\,|\varphi_c\rangle\ \varepsilon_c\,\langle\varphi_c| + \Sigma_v\,|\varphi_v\rangle\ \varepsilon_v\,\langle\varphi_v\,| + \Sigma_e\,|\varphi_e\rangle\ \varepsilon_e\ \langle\varphi_e\,|\quad , \tag{2.7}$$

in terms of the core (*c*), valence (*v*) and excited (*e*) orbitals and their corresponding orbital energies. The orbital energies are defined as

$$F\,|\varphi_i\rangle = \varepsilon_I\,|\varphi_i\,\rangle\,, \tag{2.8}$$

where *F* is a one-electron Fock operator described below. The H^v method departs from traditional MR-MBPT approaches that are based on a Moller-Plesset (MP) partitioning scheme in which a *single* one-electron Fock operator *F* is used to define all orbitals and orbital energies,

$$F{=}h{+}\ \Sigma_i^{occ}\ (2J_i - K_i), \tag{2.9}$$

where the sum runs over all the orbitals occupied in some reference state (often chosen as the ground state). Here *h* denotes the one-electron portion of the Hamiltonian, and J_i and K_i are Coulomb and exchange operators, respectively, for the occupied Hartree-Fock molecular orbital φ_i of the reference state. Since this single Fock operator produces V^N potential orbitals and orbital energies for those valence orbitals that are unoccupied in the reference state, these V^N

Downloaded by COLUMBIA UNIV on September 14, 2012 | http://pubs.acs.org
Publication Date: August 14, 2002 | doi: 10.1021/bk-2002-0828.ch007

potential orbitals are, *at best*, more suitable for describing negative ions than the low lying states of neutral species that emerge from the eigenvalues of H^v of Eq. (2.4). Consequently, this traditional single Fock operator choice is quite *unphysical* and provides a poor first order approximation (*PHP*) to the low lying states, leaving large contributions to be recovered by the higher order perturbation expansion.[20-22]

To improve the perturbative convergence and to eliminate notorious intruder state problems, Freed and coworkers use *multiple* Fock operators to define the valence orbitals.[28-30] In their formalism, all the valence orbitals and orbital energies are obtained from $V^{(N-1)}$ potentials, thereby providing a good first order approximation (*PHP*) to the low lying excited states and thus minimizing the residual corrections to be recovered by the perturbation expansion. The unoccupied valence orbitals are chosen as improved virtual orbitals as described in the next section. Moreover, intruder state problems are further reduced in the H^v method by defining the zeroth order Hamiltonian H_0 as

$$H_0(i) = \Sigma_c |\varphi_c\rangle \varepsilon_c \langle \varphi_c| + \Sigma_v |\varphi_v\rangle \varepsilon'_v \langle \varphi_v| + \Sigma_e |\varphi_e\rangle \varepsilon_e \langle \varphi_e| , \qquad (2.10)$$

where the average valence orbital energy ε'_v is obtained from the original set of valence orbital energies by the democratic averaging,

$$\varepsilon'_v = \Big(\sum_i^N \varepsilon_i \Big) /N , \qquad (2.11)$$

with N the number of valence orbitals spanning the complete active *P* space (CAS). The forced degeneracy condition introduces a diagonal perturbation $\delta V = \varepsilon_v - \varepsilon'_v$ that begins to contribute in third order. Since the magnitude of δV directly depends upon the spread of the original valence orbital energies $\{\varepsilon_v\}$ prior to averaging, the forced degeneracy condition is unnecessary for highly quasidegenerate CASs because these systems yield $\delta V \approx 0$.

III. Generation of Improved Virtual Orbitals (IVO)

The generation of improved virtual orbitals (IVOs) and orbital energies presents a non-trivial problem for systems, such as C_3H_4, $C_3H_4^+$ etc., where the highest occupied molecular orbitals (HOMOs) are doubly degenerate. Unless appropriate Fock operators *F* are used, the IVOs may break molecular symmetry (see below).

Here we describe briefly the essential aspects of generating the IVOs by the simple diagonalization of a restricted CIS matrix. A more detailed discussion of the formulation and its computational aspects is given elsewhere.[31-32] When

Downloaded by COLUMBIA UNIV on September 14, 2012 | http://pubs.acs.org
Publication Date: August 14, 2002 | doi: 10.1021/bk-2002-0828.ch007

the ground (or reference) state of the system is a closed shell, we begin with the Hartree-Fock (HF) molecular orbitals (MOs) for the ground state wavefunction, $\Phi_0 = \mathbf{A}[\varphi_1\,\varphi_1'\,\varphi_2\,\varphi_2'\ldots\varphi_n\,\varphi_n']$ where **A** is an appropriate antisymmetrizer. The indices *i,j,k,..* refer to occupied HF MOs $\{\varphi_I\}$ and *u,v,w,...* to unoccupied HF MOs. All the HF MOs are determined by diagonalizing the one electron Hartree-Fock operator ${}^1F$,

$$ {}^1F_{lm} = \langle \varphi_l \,|\, h + \sum_{k}^{occ} (2J_k - K_k) \,|\, \varphi_m \rangle , \qquad (3.1) $$

where *l* and *m* designate any (occupied or unoccupied) HF MOs and ε_l is the HF orbital energy. An excited state HF computation for the low lying singly excited $\Psi_{\alpha\to\mu}$ state would provide a new set $\{\chi\}$ of MOs that minimize the energy of $\Psi_{\alpha\to\mu}$,

$$ \Psi_{\alpha\to\mu} = \mathbf{A}\,[\,\chi_1\,\chi_1'\,\chi_2\chi_2' \cdots (\,\chi_\alpha\,\chi_\mu' \pm \chi_\mu\,\chi_\alpha'\,) \ldots \chi_n\,\chi_n'\,] , \qquad (3.2) $$

corresponding to the excitation of an electron from the orbital χ_α to χ_μ, where the + and - signs refer to triplet and singlet states, respectively. The new MOs $\{\chi_\alpha\}$ and $\{\chi_\mu\}$ may be expressed as linear combinations of the ground state MOs $\{\varphi_I, \varphi_u\}$. If, however, the orbitals are restricted such that the $\{\chi_\alpha\}$ are linear combinations of only the occupied ground state MOs $\{\varphi_i\}$ and the $\{\chi_\mu\}$ are expanded only in terms of the unoccupied $\{\varphi_u\}$,

$$ \chi_\alpha = \sum_{i}^{occ} a_{\alpha i}\,\varphi_i \quad ; \quad \chi_\mu = \sum_{u}^{unocc} c_{\mu u}\,\varphi_u , \qquad (3.3) $$

then the new orbital set $\{\,\chi_\alpha, \chi_\mu\,\}$ not only leaves the ground (or reference) state wavefunction unchanged but also ensures the orthogonality and applicability of Brillouin's theorem between the HF ground state and the singly excited $\Psi_{\alpha\to\mu}$ states. In addition, this choice also benefits from the use of a common set of MOs for the ground and excited states for calculations of oscillator strengths, etc. However, if we avoid the computationally laborious reoptimization of the occupied orbitals by setting $\{\chi_\alpha\} \equiv \{\varphi_\alpha\}$, i.e., by choosing $a_{\alpha j} = \delta_{\alpha j}$, the procedure for generating IVOs simplifies enormously. Hence, the coupled equations determining the $a_{\alpha j}$ and $c_{\mu u}$ coefficients in Eq. (3.3) reduces to a single eigenvalue equation of the form $F'\,C = C\,\Gamma$, where the operator F' is given by Hunt and Goddard and by Huzinaga[33] as

$$ F'_{vw} = {}^1F_{vw} + A_{ve}{}^{\alpha} , \qquad (3.4) $$

where ${}^1F$ is the ground (or reference) state Fock operator and where the additional term $A_{vw}{}^{\alpha}$ accounts for the excitation of an electron out of orbital φ_α.

Downloaded by COLUMBIA UNIV on September 14, 2012 | http://pubs.acs.org
Publication Date: August 14, 2002 | doi: 10.1021/bk-2002-0828.ch007

$$A_{vw}{}^{\alpha} = \langle \chi_v | -J_\alpha + K_\alpha \pm K_\alpha | \chi_w \rangle \ . \tag{3.5}$$

The minus sign in Eq. (3.5) applies for ${}^3\Psi_{\alpha\rightarrow\mu}$ a triplet state, while the plus sign is for the singlet ${}^1\Psi_{\alpha\rightarrow\mu}$ state.[33] The corresponding transition energy is

$$^{1,3}\Delta E\,(\alpha\rightarrow\mu) = E_0 + \gamma_\mu - {}^1F_{\alpha\alpha} \ , \tag{3.6}$$

where E_0 is the HF ground state energy and γ_μ is the eigenvalue of $F' C = C\Gamma$ for the μ-th orbital.

In order that the $\{\chi_\mu\}$ retain molecular symmetry, the construction of F' must be modified from the Hunt-Goddard-Huzinaga scheme to handle systems like C_3H_4 where the HOMO is doubly degenerate. If φ_α and φ_β designate the pair of highest occupied degenerate HF MOs, then the matrix element A_{vw} in equation (3.5) is replaced for these degenerate systems by $A_{vw}{}^{\alpha,\beta}$ where

$$A_{vw}{}^{\alpha,\beta} = (1/2)\,[\,\langle\chi_v | -J_\alpha + K_\alpha \pm K_\alpha | \chi_w \rangle \ + \ \langle\chi_v | -J_\beta + K_\beta \pm K_\beta | \chi_w\rangle\,] \ . \tag{3.7}$$

It may readily be shown that the excitation energies computed from the single excitation configuration interaction (CIS) and the Hunt-Goddard-Huzinaga IVO schemes become equivalent when the CIS configurations involve only the promotion of an electron from the highest molecular orbital to excited orbitals. Consequently, the combination of ground state HF occupied orbital energies and the IVO orbital energies provide a zeroth order Koopmans theorem type approximation to the low lying excitation energies. More importantly, these orbitals are then used in the first order H^v method (called the IVO-CASCI method) to provide a computationally quite efficient first order approximation (from *PHP*) to excitation energies and excited state properties. Our recent works[31,32] demonstrate that the IVO-CASCI method provides comparable accuracy to the more laborious CASSCF treatments without the need for iterations beyond the initial SCF calculation for the reference state. Furthermore, previous discussions of the H^v method [18] explain why the first order H^v wavefunctions provide good starting points for higher level treatments of the residual dynamic correlation.

IV. Computational details

The molecular geometry of allene is of D_{2d} symmetry with R_{CC} =1.308 A°, R_{CH}=1.087 A°, and ∠HCH=118.2° [34], where the *z*- axis is defined as lying along the carbon skeleton and the dihedral planes bisect the *xy* and *yz* planes. The atomic basis is chosen as Dunning's (9s5p/4s2p) contraction[35] centered on each

Downloaded by COLUMBIA UNIV on September 14, 2012 | http://pubs.acs.org
Publication Date: August 14, 2002 | doi: 10.1021/bk-2002-0828.ch007

Downloaded by COLUMBIA UNIV on September 14, 2012 | http://pubs.acs.org
Publication Date: August 14, 2002 | doi: 10.1021/bk-2002-0828.ch007

carbon atom and (4s/2s) contractions centered on each of the hydrogen atoms. A full set of n=3 (s, p, d) Cartesian Gaussian (ξ_s=0.23, ξ_p=0.021, ξ_d=0.015) is added for the central carbon atom. This basis generates 48 contracted Gaussian type orbitals (CGTO) and is quite similar to that employed by Diamond *et al.*[36] The total SCF energy in this basis is -115.8302 au and is comparable to the results of Diamond,[36] Dykstra,[37] and Rauk [38] which are -115.8258 au, -115.8303 au, and -115.8302 au, respectively. Although the basis set is not very large, it is employed to here to treat the IVO-CASCI, H^v_{3rd} and MRSDCI methods on equal footing and to compare their efficiencies. Comparisons with experimental transition energies and ionization potentials use computations with considerably larger basis sets that are described below.

It is well known that the choice of orbitals, orbital energies, and reference space represents the most significant factor determining the convergence and accuracy of multireference many-body perturbative methods of both the "perturb then diagonalize" and "diagonalize then perturb" varieties, with the selection of the appropriate reference space being the most non-trivial. In general, the reference space orbitals are selected on the basis of (i) energy criteria and (ii) the character of the states of interest. For instance, while the *e* symmetry orbitals are the most important for computing the A_1, A_2, B_1, and B_2 excited states of allene, the *e* and a_1 orbitals are prominent for describing the degenerate E states because these states arise from $e \rightarrow a_1$ or $a_1 \rightarrow e$ transitions.

However, the selection of reference space orbitals solely based on the character of the excited state alone may lead to erroneous results because symmetry considerations are also relevant. For example, the $5a_1$ unoccupied orbital in allene contributes significantly to the X^1A_1 ground state wave function but not to the excited E state wave function. Since the excitation/ionization energy is the difference between the ground and the excited/ion state energies, the unoccupied $5a_1$ orbital only indirectly contributes to the E state excitation/ionization energy. Thus, the inclusion of the $5a_1$ orbital in the reference space is necessary not only to improve transition energies but also to improve the quality of the ground state wavefunction. Similarly, orbital energy criteria are important in the selection of reference space orbitals. Inclusion of too many valence orbitals in the reference space may provide a decent first order estimate (from *PHP*) of the transition energies for the state(s) of interest, but this large valence space may severely degrade the perturbative convergence because of the reduced quasi-degeneracy of the reference space.[20-22] At this juncture, it is worthwhile mentioning that computationally inexpensive IVO-CASCI calculations may be performed for a series of test CASs to ascertain the appropriate valence space for higher order treatments. Here we describe the excited and positive ion states of allene as computed with both the IVO-CASCI and third order H^v methods for several different choices of reference spaces, where the smallest and largest valence spaces comprise *four* and *twelve* valence orbitals, respectively, to demonstrate the general principles outlined above.

Table I provides equilibrium geometry parameters for allene and for twisted allene, respectively, while Table II describes a subset of the neutral allene HF molecular orbitals and their energies. Since the energy gap between the 1*e* (HOMO-1) and 2*e* (HOMO) occupied orbitals is quite large (0.24 Hartrees), the 1*e* and 2*e* orbitals are treated as "core" and "occupied valence" orbitals, respectively. The remaining orbitals in Table II are taken as "unoccupied valence" or "excited" orbitals depending upon the size of the reference space employed in the post-HF treatment. (The orbital energies of the "unoccupied valence" and excited orbitals are, of course altered from the HF values in Table II as discussed briefly in Sect. III.) The smallest reference space chosen for the post-HF treatment is constructed from the 2*e* and 3*e* orbitals, while the largest reference space is generated by distributing four electrons among the $5a_1$, $6a_1$, $7a_1$, 2*e*, 3*e* , 4*e* , $1b_1$, $4b_2$, and $5b_2$ valence space orbitals (in all possible ways). The same set of orbitals is used to compute the transition energies for neutral allene and its positive ion, so the computation of the ionization energies requires no extra computational work apart from the diagonalization of the appropriate CASCI matrix for the allene positive ion. Calculations for the twisted geometry (D_2 point group) allene molecule are only reported using a reference space composed of the $5a_1$, $6a_1$, $7a_1$, 2*e*, 3*e*, and $4b_2$ orbitals for both neutral C_3H_4 and its positive ion.

A. Excited states of $C_3H_4^+$

Table III presents the vertical ionization potentials (VIPs) of allene as a function of reference space for production of the X^2E, X^4E, A^2E ion states, respectively. Our extensive IVO-CASCI and third order H^v calculations clearly demonstrate that (a) dynamical correlation contributes significantly to the VIPs and that (b) the difference between the experimental and the computed VIPs (from the third order H^v computations) decreases as the reference space increases from four to ten. A further increase in the size of the valence space spoils the accuracy of the computed VIPs. (c) The computations further indicate that the experimental peak at 12.7 eV can not be due to a vertical transition.

Table IV compares the VIPs of allene, as obtained from the IVO-CASCI and H^v methods, with those obtained from the MRSDCI[8] method and from experiments[1]. Although our IVO-CASCI estimate for the 2π valence ionization potential is comparable to that obtained from the MRSDCI approach, it substantially departs (≈ 0.3 eV) from the experimental value, consistent with the

Downloaded by COLUMBIA UNIV on September 14, 2012 | http://pubs.acs.org
Publication Date: August 14, 2002 | doi: 10.1021/bk-2002-0828.ch007

Downloaded by COLUMBIA UNIV on September 14, 2012 | http://pubs.acs.org
Publication Date: August 14, 2002 | doi: 10.1021/bk-2002-0828.ch007

Table I. Geometrical properties of allene.

Parameter	Experimental geometry[1]	MP2/6-311g** optimized geomertry
$R_{C\text{-}C}$	1.308 A°	1.313 A^0
$R_{C\text{-}H}$	1.087 A°	1.086 A°
∠HCH	118.2°	121.1^0

1. Ref. [34]

Table II. SCF orbital properties for allene. [All entries in au]

Orbital symmetry	*Character*	*Type*	*Exptl. Geometry*	*Optimized geometry*
1*e*	σ	HOMO-1	-0.6123	-0.6123
2*e*	π	HOMO	-0.3784	-0.3777
5a$_1$	3s	LUMO	0.0184	0.0184
6a$_1$	3d$_{z2}$	LUMO+1	0.0516	0.0516
4b$_2$	3d$_{xy}$	LUMO+2	0.0526	0.0526
3*e*	3d$_{xz,yz}$	LUMO+3	0.0531	0.0531
1b$_1$	3d$_{x2\text{-}y2}$	LUMO+5	0.0532	0.0532
5b$_2$	3p$_z$	LUMO+6	0.0587	0.0587
4	3p$_{(x,y)}$	LUMO+7	0.0594	0.0594
7a$_1$	4s	LUMO+9	0.1059	0.1058
5*e*	π*	LUMO+10	0.1629	0.1629

Downloaded by COLUMBIA UNIV on September 14, 2012 | http://pubs.acs.org
Publication Date: August 14, 2002 | doi: 10.1021/bk-2002-0828.ch007

Table III. Variation of vertical ionization potential (in eV) of allene as a function of valence space. (All calculations are performed at the experimental geometry.) [The top entry for each state is obtained the IVO-CASCI calculations, and the bottom one is from H^v_{3rd} calculations.]

State	*4V*[1]	*6V*[2]	*8V*[3]	*10V*[4]	*12V*[5]
X^2E	10.41	10.41	10.41	10.41	10.38
	10.02	10.03	10.01	10.03	9.91
X^4E	15.43	15.43	15.43	15.37	15.33
	14.49	14.58	14.57	14.67	14.58
A^2E	15.88	15.88	15.88	15.81	15.78
	14.82	14.91	14.92	15.01	14.92

1. $[2e\ 3e]^4$
2. $[2e\ 3e\ 5a_1\ 6a_1]^4$
3. $[2e\ 3e\ 5a_1\ 6a_1\ 7a_1\ 4b_2\ ]^4$
4. $[2e\ 3e\ 5a_1\ 6a_1\ 7a_1\ 4b_2\ 5b_2\ 1b_1]^4$
5. $[2e\ 3e\ 4e\ 5a_1\ 6a^1\ 7a_1\ 1b_1\ 4b_2\ 5b_2]^4$

Table IV. Ionization potential (in eV) of allene from the 10 valence (10V) orbital reference space IVO-CASCI and third order H^v calculation.

State	*IVO-CASCI*	*H^v_{3rd}*	*MRSDCI*[1]	*ADC(4)*[2]	*Expt*[3]
X^2E	10.41	10.03	10.30	10.19	10.06
X^4E	15.37	14.67			
A^2E	15.81	15.01	14.90	14.05	

1. Ref. [8]
2. Ref. [2]
3. Ref. [1]

IVO-CASCI treatment giving comparable accuracy to CASSCF calculations, but with greatly reduced computational effort. Inclusion of higher order dynamical correlation contributions significantly improves the 2π VIP, which however becomes slightly poorer for the largest valence space that begins to suffer from a lack of quasidegeneracy.

The torsional potential energy curves for the positive allene ion in Fig. 1 are generated by scanning the dihedral angle with all internal coordinates fixed at their experimental values. When the dihedral angle equals 90 degrees, $C_3H_4^+$ (as well as C_3H_4) has D_{2d} point group symmetry. As the dihedral angles increases (or decreases), the symmetry of $C_3H_4^+$ (as well as C_3H_4) changes to D_2, finally returning to D_{2h} symmetry for dihedral angles of 0 and 180 degrees. The potential energy curves depicted in Fig. 1 clearly indicate the presence of a "conical intersection" between the upper Jahn-Teller component of the X^2E state, which is labeled as $^2B_3$ for D_2 symmetry, and the lower Jahn-Teller A^2E state, which is labeled as $^2B_2$ for D_2 symmetry. This intersection occurs at approximately 12.3 eV above the X^1A_1 C_3H_4 ground state (at a torsional angle 145^o), which corresponds to 2.3 eV above the X^2E $C_3H_4^+$ ground state (at a torsional angle of 90 degrees) and is in good agreement with the MRSDCI estimate (12.3 eV) and with the experiment (12.7 eV). It is worthwhile to mention that photoioniation mass spectra of allene[39] also indicate the presence of a peak at around 12.5-13.0 eV. Furthermore, the third order H^v binding energy (15.01 eV) for the first A^2E state of the allene ion are in good agreement with experiment and MRSDCI calculations.

As seen from Table IV, the IVO-CASCI and H^v_{3rd} VIPs differ from the MRSDCI and ADC(4) values by only 0.1 eV and 0.2 eV, respectively. Our large basis set calculations for the VIPs of allene clearly indicate that the source of this deviation is purely a basis set effect. Table V compares the IVO-CASCI and H^v_{3rd} VIPs using bases of increasing size. It is evident from Tables IV and V that the IVO-CASCI and H^v_{3rd} estimates of the VIPs approach the MRSDCI and ADC(4) values, respectively, when similar size basis sets are employed in the calculations. Note that Baltzer *et al.* employ a basis with 93 CGTO functions (6s4p1d for carbon atoms and 3s1p for hydrogen atoms) in their ADC(4) treatment, which is almost twice the size of the basis (Basis I) used in the present calculation of VIPs and transition energies for allene.

B. Excited states of C_3H_4

The optically allowed transitions between the ground and excited states of allene are $X^1A_1 \rightarrow {}^1B_2$ (polarized along the molecular axis) and $X^1A_1 \rightarrow {}^1E$ (polarized perpendicular to the molecular axis). The four singlet states arising

Downloaded by COLUMBIA UNIV on September 14, 2012 | http://pubs.acs.org
Publication Date: August 14, 2002 | doi: 10.1021/bk-2002-0828.ch007

Downloaded by COLUMBIA UNIV on September 14, 2012 | http://pubs.acs.org
Publication Date: August 14, 2002 | doi: 10.1021/bk-2002-0828.ch007

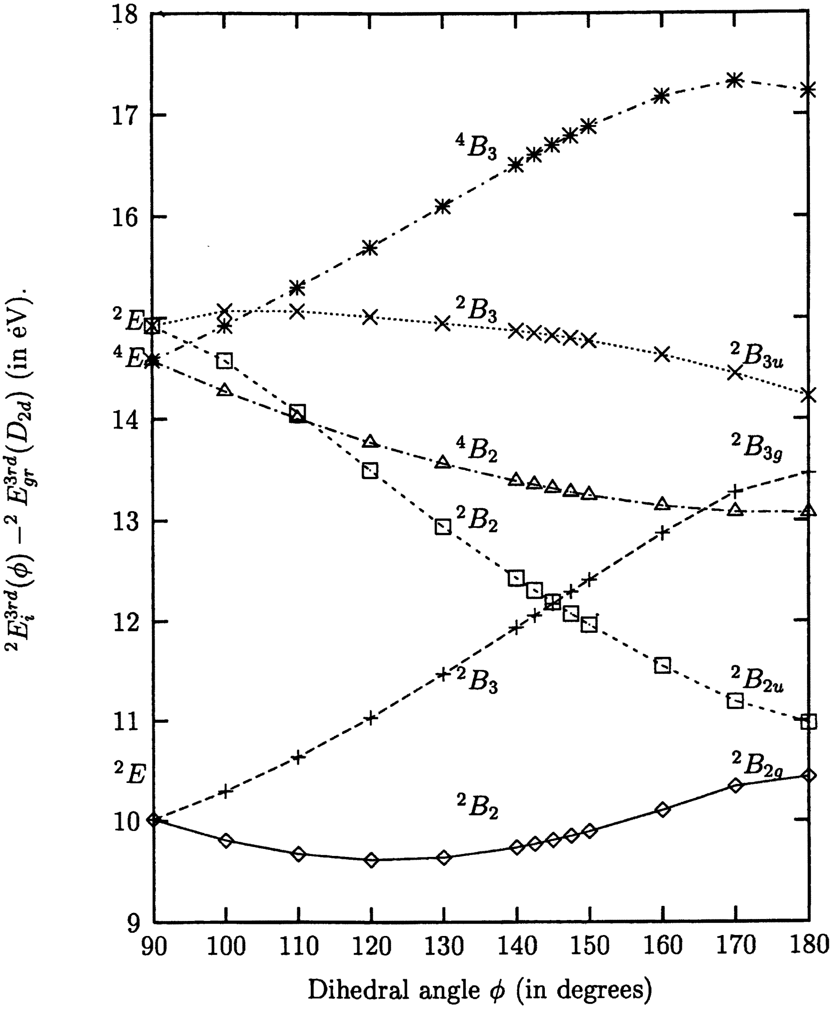

Figure 1. Plot of the ground and excited state potential curves of $C_3H_4^+$ as a function of dihedral angle ϕ.

Downloaded by COLUMBIA UNIV on September 14, 2012 | http://pubs.acs.org
Publication Date: August 14, 2002 | doi: 10.1021/bk-2002-0828.ch007

Table V. Basis set dependence of IVO-CASCI and H^{v}_{3rd} vertical ionization potential (in eV) for allene. [All calculations are performed at the experimental geometry with the 6V reference space. The top entry for each state is obtained from IVO-CASCI calculations, and the bottom is from H^{v}_{3rd} calculations.]

State	*Basis I*[1]	*Basis II*[2]	*Basis III*[3]	*Basis IV*[4]
X^2E	10.41	10.30	10.29	10.31
	10.03	10.16	10.27	10.20
X^4E	15.43	15.19	15.27	15.21
	14.58	14.54	14.67	14.58
A^2E	15.88	15.68	15.76	15.70
	14.91	14.88	15.03	14.91

1. See text. Total number of CGTO is 48.
2. Triple zeta valence (TZV) with *p* and *d* polarization for heavy atom. Total number of CGTO is 84.
3. PVDZ Correlation Consistent basis set[40]. Total number of CGTO is 95.
4. Triplet zeta valence (TZV) with *p*, *d* and *f* polarization. One *s* and one *p* diffuse function is added on each carbon atom. Total number of CGTO is 114.

Downloaded by COLUMBIA UNIV on September 14, 2012 | http://pubs.acs.org
Publication Date: August 14, 2002 | doi: 10.1021/bk-2002-0828.ch007

from π (*e*) → π* (*e**) excitations are calculated to be in the energetic order of $1^1A_2 < 1^1B_1 < 4\ ^1A_1 < 3\ ^1B_2$. The excitation energies and oscillator strengths obtained from the IVO-CASCI and $H^v{}_{3rd}$ calculations are compared with experiment and with the MRSDCI results of Diamond *et al*[36]. in Table VI. The lowest excited singlet state is an optically forbidden $^1A_2$ state. The IVO-CASCI calculation predicts this state to be 6.60 eV above the ground state, which is quite close to the MRSDCI value (6.57 eV). Although the IVO-CASCI excitation energy is in accord with the MRSDCI estimate, it overestimates the $X^1A_1 \rightarrow {}^1A_2$ transition energy by 0.15 eV. The $H^v{}_{3rd}$ calculation predicts this $X^1A_1 \rightarrow {}^1A_2$ transition energy to be 6.10 eV, in good agreement with experiment (<6.45 eV). The observed optical spectrum[10-12] in the region 6.5-6.9 eV contains a weak absorption with partially resolved vibrational structure. The calculated states in this region are the optically allowed ^1E state and the forbidden $^1B_1$ state. The $H^v{}_{3rd}$ excitation energy and oscillator strength for the optically allowed ^1E state is reasonably close to both experiment and theoretical calculations. The spectrum in the 7.0 -8.0 eV region exhibits a strong broad diffuse band. The $H^v{}_{3rd}$ calculations assign this state as due to the optically allowed $^1B_2$ state at 7.53 eV (*f*=0.233), in accord with the MRSDCI transition energy (7.45 eV) and oscillator strength (*f*=0.285) as well as with experiment. There exists another weak but allowed transition in this region. The $H^v{}_{3rd}$ assigns this state as the 2^1E state at an excitation energy of 7.68 eV (*f*=0.038). As seen from Table VI, the $H^v{}_{3rd}$ transition energies and oscillator strengths are consistently in good agreement with experiment for the low lying states. The accuracy of the H^v energies sharply falls above 8.2 eV, a deficiency that can be reduced partially by using a state selective reference space.[19,32] However, such a state selective treatment is beyond of the scope of the present analysis.

The C_3H_4 torsional potential energy curves depicted in Fig 2 are generated by scanning the dihedral angle with all internal coordinates fixed at their experimental values. Unlike $C_3H_4^+$, the high lying potential energy curves become too complicated for display at large dihedral angles, and, hence, only a portion of the curves is presented here. Figure 2 clearly demonstrates the presence of an intersection near 105° between the $^1A_2$ and 1^1B_1 excited electronic states at 6.1 eV (with respect to the $H^v{}_{3rd}$ X^1A_1 state energy computed at the experimental geometry). A similar curve crossing is also observed between the $^1B_3$ and $^1B_2$ electronic states at 7.5 eV. The present study shows that the degenerate E electronic excited states of C_3H_4 undergo curve crossings at much lower dihedral angles than those in $C_3H_4^+$, which is quite as expected.

Table VII compares the IVO-CASCI and $H^v{}_{3rd}$ vertical excitation energies (VEE) using bases of increasing size for a fixed CAS generated by allocating four valence electrons among the 2*e*, 3*e*, $5a_1$, and $6a_1$ valence orbitals in all

Downloaded by COLUMBIA UNIV on September 14, 2012 | http://pubs.acs.org
Publication Date: August 14, 2002 | doi: 10.1021/bk-2002-0828.ch007

Table VI. Vertical excitation energies (in eV) and oscillator strengths (within parentheses) of allene computed at the experimental geometry.

State	*IVO-CASCI*	*H^v_{3rd}*	*MRSDCI*[1]	*Optical absorption band*[2]	*MCD*[3]
1^3A_1	4.80	4.59			
1^3B_2	5.09	5.06			
1^3A_2	6.44	6.02			
1^1A_2	6.60	6.10	6.57	<6.45	
1^3E	7.21	6.66			
1^1E	7.38 (0.07)	6.79 (0..07)	6.88 (0.08)	6.5-6.9	6.5-6.9
1^3B_1	6.89	6.34			
1^1B_1	7.16	6.52	6.92		
1^1B_2	8.03 (0.21)	7.53 (0.23)	7.45 (0.29)	6.95-7.85 (0.34)	7.1-7.5
2^3B_2	8.24	7.71			
2^3A_1	8.22	7.72			
2^1A_1	8.31	7.74	7.61		
2^3E	8.23	7.63			
2^1E	8.28 (0.05)	7.68 (0.04)	7.69 (0.04)		
3^3E	8.79	8.26			
3^1E	8.84 (0.04)	8.30 (0.04)	8.20 (0.04)	8.02	
2^1B_2	8.97 (0.01)	8.46 (0.02)	8.34 (0.03)	8.15	
3^1A_1	9.07	8.48	8.31		
4^3E	9.04	8.57			
4^1E	9.05 (0.01)	8.58 (0.01)	8.42 (0.02)	8.25	
4^1A_1	10.37	8.76	8.53		
3^1B_2	11.01 (1.33)	9.74 (1.21)	9.07 (1.04)	8.5-9.0	

1. Ref. [36]
2. Ref. [10]
3. Ref. [12]

Downloaded by COLUMBIA UNIV on September 14, 2012 | http://pubs.acs.org
Publication Date: August 14, 2002 | doi: 10.1021/bk-2002-0828.ch007

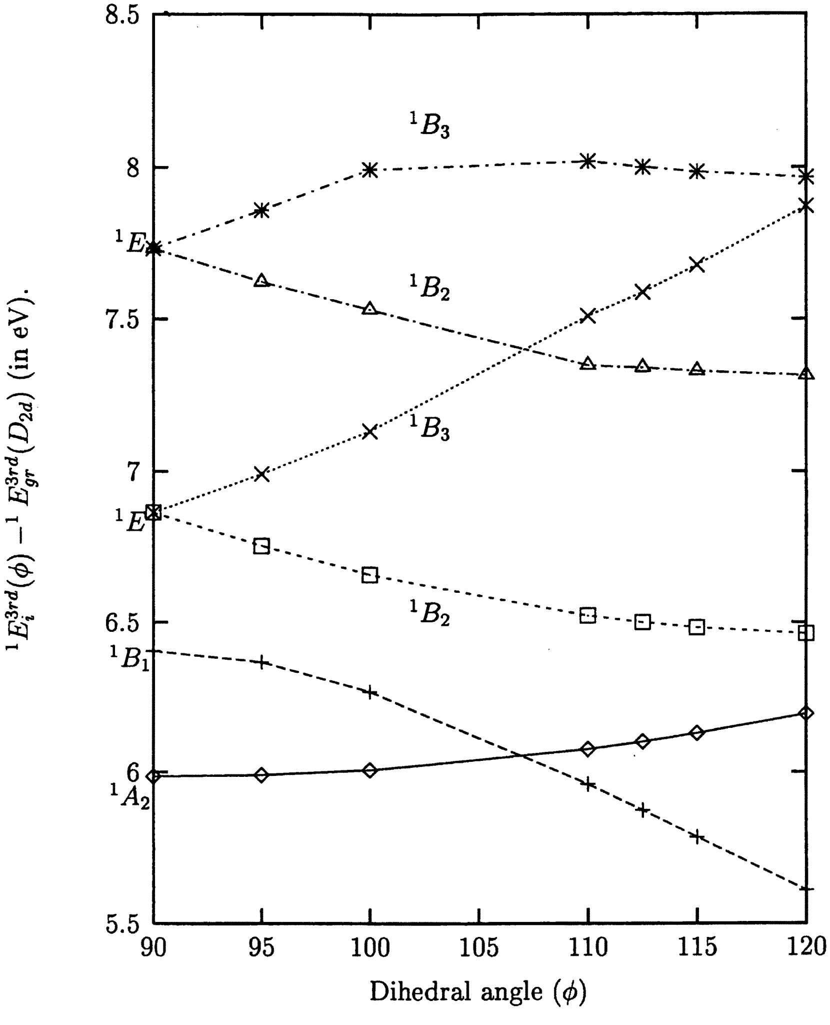

Figure 2. Plot of the excited state potential curves of C_3H_4 as a function of dihedral angle ϕ.

Downloaded by COLUMBIA UNIV on September 14, 2012 | http://pubs.acs.org
Publication Date: August 14, 2002 | doi: 10.1021/bk-2002-0828.ch007

Table VII. Basis set dependence of IVO-CASCI and H^v_{3rd} vertical excitation energies (in eV) for allene. [All calculations are performed at the experimental geometry with the 6V reference space. The top entry for each state is obtained from IVO-CASCI calculations, and the bottom one from H^v_{3rd} calculations.]

State	*Basis I*[1]	*Basis II*[2]	*Basis III*[3]	*Basis IV*[4]
1^3A_1	4.79	4.76	4.84	4.78
	4.59	4.41	4.53	4.43
1^3B_2	5.09	5.03	5.10	5.05
	5.05	4.78	4.88	4.78
1^3A_2	6.48	6.27	6.32	6.28
	5.91	5.60	5.60	5.57
1^1A_2	6.63	6.46	6.51	6.46
	5.99	5.71	5.73	5.67
1^3E	7.22	8.40	7.09	8.41
	6.72	7.95	6.84	7.98
1^1E	7.42	8.77	7.31	8.76
	6.88	8.21	7.01	8.05

1. See text. Total number of CGTOs is 48.
2. Triple zeta valence (TZV) with *p* and *d* polarization functions for heavy atom. Total number of CGTOs is 84.
3. PVDZ Correlation Consistent basis set [40]. Total number of CGTOs is 95.
4. Triplet zeta valence (TZV) with *p*, *d* and *f* polarization. One *s* and one *p* diffuse function is added on each carbon atom. Total number of CGTO is 114.

possible ways. The twin facts that the excited states of A_1, B_2, A_2, and B_1 symmetries both arise from a $2e \rightarrow 3e$ transition and that the computed VEEs for these symmetries changes insignificantly with increasing size of the basis set indicate that the presence of additional diffuse and polarization functions does not affect the character of the unoccupied (at the SCF level) $3e$ MO. On the other hand, it is also evident from Table VII that the presence of polarization and diffuse functions considerably affects the computation of the excitation energies of E symmetries which arise from $2e \rightarrow a_1^*$ transitions.

V. Concluding Remarks

We compare the vertical ionization potentials, excitation energies and oscillator strengths of allene using the IVO-CASCI and third order H^v method with experiment and with other high level computations. The optically allowed transitions in allene arise from valence→Rydberg and valence $\pi \rightarrow \pi^*$ excitations. Our computed transition energies (ionization potentials and excitation energies) and oscillator strengths are in excellent agreement with experiment and previous high level theoretical calculations. We also report singlet → triplet transition energies and quartet state ionization potentials which emerge as a byproduct of the method with "no extra" computational cost. The present study also indicates that the computationally inexpensive IVO-CASCI method is capable of providing fairly accurate molecular properties in situations where dynamical correlation is of less importance, i.e., the method is of comparable accuracy to the widely used CASSCF approach but requires considerably less CPU time.

The present calculations for the ground and excited states of $C_3H_4^+$ suggest that the experimental peak near 12.7 eV probably arises due to the presence of strong vibronic coupling between the two doublet E states that undergo a surface crossing for a torsional angle near 145^o and an energy of 12.3 eV. Alternatively, the weak peak at 12.7 eV may arise from the combined effects of spin-orbit and vibronic couplings between the doublet and quartet E state, which also exhibit a "conical intersection" (see Fig. 1) at 14 eV near a dihedral angle of 110^0.

Acknowledgment

This research is supported, in part, by NSF Grant CHE9727655. Many helpful discussions with Prof. Bruce Hudson are acknowledged. We thank Dr. M. S. Gordon and Dr. M. Schmidt for their support.

Downloaded by COLUMBIA UNIV on September 14, 2012 | http://pubs.acs.org
Publication Date: August 14, 2002 | doi: 10.1021/bk-2002-0828.ch007

References

1. Handbook of HeI photoelectron spectra of fundamental molecules; Kimura K.; Katsuamata S.; Achiba Y.; Yamazaki T.; Iwata S.: Japan Sci. Soc.Press, Tokyo (**1981**).
2. Baltzer P.; Wannberg B.; Lundqvist M.; Karlsson L.; Holland D. M. P; MacDonald M. A.; Niessen W. von; Chem. Phys. **1995,** 196, 55.
3. Mahapatra S.; Worth G. A.; Meyer H. D.; Cederbaum L.S.; H. Koppel H.; J. Chem. Phys. **1999,** 111, 10452.
4. Mahapatra S.; G. A. Worth, H.D. Meyer, L. S. Cederbaum and H. Koppel; J. Phys. Chem. **2001,** A 105, 5567.
5. Bieri G.; Burger F.; Heilbronner E.; Maier J.P.; Helv. Chim Acta **1977.** 60, 2213.
6. Niessen W. von; Tomasello P.; Schirmer J.; Cederbaum L.S.; Aust. J. Phys. **1986**, 39, 687.
7. Cederbaum L.S; Domcke W.; Schirmer J.; Niessen W. von; Adv. Chem. Phys. **1986**, 65, 115.
8. Bawagan A.D.O.; Ghanti T.K.; Davidson E.R.; Tan K.H.; Chem. Phys. Letts. **1998**, 287, 61.
9. L. H. Sutcliffe and A.D. Walsh, J. Chem. Phys. **1979**, 38, 211.
10. Rabalais J.W.; McDonald J.M.; Scherr V.; McGlynn S.P.; J. Chem. Rev. **1971**, 71, 73.
11. Iverson A.; Russell B.R., Spectrochim. Acta Part A **1972**, 28 A, 447.
12. Fuke K.; Schnepp O.; J. Chem. Phys. **1979**, 38, 211.
13. *Higher Excited States of Polyatomic Molecules*; Robin M.B; Academic Press, New York **1975**, Vol 2, p199.
14. Iwata S.; K.F. Freed K.F.; J. Chem. Phys. **1977**, 66, 1765.
15. Sun H.; Freed K.F.; Herman M.; Yeager D.L.; J. Chem. Phys. **1990**, 72, 4158.
16. Kanzler A.W.; H. Sun H.; Freed K.F.; Int. J. Quantum. Chem. **1991**, 39, 269.
17. Martin C.M.; Freed K.F.; J. Chem. Phys. **1994**, 100, 7454.
18. Stevens J.E.; Freed K.F.; Arendt F.; Graham R.L.; J. Chem. Phys. **1994**, 101,4832.
19. Stevens J.E.; Chaudhuri R.K.; Freed K.F.; J. Chem. Phys. **1996**, 105, 8754.
20. Finley J.P.; Chaudhuri R.K.; Freed K.F.; J. Chem. Phys. **1995**, 103, 4990.
21. Finley J.P.; Chaudhuri R.K.; Freed K.F.; Phys. Rev. A **1996**, 54, 343.
22. Chaudhuri R.K.; Finley J.P.; Freed K.F.; J. Chem.Phys. **1997**, 106, 4067.
23. *Lecture Notes in Chemistry*; Freed K.F.; Kaldor U., Eds.; Springer-Verlag, Berlin, **1989**, Vol. 52, p. 1.
24. Brandow B.H.; Rev. Mod. Phys. **1967, 39**, 771.

Downloaded by COLUMBIA UNIV on September 14, 2012 | http://pubs.acs.org
Publication Date: August 14, 2002 | doi: 10.1021/bk-2002-0828.ch007

25. Lindgren I.; J. Phys. B **1974**, 7, 2441.
26. 26.Wilson S.; Jankowski K.; J. Paldus J.; Int. J. Quantum. Chem. **1983,** 23, 1781.
27. Wilson S.; Jankowski K.; Paldus J.; Int. J. Quantum. Chem. **1986**, 28, 525.
28. Wang X.C.; Freed K.F.; J. Chem. Phys. **1987**, 86, 2899.
29. Graham R.L.; Freed K.F.; J. Chem. Phys. **1992**, 96, 1304.
30. Finley J.P.; Freed K.F.; J. Chem. Phys. **1995**, 102, 1306.
31. Potts D.M.; C. M. Taylor C.M.; Chaudhuri R.K.;, Freed K.F.; J. Chem. Phys. **2001**, 114, 2592.
32. Chaudhuri R.K.; Freed K.F.; Abrash S.A.; Potts D.M.; J. Mol. Structure (Theochem) (in press).
33. Hunt, W.J.; Goddard, W.A. III; Chem. Phys. Lett. **1969**, 3, 414; Huzinaga S.; Arnau C.; Phys. Rev. **1970**, A1, 1285; J. Chem. Phys. **1971,** 54, 1948; McWiiliams D.; Huzinaga S.; J. Chem. Phys. **1971**, 55, 2604.
34. Maki A.G.; Toth R.A.; J. Mol. Spectrosc. **1965**, 17, 136.
35. Dunning Jr. T.H.; J. Chem. Phys. **1970**, 53, 2823; *Modern Theoretical Chemistry*; Dunning Jr. T.H.; Hay P. J.; Schafer H.F., Eds.; Plenum Press, New York **1976**, Vol 3.
36. Diamond J.; G. A. Segal G.A.; J. Chem. Soc. **1984**, 106, 952.
37. *The Chemistry of Ketens, Allenes and Related Compounds Part 1}*; Dykstra C.E.; Schafer H.F.; Patai S., Eds.; Wiley, Chichester, **1980**, p. 1.
38. Rauk A.; Drake A.F.; Mason S.; J. Am. Chem. Soc. **1979**, 101, 2284.
39. Parr A.C.; F. A. Alder F.A.; J. Chem. Phys. **1968**, 49, 2659.
40. Dunning Jr. T.H.; J. Chem. Phys. **1989**, 90, 1007.

Downloaded by COLUMBIA UNIV on September 14, 2012 | http://pubs.acs.org
Publication Date: August 14, 2002 | doi: 10.1021/bk-2002-0828.ch007

Downloaded by UNIV MASSACHUSETTS AMHERST on September 14, 2012 | http://pubs.acs.org
Publication Date: August 14, 2002 | doi: 10.1021/bk-2002-0828.ch008

Chapter 8

Hamiltonian Matrix Elements for the Table-CI Method Using Genealogical Configuration State Functions

Yuriy G. Khait[1,2] and Mark R. Hoffmann[1,*]

[1]Chemistry Department, University of North Dakota, Grand Forks, ND 58202
[2]Permanent address: 14 Dobrolyubova Avenue, Russian Scientific Center "Applied Chemistry", St. Petersburg 197198, Russia

All necessary formulas for Hamiltonian matrix elements in the table-CI method are presented in computationally amenable form. In contrast to the initial variant of the method, as developed by Buenker, the obtained formulas allow one to avoid intermediate calculations of separate determinantal matrix elements but instead allows calculation of the Hamiltonian matrix elements directly in the basis of configuration state functions (CSFs). The recently suggested variant of a genealogical scheme for constructing CSFs in the context of table-CI is used, which results in reducing the number of contributions to typical matrix elements by approximately a factor of 2.

The configuration interaction (CI) method and, especially, its multireference variants (MRCI) have proven themselves useful for the study of both ground and excited states potential energy surfaces. Most of the developed CI algorithms rely heavily on the existence of well-defined relationships among configurations

In Low-Lying Potential Energy Surfaces; Hoffmann, M., et al.;
ACS Symposium Series; American Chemical Society: Washington, DC, 2002.

Downloaded by UNIV MASSACHUSETTS AMHERST on September 14, 2012 | http://pubs.acs.org
Publication Date: August 14, 2002 | doi: 10.1021/bk-2002-0828.ch008

of spatial orbitals [see, e.g., Refs. (*1-4*) and the recent review by Sherrill and Schaefer (*5*)]. Here, we discuss the table-CI method, originally developed by Buenker and co-workers (*6-9*), which is very efficient for performing CI calculations even when the set of configurations is thoroughly random. Although the initial variant of the method was suggested for performing multireference singles and doubles CI calculations with configuration selection and energy extrapolation procedures (*10*), the technique of the table-CI method is considerably more general and can also be used in the framework of other approaches, including methods of quasidegenerate perturbation theory (*11*).

The table-CI method is a configuration-driven algorithm in which Hamiltonian matrix elements are calculated for pairs of interacting configurations in a basis of spin-adapted configuration state functions (CSFs) and avoiding explicit comparisons of Slater determinants through the use of special compact tables. Although the efficiency of the method has been confirmed by concrete calculations and its basic ideas were described by Buenker (*6*), explicit formulas of the method have not been reported. In the present work, we present such formulas for all possible classes of interacting configurations. Furthermore, in contrast to the original variant of the table-CI method, the obtained formulas allow one to avoid intermediate calculations of separate determinantal matrix elements and instead to calculate the Hamiltonian matrix elements directly in the basis of configuration state functions (CSFs) using molecular integrals. In addition, due to the use of a genealogical scheme for constructing CSFs [see, e.g. Ref. (*12*)] that was developed recently in the context of table-CI (*13*), the number of contributions to a given matrix element is reduced by approximately a factor of 2.

The remainder of the paper is organized into three sections. The use of genealogical CSFs in the table-CI method is described briefly in the subsequent section while the basic formulas for Hamiltonian matrix elements over genealogical CSFs are discussed in Section III. A final section presents concluding remarks.

Use of Genealogical CSFs in the Table-CI Method

The table-CI method makes use of the well-known fact that the same expansion coefficients of CSFs over determinants can be employed for all configurations with a given number of open shells if an isomorphic relationship between determinants of such configurations is established. To effectively use this fact, an arbitrary N-electron configuration $\Phi(k)$ with k open and $q=(N-k)/2$ closed shells is written in the form

$$\Phi(k) = i_1^2 i_2^2 \ldots i_q^2 j_1 j_2 \ldots j_k, \qquad (1)$$

involving subsets of ordered indices of doubly ($i_1<i_2<\ldots<i_q$) and singly ($j_1<j_2<\ldots<j_k$) occupied orbitals. Then each determinant $D_t(\Phi(k))$ with a given total spin projection S_z, created by $\Phi(k)$, will be represented in second quantized form as

$$D_t = \hat{A}^+_{i_1}\hat{A}^+_{i_2}\ldots\hat{A}^+_{i_q}\hat{a}^+_{j_1 p_1^t}\hat{a}^+_{j_2 p_2^t}\ldots\hat{a}^+_{j_k p_k^t} \tag{2}$$

where $\hat{A}^+_i = \hat{a}^+_{i\alpha}\hat{a}^+_{i\beta}$ and a set $P_t = (p_1^t, p_2^t, \ldots, p_k^t)$ of integers p_j^t specifies an assignment of α ($p_j^t = 1$) and β ($p_j^t = -1$) spins to open-shell orbitals in such a way that $p_1^t + p_2^t + \ldots + p_k^t = 2S_z$. Eq. (2) permits one to set up the desired isomorphism between determinants created by different configurations, with the same number of open shells, but specified by the same spin assignment set P_t. As a result, each CSF $F_I(\Phi(k))$ with fixed spin quantum numbers S and S_z can be expanded over the determinants $D_t(\Phi(k))$ with the same S_z,

$$F_I = \sum_{t=1}^{d(k,S_Z)} C_{tI}^{(k)} D_t, \qquad I \in [1, g(k,S)], \tag{3}$$

where the coefficients $\{C_{tI}^{(k)}\}$ do not depend on the specific configuration but only on the triple index (k,S,S_z). The number of CSFs and determinants with fixed S and S_z equal

$$g(k,S) = \frac{(2S+1)}{\left(\frac{1}{2}k+S+1\right)}\binom{k}{\frac{1}{2}k+S}, \qquad d(k,S_z) = \binom{k}{\frac{1}{2}k+S_z}. \tag{4}$$

In the case of the spin-free Hamiltonian, when it suffices to use CSFs with the maximal spin projection $S=S_z$, the genealogical scheme has been recently shown (*13*) to lead to a matrix $C^{(k)} = \left\| C_{tI}^{(k)} \right\|$ with quite simple structure, if determinants $\{D_t(\Phi(k))\}$ with a fixed S_z [and, hence, spin assignments sets $\{P_t\}$ (so-called branching *trajectories*)] are ordered in a so-called lexical ordering. Since all such determinants contain the same number $k(\alpha)=k/2+S_z$ of α spins, each determinant D_t (and, hence, trajectory P_t) is uniquely specified by a vector $\boldsymbol{m}_t = (m_1^t, m_2^t, \ldots, m_{k(\alpha)}^t)$ of positions $(1 \le m_1^t < m_2^t < m_{k(\alpha)}^t \le k)$ of only α spins (e.g., if $P_t=(1,-1,1)$ then $m_t=(1,3)$). Trajectories are considered to be lexically ordered and trajectory P_t precedes $P_{\tilde{t}}$ if the first nonvanishing component in the vector $\boldsymbol{m}_{\tilde{t}} - \boldsymbol{m}_t$ is positive (e.g., if $k=3$ and $S_z=1/2$, then $d(k,S_z)=3$ and $P_1=(1,1,-1)$, $P_2=(1,-1,1)$, $P_3=(-1,1,1)$). In this case, the sequential index of an arbitrary

Downloaded by UNIV MASSACHUSETTS AMHERST on September 14, 2012 | http://pubs.acs.org
Publication Date: August 14, 2002 | doi: 10.1021/bk-2002-0828.ch008

determinant D_t, which is specified by a given vector m_t, in the set of lexically ordered determinants $\{ D_t(\Phi(k)) \}$ is equal to (*14*)

$$\binom{k}{k(\alpha)} - \sum_{j=1}^{k(\alpha)} \binom{k - m_j^t}{k(\alpha) - j + 1}. \tag{5}$$

We will refer to the subset of determinants $\{D_M\}_{M=1}^{g(k,S)}$ whose trajectories lie in the first quadrant in (k,S_z) coordinate space as *main* determinants. It has been shown that CSFs have a nonzero projection on the main determinants and, in the case of using the genealogical CSFs, the $\left\| C_{MI}^{(k)} \right\|$ block of the $C^{(k)}$ matrix turns out to be lower triangular (*13*). Such structure of the $C^{(k)}$ matrix is compatible with the idea of a double representation of CSFs, which is actively used in the table-CI method. Indeed, in addition to expansion (3), each CSF can also be written as a linear combination of only the projected main determinants

$$F_I = \sum_{M=1}^{I} W_{MI}^{(k)} \hat{P} D_M, \qquad I \in [1, g(k,S)], \tag{6}$$

where $\hat{P}$ is a projector on desired spin states. The matrix $\left\| W_{MI}^{(k)} \right\|$ is upper triangular and can easily be determined recursively using

$$\sum_{M=J}^{I} W_{MI}^{(k)} C_{MJ}^{(k)} = \delta_{IJ}, \qquad 1 \le I \le J \le g(k,S). \tag{7}$$

As a result, using representation (3) for a CSF, $F_J^{(2)}$, of a "right" configuration $\Phi_2=\Phi(k_2)$, and representation (6) for a CSF, $F_I^{(1)}$, of a "left" configuration $\Phi_1=\Phi(k_1)$ with $k_1 \ge k_2$, one gets

$$\left\langle F_I^{(1)} \middle| \hat{H} \middle| F_J^{(2)} \right\rangle = \sum_{M=1}^{I} W_{MI}^{(k_1)} \sum_{t=1}^{d(k_2,S)} C_{tJ}^{(k_2)} \left\langle D_M^{(1)} \middle| \hat{H} \middle| D_t^{(2)} \right\rangle,$$
$$I \in [1, g(k_1,S)],\ J \in [1, g(k_2,S)]. \tag{8}$$

Note that the first sum involves only the main determinants $D_M^{(1)} \in \Phi_1$ with $M \le I$, while the second sum involves formally all determinants $D_t^{(2)} \in \Phi_2$. The table-CI method allows one to specify the few determinants $\{D_{t_M}^{(2)}\} \in \Phi_2$ that have nonzero interactions with a given $D_M^{(1)}$, and thereby to effectively calculate sums

Downloaded by UNIV MASSACHUSETTS AMHERST on September 14, 2012 | http://pubs.acs.org
Publication Date: August 14, 2002 | doi: 10.1021/bk-2002-0828.ch008

Downloaded by UNIV MASSACHUSETTS AMHERST on September 14, 2012 | http://pubs.acs.org
Publication Date: August 14, 2002 | doi: 10.1021/bk-2002-0828.ch008

$\sum_{\{t_M\}} C^{(k_2)}_{t_M J} \left\langle D^{(1)}_M \middle| \hat{H} \middle| D^{(2)}_{t_M} \right\rangle$ using molecular integrals. Taking this fact into account, the following algorithm can be used for constructing Hamiltonian matrix elements $H_{IJ} = \left\langle F^{(1)}_I \middle| \hat{H} \middle| F^{(2)}_J \right\rangle$ simultaneously over all CSFs created by two configurations, without any preliminary construction of separate determinantal matrix elements:

```
1. Initialize: $\{H_{IJ} = 0\}_{I=1,J=1}^{g_1,g_2}$, $g_1=g(k_1,S)$, $g_2=g(k_2,S)$
2. Loop over main determinants: $D^{(1)}_M \in \Phi_1$, $M \in [1,g_1]$
     Construct array $\left\{ G_M[J] = \sum_{\{t_M\}} C^{(k_2)}_{t_M J} \left\langle D^{(1)}_M \middle| \hat{H} \middle| D^{(2)}_{t_M} \right\rangle \right\}_{J\in[1,g_2]}$
3.   Loop over left CSFs: $F^{(1)}_I \in \Phi_1$, $I \in [M,g_1]$
4.       Loop over right CSFs: $F^{(2)}_J \in \Phi_2$ ($J \in [1,g_2]$)
             $H_{IJ} = H_{IJ} + W^{(k_1)}_{MI} * G_M[J]$
```

Note that the algorithm: 1) permits one to determine contributions of molecular integrals simultaneously to all matrix elements over CSFs created by the configuration pair, and 2) requires, due to using genealogical CSFs, only about $g_I(g_1+1)g_2/2$ operations. Traditional schemes of generating CSFs (including, e.g., diagonalization of $\hat{S}^2$, which has been used in the conventional table-CI method) would require about two times as many operations ($\approx g_1 g_1 g_2$).

Analysis of Relationships Between Pairs of Configurations

Due to the Hermitian nature of the Hamiltonian operator, it suffices to consider only pairs of configurations with $\Delta K = \frac{1}{2}(k_1 - k_2) \geq 0$. It is clear that configurations with $\Delta K>2$ cannot interact. Buenker showed (*6*) that there are only nine non-trivial relationships between random pairs of configurations [one with $\Delta K=2$, three with $\Delta K=1$ ($P \in [1,3]$), and five with $\Delta K=0$ ($P \in [1,5]$)]. All cases are shown in Table I. Given ΔK, a parameter P labels types of molecular integrals required for calculation of interaction between configurations. Each case is determined by a diagram specifying the occupation numbers of the shells distinguishing a "left" configuration Φ_1 (at the top of the diagram) and a "right" configuration Φ_2 (on the bottom).

Following Buenker (*6*), we begin the analysis by consideration of the simplest ($\Delta K=0$, $P=4$) case, with diagram $\begin{pmatrix}\Phi_1\\ \Phi_2\end{pmatrix} = \begin{pmatrix}20\\ 02\end{pmatrix} = a^2/b^2$ ($a<b$), that describes

Table I. Possible non-vanishing relationships between random pairs of configurations

ΔK	*P*	*Main diagrams*	*No. of* R *subcases*	*Level of excitations*	*Required integrals*
2	1	$\begin{pmatrix}1111\\2200\end{pmatrix}=abcd/a^2b^2$	6	doubles	$(ac\vert bd), (ad\vert bc)$
1	1	$\begin{pmatrix}1112\\2201\end{pmatrix}=abcd^2/a^2b^2d$	3	doubles	$(ac\vert bd), (ad\vert bc)$
		$\begin{pmatrix}1110\\0021\end{pmatrix}=abc/c^2d$	3		
1	2	$\begin{pmatrix}211\\022\end{pmatrix}=a^2bc/b^2c^2$	1	doubles	$(ab\vert ac)$
		$\begin{pmatrix}011\\200\end{pmatrix}=bc/a^2$	1		
1	3	$\begin{pmatrix}11\\20\end{pmatrix}=ab/a^2$	1	singles and doubles	$h_{ab}, (ab\vert cc), (ac\vert bc)$
		$\begin{pmatrix}11\\02\end{pmatrix}=ab/b^2$	1		
0	1	$\begin{pmatrix}1100\\0011\end{pmatrix}=ab/cd$	1	doubles	$(ac\vert bd), (ad\vert bc)$
		$\begin{pmatrix}1102\\0211\end{pmatrix}=abd^2/b^2cd$	4		$(ab\vert dc), (ac\vert bd)$
		$\begin{pmatrix}1122\\2211\end{pmatrix}=abc^2d^2/a^2b^2cd$	1		$(ac\vert bd), (ad\vert bc)$
0	2	$\begin{pmatrix}210\\021\end{pmatrix}=a^2b/b^2c$	1	doubles	$(ab\vert ac)$
		$\begin{pmatrix}012\\201\end{pmatrix}=bc^2/a^2c$	1		
0	3	$\begin{pmatrix}10\\01\end{pmatrix}=a/b$	1	singles and doubles	$h_{ab}, (ab\vert cc), (ac\vert bc)$
		$\begin{pmatrix}12\\21\end{pmatrix}=ab^2/a^2b$	1		
0	4	$\begin{pmatrix}02\\20\end{pmatrix}=a^2/b^2$	1	doubles	K_{ab}
0	5	diagonal case	1	singles and doubles	h_{aa}, J_{ab}, K_{ab}

Downloaded by UNIV MASSACHUSETTS AMHERST on September 14, 2012 | http://pubs.acs.org
Publication Date: August 14, 2002 | doi: 10.1021/bk-2002-0828.ch008

configurations with the same set of open shells but differing in one of their closed shells ($a^2 \in \Phi_1$, $b^2 \in \Phi_2$). Since, determinants of the configurations are already connected through the double excitation $a_\alpha a_\beta \Rightarrow b_\alpha b_\beta$, a given main "left" determinant $D_M^{(1)} \in \Phi_1$ can interact with only one determinant $D_t^{(2)} \in \Phi_2$ in which the spin assignment for all singly occupied orbitals is the same as that in $D_M^{(1)}$. Hence, both these determinants are specified by the same branching trajectory and their sequential indices coincide. For all such determinants, the matrix element $\langle D_M^{(1)} | \hat{H} | D_M^{(2)} \rangle$ is always equal to the exchange integral K_{ab}. Using Eqs. (7) and (8), one can state that the block of the Hamiltonian matrix over CSFs created by the configurations under consideration is diagonal,

$$\langle F_I^{(1)} | \hat{H} | F_J^{(2)} \rangle = \delta_{IJ} K_{ab}, \quad I, J \in [1, g(k,S)]. \tag{9}$$

Analysis of the ΔK=2 Case (k_1=k_2+4)

Although the ΔK=2 case is also sufficiently simple, it permits one to demonstrate Buenker's technique to avoid explicit comparisons of determinants through the use of special tables. As seen from Table I, the ΔK=2 case is described by only one diagram $\begin{pmatrix} \Phi_1 \\ \Phi_2 \end{pmatrix} = \begin{pmatrix} 1111 \\ 2200 \end{pmatrix} = abcd/a^2b^2$; the four ordered open shells a, b, c, and d in Φ_1 ($a<b<c<d$) are balanced by two closed a^2 and b^2 shells in Φ_2, while all the remaining singly and doubly occupied orbitals are the same in both configurations. Since determinants $D_M^{(1)}$ and $D_t^{(2)}$ are already connected through a double excitation, they can interact only if their spin assignments for common open shells are identical. Since the total spin projection of four electrons, described in $D_M^{(1)}$ by the a, b, c, and d orbitals, must be zero, the first sum in Eq. (8) can involve only main determinants $D_M^{(1)}$ whose trajectories include two α and two β spins for these four orbitals. All possible six spin assignments ($\alpha\alpha\beta\beta$, $\alpha\beta\alpha\beta$, etc.) for the a, b, c, d orbitals in $D_M^{(1)}$ are labeled in Table II with a parameter $Z_M \in [1,6]$. Each determinant $D_M^{(1)}$ of such type, with trajectory P_M, can interact with only one determinant $D_{t_M}^{(2)}$, whose trajectory P_{t_M} is obtained from P_M by removing four spins at the positions (n_a,n_b,n_c,n_d) of the a, b, c, and d orbitals among all k_1 open shells in Φ_1 ($1 \le n_a < n_b < n_c < n_d \le k_1$).

To simplify calculation of the matrix element $\langle D_M^{(1)} | \hat{H} | D_{t_M}^{(2)} \rangle$, it is convenient to transfer the orbitals distinguishing the configurations to the first positions in the determinants. The permutation of the a^2 and b^2 closed shells to

Downloaded by UNIV MASSACHUSETTS AMHERST on September 14, 2012 | http://pubs.acs.org
Publication Date: August 14, 2002 | doi: 10.1021/bk-2002-0828.ch008

Table II. Electron repulsion integrals (I_1,I_2) and linear coefficients (f_1,f_2) for the ΔK=2 case

R-subcases	*Basis Integrals* (I_1,I_2)	$Z_M=1$ $\alpha\alpha\beta\beta$	$Z_M=2$ $\alpha\beta\alpha\beta$	$Z_M=3$ $\alpha\beta\beta\alpha$	$Z_M=4$ $\beta\alpha\alpha\beta$	$Z_M=5$ $\beta\alpha\beta\alpha$	$Z_M=6$ $\beta\beta\alpha\alpha$
1 $\begin{pmatrix}1111\\2200\end{pmatrix}$	$(ac\|bd)$, $(ad\|bc)$	(-1,1)	(0,-1)	(1,0)	(1,0)	(0,-1)	(-1,1)
2 $\begin{pmatrix}1111\\2020\end{pmatrix}$	$(ab\|cd)$, $(ad\|cb)$	(0,1)	(1,-1)	(-1,0)	(-1,0)	(1,-1)	(0,1)
3 $\begin{pmatrix}1111\\2002\end{pmatrix}$	$(ab\|dc)$, $(ac\|db)$	(0,-1)	(1,0)	(-1,1)	(-1,1)	(1,0)	(0,-1)
4 $\begin{pmatrix}1111\\0220\end{pmatrix}$	$(ab\|dc)$, $(ac\|db)$	(0,-1)	(1,0)	(-1,1)	(-1,1)	(1,0)	(0,-1)
5 $\begin{pmatrix}1111\\0202\end{pmatrix}$	$(ab\|cd)$, $(ad\|cb)$	(0,1)	(1,-1)	(-1,0)	(-1,0)	(1,-1)	(0,1)
6 $\begin{pmatrix}1111\\0022\end{pmatrix}$	$(ac\|bd)$, $(ad\|bc)$	(-1,1)	(0,-1)	(1,0)	(1,0)	(0,-1)	(-1,1)

NOTE: Since for any pair (R,Z_M) $f_i(7-R,Z_M)=f_i(R,7-Z_M)=f_i(R,Z_M)$ (i=1,2), it suffices to store only coefficients $f_i(R,Z_M)$ for pairs (R,Z_M) with R,Z_M =1,2,3.

their first two places within $D_{t_M}^{(2)}$ leads to the so-called paradigmatic determinant $\tilde{D}_{t_M}^{(2)}$ with the same sign as $D_{t_M}^{(2)}$. But the permutation $Q^{(1)}$ of the a, b, c, and d orbitals within $D_M^{(1)}$ leads to the paradigmatic determinant $\tilde{D}_M^{(1)} = w(Q^{(1)})D_M^{(1)}$, where

$$w(Q^{(1)})=(-1)^{n_a+n_b+n_c+n_d} \tag{10}$$

is the parity of the permutation $Q^{(1)}$. The Hamiltonian matrix element between the paradigmatic determinants may easily be determined for any Z_M using Slater's rules (*15*). E.g., in the Z_M=1 case, when a spin assignment for the four orbitals *abcd* in $D_M^{(1)}$ is $\alpha\alpha\beta\beta$, one has $\tilde{D}_M^{(1)} = \left|a_\alpha b_\alpha c_\beta d_\beta \ldots\right|$, $\tilde{D}_{t_M}^{(2)} = \left|a_\alpha a_\beta b_\alpha b_\beta \ldots\right|$, and

$$\left\langle \tilde{D}_M^{(1)} \middle| H \middle| \tilde{D}_{t_M}^{(2)} \right\rangle = -(ac\,|\,bd) + (ad\,|\,bc), \tag{11}$$

Downloaded by UNIV MASSACHUSETTS AMHERST on September 14, 2012 | http://pubs.acs.org
Publication Date: August 14, 2002 | doi: 10.1021/bk-2002-0828.ch008

where the bracketed quantities denote electron repulsion integrals in chemists' notation

$$(ac\,|\,bd) = \left\langle a(1)\,b(2)\left|\frac{1}{r_{12}}\right|c(1)\,d(2)\right\rangle \cdot \tag{12}$$

In the above-mentioned diagram, the a and b orbitals were selected as doubly occupied in Φ_2. One could also select other pairs (a^2c^2, b^2d^2 etc.) as closed shells in Φ_2. All such possibilities are labeled in Table II with a parameter $R \in [1,6]$, and, for each R, the same six spin assignments $Z_M \in [1,6]$ for the orbitals $abcd$ in $D_M^{(1)}$ are possible. For an arbitrary pair (R,Z_M) one has

$$\left\langle D_M^{(1)}\left|H\right|D_{t_M}^{(2)}\right\rangle = w(Q^{(1)})\left[f_1(R,Z_M)I_1(R) + f_2(R,Z_M)I_2(R)\right] \cdot \tag{13}$$

The electron repulsion integrals $I_1(R)$ and $I_2(R)$ for different R, and specific values of the linear coefficients $f_1(R,Z_M)$ and $f_2(R,Z_M)$, for all 36 possible pairs (R,Z_M) are given in Table II. Since for each $D_M^{(1)}$ there is only one interacting determinant $D_{t_M}^{(2)}$, using Eqs. (8) and (13) one finally gets the desired equation for the Hamiltonian matrix elements over CSFs created by the configurations under consideration,

$$\left\langle F_I^{(1)}\left|H\right|F_J^{(2)}\right\rangle = w(Q^{(1)})\sum_{M=1}^{l} W_{MI}^{(k_1)} C_{t_M,J}^{(k_2)}\left[f_1(R,Z_M)I_1(R) + f_2(R,Z_M)I_2(R)\right] \cdot \tag{14}$$

The concrete numbers of the a, b, c, and d orbitals are only required for determining integrals $I_l(R)$ and $I_2(R)$ and they can easily be obtained as a result of comparison of orbital occupation numbers of the configurations. The task of determination of the Z_M and t_M values for each $D_M^{(1)}$ is more complex and could require an analysis at the determinantal level. Taking into account, however, that both the Z_M and t_M values and $w(Q^{(1)})$ do not depend on concrete a, b, c, and d orbitals but only on their (n_a,n_b,n_c,n_d) positions among k_1 open shells in Φ_1, Buenker suggested to tabulate pairs (Z_M, t_M) for all $D_M^{(1)}$ (created by configurations with the required numbers k_1 of open shells) and for all possible permutations $Q^{(1)}$=(n_a,n_b,n_c,n_d) in advance. Given k_1, such a table (which we refer to as a *Z-table*) consists of $\binom{k_1}{4}$ subtables, each of which is associated with a concrete permutation $Q^{(1)}$, and each subtable consists of $2g_1$+1 entries, $g_1 = g(k_1,S)$, involving $w(Q^{(1)})$ and g_1 pairs (Z_M,t_M) (one pair for each main determinant $D_M^{(1)}$). Thus, in the (k_1,ΔK=2) case, the total dimension of the Z-table is $\binom{k_1}{4}(2g_1+1)\cdot$

Downloaded by UNIV MASSACHUSETTS AMHERST on September 14, 2012 | http://pubs.acs.org
Publication Date: August 14, 2002 | doi: 10.1021/bk-2002-0828.ch008

Downloaded by UNIV MASSACHUSETTS AMHERST on September 14, 2012 | http://pubs.acs.org
Publication Date: August 14, 2002 | doi: 10.1021/bk-2002-0828.ch008

Effective implementation of the table-CI technique requires that the set of configurations be ordered such that species with the same number of open shells follow each other *contiguously*. The value of ΔK for each configuration pair is then known *before* the occupation numbers of two specific configurations are compared, and the loop structure of a program is organized in such a way that no pairs with $\Delta K>2$ appear. Moreover, given a pair (k_1,k_2) of numbers of open shells $(k_1 \geq k_2)$, the same genealogical $W^{(k_1)}$ and $C^{(k_2)}$ matrices and the same common Z-table(s) can be used for all configuration pairs belong to the class (k_1,k_2). Comparison of orbital occupancies of a specific configuration pair (Φ_1,Φ_2) permits one to determine whether the configurations can interact or not. If configurations can interact, on the basis of the foregoing comparison, the values of R, the molecular integrals $I_1(R)$ and $I_2(R)$, and the permutation $Q^{(1)}$ are specified and, hence, the beginning address of the required subtable within the Z-table can be determined. By combining values of Z_M and t_M from the subtable with the value of R, the desired block of Hamiltonian matrix elements over CSFs can be calculated using Eq. (14) and the algorithm described in Section II. It is clear that such an approach is most effective if all required integrals are available in core storage. Otherwise, the less efficient three-step algorithm originally developed by Buenker (*6*) must be used.

Analysis of ΔK=1 (k₁=k₂+2) Cases

ΔK=1, P=1

The $(\Delta K=1, P=1)$ case is described by two main diagrams: $\begin{pmatrix}1112\\2201\end{pmatrix}=abcd^2/a^2b^2d$ and $\begin{pmatrix}1110\\0021\end{pmatrix}=abc/c^2d$ $(a<b<c)$. In both cases, configurations are connected through double excitations. In the first diagram, c is empty in Φ_2 but there are two additional possibilities depending whether a or b is empty. There are also three variants of the second diagram, depending on whether the orbital doubly occupied in Φ_2 is a, b or c. In all six diagrams, labeled in Table III with a parameter $R\in[1,6]$, the total spin of the a, b, c orbitals in a main determinant $D_M^{(1)}\in\Phi_1$ must be balanced by the spin of the d orbital in $D_{t_M}^{(2)}\in\Phi_2$. As a result, only six spin assignments $Z_M\in[1,6]$ ($\alpha\alpha\beta/\alpha, \alpha\beta\alpha/\alpha$, etc.) for the four open-shells (*abc/d*) are possible but, again, there is only one determinant $D_{t_M}^{(2)}$ that can have nonzero interaction with a specific $D_M^{(1)}$. Electron repulsion

Table III. Electron repulsion integrals (I_1,I_2) and linear coefficients (f_1,f_2) for the (ΔK=1,P=1) case

R-subcases	*Basis Integrals* (I_1,I_2)	Z_M=1 $\alpha\alpha\beta/\alpha$	Z_M=2 $\alpha\beta\alpha/\alpha$	Z_M=3 $\beta\alpha\alpha/\alpha$	Z_M=4 $\alpha\beta\beta/\beta$	Z_M=5 $\beta\alpha\beta/\beta$	Z_M=6 $\beta\beta\alpha/\beta$
1 $\begin{pmatrix}1112\\2201\end{pmatrix}$	*(ac|bd)*, *(ad|bc)*	(1,-1)	(0,1)	(-1,0)	(1,0)	(0,-1)	(-1,1)
2 $\begin{pmatrix}1112\\2021\end{pmatrix}$	*(ab|cd)*, *(ad|cb)*	(0,-1)	(-1,1)	(1,0)	(-1,0)	(1,-1)	(0,1)
3 $\begin{pmatrix}1112\\0221\end{pmatrix}$	*(ab|dc)*, *(ac|db)*	(0,1)	(-1,0)	(1,-1)	(-1,1)	(1,0)	(0,-1)
4 $\begin{pmatrix}1110\\2001\end{pmatrix}$	*(ab|dc)*, *(ac|db)*	(0,-1)	(1,0)	(-1,1)	(1,-1)	(-1,0)	(0,1)
5 $\begin{pmatrix}1110\\0201\end{pmatrix}$	*(ab|cd)*, *(ad|cb)*	(0,1)	(1,-1)	(-1,0)	(1,0)	(-1,1)	(0,-1)
6 $\begin{pmatrix}1110\\0021\end{pmatrix}$	*(ac|bd)*, *(ad|bc)*	(-1,1)	(0,-1)	(1,0)	(-1,0)	(0,1)	(1,-1)

NOTE: Since for any pair (R,Z_M) $f_i(7-R,Z_M)=f_i(R,7-Z_M)=-f_i(R,Z_M)$ (i=1,2), it suffices to store only coefficients $f_i(R,Z_M)$ for pairs (R,Z_M) with R,Z_M =1,2,3.

integrals and linear coefficients for all 36 pairs (R,Z_M) that are possible in the (ΔK=1,P=1) case are also given in Table III (N.B. A slightly different enumeration of R-subcases and Z_M-spin assignments than that used by Buenker in Ref. (*7*) is used). As was the case for Table II, Table III was obtained for paradigmatic determinants in which the shells distinguishing the configurations are placed in the lowest positions. Let $Q^{(1)}$ and $Q^{(2)}$ label permutations of the open shells (a, b, and c in Φ_1 and d in Φ_2) among all such species in each configuration. $Q^{(1)}$ is specified by a set $\left(n_a^{(1)}, n_b^{(1)}, n_c^{(1)}\right)$ of the positions of the a, b, c orbitals in Φ_1, while $Q^{(2)}$ is determined by the position $n_d^{(2)}$ of the d orbital among all open shells in Φ_2. Using the same technique as before, one obtains

$$\left\langle F_I^{(1)} \middle| H \middle| F_J^{(2)} \right\rangle = w(Q^{(1)}) w(Q^{(2)}) \sum_{M=1}^{I} W_{MI}^{(k_1)} C_{t_M,J}^{(k_2)} \left[f_1(R,Z_M) I_1(R) + f_2(R,Z_M) I_2(R) \right], \tag{15}$$

where

$$w(Q^{(1)}) = (-1)^{n_a^{(1)}+n_b^{(1)}+n_c^{(1)}}, \qquad w(Q^{(2)}) = (-1)^{n_d^{(2)}+1}, \tag{16}$$

Downloaded by UNIV MASSACHUSETTS AMHERST on September 14, 2012 | http://pubs.acs.org
Publication Date: August 14, 2002 | doi: 10.1021/bk-2002-0828.ch008

and t_M is the number of the determinant $D_{t_M}^{(2)}$ whose trajectory P_{t_M} is obtained from the trajectory P_M of $D_M^{(1)}$ by removing three spins at positions $\left(n_a^{(1)}, n_b^{(1)}, n_c^{(1)}\right)$ and adding the spin determined by Z_M for the d orbital at position $n_d^{(2)}$.

In the (k_1,ΔK=1,P=1) case, the Z-table consists of $\begin{pmatrix}k_1\\3\end{pmatrix}(k_1\text{-}2)$ subtables, associated with permutation pairs ($Q^{(1)}$,$Q^{(2)}$). Each subtable consists of $2g_1+1$ entries and has the same structure as in the ΔK=2 case.

ΔK=1, P=2

In the case under consideration, only two diagrams are possible: $\begin{pmatrix}211\\022\end{pmatrix}$=$a^2bc/b^2c^2$ (R=1) and $\begin{pmatrix}011\\200\end{pmatrix}$=$bc/a^2$ (R=2), where $b<c$. Since configurations are connected through double excitations, their determinants can interact only if the total spin for the b and c orbitals in $D_M^{(1)}$ is zero, and, hence, only two possible spin assignments, $\alpha\beta$ (Z_M=1) and $\beta\alpha$ (Z_M=2), for these two orbitals in $D_M^{(1)}$ are possible. A simple analysis shows that both diagrams have only one electron repulsion integral $(ab|ac)$ associated and that the linear coefficient $f(R,Z_M)$ for any pair (R,Z_M) equals $(-1)^{R+Z_M+1}$. As a result, by analogy with Eq. (14), one gets

$$\left\langle F_I^{(1)}\middle|H\middle|F_J^{(2)}\right\rangle = (-1)^{R+Z_M+1}\, w(Q^{(1)})\,(ab\,|\,ac)\sum_{M=1}^{I} W_{MI}^{(k_1)} C_{t_M,J}^{(k_2)}\,, \qquad (17)$$

where the permutation $Q^{(1)}$ is determined by the positions $\left(n_b^{(1)}, n_c^{(1)}\right)$ of the open shells b and c among all such species in Φ_1,

$$w(Q^{(1)}) = (-1)^{n_b^{(1)}+n_c^{(1)}+1}\,, \qquad (18)$$

and the trajectory P_{t_m} is obtained from P_M by removing two spins at positions $\left(n_b^{(1)}, n_c^{(1)}\right)$.

In the (k_1,ΔK=1,P=2) case, the Z-table consists of $\begin{pmatrix}k_1\\2\end{pmatrix}$ subtables associated

Downloaded by UNIV MASSACHUSETTS AMHERST on September 14, 2012 | http://pubs.acs.org
Publication Date: August 14, 2002 | doi: 10.1021/bk-2002-0828.ch008

with permutations $Q^{(1)}$, and the structure of each subtable, consisting of $2g_1+1$ entries, is again the same as that in the $\Delta K=2$ case.

$\Delta K=1$, $P=3$

The ($\Delta K=1,P=3$) case is described by two diagrams: $\begin{pmatrix}11\\20\end{pmatrix}=ab/a^2$ ($R=1$) and $\begin{pmatrix}11\\02\end{pmatrix}=ab/b^2$ ($R=2$), where $a<b$. Although, formally, the configurations are connected through one-electron excitations, their determinants can also be connected through double excitations.

If a spin assignment for the a and b orbitals in $D_M^{(1)}$ is $\alpha\beta$ ($Z_M=1$) or $\beta\alpha$ ($Z_M=2$), then their total zero spin is balanced in $D_{t_M}^{(2)}$ by the closed shell a^2 (if $R=1$) or b^2 (if $R=2$). Such determinants will be connected through a single excitation, and the trajectory P_{t_m}, specifying $D_{t_M}^{(2)}$, can be obtained from P_M by removing two spins at the $\left(n_a^{(1)},n_b^{(1)}\right)$ positions of the a and b orbitals among all k_1 open shells in Φ_1.

If a spin assignment for the two orbitals in $D_M^{(1)}$ is $\alpha\alpha$ or $\beta\beta$ and the configurations have a common set of open shells $\{c\}$, then $D_M^{(1)}$ can interact with several determinants $D_{t_M}^{(2)}\in\Phi_2$ through two electron excitations, $abc\Rightarrow a^2c$ (if $R=1$) or $abc\Rightarrow b^2c$ (if $R=2$), in the course of which one c orbital changes its spin. Given a pair ($D_M^{(1)}$,c), only two spin assignments, $\alpha\alpha\beta/\alpha$ ($Z_M=3$) or $\beta\beta\alpha/\beta$ ($Z_M=4$), for the three orbitals abc/c in the pair $D_M^{(1)}/D_{t_M}^{(2)}$ are allowed, and the trajectory P_{t_m} specifying $D_{t_M}^{(2)}$ is obtained from P_M by removing two spins at positions $\left(n_a^{(1)},n_b^{(1)}\right)$ and inverting the spin of the c orbital.

Using the same technique as before, in the $R=1$ case, one gets

$$\left\langle F_I^{(1)}\middle|H\middle|F_J^{(2)}\right\rangle = w(Q^{(1)})\left\{\sum_{\substack{M=1\\(Z_M\in[1,2])}}^{I}(-1)^{Z_M-1}W_{MI}^{(k_1)}C_{t_MJ}^{(k_2)}\left[\tilde{h}_{ab}+(ab\,|\,aa)-S_{ab}^{(M)}(\bar{Z}_M)\right]\right.$$

$$\left.+\sum_{\substack{M=1\\(Z_M\in[3,4])}}^{I}(-1)^{Z_M}W_{MI}^{(k_1)}\sum_{c_\gamma\in D_M^{(1)}}C_{t_M(c_\gamma\to c_{\bar{\gamma}})J}^{(k_2)}(ac\,|\,cb)\right\}, \tag{19}$$

while, in the $R=2$ case, one has

Downloaded by UNIV MASSACHUSETTS AMHERST on September 14, 2012 | http://pubs.acs.org
Publication Date: August 14, 2002 | doi: 10.1021/bk-2002-0828.ch008

Downloaded by UNIV MASSACHUSETTS AMHERST on September 14, 2012 | http://pubs.acs.org
Publication Date: August 14, 2002 | doi: 10.1021/bk-2002-0828.ch008

$$\left\langle F_I^{(1)} \middle| H \middle| F_J^{(2)} \right\rangle = w(Q^{(1)}) \left\{ \sum_{\substack{M=1 \\ (Z_M \in [1,2])}}^{I} (-1)^{Z_M - 1} W_{MI}^{(k_1)} C_{t_M J}^{(k_2)} \left[\tilde{h}_{ab} + (ab \mid bb) - S_{ab}^{(M)}(Z_M) \right] \right.$$

$$\left. - \sum_{\substack{M=1 \\ (Z_M \in [3,4])}}^{I} (-1)^{Z_M} W_{MI}^{(k_1)} \sum_{c_\gamma \in D_M^{(1)}} C_{t_M (c_\gamma \to c_{\bar{\gamma}}) J}^{(k_2)} (ac \mid cb) \right\} \cdot \tag{20}$$

Here, the permutation $Q^{(1)}$ is specified by the set $\left(n_a^{(1)}, n_b^{(1)}\right)$, $\bar{Z}_M$ equals 1 (if Z_M=2) or 2 (if Z_M=1), and

$$w(Q^{(1)}) = (-1)^{n_a^{(1)} + n_b^{(1)} + 1}, \tag{21}$$

$$\tilde{h}_{ab} = \left\{ h_{ab} + \sum_{\substack{com.closed \\ shells(i)}} \left[2(ab \mid ii) - (ai \mid bi) \right] + \sum_{\substack{com.open \\ shells(c)}} (ab \mid cc) \right\}, \tag{22}$$

$$S_{ab}^{(M)}(1) = \sum_{c_\alpha \in D_M^{(1)}} (ac \mid bc), \tag{23}$$

$$S_{ab}^{(M)}(2) = \sum_{c_\beta \in D_M^{(1)}} (ac \mid bc) \cdot \tag{24}$$

The first term in Eqs. (19) and (20) only involves summation over main determinants $D_M^{(1)}$ in which spin assignment for the a and b orbitals is $\alpha\beta$ (Z_M=1) or $\beta\alpha$ (Z_M=2). In the second term in these equations, the first sum involves determinants $D_M^{(1)}$ whose spin assignments for the a and b orbitals are $\alpha\alpha$ (Z_M=3) or $\beta\beta$ (Z_M=4) and the second summation is only over those common open shell orbitals c that have a specific spin in $D_M^{(1)}$ (β, if Z_M=3, or α, if Z_M=4). The function $S_{ab}^{(M)}(1)$ involves summation over common c orbitals having spin α in $D_M^{(1)}$ while the summation in $S_{ab}^{(M)}(2)$ is performed over common c orbitals with spin β in the determinant.

In the (k_1,ΔK=1,P=3) case, the Z-table consists of $\binom{k_1}{2}$ subtables associated with permutations $Q^{(1)}$. Each subtable involves $w(Q^{(1)})$ and, for each main determinant $D_M^{(1)}$, involves the value of Z_M ($Z_M \in [1,4]$) and the following information. If $Z_M \in [1,2]$, then the subtable includes: 1) the number of the determinant $D_{t_M}^{(2)}$ whose trajectory P_{t_M} is obtained from P_M by removing two spins at the $\left(n_a^{(1)}, n_b^{(1)}\right)$ positions; 2) the set of ($k(\alpha)$-1) locations $\left\{ n_{c_\alpha} \right\}$ of the common c orbitals having α spin in P_M; and 3) the set of $(k(\beta)$-1) locations $\{n_{c_\beta}\}$ of the common orbitals with β spin in P_M (n.b. this information is required for calculating $\tilde{h}_{ab}$ and $S_{ab}^{(M)}$). If $Z_M \in [3,4]$, then, for each common c orbital having spin γ in P_M (γ=β if Z_M=3 or α if Z_M=4), the subtable includes the pair $(\tilde{t}_M, n_{c_\gamma})$, where n_{c_γ} is the position of a specific spin-orbital c_γ in P_M and $\tilde{t}_M$ is the number of the trajectory that is obtained from P_M by inverting the spin γ at position n_{c_γ}. Thus, the total length of each subtable will be equal to $(g_1(k_1+2S+1)+1)$.

Analysis of pairs of configurations with the same number of open shells (k_1=k_2=k)

ΔK=0, P=1

In the (ΔK=0, P=1) case, there are three main diagrams: $\begin{pmatrix}1100\\0011\end{pmatrix}$=$ab/cd$, $\begin{pmatrix}1102\\0211\end{pmatrix}$=$abd^2/b^2cd$, and $\begin{pmatrix}1122\\2211\end{pmatrix}$=$abc^2d^2/a^2b^2cd$, where $a<b$ and $c<d$. There are three additional variants of the second diagram, depending on what pair of orbitals (d/a, c/b or c/a) is doubly occupied in Φ_1/Φ_2. Table IV labels all six possible diagrams with a parameter $R \in [1,6]$ and shows six possible spin assignments ($Z_M \in [1,6]$) for the four orbitals, ab/cd, in pairs $D_M^{(1)}/D_{t_M}^{(2)}$. In all diagrams, configurations are connected through double excitations. Electron repulsion integrals $I_1(R)$ and $I_2(R)$ and the linear coefficients $f_1(R,Z_M)$ and $f_2(R,Z_M)$, required for calculation of Hamiltonian matrix elements between paradigmatic determinants, are given in Table IV (which differs from the analogous table in Ref. (*8*) in details such as ordering). It is not difficult to realize that, if spin assignment for the a and b orbitals in $D_M^{(1)}$ is $\alpha\alpha$ or $\beta\beta$, then there is only one determinant $D_{t_M}^{(2)}$, which interacts with $D_M^{(1)}$, and whose trajectory P_{t_M} is obtained from P_M by removing the two spins at positions $\left(n_a^{(1)}, n_b^{(1)}\right)$ and adding the same spins at the positions $\left(n_c^{(2)}, n_d^{(2)}\right)$. But, if spin assignment for the a and b orbitals in $D_M^{(1)}$ is $\alpha\beta$ or $\beta\alpha$, then there are two determinants, $D_{t_M}^{(2)}$ and $D_{\tilde{t}_M}^{(2)}$, interacting with $D_M^{(1)}$, in which spin assignments of the c and d orbitals are $\alpha\beta$ and $\beta\alpha$, respectively. The trajectories P_{t_M} and $P_{\tilde{t}_M}$ of such determinants are

Downloaded by UNIV MASSACHUSETTS AMHERST on September 14, 2012 | http://pubs.acs.org
Publication Date: August 14, 2002 | doi: 10.1021/bk-2002-0828.ch008

Table IV. Electron repulsion integrals and linear coefficients (f_1,f_2) for the $\Delta K=0, P=1$ case

R-subcases	*Basis Integrals* (I_1,I_2)	$Z_M=1$ $\alpha\alpha/\alpha\alpha$	$Z_M=2$ $\alpha\beta/\alpha\beta$	$Z_M=3$ $\beta\alpha/\alpha\beta$	$Z_M=4$ $\alpha\beta/\beta\alpha$	$Z_M=5$ $\beta\alpha/\beta\alpha$	$Z_M=6$ $\beta\beta/\beta\beta$
1 $\begin{pmatrix}1100\\0011\end{pmatrix}$	$(ac\|bd)$, $(ad\|bc)$	(1,-1)	(1,0)	(0,-1)	(0,-1)	(1,0)	(1,-1)
2 $\begin{pmatrix}1102\\0211\end{pmatrix}$	$(ab\|dc)$, $(ac\|db)$	(0,-1)	(1,-1)	(-1,0)	(-1,0)	(1,-1)	(0,-1)
3 $\begin{pmatrix}1102\\2011\end{pmatrix}$	$(ab\|cd)$, $(ad\|cb)$	(0,1)	(1,0)	(-1,1)	(-1,1)	(1,0)	(0,1)
4 $\begin{pmatrix}1120\\0211\end{pmatrix}$	$(ab\|cd)$, $(ad\|cb)$	(0,1)	(1,0)	(-1,1)	(-1,1)	(1,0)	(0,1)
5 $\begin{pmatrix}1120\\2011\end{pmatrix}$	$(ab\|dc)$, $(ac\|db)$	(0,-1)	(1,-1)	(-1,0)	(-1,0)	(1,-1)	(0,-1)
6 $\begin{pmatrix}1122\\2211\end{pmatrix}$	$(ac\|bd)$, $(ad\|bc)$	(1,-1)	(1,0)	(0,-1)	(0,-1)	(1,0)	(1,-1)

NOTE: Since for any pair (R,Z_M) $f_i(7-R,Z_M)=f_i(R,7-Z_M)=f_i(R,Z_M)$ (i=1,2), it suffices to store only coefficients $f_i(R,Z_M)$ for pairs (R,Z_M) with $R,Z_M=1,2,3$.

obtained from P_M by removing two spins ($\alpha\beta$ or $\beta\alpha$) at positions $\left(n_a^{(1)},n_b^{(1)}\right)$ and adding two spins ($\alpha\beta$ for P_{t_M} and $\beta\alpha$ for $P_{\tilde{t}_M}$, respectively) at positions $\left(n_c^{(2)},n_d^{(2)}\right)$. If the coefficients for the pair $D_M^{(1)}/D_{t_M}^{(2)}$ are $f_i(R,Z_M)$, then the coefficients required for the pair $D_M^{(1)}/D_{\tilde{t}_M}^{(2)}$ will be $f_i(R,Z_M+2)$. Taking into account that $f_i(R,Z_M)=f_i(R,7-Z_M)$ (see Table IV), one finally has

$$\begin{aligned}\left\langle F_I^{(1)}\middle|H\middle|F_J^{(2)}\right\rangle &= w(Q^{(1)})w(Q^{(2)})\\ &\times\left\{\sum_{\substack{M=1\\(Z_M=1,6)}}^{I} W_{MI}^{(k)}C_{t_MJ}^{(k)}\left[f_1(R,Z_M)I_1(R)+f_2(R,Z_M)I_2(R)\right]\right.\\ &\left.+\sum_{\substack{M=1\\(Z_M=2,3)}}^{I} W_{MI}^{(k)}\begin{bmatrix}C_{t_MJ}^{(k)}\left(f_1(R,Z_M)I_1(R)+f_2(R,Z_M)I_2(R)\right)\\ +C_{\tilde{t}_MJ}^{(k)}\left(f_1(R,5-Z_M)I_1(R)+f_2(R,5-Z_M)I_2(R)\right)\end{bmatrix}\right\},\end{aligned} \tag{25}$$

where

Downloaded by UNIV MASSACHUSETTS AMHERST on September 14, 2012 | http://pubs.acs.org
Publication Date: August 14, 2002 | doi: 10.1021/bk-2002-0828.ch008

$$w(Q^{(1)}) = (-1)^{n_a^{(1)}+n_b^{(1)}+1}, \qquad w(Q^{(2)}) = (-1)^{n_c^{(2)}+n_d^{(2)}+1}, \tag{26}$$

and permutations $Q^{(1)}$ and $Q^{(2)}$ are specified by the sets $\left(n_a^{(1)}, n_b^{(1)}\right)$ and $\left(n_c^{(2)}, n_d^{(2)}\right)$. Note that the first sum in Eq. (25) only involves determinants $D_M^{(1)}$ in which spin assignment for the *a* and *b* orbitals is $\alpha\alpha$ or $\beta\beta$, and the second sum involves determinants with spin assignments $\alpha\beta$ or $\beta\alpha$.

In the (k,ΔK=0,P=1) case, the Z-table consists of $\frac{1}{2}\binom{k}{2}\left(\binom{k}{2}+1\right)$ subtables associated with permutation pairs ($Q^{(1)} \leq Q^{(2)}$). Each subtable consists of ($3g$+1) entries, namely $w(Q^{(1)})w(Q^{(2)})$ and, for each main determinant $D_M^{(1)}$, the triple index $\left(Z_M, t_M, \tilde{t}_M\right)$.

ΔK=0, P=2

In the (ΔK=0, P=2) case, there are two main diagrams: $\begin{pmatrix}210\\021\end{pmatrix}$=$a^2b/b^2c$ (R=1) and $\begin{pmatrix}012\\201\end{pmatrix}$=$bc^2/a^2c$ (R=2), describing configuration pairs connected through the double excitation $a^2 \Rightarrow bc$ ($a<b<c$). Only two spin assignments, α/α (Z_M=1) and β/β (Z_M=2), are possible for the open shells b/c in pairs $D_M^{(1)} / D_{t_M}^{(2)}$. The trajectory P_{t_m} of the only determinant $D_{t_M}^{(2)}$ interacting with a given $D_M^{(1)}$ is obtained from P_M by removing a spin at position $n_b^{(1)}$ and adding the same spin at position $n_c^{(2)}$. In all four cases, interactions between paradigmatic determinants are described by the electron repulsion integrals *(ab|ac)* and the linear coefficient is always equal to -1. Taking these results into account, one gets

$$\left\langle F_I^{(1)} \middle| H \middle| F_J^{(2)} \right\rangle = -w(Q^{(1)})w(Q^{(2)})(ab \mid ac)\left(\sum_{M=1}^{I} W_{MI}^{(k)} C_{t_M J}^{(k)}\right), \tag{27}$$

where permutations $Q^{(1)}$ and $Q^{(2)}$ label the positions $n_b^{(1)}$ and $n_c^{(2)}$ of the *b* and *c* orbitals in the configurations, and

$$w(Q^{(1)}) = (-1)^{n_b^{(1)}+1}, \qquad w(Q^{(2)}) = (-1)^{n_c^{(2)}+1}. \tag{28}$$

Downloaded by UNIV MASSACHUSETTS AMHERST on September 14, 2012 | http://pubs.acs.org
Publication Date: August 14, 2002 | doi: 10.1021/bk-2002-0828.ch008

In the (k,ΔK=0,P=2) case, the Z-table consists of $\begin{pmatrix} k+1 \\ 2 \end{pmatrix}$ subtables associated with permutation pairs ($Q^{(1)} \leq Q^{(2)}$). Each subtable consists of (g+1) entries, namely $w(Q^{(1)})w(Q^{(2)})$ and, for each $D_M^{(1)}$, the value of t_M.

ΔK=0, P=3

The case under consideration is described by two diagrams: $\begin{pmatrix} 10 \\ 01 \end{pmatrix}$=$a/b$ (R=1) and $\begin{pmatrix} 12 \\ 21 \end{pmatrix}$=$ab^2/a^2b$ (R=2). This case is similar to the (ΔK=1,P=3) case discussed earlier. Again, although configurations are connected formally through single excitations, their determinants can additionally be connected through double excitations.

If spins of the a/b orbitals in the pair $D_M^{(1)} / D_{t_M}^{(2)}$ are the same (α/α (Z_M=1) or β/β (Z_M=2)), then the determinants will be connected through a single excitation and the trajectory P_{t_M} of $D_{t_M}^{(2)}$ is obtained from P_M by removing a spin at position $n_a^{(1)}$ and adding the same spin at the position $n_b^{(2)}$.

If spins of the orbitals a/b in the pair $D_M^{(1)} / D_{t_M}^{(2)}$ are different (α/β (Z_M=3) or β/α (Z_M=4)) and the configurations have a common set $\{c\}$ of open shells, then the determinants will be connected through a double excitation ($a_\alpha c_\beta \Rightarrow b_\beta c_\alpha$ (if Z_M=3) or $a_\beta c_\alpha \Rightarrow b_\alpha c_\beta$ (if Z_M=4)), in the course of which one common c orbital changes its spin. In this case, the trajectory P_{t_M} specifying $D_{t_M}^{(2)}$ is obtained from P_M by removing a spin at position $n_a^{(1)}$, adding the opposite spin at position $n_b^{(2)}$, and inverting the spin of a c orbital.

Again using Slater's rules, in the R=1 case, one gets

$$\left\langle F_I^{(1)} \middle| H \middle| F_J^{(2)} \right\rangle = w(Q^{(1)})w(Q^{(2)}) \left\{ \sum_{\substack{M=1 \\ (Z_M \in [1,2])}}^{I} W_{MI}^{(k)} C_{t_M J}^{(k)} \left[\tilde{h}_{ab} - S_{ab}^{(M)}(Z_M) \right] \right.$$

$$\left. - \sum_{\substack{M=1 \\ (Z_M \in [3,4])}}^{I} W_{MI}^{(k)} \sum_{c_\gamma \in D_M^{(1)}} C_{t_M (c_\gamma \to c_{\bar{\gamma}}) J}^{(k)} (ac \mid cb) \right\}, \tag{29}$$

while, in the R=2 case, one has

Downloaded by UNIV MASSACHUSETTS AMHERST on September 14, 2012 | http://pubs.acs.org
Publication Date: August 14, 2002 | doi: 10.1021/bk-2002-0828.ch008

$$\left\langle F_I^{(1)} \middle| H \middle| F_J^{(2)} \right\rangle = -w(Q^{(1)})w(Q^{(2)})$$

$$\times \left\{ \begin{array}{l} \sum\limits_{\substack{M=1 \\ (Z_M \in [1,2])}}^{I} W_{MI}^{(k)} C_{t_M J}^{(k)} \left[\tilde{h}_{ab} + (ab \mid aa) + (ab \mid bb) - S_{ab}^{(M)}(\bar{Z}_M) \right] \\ \qquad - \sum\limits_{\substack{M=1 \\ (Z_M \in [3,4])}}^{I} W_{MI}^{(k)} \sum\limits_{c_\gamma \in D_M^{(1)}} C_{t_M (c_\gamma \to c_{\bar{\gamma}}) J}^{(k)} (ac \mid cb) \end{array} \right\}. \tag{30}$$

Here, permutation $Q^{(1)}$ and $Q^{(2)}$ are determined by the positions $n_a^{(1)}$ and $n_b^{(2)}$, $\bar{Z}_M$ equals 1 (if Z_M=2) or 2 (if Z_M=1),

$$w(Q^{(1)}) = (-1)^{n_a^{(1)}+1}, \qquad w(Q^{(2)}) = (-1)^{n_b^{(2)}+1}, \tag{31}$$

and $\tilde{h}_{ab}$ and $S_{ab}^{(M)}(Z)$ are defined by Eqs. (22)-(24). The first term in Eqs. (29) and (30) involves summation over all main determinants $D_M^{(1)}$. $S_{ab}^{(M)}(Z_M)$ in Eq. (29) involves those common orbitals *c* which have the same spin in $D_M^{(1)}$ as does orbital *a*, while $S_{ab}^{(M)}(\bar{Z}_M)$ in Eq. (30) involves the common orbitals whose spin is opposite to that of the *a* orbital in $D_M^{(1)}$. The second term in Eqs. (29) and (30) involves main determinants $D_M^{(1)}$ in which the spin of the *c* orbitals is opposite to that of the orbital *a*.

In the (k,ΔK=0,P=3) case, the Z-table consists of $\begin{pmatrix} k+1 \\ 2 \end{pmatrix}$ subtables associated with separate pairs ($Q^{(1)} \le Q^{(2)}$) of permutations specifying the positions $n_a^{(1)}$ and $n_b^{(2)}$. Each subtable consists of (2kg+1) entries, namely $w(Q^{(1)})w(Q^{(2)})$, and, for each main determinant $D_M^{(1)}$, the subtable includes 3 pieces of information: 1) the spin γ of the electron at position $n_a^{(1)}$ in $D_M^{(1)}$ and the number of the determinant $D_{t_M}^{(2)}$ whose trajectory is obtained from P_M by removing the spin γ at position $n_a^{(1)}$ and adding the same spin at position $n_b^{(2)}$; 2) the positions n_{c_γ} of the common orbitals with spin γ in $D_M^{(1)}$; and 3) the positions $n_{c_{\bar{\gamma}}}$ of the common orbitals with spin opposite to γ in $D_M^{(1)}$. The information in (3) is paired with the number, t_M, of the determinant, $D_{t_M}^{(2)}$, with trajectory P_{t_M} that is obtained from P_M by removing spin γ at position $n_a^{(1)}$, adding the opposite spin $\bar{\gamma}$ at position

Downloaded by UNIV MASSACHUSETTS AMHERST on September 14, 2012 | http://pubs.acs.org
Publication Date: August 14, 2002 | doi: 10.1021/bk-2002-0828.ch008

$n_b^{(2)}$, and inverting the spin at position $n_{c_{\bar{\gamma}}}$. To facilitate storage and indexing, the information in (2) is paired with unused values.

The case of the same configuration

In the case when the configurations are the same (Φ_1=Φ_2=Φ), it suffices to consider only the lower triangle of the required Hamiltonian matrix block. On the basis of Eq. (8), one has

$$\langle F_I|\hat{H}|F_J\rangle = \sum_{M=J}^{I} W_{MI}^{(k)} C_{MJ}^{(k)} \langle D_M|\hat{H}|D_M\rangle + \sum_{M=1}^{I} W_{MI}^{(k)} \sum_{t(\neq M)}^{d(k,S)} C_{tJ}^{(k)} \langle D_M|\hat{H}|D_t\rangle, \quad 1 \leq J \leq I \leq g, \tag{32}$$

where the first and second terms involve diagonal and off-diagonal determinantal matrix elements, respectively. In the last equation, it has been taken into account that, when using genealogical CSFs, the block $\left\| C_{MJ}^{(k)} \right\|$ is lower triangular. The diagonal matrix elements can be written in the form (*8*)

$$\langle D_M|\hat{H}|D_M\rangle = I_0(\Phi) - \sum_{\gamma=\alpha,\beta} \sum_{\substack{a_\gamma<b_\gamma \\ (a_\gamma, b_\gamma \in D_M)}}^{open} K_{ab}, \tag{33}$$

where the first term

$$I_0(\Phi) = \sum_{i}^{closed} (2h_{ii} + J_{ii}) + \sum_{i<i}^{closed} (4J_{ij} - 2K_{ij}) + \sum_{a}^{open} \left(h_{aa} + \sum_{i}^{closed} (2J_{ia} - K_{ia}) \right) + \sum_{a<b}^{open} J_{ab} \tag{34}$$

depends only on the configuration and is common for all D_M, and the second term involves summation over all pairs of open-shell spin-orbitals $a_\gamma<b_\gamma$ (γ=α,β) occupied in a given determinant D_M (N.B. J_{ia} and K_{ia} are Coulomb and exchange integrals).

Since all determinants, created by the same configuration, with a given S_z are related by double and higher excitations (*8*), determinants D_M and D_t can interact only if exactly two open-shell orbitals a and b of opposite spin in D_M have inverse spins in D_t. Taking into account that the Hamiltonian matrix element between such determinants is -K_{ab}, on the basis of Eqs. (6), (32) and (33), one has

Downloaded by UNIV MASSACHUSETTS AMHERST on September 14, 2012 | http://pubs.acs.org
Publication Date: August 14, 2002 | doi: 10.1021/bk-2002-0828.ch008

$$\left\langle F_I \middle| \hat{H} \middle| F_J \right\rangle = I_0(\Phi) - \sum_{M=J}^{I} W_{MI}^{(k)} C_{MJ}^{(k)} \sum_{\gamma=\alpha,\beta} \sum_{\substack{a_\gamma<b_\gamma \\ (a_\gamma, b_\gamma \in D_M)}} K_{ab} - \sum_{M=1}^{I} W_{MI}^{(k)} \sum_{\substack{a_\gamma<b_\delta\,(\gamma\neq\delta) \\ (a_\gamma, b_\delta \in D_M)}} C_{t_M J}^{(k)} K_{ab}, \quad (35)$$

where, in contrast to the second term, the third term involves summation over all pairs of open-shell spin-orbitals $a_\gamma<b_\delta$ whose spins are opposite ($\gamma\neq\delta$) in a given determinant D_M.

For each main determinant D_M, the Z-table involves 1) the sets $\{n_\alpha^{(1)}, n_\alpha^{(2)}, \ldots, n_\alpha^{(k(\alpha))}\}$ and $\{n_\beta^{(1)}, n_\beta^{(2)}, \ldots, n_\beta^{(k(\beta))}\}$, specifying locations of open shells electrons in D_M with α- and β-spins, respectively, and 2) the set of triple indices $\{(n_\gamma^{(i)}, n_\delta^{(i)}, t_M^{(i)})\}_{i=1}^{k(\alpha)k(\beta)}$ determining locations ($n_\gamma^{(i)} < n_\delta^{(i)}$) of pairs of open shell electrons with opposite spins in D_M and the number $t_M^{(i)}$ of the determinant, interacting with D_M, whose trajectory is obtained from P_M by flipping two spins at the positions ($n_\gamma^{(i)} < n_\delta^{(i)}$). Since the numbers $k(\alpha)$ and $k(\beta)$ of α- and β-electrons in D_M are equal to $k/2+S$ and $k/2-S$, respectively, the total dimension of the Z-table required for calculation of all Hamiltonian matrix elements over CSFs of the same configuration is equal to $g[k+3(k^2/4-S^2)]$.

Concluding remarks

Formulas for Hamiltonian matrix elements in a spin-adapted basis have been obtained in the framework of the table-CI method. In particular, intermediate transformations of the Hamiltonian matrix from the determinant basis to a basis of CSFs are eliminated. Furthermore, the genealogical scheme of constructing CSFs is shown to produce efficient formulas.

The formulas presented herein have been implemented and numerically tested in a program realizing second-order generalized Van Vleck perturbation theory (GVVPT2) [see, e.g., Ref. (*16*)]. Preliminary results support the assertion that the method of constructing Hamiltonian matrix elements is highly efficient. Computational details of implementation in the context of GVVPT2 and other specific methods of molecular electronic structure theory will be considered in separate publications.

Finally, we note that the formulas discussed in this paper are compatible with our so-called macroconfiguration concept, which has been realized recently (*17*). Specifically, the need for explicit storage of highly excited configurations is eliminated and, at the same time, a vast number of noninteracting Hamiltonian matrix elements are prescreened. This development is critical to our recently presented MR-CISD(TQ) method (*18*).

Downloaded by UNIV MASSACHUSETTS AMHERST on September 14, 2012 | http://pubs.acs.org
Publication Date: August 14, 2002 | doi: 10.1021/bk-2002-0828.ch008

Acknowledgments

The authors gratefully acknowledge the National Science Foundation (Grant No. CHE-9975429) for financial support of the research presented herein.

References

1. Shavitt, I. The Method of Configuration Interaction. In *Methods of Electronic Structure Theory*; Schaefer, H. F., Ed.; Plenum Press: New York, 1977; pp 189-275.
2. Siegbahn, P. E. M. The Configuration Interaction Method. In *Lecture Notes in Quantum Chemistry: European Summer School in Quantum Chemistry*; Roos, B. O., Ed.; Springer-Verlag: New York, 1992; Vol. 58, pp 255-293.
3. Karwowski, J. The Configuration Interaction Approach to Electron Correlation. In *Methods in Computational Molecular Physics*; Wilson, S., Diercksen, G. H. F., Eds.; Plenum Press: New York, 1992; pp 65-98.
4. Duch, W. *THEOCHEM* **1991,** *80,* 27.
5. Sherrill, C. D.; Schaefer, H. F. The Configuration Interaction Method: Advances in Highly Correlated Approaches. *Adv. Quantum Chem.* **1999,** *34,* 143-270.
6. Buenker, R. J. The Configuration-Driven Table CI Method and Comparison With Integral-Driven CI Procedures. In *Molecular Physics and Quantum Chemistry into the 1980's*; Burton, P. G., Ed.; University of Wollongong Press: Wollongong, Australia, 1980; pp 1.5.1 - 1.5.37.
7. Buenker, R. J. Implementation of the Table CI Method: Configurations Differing by Two in the Number of Open Shells. *Stud. Phys. Theor. Chem.*, **1982,** *21,* 17-34.
8. Buenker, R. J.; Phillips, R. A. *THEOCHEM* **1985,** *123,* 291.
9. Krebs, S.; Buenker, R. J. *J. Chem. Phys.* **1995,** *103,* 5613.
10. Buenker, R. J.; Peyerimhoff, S. D. *Theor. Chim. Acta* **1974,** *35,* 33.
11. Hoffmann, M. R. Quasidegenerate Perturbation Theory Using Effective Hamiltonians. In *Modern Electronic Structure Theory*; Yarkony, D. R., Ed.; World Scientific: Singapore, 1995; pp 1166-1190.
12. Pauncz, R. *The Construction of Spin Eigenfunctions (An Exercise Book);* Plenum Press: New York, 2000.
13. Khait, Y. G.; Hoffmann, M. R. *Int. J. Quantum Chem.* **2001,** *81,* 130.
14. Reingold, E. M.; Nievergel, J.; Deo, N. *Combinatorial Algorithms*; Prentice-Hall: Englewood Cliffs, NJ, 1977.
15. Slater, J. C. *Phys. Rev.* **1929,** *34,* 1293.
16. Hoffmann, M. R. *Chem. Phys. Lett.* **1992,** *195,* 127; **1993,** *210,* 193.

Downloaded by UNIV MASSACHUSETTS AMHERST on September 14, 2012 | http://pubs.acs.org
Publication Date: August 14, 2002 | doi: 10.1021/bk-2002-0828.ch008

17. Khait, Y. G.; Song, J.; Hoffmann, M. R. Macroconfigurations in Molecular Electronic Structure. Theory and Application to Cr_2. *J. Chem. Phys.*, submitted for publication, 2001.
18. Hoffmann, M. R.; Khait, Y. G. *Abstracts of Papers,* 221st National Meeting of the American Chemical Society, San Diego, CA, Mar 30-Apr 4, 2001; American Chemical Society: Washington, DC, 2001; PHYS 277.

Downloaded by UNIV MASSACHUSETTS AMHERST on September 14, 2012 | http://pubs.acs.org
Publication Date: August 14, 2002 | doi: 10.1021/bk-2002-0828.ch008

Downloaded by UNIV OF GUELPH LIBRARY on September 14, 2012 | http://pubs.acs.org
Publication Date: August 14, 2002 | doi: 10.1021/bk-2002-0828.ch009

Chapter 9

Jacob's Ladder for Time-Dependent Density-Functional Theory: Some Rungs on the Way to Photochemical Heaven

Mark E. Casida

**Laboratoire d'Etudes Dynamiques et Structurales de la Sélectivité (LEDSS),
Université Joseph Fourier (Grenoble I), 38041 Grenoble, France
(email: Mark.CASIDA@ujf-grenoble.fr)**

Abstract

The time-dependent extension of density-functional theory (TDDFT) provides a rigorous formalism allowing the treatment of electronic excitations and excited states. However, just as in traditional (ground-state) density-functional theory (DFT), the quality of the results depends upon the approximation used for the unknown exchange-correlation (xc) functional. Perdew and Schmidt have described the various functionals developed for ground state DFT in terms of a Jacob's ladder, where the rungs correspond to successive levels of approximation of the xc-functional[1]. Within the adiabatic approximation, these functionals can also be used in TDDFT. However, TDDFT places additional demands on the functional that are not typically satisfied by approximations developed for the ground-state. The simple time-dependent local approximation already gives remarkably good results for many excited states. However other excitations require more accurate treatment of the xc potential. Our work on this problem will be summarized in terms of a "Jacob's ladder" adopted to the special needs of applied TDDFT.

Downloaded by UNIV OF GUELPH LIBRARY on September 14, 2012 | http://pubs.acs.org
Publication Date: August 14, 2002 | doi: 10.1021/bk-2002-0828.ch009

Long accepted as an important fundamental theoretical tool in solid state physics, density-functional theory (DFT) has now also come to be accepted as an important fundamental tool in the quantum chemistry community. The 1998 Nobel Prize in Chemistry awarded "to Walter Kohn for his development of the density-functional theory and to John Pople for his development of computational methods in quantum chemistry" certainly emphasized this acceptance [2]. In comparison with *ab initio* methods, DFT has the important advantage that it includes electron-correlation effects in a simple Hartree-Fock (or Hartree-like) manner. When suitably programmed, this allows DFT to be applied to larger molecules, and hence to more molecules of practical importance, than is the case with traditional *ab initio* methods. It is also simple enough for on-the-fly calculation of forces needed in so-called *ab initio* molecular dynamics methods (most of which are based on DFT), such as that of Car and Parrinello [3]. Nevertheless, with all its advantages, traditional Hohenberg-Kohn-Sham DFT [4, 5] was born an incomplete theory, limited to calculating the energy and charge density for the static ground electronic stationary state. Here I review the time-dependent generalization of DFT, and particularly how different levels of sophistication of functionals can be important for time-dependent DFT (TDDFT) calculations of electronic excited state potential energy surfaces.

To the extent that we can solve the "problem of the unknown functional" in TDDFT, we can look forward to an ever widening list of applications. Since our formulation [6] and implementation [7] of TDDFT in a manner suitable for molecular applications, some form of TDDFT has been implemented in nearly every major quantum chemistry program. Most applications have been to the calculation of electronic excitation energies and spectra, including for chlorophyll a [8], fullerenes [9], polyacetylenes [10, 11, 12, 13], transition metal coordination compounds [14, 15, 16], and phototoxic drugs [17]. Nevertheless there have now been several calculations of potential energy surfaces [18, 19, 20, 21, 22, 23] and the implementation of analytic derivatives for TDDFT [24, 25] has allowed automatic geometry optimizations to be carried out for excited states. These developments make me optimistic that we will soon see some type of Car-Parrinello treatment of a photodynamics problem. Certainly first attempts are already being made in this direction. These include Car-Parrinello for a single excited state using the multiplet sum formalism [26] and implementation of TDDFT to take into account finite temperature vibrational structure for excitation spectra in Car-Parrinello codes [27]. Very recent work of relevance to this problem is also being carried out in the Röthlisberger group [28].

In the remainder of this chapter, I first review the status of the treatment of excited states in DFT and then go into a detailed analysis of where and how functionals can be improved.

EXCITED STATES IN DFT

Traditional DFT is based upon two theorems due to Hohenberg and Kohn [4]: (1) For a nondegenerate system of electrons in its ***ground stationary state*** the charge density determines the external potential up to an arbitrary additive constant. (2) In principle, the ***ground state*** energy and charge density may be obtained by minimizing a certain functional $E[\rho]$ (for which a practical exact form is unfortunately not known.) I have deliberately emphasized the references to "ground" and "stationary state." Before seeing how we can generalize the traditional theory to get around these limitations, it is useful to review the status of "ordinary" DFT.

In practice, the Kohn-Sham formulation [5] of DFT is almost always used. This overcomes the major difficulty with finding a density-functional for the kinetic energy by introducing a set of orthonormal auxiliary functions (i.e. the Kohn-Sham orbitals), ψ_i with occupation numbers f_i, which sum to the ground state density,

$$\rho(\mathbf{r}) = \sum_i f_i |\psi_i(\mathbf{r})|^2 , \tag{1}$$

and allow us to express the ground state energy as

$$E = \sum_i f_i \langle \psi_i | \hat{h}_{core} | \psi_i \rangle + \frac{1}{2} \int \int \frac{\rho(\mathbf{r})\rho(\mathbf{r}')}{|\mathbf{r}-\mathbf{r}'|} d\mathbf{r}d\mathbf{r}' + E_{xc}[\rho] . \tag{2}$$

These orbitals are to be found by minimizing the energy subject to the orthonormality constraint. The result is the Kohn-Sham equation,

$$\left[-\frac{1}{2}\nabla^2 + v_{ext}(\mathbf{r}) + \int \frac{\rho(\mathbf{r}')}{|\mathbf{r}-\mathbf{r}'|} d\mathbf{r}' + v_{xc}(\mathbf{r}) \right] \psi_i(\mathbf{r}) = \epsilon_i \psi_i(\mathbf{r}) . \tag{3}$$

Since no practical exact form of the exchange-correlation functional

$$E_{xc}[\rho] = \int \epsilon_{xc}[\rho](\mathbf{r})\rho(\mathbf{r})\, d\mathbf{r} \tag{4}$$

is known, it is approximated in practice. There are several levels of sophistication that can be used for constructing approximate functionals. Recently, Perdew and Schmidt[1] have organized the different families of density functionals into a "Jacob's ladder of density functional approximations." A generalization of this ladder is given in Fig. 1. The lowest level represents the simplest approximation which is the local density approximation (LDA) in which the exchange-correlation energy density is approximated by that of the homogeneous electron gas (HEG),

$$\epsilon_{xc}[\rho](\mathbf{r}) = \epsilon_{xc}^{HEG}(\rho(\mathbf{r})) . \tag{5}$$

Downloaded by UNIV OF GUELPH LIBRARY on September 14, 2012 | http://pubs.acs.org
Publication Date: August 14, 2002 | doi: 10.1021/bk-2002-0828.ch009

Downloaded by UNIV OF GUELPH LIBRARY on September 14, 2012 | http://pubs.acs.org
Publication Date: August 14, 2002 | doi: 10.1021/bk-2002-0828.ch009

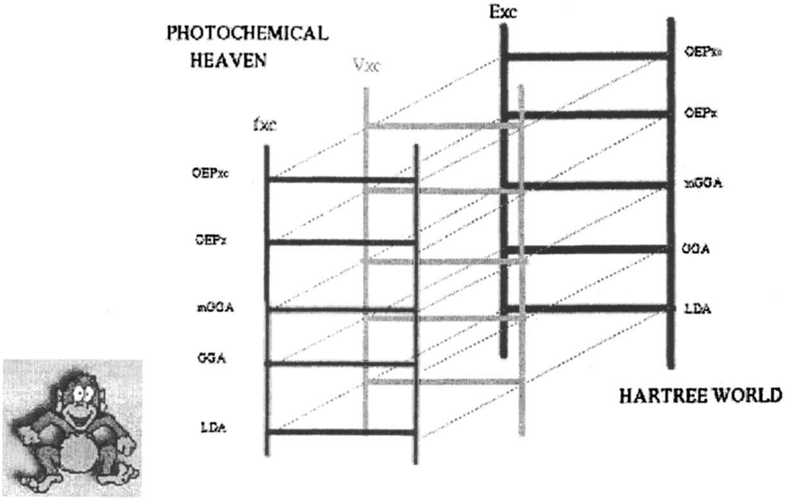

Figure 1: Jacob's jungle gym for TDDFT.

This works remarkably well, especially for properties such as ionization potentials and molecular geometries of "ordinary" molecules. It is normally used in its spin-dependent form (the local spin density approximation), but for simplicity I will neglect spin except where it is explicitly necessary to include it. Unfortunately the LDA tends to overbind. The next level of approximation are the generalized gradient approximations (GGAs) which include an explicit dependence on the reduced gradient of the charge density, $x(\mathbf{r}) = |\vec{\nabla}\rho(\mathbf{r})|/\rho^{4/3}(\mathbf{r})$. Well-constructed GGAs are able to give significantly better chemical binding energies. The third level of approximation is the meta-GGAs which include a dependence on the kinetic energy density, $\tau(\mathbf{r}) = \sum_i f_i|\vec{\nabla}\psi_i(\mathbf{r}|^2$. Older and more explored is the fourth level of the ladder (labelled OEPx here) in which some explicit dependence on occupied orbitals is included, typically through some portion of Hartree-Fock exchange. This inclusion of an orbital dependence in the density-functional may seem a little strange, until it is recalled that the orbitals themselves are implicit functionals of the charge density. These hybrid functionals were introduced because they are able to give near chemical accuracy for thermochemistry — something which GGAs alone were unable to do. The highest level of the ladder (OEPxc) includes also a dependence on the unoccupied orbitals. At this level, we have enough degrees of freedom to construct "exact" exchange-correlation potentials from *ab initio* theory, giving rise to the term "*ab initio* density-functional theory" [29]. Work at this level is only just beginning. The reader is referred to the book by Koch and Holthausen for a property-by-property assessment of the accuracy of many popular functionals [30].

In thinking about the impact of a particular choice of functional on any given property, it is important to realize that the historical emphasis in creating approximate density-functionals has been to obtain accurate total energies. Hence most work has concentrated on understanding and approximating the exchange-correlation *energy*, $E_{xc}[\rho]$. As we go to higher and higher functional derivatives of the exchange-correlation energy, less and less is known about their exact properties and how to approximate them. Since the exchange-correlation *potential*, $v_{xc}[\rho](\mathbf{r}) = \delta E_{xc}[\rho]/\delta\rho(\mathbf{r})$, enters into the orbital equation, it has a direct effect effect on the charge density. It also enters into the calculation of analytic first-derivatives used in automatic geometry optimizations. These are important properties and more and more effort is being made to find better approximations for the exchange-correlation potential [31, 32, 33, 18, 34, 35, 33, 36, 37]. The second derivative is the exchange-correlation *kernel*, $f_{xc}[\rho](\mathbf{r},\mathbf{r}') = \delta^2 E_{xc}[\rho]/\delta\rho(\mathbf{r})\delta\rho(\mathbf{r}')$. It is needed for the calculation of static response properties such as electronic dipole polarizabilities and for the calculation of analytic second-derivatives. We can, of course, go on taking derivatives, but this is high enough for present purposes.

Excited States. It is interesting to note that the first Hohenberg-Kohn theorem implies that the ground state charge density, by determining the external potential up to an additive constant, also implicitly determines the entire manifold of electronic ground and excited states up to an arbitrary energy zero. The problem has been how to find a practical approximate scheme for treating excited states based on either (or both) the ground and excited state charge densities. Several methods have been proposed for doing this (see Ref. [21] for a recent review.) Practical calculations typically use one of two approaches: either (i) the DFT ΔSCF approach or (ii) TDDFT. Both approaches have advantages and disadvantages and until the two are united into a single formalism, we must learn to pick and choose depending upon our application.

The ΔSCF approach is historically the older of the two approaches. It is based on the idea that DFT should be valid for the lowest state of each symmetry (especially if the state is well described by a single-determinantal wave function!) If this is true, it suffices to take the energy difference of two SCF calculations with different orbital occupancies. This approach is formally exact for the first ionization potential of a molecule (but is often also useful for other ionization potentials). It is also exact for the lowest excited state of a given symmetry (and it is very commonly applied in this form to calculate the lowest triplet state of a closed-shell molecule). In

Downloaded by UNIV OF GUELPH LIBRARY on September 14, 2012 | http://pubs.acs.org
Publication Date: August 14, 2002 | doi: 10.1021/bk-2002-0828.ch009

Downloaded by UNIV OF GUELPH LIBRARY on September 14, 2012 | http://pubs.acs.org
Publication Date: August 14, 2002 | doi: 10.1021/bk-2002-0828.ch009

more complicated situations, *afficianados* of the ΔSCF approach use the Ziegler-Rauk-Baerends multiplet sum method[38, 39] to *estimate* energies for excited states. In this variation on the ΔSCF method, first-order energies of multi-determinantal states are estimated by a weighted sum of the energies of single-determinantal states based upon a group theoretical guess of the form of the multi-determinantal wave function. In the case of a singlet one-electron excited state of a closed-shell molecule,

$$E_{i \to a}^{singlet} \cong 2E_{i\downarrow \to a\downarrow} - E_{i\downarrow \to a\uparrow} \,. \tag{6}$$

The *strength* of the ΔSCF approach is that it can handle two-electron and higher-electron excited states easily. The *weakness* of ΔSCF lies in its lack of formal justification (except for particular special situations, such as the first ionization potential), and in its inability to handle nontrivial configuration mixing, such as would be encountered, say, near avoided crossings of two excited states.

Time-dependent density-functional theory operates very differently. Although TDDFT was initially viewed as an *ad hoc* method, a substantial body of work has now given it a rigorous formal footing [40, 41, 42, 43, 44, 45, 46, 47, 48] (see especially reviews by Gross and coworkers [49, 50, 51].) In analogy with experiment, TDDFT excitation energies are determined by finding the resonant frequencies for the response of the charge density to a time-dependent electric field (*think photon!*). The *strength* of TDDFT is that it is formally well-founded (though there is an unknown functional) and configuration mixing in excited states emerges as a natural consequence of the formalism. The *weakness* of TDDFT in practice is in the functionals and in the adiabatic approximation which restricts it to one-electron excitations. Practical calculations solve the equation,

$$\begin{bmatrix} \mathbf{A} & \mathbf{B} \\ \mathbf{B} & \mathbf{A} \end{bmatrix} \begin{pmatrix} \vec{X}_I \\ \vec{Y}_I \end{pmatrix} = \omega_I \begin{bmatrix} 1 & 0 \\ 0 & -1 \end{bmatrix} \begin{pmatrix} \vec{X}_I \\ \vec{Y}_I \end{pmatrix} , \tag{7}$$

where

$$A_{ia\sigma,jb\tau} = \delta_{i,j}\delta_{a,b}\delta_{\sigma,\tau}(\epsilon_{a\sigma} - \epsilon_{i\sigma}) + K_{ia\sigma,jb\tau} \tag{8}$$

$$B_{ia\sigma,jb\tau} = K_{ia\sigma,bj\tau} \,, \tag{9}$$

and the "coupling matrix,"

$$\begin{aligned} K_{ia\sigma,jb\tau} &= \int\int \psi_{i\sigma}(\mathbf{r})\psi_{a\sigma}(\mathbf{r}) \left(\frac{1}{|\mathbf{r} - \mathbf{r}'|} + f_{xc}^{\sigma,\tau}(\mathbf{r},\mathbf{r}') \right) \\ &\times \psi_{j\tau}(\mathbf{r}')\psi_{b\tau}(\mathbf{r}') \, d\mathbf{r}d\mathbf{r}' \,. \end{aligned} \tag{10}$$

Thus the excitation energy, ω_I, depends upon both the exchange-correlation potential through the orbitals, $\psi_{i\sigma}$, and orbital energies, $\epsilon_{i\sigma}$, and on the exchange-correlation kernel, $f_{xc}^{\sigma;\tau}(\mathbf{r},\mathbf{r}')$.

Had the adiabatic approximation *not* been made, then the exchange-correlation kernel would also have a frequency dependence, $f_{xc}^{\sigma;\tau}(\mathbf{r},\mathbf{r}';\omega)$. The adiabatic approximation assumes that the exchange-correlation potential, $v_{xc}^{\sigma}(\mathbf{r},t)$, reacts instantly to any temporal change in the charge density. The exact theory includes "memory effects" whereby the response of the potential at time t depends not only on the charge density at time t but also on the charge density at previous times. In principle the adiabatic approximation is valid only in the low frequency (i.e. low energy $= \hbar\omega$) limit. In practice, the limit of validity of the adiabatic approximation can only be determined through explicit calculation and comparison with reliable experimental and theoretical results.

Jacob's Jungle Gym. Potential energy surfaces can be calculated by adding the excitation energies from TDDFT directly to the total ground state energy obtained from traditional DFT. This transforms the problem of Jacob's ladder into that of Jacob's jungle gym (Fig. 1) because we can expect to need reasonably high-quality approximations for both the exchange-correlation energy and for its functional derivatives. In particular, the ground state energy depends heavily on the approximation for E_{xc} and also to some extent on the quality of the first functional derivative, v_{xc}. The excitation energy, ω_I depends on v_{xc} and also on f_{xc}.

Nevertheless, we can do surprisingly well on the lowest level of the jungle gym, which is known as either the time-dependent local density approximation (TDLDA) or as the adiabatic local density approximation (ALDA). Experience has shown that one should expect excitation energies which are better than those given by the time-dependent Hartree-Fock (TDHF) approximation or by configuration interaction singles (CIS) for comparable or less effort *provided*, (i) excitations are vertical and at the ground state equilibrium geometry, (ii) only excitation energies are considered which are below the TDDFT ionization threshold at minus the HOMO orbital energy, and (iii) there is not too much change in the charge densities before and after the excitation process. TDLDA results for N_2 are given in Table 1.

LADDER-BY-LADDER ANALYSIS

In this section I will show several instances where it is necessary to mount the various ladders in Jacob's jungle gym, beginning with the E_{xc} ladder and continuing on to the f_{xc} ladder.

Problems with E_{xc}. Since TDDFT is based on the response of the

Downloaded by UNIV OF GUELPH LIBRARY on September 14, 2012 | http://pubs.acs.org
Publication Date: August 14, 2002 | doi: 10.1021/bk-2002-0828.ch009

Table 1: Data are from Ref. [7].

N_2 Vertical Excitation Energies (eV)				
State	TDLDA	Expt	TDHF	CIS
Singlet → Singlet Transitions				
$w^1\Delta_u$	10.22	10.27	8.75	9.09
$a'^1\Sigma_u^-$	9.66	9.92	7.94	8.51
$a^1\Pi_g$	9.10	9.31	9.76	9.60
Singlet → Triplet Transitions				
$C^3\Pi_u$	10.36	11.19	11.26	11.85
$B'^3\Sigma_u^-$	9.66	9.67	7.94	8.51
$W^3\Delta_u$	8.83	8.88	5.80	7.35
$B^3\Pi_g$	7.60	8.04	7.62	7.94
$A^3\Sigma_u^+$	7.88	7.75	3.47	6.25
Average Error for All Eight States				
	0.25		1.69	1.02

ground state, it fails when the description of the ground state fails. A classic example of such a failure is the DFT description of the ground states of biradicals. This problem is illustrated for the simple hydrogen molecule in Fig. 2. A similar problem is encountered for rotating around a double bond.

Figure 2 can be understood beginning from an analysis of symmetry breaking in the groundstate [52]. The stability of the Kohn-Sham wave function with respect to symmetry-breaking can be tested by considering an arbitrary unitary transformation of the orbitals,

$$\psi_r^\lambda(\mathbf{r}) = e^{i\lambda(\hat{R}+i\hat{I})}\psi_r(\mathbf{r})\,, \tag{11}$$

where $\hat{R}$ and $\hat{I}$ are real operators. After a fair amount of algebra, one arrives at the energy expression,

$$E_\lambda = E_0 + \lambda^2\left[\vec{R}^\dagger(\mathbf{A}-\mathbf{B})\vec{R} + \vec{I}^\dagger(\mathbf{A}+\mathbf{B})\vec{I}\right] + \mathcal{O}(\lambda^3)\,, \tag{12}$$

where matrix elements of the $\hat{R}$ and $\hat{I}$ operators have been arranged in column vectors and the $\mathcal{O}(\lambda)$ term disappears because the energy has already been minimized before considering symmetry-breaking. The presence of the terms $(\mathbf{A}\pm\mathbf{B})$ shows the connection with the pseudoeigenvalue problem (7). In fact, Eq. (7) can be rewritten as the eigenvalue equation

$$(\mathbf{A}+\mathbf{B})(\mathbf{A}-\mathbf{B})\vec{Z}_I = \omega_I^2\vec{Z}_I\,. \tag{13}$$

Downloaded by UNIV OF GUELPH LIBRARY on September 14, 2012 | http://pubs.acs.org
Publication Date: August 14, 2002 | doi: 10.1021/bk-2002-0828.ch009

Downloaded by UNIV OF GUELPH LIBRARY on September 14, 2012 | http://pubs.acs.org
Publication Date: August 14, 2002 | doi: 10.1021/bk-2002-0828.ch009

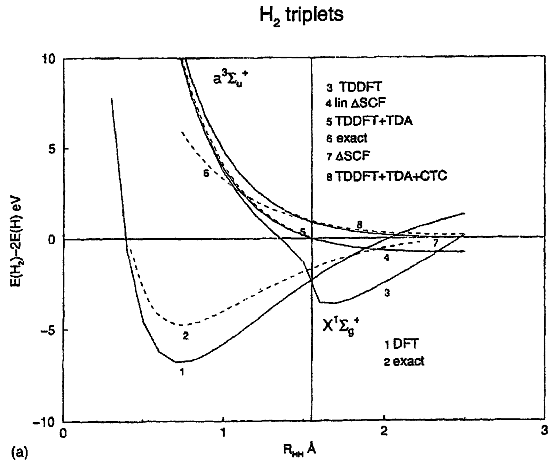

(a) Ground and triplet excited state surfaces.

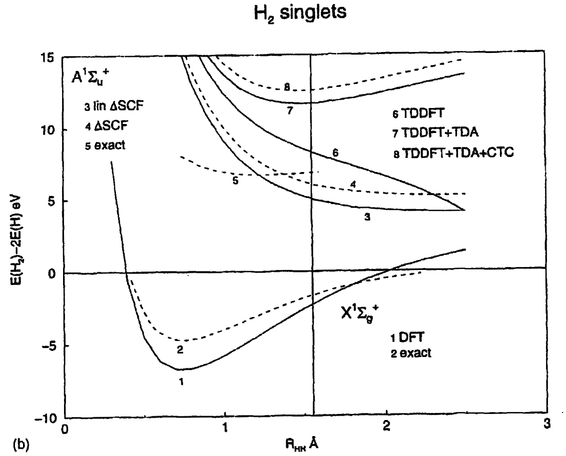

(b) Ground and singlet excited state surfaces.

Figure 2: H_2 ground and excited state surfaces. Adapted from Ref. [22].

Assuming that the *aufbau* principle is obeyed, the matrix $(\mathbf{A}-\mathbf{B})$ is always positive definite. However $(\mathbf{A}+\mathbf{B})$ may have negative eigenvalues. In that case, the energy E_λ will fall below E_0 for some value of $\vec{I}$. At the same time, this will correspond to a negative value of ω_I^2 (i.e. an imaginary value of ω_I.) This is exactly what happens in Fig. 2. At the bond distance given by the vertical line, the Kohn-Sham energy can be further lowered by allowing for different orbitals with different spin, though these orbitals no longer belong to proper representations of the molecular symmetry group. This is a disaster for calculating excited state surfaces because the triplet excitation energy falls to zero and then becomes imaginary. We might have hoped that the excitation energy would remain reasonable until fairly close to the symmetry breaking point, however Fig. 2 shows that we actually have a problem significantly before symmetry breaking occurs. (A stability analysis for the Kohn-Sham equation was also carried out by Bauernschmitt and Ahlrichs [53], but no connection was made with TDDFT excitation energies.)

In the absence of the exact exchange-correlation functional, the ultimate solution to the symmetry-breaking problem is probably some sort of multi-determinantal generalization of DFT for the groundstate. However it is interesting to note that the ΔSCF approach is in principle valid for the lowest triplet state of H_2 and the excitation energy curve is in fact quite reasonable. So one way to try to improve the TDDFT excitation energy curves is to try to incorporate some features of the ΔSCF approach. We have done this in Ref. [22]. We find that, loosely speaking, 90% of the solution to this problem comes from using the Tamm-Dancoff approximation (TDA) which consists of setting $\mathbf{B}=\mathbf{0}$. The resultant equation for excitation energies,

$$\mathbf{A}\vec{X}_I = \omega_I \vec{X}_I \,, \tag{14}$$

decouples the excitation energy problem from the problem of the stability of the ground state wave function. Results for H_2 are shown in Fig. 2. A second part of the solution is a *charge transfer correction* (CTC) [22],

$$A_{ia\sigma,ia\sigma} \leftarrow A_{ia\sigma,ia\sigma} + \omega^{\Delta \mathrm{SCF}}_{i\sigma\rightarrow a\sigma} - \Delta\epsilon_{i\sigma\rightarrow a\sigma} \,. \tag{15}$$

As shown in Fig. 2, the TDDFT+TDA+CTC triplet curve is virtually identical to the ΔSCF triplet curve. In the singlet case, the ΔSCF method is hard to justify and indeed the excited singlet curve seems to be dissociating to the wrong limit, while the TDDFT+TDA+CTC singlet curve is at least qualitatively correct.

Problems with v_{xc}. Consider now just vertical excitation energies near the equilibrium ground state geometry. It can be shown that the TDDFT ionization threshold is at $-\epsilon_{HOMO}$ [54]. As illustrated in Table 2, this

Downloaded by UNIV OF GUELPH LIBRARY on September 14, 2012 | http://pubs.acs.org
Publication Date: August 14, 2002 | doi: 10.1021/bk-2002-0828.ch009

Table 2: Data are from Refs. [54] and [36].

	Ionization Potential (eV)			
Molecule	$-\epsilon_{HOMO}^{LDA}$	$-\epsilon_{HOMO}^{AC-LDA}$	ΔSCF	Expt
N_2	10.36	15.36	15.62	15.60
CO	9.10	13.78	14.10	14.01
CH_2O	6.32	10.85	10.92	10.88
C_2H_4	6.91	11.01	10.94	10.68

threshold is too low. The reason is known and is because the asymptotic behavior of v_{xc} for nearly all common functionals falls off too quickly, leading to underbinding. Unless this is corrected, TDDFT excitation energies calculated with an extended basis set will show variational collapse. As in Fig. 3, TDLDA excitation energies above $-\epsilon_{HOMO}^{LDA}$ collapse because we are trying to describe with a finite basis set a continuum which has set in too early. A very simple correction of the asymptotic behavior of the potential is,

$$
\begin{aligned}
v_{xc}^{AC-LDA}(\mathbf{r}) &= v_{xc}^{LDA}(\mathbf{r}) \\
&- \min(IP_{\Delta \mathrm{SCF}} + \epsilon_{HOMO}, \beta\rho_\sigma^{1/3}\frac{x_\sigma^2}{1+3\beta x_\sigma \sinh^{-1} x_\sigma}), \qquad (16)
\end{aligned}
$$

where x_σ is the reduced gradient defined earlier. (Since the correction is just a rigid shift of the potential except at large r, the density and total energy remain largely unaffected.) The resultant ionization potentials are shown in Table 2. Figure 3 shows that this does indeed fix the problem of variational collapse. Since this allows us to treat higher excited states such as Rydberg states, it also allows us to treat avoided crossings between valence-type and Rydberg-type excitations, such as those in the $^1A_1$ manifold of CH_2O [18].

Ethylene is an important molecule for photochemistry, so it is important to describe its excited states as well as possible. While correcting the asymptotic behavior of v_{xc} helps immensely in the TDDFT description of higher π excited states, we have noticed that certain excitations out of the σ manifold of orbitals are too low in TDDFT [54]. This is particularly problematic because these σ excitations mix artifactually with the π excitations around 8 eV to give a false picture of the nature of the excited states (Fig. 4). We have traced this back to problems with the relative energies of the occupied σ and π orbitals[36], by using the fact that the TDA is often a good approximation near the ground state equilibrium geometry and that relaxation is often relatively small in DFT. This latter point makes

Downloaded by UNIV OF GUELPH LIBRARY on September 14, 2012 | http://pubs.acs.org
Publication Date: August 14, 2002 | doi: 10.1021/bk-2002-0828.ch009

Downloaded by UNIV OF GUELPH LIBRARY on September 14, 2012 | http://pubs.acs.org
Publication Date: August 14, 2002 | doi: 10.1021/bk-2002-0828.ch009

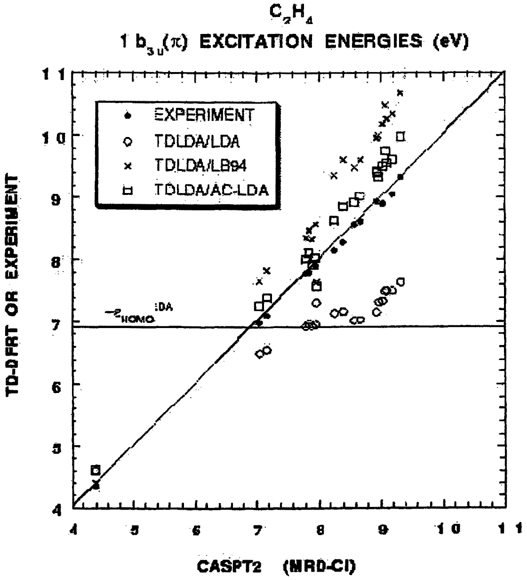

Figure 3: Variational collapse of ethylene π excitation energies of above the TDLDA ionization threshold at $-\epsilon_{HOMO}^{LDA}$. From Ref. [36].

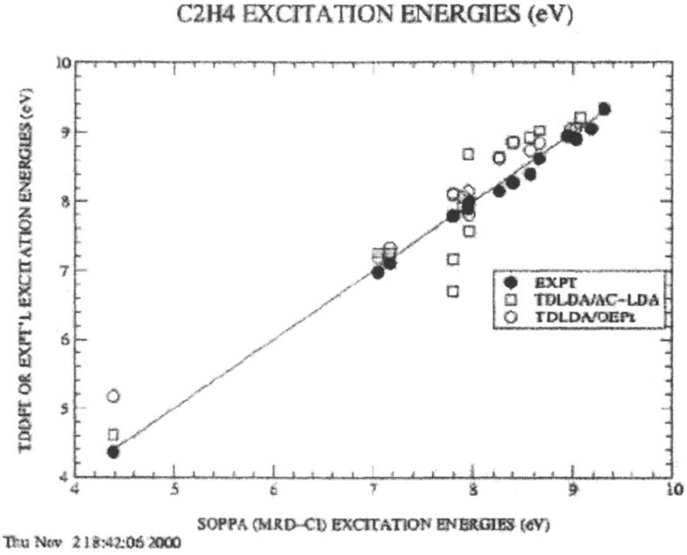

Figure 4: Comparison of *all* one-electron excitation energies of C_2H_4 with those from good *ab initio* calculations.

Table 3: C_2H_4 $^{1,3}B_{1g}[1b_{3g}(\pi'_{CH_2}), 1b_{2g}(\pi^*)]$ Excitation Energies (eV). Data from Refs. [36] and [55].

Method	ω_T	ω_S	$\Delta\epsilon$
TDLDA/LB94	6.59	7.08	6.83
TDLDA/AC-LDA	6.70	7.16	6.92
TDLDA/LDA	6.93	6.98	7.19
ΔSCF/LDA	7.13	7.19	7.52
TDLDA/OEPx	8.1	8.46	8.34
Expt		9.2	
TDHF		9.22	
CIS	8.56	9.28	
CIS-MP2	8.96	9.31	

DFT very different than Hartree-Fock. It is well-known that Hartree-Fock orbitals are ill-adapted for describing the excitation process because the unoccupied orbitals see one more electron than do the occupied orbitals. In contrast, DFT orbitals are much better adapted to describing the excitation process because the occupied and unoccupied orbitals see the same potential. Thus, as long as the charge density remains roughly the same for the initial and final states and we are not near an avoided crossing where there are nontrivial configuration mixing effects, the excitation can be described in terms of a simple two-level model (2LM) as a single promotion $\psi_i \rightarrow \psi_a$ plus singlet and triplet spin coupling. Within the 2LM+TDA, it can be shown that,

$$\omega_T \leq \Delta\epsilon \leq \omega_S \tag{17}$$

and the singlet-triplet splitting gets smaller as we go to Rydberg states[36]. This and Table 3 allow us to see that the problem in ethylene with TDDFT excitations out of the σ system of ethylene lies at the orbital energy level, at least in the case of the $1b_{3g}(\pi'_{CH_2}) \rightarrow 1b_{2g}(\pi^*)$ excitation (the $1b_{3g}(\pi'_{CH_2})$ looks like an in-plane π^*-like arrangement of CH sigma bonds.) In particular, with the LDA, LB94, and AC-LDA functionals, the simple orbital energy difference lies ***significantly lower*** than the expected triplet excitation energy around 8.5 eV.

This indicates that v_{xc} is not only incorrect in the large r region, but is also subtly incorrect in regions of space important for occupied orbitals. In order to solve this problem, it suffices to calculate a more accurate potential. According to Kohn and Sham[5], the exact exchange-correlation potential is simply that which satisfies the condition that the *difference* of the charge

Downloaded by UNIV OF GUELPH LIBRARY on September 14, 2012 | http://pubs.acs.org
Publication Date: August 14, 2002 | doi: 10.1021/bk-2002-0828.ch009

Downloaded by UNIV OF GUELPH LIBRARY on September 14, 2012 | http://pubs.acs.org
Publication Date: August 14, 2002 | doi: 10.1021/bk-2002-0828.ch009

densities is zero:

$$0 = \Delta\rho_\sigma(\mathbf{r}) = \rho_\sigma^{\text{exact}}(\mathbf{r}) - \rho_\sigma^{\text{DFT}}(\mathbf{r})\,. \tag{18}$$

This is almost the same in the exchange-only case as the optimized effective potential which is defined by requiring that the *linear response* of the charge density is zero,

$$0 = \delta\rho_\sigma(\mathbf{r}) = \int\int \left(\Sigma_x^\sigma[\gamma_{DFT}](\mathbf{r};\mathbf{r}') - v_x^\sigma(\mathbf{r})\delta(\mathbf{r}-\mathbf{r}')\right)\gamma_{DFT}^\sigma(\mathbf{r}';\mathbf{r})\,d\mathbf{r}d\mathbf{r}'\,, \tag{19}$$

where $\hat{\Sigma}_x^\sigma$ is the HF exchange potential. Equivalently v_x^σ is the multiplicative potential whose orbitals minimize the HF energy expression [56, 57]. We have programmed and carried out exchange-only OEP calculations for molecules within a resolution-of-the-identity methodology, without use of 4-center integrals [55]. To be fair, these calculations entail numerous subtle numerical difficulties [55, 58], but we are reasonably confident about the quality of the results presented here. Figures 5 and 6 show what happens to the orbital energies in C_2H_4. In both cases, the simple AC-LDA gives orbital energies in reasonably good agreement with our OEP calculations. However the small relative differences for the σ and π orbitals are important, bringing the OEP orbital energy difference in Table 3 much more in-line with the expected value. Figure 4 shows that although our TDLDA/OEPx calculations have neglected correlation in v_{xc} (though not in f_{xc}) we are, as hoped, able to clean up the structure of the excited states around 8 eV.

Problems with f_{xc}. As mentioned earlier, the adiabatic approximation is a low frequency (low energy) approximation. It is thus natural to ask how and where the frequency dependence of f_{xc} should become important. Two rather different types of frequency dependence are important in this context [59]. The first type (dispersion) consists of a continuous variation of $f_{xc}(\omega)$ as a function of ω, and will result in shifted excitation energies. The second type (pole structure) consists of the probable presence of singularities in $f_{xc}(\omega)$ at particular values of ω. This pole structure is associated with the appearance of additional satellite peaks in the electronic absorption spectra, due to mixing of many-electron with one-electron excitations.

The development of useful exchange-correlation kernels which go beyond the adiabatic approximation has been a slow process, but a recent application of one such kernel to semiconductors is encouraging [60]. I will give a brief overview of some of the principal work leading up to this recent application. The first attempt at a frequency-dependent exchange-correlation kernel was given by Gross and Kohn [61]. Almost a decade later, Dobson proved the harmonic potential theorem (HPT) which must be obeyed by

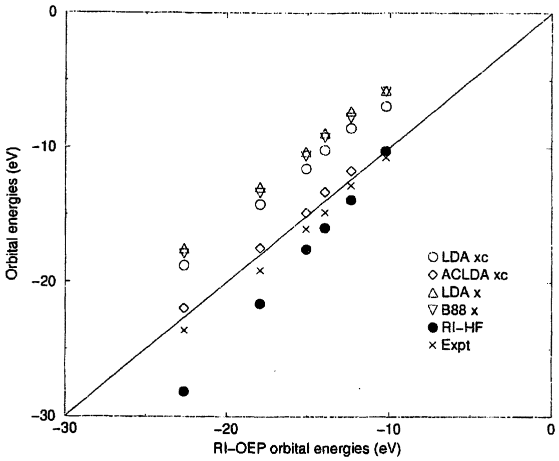

Figure 5: Correlation graph between various exchange, exchange-correlation methods, and OEP for C_2H_4: all 6 occupied valence orbitals. From Ref. [55].

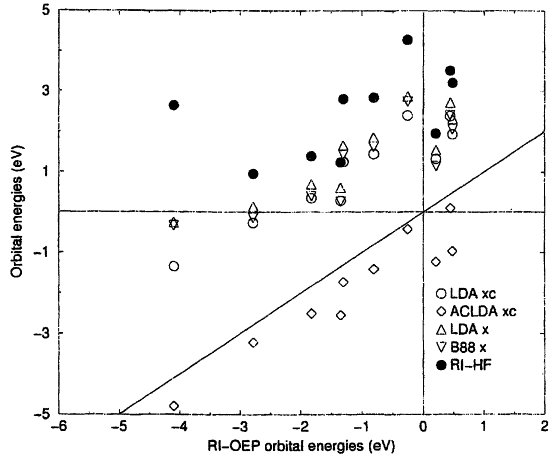

Figure 6: Correlation graph between various x-only method and OEP for C_2H_4: 10 unoccupied orbitals. From Ref. [55]

Downloaded by UNIV OF GUELPH LIBRARY on September 14, 2012 | http://pubs.acs.org
Publication Date: August 14, 2002 | doi: 10.1021/bk-2002-0828.ch009

any admissible $f_{xc}(\omega)$ [62]. He showed that the adiabatic approximation satisfies the HPT but that the suggestion of Gross and Kohn does not. Vignale gave a general condition guaranteeing that exchange-correlation functionals obey the HPT [63]. Vignale and Kohn [64] showed that the exchange-correlation potential in TDDFT is an intrinsically nonlocal functional of the charge density which does not admit a gradient expansion, unless the theory is reformulated to also include a dependence on the current density, $\vec{j} = (1/2i)\sum_i f_i(\psi_i^* \vec{\nabla}\psi_i + \psi_i \vec{\nabla}\psi_i^*)$. They gave an explicit form for the exchange-correlation functional in the case of a perturbation of the homogeneous electron gas which is slowly varying on the scales of k_F^{-1} ($\sim$ interelectron distance) and v_F/ω ($\sim$ distance traveled by an electron during a period of the perturbing field.) Vignale, Ullrich, and Conti reformulated the Vignale-Kohn theory in terms of the exchange-correlation viscoelastic stress tensor [65]. Dobson, Bünner, and Gross have presented a generalization of the Vignale-Kohn theory [66]. In order to apply these theories, one must also know the frequency dependence of $f_{xc}(\omega)$ for the homogeneous electron gas. This has been studied by Nifosì, Conti, and Tosi [67]. The exchange-correlation kernel for the homogeneous electron gas is a relatively flat function of frequency at low frequency, varies more rapidly as the plasmon frequency is approached, and has a sharp mininum at twice the plasmon frequency where two plasmon excitations become possible. Such a minimum is a typical sign of residual pole structure when going from a discrete bound state problem to a continuum problem such as the homogeneous electron gas. However this particular feature is not especially relevant for the Vignale-Kohn-Ullrich-Conti theory which is for slowly varying perturbations. The problem addressed by de Boeij, Kootstra, Berger, van Leeuwen, and Snijders [60] was to include the macroscopic exchange-correlation electric field in calculations of semiconductor excitation spectra. This is a nontrivial highly nonlocal contribution to the exchange-correlation functional associated with the development of surface charges and changes in the reaction field due to these charges when a polarizable solid is placed in an electric field. de Boeij *et al.* show how to derive an expression for the macroscopic exchange-correlation electric field in terms of the Vignale-Kohn-Ullrich-Conti theory and demonstrate how this improves absorption spectra for semiconductors, thus giving the first explicit example of a density-polarization functional.

It has been the author's contention that, at least for small molecules, the breakdown of the adiabatic approximation is rather minor for one-electron excitations compared to errors already present when common popular functionals are used in the adiabatic approximation. This contention has been largely confirmed by the general quality of excitation energies obtained by asymptotically-corrected functionals. Nevertheless it is known that, in con-

Downloaded by UNIV OF GUELPH LIBRARY on September 14, 2012 | http://pubs.acs.org
Publication Date: August 14, 2002 | doi: 10.1021/bk-2002-0828.ch009

trast to common practical functionals which are relatively short ranged,

$$f_x^{\sigma,\tau}(\mathbf{r},\mathbf{r}') \cong \delta(\mathbf{r}-\mathbf{r}')f_x^{\sigma,\tau}(\mathbf{r},\mathbf{r}) \,, \tag{20}$$

the exact adiabatic exchange-correlation kernel is most likely rather long ranged. Thus Petersilka, Gossmann, and Gross[68] have shown that the kernel corresponding to Slater's model for the exchange-only potential, v_x, is

$$f_x^{\sigma,\tau}(\mathbf{r},\mathbf{r}') = -\delta_{\sigma,\tau}\frac{|\gamma^\sigma(\mathbf{r},\mathbf{r}')|^2}{\rho_\sigma(\mathbf{r})|\mathbf{r}-\mathbf{r}'|\rho_\sigma(\mathbf{r}')} \,. \tag{21}$$

It might also contain particle-number derivative discontinuities [59]. Fortunately neglect of these effects in approximate adiabatic kernels does not seem to be a problem in many applications.

Applications where the overlocality of the kernel *does* seem to be a problem include finite segments of conducting polymers where the TDDFT method overestimates the dipole polarizability along the chain and this overestimate can be made as large as you like by simply making the segment longer and longer, [69] and improper scaling with respect to the number of K points in periodic calculations. [13] Since the hope is that DFT calculations should be useful for larger molecules than traditional *ab initio* calculations, it is disappointing to see cases where the error due to the functional seems to grow with the size of the molecule. Errors due to the overlocality of the kernel have also been seen as underestimated charge-transfer excitations in small molecules. [52, 35]

The solution at this point is not entirely clear but the area is under very active investigation. Certainly part of the solution for conducting polymers would seem to be the density-polarization functional of Boeij *et al.* [60], if it can be adopted for molecular solids and for isolated molecules. I have also already mentionned the Slater approximation for the kernel [68], and the charge-transfer correction [52, 22]. Recently, Burke, Petersilka, and Gross have combined these two ideas to suggest a hybrid method in which the parallel-spin component of the kernel is approximated by the Slater approximation while the TDLDA is retained for the antiparallel component of the kernel. [70] Since the basis for the charge-transfer correction was the idea that, at least under certain circumstances, the TDDFT and DFT ΔSCF methods should give the same excitation energies, I am excited by the recent demonstration of Gonze and Scheffler [71] that TDDFT with the TDA and 2LM gives the same answer as the ΔSCF method applied in the context of Görling-Levy adiabatic connection perturbation theory provided the exact exchange-only optimized potential theory is used within the Keldysh formalism of van Leeuwen [72].

Downloaded by UNIV OF GUELPH LIBRARY on September 14, 2012 | http://pubs.acs.org
Publication Date: August 14, 2002 | doi: 10.1021/bk-2002-0828.ch009

CONCLUSION

The presence of TDDFT in most well-known quantum chemistry packages and its present popularity for applications, is an indication of the fact that TDDFT often works reasonably well in comparison with traditional *ab initio* methods, especially for larger molecules. It is in fact remarkable that a method which was virtually unknown in the quantum chemistry community as little as half a decade ago should have been so widely accepted. It has been the purpose of this chapter to give a (necessarily biased) overview of present-day limitations of this still-young method and to suggest what directions should be pursued to improve functionals for practical applications of TDDFT. Together we have climbed the rungs of the ladders on Jacob's jungle gym (Fig. 1). It is my hope that the reader will be able to take this information and be able to make somewhat wiser decisions about the choice of rungs appropriate for their accuracy requirements and computational resources.

ACKNOWLEDGEMENT The work reported here was carried out while the author was employed as Chemistry Computing Professional at the Université de Montréal. I would like to thank my numerous coauthors. I am particularly grateful to Professor Dennis R. Salahub for his friendship and support over the years. Financial support for this work came from a variety of funding sources over the years, including the Canadian Centre of Excellence in Molecular and Interfacial Dynamics (CEMAID), the Natural Sciences and Engineering Research Council (NSERC) of Canada, the Canadian Institute for Photonics Innovation (CIPI), the Fonds pour la formation des chercheurs et l'aide à la recherche (FCAR) of Québec, and the Conseil National de Recherche Scientifique (CNRS) of France (while I was in Toulouse.)

References

[1] Perdew, J.P.; Schmidt, K.; in: *Density Functional Theory and Its Applications to Materials*, edited by V.E. Van Doren, K. Van Alseoy, and P. Geerlings (American Institute of Physics, 2001). See also http://www-chimie.ujf-grenoble.fr/PERSONNEL/LEDSS7/casida/CompChem/DFT.html

[2] http://www.nobel.se/chemistry/laureates/1998/press.html .

[3] Car, R.; Parrinello, M *Phys. Rev. Lett.* **1985**, *55*, 2471.

Downloaded by UNIV OF GUELPH LIBRARY on September 14, 2012 | http://pubs.acs.org
Publication Date: August 14, 2002 | doi: 10.1021/bk-2002-0828.ch009

[4] Hohenberg, P.; Kohn, W.; *Phys. Rev.* **1964** *136*, B864.

[5] Kohn, W.; Sham, L.J.; *Phys. Rev.* **1965**, *140*, A1133.

[6] Casida, M.E.; in *Recent Advances in Density Functional Methods, Part I*, edited by D.P. Chong (World Scientific, Singapore, 1995), p. 155.

[7] Jamorski, C.; Casida, M.E.; Salahub, D.R.; *J. Chem. Phys.* **1996** *104*, 5134.

[8] Sundholm, D.; *Chem. Phys. Lett.* **1999**, *26*, 480.

[9] Bauernschmitt, R.; Ahlrichs, R.; Hennrich, F.H.; Kappes, M.M.; *J. Am. Chem. Soc.* **1998**, *120*, 5052.

[10] Champagne, B.; Perpète, E.A.; van Gisbergen, S.J.A; Baerends, E.J.; Snijders, J.G.; Soubra-Ghaoui, C.; Robins, K.A.; Kirtman, B.; *J. Chem. Phys.* **1998** *109*, 10489.

[11] van Gisbergen, S.J.A.; Schipper, P.R.T.; Gritsenko, O.V.; Baerends, E.J.; Snijders, J.G.; Champagne, B.; Kirtman, B.; *Phys. Rev. Lett.* **1999**, *83*, 694.

[12] Yabana K.; Bertsch, G.F.; *Int. J. Quant. Chem.* **1999** *75*, 55.

[13] Hirata, S.; Head-Gordon, M.; Bartlett, R.J.; *J. Chem. Phys.* **1999** *111*, 10774.

[14] van Gisbergen, S.J.A.; Groeneveld, J.A.; Rosa, A.; Snijders, J.G.; Baerends, E.J.; *J. Phys. Chem.* **1999**, *103*, 6835.

[15] Boulet, P.; Chermette H.; Daul C.; Gilardoni, F.; Rogemond, F.; Weber, J.; Zuber, G.; *J. Phys. Chem. A* **2001**, *105*, 885.

[16] Nguyen, K.A.; Day, P.N.; Pachter, R.; *J. Chem. Phys.* **1999**, *110*, 9135.

[17] Lhiouhet, V.; Gutierrez, F.; Penaud, F.; Amouyal, E.; Daudey, J.-P.; Poteau, R.; Chouini-Lalanne, N.; Paillous, N.; *New Journal of Chemistry* **2000** *24*, 403.

[18] Casida, M.E.; Casida, K.C.; Salahub, D.R.; *Int. J. Quant. Chem.* **1998** *70*, 933.

[19] Spielfiedel, A.; Handy, N.C.; *Phys. Chem. Chem. Phys.* **1999**, *1*, 2401.

[20] Ben-Nun, M.; Martínez, T.J.; *Chem. Phys.* **2000**, *257*, 237. (See footnote 2.)

Downloaded by UNIV OF GUELPH LIBRARY on September 14, 2012 | http://pubs.acs.org
Publication Date: August 14, 2002 | doi: 10.1021/bk-2002-0828.ch009

[21] Singh, R.; Deb, B.M.; *Physics Reports* **1999**, *311*, 47.

[22] Casida, M.E.; Gutierrez, G.; Guan, J.; Gadea, F.-X.; Salahub, D.R.; Daudey, J.-P.; *J. Chem. Phys.* **2000**, *113*, 7062.

[23] Gritsenko, O.V.; van Gisbergen, S.J.A.; Görling, A.; Baerends, E.J.; *J. Chem. Phys.* **2000**, *113*, 8478.

[24] Van Caillie, C.; Amos, R.D.; *Chem. Phys. Lett.* **1999**, *308*, 249.

[25] Van Caillie, C.; Amos, R.D.; *Chem. Phys. Lett.* **2000**, *317*, 159.

[26] Frank, I.; Hutter, J.; Marx, D.; Parrinello, M.; *J. Chem. Phys.* **1998**, *108*, 4060.

[27] Dotsinis, N.L.; Sprik, M.; *Chem. Phys. Lett.* **2000**, *330*, 563.

[28] Röhrig, U.; Laio, A.; VandeVondele, J.; Hullo, J; Röthlisberger, U; *unpublished.*

[29] Bartlett, R.J.; in *Chemistry for the 21st Century*, edited by E. Keinan and I. Schechter (Wiley-VCH, Weinheim, 2000), p. 271.

[30] Koch, W.; Holthausen, M.C.; *A Chemist's Guide to Density Functional Theory* (Wiley-VCH, New York, 2000),

[31] Hamprecht, F.A.; Cohen, A.J.; Tozer, D.J.; Handy, N.C.; *J. Chem. Phys.* **1998** *109*, 6264.

[32] van Leeuwen, R.; Baerends, E.J.; *Phys. Rev. A* **1994** *49* 2421.

[33] Gritsenko, O.V.; Schipper, P.R.T.; Baerends, E.J.; *Chem. Phys. Lett.* **1999** *302*, 199.

[34] Tozer, D.J.; Handy, N.C.; *J. Chem. Phys.* **1998**, *108*, 2545.

[35] Tozer, D.J.; Amos, R.D.; Handy, N.C.; Roos, B.O.; Serrano-Andrés, L.; *Mol. Phys.* **1999** *97*, 859.

[36] Casida, M.E.; Salahub, D.R.; *J. Chem. Phys.* **2000**, *113*, 8918.

[37] Grüning, M.; Gritsenko, O.V.; van Gisbergen, S.J.A.; Baerends, E.J.; *J. Chem. Phys.* **2001**, *114*, 652.

[38] Ziegler,T; Rauk, A.; Baerends, E.J.; *Theor. Chim. Acta* **1977**, *43*, 877.

[39] Daul, C.; *Int. J. Quant. Chem.* **1994**, *52*, 867.

[40] Peuckert, V; *J. Chem. Phys. C* **1978**, *11*, 4945.

Downloaded by UNIV OF GUELPH LIBRARY on September 14, 2012 | http://pubs.acs.org
Publication Date: August 14, 2002 | doi: 10.1021/bk-2002-0828.ch009

[41] Chakravarty, S.; Fogel, M.B.; Kohn, W.; *Phys. Rev. Lett.* **1979**, *43*, 775.

[42] Bartolotti, L.J.; *Phys. Rev. A* **1981**, *24*, 1661.

[43] Bartolotti, L.J.; *Phys. Rev. A* **1982**, *26*, 2243.

[44] Deb, B.H.; Ghosh, S.K.; *J. Chem. Phys.* **1982**, *77*, 342.

[45] Runge, E.; Gross, E.K.U.; *Phys. Rev. Lett.* **1984**, *52*, 997.

[46] Kohl, H.; Dreizler, R.M.; *Phys. Rev. Lett.* **1986**, *56*, 997.

[47] Mearns, D.; Kohn, W.; *Phys. Rev. A* **1987**, *35*, 4796.

[48] van Leeuwen, R.; *Phys. Rev. Lett.* **1998**, *80*, 1280.

[49] Gross, E.K.U.; Kohn, W.; *Adv. Quant. Chem.* **1990**, *21*, 255.

[50] Gross, E.K.U.; Ullrich, C.A.; Gossmann, U.J.; in *Density Functional Theory*, edited by E.K.U. Gross and R.M. Dreizler, NATO ASI Series (Plenum, New York, 1994), p. 149.

[51] Gross, E.K.U.; Dobson, J.F.; Petersilka, M.; in *Density Functional Theory II*, Vol. 181 of *Topics in Current Chemistry*, edited by R.F. Nalewajski (Springer, Berlin, 1996), p. 149.

[52] M.E. Casida, in the *On-line Workshop Proceedings of the Joint ITP/INT Workshop on Time-Dependent Density Functional Theory*, 15-17 April 1999, Institute for Theoretical Physics, University of California at Santa Barbara: http://www.itp.ucsb.edu/online/tddft_c99/

[53] Bauernschmitt, R.; Ahlrichs, R.; *J. Chem. Phys.* **1996**, *104*, 9047.

[54] Casida, M.E.; Jamorski, C.; Casida, K.C.; Salahub, D.R.; *J. Chem. Phys.* **1998** *108*, 4439.

[55] Hamel, S.; Casida, M.E.; Salahub, D.R.; *J. Chem. Phys.* in press.

[56] Sharp, R.T.; Horton, G.K.; *Phys. Rev.* **1953**, *90*, 317.

[57] Talman, J.D.; Shadwick, W.F.; *Phys. Rev. A* **1976**, *14*, 36.

[58] Hirata, S.; Ivanov, S.; Grabowski, I.; Bartlett, R.J.; Burke, K.; Talman, J.D.; *J. Chem. Phys.* **2001**, *115*, 1635.

[59] Casida, M.E.; in *Recent Developments and Applications of Modern Density Functional Theory*, edited by J.M. Seminario (Elsevier, Amsterdam, 1996), p. 391.

Downloaded by UNIV OF GUELPH LIBRARY on September 14, 2012 | http://pubs.acs.org
Publication Date: August 14, 2002 | doi: 10.1021/bk-2002-0828.ch009

[60] de Boeij, P.L.; Kootstra, F.; Berger, J.A.; van Leeuwen, R.; Snijders, J.G.; *J. Chem. Phys.* **2001**, *115*, 1995.

[61] Gross, E.K.U.; Kohn, W.; *Phys. Rev. Lett.* **1985**, *55*, 2850.

[62] Dobson, J.F.; *Phys. Rev. Lett.* **1994**, *73*, 2244.

[63] Vignale, G.; *Phys. Rev. Lett.* **1995**, *74*, 3233.

[64] Vignale, G.; Kohn, W.; *Phys. Rev. Lett.* **1996**, *77*, 2037.

[65] Vignale, G.; Ullrich, C.A.; Conti, S.; *Phys. Rev. Lett.* **1997**, *79*, 4878.

[66] Dobson, J.F.; Bünner, M.J.; Gross, E.K.U.; *Phys. Rev. Lett.* **1997**, *79*, 1905.

[67] Nifosì, R.; Conti, S.; Tosi, P.; *Phys. Rev. B*, **1998**, *58*, 12758.

[68] Petersilka, M.; Gossmann, U.J.; Gross, E.K.U.; *Phys. Rev. Lett.* **1996** *76*, 1212.

[69] Champagne, B.; *et al.*; *J. Chem. Phys.* **1998**, *109*, 10489.

[70] Burke, K.; Petersilka, M.; and Gross, E.K.U.; in ***Recent Advances in Density Functional Methods, Vol III***, edited by P. Fantucci and A. Bencini (World Scientific Press, 2000).

[71] Gonze, X.; Scheffler, M.; *Phys. Rev. Lett.* **1999** *82*, 4416.

[72] van Leeuwen, R.; *Phys. Rev. Lett.* **1998** *80*, 1280.

Downloaded by UNIV OF GUELPH LIBRARY on September 14, 2012 | http://pubs.acs.org
Publication Date: August 14, 2002 | doi: 10.1021/bk-2002-0828.ch009

Downloaded by COLUMBIA UNIV on September 14, 2012 | http://pubs.acs.org
Publication Date: August 14, 2002 | doi: 10.1021/bk-2002-0828.ch010

Chapter 10

Spectral Theory of Chemical Bonding

P. W. Langhoff[1-3], J. A. Boatz[3], R. J. Hinde[4], and J. A. Sheehy[3]

[1]**Department of Chemistry, Indiana University, Bloomington, IN 47405–4001**
[2]**San Diego Supercomputer Center, University of California at San Diego,**
9500 Gilman Drive, La Jolla, CA 92093–0505
[3]**Air Force Research Laboratory, AFRL/PRSP, 10 East Saturn Boulevard,**
Edwards Air Force Base, CA 93524–7680
[4]**Department of Chemistry, University of Tennessee, Knoxville, TN 37996–1600**

New theoretical methods are reported for obtaining the binding energies of molecules and other chemical aggregates employing the spectral eigenstates and related properties of their atomic constituents. Wave function antisymmetry in the aggregate atomic spectral-product basis is enforced by unitary transformation performed subsequent to formation of the Hamiltonian matrix, greatly simplifying its construction. Spectral representatives of the individual atomic number-density operators, which can be determined once and for all and tabulated for future use, provide the computational invariants of the development. Calculations of the lowest-lying attractive and repulsive states of the two-electron pair bond (H_2) as functions of atomic separation illustrate the nature of the formalism and its convergence to values in accord with results obtained employing conventional methods.

[†] Work supported in part by grants from the U.S. Air Force Office of Scientific Research.

In Low-Lying Potential Energy Surfaces; Hoffmann, M., et al.;
ACS Symposium Series; American Chemical Society: Washington, DC, 2002.

Introduction

Adiabatic electronic wave functions (*1*) have long provided a useful starting point for quantitative predictions of chemical structures and the pathways of chemical reactions (*2*). Computational methods for such purposes commonly employ totally antisymmetric basis functions in repeated calculations of the total electronic energy of a molecule or other chemical aggregate at a large number of atomic configurations, with binding energies at stable structures obtained in this way by subtracting the calculated energies of the non-interacting constituent atoms. A similar strategy is adopted in density-functional methods (*3*), which cleverly circumvent determinations of correlated many-electron wavefunctions but nevertheless calculate total energies, rather than binding energies, over the relevant range of aggregate geometries. Such methods have provided a great wealth information on structures and selected physical properties of molecules, but they arguably do not constitute a quantum theory of bonding in which chemical interaction energies are expressed in terms of intrinsic atomic properties (*4*).

Downloaded by COLUMBIA UNIV on September 14, 2012 | http://pubs.acs.org
Publication Date: August 14, 2002 | doi: 10.1021/bk-2002-0828.ch010

Role of the Symmetric Group

A significant barrier to development of an atomic-interaction-based theory of chemical bonding is found in the antisymmetry requirement placed on physically admissible solutions of the Schrödinger equation (*5*). Specifically, the permutation symmetry group of a collection of N non-interacting atoms is given by the direct product group $S_{n_1} \otimes S_{n_2} \otimes \cdots S_{n_N}$ of the electron permutation groups $S_{n_1}, S_{n_2}, \cdots S_{n_N}$ of the individual atoms, which is a *sub-group* of the permutation group $S_{n_{total}}$ ($n_{total} = n_1 + n_2 + \cdots + n_N$) for the entire aggregate (*6*). As a consequence, the outer product of atomic eigenstates familiar from the perturbation theory of long-range interactions (*7*), which is correct in the atomic separation limit and provides an appropriately universal basis for describing chemical interactions (*8,9*), is reducible in $S_{n_{total}}$ and generally contains irreducible representations of $S_{n_{total}}$ other than the desired totally antisymmetric representation (*6,10*). Moreover, some of these non-totally-antisymmetric representations are known to contain unphysical continua in which the physical Schrödinger eigenstates can be embedded (*11,12*). Outer-product reduction methods for isolating the totally antisymmetric subspace of the atomic spectral-product basis (*6*) are not generally suitable for this construction (*10*), and symmetry-adapted perturbative approaches which adopt alternative strategies to accomplish the required isolation of the totally antisymmetric subspace are either ineffectual or are inappropriate for the large charge distortions consequent of chemical bonding (*12,13*). Of course, the usual prior antisymmetrization of the basis does not allow the desired separation of the Hamiltonian

Downloaded by COLUMBIA UNIV on September 14, 2012 | http://pubs.acs.org
Publication Date: August 14, 2002 | doi: 10.1021/bk-2002-0828.ch010

matrix into constituent atomic energies and their interactions in the aggregate, and can give rise to linear dependence and associated computational instablities. New approaches which can overcome the difficulties associated with employing an atomic-product representation in studies of chemical interactions, while retaining the conceptual and computational advantages associated with such an interaction-energy-based approach, are clearly required.

Spectral Theory

In the present report, a new theoretical approach to chemical bonding is described based on the outer spectral-product representation of the interacting atoms (*7-9*). The aforementioned symmetric-group issues are overcome by deferring enforcement of wave function antisymmetry until *after* the construction of the matrix representative of the Hamiltonian in the spectral-product basis. The aggregate Hamiltonian matrix obtained in this way is additive in the energies of the atomic constituents and in their pairwise interactions. The atomic interaction-energy matrices can be expressed entirely in terms of spectral representatives of the electronic number-density operators of the individual atoms, which provide the computational invariants of the formalism. Since the required atomic spectral information can be determined once and for all from conventional electronic structure theory calculations, there is no need for the repeated evaluations of Hamiltonian matrix elements as integrals over antisymmetric many-electron basis functions required in standard molecular calculations (*2,3*). Construction and storage of the potentially very large Hamiltonian matrix that can arise in the spectral-product representation can be avoided by employing chemically relevant test functions and recursion methods in performing a unitary transformation to isolate its much smaller totally antisymmetric block. In this way, a physically significant Hamiltonian matrix is obtained from the non-interacting atomic energies, Heitler-London-like Coulomb and exchange terms, and contributions from spectral excitations which correspond to dispersion and polarization terms familiar from long-range pertubation theory (*7*).

Theoretical Formalism

The essential features of the formalism are described here for an aggregate of n hydrogen atoms, with more general results reported elsewhere (*14*). The orthonormal spectral-product basis in this case is the outer product row vector $\boldsymbol{\Phi}(\mathbf{1},\mathbf{2},\ldots\boldsymbol{n}) = \{\boldsymbol{\Phi}^{(1)}(\mathbf{1}) \otimes \boldsymbol{\Phi}^{(2)}(\mathbf{2}) \otimes \cdots \boldsymbol{\Phi}^{(n)}(\boldsymbol{n})\}$ of n-electron product functions, each of which consists of products of n functions, one each taken from the indicated one-electron spin-orbital row vectors $\Phi^{(1)}(\mathbf{1}), \Phi^{(2)}(\mathbf{2}), \ldots \Phi^{(n)}(\boldsymbol{n})$. Although the n-electron functions so defined are not individually antisymmetric, the spectral-product basis is nevertheless complete for representations of antisymmetric states (*7,8*), and contains the totally antisymmetric representation once and only once (*14*).

The many-electron (Coulombic) Hamiltonian operator in the spectral-product basis is

$$\mathbf{H}(\boldsymbol{R}) = \sum_{\alpha=1}^{n} \left\{ \mathbf{H}^{(\alpha)} + \sum_{\beta=1}^{n} (\beta > \alpha)\, \mathbf{V}^{(\alpha,\beta)}(\boldsymbol{R}_{\alpha\beta}) \right\}, \tag{1}$$

where

$$\mathbf{H}^{(\alpha)} = \mathbf{I}^{(1)} \otimes \mathbf{I}^{(2)} \otimes \cdots \mathbf{E}^{(\alpha)} \otimes \cdots \mathbf{I}^{(n)} \tag{2}$$

and

$$\mathbf{V}^{(\alpha,\beta)}(\boldsymbol{R}_{\alpha\beta}) = \mathbf{I}^{(1)} \otimes \mathbf{I}^{(2)} \otimes \cdots \mathbf{v}^{(\alpha,\beta)}(\boldsymbol{R}_{\alpha\beta}) \otimes \cdots \mathbf{I}^{(n)} \tag{3}$$

are the indicated outer matrix products. Here, $\boldsymbol{R}$ specifies the entire aggregate atomic configuration, $\boldsymbol{R}_{\alpha\beta}$ is an atomic separation vector, and $\mathbf{I}^{(\alpha)}$ is the unit matrix and $\mathbf{E}^{(\alpha)}$ the diagonal matrix of energies for the atom α. As has been noted previously (*14*), the Hamiltonian matrix of Eq. (1) is rigorously additive in the pairwise interaction-energy matrices $\mathbf{V}^{(\alpha,\beta)}(\boldsymbol{R}_{\alpha\beta})$ of Eq. (3). In the latter equation

$$\mathbf{v}^{(\alpha,\beta)}(\boldsymbol{R}_{\alpha\beta}) = \mathbf{D}^{(\alpha,\beta)}(\hat{\boldsymbol{R}}_{\alpha\beta})^{\dagger} \cdot \mathbf{v}^{(\alpha,\beta)}(R_{\alpha\beta}) \cdot \mathbf{D}^{(\alpha,\beta)}(\hat{\boldsymbol{R}}_{\alpha\beta}), \tag{4}$$

where $\mathbf{D}^{(\alpha,\beta)}(\hat{\boldsymbol{R}}_{\alpha\beta})$ is comprised of products of rotation matrices (*15,16*) at the sites α and β, $\hat{\boldsymbol{R}}_{\alpha\beta}$ is the angular orientation of atom β relative to the site α, $R_{\alpha\beta}$ is the corresponding scalar separation, and $\mathbf{v}^{(\alpha,\beta)}(R_{\alpha\beta})$ is a reduced interaction-energy matrix for the interacting pair oriented along a standard z coordinate axis. The latter matrix is given by the expression

$$\mathbf{v}^{(\alpha,\beta)}(R_{\alpha\beta}) = \frac{1}{2\pi^2} \int_{\mathbf{k}} d\mathbf{k}\, e^{ik_z R_{\alpha\beta}} \left\{ \boldsymbol{\alpha}(\mathbf{k}) \otimes \boldsymbol{\beta}(\mathbf{k})^{\dagger} \right\}, \tag{5}$$

with

$$\boldsymbol{\alpha}(\mathbf{k}) = (e/k) \int_{\boldsymbol{r}_\alpha} d\boldsymbol{r}_\alpha\, \boldsymbol{\gamma}^{(\alpha)}(\boldsymbol{r}_\alpha)\{1 - e^{i\mathbf{k}\cdot\boldsymbol{r}_\alpha}\}, \tag{6}$$

where

$$\boldsymbol{\gamma}^{(\alpha)}(\boldsymbol{r}_\alpha) = \langle \Phi^{(\alpha)}(\mathbf{1}) | \delta^{(\alpha)}(\mathbf{1} - \boldsymbol{r}_\alpha) | \Phi^{(\alpha)}(\mathbf{1}) \rangle. \tag{7}$$

Downloaded by COLUMBIA UNIV on September 14, 2012 | http://pubs.acs.org
Publication Date: August 14, 2002 | doi: 10.1021/bk-2002-0828.ch010

Downloaded by COLUMBIA UNIV on September 14, 2012 | http://pubs.acs.org
Publication Date: August 14, 2002 | doi: 10.1021/bk-2002-0828.ch010

Equations (5) to (7), which follow from a Fourier representation of the Coulombic interactions in the Hamiltonian operator (*14*), indicate that the atomic transition density matrices (*17*) of Eq. (7) provide the computational invariants required for construction of both the (Coulombic) response matrices of Eq. (6) and the reduced pair-interaction matrices of Eq. (5). Use of the familiar Rayleigh plane-wave expansion and of standard expressions for the resulting angular integrations (*15*) reduces evaluation of Eq. (5) to a single quadrature over the scalar k, whereas the integrals of Eqs. (6) and (7) can generally be evaluated in closed forms when Gaussian basis orbitals are employed.

Antisymmetric Subspace

Although the eigenfunctions obtained from the Hamiltonian $\mathbf{H}(\boldsymbol{R})$ of Eq. (1) span all irreducible representations of the symmetric group S_n, they do not necessarily transform irreducibly under the symmetry group defined by the complete set of commuting observables, and they exhibit a high degree of degeneracy (*14*). To demonstrate formally that the totally antisymmetric or physical block of $\mathbf{H}(\boldsymbol{R})$ can be isolated and solutions obtained in symmetry-adapted form, the unitary transformation

$$\mathbf{U_S}(\boldsymbol{R})^\dagger \cdot \mathbf{H}(\boldsymbol{R}) \cdot \mathbf{U_S}(\boldsymbol{R}) \to \begin{pmatrix} \mathbf{H_S^{(p)}}(\boldsymbol{R}) & \mathbf{0} \\ \mathbf{0} & \mathbf{H_S^{(r)}}(\boldsymbol{R}) \end{pmatrix} \tag{8}$$

is employed. Here, the transformation $\mathbf{U_S}(\boldsymbol{R})$ is obtained from the diagonalization

$$\mathbf{U_S}(\boldsymbol{R})^\dagger \cdot \mathbf{S}(\boldsymbol{R}) \cdot \mathbf{U_S}(\boldsymbol{R}) \to n! \begin{pmatrix} \mathbf{I}^{(p)} & \mathbf{0} \\ \mathbf{0} & \mathbf{0}^{(r)} \end{pmatrix}, \tag{9}$$

where

$$\mathbf{S}(\boldsymbol{R}) = (n!)^{1/2} \langle \boldsymbol{\Phi}(\mathbf{1},\mathbf{2},\ldots,\boldsymbol{n}) | \hat{P}_A | \boldsymbol{\Phi}(\mathbf{1},\mathbf{2},\ldots,\boldsymbol{n}) \rangle \tag{10}$$

is the matrix representative of the antisymmetrizer $\hat{P}_A$ (*5*), $n!$ is the redundancy of the spectral-product basis when antisymmetrized, (p) and (r) refer, respectively, to physical and remainder subspaces of $\boldsymbol{\Phi}(\mathbf{1},\mathbf{2},\ldots\boldsymbol{n})$, $\mathbf{I}^{(p)}$ and $\mathbf{0}^{(r)}$ are the unit and null matrices in the indicated subspaces, and the right-hand sides of Eqs. (8) and (9) are reached in the closure limit. In this limit, the eigenvalues and functions obtained from $\mathbf{H_S^{(p)}}(\boldsymbol{R})$ converge to values obtained in the prior antisymmetrized basis $\hat{P}_A\boldsymbol{\Phi}(\mathbf{1},\mathbf{2},\ldots\boldsymbol{n})$ when its $(n!-1)$ redundant components are are removed (*7,14*).

Although Eqs. (8) to (10) provide formal expressions to isolate the physical eigenstates from the unphysical states in which they can be embedded, and to correspondingly demonstrate equivalence with results obtained from prior antisymmetry (*14*), an efficient recursive scheme using appropriately chosen antisymmetrized starting functions is sufficient to construct $\mathbf{H}_{\mathbf{S}}^{(p)}(\boldsymbol{R})$. Specifically, a transformation of the Hamiltonian matrix which is equivalent to that of Eq. (8) is obtained from the recurrence equations (*18*)

$$\beta_j(\boldsymbol{R})\ \mathbf{v}_{j+1}(\boldsymbol{R}) = (\mathbf{H}^{(+)}(\boldsymbol{R}) - \alpha_j(\boldsymbol{R})\ \mathbf{I})\cdot\mathbf{v}_j(\boldsymbol{R}) - \beta_{j-1}(\boldsymbol{R})\ \mathbf{v}_{j-1}(\boldsymbol{R}), \quad (11)$$

where the column vectors $\mathbf{v}_j(\boldsymbol{R})$ for $j = 1, 2, \ldots p$ define a set of p orthonormal Krylov-Lanczos functions in the spectral-product basis, the recurrence coefficients $\alpha_j(\boldsymbol{R})$ and $\beta_j(\boldsymbol{R})$ give the diagonal and off-diagonal terms, respectively, of a p-dimensional tri-diagonal matrix which is unitarily equivalent to the Hamiltonian matrix $\mathbf{H}_{\mathbf{S}}^{(p)}(\boldsymbol{R})$ of Eq. (8), and $\mathbf{H}^{(+)}(\boldsymbol{R})$ is the spectral-product Hamiltonian matrix supplemented with an additional row and column. The latter is constructed with an asymptotically ($\boldsymbol{R} \to \infty$) correct antisymmetrized-product test function which insures that the totally antisymmetric subspace of the spectral-product representation is isolated in the Krylov-Lanczos basis, that the correct number of multiplet states and their exchange splittings are included in the atomic separation limit, and that an appropriate starting vector is provided for the recurrence of Eq. (11) (*14*). This iterative approach requires only sequential calculations of individual rows of the potentially very large Hamiltonian matrix in the spectral-product basis, avoiding construction and tabulation of the entire matrix at one time. Moreover, the resulting unitary transformation provides a much lower-dimension physically significant Hamiltonian matrix from the zeroth-order non-interacting atomic energies, first-order Coulomb and exchange terms, and higher-order contributions which correspond to dispersion and polarization terms familiar from long-range pertubation theory (*7,14*).

Computational Applications

Calculations of the lowest-lying attractive and repulsive states of the electron-pair bond (H_2) illustrate the attributes of the formalism and the convergence achieved. In this case ($n_{total} = 2$), the spin functions factor out, there are no unphysical irreducible representations to contend with, and the development deals only with spatial functions which are symmetric (singlet) or antisymmetric (triplet) under electron transposition (*6*). The spectral-product representation spans these spatially symmetric and antisymmetric

Downloaded by COLUMBIA UNIV on September 14, 2012 | http://pubs.acs.org
Publication Date: August 14, 2002 | doi: 10.1021/bk-2002-0828.ch010

representations of the group S_2 once and only once, whereas the symmetric or antisymmetric forms of the basis are 2-fold redundant in the limit of closure. The absence of unphysical irreducible representations in this special case allows construction of solutions by direct diagonalization of the Hamiltonian matrix of Eq. (1) for comparisons with results obtained from the unitary-transformation [Eqs. (8) to (10)] and recursion [Eq. (11)] methods described above.

The spectral-product basis in this case corresponds formally to all products of discrete and continuum hydrogenic orbitals for the two atoms. To avoid dealing explicitly with continuum hydrogenic states, denumerable representational basis sets are employed in the calculations in the usual way (*2*). Even-tempered Gaussian functions $(s, p, d, f, \ldots)$ having exponents chosen to represent the lowest-lying atomic hydrogen orbitals accurately, and to span the corresponding Rydberg states and low-lying continua in the form of spectral packets (*18*), are employed in evaluating the matrix elements required in forming the spectral-product Hamiltonian matrix and the other integrals needed to implement the development.

In Table I are shown the spectra of atomic energies obtained for s, p, d and f orbitals constructed in even-tempered Gaussian basis sets (*19*), with orbital exponents chosen so the discrete and lower continuum states are spanned by the numbers of orbitals shown for each angular momentum value. Although no systematic studies of orbital selection are reported here, it should be noted that considerable experience has been gained in this connection through previous studies of the discrete and continuum states of atoms and polyatomic molecules (*18*). The spectra of Table I are judged to be suitable for describing the charge distortions accompanying chemical bond formation in H_2 in the interval $R \approx 1$ to $5\ a_0$, to correctly describe wavefunction antisymmetry in this interval in the absence of explicit electron exchange terms, and to otherwise approximate spectral closure in this interval. Consequently, the atomic basis sets so devised are seen to be significantly larger than those commonly employed in molecular electronic structure calulations (*2*). This use of larger atomic basis sets in the spectral theory is largely ameliorated by the need to perform electronic integral evaluations once and only once, and by the associated avoidance of repeated calculations of molecular integrals over antisymmetric basis states required in conventional developments.

In Figure 1 are shown as an example selected eigenvalues s_i of the metric matrix $\mathbf{S}(R)$ of Eq. (10) for H_2, evaluated employing the [*sp*] basis sets indicated in Table I. Only the fifty largest ($s_i \approx 2$) and the fifty smallest ($s_i \approx 0$) eigenvalues are shown as functions of the interatomic separation. The eigenstates of $\mathbf{S}(R)$ corresponding to eigenvalues $s_i \approx 2$ refer to ap-

Downloaded by COLUMBIA UNIV on September 14, 2012 | http://pubs.acs.org
Publication Date: August 14, 2002 | doi: 10.1021/bk-2002-0828.ch010

Downloaded by COLUMBIA UNIV on September 14, 2012 | http://pubs.acs.org
Publication Date: August 14, 2002 | doi: 10.1021/bk-2002-0828.ch010

Table I. Spectral Energies for Atomic Hydrogen.[a]

s-basis[b]	p-basis[b]	d-basis[b]	f-basis[b]
−0.499991	−0.124998	−0.055256	−0.026707
−0.124994	−0.053439	−0.011199	0.028807
−0.048465	0.025060	0.108901	0.187597
0.088668	0.274825	0.450236	0.617389
0.563368	0.986192	1.361055	1.748440
1.951139	2.880038	3.708833	4.791877
5.660465	7.854649	9.719458	
15.152536	21.314359	25.786063	
38.982050			
98.333482			
249.224098			
657.488778			

[a] Orbital energies (*a.u.*) obtained from diagonalization of the atomic hydrogen Hamiltonian employing the indicated basis sets.

[b] Basis sets employed are the most diffuse ($12s8p8d6f$) hydrogenic orbitals constructed from 12 regularized even-tempered primitive Gaussian orbitals of each angular momentum symmetry (*19*), supplemented with two additional diffuse functions having exponents of 0.02786 and 0.01156 in each case.

Downloaded by COLUMBIA UNIV on September 14, 2012 | http://pubs.acs.org
Publication Date: August 14, 2002 | doi: 10.1021/bk-2002-0828.ch010

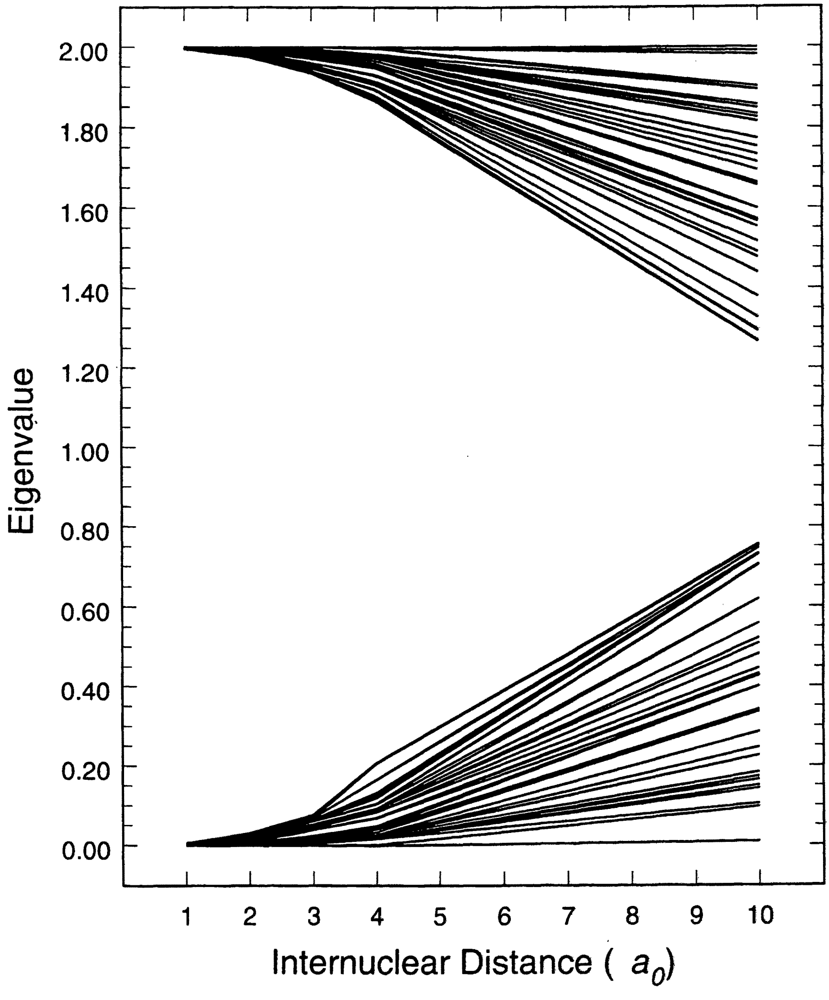

Figure 1. Eigenvalues s_i of the metric matrix of Eq. (10) for H_2, constructed in the [*sp*] basis set of Table I as functions of interatomic separation $R(a_0)$. Values $s_i \approx 2$ refer to approximately antisymmetric eigenfunctions of electron coordinates constructed in the spectral-product basis, whereas vlues $s_i \approx 0$ refer to approximately symmetric functions of electron coordinates, as is discussed more fully in the text.

proximately antisymmetric states in the spectral-product basis, whereas those correponding to $s_i \approx 0$ refer to approximately symmetric states. On the other hand, states constructed in the prior antisymmetrized basis corresponding to the $s_i \approx 2$ values refer to linearly independent spatially antisymmetric states, while those corresponding to $s_i \approx 0$ values refer to linearly dependent combinations of the prior antisymmetrized basis. When the two-electron symmetric projector is employed in place of the antisymmetrizer, results identical to the foregoing are obtained, but with the states previously corresponding to $s_i \approx 2$ and $s_i \approx 0$ interchanging their identities.

A significant number of the eigenvalues of $\mathbf{S}(R)$ depicted in Figure 1 evidently maintain their extreme values ($s_i \approx 0$ or 2) over the chemical interaction region ($R \approx 1$ to 5 a_0), whereas only a very few of these survive into the van der Waals region ($R \approx 5$ to 10 a_0). These behaviors are entirely in accord with the spatial characteristics of the spectral states corresponding to the eigenvalues of Table I employed in constructing $\mathbf{S}(R)$, which have relatively small amplitudes at distances ≈ 5 to 10 a_0 from the atomic origins. Accordingly, the basis of Table I can be expected to give converged results in the chemical interaction region, and particularly at the equilibrium interatomic separation ($R = 1.40\ a_0$), whereas alternative basis sets will likely be required to achieve closure at larger interatomic separations. These can be devised employing more diffuse Gaussian basis sets following previously described selection criteria (*18*).

The spectra of Table I are employed in calculations of energies and expectation values for the lowest-lying ${}^1\Sigma_g^+$ and ${}^3\Sigma_u^+$ states in H_2 at the equilbrium interatomic separation following the development of Eqs. (1) to (10). The total energies, binding energies, and expectation values of the electron transposition operator $\hat{P}_{12}$ for both states, shown in Table II, evidently converge monotonically to known values with increase in basis-set angular momentum. Similarly, the norms of the familiar singlet and triplet Heitler-London functions (*4*) represented in the spectral-product basis, also shown in Table II, give additional indication of the closure achieved for exchange terms in this case. As indicated above, the values shown in Table II can be obtained directly from diagonalization of the spectral-product Hamiltonian of Eq. (1) or from the unitary transformation of Eqs. (8) to (10), with identical values resulting from the two procedures in the limit of closure. It is found in the smaller basis sets ([*s*], [*sp*]) of Table I, however, that relatively large blocks of the transformed Hamiltonian matrix of Eq. (8) are required in order to reproduce accurately the results obtained from the complete spectral-product Hamiltonian matrix. That is, the totally symmetric subspace in these cases is not completely isolated into a physical block which is small relative to the original spectral-product Hamiltonian

Downloaded by COLUMBIA UNIV on September 14, 2012 | http://pubs.acs.org
Publication Date: August 14, 2002 | doi: 10.1021/bk-2002-0828.ch010

Downloaded by COLUMBIA UNIV on September 14, 2012 | http://pubs.acs.org
Publication Date: August 14, 2002 | doi: 10.1021/bk-2002-0828.ch010

Table II. Electron Pair-Bond Calculations.[a]

Basis[b]	Energy(a.u.)[c]	Binding(eV)[c]	$\langle \hat{P}_{12} \rangle^c$	$(\lvert\Phi^{(HL)}\rvert^2)^c$
		$^1\Sigma_g^+$ state		
[*s*]	−1.0096	+0.2618	+0.5255	+0.8052
[*sp*]	−1.0691	+1.8809	+0.8409	+0.9469
[*spd*]	−1.1140	+3.1027	+0.9525	+0.9872
[*spdf*]	−1.1384	+3.7667	+0.9847	+0.9967
Exact (*20*)	−1.1745	+4.7478	+1.0000	+1.0000
		$^3\Sigma_u^+$ state		
[*s*]	−0.5586	-12.0109	-0.6226	+0.2950
[*sp*]	−0.6641	-9.1400	-0.6905	+0.8078
[*spd*]	−0.7249	-7.4856	-0.9317	+0.9538
[*spdf*]	−0.7524	-6.7372	-0.9801	+0.9870
Exact (*20*)	−0.7842	−5.8737	−1.0000	+1.0000

[a] Values at $R = 1.40\ a_0$ obtained from diagonalization of the Hamiltonian matrix of Eqs. (1) to (3) for H_2, or, equivalently, from the unitary transformation of Eqs. (8) to (10) in the text.

[b] Denotes the portion of the (12*s*8*p*8*d*6*f*) basis set indicated in Table I employed in the calculation.

[c] Total and binding energies as indicated; $\langle \hat{P}_{12} \rangle$ refers to the expectation value of the electron transposition operator $\hat{P}_{12}$; $\lvert\Phi^{(HL)}\rvert^2$ is the norm of the Heitler-London function as represented in the indicated spectral-product basis sets.

matrix of Eq. (1) by the the unitary transformation of Eq. (8). These observations serve to emphasize that the development of Eqs. (8) to (10) provides a formal proof of the convergence of the spectral method in the closure limit, rather than an optimal computational implementation of the approach.

The rate of convergence of the results of Table II with increasing angular momentum in the atomic basis is related to the nature of the charge distortions in H_2 consequent of bond and antibond formation at the equilibrium interatomic separation. In Figure 2 is shown the one-electron charge distribution in the plane of the two nuclei for the ${}^1\Sigma_g^+$ ground state obtained as indicated in the figure, with the undisturbed atomic charges of the two atoms in their $1s$ states subtracted out. Evidently, there is a distinct line of electronic charge connecting the two nuclei in this density difference map which provides sufficient attraction to form the bond in this case, in accordance with the predictions of the Hellmann-Feynman theorem. This additional "exchange charge," in an integrated amount equal to ≈ 0.25 electrons gathered from the outer-lying regions and concentrated between the two nuclei, is represented in the spectral-product basis by single-center overlap factors in the charge-density expression

$$\rho(\boldsymbol{r}) = \sum_{i,i'} \Gamma_{ii'} \phi_i^{(\alpha)}(\boldsymbol{r}) \phi_{i'}^{(\alpha)}(\boldsymbol{r})^* + \sum_{j,j'} \Gamma_{jj'} \phi_j^{(\beta)}(\boldsymbol{r}) \phi_{j'}^{(\beta)}(\boldsymbol{r})^*, \qquad (12)$$

where $\Gamma_{ii'}$ and $\Gamma_{jj'}$ form the one-electron density matrix in the orbital-product basis, with two-center differential overlap factors absent consequent of the orthonormality of the spectral-product fucntions. The exchange charge confined between the two atoms depicted in Figure 2 evidently requires the higher angular momentum functions of Table I for an accurate description of this accumulation upon bond formation, and also for corresponding convergence in the total energy and exchange factors of Table II.

The recursive projection procedure described above provides an alternative and potentially more efficient method for obtaining eigenstates than does the development of Eqs. (8) to (10). In the two-electron case, this procedure serves to separate the symmetric and antisymmetric subspaces spanned in the absence of unphysical representations, and can accelerate the convergence relative to that of Table II through incorporation of explicitly symmetric or antisymmetric test functions. In Figure 3 are shown ${}^1\Sigma_g^+$ and ${}^3\Sigma_u^+$ potential energy curves in H_2 obtained from the recursive development and the basis states of Table I employing Heitler-London test functions in each case. These functions serve as appropriate chemical reference states

Downloaded by COLUMBIA UNIV on September 14, 2012 | http://pubs.acs.org
Publication Date: August 14, 2002 | doi: 10.1021/bk-2002-0828.ch010

Downloaded by COLUMBIA UNIV on September 14, 2012 | http://pubs.acs.org
Publication Date: August 14, 2002 | doi: 10.1021/bk-2002-0828.ch010

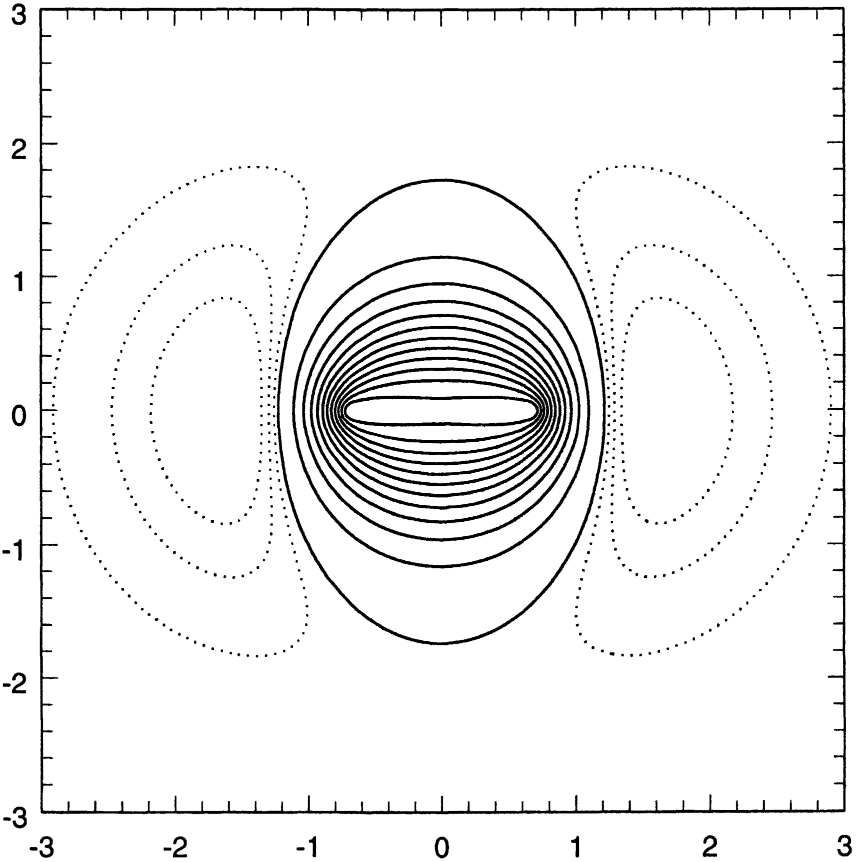

Figure 2. Charge-density difference map for H_2 in the plane of the two nuclei, depicting the accumulation of charge between the two atoms upon bond formation in the ground $^1\Sigma_g^+$ state. The quantity plotted is the total one-electron molecular change density obtained from a configuration-interaction calculation using the [*sp*] basis of Table I, minus the charge density corresponding to the two unperturbed H atoms in their 1*s* ground states. The H_2 bond length is fixed at 1.40 a_0. The outermost solid contour represents a zero charge-density difference; successive solid contours are at charge-density difference intervals of 0.02 *a.u.*, with the innermost solid contour representing a charge-density difference of 0.1 *a.u.*; the outermost dashed contour corresponds to -0.003 *a.u.* and the innermost dashed contour to -0.006 *a.u.*; a total of ≈ 0.25 additional electrons are accumulated in the bond.

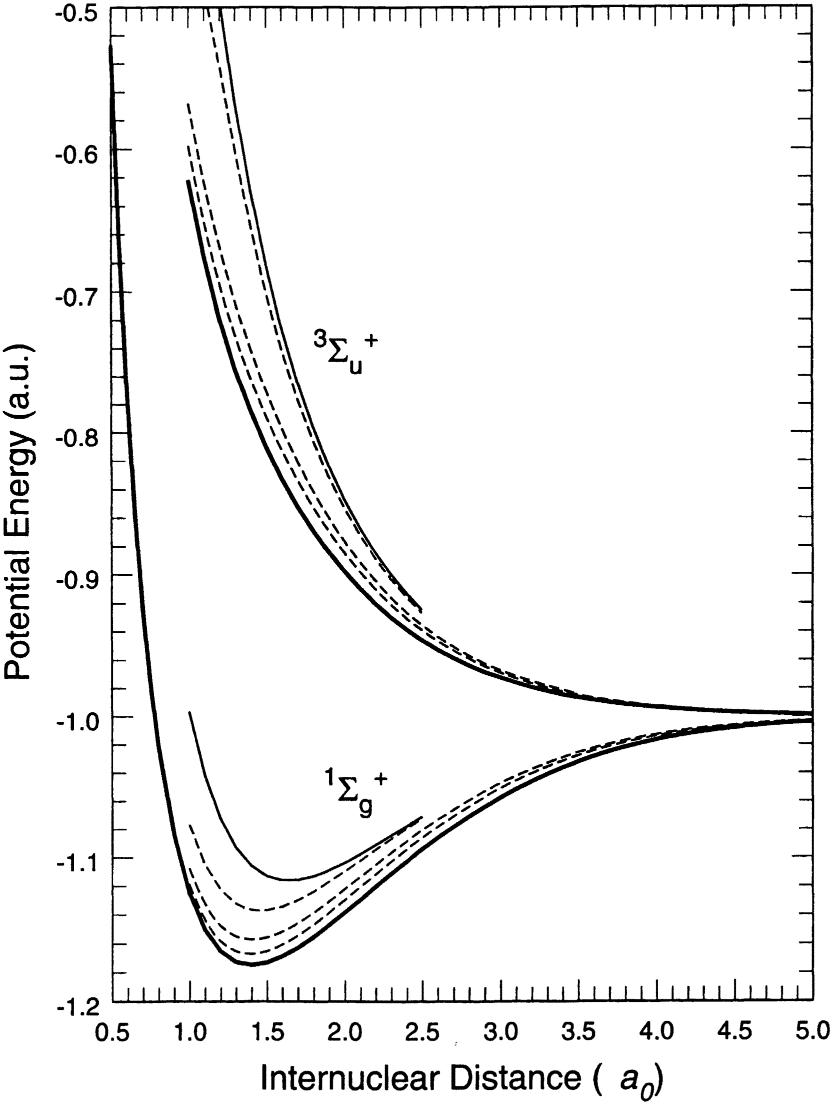

Figure 3. Potential energy (*a.u.*) curves for the $^1\Sigma_g^+$ and $^3\Sigma_u^+$ states of H_2 as functions of atomic separation $R(a_0)$. Solid lines refer to Heitler-London (HL) (*4*) and previously determined accurate values (KW) (*20*), whereas the dashed lines give the present results obtained from the recursion procedure indicated in the text employing the [*s*], [*sp*], and [*spd*] basis states of Table I and Heitler-London test functions in each case.

Downloaded by COLUMBIA UNIV on September 14, 2012 | http://pubs.acs.org
Publication Date: August 14, 2002 | doi: 10.1021/bk-2002-0828.ch010

at all interatomic separations, and also provide the starting functions required to generate recursively the correct permutation symmetries in the spectral-product subspaces. Evidently, the spectral-theory potential curves of Figure 3 converge rapidly in the chemical region ($R \approx 1$ to $5\ a_0$) as larger angular momentum values are included in the basis, the [*sp*] limit already providing ≈ 90% of the chemical bonding energy at the equilibrium interatomic separation, and the [*spd*] limit providing ≈ 96% of this value. Finally, although the basis of Table I is insufficient to accurately determine the exchange energy splitting in the van der Waals region ($R \approx 5$ to $10\ a_0$), the average value of the singlet and triplet energies obtainded in the basis in this region is found to give accurate results for the leading ($C_6, C_8, \ldots$) van der Waals coeffcients.

Downloaded by COLUMBIA UNIV on September 14, 2012 | http://pubs.acs.org
Publication Date: August 14, 2002 | doi: 10.1021/bk-2002-0828.ch010

Concluding Remarks

A new method is reported for determining the adiabatic electronic wave functions and energies of molecules and other chemical aggregates. The spectral-product basis, formally comprised of all simple products of the physical eigenstates of the individual atoms in the aggregate, gives a Hamiltonian matrix that is rigorously additive in pairwise-atomic interaction-energy matrices, greatly simplifying its evaluation relative to conventional methods which employ antisymmetrized basis states (*2,3*). In this approach, ***atomic*** structure calculations of electronic transition density matrices employed in evaluation of the Hamiltonian matrix need be performed once and only once, avoiding the repeated evaluations of many-electron matrix elements over antisymmetric molecular basis functions required in conventional potential-energy surface determinations. Procedures for isolating the totally antisymmetric subspace of the spectral-product basis are indicated which avoid construction and storage of the entire Hamiltonian matrix at one time, and which also largely overcome the symmetric-group complications which have hindered previous developments employing the atomic spectral-product representation (*7-13*).

Applications of the formalism to the lowest-lying singlet and triplet states of H_2 illustrate the convergence achieved to results obtained from conventional methods, and indicate that prior basis-set antisymmetry is not required in molecular electronic structure calculations. Although observations based on the illustrative calculations reported here are useful, additional computational applications of the spectral method are required to clarify the nature of the spectral-product representation required more generally to accurately describe charge distortions consequent of chemical bonding. It should be noted that the Hamiltonian matrix for any aggregate of interacting hydrogen atoms can be formed employing the calculated pair-interaction energy matrices reported here and the development of Eqs. (1) to (4) employing explicit computational algorithims devised for this purpose. Applications of the spectral theory to more complex heteronuclear chemical systems entail additional computational evaluations of the appropriate atomic matrices Eqs. (5) to (7), obviating the need for additional calculations at the molecular or aggregate level. The results of such calculations, as well as other theoretical and computational aspects of the formalism, are reported separately elsewhere (*14*). The desirable atributes of an atomic-based approach to molecular structure determinations suggests further studies of the spectral method reported here are warrented.

Downloaded by COLUMBIA UNIV on September 14, 2012 | http://pubs.acs.org
Publication Date: August 14, 2002 | doi: 10.1021/bk-2002-0828.ch010

Acknowledgments

This work was funded in part by the U.S. Air Force Office of Scientific Research. We thank Dr. Peter Taylor for his hospitality to PWL at the San Diego Supercomputer Center during the course of the investigation, and Drs. Michael Berman, Stephen Rogers and Mario Fajardo for advice, encouragement and support.

References

1. Born, M.; Oppenheimer, J.R. Ann. Physik **1927** *84*, 457.
2. *Modern Electronic Structure Theory*; Yankony, D.R., Ed.; World Scientific, London, 1995, Parts I & II.
3. Parr, R.G.; Yang, W. *Density-Functional Theory of Atoms and Molecules*; Oxford University Press, New York, 1989.
4. Heitler, W.; London, F. Z. Physik **1927** *44*, 455.
5. Dirac, P.A.M. *The Principles of Quantum Mechanics*; Oxford University Press, New York, 1958; 4th Edition, Chapter IX.
6. Hammermesh, M. *Group Theory*; Addison-Wesley, Reading, Massacusetts, 1962; Chapter 7.
7. Eisenschitz, H.; London, F. Z. Physik **1930** *60*, 491.
8. Amos, A.T.; Musher, J.I. Chem. Phys. Letters **1967** *1*, 149.
9. Moffitt, W. Proc. Roy. Soc. (Lond.) **1951** *A210*, 245.
10. Claverie, P. Int. J. Quantum Chem. **1971** *5*, 273.

11. Morgan, III, J.D.; Simon, B. Int. J. Quantum Chem. **1980** *17*, 1143.

12. Adams, W. H. Int. J. Quantum Chem. **1996** *60*, 273.

13. Jeziorski, B.; Moszynski, R.; Szalewicz, K. Chem. Rev. **1994** *94*, 1887.

14. Langhoff, P.W. J. Phys. Chem. **1996** *100*, 2974; Langhoff, P.W.; Boatz, J.A.; Hinde, R.J.; Sheehy, J.A. Theor. Chem. Acc. (submitted).

15. Edmonds, A.R. *Angular Momentun in Quantum Mechanics*; Princeton, NJ, 1957.

16. Tully, J.C. in *Modern Theoretical Chemistry*; G.A. Segal, Ed.; Plenum, NY, 1977; Vol. 7, pp. 173-200.

17. Friedman, W.A. Annals of Physics **1967** *45*, 265.

18. Langhoff, P.W. in *Mathematical Frontiers in Computational Chemical Physics*; D.G. Truhlar, Ed.; Springer, Berlin, 1988; pp. 85-135.

19. Schmidt, M.W.; Ruedenberg, K. J. Chem. Phys. **1979** *71*, 3951.

20. Kolos W.; Wolniewicz, L. J. Chem. Phys. **1965** *43*, 2429.

Downloaded by COLUMBIA UNIV on September 14, 2012 | http://pubs.acs.org
Publication Date: August 14, 2002 | doi: 10.1021/bk-2002-0828.ch010

Downloaded by NORTH CAROLINA STATE UNIV on September 14, 2012 | http://pubs.acs.org
Publication Date: August 14, 2002 | doi: 10.1021/bk-2002-0828.ch011

Chapter 11

Comparison of CaF, ZnF, CaO, and ZnO: Their Anions and Cations in Their Ground and Low-Lying Excited States

J. F. Harrison[1], R. W. Field[2], and C. C. Jarrold[3]

[1]Department of Chemistry, Michigan State University, East Lansing, MI 48824–1322
[2]Department of Chemistry, Massachusetts Institute of Technology, Cambridge, MA 02139–4307
[3]Department of Chemistry, University of Illinois at Chicago, Chicago, IL 60607–7061

Abstract

The results of large basis set ab initio electronic structure calculations using the RCCSD(T) method are reported for the bond lengths, bond energies, excitation energies, vibrational frequencies, dipole moments and charge distributions for the titled molecules and where possible compared with experiment and previous calculations The striking differences between the Ca and Zn compounds are discussed in terms of their relative ionic character.

Introduction

The excited electronic states of CaO and CaF may be understood in terms of a ligand field model (1,2) in which Ca is essentially Ca^+ and hosts a 4s, 4p or 3d electron which is perturbed by the companion anion. Since Ca and Zn are ostensibly similar, both having an outer $4s^2$ configuration, the question arises whether the excited states of ZnO and ZnF can be understood in terms of a similar ligand field model. Recent work on the photoelectron spectrum of ZnO and ZnF by Moravec et. al. (3) suggests that the answer is no and we will demonstrate that the reason is, primarily, because the Zn compounds are considerably less ionic than the corresponding Ca compounds. In this paper we compare and contrast the electronic structure of the title compounds.

In Low-Lying Potential Energy Surfaces; Hoffmann, M., et al.;
ACS Symposium Series; American Chemical Society: Washington, DC, 2002.

Technical Details

Unless otherwise noted, all calculations used the MOLPRO (4,5) system of programs (Versions 96.4 and higher) and the RCCSD(T) (6,7,8) method. The F and O basis sets were the ANO contraction of the Dunning aug-cc-pvqz set (9) with the g functions deleted (13s7p4d3f contracted to 6s5p4d3f). The Zn basis is from Heineman, Koch and Partridge(10) and is a 20s15p9d6f4g primitive set with an ANO contraction to 7s6p4d3f2g , while for Ca we use the basis of Bauschlicher, Rosi and Langhoff(11), which is a primitive 20s15p9d5f2g, contracted to 8s7p7d5f2g. Electron affinities, ionization energies and T_0's are corrected for zero point vibration and scalar relativistic effects. The relativistic corrections and electron populations were obtained from a CISD calculation at the RCCSD(T) equilibrium geometry. All dissociation energies, D_0, are reported relative to the lowest energy neutral adiabatic asymptote appropriate to the molecular symmetry. For example, D_0 for CaO($X^1\Sigma^+$) is relative to Ca(^3P) + O(^3P) while for ZnO ($X^1\Sigma^+$) it is relative to Zn(^1S) + O(^1D).

Previous Theoretical Work

Theoretical work on CaO dates from the early single configuration studies of Yoshimine (12), McLean and Yoshimine (13) and Carlson et. al. (14), all of which predicted the wrong ground state. Bauschlicher and Yarkony (15) pointed out the inadequacy of the single configuration representation of the $X^1\Sigma^+$ state, while calculations by England (16) were the first to obtain $^1\Sigma^+$ as the ground state, in agreement with experiment (17). England also noted that the bond lengths calculated without core-valence correlation were too long. In 1982 Diffenderfer and Yarkony (18,19) studied the low-lying $X^1\Sigma^+$ and $^1\Pi$ excited states while Bauschlicher and Partridge (20) corroborated the experimental dissociation energy of Irvin and Dagdigian (21) for the $X^1\Sigma^+$ state. More recent work on CaF (22,23), CaO(24), CaO^+ and CaF^+ (25) will be discussed latter. Bauschlicher and Langhoff published (26) the first high-level calculation of ZnO and pointed out the sensitivity of the predicted ground state to the level of electron correlation. Subsequent work on ZnF(27,28), ZnO(28,29), and ZnO^-(29,30) will be discussed latter.

Downloaded by NORTH CAROLINA STATE UNIV on September 14, 2012 | http://pubs.acs.org
Publication Date: August 14, 2002 | doi: 10.1021/bk-2002-0828.ch011

Atomic Characteristics

As one goes from Ca to Zn the 3d shell fills but does not completely shield the additional nuclear charge, resulting in the ionization energy (31) of Zn (9.391eV) being much larger than Ca (6.111eV). In addition, the atomic energy level pattern in Figure 1 shows that the $^3P(4s4p)$ and the ^3D (4s3d) states of Ca are 1.892 and 2.525eV above the ground state while in Zn the $^3P(4s4p)$ is at 4.054eV and the 4d orbitals lie 7.7eV above the ground ^1S. These low lying atomic states in Ca permit the atom to use pπ and dπ electrons in bonding, an option not energetically available to Zn. The situation in the positive ion is much more dramatic (31). The first excited state of Ca^+ is a $^2D(3d)$ state at 1.697eV while the $^2P(4p)$ is only 3.142eV above the $Ca^+(^2S)$. In contrast, the first excited state of Zn^+ is a $^2P(4p)$ state at 6.083eV. Clearly, Ca is a transition element in waiting! The proximity of the Ca 3d orbital to the ground state in both the neutral atom and positive ion plays a significant role in the electronic structure of CaF and CaO (vide infra).

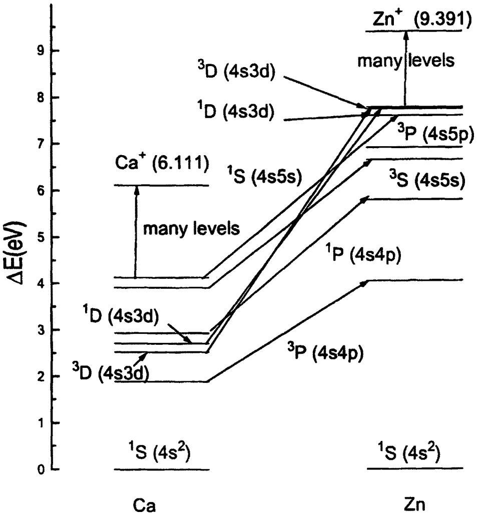

Figure 1. Selected energy levels of Ca and Zn

Downloaded by NORTH CAROLINA STATE UNIV on September 14, 2012 | http://pubs.acs.org
Publication Date: August 14, 2002 | doi: 10.1021/bk-2002-0828.ch011

Downloaded by NORTH CAROLINA STATE UNIV on September 14, 2012 | http://pubs.acs.org
Publication Date: August 14, 2002 | doi: 10.1021/bk-2002-0828.ch011

CaF and ZnF Results

Neutrals

Consider first the $X^2\Sigma^+$ state of CaF and ZnF. The lowest neutral asymptote is the ^1S (metal) + ^2P_u (F) and we envision a bond being formed between a sz hybrid on the metal (pointing toward the F) and the F $2p_z$ orbital with the unpaired electron in the $s\bar{z}$ hybrid on the metal pointing away from F. The valence electron configuration is $s\bar{z}^{1}(sz+p_\sigma)^2\pi^4$ where the π electrons are localized on F. In the ionic limit the σ bonding electron pair will be transferred to F resulting in the configuration $s\bar{z}^{1}p_\sigma^{2}\pi^{4}$.

The population analysis shown in Table 1 suggests that while both molecules are considerably ionic, CaF is more so. This is consistent with the lowest ionic asymptote in CaF being 2.71eV above the ground state products and the resulting ionic curve crossing this asymptote at 5.31Å (2.7 R_e) while the ionic products in ZnF are 5.99eV above ground and cross at 2.40Å (1.4 R_e). The calculated spectroscopic properties of CaF (Table 2) are in reasonable agreement with experiment and previous calculations. Our calculated ionization energy (Table 3) of CaF (5.821eV) is in good agreement with experiment (32)(5.828eV) and is approximately 0.3eV lower than the IP of Ca. Since the IP of CaF is equal to the IP of Ca plus the difference between the D_0 of the neutral and positive molecule, $CaF^+(^1\Sigma^+)$ is more bound by approximately 0.3eV than $CaF(^2\Sigma^+)$ (vide infra). Similarly since the electron affinity of CaF (calc. 1.028eV) is equal to the EA of F(calc, 3.329eV) plus the difference between the D_0 of the anion and the neutral molecule, the neutral is bound by 2.3eV more than the anion. Note that because our calculated EA of $F(^2P)$ is too small (33) by 0.072eV, a better estimate of the EA of CaF is our calculated value plus this differential, or 1.095eV. The molecular EA corrected for the error in the atom is shown in parenthesis in Table 3. The calculated IP of ZnF is 9.30eV, which is slightly smaller than our calculated IP of Zn (9.319eV, exp 9.391eV) and so the bond energies in the neutral and positive ion are very similar. Our calculated EA of ZnF, corrected for the error in the EA of atomic F and for relativity (0.048eV) is 1.929eV, somewhat smaller than the experimental (3) value of 1.974(8)eV. Our calculations imply that D_0 of $ZnF(^2\Sigma^+)$ is 1.435eV larger than $ZnF^-(^1\Sigma^+)$ in reasonable agreement with the experimental value of 1.427eV.

Downloaded by NORTH CAROLINA STATE UNIV on September 14, 2012 | http://pubs.acs.org
Publication Date: August 14, 2002 | doi: 10.1021/bk-2002-0828.ch011

Table 1. Fluoride Population Analysis

Molecule	4s	$4p_\sigma$	$4p_{\pi x}$	$4p_{\pi y}$	$3d_{\sigma+\delta}$	$3d_{\pi x}$	$3d_{\pi y}$	$3d_{\delta+}$	2s	$2p_\sigma$	$2p_{\pi x}$	$2p_{\pi y}$	Q(M)	Q(F)
$CaF(X^2\Sigma^+)$	0.79	0.13	0.02	0.02	0.11	0.06	0.06	0.01	2.02	1.93	1.94	1.94	+0.86	-0.86
$ZnF(X^2\Sigma^+)$	0.96	0.26	0.02	0.02	4.0	2.0	2.0	2.0	1.97	1.80	1.96	1.96	+0.72	-0.72
$CaF(^2\Pi_r)$	-0.03	-0.08	0.38	0.38	0.11	0.27	0.05	0.01	2.03	1.92	1.94	1.93	+0.86	-0.86
$ZnF(^2\Pi_r)$	0.19	0.07	1.14	0.02	4.0	2.0	2.0	2.0	1.98	1.75	1.85	1.95	+0.55	-0.55
$CaF^-(^1\Sigma^+)$	1.66	0.20	-0.02	-0.02	0.11	0.04	0.04	0.01	2.04	1.95	1.96	1.96	-0.07	-0.93
$ZnF^-(^1\Sigma^+)$	2.09	0.21	0.02	0.02	4.0	2.0	2.0	2.0	1.87	1.80	1.98	1.98	-0.36	-0.64
$CaF^-(^3\Pi_r)$	1.83	0.08	0.87	-0.02	0.12	0.15	0.04	0.01	2.02	1.93	1.96	1.95	-0.11	-0.89
$ZnF^-(^3\Pi_r)$	1.06	0.18	1.14	0.02	4.0	2.0	2.0	2.0	1.93	1.81	1.84	1.97	-0.43	-0.57
$CaF^+(^1\Sigma^+)$	-0.03	-0.05	-0.02	-0.02	0.14	0.07	0.07	0.01	2.03	1.89	1.91	1.91	+1.79	-0.79
$ZnF^+(^1\Sigma^+)$	0.22	0.07	0.03	0.03	4.0	2.0	2.0	2.0	1.98	1.72	1.94	1.94	+1.62	-0.62

Downloaded by NORTH CAROLINA STATE UNIV on September 14, 2012 | http://pubs.acs.org
Publication Date: August 14, 2002 | doi: 10.1021/bk-2002-0828.ch011

Table 2. Fluoride results, previous calculations and experiment

Molecule	Source	Re(Å)	ω_e(cm^{-1})	D_0(eV)	T_0(eV)
$CaF(X^2\Sigma^+)$	This work	1.957	587	5.47[a]	0.0
	Previous[22]	1.966	583	5.51[a]	0.0
	Experiment	1.967[38]	581[38]	5.55[a,39,40]	0.0
$ZnF(X^2\Sigma^+)$	This work	1.775	633	3.12[a]	0.0
	Previous[28]	1.796	593		0.0
	Previous[27]	1.787	601	1.99[a]	0.0
	Experiment[3]		620(10)		
$CaF(^2\Pi_r)$	This work	1.943	594	5.30[b]	2.05
	Experiment[38]	1.952	587	5.40[b]	2.044
$ZnF(^2\Pi_r)$	This work	1.757	659	2.59[b]	4.63
	Experiment[29]		630		4.586
$CaF^-(X^1\Sigma^+)$	This work	2.018	509	3.17[c]	0.0
$ZnF^-(X^1\Sigma^+)$	This work	1.913	425	1.60[c]	0.0
	Experiment[3]	$X^2\Sigma^+$+0.15	420(10)		0.0
$CaF^-(^3\Pi_r)$	This work	1.992	537	4.04[d]	1.08
$ZnF^-(^3\Pi_r)$	This work	1.826	541	3.19[d]	2.53
$CaF^+(^1\Sigma^+)$	This work	1.876	692	5.80[e]	0.0
	Previous[25]	1.881	756	5.67[e]	0.0
$ZnF^+(^1\Sigma^+)$	This work	1.708	748	3.15[e]	0.0

a. Relative to $M(^1S) + F(^2P)$
b. Relative to $M(^3P) + F(^2P)$
c. Relative to $M(^1S) + F^-(^1S)$
d. Relative to $M(^3P) + F^-(^1S)$
e. Relative to $M^+(^2S) + F(^2P)$

The first excited state of CaF and ZnF is $A^2\Pi_r$ with the configuration $\pi_m^1(sz+p_\sigma)^2\pi^4$ where the singly occupied π_m electron is localized on the metal. The lowest energy asymptote is ^3P_u (metal) + ^2P_u (F), which is 1.86eV and 3.966eV above the ground state products in CaF and ZnF. In the ionic limit the configuration is $\pi_m^1 p_\sigma{}^2\pi^4$ and the lowest $^2\Pi_r$ ionic asymptote has the metal ion in a ^2P state. The ionic curves will cross the neutral asymptote at 5.65Å (2.9 R_e) in CaF and 1.78Å (1.0 R_e) in ZnF and accordingly we expect CaF to be significantly more ionic than ZnF and this is supported by the population analysis (Table 1).

The singly occupied π_m in CaF has the composition $p_\pi^{0.70}d_\pi^{0.27}$ while in ZnF it is $p_\pi^{1.0}$. Given that the energy of the 3d orbital in Ca^+ $^2D(3d)$ is 1.697 eV above the $^2S(4s)$, while the $^2P(4p)$ is 3.142eV, it is surprising, in so ionic a molecule, that the 3d orbital is not dominant. It could be that this composition is energetically favored over a single d electron because of the increased polarizability of the 4p component, the reduced repulsion with the F π orbitals that obtains when the $p_\pi d_\pi$ orbital hybridizes away from F, and the more favorable quadrupolar interaction with F^-(the zz component of the quadrupole tensor of the 4pπ orbital is positive while that of the dπ is negative). As first noted by Ernst and Kandler (35) this $p_\pi d_\pi$ mixing explains why the dipole moment of CaF (Table 4) in the $A^2\Pi_r$ state (2.57D calc, 2.44D experiment) is significantly smaller than that of ZnF while in the ground state they are comparable (3.05D vs. experiment (36), 3.12D). Note that, for ZnF, the $A^2\Pi_r$ state is stabilized by the quadrupolar interaction of the metal centered p_π orbital with F^-. The bond length of both CaF and ZnF in the excited $A^2\Pi_r$ state is smaller than in the ground $X^2\Sigma^+$, state, contracting by 0.014 and 0.018Å, while the corresponding frequencies increase by 7 and 26 cm^{-1} respectively.

The generalized Morse potentials (37) in which the molecules dissociate to their lowest neutral asymptotes, are shown in Figures 2 and 3 and illustrate the significantly larger D_0 of CaF (an ionic effect) and the significantly smaller T_0 which is a consequence of the much smaller ^1S, ^3P separation in Ca relative to Zn. This small separation also permits the $A^2\Pi_r$ state in CaF to be bound relative to the ground state atoms .

Anions

Adding an electron to the singly occupied metal centered σ orbital in either the $X^2\Sigma^+$ state, or $A^2\Pi_r$ state results in a state in which the additional

Downloaded by NORTH CAROLINA STATE UNIV on September 14, 2012 | http://pubs.acs.org
Publication Date: August 14, 2002 | doi: 10.1021/bk-2002-0828.ch011

Downloaded by NORTH CAROLINA STATE UNIV on September 14, 2012 | http://pubs.acs.org
Publication Date: August 14, 2002 | doi: 10.1021/bk-2002-0828.ch011

Table 3. Ionization Energies and Electron Affinities

Molecule	IP(eV)		EA(eV)	
	Calculated	Experiment	Calculated	Experiment
CaO($^1\Sigma^+$)	6.767	6.66(8)[42]	0.865(0.977)	
ZnO($^1\Sigma^+$)	9.260		1.927(2.039)	2.087[3,34]
CaF ($^2\Sigma^+$)	5.821	5.828[36]	1.028(1.095)	
ZnF($^2\Sigma^+$)	9.303		1.857(1.929)	1.974(8)[3]
Ca(^{1}S)	6.097	6.111[31]		
Zn(^{1}S)	9.319	9.391[31]		
F(^{2}P)			3.329	3.401[33]
O(^{3}P)			1.349	1.461[33]

Table 4. Dipole moments (Debye)

Molecule	This Work	Experiment	Previous Calculation
CaF(X$^2\Sigma^+$)	3.05	3.07(7)[36]	3.06[23]
ZnF(X$^2\Sigma^+$)	3.12		3.24[28]
CaF($^2\Pi_r$)	2.57	2.44[35]	
ZnF($^2\Pi_r$)	3.80		
CaO(X$^1\Sigma^+$)	8.84		8.64[16]
ZnO(X$^1\Sigma^+$)	5.49		5.37[28]
CaO($^3\Pi_i$)	3.48		3.39[16]
ZnO($^3\Pi_i$)	2.62		2.61[28]
CaO($^3\Sigma^+$)	2.61		2.55[16]
ZnO ($^3\Sigma^+$)	3.11		3.12[28]/3.09[38]

electron is localized on the metal (see Table 1). In the ${}^1\Sigma^+$ and ${}^3\Pi_r$ states of CaF^- and ZnF^-, F has a Mulliken charge very similar to its charge in the neutral predecessors. There are no previous calculations on these molecules and the only experimental (3) data is the bond length of ZnF^- ($X^1\Sigma^+$) relative to ZnF

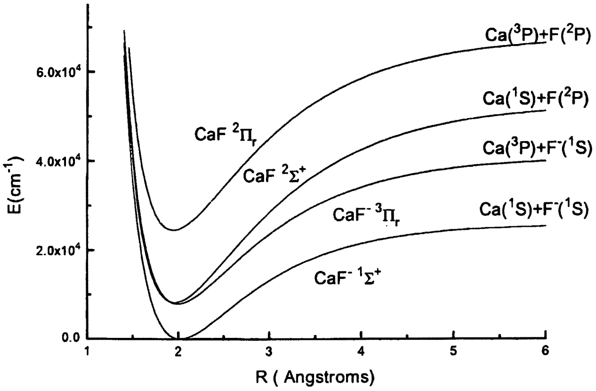

Figure 2. Generalized Morse Potentials for CaF and CaF⁻

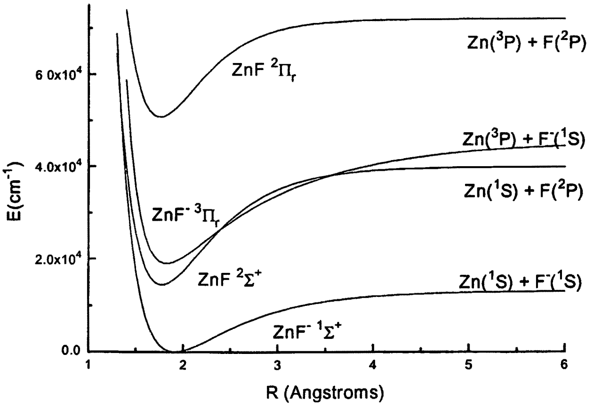

Figure 3. Generalized Morse Potentials for ZnF and ZnF⁻

($X^2\Sigma^+$). Our calculated differential is +0.138Å, in reasonable agreement with the experimental value of +0.150Å. The bond length contraction upon

Downloaded by NORTH CAROLINA STATE UNIV on September 14, 2012 | http://pubs.acs.org
Publication Date: August 14, 2002 | doi: 10.1021/bk-2002-0828.ch011

excitation discussed earlier for the neutral fluorides is also seen in the anions. In CaF^- the $^3\Pi_r$ bond length is 0.02Å shorter than in the $X^1\Sigma^+$ state while in ZnF^- the contraction is a substantial 0.087Å.

The Morse potential curves shown in Figures 2 and 3 illustrate several interesting features. The $^3\Pi_r$ state of CaF^- and the $^2\Sigma^+$ state of CaF are both bound relative to the $Ca(^1S)$ + $F^-(^1S)$ asymptote while neither $ZnF(^2\Sigma^+)$ nor $ZnF^-(^3\Pi_r)$ are bound relative to Zn (^1S) + $F^-(^1S)$. As noted, the small $Ca(^1S, {}^3P)$ separation of 1.86eV (less than the electron affinity of F) plays a major role in this. Also, the $CaF^-(^3\Pi_r)$ state is 0.03eV below the $CaF(^2\Sigma^+)$ state while $ZnF^-(^3\Pi_r)$ is 0.60eV above the $ZnF(^2\Sigma^+)$. These energy separations at the equilibrium geometry for each state are summarized in Figure 4.

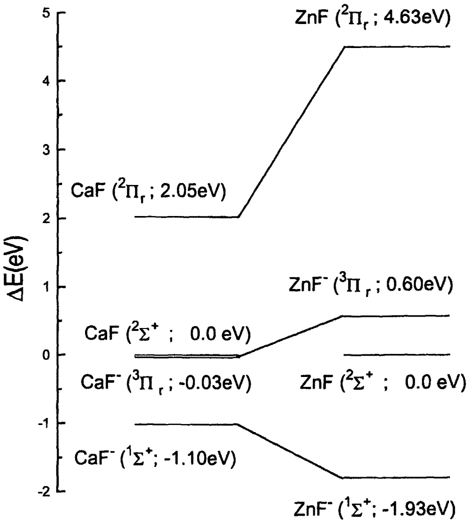

Figure 4.Comparison of CaF and ZnF and their Anions

Cations

Removing an electron in the singly occupied σ orbital from the $X^2\Sigma^+$ state of either ZnF or CaF results in a $X^1\Sigma^+$ state. The population analysis in

Downloaded by NORTH CAROLINA STATE UNIV on September 14, 2012 | http://pubs.acs.org
Publication Date: August 14, 2002 | doi: 10.1021/bk-2002-0828.ch011

Table 1 supports the view that the removed electron comes from the metal, as the Mulliken charge on F is only slightly less negative than in the neutral molecule. Clearly the large electrostatic stabilization that results from the highly positive metal and the negative F makes electron transfer to the metal energetically unfavorable. In both cations the calculated D_0 is larger than that of the neutral parent, another reflection of the increased ionic character. There are no experimental data on these cations . While our D_0 and R_e for CaF^+ are in reasonable agreement with the previous calculations of Partridge et al (25), our vibration frequency is significantly smaller.

CaO and ZnO Results

Neutrals

While both CaO and ZnO have a $X^1\Sigma^+$ ground state they dissociate to different atomic electronic states. The lowest neutral asymptote for CaO has Ca in an excited ^3P_u and O in the ground ^3P_g. This asymptote permits a sigma bond between the Ca 4s and O 2pz orbitals (taking the internuclear line as the z axis) and a π bond that is a mixture of a covalent interaction between the Ca πx orbital and the O px and a dative bond involving donation from the O py lone pair into the formally empty Ca πy orbital. The proximity of the ^3P_u and ^3D states of Ca ensures significant 3d character in the Ca π orbital. The lowest ionic asymptote (Ca^+O^-) permits a sigma bond between the Ca^+ 4s and the O^- 2pz orbitals, and two dative bonds from the O lone pairs in the π system. The low-lying pπ and dπ orbitals on Ca^+ facilitate significant back donation. This ionic curve will cross the neutral asymptote around 5.16Å, which is 2.8 times R_e (vide infra) while the doubly ionic asymptote ($Ca^{++}O^{--}$) will cross the neutral asymptote around 3.9Å (2.1 R_e). The early crossing of these two ionic curves with the neutral asymptote insures that the $X^1\Sigma^+$ state will have considerable ionic character. The lowest neutral asymptote for ZnO has Zn in the ground ^1S and O in the excited ^1D_g state. This asymptote permits a dative sigma bond between the Zn 4s pair and the empty O pz. Both ionic asymptotes (Zn^+O^- and $Zn^{++}O^{--}$) cross the neutral asymptote at 2.41Å or 1.4 R_e and accordingly one expects less ionic character than in CaO. The lowest ionic asymptote permits a covalent bond between the singly occupied 4s and $2p_z$ on Zn^+ and O^- and the same dative bonds as in Ca^+O^-, however, since the pπ orbital in Zn^+ lies at much higher energy than the dπ orbitals in Ca^+ they are not expected to participate as fully. The population analysis in Table 5 suggests that CaO be viewed as $Ca^{++}O^{--}$ with considerable back-donation from O to the Ca 3d orbitals, resulting in a 3d population of 0.77 electrons. ZnO however does appear to be consistent with a single bond between Zn^+(4s) and O^- ($2p_\sigma$).

Downloaded by NORTH CAROLINA STATE UNIV on September 14, 2012 | http://pubs.acs.org
Publication Date: August 14, 2002 | doi: 10.1021/bk-2002-0828.ch011

Downloaded by NORTH CAROLINA STATE UNIV on September 14, 2012 | http://pubs.acs.org
Publication Date: August 14, 2002 | doi: 10.1021/bk-2002-0828.ch011

Table 5.Oxide Population Analysis

Molecule	4s	$4p_\sigma$	$4p_{\pi x}$	$4p_{\pi y}$	$3d_{\sigma+\delta}$	$3d_{\pi x}$	$3d_{\pi y}$	$3d_{\delta+}$	2s	$2p_\sigma$	$2p_{\pi x}$	$2p_{\pi y}$	Q(M)	Q(X)
$CaO(X^1\Sigma^+)$	0.01	-0.04	0.02	0.02	0.31	0.23	0.23	0.01	2.03	1.67	1.72	1.72	+1.18	-1.18
$ZnO(X^1\Sigma^+)$	0.95	0.05	0.09	0.09	4.0	2.0	2.0	2.0	1.90	1.11	1.88	1.88	+0.82	-0.82
$CaO(^3\Pi_i)$	0.78	0.16	-0.01	-0.04	0.13	0.03	0.07	0.01	2.03	1.89	0.98	1.91	+0.85	-0.85
$ZnO(^3\Pi_i)$	1.04	0.29	0.01	0.04	4.0	2.0	2.0	2.0	1.94	1.70	0.99	1.94	+0.61	-0.61
$CaO(^3\Sigma^+)$	0.75	0.14	-0.02	-0.02	0.08	0.08	0.08	0.01	2.03	0.98	1.90	1.90	+0.85	-0.85
$ZnO(^3\Sigma^+)$	0.91	0.27	0.04	0.04	4.0	2.0	2.0	2.0	1.92	0.91	1.93	1.93	+0.72	-0.72
$CaO^-(^2\Sigma^+)$	0.71	0.28	0.03	0.03	0.24	0.19	0.19	0.01	2.00	1.77	1.75	1.75	+0.32	-1.32
$ZnO^-(^2\Sigma^+)$	1.17	0.43	0.11	0.11	4.0	2.0	2.0	2.0	1.92	1.48	1.87	1.87	+0.17	-1.17
$CaO^-(^2\Pi_i)$	1.77	0.18	-0.02	-0.01	0.13	0.02	0.05	0.02	2.00	1.88	0.99	1.93	-0.16	-0.84
$ZnO^-(^2\Pi_i)$	2.17	0.24	0.01	0.03	4.0	2.0	2.0	2.0	1.83	1.73	0.99	1.96	-0.47	-0.53
$CaO^-(^2\Pi_r)$	0.0	-0.04	0.67	0.02	0.26	0.48	0.21	0.01	2.03	1.73	1.81	1.74	+0.35	-1.35
$ZnO^-(^2\Pi_r)$	0.90	0.07	1.28	0.08	4.0	2.0	2.0	2.0	1.90	1.16	1.70	1.90	-0.32	-0.68
$CaO^+(^2\Pi_i)$	-0.03	-0.05	-0.02	-0.01	0.17	0.03	0.10	0.01	2.04	1.84	0.97	1.87	+1.77	-0.77
$ZnO^+(^2\Pi_i)$	0.39	0.08	0.01	0.05	4.0	2.0	2.0	2.0	1.95	1.55	0.98	1.92	+1.45	-0.45
$CaO^+(^2\Sigma^+)$	-0.05	-0.06	-0.01	-0.01	0.10	0.12	0.12	0.01	2.02	0.96	1.86	1.86	+1.75	-0.75
$ZnO^+(^2\Sigma^+)$	0.16	0.07	0.07	0.07	4.0	2.0	2.0	2.0	1.90	0.86	1.90	1.90	+1.60	-0.60

Calculated and experimental spectroscopic properties of the neutral oxides are collected in Table 6

The a$^3\Pi_i$ state of both molecules correlate to the lowest atomic asymptotes, which permits a sigma bond between the singly occupied O 2p$_z$ orbital and an *sz* hybrid on the metal, leaving the triplet coupled electrons in the companion $s\bar{z}$ hybrid on the metal and on O in the pπ orbital. Note that only a singly charged ionic asymptote can contribute to this state (and the $^3\Sigma^+$, vide infra) and the lowest ionic crossings occur at 3.10Å (2.1 R$_e$) and 1.8Å (1.0 R$_e$) for CaO and ZnO respectively, consistent with the population analysis results (Table 5) that CaO is the more ionic.

The $^3\Sigma^+$ states of both molecules correlate to the excited ^3P_u state of the metal and the ground ^3P_g state of O. The four unpaired electrons in this asymptote can be triplet coupled in three ways and this permits the wave function to be a mixture of a σ bond with the π electrons triplet coupled and a π bond with the σ electrons triplet coupled. The lowest ionic asymptote, metal (4s) + O$^-$(2p^5) has the π electrons singlet coupled and crosses the neutral asymptotes at 5.16Å (2.6 R$_e$, Ca$^+$O$^-$) and 3.66Å (2.0 R$_e$, Zn$^+$O$^-$) suggesting that the triplet coupled electrons will be primarily in the σ system. Because the ^{2}S-^{2}D separation in Ca$^+$ is only 1.697 eV, a second ionic asymptote, Ca$^+$(^{2}D) + O$^-$(^{2}P) is important and crosses at 3.21Å (1.6 R$_e$), differentially stabilizing CaO, over ZnO. The relative locations of these states are shown in Figures 5 and 6.

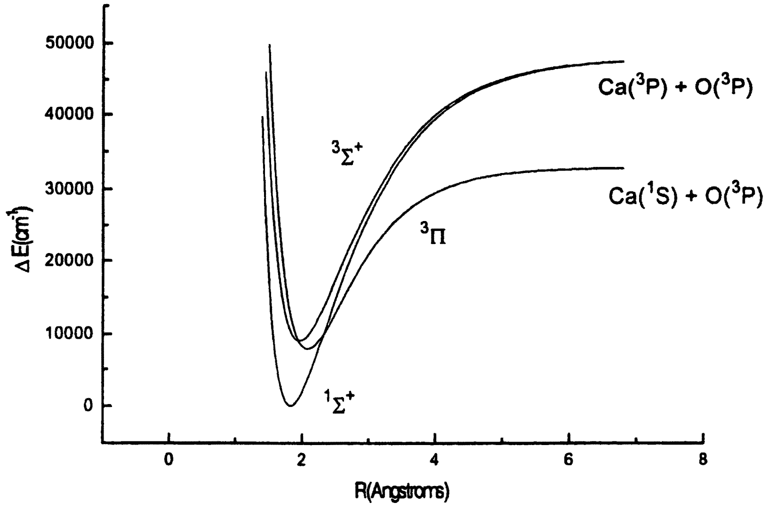

Figure 5. Generalized Morse Potentials for CaO

Downloaded by NORTH CAROLINA STATE UNIV on September 14, 2012 | http://pubs.acs.org
Publication Date: August 14, 2002 | doi: 10.1021/bk-2002-0828.ch011

Downloaded by NORTH CAROLINA STATE UNIV on September 14, 2012 | http://pubs.acs.org
Publication Date: August 14, 2002 | doi: 10.1021/bk-2002-0828.ch011

Table 6. Oxide results, previous calculations and experiment

Molecule	Source	Re(Å)	ω_e(cm^{-1})	D_0(eV)	T_0(eV)
$CaO(X^1\Sigma^+)$	This work	1.829	721	5.91[a]	0.0
	Previous	1.886[16]	677[16]	6.03[a,41]	0.0
	Experiment	1.8221	732	5.96[a,21]	0.0
$ZnO(X^1\Sigma^+)$	This work	1.715	741	3.54[b]	0.0
	Previous[29]	1.719	727	3.59[b]	0.0
	Previous[28]	1.733	690	3.25[b]	0.0
	Experiment		805(40)[34]	3.57[b,42]	
	Experiment[3]		720(20)		
$CaO(^3\Pi_i)$	This work	2.082	543	3.07[c]	0.92
	Previous[24]	2.086	544	3.08[c]	
	Previous[16]	2.153	508		
	Experiment[17]	2.099	556		1.031
$ZnO(^3\Pi_i)$	This work	1.850	577	1.31[c]	0.35
	Previous[29]	1.857	567	1.38[c]	0.26
	Previous[28]	1.873	525		0.04
	Experiment	$X^1\Sigma^+$+0.126[3]	550(20)[3]	1.36[c,34]	0.313(10)[3]
$CaO(^3\Sigma^+)$	This work	1.964	587	4.78[a]	1.07
	Previous[16]	2.031	554		
$ZnO(^3\Sigma^+)$	This work	1.801	596	3.87[d]	1.83
	Previous[28]	1.818	561		1.512
	Previous[38]	1.816	611		1.465
	Experiment[3]	$X^1\Sigma^+$+0.086	560(20)		1.875(10)

a. Relative to $Ca(^3P) + O(^3P)$
b. Relative to $Zn(^1S) + O(^1D)$
c. Relative to ground state products
d. Relative to $Zn(^3P) + O(^3P)$

Downloaded by NORTH CAROLINA STATE UNIV on September 14, 2012 | http://pubs.acs.org
Publication Date: August 14, 2002 | doi: 10.1021/bk-2002-0828.ch011

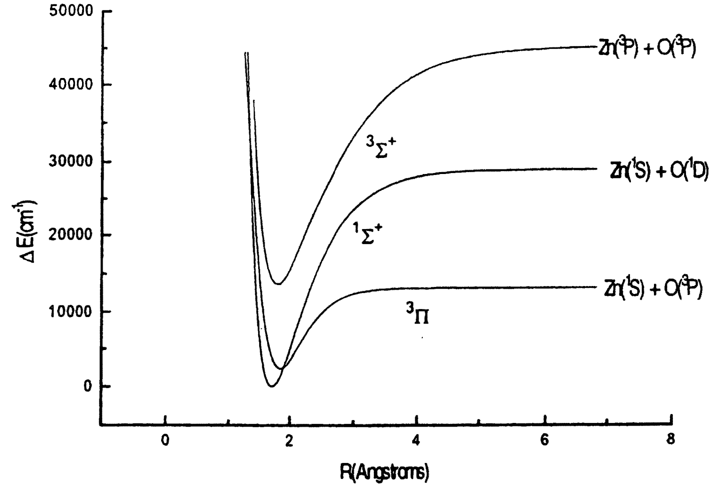

Figure 6. Generalized Morse Potentials for ZnO

The Mulliken populations (Table 5) are consistent with the long standing view that CaO is essentially Ca^+O^- and has a comparable ionicity in the $a^3\Pi_i$ and $^3\Sigma^+$ states and that they differ primarily in the orientation of the p hole on O^-, with the $a^3\Pi_i$ hosting a π hole and the $^3\Sigma^+$ the σ hole. In ZnO however the $a^3\Pi_i$ state is less ionic than the $^3\Sigma^+$ state and both are less ionic than CaO. The difference in ionicity between CaO and ZnO contributes to the significantly different $a^3\Pi_i$ - $^3\Sigma^+$ energy separation. In CaO the $a^3\Pi_i$ state lies 0.143eV (calculated, 0.142eV) below the $^3\Sigma^+$ state while in ZnO the states are in the same order but separated by 1.56eV (calculated, 1.41eV). The order of the two states and their separation in CaO has been attributed to the differential in the monopole-quadrupole interaction between Ca^+ and the two orientations of O^-, and while this interaction is certainly present in ZnO the ionic character has not overcome the residual covalence in the $^3\Sigma^+$ state, resulting in much larger separations. As shown in Figure 6, the $^3\Sigma^+$ state traces its lineage to the Zn(^{3}P) + O(^{3}P) asymptote, 3.996 eV above the ground state products, while the corresponding asymptote in CaO is only 1.86eV above ground state products (Figure 5).

Not surprisingly the dipole moment of CaO ($X^1\Sigma^+$), 8.84D, is very close to that expected for two unit charges separated by the calculated bond length, 8.79D, and is significantly larger than that of ZnO ($X^1\Sigma^+$), 5.49D . The same model predicts the dipole moment of Zn^+O^- to be 8.24D and scaling this by the Mulliken charge gives 6.75D, still larger than the *ab initio* value. Since the 4s on Zn seems unhybridized it will not contribute to a decrease in the dipole moment. However, the 2s-2pσ hybrid on O will be polarized toward Zn and away from O and this could account for the

Downloaded by NORTH CAROLINA STATE UNIV on September 14, 2012 | http://pubs.acs.org
Publication Date: August 14, 2002 | doi: 10.1021/bk-2002-0828.ch011

decrease from 6.75D to 5.49D. There are no experimental values for these dipole moments. Our calculated bond lengths for the $X^1\Sigma^+$ and $a^3\Pi_i$ states of CaO differ from experiment by +0.007Å and -0.017Å respectively. While there are no experimental ZnO bond lengths, Moravec et. al. (3) have reported the equilibrium bond lengths of ZnO $a^3\Pi_i$ and $^3\Sigma^+$ relative to $X^1\Sigma^+$ of +0.126Å, and +0.086Å and we calculate +0.135Å and +0.086Å. Unlike the fluorides, the bond length in the oxides increases upon electronic excitation. Our calculated vibration frequencies for CaO in the $X^1\Sigma^+$ and $a^3\Pi_i$ states are less than experiment by 11cm^{-1} and 13cm^{-1} while for the three reported states of ZnO we are larger than experiment (21cm^{-1} in $X^1\Sigma^+$; 27cm^{-1} in $a^3\Pi_i$, and 36cm^{-1} in $^3\Sigma^+$) although there is a 20cm^{-1} uncertainty in the experimental numbers. D_0 values for the $X^1\Sigma^+$ states, referred to the Ca (^3P) + O(^3P) and Zn(^1S) + O(^1D) asymptotes are in good agreement with experiment. T_0's for CaO($a^3\Pi_i$) and ZnO($a^3\Pi_i$) both differ from experiment by -0.05eV while our ZnO($^3\Sigma^+$) is too low by 0.178eV. Our calculated ionization potentials for both CaO and ZnO are in reasonable agreement with experiment (calculated, 6.77 and 9.26eV ; experimental, 6.66(18) and 9.095eV).

Anions

Calculated and experimental spectroscopic properties for the anions are collected in Table 7. Adding an electron to the $X^1\Sigma^+$ state of CaO or ZnO results in a $^2\Sigma^+$ state in which the additional electron is localized in the sigma system and shared between the metal and O. In CaO$^-$ most of the electron stays on Ca as the in-situ charge on Ca decreases from 1.18 to 0.32, accounting for 0.86 of the added electron, while in ZnO$^-$ the Zn charge decreases from 0.82 to 0.17, accounting for 0.65 of the added electron and reflecting the larger ionic character of CaO. The bond lengths in CaO$^-$ and ZnO$^-$ both increase (0.064Å and 0.044Å), while the vibration frequencies decrease by 50cm^{-1} and 76cm^{-1} respectively. Adding an electron to the $a^3\Pi_i$ state of the neutral oxide results in a $^2\Pi_i$ state in which the added electron is essentially localized in the sigma system of the metal. In CaO$^-$ the *in situ* charge decreases from 0.85 to -0.16 while in ZnO it drops from 0.61 to -0.47 accounting for 1.01 and 0.86 electrons respectively. The $^2\Pi_r$ state of the anions is best thought of as obtaining from the addition of an electron to the $X^1\Sigma^+$ state. In CaO$^-$ the added electron is in a metal centered π orbital with the composition $p_\pi^{0.67} d_\pi^{0.25}$, remarkably similar to the $p_\pi^{0.70} d_\pi^{0.27}$ occupancy in CaF ($^2\Pi_r$).

There are no experimental data on the CaO anions and little on ZnO$^-$. The photoelectron spectroscopic study of Fancher et al (35) suggests that

Downloaded by NORTH CAROLINA STATE UNIV on September 14, 2012 | http://pubs.acs.org
Publication Date: August 14, 2002 | doi: 10.1021/bk-2002-0828.ch011

Table 7. Oxide Ion results; previous calculations and experiment

Molecule	Source	Re(Å)	ω_e(cm^{-1})	D_0(eV)	T_0(eV)
$CaO^-(X^2\Sigma^+)$	This work	1.893	671	3.54[a]	0.0
$ZnO^-(X^2\Sigma^+)$	This work	1.759	665	2.19[a]	0.0
	Previous[29]	1.764	664	2.20[a]	0.0
	Experiment[34]	$X^1\Sigma^+$+0.068	625(40)	2.24(5)[a]	0.0
	Experiment[3]	$X^1\Sigma^+$+0.048	650(50)		
$CaO^-(^2\Pi_i)$	This work	2.151	467	2.79[a]	0.72
$ZnO^-(^2\Pi_i)$	This work	1.984	407	1.50[a]	0.71
	Experiment[3]				0.73
$CaO^-(^2\Pi_r)$	This work	1.869	665	4.18[b]	1.36
$ZnO^-(^2\Pi_r)$	This work	1.762	641	3.27[b]	2.89
$CaO^+(^2\Pi_i)$	This work	1.992	638	3.33[c]	0.0
	Previous[25]	1.996	669	3.29[c]	0.0
$ZnO^+(^2\Pi_i)$	This work	1.798	644	1.66[c]	0.0
$CaO^+(^2\Sigma^+)$	This work	1.875	704	4.94[d]	0.08
	Previous[25]	1.885	728	3.29[d]	0.09
$ZnO^+(^2\Sigma^+)$	This work	1.708	759	1.74[e]	1.99

a. Relative to $M(^1S) + O^-(^2P)$
b. Relative to $M(^3P) + O^-(^2P)$
c. Relative to $M^+(^2S) + O(^3P)$
d. Relative to $Ca^+(^2D) + O(^3P)$
e. Relative to $Zn^+(^2S) + O(^1D)$

Downloaded by NORTH CAROLINA STATE UNIV on September 14, 2012 | http://pubs.acs.org
Publication Date: August 14, 2002 | doi: 10.1021/bk-2002-0828.ch011

the bond length in ZnO^-($X^2\Sigma^+$) is 0.068Å larger than in $ZnO(X^1\Sigma^+)$ while Moravec et al (3) suggest 0.048Å, much closer to our computed value of 0.044Å. Additionally our computed frequency, 665cm^{-1} agrees better with the 650cm^{-1} result of Moravec et al than with the 625cm^{-1} result of Fancher et al, although both experimental frequencies have large uncertainties. The relative energies of CaO, ZnO and their anions are shown in figure 7, while the Morse potentials comparing CaO and CaO^- and ZnO and ZnO^- are shown in figures 8 and 9 respectively.

Cations

The $^2\Pi_i$ ground states of both CaO^+ and ZnO^+ dissociate to the metal$^+$(^{2}S) + O(^{3}P) asymptote while the excited $^2\Sigma^+$ state dissociate to $Ca^+(^2D)$ + $O(^3P)$ and $Zn^+(^2S)$ + $O(^1D)$. Our calculations suggest that CaO^+ in both the $^2\Pi_i$ and $^2\Sigma^+$ states should be considered $Ca^{++}O^-$ with some back donation (0.25 electrons) into the 3d orbitals of Ca, resulting in a charge of approximately +1.75. This Ca^{++} character is consistent with the location of the lowest doubly positive asymptote, Ca^{++} (^{1}S) + $O^-(^2P)$, which is 8.71eV above the $Ca^+(^2D)$ + $O(^3P)$ asymptote. The resulting doubly positive curve intersects the lower asymptote at 3.31Å or 1.8 R_e, permitting considerable charge transfer. There is also significant $Zn^{++}O^-$ character to ZnO^+ in the $^2\Sigma^+$ state (the Zn charge is +1.60) but somewhat less in the $^2\Pi_i$ ground state where Zn has a charge of +1.45. These charges are also consistent with the doubly positive Zn asymptote being 14.5 and 16.5eV above the $^2\Pi_i$ and $^2\Sigma^+$ asymptotes. The charge distribution on O in the $^2\Pi_i$ and $^2\Sigma^+$ states of CaO^+ is remarkably similar to that on O in the $^3\Pi_i$ and $^3\Sigma^+$ states of neutral CaO and this similarity is reflected in the comparable Π_i - Σ^+ energy separation in the neutral (0.15eV) and positive ion (0.08eV), reinforcing the idea that this separation is dominated by the same quadrupolar interaction in both systems. The Π_i - Σ^+ separation in ZnO^+ (1.97eV) is comparable to that in ZnO (1.48eV) and considerably larger than in the corresponding CaO system, reflecting the effects of residual covalent bonding in the ZnO system. There are no experimental data on either of these cations, but there are calculations (25) on CaO^+ with which we are in reasonable agreement (see Table 7)

Conclusions

On the basis of the many detailed results presented in this work we conclude that the fundamental difference between the electronic structures of CaX and ZnX molecules is that CaX is much more ionic than ZnX. Although the 3d shell fills completely in going from Ca to Zn, it does not

Downloaded by NORTH CAROLINA STATE UNIV on September 14, 2012 | http://pubs.acs.org
Publication Date: August 14, 2002 | doi: 10.1021/bk-2002-0828.ch011

completely shield the increased nuclear charge on Zn and its ionization energy, 9.391eV is much larger than that of Ca (6.111 eV). This results in an ionic-covalent curve crossing at a much shorter internuclear distance in ZnO than in CaO. For example, the $X^1\Sigma^+$ state of CaO correlates with the Ca(^{3}P) + O(^{3}P) neutral asymptote, and the potential energy curve of the lowest ionic products, Ca$^+$(^{2}P) + O$^-$(^{2}P) crosses this asymptote at 5.2 Å. However, the $X^1\Sigma^+$ state of ZnO correlates with the Zn(^{1}S) + O(^{1}D) neutral products and the lowest energy ionic products cross this neutral asymptote at 2.41 Å with the result that CaO is more ionic than ZnO.

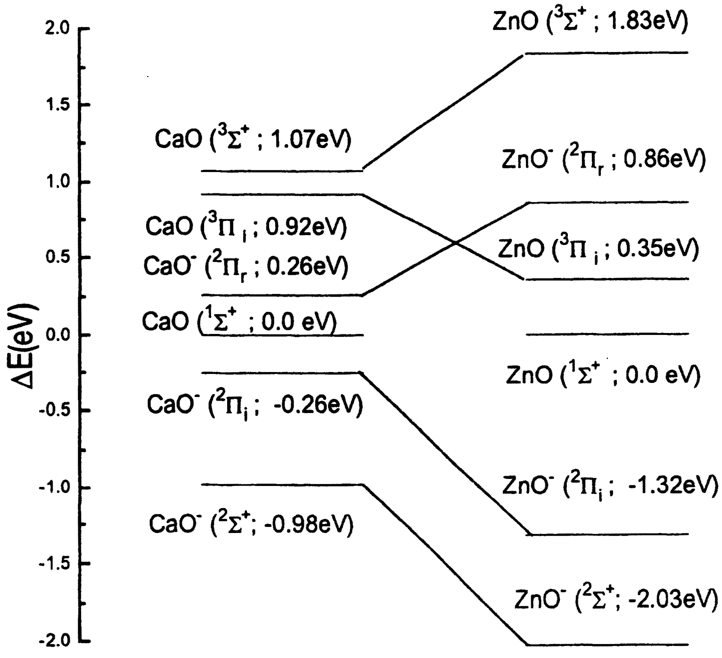
2.0
1.5
1.0
0.5
0.0
-0.5
-1.0
-1.5
-2.0
ΔE(eV)
CaO ($^3\Sigma^+$; 1.07eV)
CaO ($^3\Pi_i$; 0.92eV)
CaO$^-$ ($^2\Pi_r$; 0.26eV)
CaO ($^1\Sigma^+$; 0.0 eV)
CaO$^-$ ($^2\Pi_i$; -0.26eV)
CaO$^-$ ($^2\Sigma^+$; -0.98eV)
ZnO ($^3\Sigma^+$; 1.83eV)
ZnO$^-$ ($^2\Pi_r$; 0.86eV)
ZnO ($^3\Pi_i$; 0.35eV)
ZnO ($^1\Sigma^+$; 0.0 eV)
ZnO$^-$ ($^2\Pi_i$; -1.32eV)
ZnO$^-$ ($^2\Sigma^+$; -2.03eV)

Figure 7. Comparison of CaO and ZnO and their anions

Downloaded by NORTH CAROLINA STATE UNIV on September 14, 2012 | http://pubs.acs.org
Publication Date: August 14, 2002 | doi: 10.1021/bk-2002-0828.ch011

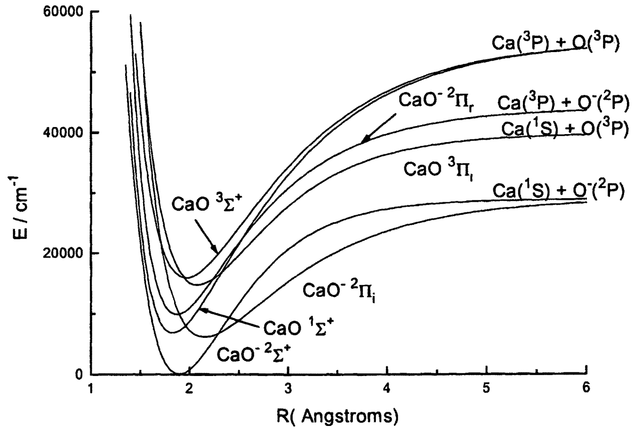

Figure 8. Generalized Morse Potentials for CaO and CaO^-

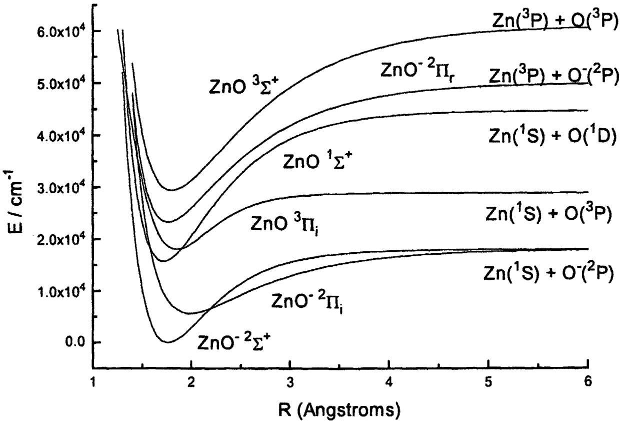

Figure 9. Generalized Morse Potentials for ZnO and ZnO^-

References

1. Rice, S. F.; Martin, H.; Field, R. W. *J. Chem. Phys.* **1985**,*82*,5023
2. Norman, J. B.; Cross, K. J.; Schweda, M. P.; Field, R. W. *Mol. Phys.* **1989**,*66*,235

3. Moravec, V.; Klopcic, S. A.; Chatterjee, B.; Jarrold, C. C. Chem. Phys. Lett. **2001**,*341*,313
4. *Molpro* is a package of ab initio programs written by H. J. Werner, H.J; Knowles, P.J; with contributions from Amos, R. D; Bernhardsson, A.; Berning, A.; Celani,P.; Cooper, D.L.; Deegan, M.J.O.; Dobbyn, A.J.;Eckert, F.;Hampel, C.;Hetzer, G.;Korona, T.;Lindh, R.;Loyd, A.W.;McNicholas, S.J.;Manby. F.R.;Meyer, W.;Mura, M.E.;Nicklass, A.;Palmieri, P.;Rauhut, G.;Schutz, M.;Stoll, H.;Stone, A.J.;Tarroni, R.;Thorsteinsson, T.
5. Lindh, R.; Ryu, U.; Liu, B. *J. Chem. Phys.* **1991**,*95*,5889
6. Cizek, J. *J. Chem. Phys.* **1966**,*45*,4526
7. Cizek, J. *Adv. Chem. Phys.* **1969**,*14*,35
8. Knowles, P. J.; Hampel, C.; Werner, H. J. *J. Chem. Phys.* **1993**,*99*,5219
9. Kendall,R.A; Dunning,Jr.,T.H.; Harrison,R.J. *J. Chem. Phys.* **1992**,*96*,6769-6806
10. Heineman,C.; Koch,W.; Partridge,H. *Chem. Phys. Lett* **1998**,*286*,131-137
11. Bauschlicher, Jr. C.W.;Rosi, M.;Langhoff, S.R. *Chem. Phys.* **1990**,*146*,237-243
12. Yoshimine, M. *J. Phys. Soc. Jpn.* **1968**,*25*,1100
13. McLean, A.D.; Yoshimine, M. *IBM J. Res. Dev.* **1968**,*12*,206
14. Carlson, K. D.; Kaiser, K.; Moser, C.; Wahl, A. C. *J. Chem. Phys.* **1970**,*52*,4678
15. Bauschlicher, Jr. C. W.; Yarkony, D. R. *J. Chem. Phys.* **1978**,*68*,3990
16. England, W. B. *Chemical Physics* **1980**,*53*,1
17. Field, R. W. *J. Chem. Phys.* **1974**,*60*,2400
18. Diffenderfer, R. N.; Yarkony, D. R. *J. Chem. Phys.* **1982**,*77*,5573
19. Diffenderfer, R. N.; Yarkony, D. R. *J. Chem. Phys.* **1983**,*78*,7017
20. Bauschlicher, Jr., C. W.; Partridge, H. *Chem. Phys. Lett.* **1983**,*94*,366
21. Irvin, J. A.; Dagdigian, P. J. *J. Chem. Phys.* **1980**,*73*,176
22. Langhoff, S. R.; Bauschlicher, Jr., C. W.; Partridge, H. *J. Chem. Phys.* **1986**,*84*,1687
23. Langhoff, S. R.; Bauschlicher, Jr., C. W.; Partridge, H.;Ahlrichs, R. *J. Chem. Phys.* **1986**,*84*,5025
24. Langhoff, S. R.; Bauschlicher, Jr., C. W.; Partridge, H. *J. Chem. Phys.* **1986**,*84*,4474
25. Partridge, H.; Langhoff, S. R.; Bauschlicher, Jr., C. W. *J. Chem. Phys.* **1986**,*84*,4489
26. Bauschlicher, Jr., C. W.; Langhoff, S. R. *Chem. Phys. Lett.* **1986**,*126*,163
27. Bowmaker, G. A.; Schwerdtfeger, P. *J. Mol. Structure (Theochem)* **1990**,*205*,295
28. Boldyrev, A. I.; Simons, *J. Mol. Phys.* **1997**,*92*,365
29. Bauschlicher, Jr., C. W.; Partridge, H. *J. Chem. Phys.* **1998**,*109*,8430
30. Gutsev, G. L.;Rao, B. K.;Jena, P. *J. Phys. Chem. A.* **2000**,*104*,5374

Downloaded by NORTH CAROLINA STATE UNIV on September 14, 2012 | http://pubs.acs.org
Publication Date: August 14, 2002 | doi: 10.1021/bk-2002-0828.ch011

31. Moore, C. E. Atomic Energy Levels, *Natl. Bur. Stand. (US)*, **1949**, Circ. 467
32. Jakubek, Z.J.; Harris, N.A.; Field, R.W.; Gardner, J.A.; Murad, E. *J. Chem. Phys.* **1994**,*100*,622
33. Hotop, H.; Lineberger, W. C. *J. Phys. Chem. Ref. Data*, **1985**,*14*,731
34. Fancher, C.A.; de Clercq, H.L.; Thomas, O.C.; Robinson, D.W.; Bowen, K.H. *J. Chem. Phys.* **1998**,*109*,8426
35. Ernst, W. E.; Kandler, J. *Phys. Rev. A.* **1989**,*39*,1575
36. Childs, W. J;Goodman, L. S.;Nielsen, U.; Pfeufer, V. *J.Chem.Phys.* **1984**,*80*,2283
37. Coxon, J. A.; Hajigeorgiou, P. G. *J. Mol. Spectrosc.* **1991**,*150*,1
38. Huber, K. P.; Herzberg, G. *Molecular Spectra and Molecular Structure, Constants of Diatomic Molecules* , **1979** (New York; van Nostrand Reinhold)
39. Kleinschmidt, P. D.; Hildenbrand, D. L. *J. Chem. Phys.* **1978**,*68*,2819
40. Karny, Z.; Zare, R. N. *J. Chem. Phys.* **1978**,*68*,3360
41. Bauschlicher, Jr., C. W.; Partridge, H.; Sodupe, M.; Langhoff, S. R.. *J. Phys. Chem.* **1992**,*96*,9259
42. Dalleska, N. F.; Armentrout, P.B. *J. Mass Spectrom. Ion Processes* **1994**,*134*,203-212

Downloaded by NORTH CAROLINA STATE UNIV on September 14, 2012 | http://pubs.acs.org
Publication Date: August 14, 2002 | doi: 10.1021/bk-2002-0828.ch011

Downloaded by COLUMBIA UNIV on September 14, 2012 | http://pubs.acs.org
Publication Date: August 14, 2002 | doi: 10.1021/bk-2002-0828.ch012

Chapter 12

The $X_1(^2\Pi_{3/2})$ and $X_2(^2\Pi_{1/2})$ Potentials of the Halogen Monoxides: A Comparison of RKR and Ab Initio Results

Charles E. Miller

Department of Chemistry, Haverford College, Haverford, PA 19041–1392

Experimentally determined RKR potentials for the $X_1(^2\Pi_{3/2})$ and $X_2(^2\Pi_{1/2})$ states of the halogen monoxides FO, ClO, BrO and IO are compared to available ab initio potentials. The results suggest that fully relativistic ab initio calculations have the capability to reproduce the experimental bond lengths, harmonic vibrational frequencies and fine structure intervals of the XO series with reasonable accuracy. The quest for spectroscopically accurate XO potentials will provide an excellent benchmark for future theoretical methods.

This paper addresses the question of what it means to have a spectroscopic quality potential energy surface. The literature of the last few years contains numerous references to spectroscopic quality ab initio molecular potentials, yet the definition of spectroscopic quality necessarily depends on the resolution of the experimental spectrum and the theoretical calculation. The accuracy of a molecular potential is perhaps better characterized by asking how well it reproduces experimental observables. This topic is explored by comparing the $X_1(^2\Pi_{3/2})$ and $X_2(^2\Pi_{1/2})$ potentials of the halogen monoxides determined from high-resolution spectroscopic studies with potentials computed using ab initio methods. The RKR potentials determined from spectroscopic data provide

In Low-Lying Potential Energy Surfaces; Hoffmann, M., et al.;
ACS Symposium Series; American Chemical Society: Washington, DC, 2002.

faithful representations of the XO experimental information and serve as valuable benchmarks for ab initio work.

The halogen monoxides, XO (where X = F, Cl, Br, I), represent a fundamental series of main group inorganic oxides that should have interesting chemical bonding due to the competition between the two highly electronegative atoms and the presence of an unpaired valence electron. They are diatomic molecules, so that, in principle, one may obtain "exact" quantum mechanical potentials from spectroscopic data inversions. Similarly, determining the potentials from ab initio methods should prove a tractable problem. Examination of the entire XO series enables one to investigate periodic trends, comment on structure/reactivity relationships and begin to understand the bonding likely to occur in larger halogen oxides.

The high-resolution spectroscopic data used to derive the RKR potentials for FO, ClO, BrO and IO has been described in a series of recent publications (*1-4*). The potentials include transitions between molecular eigenstates with up to 10,000 cm^{-1} of internal energy (~40% of the X-O bond dissociation energy) measured with microwave accuracy. The XO ground state possesses the electronic configuration $(z\sigma)^2(y\sigma^*)^2(x\sigma)^2(w\pi)^4(v\pi^*)^3$ where the values of v, w, x, y and z vary with the identity of the halogen atom. The unpaired π^* electron gives rise to an inverted $^2\Pi$ state with the $X_1(^2\Pi_{3/2})$ lying below the $X_2(^2\Pi_{1/2})$ state. The fine structure splitting between $X_1(^2\Pi_{3/2})$ and $X_2(^2\Pi_{1/2})$ scales with the $^2P_{3/2}$ – $^2P_{1/2}$ splitting of the halogen atom. All four members of the XO series examined here are good examples of Hund's case (*a*) coupling, the limit in which the fine structure splitting is much larger than the rotational constant, $A/B >> 1$.

Downloaded by COLUMBIA UNIV on September 14, 2012 | http://pubs.acs.org
Publication Date: August 14, 2002 | doi: 10.1021/bk-2002-0828.ch012

FO

The $X_1(^2\Pi_{3/2})$ and $X_2(^2\Pi_{1/2})$ potentials of FO were derived from a combined fit to the existing microwave, LMR and high-resolution FTIR spectroscopic data (*2*). The data included transitions for vibrational levels up to $v = 7$ and direct measurements of $X_1(^2\Pi_{3/2})$ – $X_2(^2\Pi_{1/2})$ fine structure transitions. The RKR potentials and associated vibrational intervals are shown in Figure 1. Figure 2 compares the $X\ ^2\Pi$ RKR potential with available ab initio potential energy points (*5-7*).

A broader comparison with ab initio work is made in Table I where r_e, ω_e and $\omega_e x_e$ values are collected. One notes that all of the calculations in Table I report effective $^2\Pi$ equilibrium properties. Additionally, the majority of calculations are unable to reproduce simultaneously the equilibrium bond length and the harmonic vibrational frequency. The MRCI/aug-cc-pVQZ calculations

Downloaded by COLUMBIA UNIV on September 14, 2012 | http://pubs.acs.org
Publication Date: August 14, 2002 | doi: 10.1021/bk-2002-0828.ch012

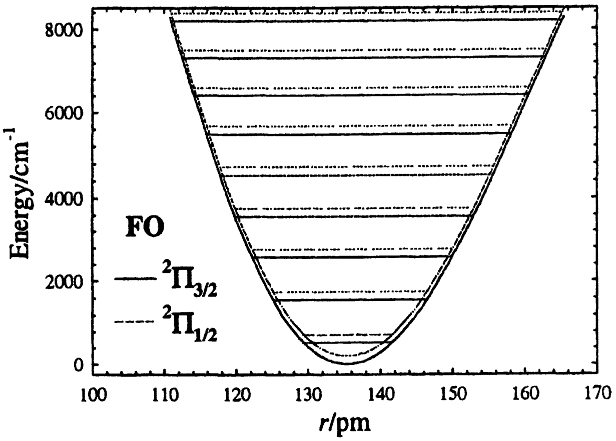

Fig. 1. FO $^2\Pi_{3/2}$ and $^2\Pi_{1/2}$ RKR potentials and vibrational levels (2).

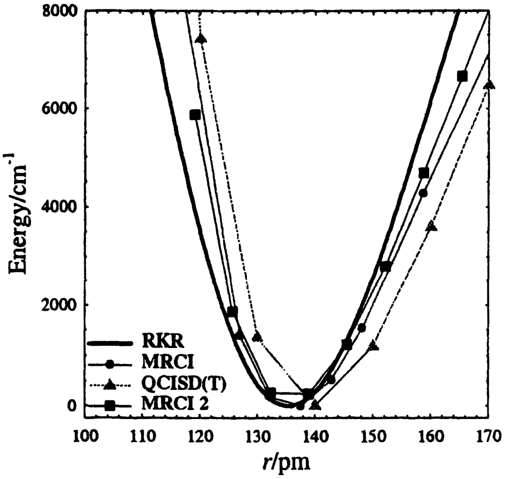

Fig. 2. A comparison of the FO RKR $^2\Pi$ potential with several ab initio potentials (2).

of Leonard et al. (*7*) provide the most accurate characterization of FO *X* ($^2\Pi$) but closer examination of Figure 2 shows that these calculations yield a potential that is too anharmonic for energies above 2000 cm^{-1}.

Table I. Ab Initio Characterization of FO *X* ($^2\Pi$)

Level of Theory	r_e/pm	ω_e/cm^{-1}	*Reference*
B3LYP/6-311++G(3df,3pd)	134.6	1120	(*8*)
MP2/6-31G(d)	134.4	1542	(*9*)
UMP4/5s4p2d	135.2	1468	(*10*)
AUMP2/6-31G*	136.53	1092	(*11*)
QCISD(T)/ 6-31+G*	138	1017	(*6*)
QCISD(T)/ 6-311++G(3df)	135.6	1027	(*12*)
CCSD(T)/cc-pVTZ	137.33	1072	(*13*)
UCCSD(T)/5s4p2d	137.0	1060	(*10*)
UGA-CCSD/6-31G*	138.3	1075	(*14*)
UGA-CCSD/TZ2P	135.4	1085	(*14*)
MRCI/aug-cc-pVQZ	135.5	1047	(*7*)
MRCI/extended gaussian	136.1	992	(*5*)
Experiment ($^2\Pi_{eff}$)	135.411	1053.01	(*2*)

ClO

The $X_1(^2\Pi_{3/2})$ and $X_2(^2\Pi_{1/2})$ potentials of ClO were derived from a combined fit to the existing microwave, FIR and high-resolution FTIR spectroscopic data (*3*). The data included transitions from ^{35,37}Cl^{16,18}O isotopomers in vibrational levels up to $v = 2$. Figure 3 shows the ^{35}Cl^{16}O potentials and their associated vibrational levels. Pettersson et al. (*15*) reported a tabulated set of CCI+Q potential energy points and these are plotted against the RKR $X(^2\Pi)$ potential in Figure 4. The agreement between the experimental and ab initio potentials is very good. The small discrepancies for energies above 4000 cm^{-1} may be due to the extrapolation of the RKR potential to energies not included in the inversion.

Table II compares the experimental $X(^2\Pi)$ parameters with available ab initio values; again no ab initio calculations report resolved $^2\Pi$ equilibrium properties. The theoretical characterizations of ClO agree much better with experiment than the corresponding FO calculations, probably reflecting difficulties with the anomalous properties of the F-O bond (see below). Methods employing sophisticated electron correlation effects perform very well, with the

Downloaded by COLUMBIA UNIV on September 14, 2012 | http://pubs.acs.org
Publication Date: August 14, 2002 | doi: 10.1021/bk-2002-0828.ch012

Downloaded by COLUMBIA UNIV on September 14, 2012 | http://pubs.acs.org
Publication Date: August 14, 2002 | doi: 10.1021/bk-2002-0828.ch012

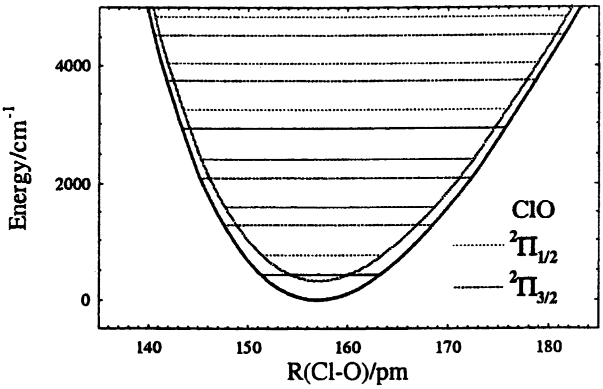

Fig. 3. ClO $X_1(^2\Pi_{3/2})$ and $X_2(^2\Pi_{1/2})$ RKR potentials and vibrational levels

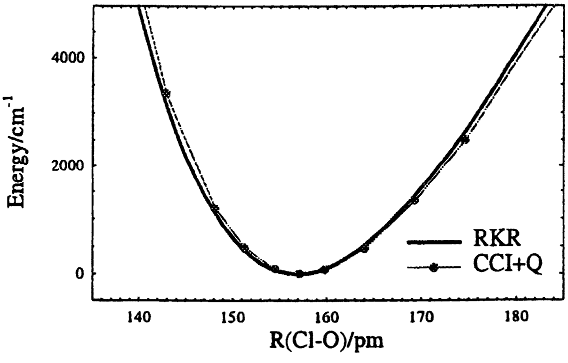

Fig. 4. A comparison of the RKR and CCI+Q potential for ClO X *($^2\Pi$).*

Table II. Ab Initio Characterization of ClO X ($^2\Pi$)

Level of Theory	r_e/*pm*	ω_e/*cm*$^{-1}$	$\omega_e x_e$ /*cm*$^{-1}$	*Reference*
HCTH/TZ2P	157.0			(*17*)
QCISD(T)/ 6-311++G(3df)	158.0	840.9	6.7	(*12*)
CCI(9)+Q	157.2	845		(*15*)
CCI(13)+Q+rel	158.5	810		(*15*)
EHFACE2U	157.0	848.5	4.74	(*16*)
MRCI/aug-cc-pV5Z	157.9	852.3	4.9	(*7*)
Experiment ($^2\Pi_{eff}$)	157.01	852.3	5.528	(*3*)

MRCI/aug-cc-pV5Z (*7*) and EHFACE2U (*16*) calculations approaching spectroscopic accuracy.

BrO

The $X_1(^2\Pi_{3/2})$ and $X_2(^2\Pi_{1/2})$ potentials of BrO were derived from a combined fit to the existing microwave, LMR and high-resolution FTIR spectroscopic data (*1*). The data included transitions from $^{79,81}Br^{16,18}O$ isotopomers in vibrational levels up to $v = 8$. Figure 5 shows the BrO potentials and their associated vibrational levels. The MRCI+Q/aug-cc-pVQZ potential (no spin-orbit coupling) recently reported by Li et al.(*18*) is compared to the $X(^2\Pi_{\text{eff}})$ potential in Figure 6. Note that the ab initio potential has been shifted by −1.0 pm for better agreement with the RKR potential. The two potentials exhibit minimal differences for energies up to 8000 cm^{-1}. This suggests that MRCI calculations with sufficiently large basis sets and explicit inclusion of spin-orbit coupling should be able to reproduce the XO RKR potentials accurately.

Comparisons of the experimental and ab initio $X(^2\Pi)$ characterizations of the potential minimum are given in Table III, including the spin-orbit state resolved bond lengths and vibrational frequencies determined by Li et al. (*18*). The MRCI calculations do an outstanding job of reproducing the experimental harmonic vibrational frequency. They also reproduce the relative values of r_e in both $^2\Pi$ states, although they systematically overestimate the Br-O bond length by 1.0 pm. In fact, all of the theoretical methods overestimate the Br-O bond length. Analysis of the magnetic hyperfine structure and quadrupole coupling parameters (see below) indicates that relativistic effects make a measurable impact on the BrO electronic structure; the discrepancy between the experimental and theoretical bond lengths may reflect a small relativistic contraction.

Downloaded by COLUMBIA UNIV on September 14, 2012 | http://pubs.acs.org
Publication Date: August 14, 2002 | doi: 10.1021/bk-2002-0828.ch012

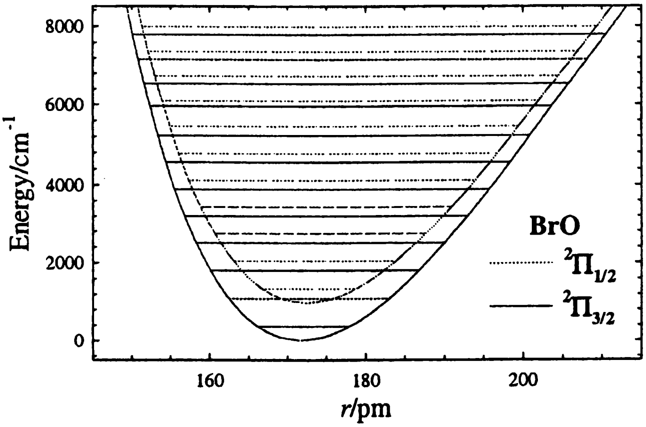

Fig. 5. BrO $X_1(^2\Pi_{3/2})$ and $X_2(^2\Pi_{1/2})$ RKR potentials and vibrational levels.

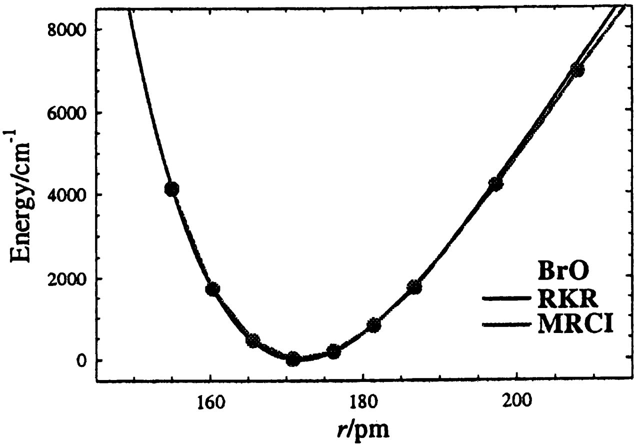

Fig. 6. A comparison of the RKR and MRCI potential for BrO X *($^2\Pi_{eff}$).*

Downloaded by COLUMBIA UNIV on September 14, 2012 | http://pubs.acs.org
Publication Date: August 14, 2002 | doi: 10.1021/bk-2002-0828.ch012

Table III. Ab Initio Characterization of BrO X ($^2\Pi$)

Level of Theory	r_e/pm	ω_e/cm^{-1}	$\omega_e x_e$ /cm^{-1}	*Reference*
UMP2/TZ2P	172.4			(22)
MP2/AREP-311G**	175.0	813		(*23*)
QCISD(T)/ 6-311+G(3df)	173.1	705.8	6.5	(*12*)
CISD/AREP-311G**	176.9	741		(*23*)
CCSD(T)/ANO4	172.7	728		(22)
MRCI/aug-cc-pVQZ	172.6	728.5	3.5	(*7*)
$^2\Pi_{3/2}$				
MRCI+Q/aug-cc-pVQZ	172.7	730		(*18*)
Experiment	171.72	732.88	4.649	(*1*)
$^2\Pi_{1/2}$				
MRCI+Q/aug-cc-pVQZ	173.3	719		(*18*)
Experiment	172.41	717.95	4.658	(*1*)

IO

The $X_1(^2\Pi_{3/2})$ and $X_2(^2\Pi_{1/2})$ potentials of IO were derived from a fit to the extensive microwave data reported by Miller and Cohen(*4*), augmented by the MOODR transitions measured by Bekooy et al.(*19*) and the fine structure splitting of 2091 ± 40 cm^{-1} measured by Gilles et al.(*20*) The data included transitions from $I^{16,18}O$ isotopomers in vibrational levels up to $v = 13$. The IO potentials and their associated vibrational levels are shown in Figure 7. The RKR and MRD-CI/RECP potentials of Roszak et al.(*21*) are plotted in Figure 8. The ab initio potentials have been shifted by −5.0 pm in this plot for a better comparison with experiment. The MRD-CI calculations overestimate the I-O bond length due to freezing of the iodine 4*d* electrons at the configuration interaction step (*21*). The diffuse 4*d* electrons in IO are significantly polarized by the electronegative oxygen atom, resulting in stronger bonding than reflected in the calculations. The relative agreement of the experimental and ab initio potentials for both the $X_1(^2\Pi_{3/2})$ and $X_2(^2\Pi_{1/2})$ states is impressive given the difficulty of treating the large number of electrons in IO with an explicit inclusion of spin-orbit coupling in the ab initio code. The ab initio potentials become too anharmonic above 3000 cm^{-1} but this behavior was noted for the theoretical potentials of all of the lighter halogen monoxides and appears to be a systematic difficulty.

Downloaded by COLUMBIA UNIV on September 14, 2012 | http://pubs.acs.org
Publication Date: August 14, 2002 | doi: 10.1021/bk-2002-0828.ch012

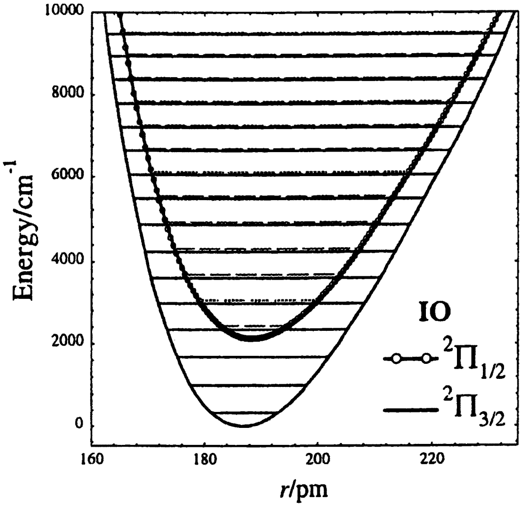

Fig. 7. IO $X_1(^2\Pi_{3/2})$ and $X_2(^2\Pi_{1/2})$ RKR potentials and vibrational levels.

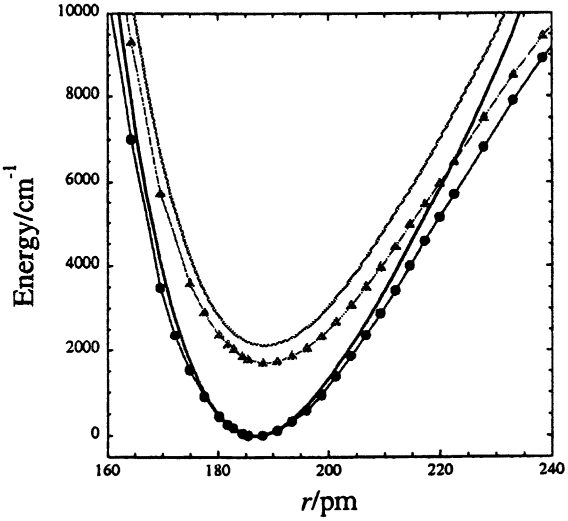

Fig. 8. The RKR and MRD-CI potentials for IO X ($^2\Pi$). The solid lines mark the RKR potentials while the lines with symbols mark the adjusted ab initio potentials from Ref(21).

Downloaded by COLUMBIA UNIV on September 14, 2012 | http://pubs.acs.org
Publication Date: August 14, 2002 | doi: 10.1021/bk-2002-0828.ch012

Downloaded by COLUMBIA UNIV on September 14, 2012 | http://pubs.acs.org
Publication Date: August 14, 2002 | doi: 10.1021/bk-2002-0828.ch012

Table IV. Ab Initio Characterization of IO X ($^2\Pi$)

Level of Theory	r_e/*pm*	ω_e/*cm*$^{-1}$	$\omega_e x_e$ /*cm*$^{-1}$	*Reference*
MP2/6-311+G(3df)	188.8	724		(*24*)
CASPT2(9,6)	187.99	652	4.76	(*25*)
CCSD(T)/6-311+G(3df)	189.39	664	3.7	(*25*)
MRCI/aug-cc-pVQZ	187.9	694.5	4.6	(*7*)
QCISD(T)/ 6-311+G(3df)	190.0	644.4	5.5	(*12*)
$^2\Pi_{3/2}$				
MRD-CI/RECP	192.2	650		(*21*)
Experiment	186.769	681.7	4.35	(*4*)
$^2\Pi_{1/2}$				
MRD-CI/RECP	193.9	626		(*21*)
Experiment	188.475	645.3	4.31	(*4*)

Experimental and ab initio characterizations of the $X(^2\Pi)$ potential minima are given in Table IV. It is difficult to compare the calculations without resolved spin-orbit components to the experimental data since changing from $X_1(^2\Pi_{3/2})$ to $X_2(^2\Pi_{1/2})$ increases the I-O bond length by 1.7 pm and decreases the harmonic vibrational frequency by 36 cm^{-1}. These results suggest that the two spin-orbit states may have significant differences in their electron configurations. This hypothesis is explored further in the treatment of relativistic effects given below.

Relativistic Effects

The intrinsically relativistic nature of the electronic structure of the halogen monoxides is dictated by the presence of two spin-orbit components in the ground electronic state. Any accurate characterization of the XO X_1 $^2\Pi_{3/2}$ and X_2 $^2\Pi_{1/2}$ potentials must therefore treat relativistic effects explicitly. However, this requirement greatly increases the cost and complexity of the ab initio effort(*26*), resulting in few relativistic potential surface calculations such as the IO study by Roszak *et al.*(*21*) One more frequently finds relativistic effects incorporated as corrections to non-relativistic energies or treated through the use of effective core potentials (*23*).

The fine structure splittings of the XO series provide the most direct insight into the relativistic contributions in these molecules and the role of the halogen

Table V. XO X ($^2\Pi$) Fine Structure Splittings

Level of Theory	A_e/cm^{-1}	*Reference*
FO		
MCSCF/6-31G(d,p)/SBK	−185.7	(*27*)
RELCCSD-T/aug-cc-pVTZ	−194.6	(*26*)
Experiment	−196.6	(2)
ClO		
MCSCF/6-31G(d,p)/SBK	−290.0	(*27*)
RELCCSD-T/aug-cc-pVTZ	−314.5	(*26*)
Experiment	−321.8	(*3*)
BrO		
MRCI+Q/aug-cc-pVQZ	−726	(*18*)
Experiment	−975.4	(*1*)
IO		
MRD-CI/RECP	−1683	(*21*)
Experiment	−2091	(*20*)

Downloaded by COLUMBIA UNIV on September 14, 2012 | http://pubs.acs.org
Publication Date: August 14, 2002 | doi: 10.1021/bk-2002-0828.ch012

atom spin-orbit coupling in defining their electronic structures. The fine structure interval separating the $X_1\ ^2\Pi_{3/2}$ and $X_2\ ^2\Pi_{1/2}$ states increases as halogen atom spin-orbit coupling increases (Table V). The RELCCSD calculations reported by Visscher et al.(*26*) perform remarkably well for FO and ClO, reproducing the experimental fine structure splittings within a few wavenumbers. These calculations approach the accuracy one would hope to achieve for spectroscopic quality ab initio potential. It would be very interesting to learn if the RELCCSD calculations perform as well for values of r away from the r_e position, especially if they can reproduce the observed vibrational state dependence of the fine structure splitting. It is also unclear whether the performance of this method extends to BrO and IO where the impact of the relativistic effects is significantly larger.

The performance of multi-reference configuration interaction (MRCI) methods for BrO(*18*) and IO(*21*) illustrate the difficulties associated with capturing the correct form of the $^2\Pi$ potentials as well as an accurate characterization of the fine structure splitting. Figures 6 and 8 show that the shifted MRCI calculations describe the contours of the BrO and IO potentials quite well. However, the calculated fine structure splittings are systematically low, differing by −26% for BrO and −20% for IO. Despite these discrepancies, it appears that MRCI methods are approaching the accuracy necessary to calculate high quality ab initio potentials for the XO series.

The magnetic hyperfine structure and quadrupole coupling parameters provide detailed information on the electron distributions of the XO series. The relationships between these parameters and various expectation values reflect contributions from only those electrons which contribute to the orbital angular momentum (designated **L**), only those electrons which contribute to the spin angular momentum (designated **S**), and all electrons (designated **T**). The variable θ defines the angular orientation of the electron distribution relative to the internuclear axis.

$$\begin{aligned}
a &= 2g_N\beta\beta_N\left\langle r^{-3}\right\rangle_L \\
b_F &= \frac{8\pi}{3}g_e g_N\beta\beta_N\left\langle \Psi^2(0)\right\rangle_S \\
c &= \frac{3}{2}g_e g_N\beta\beta_N\left\langle \frac{3\cos^2\theta-1}{r^3}\right\rangle_S \\
d &= \frac{3}{2}g_e g_N\beta\beta_N\left\langle \frac{\sin^2\theta}{r^3}\right\rangle_S \\
eQq_1 &= eQ\left\langle \frac{3\cos^2\theta-1}{r^3}\right\rangle_T \\
eQq_2 &= -3eQ\left\langle \frac{\sin^2\theta}{r^3}\right\rangle_T
\end{aligned} \tag{1}$$

The experimentally derived expectation values for all four XO molecules are summarized in Table VI. The spin density on the halogen atom is derived by the ratio of the molecular and relativistic atomic radial and angular expectation values. The spin density on the F atom in FO is anomalously low, 20%, a characteristic that is also reflected in the unusually small dipole moment for this molecule.(*5, 7*) The spin densities found on the halogen atoms in ClO, BrO and IO are between 37 and 39% and exhibit little dependence on the identity of the halogen atom. The spin densities calculated using non-relativistic radial integrals for the evaluation of the halogen atomic expectation values lead to an unphysical increases in the calculated spin density on the halogen atom, reaching 62% for IO.

Another indication of the importance of relativistic contributions to the bonding in the XO series is given by the trend in $\left\langle \Psi^2(0)\right\rangle_S$, the probability of finding the spin inducing electron at the halogen nucleus. Table VI shows that

Downloaded by COLUMBIA UNIV on September 14, 2012 | http://pubs.acs.org
Publication Date: August 14, 2002 | doi: 10.1021/bk-2002-0828.ch012

Downloaded by COLUMBIA UNIV on September 14, 2012 | http://pubs.acs.org
Publication Date: August 14, 2002 | doi: 10.1021/bk-2002-0828.ch012

there is a clear periodic decrease in this expectation value, passing through zero and reaching a negative value for IO. Examination of the expression for the Fermi contact term, b_F, from which this expectation value is derived shows that b_F should be a positive number since it is the product of nominally positive parameters. Many authors attribute such unphysical behavior to spin polarization but it appears quite consistent with the other results from the XO series, demonstrating the importance of relativistic corrections. Note that the angular distribution of the electrons which contribute to the molecular spin, $\left\langle \sin^2\theta \right\rangle_S$, shows a very reasonable decreasing trend through the series without any unphysical behavior, most likely due to the contraction of the halogen atom p-π* orbital to optimize overlap with the oxygen p-π* orbital.

Table VI. Derived XO X ($^2\Pi$) Electron Distribution Expectation Values

Molecular Values	*FO (Ref. 2)*	*^{35}ClO (Ref. 3)*	*^{79}BrO (Ref. 1)*	*IO (Ref. 4)*
$\left\langle r^{-3}\right\rangle_S$	10.452	18.232	35.686	61.676
$\left\langle r^{-3}\right\rangle_L$	10.485	17.583	32.310	48.789
$\left\langle \Psi^2(0)\right\rangle_S$	0.3300	0.2461	0.0964	-0.7170
$\left\langle \sin^2\theta\right\rangle_S$	0.8383	0.8163	0.7982	0.7612

Atomic Values	*X Calc.*	*XO/X Ratio*	*X Calc.*	*XO/X Ratio*	*X Calc.*	*XO/X Ratio*	*X Calc.*	*XO/X Ratio*
$\left\langle r^{-3}\right\rangle_S$	51.5	20.3	46.9	38.8	97.9	36.5	162.8	37.9
$\left\langle r^{-3}\right\rangle_L$	51.1	20.5	45.7	38.5	86.5	37.4	122.2	39.9
$\left\langle \Psi^2(0)\right\rangle_S$	-0.018		-0.056		-0.500		-1.72	

The axial and non-axial quadrupole coupling parameters, eQq_1 and eQq_2, provide a measure of the electric field gradient at the halogen nucleus. This very specific electron distribution information also bears the signature of relativistic effects. The subtle differences in the electronic structures of the $X_1\ ^2\Pi_{3/2}$ and $X_2\ ^2\Pi_{1/2}$ states produce changes in the value of eQq_1. These changes have been fit in the analysis of the ClO, BrO and IO spectra using the parameter eQq_S.

There are two major contributions to eQq_S : a structural component

$$\Delta eQq_1(struc) = -eQq_{1(10)}\frac{A_{01}}{Y_{11}}$$

related to the differences in the equilibrium structures of the $X_1\ {}^2\Pi_{3/2}$ and $X_2\ {}^2\Pi_{1/2}$ states and a relativistic correction

$$\Delta eQq_1(rel) = \frac{2\rho_S\left(C_{++} - C_{+-}\right)eQq_{n(10)}}{3C_{++}}$$

obtained from the appropriate relativistic integrals (*1*). The calculated contributions to eQq_S for ClO, BrO and IO are collected in Table VII along with the fitted values of eQq_S. These results show that the predicted changes are of the same sign and order of magnitude as the fitted values of eQq_S. Additionally, one notes that the relativistic contribution is systematically a factor of three larger than the structural contribution. These trends hold despite the fact that the changes vary from 0.4 to 119 MHz. The increasing deviation of the calculated and observed eQq_S values as X changes from Cl to I may reflect the increased mixing of neighboring Σ^+ state(s) into the $X_2\ {}^2\Pi_{1/2}$ configuration (*4*), although this explanation awaits direct theoretical confirmation. Nevertheless, the good agreement between the calculated and experimental eQq_S values supports the assertion that relativistic effects play an important role in determining accurate potentials for the XO molecules.

Table VII. Structural and Relativistic Contributions (MHz) to eQq_S

XO	$eQq_{n(10)}(X)$	*Δ(struc)*	*Δ(rel)*	*Δ(total)*	eQq_S
ClO	109.74	0.09	0.32	0.41	0.37
BrO	-769.76	-4.0	-10.1	-14.1	-21.82
IO	2292.71	38.5	81.4	119.1	198.14

Conclusions

This paper has summarized the current state of knowledge concerning the $X_1\ {}^2\Pi_{3/2}$ and $X_2\ {}^2\Pi_{1/2}$ potentials of the halogen monoxides. A comparison of RKR and ab initio potentials shows that the theoretical potentials reproduce the experimentally derived potentials quite well but generally lack spectroscopic accuracy. Recent advances in relativistically corrected MRCI and CCSD methods show great promise for achieving accurate characterizations of the XO potential curves for the entire range of energies up to the dissociation limit. New experimental data has also provided detailed information on the electron distributions around the halogen nucleus and the impact of relativistic effects on

Downloaded by COLUMBIA UNIV on September 14, 2012 | http://pubs.acs.org
Publication Date: August 14, 2002 | doi: 10.1021/bk-2002-0828.ch012

these distributions. The combination of the RKR potentials and electron distributions provide a valuable benchmark with which to assess the performance of future ab initio calculations on these systems.

Acknowledgments

This work was performed while the author was on leave at the NASA Jet Propulsion Laboratory. He wishes to thank E. A. Cohen and B. J. Drouin for helpful discussions.

Downloaded by COLUMBIA UNIV on September 14, 2012 | http://pubs.acs.org
Publication Date: August 14, 2002 | doi: 10.1021/bk-2002-0828.ch012

References

1. Drouin, B. J.; Miller, C. E.; Muller, H. S. P.; Cohen, E. A. *J. Mol. Spectrosc.*, **2001**, *205*, 128-138.
2. Miller, C. E.; Drouin, B. J. *J. Mol. Spectrosc.*, **2001**, *205*, 312-318.
3. Drouin, B. J.; Miller, C. E.; Cohen, E. A.; Wagner, G.; Birk, M. *J. Mol. Spectrosc.*, **2001**, *209*.
4. Miller, C. E.; Cohen, E. A. *J. Chem. Phys.*, in press, **2001**.
5. Langhoff, S. R.; Bauschlicher, C. W.; Partridge, H. *Chem. Phys. Lett.*, **1983**, *102*, 292-298.
6. Haaland, P. *Chem. Phys. Lett.*, **1991**, *176*, 287-292.
7. Leonard, C.; Le Quere, F.; Rosmus, P.; Puzzarini, C.; Castells, M. P. D. *PCCP Phys. Chem. Chem. Phys.*, **2000**, *2*, 1117-1122.
8. Kieninger, M.; Segovia, M.; Ventura, O. N. *Chem. Phys. Lett.*, **1998**, *287*, 597-600.
9. Zhao, Y.; Francisco, J. S. *Chem. Phys. Lett.*, **1990**, *167*, 285-290.
10. Tozer, D. J.; Handy, N. C.; Amos, R. D.; Pople, J. A.; Nobes, R. H.; Xie, Y. M.; Schaefer, H. F. *Mol. Phys.*, **1993**, *79*, 777-793.
11. Jensen, F. *Chem. Phys. Lett.*, **1990**, *169*, 519-528.
12. McGrath, M. P.; Rowland, F. S. *J. Phys. Chem.*, **1996**, *100*, 4815-4822.
13. Johnson, R. D. *Chem. Phys. Lett.*, **1995**, *245*, 484-487.
14. Li, X. Z.; Paldus, J. *J. Chem. Phys.*, **1996**, *104*, 9555-9562.
15. Pettersson, L. G. M.; Langhoff, S. R.; Chong, D. P. *J. Chem. Phys.*, **1986**, *85*, 2836-2844.
16. Pena-Gallego, A.; Abreu, P. E.; Varandas, A. J. C. *J. Phys. Chem. A*, **2000**, *104*, 6241-6246.
17. Menconi, G.; Wilson, P. J.; Tozer, D. J. *J. Chem. Phys.*, **2001**, *114*, 3958-3967.
18. Li, Y. M.; Francisco, J. S.; Peterson, K. A. *J. Chem. Phys.*, **2000**, *113*, 8556-8560.

19. Bekooy, J. P.; Meerts, W. L.; Dymanus, A. *J. Mol. Spectrosc.*, **1983**, *102*, 320-343.
20. Gilles, M. K.; Polak, M. L.; Lineberger, W. C. *J. Chem. Phys.*, **1992**, *96*, 8012-8020.
21. Roszak, S.; Krauss, M.; Alekseyev, A. B.; Liebermann, H. P.; Buenker, R. J. *J. Phys. Chem. A*, **2000**, *104*, 2999-3003.
22. Francisco, J. S.; Parthiban, S.; Lee, T. J. *J. Chem. Phys.*, **1998**, *109*, 10818-10822.
23. Pacios, L. F.; Gomez, P. C. *Int. J. Quantum Chem.*, **1994**, *49*, 817-833.
24. Misra, A.; Marshall, P. *J. Phys. Chem. A*, **1998**, *102*, 9056-9060.
25. Hassanzadeh, P.; Irikura, K. K.; Johnson, R. D. *J. Phys. Chem. A*, **1997**, *101*, 6897-6902.
26. Visscher, L.; Lee, T. J.; Dyall, K. G. *J. Chem. Phys.*, **1996**, *105*, 8769-8776.
27. Koseki, S.; Gordon, M. S.; Schmidt, M. W.; Matsunaga, N. *J. Phys. Chem.*, **1995**, *99*, 12764-12772.

Downloaded by COLUMBIA UNIV on September 14, 2012 | http://pubs.acs.org
Publication Date: August 14, 2002 | doi: 10.1021/bk-2002-0828.ch012

Downloaded by NORTH CAROLINA STATE UNIV on September 14, 2012 | http://pubs.acs.org
Publication Date: August 14, 2002 | doi: 10.1021/bk-2002-0828.ch013

Chapter 13

Symmetry in Spin-Orbit Coupling

Dmitri G. Fedorov[1,2] and Mark S. Gordon[1]

[1]Department of Chemistry and Ames Laboratory, Iowa State University, Ames, IA 50011
[2]Current address: Department of Applied Chemistry, School of Engineering, University of Tokyo, Tokyo 113, Japan

A thorough review of the symmetry properties of the spin-orbit coupling operator and its matrix elements is presented. Various consequences of symmetry upon the practical calculations of spin-orbit coupling matrix elements at both point and double group level are illuminated. A parallelisation scheme and various steps unrelated to symmetry toward making the calculations more efficient are discussed. Tests of scalability of the code as implemented into the distributed version of GAMESS are presented.

Introduction

Recent progress in studying molecular dynamics involving states of different multiplicities, such as conical intersection studies *(1,2)*, relies to a large degree on the ability to calculate spin-orbit coupling matrix elements. Conventional scalar (spin-independent) calculations involving average-sized elements, such as those in the 4th or 5th row of the Periodic Table, can be greatly improved in

In Low-Lying Potential Energy Surfaces; Hoffmann, M., et al.;
ACS Symposium Series; American Chemical Society: Washington, DC, 2002.

terms of energy level splittings by using either perturbative treatments involving spin-orbit (SO) coupling in a manner of *(3,4)* or non-perturbatively, known as SO CI (configuration interaction) *(5,6)*. There are many different techniques available to obtain numerical results *(7,8,9,10)* for a given system. The study of SO coupling (SOC) in molecules is relatively new are but a few books and book chapters are available *(11,12,13)* and many references can be found in the bibliography by Pyykkö *(14)*.

An efficient spin-orbit coupling calculation will take advantage of symmetry and various computational techniques to improve the efficiency. This paper begins with a consideration of the applicable symmetry rules. This will be followed by a discussion of the computational aspects of the spin-orbit coupling matrix elements. The symmetry rules elucidated in this work are applicable to the recently developed relativistically transformed spin-orbit coupling operators, provided that the rotational properties of the transformed operators are unchanged, which is the case for transformations explicitly dependent upon momentum p^2, *(15,16, 17)*.

The number of non-zero elements that must be calculated can be greatly reduced by predicting ahead of time which matrix elements are zero due to symmetry. The general SO matrix element can be written as:

$$<\alpha\Gamma i S M_S \mid \hat{H}_{so} \mid \alpha'\Gamma' i' S' M_S'> \quad (1)$$

where the spin-orbit coupling part of the Pauli-Breit Hamiltonian *(18)* spin-orbit coupling $\hat{H}_{so}$ contains both one and two electron operators. The state $|\alpha\Gamma i S M_S>$ contains the symmetry labels of the wavefunction obtained from a conventional spin-independent calculation: Γ denotes the irreducible representation (irrep) of the point group G of the molecule, i distinguishes degenerate components of Γ, α distinguishes equivalent irreps, $S(S+1)$ and M_S are the eigenvalues (in atomic units) of the spin operators $\hat{S}^2$ and $\hat{S}_z$, respectively.

The matrix element in eq 1 represents a relativistic spin-dependent correction. Since the conventional scalar Hamiltonian commutes with $\hat{S}^2$ and $\hat{S}_z$, one significant use of symmetry is to apply the Wigner-Eckart theorem *(19)*. Secondly, $\hat{H}_{so}$ commutes with a set of rotation and reflection operators, applied to both orbital and spin variables, forming the double group *(21)* $\overline{G}$, just as the scalar Hamiltonian commutes with a set of space rotations and reflections forming group G. The eigenvectors of the matrix representation of $\hat{H}_{so}$ in the basis $|\alpha\Gamma i S M_S>$ can therefore be classified according to the irreps of the double group. Linear combinations of the original states $|\alpha\Gamma i S M_S>$ with eigenvectors of the H_{so} matrix as expansion coefficients form states with a distinct double group symmetry in which $\hat{H}_{so}$ is diagonal. *The following discussion is intended mainly*

Downloaded by NORTH CAROLINA STATE UNIV on September 14, 2012 | http://pubs.acs.org
Publication Date: August 14, 2002 | doi: 10.1021/bk-2002-0828.ch013

for the finite groups, and, although it is valid for arbitrary molecular or atomic symmetry, we do not explicitly use the notation of the groups with infinite rotation axes and conserved angular momenta. The exact type of the conventional scalar wavefunction is irrelevant as long as it can be described by the labels specified above. A notable exception is the unrestricted Hartree-Fock (UHF) wavefunction, where the rules involving spin angular momentum symmetry are not applicable because the wavefunction is not an eigenfunction of $\hat{S}^2$.

It should be noted that most of the symmetry rules presented here have been known but not gathered together prior to this work (see, for example, *(2,20,21)*). Despite the fact that many papers on SOC give the selection rules for particular point groups, there appears to be no general formulation useful from both theoretical and algorithmic point of view, in particular formulated for the scalar wavefunction as it comes from spin-independent methods. In practice it is convenient to use such wavefunction as the formalism to compute SOC is similar to spin-free computations with simple spin dependence so that even the alternative approaches aimed at making the SOC matrix real or using time-reversal symmetry often reduce to the computation of SOC in the basis of wavefunctions obtained from spin-independent methods. In addition to consideration of symmetry, methods for improving the efficiency of spin-orbit coupling calculations, including the use of parallelisation, are presented.

The Wigner-Eckart Theorem

The theorem proved to be very useful for SOC calculations as applied by McWeeny *(22)*, states that:

$$\left\langle \alpha jm \middle| \hat{T}_q^k \middle| \alpha' j' m' \right\rangle = (j',k,m',q \mid j,m) \frac{\left\langle \alpha j \middle| \hat{T}^k \middle| \alpha' j' \right\rangle}{\sqrt{2j'+1}} \qquad (2)$$

where $\hat{T}_q^k$ is an irreducible spherical tensor operator of rank *k*, $\hat{T}^k$ is the so called reduced tensor operator, $(j',k,m',q|j,m)$ are Clebsch-Gordan coefficients (assumed below to be real), $|\alpha jm\rangle$ are eigenvectors of angular momentum operators $\hat{J}^2$ and $\hat{J}_z$ and α is used to denote any other labels. Now, $\hat{\mathrm{H}}_{\mathrm{so}}$ transforms as $\sum_i \left(\hat{l}_i \cdot \hat{s}_i\right)$ or for the spin selection rules *(11)* as

$(\hat{L}\cdot\hat{\mathrm{S}}) = \hat{\mathrm{L}}_0\hat{\mathrm{S}}_0 - (\hat{\mathrm{L}}_+\hat{\mathrm{S}}_- + \hat{\mathrm{L}}_-\hat{\mathrm{S}}_+)/2$ and $\hat{J}_\pm = \mp\left(\hat{J}_x \pm i\hat{J}_y\right)$. The latter can be seen from the explicit separation of spin and orbital operators in the second quantised

Downloaded by NORTH CAROLINA STATE UNIV on September 14, 2012 | http://pubs.acs.org
Publication Date: August 14, 2002 | doi: 10.1021/bk-2002-0828.ch013

formalism *(23)*. Taking $\hat{T}_q^k$ to be $\hat{S}_+, \hat{S}_0, \hat{S}_-$ where k=1 and q=1,0,-1, it is therefore possible to rewrite the matrix element in eq 1 as:

$$\left\langle \alpha\Gamma iSM_S \middle| \hat{H}_{so} \middle| \alpha\Gamma' i' S' M'_S \right\rangle \cong \sum_{q=-1}^{1} (S',1,M'_S,q|S,M_S) \left\langle \alpha\Gamma iS \middle| \hat{L}_{-q}\hat{S} \middle| \alpha\Gamma' i' S' \right\rangle (-1)^q \tag{3}$$

where the numerical constants are included into the operator transforming as angular momentum $\hat{L}_q$ and the vector spin operator $\hat{\hat{S}}$ has been reduced to the scalar operator $\hat{S}$. The sign ≅ is to be understood as "transforms as". For $S=0$ and $S'=0$ the coefficient $(S',1,0,0|S,0)= 0$, so it follows that:

(a) A matrix element between two singlets is zero.

Secondly, using the property of the Clebsch-Gordan coefficients

$(S,1,M_S,q|S',M_S')= 0$ if $|S-S'|>1$ or $M_S+q\neq M_S'$, one obtains:

(b) The SO matrix elements are zero unless $|S-S'|\leq 1$

Furthermore,

(c) at most three elements need to be explicitly calculated, given S and S'

$$<\alpha\Gamma iSM_S'-1|\hat{H}_{so}|\,\alpha'\Gamma' i'S'M_S'>=(S',1,M_S',-1|S,M_S'-1)<\alpha\Gamma iS\,|\hat{L}_+\hat{S}|\,\alpha'\Gamma' i'S'>(-1) \tag{4}$$

$$<\alpha\Gamma iSM_S'|\hat{H}_{so}|\,\alpha'\Gamma' i'S'M_S'> \;= (S',1,M_S',0|S,M_S')<\alpha\Gamma iS\,|\hat{L}_0\hat{S}|\,\alpha'\Gamma' i'S'> \tag{5}$$

$$<\alpha\Gamma iSM_S'+1|\hat{H}_{so}|\,\alpha'\Gamma' i'S'M_S'>=(S',1,M_S',+1|S,M_S'+1)<\alpha\Gamma iS\,|\hat{L}_-\hat{S}|\,\alpha'\Gamma' i'S'>(-1) \tag{6}$$

The remaining elements are:

1) zero if $|M_S-M_S'|>1$

The H_{so} matrix is tridiagonal (diagonal being defined as $M_S=M_S'$).

2) calculated for an arbitrary M_S by using one of the basic three expressions in (c) e.g.:

$$\begin{aligned} <\alpha\Gamma iS\, M_S -1|\, \hat{H}_{so}\,|\,\alpha'\Gamma' i'S'\, M_S> &= (S',1,\, M_S -1|S,M_S -1) \\ &\times <\alpha\Gamma iS|\,\hat{L}_+\hat{S}\,|\,\alpha'\Gamma' i'S'>/(S',1,M_S',-1|S,M_S'-1)(-1) \end{aligned} \tag{7}$$

where the reduced matrix element is calculated from the above defining relation (for M_S').

It should be noted that some Clebsch-Gordan coefficients are equal to zero, for example, (1,1,0,0|1,0) and (2,2,0,0|1,0). It is important to keep this in mind

Downloaded by NORTH CAROLINA STATE UNIV on September 14, 2012 | http://pubs.acs.org
Publication Date: August 14, 2002 | doi: 10.1021/bk-2002-0828.ch013

when actually implementing the Wigner-Eckart usage of the reduced matrix elements. It is not possible to use $M_S=M_S'=0$ to get the reduced matrix element in these cases as it would lead to division by zero. Using the largest possible M_S, that is, $M_S=S,\ M_S'=S'$, however, always leads to non-zero Clebsch-Gordan coefficients.

Hermiticity and Time reversal, States Represented by Real Valued Wavefunctions

If one uses states represented by real valued wavefunction, it is possible to **reduce** the number of matrix elements one must explicitly calculate from **three** to **two**. Note that this corresponds to calculating matrix elements of the three operators represented schematically by $\hat{L}_x\hat{S}, \hat{L}_y\hat{S}, \hat{L}_z\hat{S}$.

Elements along subdiagonals are bound by a simple relation. To see this, consider states of different multiplicity and use explicit form of the angular momentum operators *(18)* in order to see the relations between real and imaginary parts of the two matrix elements below:

$$\begin{aligned}
&\langle \alpha\Gamma iS, M_S\,|\hat{H}_{so}|\,\alpha\Gamma' i'S+1, M_S+1\rangle \\
&\quad = \left(S+1,1,M_S+1,-1\middle|S,M_S\right)\left\langle \alpha\Gamma iS\middle|\hat{L}_+\hat{S}\middle|\alpha\Gamma' i'S+1\right\rangle(-1) \\
&\quad = \left(S+1,1,M_S+1,-1\middle|S,M_S\right)(-1) \\
&\quad \times\left[-i\left\langle\alpha\Gamma iS\middle|\left[\hat{\vec{r}}\times\hat{\vec{p}}\right]_x\hat{S}\middle|\alpha\Gamma' i'S+1\right\rangle+(-i)i\left\langle\alpha\Gamma iS\middle|\left[\hat{\vec{r}}\times\hat{\vec{p}}\right]_y\hat{S}\middle|\alpha\Gamma' i'S+1\right\rangle\right](-1)
\end{aligned} \tag{8}$$

$$\begin{aligned}
&\langle \alpha\Gamma iS, -M_S\,|\hat{H}_{so}|\,\alpha\Gamma' i'S+1, -M_S-1\rangle \\
&\quad = \left(S+1,1,-M_S-1,1\middle|S,-M_S\right)\left\langle \alpha\Gamma iS\middle|\hat{L}_-\hat{S}\middle|\alpha\Gamma' i'S+1\right\rangle(-1) \\
&\quad = \left(S+1,1,-M_S-1,1\middle|S,-M_S\right) \\
&\quad \times\left[-i\left\langle\alpha\Gamma iS\middle|\left[\hat{\vec{r}}\times\hat{\vec{p}}\right]_x\hat{S}\middle|\alpha\Gamma' i'S+1\right\rangle-i(-i)\left\langle\alpha\Gamma iS\middle|\left[\hat{\vec{r}}\times\hat{\vec{p}}\right]_y\hat{S}\middle|\alpha\Gamma' i'S+1\right\rangle\right](-1)
\end{aligned} \tag{9}$$

It can be proven generally that $(S+1,1,M_S+1,-1|S,M_S)= (S+1,1,-M_S-1,1|S,-M_S)$ (Appendix III), so that by comparing the right-hand sides of eqs 8 and 9 it can be seen that their left-hand sides are bound by the relation:

$$<\alpha\Gamma iS\ M_S\,|\,\hat{\mathrm{H}}_{so}\,|\,\alpha'\Gamma' i'S+1,\ M_S+1>=<\alpha\Gamma iS\,,-M_S\,|\,\hat{\mathrm{H}}_{so}\,|\,\alpha'\Gamma' i'S+1,\ -M_S-1>^{*} \tag{10}$$

Downloaded by NORTH CAROLINA STATE UNIV on September 14, 2012 | http://pubs.acs.org
Publication Date: August 14, 2002 | doi: 10.1021/bk-2002-0828.ch013

Similarly, for states of the same multiplicity:

$$\begin{aligned}
&\langle \alpha\Gamma iS,M_S-1|\hat{H}_{so}|\alpha\Gamma' i'S,M_S\rangle \\
&\quad=(S,1,M_S,-1|S,M_S-1)\langle \alpha\Gamma iS|\hat{L}_+\hat{S}|\alpha\Gamma' i'S\rangle(-1) \\
&\quad=(S,1,M_S,-1|S,M_S-1)(-1) \\
&\quad\times\left[-i\langle \alpha\Gamma iS|[\hat{r}\times\hat{p}]_x\hat{S}|\alpha\Gamma' i'S\rangle+i(-i)\langle \alpha\Gamma iS|[\hat{r}\times\hat{p}]_y\hat{S}|\alpha\Gamma' i'S\rangle\right](-1)
\end{aligned} \tag{11}$$

$$\begin{aligned}
&\langle \alpha\Gamma iS,M_S|\hat{H}_{so}|\alpha\Gamma' i'S,M_S-1\rangle \\
&\quad=(S,1,M_S-1,1|S,M_S)\langle \alpha\Gamma iS|\hat{L}_-\hat{S}|\alpha\Gamma' i'S\rangle(-1) \\
&\quad=(S,1,M_S-1,1|S,M_S) \\
&\quad\times\left[-i\langle \alpha\Gamma iS|[\hat{r}\times\hat{p}]_x\hat{S}|\alpha\Gamma' i'S\rangle-i(-i)\langle \alpha\Gamma iS|[\hat{r}\times\hat{p}]_y\hat{S}|\alpha\Gamma' i'S\rangle\right](-1)
\end{aligned} \tag{12}$$

However, $(S,1,M_S,-1|S,M_S-1)=(-1)\,(S,1,M_S-1,1|S,M_S)$ (Appendix III), so by comparing the eqs 11 and 12 it is seen that:

$$<\alpha\Gamma iS\,M_S-1|\,\hat{H}_{so}|\,\alpha'\Gamma'i'S\,M_S>=<\alpha\Gamma iS\,M_S\,|\,\hat{H}_{so}|\,\alpha'\Gamma'i'S\,M_S-1>^*(-1) \tag{13}$$

For states represented by real-valued wavefunction, only the diagonal and one subdiagonal need to be explicitly calculated. The other subdiagonal is readily calculated as the complex conjugate (different multiplicities) or negative complex conjugate(same multiplicities) of the first subdiagonal.

Hermitian Character of $\hat{H}_{so}$

Consider $<\alpha\Gamma iSM_S|\,\hat{H}_{so}|\,\alpha\Gamma iSM_S> \propto <\alpha\Gamma iSM_S|\,\hat{L}_0\hat{S}\,|\,\alpha\Gamma iSM_S>$. The matrix element must be real since the operator is Hermitian, but the angular momentum operator is proportional to i, imaginary unity. So, provided that **real basis functions** are used, this matrix element is purely imaginary. This implies that:

$$<\alpha\Gamma iSM_S|\,\hat{H}_{so}|\alpha\Gamma iSM_S> = 0 \tag{14}$$

Using the previously obtained eq 9 for $\alpha=\alpha',\Gamma=\Gamma',i=i'$

$$<\alpha\Gamma iSM_S-1|\,\hat{H}_{so}|\,\alpha\Gamma iSM_S>=<\alpha\Gamma iSM_S|\,\hat{H}_{so}|\alpha\Gamma iSM_S-1>^*\,(-1)$$

Downloaded by NORTH CAROLINA STATE UNIV on September 14, 2012 | http://pubs.acs.org
Publication Date: August 14, 2002 | doi: 10.1021/bk-2002-0828.ch013

Since $\hat{H}_{so}$ is Hermitian,

$$<\alpha\Gamma i SM_S\text{-}1|\ \hat{H}_{so}|\alpha\Gamma i SM_S>=<\alpha\Gamma i SM_S|\ \hat{H}_{so}|\alpha\Gamma i SM_S\text{-}1>^*$$

This implies that

$$<\alpha\Gamma i SM_S\text{-}1|\ \hat{H}_{so}|\alpha\Gamma i SM_S>=<\alpha\Gamma i SM_S|\ \hat{H}_{so}|\alpha\Gamma i SM_S\text{-}1> = 0 \qquad (15)$$

From eqs 14, 15 and 7 one concludes that:
Diagonal matrix elements (i.e. bra equal to ket) are zero provided that the state is represented by a real-valued wavefunction.
The same is true for states represented by a purely complex wavefunction.

Time-Reversal Symmetry

It can be proven generally *(19)* that the matrix elements of operators invariant under time reversal (such as $\hat{H}_{so}$) in **the time-reversal invariant basis set** are real, which can be used to find a set of states in which the SOC matrix is real, a matter of practical importance for large spin-orbit CI. The wavefunction obtained from a spin-independent calculation, denoted by $|\alpha\Gamma i SM_S>$, in general is not an eigenfunction of the time reversal operator and thus this symmetry can be used only for certain linear combinations of such wavefunctions. The details go beyond the scope and aim of this paper and can be found elsewhere *(5,6,24)*.

Double Group Symmetry

As is well known, in order for a matrix element to be non-zero, the direct product of irreps to which bra, ket and the operator belong must contain the totally symmetric irrep. This is a consequence of the requirement that the matrix element taken as an integral over space variables and as a scalar product for the spin coordinates be independent of an arbitrary rotation of the entire system, that is,

$$\left\langle \Psi^{\Gamma_1} \middle| A^{\Gamma_A} \middle| \Psi^{\Gamma_2} \right\rangle = 0, \text{ unless } \Gamma_1 \otimes \Gamma_A \otimes \Gamma_2 \text{ contains the totally symmetric irrep.} \qquad (16)$$

Downloaded by NORTH CAROLINA STATE UNIV on September 14, 2012 | http://pubs.acs.org
Publication Date: August 14, 2002 | doi: 10.1021/bk-2002-0828.ch013

Since $\hat{H}_{so}$ transforms as a scalar product of two pseudovectors **L** and **S**, it transforms as a scalar, or in other words it belongs to the totally symmetric irreducible representation. Thus the requirement for the matrix element to be non-zero is:

$\sum_{g\in G}\chi^{\Gamma_1 *}(g)\chi^{\Gamma_2}(g)=\delta_{\Gamma_1,\Gamma_2} \quad \Leftrightarrow \quad \Gamma_1=\Gamma_2$, where χ are the characters and δ is the Kronecker δ symbol.

The conventional scalar wavefunctions will mix in general into several irreps of the double group, thus the matrix element in eq 16 is zero unless there is an irrep of the double group to which both bra and ket belong.

The procedure for determining the double group irreps to which the scalar wavefunctions belong will be outlined below. This procedure can also be reversed to find bases of the irreducible representations of the double groups as well. Since the number of electronic states included in the SO calculation is usually small, and in order to take advantage of conventional algorithms for the matrix element calculation, the states obtained from spin-independent calculations are used as a basis. Consequently, the H_{SO} matrix in this basis is diagonalised (as opposed to using the symmetry adapted states as the basis in which $\hat{H}_{so}$ is diagonal).

In the discussion below, bars above symbols (eg $\bar{G}$) denote double group entities. The following projection operators extract the functions belonging to the irrep of the double group:

$$P_k^{\bar\Gamma} = \frac{n_{\bar\Gamma}}{n_{\bar g}} \sum_{\bar g \in \bar G} D_{kk}^{\bar\Gamma *}(\bar g) T_{\bar g} \qquad (17)$$

where $T_{\bar g}$ is the rotation operator representation of the double group elements, $D_{kk}^{\bar\Gamma}(\bar g)$ are the diagonal elements of the matrices of the irreps of $\bar G$, $n_{\bar\Gamma}$ is the order(degeneracy) of $\bar\Gamma$, $n_{\bar g}$ is the order(size) of $\bar G$. The condition for a state $|\alpha\Gamma i S M_S>$ to mix into row k of an irrep $\bar\Gamma$ is

$$P_k^{\bar\Gamma} \,|\, \alpha\Gamma i S M_s > \neq 0 \qquad (18)$$

Before explicit formulae are obtained, it should be noted that generally for non-Abelian groups when doing quantum-mechanical calculations, one does not obtain states with a pretabulated irreducible representation row-symmetry. Unless special measures are taken, row symmetry specific components of degenerate irreps mix with each other. Thus, instead of having a distinct row label "*i*", a more general case will be considered, namely with label *j* which simply numbers degenerate components and does not correspond to row

Downloaded by NORTH CAROLINA STATE UNIV on September 14, 2012 | http://pubs.acs.org
Publication Date: August 14, 2002 | doi: 10.1021/bk-2002-0828.ch013

symmetry in the sense of transformation properties with pretabulated matrices. The case with the row symmetry present will be derived as a special case at the end.

A state with mixed row symmetry (i) can be written as

$$\left|\alpha\Gamma jSM_s\right\rangle = \sum_{i=1}^{n_\Gamma} a_{ij}\left|\alpha\Gamma iSM_s\right\rangle \tag{19}$$

Next, consider the relation

$$P_k^\Gamma \mid \alpha\Gamma jSM_s >= 0 \tag{20}$$

$$\begin{aligned} T_{\bar{g}}\left|\alpha\Gamma jSM_S\right\rangle &= \sum_{i=1}^{n_\Gamma} a_{ij} T_{\bar{g}}\left|\alpha\Gamma iSM_S\right\rangle \\ &= \sum_{i=1}^{n_\Gamma} a_{ij} \sum_{i'}^{n_\Gamma} D_{i'i}^\Gamma(g) \sum_{M_s'=-S}^{S} D_{M_s'M_s}^S(\bar{g}) \left|\alpha\Gamma i'SM_S{}'\right\rangle = 0 \end{aligned} \tag{21}$$

where D^Γ and D^S are the matrices of the irreducible representations of groups G and K_h, respectively, and a_{ij} are the coefficients. It should be noted that $D^\Gamma(g)$ does not depend on the colour (colour can be defined as the phase δ in the Euler angle representation: e.g., white colour set to δ=0 and black to δ=2π as added to Euler angle α, spin-wavefunction changes sign when rotated by 2π) of $\bar{g}$ as the states $|\alpha\Gamma jSM_S>$ are classified in the group G (or in other words, as single-valued representations of the double group). The a_{ij} are unknown and form linearly independent vectors $\boldsymbol{a}_i$. Thus the eq 20 becomes:

$$P_k^{\bar{\Gamma}} \mid \alpha\Gamma jSM_s >= \frac{n_{\bar{\Gamma}}}{n_{\bar{g}}} \sum_{\bar{g}\in\bar{G}} D_{kk}^{\bar{\Gamma}^*}(\bar{g}) \sum_{i=1}^{n_\Gamma} a_{ij} \sum_{i'}^{n_\Gamma} D_{i'i}^\Gamma(g) \sum_{M_s'=-S}^{S} D_{M_s'M_s}^S(\bar{g}) \left|\alpha\Gamma i'SM_s'\right\rangle = 0 \tag{22}$$

Using the linear independence of $\left|\alpha\Gamma i'SM_s'\right\rangle$, the individual coefficients are zero for all i' and M_s'.

$$\forall i', M_s': \sum_{i=1}^{n_\Gamma} a_{ij} \sum_{\bar{g}\in\bar{G}} D_{kk}^{\bar{\Gamma}^*}(\bar{g}) D_{i'i}^\Gamma(g) D_{M_s'M_s}^S(\bar{g}) = 0 \tag{23}$$

Finally, using the linear independence of $\boldsymbol{a}_i$, the individual coefficients for all i, i' and M_s' are zero:

Downloaded by NORTH CAROLINA STATE UNIV on September 14, 2012 | http://pubs.acs.org
Publication Date: August 14, 2002 | doi: 10.1021/bk-2002-0828.ch013

$$\forall i,i',M_s' : \sum_{\bar{g}\in\bar{G}} D^{\bar{\Gamma}^*}_{kk}(\bar{g}) D^{\Gamma}_{i'i}(g) D^{S}_{M_s'M_s}(\bar{g}) = 0 \qquad (24)$$

Therefore,

$$\sum_{\bar{g}\in\bar{G}} D^{\bar{\Gamma}^*}_{kk}(\bar{g}) D^{\Gamma}(g) \times D^{S}(\bar{g}) = 0 \qquad (25)$$

in terms of the tensor product for all M_S, and one can replace the D^S matrix by the M_S -column of D^S for a specific M_S. This is easily identifiable as the relation stating that the product of two irreducible representations Γ and S does not contain $\bar{\Gamma}$.

The final result given in eq 25 is easy to apply. It can be readily deduced that the states of odd $2S$ mix into double-valued irreps $\bar{\Gamma}$ only, and correspondingly even $2S$ states mix into single-valued irreps only. This follows from $D^{\bar{\Gamma}}_{kk}(\bar{g}) = \pm D^{\bar{\Gamma}}_{kk}(g)$ where the plus/minus refer to single/double valued irreps respectively; and from $D^S(\bar{g}) = \pm D^S(g)$ where the plus/minus refer to even/odd values of $2S$, respectively. Note that $\bar{g}$ and g differ by a rotation of 2π about the z-axis (in the Euler angle representation).

Thus states of integer and half -integer S do not mix with each other.

Eq 25 can finally be simplified to:

$$\sum_{g\in G} D^{\bar{\Gamma}^*}_{kk}(g) D^{\Gamma}(g) \times D^{S}(g) = 0 \qquad (26)$$

Note that the sum runs over the white elements of $\bar{G}$ (i.e. over a subgroup of $\bar{G}$ isomorphic to G). In the case of distinct row symmetry i, the direct product $D^{\Gamma} \times D^S$ is replaced by $D^{\Gamma}_i \times D^S$, where D^{Γ}_i stands for i-th column of D .

Matrices $D^S(g)$, also known as Wigner functions, are straightforward to calculate. Parametrisation of g by the three Euler angles is convenient (see Appendix I).

To summarise briefly, the double group selection rule is:

$<\alpha\Gamma i S M_S \mid \hat{H}_{so} \mid \alpha'\Gamma' i' S' M_S'>$ is zero if there are no $\bar{\Gamma}$ and k such that

$$\sum_{g\in G} D^{\bar{\Gamma}^*}_{kk}(g) D^{\Gamma}(g) \times D^{S}_{M_s}(g) \neq 0 \; and$$

$$\sum_{g\in G} D^{\bar{\Gamma}^*}_{kk}(g) D^{\Gamma'}(g) \times D^{S'}_{M_s'}(g) \neq 0 \qquad (27)$$

Downloaded by NORTH CAROLINA STATE UNIV on September 14, 2012 | http://pubs.acs.org
Publication Date: August 14, 2002 | doi: 10.1021/bk-2002-0828.ch013

where $D^S_{M_s}$ *is the* M_S *column of* D^S. *In addition: S and S' should be both integer or both half-integer and* $\overline{\Gamma}$ *single or double valued respectively;* D^Γ_1 *is to be used in place of* D^Γ *if row symmetry is present.*

As was pointed out earlier, only half-integer spins mix into double-valued irreps of $\overline{G}$, thus double group symmetry per se is used only for half-integer spins.

Downloaded by NORTH CAROLINA STATE UNIV on September 14, 2012 | http://pubs.acs.org
Publication Date: August 14, 2002 | doi: 10.1021/bk-2002-0828.ch013

Point Group Symmetry

A somewhat different kind of selection rule can be derived from a combination of the Wigner-Eckart theorem and point group symmetry. After application of the Wigner-Eckart theorem one is left with matrix elements of the type:

$<\alpha\Gamma iSM_S' -q|\, \hat{\mathrm{H}}_{so} \,|\alpha'\Gamma' i'S'M_S'> \propto <\alpha\Gamma iSM_S' -q|\, \hat{L}_q\hat{S}\,|\,\alpha'\Gamma' i'S'M_S'>$

This matrix element is equal to zero unless $\Gamma\times\Gamma^{L_q}\times\Gamma'$ *contains the totally symmetric representation of G.* $\hat{L}_q$ itself transforms as linear combinations of the pseudovector components $\hat{L}_x, \hat{L}_y, \hat{L}_z$ (which transform as x,y,z except that they are even under inversion). Depending on implementation of actual calculations, it may be beneficial to explicitly rewrite the matrix elements in terms of $\hat{L}_x, \hat{L}_y, \hat{L}_z$, because for the more common groups it is $\hat{L}_x$ and $\hat{L}_y$ that have unique irrep labels rather than $\hat{L}_+$ and $\hat{L}_-$.

Comparison of the Point and Double Group Selection Rules

Even though the point group rules may seem less powerful due to the absence of spin dependence, they are in fact more restrictive and useful than the double group rules. There are two reasons for this: the spin dependence is actually not neglected, but taken full advantage of by means of the Wigner-Eckart theorem, and secondly the basis set in terms of which the rules are formulated (scalar wavefunction) is naturally suited for point group rules. The bases of the irreps of the double groups are often built from several scalar functions, so the latter functions themselves are unwieldy and a poor choice for the rules in the double group.

A pictorial example of this is a matrix element between two states having the same point group symmetry and spin (both S and M_S) (equivalent terms), e.g., $<1\text{-}^3A_1(M_S=0)|\, \hat{\mathrm{H}}_{so}\, |2\text{-}^3A_1(M_S'=0)>$. Such a matrix element is not predicted to be zero according to the double group rules, as the radial and the spin symmetries are identical, however in the point group the symmetry rule reduces to the symmetry of the component of L_z. This deems the element equal to zero in those point groups in which L_z belongs to an irrep other than the totally symmetric one (e. g., in C_{2v}).

Computational Speed-up

Downloaded by NORTH CAROLINA STATE UNIV on September 14, 2012 | http://pubs.acs.org
Publication Date: August 14, 2002 | doi: 10.1021/bk-2002-0828.ch013

The symmetry selection rules can be used in several different ways. First, let us consider techniques to accelerate scalar (single CPU) code. As the size of the active space and the level of electron correlation increases, the number of either determinants or configuration state functions (CSFs) increases dramatically. The main computational difficulty in a SOC calculation usually is confined to having to deal with a large CI expansion. Although working in the determinant basis set has its own benefits, such as its relative simplicity and efficiency at the same time, the smaller expansion in the CSF basis can prove to be a significant advantage. Most techniques described below are applicable to both types of wavefunction expansion, the main difference being that CSFs are eigenfunctions of $\hat{S}^2$ and $\hat{S}_z$, whereas determinants are eigenfunctions of $\hat{S}_z$ only.

The approaches presented below are incorporated into the GAMESS package *(25)* as modifications of the original SOC code written by Koseki *(9)*, based upon graphic unitary group approach (GUGA) *(26)* used to generate CI wavefunction. Perturbative treatment is assumed whereas a recent paper by Yabushita et al developed spin-orbit CI method using GUGA *(5)*.

For a CSF-driven algorithm, a SOC code contains a loop over pairs of CSFs. The following criteria can be used to avoid calculating the matrix element between two CSFs.

a) Overall number of open shells:

GUGA provides the number of unpaired electrons for each CSF. These numbers for the two CSFs cannot differ by more than 1 (one-electron $\hat{H}_{so}$) or 2 (full Pauli-Breit Hamiltonian).

b) Orbital occupancies:

Each CSF has a unique orbital occupancy, consisting of determinants that differ only by spin occupations. The maximum allowed number of orbital discoincidences n is determined by the structure of the operator: n=1 if only one-electron terms are included and n=2 for the full Pauli-Breit Hamiltonian. To make this heavily used part of the code more efficient, the orbital occupancies (which can be 0, 1 or 2 for each orbital) are packed into integer arrays, 2 bits per orbital. To determine the number of occupancies exclusive or (XOR) is performed, in the same fashion as developed by Furlani *(10)*. The resultant array is split into 2-byte integer numbers. Each of these numbers is taken as an

In Low-Lying Potential Energy Surfaces; Hoffmann, M., et al.;
ACS Symposium Series; American Chemical Society: Washington, DC, 2002.

argument to a pretabulated function giving the number of discoincidences. The total number of discoincidences is then obtained as a sum of the values of the precalculated array over all 2-byte numbers. This reduces the linear dependency on the number of orbitals to a logarithmic dependency.

c) If the absolute value of the product of the two CI expansion coefficients is smaller than some threshold value (given by the user), there is no need to proceed further.
d) Symmetry selection rules. By using the selection rules discussed above, the calculation of matrix elements that are zero by symmetry can be avoided.

The parallelisation of this scheme can be achieved quite easily by dividing the loop over CSFs into all computer nodes available for the parallel run. Each node will then calculate its share of the CSF pairs, and the resultant matrix elements are then summed over all nodes, using static load balancing to avoid either dynamically retrieving or complete in-core storing of CSF occupations and coefficients. The integrals are either completely or partially kept in memory, depending upon the amount of memory needed/available. A few timings obtained with the parallel version of GAMESS will be presented below. A parallel implementation of spin-orbit CI also exists *(27)*.

As a test case a calculation of ArO has been chosen. All calculations have been run on the Scalable Computing Laboratory 64 node Pentium cluster ALICE *(28)*. Each node is a 200 MHz Pentium Pro with a 2GB hard disk and 256MB RAM. All timings are wall-clock and are given in seconds. The basis set *(29,30)* used is Ar=(11s,7p,1d)/[4s,3p,1d], O=(9s,5p,1d)/[3s,2p,1d], the orbitals were optimised with 14 electrons in 8 orbitals complete active space self consistent field (CASSCF) method and finally single and double (SOCI) excitations into the virtual space were performed. The internuclear distance was set[29] to 1.9844 Å. The following states were included in the spin-orbit coupling study: $1\text{–}^1\Sigma^+$, $^1\Pi$, $^1\Delta$, $2\text{–}^1\Sigma^+$, $^3\Pi$, $^3\Sigma^-$. There are 145776 singlet and 232848 triplet CSFs. CSFs were generated in C_1 symmetry to obtain all states at once, and SOC and ordinary integrals were calculated in C_{2v} symmetry.

The scalability of SOC is given in Figure 1. Two-electron SO integrals in the AO basis as well as transformations into the MO basis are performed on each node independently to reduce the amount of communication traffic. As seen from the figure the scalability of the full Pauli-Breit Hamiltonian is the best. The overall scalability is dragged down by the CI code.

Summary and conclusions

General group-theoretical methods have been used to derive important selection rules for spin-orbit coupling matrix elements. Whereas some of the results have been known prior to this publication, some useful new procedures have been introduced, and as complete a symmetry analysis as possible has been

Downloaded by NORTH CAROLINA STATE UNIV on September 14, 2012 | http://pubs.acs.org
Publication Date: August 14, 2002 | doi: 10.1021/bk-2002-0828.ch013

Downloaded by NORTH CAROLINA STATE UNIV on September 14, 2012 | http://pubs.acs.org
Publication Date: August 14, 2002 | doi: 10.1021/bk-2002-0828.ch013

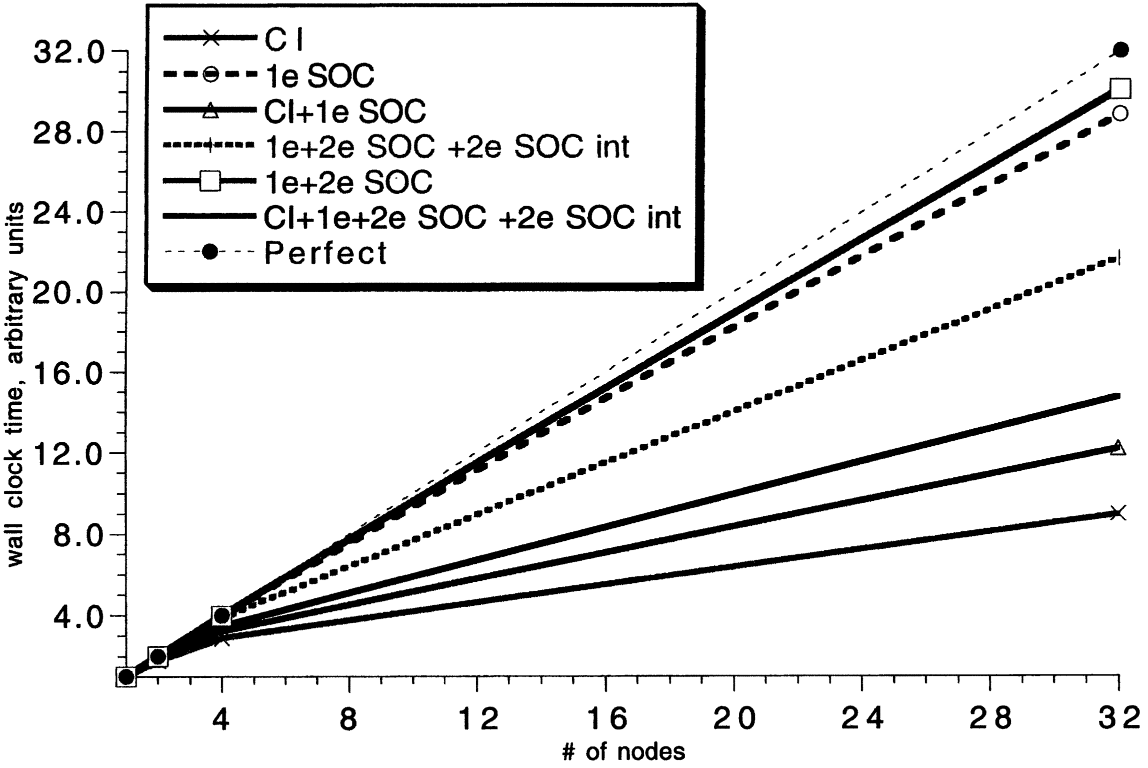

Figure 1. Scalability of SOC code

presented. Selection rules for the spin-orbit coupling matrix elements have been given in terms of both double and point groups. The computational procedure for an efficient spin-orbit coupling code has been described and the results of parallel tests have been presented.

A typical spin-orbit coupling matrix is given in Appendix IV.

Acknowledgements

The authors wish to express their gratitude to Professors Michael Schmidt, Satoshi Yabushita, David Yarkony and Pekka Pyykkö for their helpful comments. The parallel calculations were performed on the Alice cluster, obtained via funds from the Ames Laboratory-USDOE and Iowa State University. This work was supported by the Ames Laboratory via the Department of Energy Basic Energy Sciences Office. Development of scalable codes was supported by a DoD software grant administered by the Air Force Office of Scientific Research.

Downloaded by NORTH CAROLINA STATE UNIV on September 14, 2012 | http://pubs.acs.org
Publication Date: August 14, 2002 | doi: 10.1021/bk-2002-0828.ch013

Appendix I. Wigner Functions

Wigner functions in the Euler angle representation can be calculated as follows *(31)*:

$$\begin{aligned} D^{j}_{mm'}(\alpha,\beta,\gamma) &= \exp(-im\alpha - im'\gamma)\, d^{j}_{mm'}(\beta) \\ d^{j}_{mm'}(\beta) &= (-1)^{j-m'}\sqrt{(j+m)!(j-m)!(j+m')!(j-m')!}\,\times \\ &\sum_{k=\min(j-m,j-m')}^{\max(-m-m',0)} (-1)^{k} \frac{\cos^{m+m'+2k}(\beta/2)\sin^{2j-m-m'-2k}(\beta/2)}{k!(j-m-k)!(j-m'-k)!(m+m'+k)!} \end{aligned} \tag{28}$$

Appendix II. Arbitrary CI Wavefunction Symmetry Labelling

While this labelling is a technical issue, it appears sufficiently important to be briefly outlined. The necessity for this lies in the fact that especially for non-Abelian point groups, existing CI implementations are not always able to assign symmetry labels to the states obtained in a determinant-based calculation, such as CASSCF or MRCI. In particular, the non-Abelian GUGA approach does not appear to be widely used. Consider a wavefunction

$$\Psi = \sum_{I} C_I D_I \tag{29}$$

where D_I are the determinants and C_I the expansion coefficients. It is assumed that molecular spin-orbitals $\psi=\varphi\sigma$ in the determinants are already symmetry labelled. For simplicity the spin part σ is omitted in the equations below, except where relevant. The statement that Ψ does not belong to row a of irrep Γ is equivalent to:

$P^{\Gamma a}\Psi = 0$ where P is a projection operator. (30)

$$P^{\Gamma a}\Psi = \frac{n^{\Gamma}}{n_g}\sum_g D_{aa}^{\Gamma\,*}(g) T_g \sum_I C_I \det\{\varphi_1 \ldots \varphi_N\}_I = \frac{n^{\Gamma}}{n_g}\sum_g D_{aa}^{\Gamma\,*}(g) \sum_I C_I \det\{T_g\varphi_1 \ldots T_g\varphi_N\}_I \tag{31}$$

Unless special measures are taken, φ will usually be labelled without a distinct row symmetry. This corresponds to mixing degenerate components, such as p_x and p_y for atoms. In order to find their transformation law, they can be decomposed into linear combinations of row-adapted functions. In the following, k_μ below simply numbers degenerate components, e. g. one can assign k=1 for an orbital $\varphi=p_x+p_y$ and k=2 for p_x-p_y so k=1 does not imply pure p_x or p_y.

$$\begin{aligned}
&\varphi_\mu \equiv \varphi_\mu^{\Gamma_\mu k_\mu} = \sum_{\alpha=1}^{n^\Gamma} a_{\alpha k_\mu}^{\Gamma_\mu} \phi_\mu^{\Gamma_\mu \alpha} \quad and \quad \phi_\mu^{\Gamma_\mu \alpha} = \sum_{k_\mu=1}^{n^\Gamma} (a^{-1})_{k_\mu \alpha}^{\Gamma_\mu} \varphi_\mu^{\Gamma_\mu k_\mu} \\
&T_g \phi_\mu^{\Gamma_\mu \alpha} = \sum_{\alpha'=1}^{n^\Gamma} D_{\alpha'\alpha}^{\Gamma_\mu}(g) \phi_\mu^{\Gamma_\mu \alpha'} = \sum_{\alpha'=1}^{n^\Gamma} D_{\alpha'\alpha}^{\Gamma_\mu}(g) \sum_{k_\mu=1}^{n^\Gamma} (a^{-1})_{k_\mu \alpha'}^{\Gamma_\mu} \varphi_\mu^{\Gamma_\mu k_\mu} \\
&T_g \varphi_\mu^{\Gamma_\mu k_\mu} = \sum_{\alpha=1}^{n^\Gamma} a_{\alpha k_\mu}^{\Gamma_\mu} \sum_{\alpha'=1}^{n^\Gamma} D_{\alpha'\alpha}^{\Gamma_\mu}(g) \sum_{k_\mu=1}^{n^\Gamma} (a^{-1})_{k_\mu \alpha'}^{\Gamma_\mu} \varphi_\mu^{\Gamma_\mu k_\mu} \\
&D'^{\Gamma_\mu}(g) = a^{-1} D^{\Gamma_\mu}(g) a
\end{aligned} \tag{32}$$

where ϕ transform according to row α of the irreducible representation Γ and the coefficients "a" will be found later. D' gives the transformation law in the new basis.

$$\begin{aligned}
P^{\Gamma a}\Psi &= \frac{n^{\Gamma}}{n_g}\sum_g D_{aa}^{\Gamma\,*}(g) \sum_I C_I \det\{T_g \varphi_1^{\Gamma_1 k_1} \ldots T_g \varphi_N^{\Gamma_N k_N}\}_I \\
&= \frac{n^{\Gamma}}{n_g}\sum_g D_{aa}^{\Gamma *}(g) \sum_I C_I \sum_{k_1'} D'^{\Gamma_1}_{k_1' k_1}(g) \ldots \sum_{k_N'} D'^{\Gamma_N}_{k_N' k_N}(g) \det\{\varphi_1^{\Gamma_1 k_1'} \ldots \varphi_N^{\Gamma_N k_N'}\}_I
\end{aligned} \tag{33}$$

Some of the determinants $\det\{\varphi_1^{\Gamma_1 k_1'} \ldots T_g \varphi_N^{\Gamma_N k_N'}\}_I$ are linearly dependent. These are only the determinants which include degenerate MO's belonging to the

Downloaded by NORTH CAROLINA STATE UNIV on September 14, 2012 | http://pubs.acs.org
Publication Date: August 14, 2002 | doi: 10.1021/bk-2002-0828.ch013

same Γ_μ and only for certain combinations of spin functions, e.g., for doubly degenerate MOs $\det\{\ldots\varphi_1\alpha\varphi_2\alpha\ldots\}$ *and* $\det\{\ldots\varphi_2\alpha\varphi_1\alpha\ldots\}$ arise from $T_g\det\{\ldots\varphi_1\alpha\varphi_2\alpha\ldots\}$. These linearly independent cases are small in number and are readily accounted for.

The weight of the irreducible representation Γ row α in the wavefunction Ψ is:

$$W^{\Gamma\alpha}[\Psi]=\sum_I\left|\frac{n^\Gamma}{n_g}\sum_J C_J[-1]^{I,J}\sum_g D_{aa}^{\Gamma^*}(g)D'^{\Gamma_1}_{k_1'k_1}(g)\ldots D'^{\Gamma_N}_{k_N'k_N}(g)\right|^2 \tag{34}$$

The sum over *I* runs over all determinants in Ψ and the sum over *J* runs over determinants generating linearly dependent determinants in D_I upon application of T_g. Unprimed indices correspond to orbitals found in D_I and primed indices are from D_J. $[-1]^{I,J}$ arises after an even *1* or odd *(-1)* permutation producing *I* from *J*.

Determinants to be included in the *J* sum are easy to identify, because they have the same orbital **and** spin occupancies except for one possible degree of freedom: MOs belonging to a degenerate Γ_μ can replace one another. So a determinant containing p_x, det $\{\ldots p_x\ldots\}$, can be reproduced upon rotation from a determinant with p_y in place of p_x, det $\{\ldots p_y\ldots\}$, and identical in other orbitals. It should be noted that Γ_μ is understood to include a label distinguishing equivalent irreps, such as 2 in $2p_x$, so that $2p_x$ does not interact with $3p_y$ in the above sense. For determinants containing a degenerate irrep, for MOs multiplied by the same spin function it is necessary to add determinants to *J* obtained from those in *I* by a permutation. This can be seen to correspond to restricting *J* to only determinants found in *I* and replacing the product of *D'* matrix elements with det D'^Γ. Since the choice of *J* for a given *I* is crucial, the following examples should clarify the choice of *J*.

Consider a wavefunction consisting of only three determinants in C_{3v} (case A), for any spin occupancies:

$D_1=det\{1a_11e_12\ a_1\}$
$D_2=det\{1\ a_11e_22\ a_1\}$
$D_3=det\{1\ a_11e_23\ a_1\}$

The phases and determinants to be included into the *J* sum are given in Table I; *I*, *J* and $[-1]^{I,J}$ are defined as in Eq. 34.

Another example involving negative phase might be (case B):

$D_1=det\{1a_1\alpha 1e_1\beta 1e_2\beta\}$
$D_2=det\{1a_1\alpha 1e_2\beta 2\ a_1\beta\}$
$D_3=det\{1a_1\beta 1e_2\beta 2\ a_1\alpha\}$
$(D_{1'}=det\{1a_1\alpha 1e_2\beta 1e_1\beta\})$

Downloaded by NORTH CAROLINA STATE UNIV on September 14, 2012 | http://pubs.acs.org
Publication Date: August 14, 2002 | doi: 10.1021/bk-2002-0828.ch013

Downloaded by NORTH CAROLINA STATE UNIV on September 14, 2012 | http://pubs.acs.org
Publication Date: August 14, 2002 | doi: 10.1021/bk-2002-0828.ch013

The phases and determinants are given in Table II.

Finally to find the necessary coefficients a, the following procedure can be used. Application of $P^{\Gamma\alpha}$ on the set $\varphi^{\Gamma k}$ produces either zero if $\varphi^{\Gamma k}$ has no projection in the space of Γ,α or $\varphi^{\Gamma\alpha}$ otherwise and $\varphi^{\Gamma\alpha}$ can be normalised for convenience. Functions $\varphi^{\Gamma\alpha}$ can be explicitly written in terms of atomic orbitals.

$$\begin{aligned}\varphi^{\Gamma k}(r) &= \sum_{pst} c^{\Gamma k}_{pst}\chi_{ps}(r-R_t)\\ \phi^{\Gamma\alpha}(r) &= \sum_{pst} C^{\Gamma\alpha}_{pst}\chi_{ps}(r-R_t)\end{aligned} \tag{35}$$

The index p corresponds to l (angular momentum quantum number) in case spherical harmonics are used or to the rank of the Cartesian direct product tensor (i.e., 1 for x, 2 for xy, z^2 etc) for real Cartesian basis sets, s being correspondingly m or denoting a component of the tensor of rank p. R_t stands for Cartesian coordinates of atom t.

$$\begin{aligned}\phi^{\Gamma\alpha}(r) &= \sum_{pst} C^{\Gamma\alpha}_{pst}\chi_{ps}(r-R_t) = P^{\Gamma\alpha}\varphi^{\Gamma k}(r) = \frac{n^{\Gamma}}{n_g}\sum_{pst} c^{\Gamma k}_{pst}\sum_{g} D^{\Gamma}_{aa}{}^{*}(g)T_g\chi_{ps}(r-R_t) =\\ &= \frac{n^{\Gamma}}{n_g}\sum_{pst} c^{\Gamma k}_{pst}\sum_{g} D^{\Gamma}_{aa}{}^{*}(g)\sum_{s'} F^{p}_{s's}(g)\chi_{ps'}(r-gR_t)\end{aligned} \tag{36}$$

Matrices $F(g)$ give the transformation law for χ. They are the Wigner functions for χ having angular dependence of spherical harmonics. For Cartesian angular dependence they can be explicitly written down with some algebra as linear combinations of Wigner functions.

$$C^{\Gamma\alpha}_{ps} = \frac{n^{\Gamma}}{n_g}\sum_{g} D^{\Gamma}_{aa}{}^{*}(g)\sum_{s'} F^{p}_{ss'}(g)c^{\Gamma k}_{ps',g^{-1}t} \tag{37}$$

where $g^{-1}t$ is understood to mean atom t' such that $R_{t'}=g^{-1}R_t$.
Using the orthonormality of $\langle\varphi^{\Gamma\alpha}|\varphi^{\Gamma\alpha'}\rangle = \delta_{\alpha\alpha'}$

$$\begin{aligned}\varphi^{\Gamma k} &= \sum_{\alpha=1}^{n^{\Gamma}} a^{\Gamma}_{\alpha k}\phi^{\Gamma\alpha}\\ a^{\Gamma}_{\alpha k} &= \langle\phi^{\Gamma\alpha}|\varphi^{\Gamma k}\rangle\end{aligned} \tag{38}$$

Appendix III. Clebsch-Gordan Coefficient Relations

The following relations used above can be readily proved by using the properties of 3j Wigner symbols *(19)*.

Downloaded by NORTH CAROLINA STATE UNIV on September 14, 2012 | http://pubs.acs.org
Publication Date: August 14, 2002 | doi: 10.1021/bk-2002-0828.ch013

Table I. Determinants and phase factors for Non-Abelian groups, case A.

I	*J*	$[-1]^{I,J}$
1	1	1
	2	1
2	1	1
	2	1
3	3	1

Table II. Determinants and phase factors for Non-Abelian groups, case B.

I	*J*	$[-1]^{I,J}$
1	1	1
	1'	-1
2	2	1
3	3	1

Downloaded by NORTH CAROLINA STATE UNIV on September 14, 2012 | http://pubs.acs.org
Publication Date: August 14, 2002 | doi: 10.1021/bk-2002-0828.ch013

$$\left(S,1,M_s-1,1\middle|S,M_s\right)=(-1)^{S-1+M_s}\sqrt{2S+1}\begin{pmatrix} S & 1 & S \\ M_s-1 & 1 & -M_s \end{pmatrix}$$

$$\left(S,1,M_s,-1\middle|S,M_s-1\right)=(-1)^{S-1+M_s-1}\sqrt{2S+1}\begin{pmatrix} S & 1 & S \\ M_s & -1 & -(M_s-1) \end{pmatrix}=$$

$$(-1)^{S-1+M_s-1}\sqrt{2S+1}(-1)^{2S+1}\begin{pmatrix} S & 1 & S \\ -M_s & 1 & M_s-1 \end{pmatrix}=$$

$$(-1)^{S-1+M_s-1}\sqrt{2S+1}(-1)^{2S+1}(-1)^{2S+1}\begin{pmatrix} S & 1 & S \\ M_s-1 & 1 & -M_s \end{pmatrix}=$$

$$-(-1)^{S-1+M_s}\sqrt{2S+1}\begin{pmatrix} S & 1 & S \\ M_s-1 & 1 & -M_s \end{pmatrix}=-\left(S,1,M_s-1,1\middle|S,M_s\right)$$

And similarly,

$$\left(S+1,1,M_s+1,-1\middle|S,M_s\right)=(-1)^{S+1-1+M_s}\sqrt{2S+1}\begin{pmatrix} S+1 & 1 & S \\ M_s+1 & -1 & -M_s \end{pmatrix}$$

$$\left(S+1,1,-M_s-1,1\middle|S,-M_s\right)=(-1)^{S+1-1-M_s}\sqrt{2S+1}\begin{pmatrix} S+1 & 1 & S \\ -M_s-1 & 1 & M_s \end{pmatrix}=$$

$$(-1)^{S+1-1-M_s}\sqrt{2S+1}(-1)^{S+1+1+S}\begin{pmatrix} S+1 & 1 & S \\ M_s+1 & -1 & -M_s \end{pmatrix}=$$

$$(-1)^{M_s-M_s}(-1)^{S+1-1-M_s}\sqrt{2S+1}(-1)^{S+1+1+S}\begin{pmatrix} S+1 & 1 & S \\ M_s+1 & -1 & -M_s \end{pmatrix}=$$

$$(-1)^{S+1+1+S-2M_s}(-1)^{S+1-1+M_s}\sqrt{2S+1}\begin{pmatrix} S+1 & 1 & S \\ M_s+1 & -1 & -M_s \end{pmatrix}=$$

$$(-1)^{S+1-1+M_s}\sqrt{2S+1}\begin{pmatrix} S+1 & 1 & S \\ M_s+1 & -1 & -M_s \end{pmatrix}=\left(S+1,1,M_s+1,-1\middle|S,M_s\right)$$

where $S+1+1+S-2M_S$ is always an even number as S and M_S are both integers or half-integers.

Appendix IV. Detailed structure of the H_{so} matrix

As pointed out above, the matrix is tridiagonal and only two matrix elements need to be calculated explicitly. The detailed structure is provided below, the cases of equal and different multiplicities are given separately in Table III and Table IV. The orbital part is assumed to be different for the two states. The only two matrix elements which are explicitly calculated are A and B, the rest are obtained from these two.

Table III. H_{so} matrix for equal multiplicities.

	S	S-1	S-2	...	← M_S'
S	A	-B*	0	0	0
S-1	B	AA	-bB*	0	0
S-2	0	bB*	...	...	0
...	0	0	...	...	...
M_S ↑	0	0	0	...	...

A,*B* – calculated matrix elements, while *a* and *b* are Clebsch-Gordan coefficients:

$a \equiv (S,1,S\text{-}1,0|S,S\text{-}1)/(S,1,S,0|S,S)$ and $b \equiv (S,1,S\text{-}1,\text{-}1|S,S\text{-}2)/(S,1,S,\text{-}1|S,S\text{-}1)$

"... " denote further propagation of *A* and *B* by means of eq 7.

Table IV. H_{so} matrix for different multiplicities.

	S+1	S	S-1	...	←M_S'→	-S	-S-1
S	B	A	bB*	0	0	0	0
S-1	0	aB	cA	...	0	0	0
S-2	0	0	...	...	...	0	0
M_S ↑	0	0	0	...	...	...	0
-S	0	0	0	0	...	...	B*

A,*B* – calculated matrix elements and a,b,c are Clebsch-Gordon coefficients:

$a \equiv (S+1,1,S,\text{-}1|S,S\text{-}1)/(S+1,1,S+1,\text{-}1|S,S)$,

$b \equiv (S+1,1,S\text{-}1,1|S,S)/(S+1,1,\text{-}S\text{-}1,1|S,\text{-}S)$

$c \equiv (S+1,1,S\text{-}1,0|S,S\text{-}1)/(S+1,1,S,0|S,S)$

References

---

1. Yarkony, D. R. J. Phys. Chem. A **1997**, 101, 4263.
2. Yarkony, D. R. Int Rev in Phys. Chem. **1992**, Vol II No 2, 195-242.
3. Hay, P. J. J. Am. Chem. Soc. **1982**, 104, 7007.
4 Hay, P. J. J. Chem. Phys. **1983**, 79, 5469.
5. Yabushita, S.; Zhang, Z.; Pitzer, R. M. J. Phys. Chem. **1999**, 103, 5791.
6. Sjøvoll, M.; Gropen, O.; Olsen, J. Theor. Chem. Acc. **1997**, 97, 301.

Downloaded by NORTH CAROLINA STATE UNIV on September 14, 2012 | http://pubs.acs.org
Publication Date: August 14, 2002 | doi: 10.1021/bk-2002-0828.ch013

7. Furlani, T. R.; King, H. F. J. Chem. Phys. **1985**, 82, 5577.
8. Yarkony, D. R. J. Chem. Phys. **1986**, 84, 2075.
9. Koseki, S.; Gordon, M. S.; Schmidt, M. W.; Matsunaga N. **1995**, J. Phys. Chem. 99,12764.
10. Furlani, T. R. PhD Thesis, SUNY, NY, **1984**.
11. *Applications of Electronic Structure Theory*, Ed. by Schaefer H.F. III, Plenum,New York, **1977**.
12. Richards, W. G.; Trivedi, H. P.; Cooper, D. L. *Spin-orbit coupling in molecules*, Clarendon Press, Oxford, **1981**.
13. Dolg, M.; Stoll, H. *Handbook on the Physics and Chemistry of Rare Earths*, Elsevier, New York, **1978**, vol. 22.
14. Pyykkö, P. *Relativistic Theory of Atoms and Molecules, A bibliography 1916-1985*. Springer-Verlag **1986**; *A bibliography 1986-1992*, Springer-Verlag **1993.**
15. Hess, B. A. Phys. Rev. A **1985**, 32, 756.
16. Hess, B. A. Phys. Rev. A **1986**, 33, 3742.
17. Nakajima, T.; Hirao, K. Chem. Phys. Lett. **1999**, 302, 383.
18. Bethe, H. A.; Salpeter, E. E. *Quantum Mechanics of One- and Two Electron Atoms*, New York, Plenum, **1977**.
19. Brink, D. M.; Satchler, G. R. *Angular Momentum*. Charedon Press, Oxford, **1968**.
20. Yarkony, D. R. *Modern Electronic Structure Theory*. World Scientific, 174ff, **1995**.
21. Balasubramanian, K. *Relativistic Effects In Chemistry*. John Wiley, New York, **1997**.
22. McWeeny, R. J. Chem. Phys. **1965**, 42, 1717.
23. Fedorov, D. G.; Finley, J. P. Phys. Rev. A **2001**, 64, 04250, specifically, Eq (3.19).
24. Pitzer, R. M.; Winter, N. W. J. Phys. Chem. **1988**, 92, 3061.
25. Schmidt, M. W.; Baldridge, K. K.; Boatz, J. A.; Elbert, S. T.; Gordon, M. S., Jensen, J. H.; Koseki, S.; Matsunaga, N.; Nguyen, K. A.; Su, S. J.; Windus, T.L., Dupuis; M., Montgomery, J. A. J. Comput. Chem. **1993**, 14, 1347
26. Brooks, B. R.; Schaefer, H. F. III J. Chem. Phys. **1979**, 70, 5092.
27. Tilson, J. L., Ermler, W. C., Pitzer, R. M. Comp. Phys. Comm. **2000**, 128, 128.
28. http://www.scl.ameslab.gov.
29. Dunning, T. H., Hay, P. J. J. Chem. Phys. **1977**, 66, 3767.
30. Cohen, J. S., Wadt, W. R., Hay, P. J. J Chem. Phys. **1979**, 71, 2955.
31. Warshalovich, D. A., Moskalev, L. N., Kersunski, V. K. *Quantum theory of angular momentum*. Nauka, Moscow, **1975** (in Russian).

Downloaded by NORTH CAROLINA STATE UNIV on September 14, 2012 | http://pubs.acs.org
Publication Date: August 14, 2002 | doi: 10.1021/bk-2002-0828.ch013

Chapter 14

Non-Adiabatic Bending Dissociation of OCS Induced by Orbital Unlocking

Toshinori Suzuki[1,2] and Shinkoh Nanbu[2,3]

[1]Institute for Molecular Science, [2]Graduate University for Advanced Studies,
and [3]Research Center for Computional Science, Okazaki National Research Institutes,
Myodaiji, Okazaki 444–8585, Japan

Downloaded by COLUMBIA UNIV on September 14, 2012 | http://pubs.acs.org
Publication Date: August 14, 2002 | doi: 10.1021/bk-2002-0828.ch014

UV photodissociation of OCS via 2A'($^1\Delta$) leads to a bimodal speed distribution of S($^1D_2$) fragment atoms whereas a single speed distribution characterizes the S atoms emerging from the 1A"($^1\Sigma^-$) surface. The potential energy surfaces of these two states are almost degenerate, meaning that the bimodal state distribution observed for the 2A' state cannot be explained by the topography of the adiabatic surfaces. It is shown that the bimodal distribution originates from concomitant adiabatic and non-adiabatic dissociation processes from the 2A' state. The non-adiabatic transition is due to unlocking of an S atom electron orbital from the C-S axis by rapid rotation of CO.

INTRODUCTION

Within the adiabatic (or Born-Oppenheimer) approximation, a chemical reaction is viewed as the nuclear motion on a single potential energy surface (PES). The nuclear motion over the PES occurs with little or no recrossing in direct reactions, resulting in short trajectories, while long and (pseudo)chaotic trajectories are

In Low-Lying Potential Energy Surfaces; Hoffmann, M., et al.;
ACS Symposium Series; American Chemical Society: Washington, DC, 2002.

observed in compound reactions. However, in so far as the nuclear motion occurs on a single PES, these modes of reaction are only different in their complexities. On the other hand, when the energies of different electronic states approach each other at a certain nuclear position, the Born-Oppenheimer approximation becomes totally inaccurate, which is observable by 'non-adiabatic transitions' between the adiabatic PES's (1-4). Their consideration is particularly important when discussing the dynamics of polyatomic molecules, where a number of surface crossing occur between close-lying electronic states. Photodissociation of OCS leads to the same product, $CO(^1\Sigma^+)+S(^1D_2)$, from both adiabatic and non-adiabatic dissociation channels. Because of this, the importance of non-adiabatic coupling in OCS was not readily recognized in the past. In this contribution, we describe how the non-adiabatic dissociation dynamics in OCS have been disentangled by two-dimensional photofragment imaging and *ab initio* wavepacket calculations. In the process we will show that one-electron molecular orbital pictures such as Walsh diagrams (5) well illustrate the electronic origin of the non-adiabatic interactions.

Downloaded by COLUMBIA UNIV on September 14, 2012 | http://pubs.acs.org
Publication Date: August 14, 2002 | doi: 10.1021/bk-2002-0828.ch014

TWO-DIMENSIONAL PHOTOFRAGMENT IMAGING

A pump laser pulse dissociates parent molecules to create a rapidly expanding sphere of neutral fragments. In the ion imaging method (6), the neutral fragments are state-selectively ionized by a probe laser pulse and the resulting ion cloud is projected onto an imaging detector that consists of a microchannel plate (MCP) together with a phosphor screen and a CCD (charge-coupled device) camera. When an ion enters one of the channels (10 μm in diameter) in the MCP, secondary electrons are amplified in the channel and accelerated toward the phosphor screen. The electron impact on the phosphor provides a bright light spot that indicates the arrival position of an ion on the MCP. The image on the phosphor screen is captured by the CCD camera and integrated for a number of laser shots. The photofragment velocity components parallel to the detector face (v_x and v_y) are readily determined from the flight time (t) and the arrival position (x, y) of an ion from the relation $v_x=x/t$ and $v_y=y/t$. The ions with different masses are discriminated by the flight times from the ionization region to the detector. Thus, an ion image can be selectively observed for a particular mass of interest by time gating the MCP or the camera. Photofragment imaging uses resonance-enhanced multiphoton ionization (REMPI) to detect the atoms and molecules in a particular quantum state. Therefore, the observed image provides the scattering distribution of state-selected products. It should be noted that electron impact, one-photon, or non-resonant multi-photon ionization methods cannot provide such state-selectivity in ionization. The image obtained is a projection of the 3D fragment velocity distribution onto a 2D detector plane. The data are numerically inverted to recover the original 3D distribution for quantitative analysis (7). It can be shown mathematically that a cylindrically symmetric 3D object can be reconstructed from a single projection image, if the projection plane involves the symmetry axis. The cylindrical symmetry is ensured for the 3D ion distribution by aligning the pump and probe laser polarization parallel to each other in photodissociation experiment. Therefore, this polarization combination and a projection direction perpendicular to the symmetry axis are usually employed. Inverse Abel transform is most commonly used to invert the 2D projection to the 3D distribution (7).

In our experiment (8), OCS seeded in He or Ar was expanded from a pulsed valve with a stagnation pressure of about 1 bar and collimated by two skimmers. The molecular beam intersects, perpendicularly, the counter-propagated pump and probe laser beams. The time delay between the pump and probe laser pulses is kept less than 20 ns. Both the pump and probe beams are focused with axisymmetric lenses (f = 250 or 300 mm). The photoions produced are accelerated up to a kinetic energy of 4 keV and projected onto the MCP backed by a phosphor screen (36 mm in effective diameter). A high voltage pulse, 1600-1800 V in height and 200 ns in width, is applied to the MCP to time-gate the ions with the particular mass of interest. The transient image on the phosphor screen is captured by a video-rate (CCIR) interline CCD camera and integrated by an image capture board with 16 bit on-board memory. During the integration of an image, the probe laser frequency is scanned over the entire absorption line of the S atom to eliminate Doppler broadening effects due to the fragment recoil velocities.

Downloaded by COLUMBIA UNIV on September 14, 2012 | http://pubs.acs.org
Publication Date: August 14, 2002 | doi: 10.1021/bk-2002-0828.ch014

RESULTS AND DISCUSSION

A. 2D imaging of $S(^1D_2)$ in photodissociation of OCS

OCS is a 16 valence-electron system similar to CO_2, N_2O, and CS_2. The first absorption band of OCS in the UV region is due to transitions to the close-lying $^1\Sigma^-$ and $^1\Delta$ states that arise from the HOMO-LUMO transition. Electric dipole transitions from the ground state $^1\Sigma^+$ to the $^1\Sigma^-$ and $^1\Delta$ states are forbidden. However, bending deformation splits the $^1\Delta$ state into A' and A" and transforms $^1\Sigma^-$ to A" components ($C_{\infty v} \rightarrow C_s$), to which transitions from the ground state are weakly dipole-allowed (9-12).

There are four dissociation channels energetically open for the first absorption band of OCS,

$$\text{OCS} \rightarrow \text{CO}(^1\Sigma^+) + \text{S}(^1D_2) \qquad \Delta H = 98.3\ \text{kcal/mol} \qquad \text{(I)}$$

$$\rightarrow CO(^1\Sigma^+) + S(^3P_0) \qquad \Delta H = 73.6 \text{ kcal/mol} \qquad (IIa)$$
$$\rightarrow CO(^1\Sigma^+) + S(^3P_1) \qquad \Delta H = 73.0 \text{ kcal/mol} \qquad (IIb)$$
$$\rightarrow CO(^1\Sigma^+) + S(^3P_2) \qquad \Delta H = 71.9 \text{ kcal/mol} \qquad (IIc).$$

However, the spin-forbidden channels (IIa) - (IIc) contribute only 5% relative to the spin-allowed channel (I) (13). In the following, we focus on the main dissociation channel (I).

Since CO is produced predominantly in the ground vibrational state of $X^1\Sigma^+$ (14), the rotational distribution of CO can be determined from the translational energy distributions of the concomitantly produced S atoms using energy and momentum conservation laws. In fact, observation of the S atoms is advantageous, since it discriminates between the four exit channels unambiguously.

The inverse Abel transforms of the $S(^1D_2)$ images measured at 223, 235, and 248 nm are shown in Fig. 1. The key to assigning the electronic states involved is that dissociation from the A' and A" states leads to S atoms ejected parallel and perpendicular to the pump laser polarization, respectively. Note that the high translational energy component appearing as an outer ring in the ion images varies from an isotropic (223 nm) to anisotropic distribution (248 nm). This means that the high translational-energy component is created from both A' and A", and that the relative photoabsorption cross-section to the A" state increases with respect to A' in the longer wavelength region. Since the only A' state expected in this energy region is the A' Renner-Teller component of the $^1\Delta$ state, the observed photofragments produced parallel to the photolysis laser polarization can be assigned to it. On the other hand, there are two A" states in the region, namely the A" Renner-Teller component of $^1\Delta$ and $A"(^1\Sigma^-)$. However, from the increasing contribution of A" in the longer wavelength region, the observed perpendicular fragments are assigned to $A"(^1\Sigma^-)$ that is located at lower energy than the $^1\Delta$ state. The A" Renner-Teller component of $^1\Delta$ exists in higher energy than the A' component.

A striking experimental result is that the speed distribution of S (or the rotational distribution of CO) is bimodal (8,14,15). Since the bending wavefunction of a parent molecule and the rotational distribution of a diatomic fragment can be related by the rotational reflection principle (16), a Gaussian-shaped rotational distribution of CO may be anticipated for a single dissociation channel. The observed bimodal distribution implies that there is bifurcation in dissociation dynamics. The scattering distribution of S atoms observed by ion imaging indicates that the bimodal distribution occurs only for dissociation from the $A'(^1\Delta)$ state and not for the $A"(^1\Sigma^-)$ state. The question is why does it occur only from the $A'(^1\Delta)$ state?

Downloaded by COLUMBIA UNIV on September 14, 2012 | http://pubs.acs.org
Publication Date: August 14, 2002 | doi: 10.1021/bk-2002-0828.ch014

Downloaded by COLUMBIA UNIV on September 14, 2012 | http://pubs.acs.org
Publication Date: August 14, 2002 | doi: 10.1021/bk-2002-0828.ch014

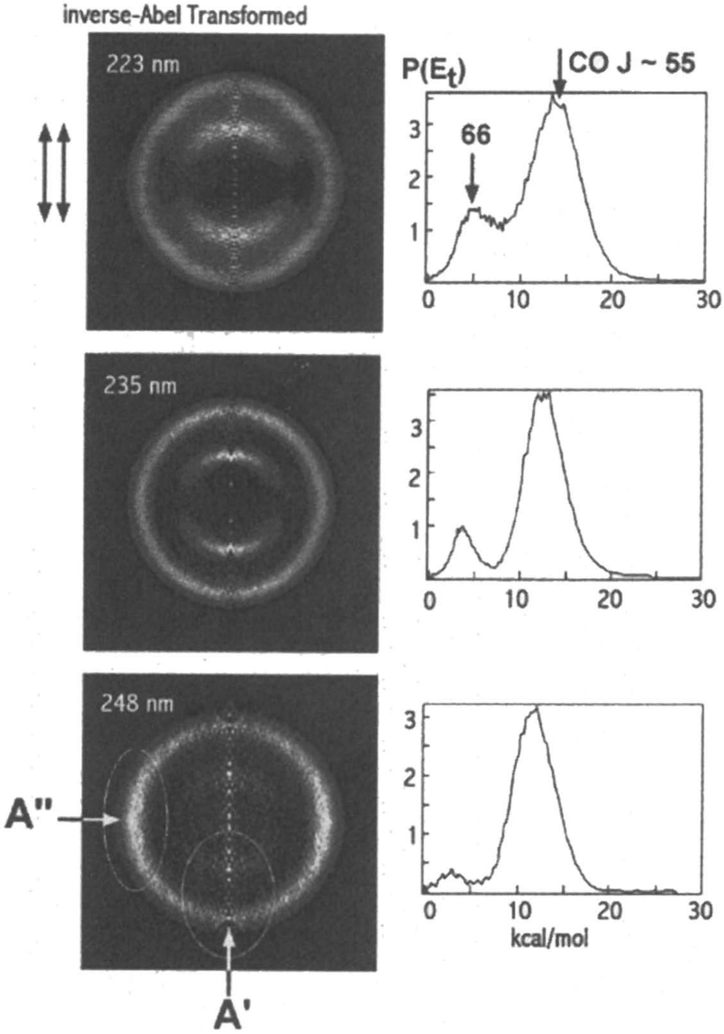

Figure 1 Inverse Abel transforms of the S($^1D_2$) images observed for photodissociation at 223, 235, and 248 nm. The center-of-mass translational energy releases calculated from these images are also shown. The fast component gradually changes from an isotropic distribution at 223 nm to an anisotropic distribution at 248 nm. The photoabsorption at 248 nm is dominated by a perpendicular transition to A". A bimodal speed distribution occurs only in dissociation from the A' state.

B. Electronic structure of OCS

To answer this, we calculated the PES's by the *ab initio* MRCI (multi-reference configuration interaction) method (8). In order to describe the low-lying electronic states accurately, the active space was selected as follows:

$$[(9\sigma)(2\pi)(3\pi)(4\pi)(10\sigma)(11\sigma)]^{10}.$$

The CASSCF calculations were performed by considering all possible configurations of the nine active orbitals filled with ten electrons. The restricted closed-shell SCF MO's were used in an initial state-averaged CASSCF calculation for the five A' and three A" states correlating with $S(^3P)$+CO, $S(^1D)$+CO, and $S(^1S)$ +CO. The natural orbitals obtained by the CASSCF calculation were used in the final internally-contracted MRCI calculations. The configuration state functions (CSFs) were generated by single and double excitations based on the reference configurations obtained by the CASSCF calculation. However, since the total number of configurations were as large as 6,600,000, only 300,000 configurations were selected in terms of the squares of the CSF coefficients. Since the CO fragment is not vibrationally excited, we fixed the C=O bond length to 1.13 Å and constructed a two-dimensional model with R and θ coordinates. The potential energies and transition dipole moments were calculated at 361 points and spline-interpolated.

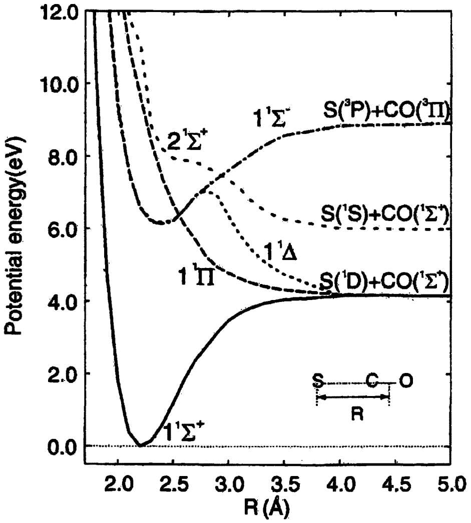

Figure 2 A section of potential energy surfaces for R coordinate in the linear geometry. The CO distance was fixed to 1.13Å. (Adopted with permission from reference 8. Copyright 1998 American Institute of Physics)

Downloaded by COLUMBIA UNIV on September 14, 2012 | http://pubs.acs.org
Publication Date: August 14, 2002 | doi: 10.1021/bk-2002-0828.ch014

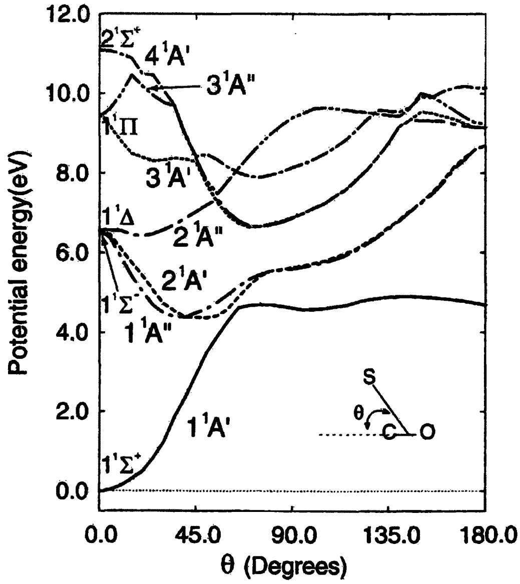

Figure 3 A section of potential energy surfaces for θ coordinate calculated with R=2.2 Å and r=1.13Å. (Adopted with permission from reference 8. Copyright 1998 American Institute of Physics)

Figures 2 and 3 show one-dimensional cuts of the calculated *ab initio* PES's for R and θ. As seen in Fig. 2, both the A'($^1\Delta$) and A"($^1\Sigma^-$) are bound in R, but show conical intersections with the repulsive $^1\Pi$ state at around R=2.5 Å which provide the adiabatic dissociation pathways. It should be noted that both the A'($^1\Delta$) and A"($^1\Sigma^-$) surfaces are steeply declined for θ, as seen in Fig. 3. Therefore, the initial motion on these surfaces is rapid bending of the molecule. Figures 2 and 3 indicate that the topographies of 2A' and 1A" PES's are quite similar.

The bond angles of triatomic molecules can often be qualitatively explained by the diagram of one-electron orbital energies as a function of bending angle known as a Walsh diagram (5). The diagram for CO_2, isovalent with OCS, is shown in Fig. 4. One can clearly see that bending deformation mostly affects the in-plane orbitals. The linearity of CO_2 in the ground state is attributed to destabilization of the HOMO ($4b_2$) by bending. On the other hand, bending deformation significantly stabilizes the LUMO ($6a_1$), so the energies of the HOMO and LUMO are reversed for smaller bond angle. The electronic structure of OCS is essentially the same as that of CO_2. However, the HOMO (12a') and

Downloaded by COLUMBIA UNIV on September 14, 2012 | http://pubs.acs.org
Publication Date: August 14, 2002 | doi: 10.1021/bk-2002-0828.ch014

LUMO (13a') fall in the same symmetry species in the C_s point group so they are symmetry repelled. The out-of-plane HOMO 3a" orbital is not much affected. As a result, 12a' and 3a" have similar orbital energies, and the 2A' and 1A" PES's become almost identical, since these arise predominantly from one electron promotion of $13a'(4\pi_x)\leftarrow 12a'(3\pi_x)$ and $13a'\leftarrow 3a''(3\pi_y)$.

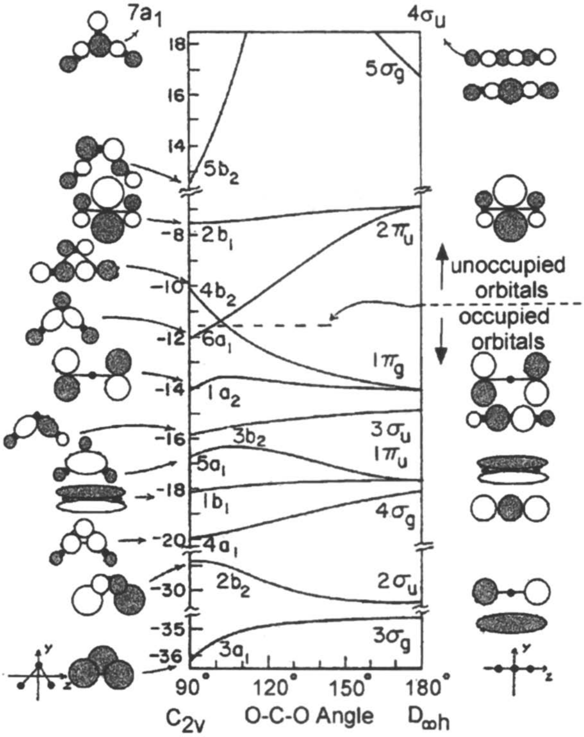

Figure 4 Walsh diagram for CO_2 and schematic MO's adopted with permission from reference 9. The gray color represents the regions of negative phase. Only one member of each pair of the degenerate $1\pi_u$, $1\pi_g$, and $2\pi_u$ orbitals is shown for clarity. The other member of each pair is identical with the one shown, except that it is rotated by 90 degrees about the internuclear axis. For the bond angle of 90 degree, except for the $1b_1$, $1a_2$, and $2b_1$ orbitals, the molecule is shown in the yz plane and all orbitals are in the same plane. For the $1b_1$, $1a_2$, and $2b_1$ orbitals, the molecule is shown in the xz plane and the orbitals are in the same plane (i.e., the orbitals are perpendicular to the molecular plane).

Downloaded by COLUMBIA UNIV on September 14, 2012 | http://pubs.acs.org
Publication Date: August 14, 2002 | doi: 10.1021/bk-2002-0828.ch014

More quantitatively, the orbital energies and shapes of the 13a', 12a', and 3a" MO's were calculated at the CASSCF level with DZP basis set, and these fully supported the qualitative argument described above.

We performed wave packet calculations on the 2A' and 1A" adiabatic *ab initio* surfaces. As is easily understood from the similarity of the 2A' and 1A" PES's and from the rotational reflection principle, dissociation on these two surfaces produce almost identical product distributions, i.e. singly-peaked Gaussians. This is clearly at odds with the observed bimodality in the product distribution and the specificity observed for 2A', suggesting that bimodality cannot be explained by adiabatic dissociation dynamics. Close inspection of Fig. 3 reveals that both the 2A'($^1\Delta$) and 1A"($^1\Sigma^-$) surfaces approach the ground state around $\theta = 65°$, where non-adiabatic transition from 2A' to 1A' might be anticipated.

C. Non-adiabatic transition in the bending coordinate

Non-adiabatic transitions are induced by off-diagonal matrix elements of the nuclear kinetic operator on the electronic wavefunctions. In the case of OCS, a rotational (Coriolis) coupling is essential. If we assume the total angular momentum J to be zero, a rotational coupling term is expressed as follows:

$$H_{rot} = \frac{L^2}{2\mu_R R^2} + \frac{j^2}{2\mu_r r^2} = \left(\frac{1}{2\mu_R R^2} + \frac{1}{2\mu_r r^2}\right)L^2 \qquad (1)$$

$$= -\left(\frac{1}{2\mu_R R^2} + \frac{1}{2\mu_r r^2}\right)\frac{\partial}{\partial\vartheta}\left(\cot\theta + \frac{\partial}{\partial\vartheta}\right)$$

where L and j are the orbital angular momentum of relative motion and the rotational angular momentum of a diatomic fragment molecule, respectively. Note that $\frac{1}{2\mu_R R^2}$ diminishes as R increases, while $\frac{1}{2\mu_r r^2}$ due to an internal rotation of CO has no apparent R-dependence, so it becomes relatively more important at large R.

If we take into account only the one-dimensional non-adiabatic coupling element, the non-adiabatic dynamics is reduced to a one-dimensional two-state problem. To solve it, a unitary transformation can be performed on the electronic wavefunctions such that the derivative coupling element $\left\langle \psi_1^e \middle| \frac{\partial}{\partial\vartheta} \middle| \psi_2^e \right\rangle$ vanishes from the coupled equations for the nuclear motion. In this way, we performed wave packet calculations on the diabatic PES's constructed from the adiabatic *ab initio* PES's (8). The bimodality was well reproduced by our calculations (8).

Downloaded by COLUMBIA UNIV on September 14, 2012 | http://pubs.acs.org
Publication Date: August 14, 2002 | doi: 10.1021/bk-2002-0828.ch014

The experimentally observed non-adiabatic transition efficiency from the 2A' to the 1A' state was 30 % at 223 nm. Such large contribution discovered for this prototypical triatomic molecule illustrates the importance of non-adiabatic transition in polyatomic molecules in general.

On the other hand, the calculated transition efficiency was only 10%. For examining whether this discrepancy is due to the non-adiabatic transition along the R coordinate neglected in the above treatment, we have evaluated it by analytical theory. We decomposed the nuclear position and momentum into the θ and R directions and applied one-dimensional non-adiabatic transition theory at the most critical point of R=2.6 Å and θ=75°. The one-dimensional bending potentials of OCS at R=2.6 Å and those of C-S stretching at θ=75° were extracted from the sections through the 2A' and 1A' PES's. We used the formulas given by Zhu and Nakamura (4) for these two curve-crossing cases to obtain the transition efficiencies. The non-adiabatic transition probabilities calculated for 223 nm photodissociation were 2-3 times larger for the bending (0.09) than the C-S stretching motion (0.03-0.04). Thus, the discrepancy is not reduced by considering the R motion. Full three dimensional analysis on more accurate PES's seems necessary for reproducing the experimental value quantitatively.

D. Non-adiabatic bending dissociation as an orbital unlocking

Fig. 5 shows the picture of MO's along the reaction coordinate with the inertial axis fixed in the same direction. The bending motion is dominated by the fast rotation of CO as we have seen in equation (1). The most critical region for the non-adiabatic transition is between 80 – 120°. An adiabatic process retains an electron in the 13a' orbital that is the p-orbital parallel to the chemical bond, while the non-adiabatic process due to electron deactivation from 13a' to 12a' corresponds to rotation of the p-orbital. In other words, the p-lobe of 13a' on the S atom is pσ in character while that of 12a' is pπ. The non-adiabatic transition of OCS from the 2A' to 1A' state is essentially an unlocking of an electron oribital from the bond axis; that is similar in nature to a pσ-pπ transition observed in atomic collision dynamics.

In Fig. 6, we present the bending potential of 2A' and 1A' around the point of the largest non-adiabatic coupling along the reacton coordinate, R=2.7 Å and θ=65°. It is seen that the separation of the two potentials is much smaller than the one at R=2.2 Å, since the interaction of S with CO is weaker at R=2.7 Å. These are the potentials sampled by the wavepacket in non-adiabatic transition.

Downloaded by COLUMBIA UNIV on September 14, 2012 | http://pubs.acs.org
Publication Date: August 14, 2002 | doi: 10.1021/bk-2002-0828.ch014

Downloaded by COLUMBIA UNIV on September 14, 2012 | http://pubs.acs.org
Publication Date: August 14, 2002 | doi: 10.1021/bk-2002-0828.ch014

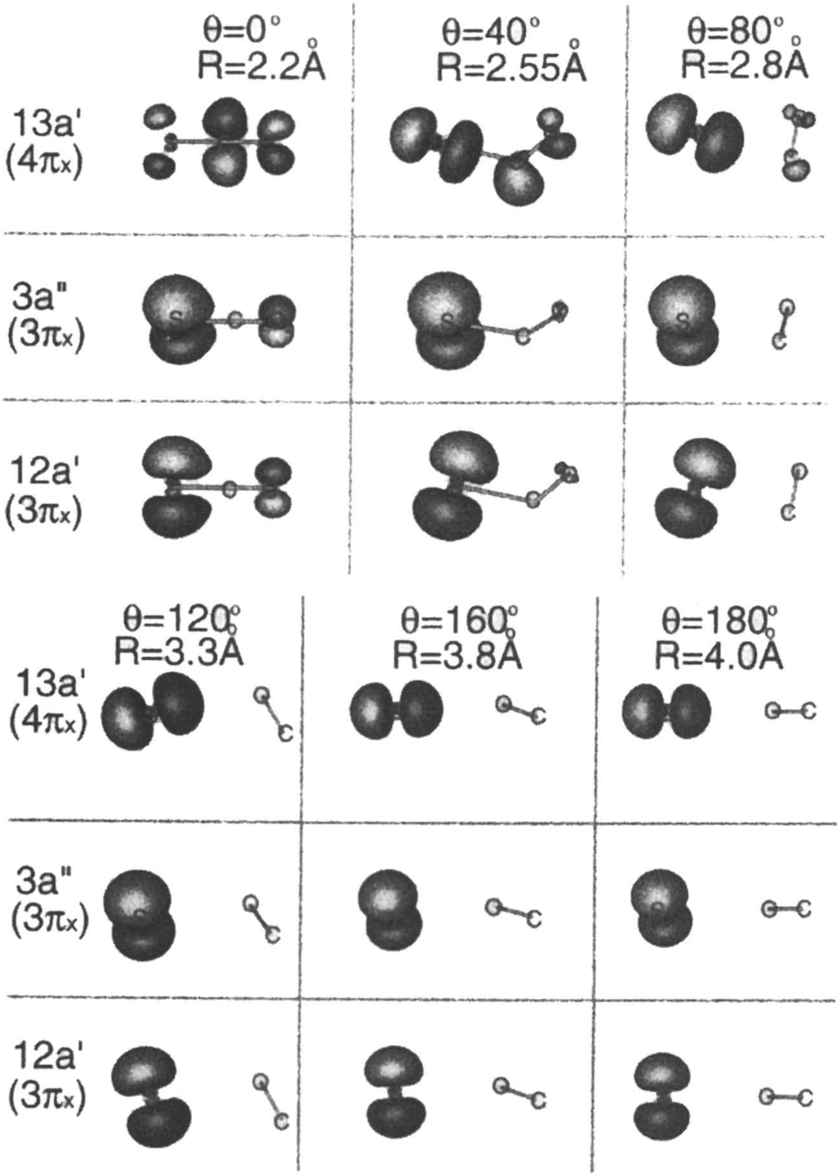
θ=0°
R=2.2Å
θ=40°
R=2.55Å
θ=80°
R=2.8Å
13a'
(4πx)
3a"
(3πx)
12a'
(3πx)
θ=120°
R=3.3Å
θ=160°
R=3.8Å
θ=180°
R=4.0Å
13a'
(4πx)
3a"
(3πx)
12a'
(3πx)
S
C

Figure 5 The shape of 13a', 12a', and 3a" molecular orbitals along the reaction coordinate calculated by CASSCF with DZP basis set.

Downloaded by COLUMBIA UNIV on September 14, 2012 | http://pubs.acs.org
Publication Date: August 14, 2002 | doi: 10.1021/bk-2002-0828.ch014

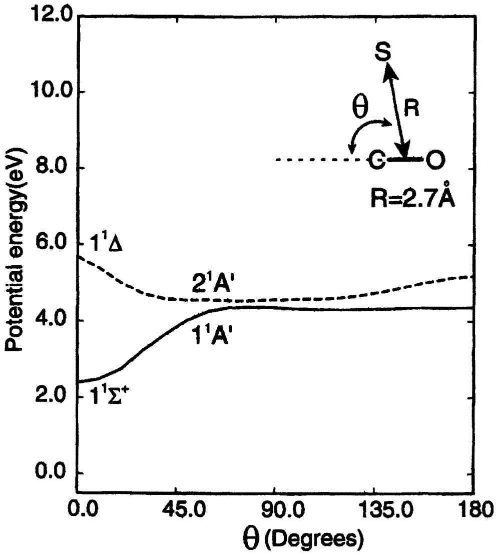

Figure 6 A section of potential energy surface along θ with R=2.7 Å and r=1.13 Å.

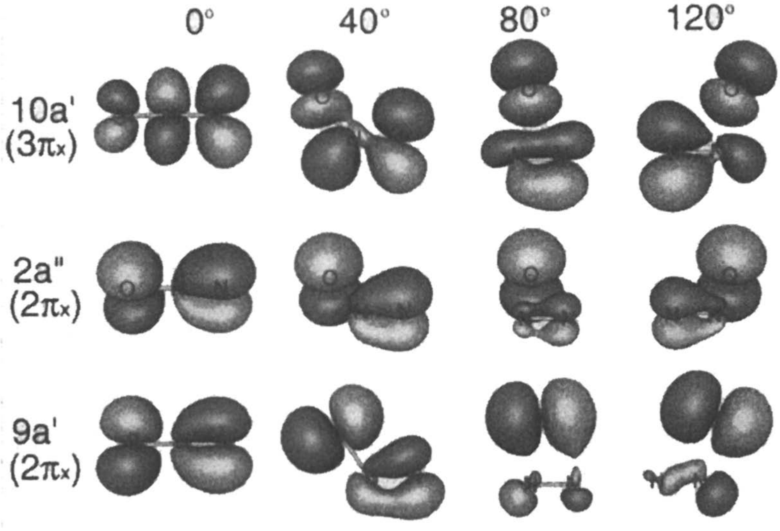

Figure 7 The shapes of HOMO and LUMO of N_2O as a function of θ. R and r were fixed to 1.8 and 1.128, respectively.

As the Walsh diagram predicts, the avoided crossing between the A'($^1\Delta$) and A'($^1\Sigma^+$) states is not specific for OCS but is general in 16 valence electron systems [5]. In order to demonstrate it, we present the HOMO 9a'($2\pi_x$) and 2a"($2\pi_y$) and LUMO 10a'($3\pi_x$) of the N_2O molecule in Fig. 7. The shapes of the MOs are extremely similar to those of OCS, except for some differences such as the MO amplitude on the central nitrogen atom. As a result, the PES's of N_2O are quite similar to those of OCS [17-19]. In the dissociation of N_2O, however, the light mass of the N atom allows 1.5 times faster motion along R than in OCS. It is quite interesting to compare the dynamics of N_2O molecule with OCS for elucidating the non-adiabatic processes in 16 valence electron systems.

Downloaded by COLUMBIA UNIV on September 14, 2012 | http://pubs.acs.org
Publication Date: August 14, 2002 | doi: 10.1021/bk-2002-0828.ch014

ACKNOWLDGMENT

This work has been supported by the Grant-in-Aid from the Ministry of Education, Science, Technology, Sports, and Culture of Japan under contract numbers 11440183 and 11359005. The authors gratefully acknowledge the essential contributions of Mr. Hideki Katayanagi in the experiments and continuous support of Professor Mutsumi Aoyagi to this work.

REFERENCES

1. Landau, L.D.; Lifshitz, E.M. *Quantum Mechanics*; Pergamon Press, Oxford, 1977.
2. Tully, J.C. In *Dynamics of Molecular Collisions;* Miller, W.H.; Plenum, New York, 1976, Part B.
3. Garrett, B.C.; Truhlar, D.G. In *Theoretical Chemistry: Advances and Perspectives*; Henderson, D.; Academic Press, New York, 1981.
4. (a) Nakamura, H., In *Dynamics of Molecules and Chemical Reactions*; Wyatt, R.E.; Zhang, J.Z.H.; Marcell Dekker, New York, 1996.
   (b) Zhu C.; Teranishi Y.; and Nakamura H. In *Advances in Chemical Physics, Volume 117*; Prigogine I. and Rice S.; John Wiley and Sons, 2001.
5. Walsh, A.D. *J. Chem. Soc.* **1953,** 2266.
6. Chandler, D.W.; Houston, P.L. *J. Chem. Phys.* **1987**, *87*, 1445.
7. Whitaker, B.J. In *Research in Chemical Kinetics, Volume I*; Compton, R.G.; Hancock G.; Elsevier, Amsterdam, 1993.
8. Suzuki, T.; Katayanagi, H.; Nanbu, S.; Aoyagi, M. *J. Chem. Phys.* **1998,** *109*, 5778.

9. Rabalais, J.W.; McDonald, J.M.; Scherr, V.; McGlynn, S.P. *Chem. Rev.* **1971**, *71*, 73.
10. Breckenridge, W.H.; Taube, H. *J. Chem. Phys.* **1970**, *52*, 1713.
11. Locker, J.R.; Burkholder, J.B.; Bair, E.J.; Webster, H.A. *J. Phys. Chem.* **1983**, *87*, 1864.
12. Joens, J.A.; Bair, E.J. *J. Phys. Chem.* **1984**, *88*, 6009.
13. Nan, G.; Burak, I.; Houston, P.L. *Chem. Phys. Lett.* **1993**, *209*, 383.
14. Sivakumar, N.; Hall, G.E.; Houston, P.L.; Hepburn, J.W.; Burak, I. *J. Chem. Phys.* **1988**, *88*, 3692.
15. Sato, Y.; Matsumi, Y.; Kawasaki, M.; Tsukiyama, K.; Bersohn, R. *J. Phys. Chem.* **1995**, *99*, 16307.
16. Schinke, R. *Photodissociation Dynamics*, Cambridge University Press, New York, 1993.
17. Hopper, D.G. *J. Chem. Phys.* **1984**, *80*, 4270.
18. Brown, A.; Jimeno, P.; Balint-Kurti, G.G. *J. Phys. Chem. A* **1999**, *103*, 11089.
19. Teule, J.M.; Groenenboom, G.C.; Neyer, D.W.; Chandler, D.W.; Janssen, M.H.M. *Chem. Phys. Lett.* **2000**, *320*, 177.

Downloaded by COLUMBIA UNIV on September 14, 2012 | http://pubs.acs.org
Publication Date: August 14, 2002 | doi: 10.1021/bk-2002-0828.ch014

Downloaded by NORTH CAROLINA STATE UNIV on September 14, 2012 | http://pubs.acs.org
Publication Date: August 14, 2002 | doi: 10.1021/bk-2002-0828.ch015

Chapter 15

Electronic Structure and Dynamics in the O_4 System

Ramón Hernández Lamoneda

Centro de Investigacionces Químicas, UAEM, 62210 Cuernavaca, Mor., México

Abstract

There has been a renewed interest in the properties of the O_4 system in recent years coming from a variety of scientific fields(high resolution spectroscopy, nature of intermolecular forces, molecular beam scattering, molecular collision dynamics, photochemistry, atmospheric chemistry, solid state physics) and aimed at a better understanding of its electronic structure and dynamics. In this contribution I will review our current knowledge of this system with particular emphasis on the electronic structure and dynamics of the $O_2(v>>0) + O_2(v=0)$ collision which we have been studying in the past several years and is still the subject of debate stemming from unsolved discrepancies between theory and experiment and also its possible relevance in determining the chemical composition of the atmosphere.

In Low-Lying Potential Energy Surfaces; Hoffmann, M., et al.;
ACS Symposium Series; American Chemical Society: Washington, DC, 2002.

The van der Waals complex

From the point of view of its electronic structure already in 1924 G.N. Lewis(*1*) speculated the formation of a diamagnetic O_4 complex in liquid oxygen and used it to explain its magnetic susceptibility. Since then the complex, better described as a dimer $(O_2)_2$, has been characterized spectroscopically(*2-8*), theoretically(*9-15*) and recently in molecular beam scattering experiments(*16,17*). There is general agreement that the ground electronic state multiplicity corresponds to a singlet with D_{2h} symmetry(rectangular) with low-lying triplet and quintet states all correlating with two oxygen molecules in their corresponding triplet ground states. The intermolecular potential is highly anisotropic and this has a profound effect on the collision dynamics(*13*). Recently Aquilanti et al(*16,17*) determined potential energy surfaces using a novel harmonic expansion functional form and fitting the radial components as to reproduce the experimentally determined total integral cross section including features which are very sensitive to the intermolecular potential. The energy surfaces obtained for the three multiplicities are in good agreement with previous theoretical work (*9-13*) considering the weak nature of the interaction and the complexity of the electronic structure for this system. There are important quantitative differences in the precise shape of the potential analyzed at fixed orientations of the monomers, particularly the internuclear distance at the minima and the well-depths for some geometries. It stands as a challenge for *ab initio* calculations to reproduce in a quantitative way the experimentally determined potential energy surfaces and the spin-spin interactions in the $(O_2)_2$ dimer.

The O_4 system is also of relevance in describing the properties of the condensed phases of oxygen as has been shown recently in high pressure studies(*18*). Most phases of solid oxygen can be understood using molecular oxygen as a basis ,ie, the molecular bond does not change significantly when the intermolecular potential increases as a result of the high pressure. For the so-called ε phase in the 10-63 Gpa pressure range a qualitative change in the nature of the intermolecular potential occurs as evidenced in the appearance of a new band in the infrared spectra and other large changes in the macroscopic properties of this phase. Furthermore the intermolecular separation between neighbouring molecules is 30 % shorter than the equilibrium distance observed for the dimer in the gas phase which is consistent with the formation of a 'new bond' in the O_4 complex. The precise nature of the intermolecular interaction in the complex still awaits more detailed experimental and theoretical studies.

Downloaded by NORTH CAROLINA STATE UNIV on September 14, 2012 | http://pubs.acs.org
Publication Date: August 14, 2002 | doi: 10.1021/bk-2002-0828.ch015

The chemically bound O_4 complex

The formation of oxygen rings in analogy with the well-known sulfur rings was the subject of theoretical studies in the eighties with modest *ab initio* calculations(*19-22*). In 1992 Schaefer and Seidl studied the chemically bound O_4 system as a potentially efficient high energy density material(*23*). Although the equilibrium structure can be reasonably well described by single configuration methods, one of the key issues for its potential practical use is its relative stability with respect to dissociation into oxygen molecules, a process which is accompanied by spin recoupling and the transformation of a closed shell system into two open shell fragments which should be more properly described with multiconfigurational wavefunctions(*23*). Very slow convergence of the saddle-point properties with respect to the inclusion of electron correlation at increasing levels of theory illustrated the limitations of using single reference methods. In particular, the barrier towards dissociation diminished dramatically as the level of treatment increased. Since the reaction has an early barrier and because electron correlation was included at the highest level of theory with the CCSD(T) method(*24*) their prediction of a stable molecule could still be considered reliable. We used the CASMP2 method(*25,26*) with large basis set in order to check the reliability of the previous predictions and found both qualitative and quantitative agreement regarding the stability of the complex(*27*). No direct experimental evidence of its existence has been given yet.

Another quantity of interest for chemically bound O_4 is its relative energy with respect to two oxygen molecules. Schaefer's group estimated it at the CCSD/DZP level and obtained a value of 83 kcal/mol (*28*). It is important to emphasize that the noniterative correction for the triple excitations was not included when calculating this property. The accurate determination of the relative stability is important because the O_4 species has been proposed as a possible intermediate to explain the dark channel observed by the Wodtke group to be described in a section below and recent photoionization spectra(*29*) arguing that under the experimental conditions there should be enough energy to form it. In particular the 83 kcal/mol value places it below the endothermicity for the reaction forming ozone 94 kcal/mol. We calculated the relative stability using the CASMP2 method with the 5s4p3d2f ANO basis set and obtained a value of 104 kcal/mol. A recent study of the O_4 chemically bound complex(*29*) showed that its relative stability exhibits a large change when the noniterative correction for triple excitations is included, CCSD(T), predicting a value 20 kcal/mol higher than with the CCSD method.

Downloaded by NORTH CAROLINA STATE UNIV on September 14, 2012 | http://pubs.acs.org
Publication Date: August 14, 2002 | doi: 10.1021/bk-2002-0828.ch015

Downloaded by NORTH CAROLINA STATE UNIV on September 14, 2012 | http://pubs.acs.org
Publication Date: August 14, 2002 | doi: 10.1021/bk-2002-0828.ch015

Highly vibrationally excited states electronic structure and dynamics

The study of highly vibrationally excited molecules is a quickly developing area which has relied on novel laser-based experimental techniques as well as theoretical models(*30*). Some of the key questions to be answered relate to the specific properties and collision dynamics of molecules containing enough internal energy to react, how they differ from the low energy non-reactive regime and how previous theoretical models have to be modified to properly reproduce their behaviour. Another source of interest is the possible relevance of highly vibrationally excited states in determining the chemical composition of the atmosphere. This issue has been the subject of great interest and debate recently(*31-38*) particularly in relation to the possibility of producing ozone from highly vibrationally excited O_2 molecules through the reaction:

$$O_2(v) + O_2(v=0) \Rightarrow O_3(X^1A_1) + O(^3P) \qquad \text{(R1)}$$

and considering that highly vibrationally excited O_2 molecules are known to be formed during the photodissociation of ozone in its triplet channel(*32,34*) in a bimodal distribution with maxima at v=14 and v=27:

$$O_3 + h\nu \Rightarrow O(^3P) + O_2(X^3\Sigma^-_g, v)$$

Our interest in this field started with the experimental determination by Wodtke's group of the self-relaxation rates of molecular oxygen in highly vibrationally excited states(v=14-28)(*37*). We developed (*13*) a potential energy surface to describe rovibrational inelastic scattering based on *ab initio* calculations of the six dimensional surface and were able to reproduce the available experimental results covering the range v=8-24. For higher values a sharp increase in the depletion rates is observed experimentally and the theoretical treatment was unable to reproduce it. At the time of the original measurements a reasonable explanation by the Wodtke group was proposed: since the observed threshold for enhanced relaxation is coincident with the opening of the reactive channel leading to ozone formation it was argued that this was the new mechanism observed and which could not be reproduced by our calculations since the PES only sampled the non-reactive region. Since then there have been a few experimental and theoretical studies aimed at confirming or suggesting alternative explanations and a brief summary of these is in order.

Wodtke's measurements can be divided in two groups according to the specific experimental scheme employed(33,37) : I) v=19-26 II) v=27. Scheme I relies on a direct determination of the total depletion rate by monitoring the decay of the initially prepared vibrational state and fitting the pressure-dependent data to an exponential from which the lifetime and rate constant is obtained. This procedure yields what we believe is an extremely accurate estimate of the total depletion rates for v=19-26. Unfortunately it cannot be applied for higher values of v since these dissappear too fast to be observed directly . Scheme II relies on monitoring the vibrational state just below the initially prepared one and hence the data obtained has to be fitted by a kinetic model based mainly on the assumption that there are three main relaxation channels: single and double quantum steps and a so-called 'dark-channel' which is suggested to be due to the ozone formation reaction. Some of the rate constants related to the different relaxation channels are used as parameters in the fitting procedure so that their final determination is indirect. Although reasonable arguments are given for the kinetic model followed the reliability of the determination can be questioned. Further indirect support for the presence of an activated chemical process was obtained by varying the temperature and comparing the dark channel rates for v=26 and v=27 and noticing the difference follows a decrease in the energy of activation corresponding to the difference in internal energy between these states(*37*). As we will show later non-reactive processes may also display this behaviour.

Downloaded by NORTH CAROLINA STATE UNIV on September 14, 2012 | http://pubs.acs.org
Publication Date: August 14, 2002 | doi: 10.1021/bk-2002-0828.ch015

a) Theoretical studies on the ozone forming reaction (R1)

Prompted by the Wodtke group measurements and analysis, a few theoretical treatments of the chemical reaction have been performed(*39-41*). The first of these(*39*) was mainly concerned with a variational transition state treatment of the reverse reaction -R1, but also performed preliminary semiclassical wavepacket calculations on R1. Although the number of trajectories computed was not enough to obtain converged results, there was little evidence of reaction taking place and rather wavepackets were inelastically scattered. We applied a quantum reduced dimensionality treatment to R1 using both time-dependent and time-independent methodology to obtain converged vibrationally-selected reaction rate constants(*40*). In that study it was shown that vibrational excitation enhances the reaction rate and a significant change occurs for v=27 in analogy with the treshold behaviour observed experimentally. Unfortunately the reaction rate values were too small compared with pure vibrational relaxation and it was considered that even with a more accurate potential energy surface and dynamical treatment the reaction rates could not change enough to explain the experimental observations.

Most theoretical treatments of R1 and -R1 have been based on the potential energy surface developed(*42*) by Varandas and Pais(VP). This surface is based on a double many-body expansion of the potential and used in a multiproperty fit including spectroscopic, dynamical and *ab initio* information. The surface has the merit of giving a relatively smooth global representation for the O_4 system, it yields accurate thermal rate constants for the reverse reaction(*39,43-45*) and other dynamical properties but displays some minima which are most likely

Downloaded by NORTH CAROLINA STATE UNIV on September 14, 2012 | http://pubs.acs.org
Publication Date: August 14, 2002 | doi: 10.1021/bk-2002-0828.ch015

spurious and given the nature of the fit one cannot expect it to reproduce finer details of the interaction potential which should be obtained via accurate *ab initio* calculations. Nevertheless it has played a key role in obtaining an initial description of the reactive scattering properties of the system. Extensive quasiclassical calculations have been performed on the VP surface by Varandas and Wang(*46*) analyzing a variety of energy transfer processes and reactions. In particular they confirm the low reactivity for initial states of relevance for the Wodtke's group experiments but go on to analyze initial combinations in which both O_2 molecules are highly vibrationally excited leading to rate constants of the same order of magnitude as estimated in the experiments. Although this finding can be of relevance for the non-equilibrium modeling of stratospheric ozone concentrations(*30-36*), we fail to see how it can explain the Wodtke group observations since the experimental conditions(*37*) guarantee the excess of O_2 in the ground vibrational state as the relaxing partner.

A combined experimental and theoretical study(*47*) of the products energy distribution for the reverse reaction(-R1) showed discrepancies which were attributed to limitations in the VP potential. More specifically, the rotational energy distribution measured in the experiment is much colder than that predicted from quasiclassical trajectory calculations on the VP surface and the translational energy release is also significantly smaller as measured in Doppler profiles. A plausible explanation for these discrepancies suggested by the authors is that in fact both O_2 molecules emerge vibrationally excited. This is in contradiction with the predictions made by quasiclassical trajectories on the VP surface in which one of the O_2 molecules remains in the ground vibrational state and acts merely as an spectator to the reaction. We have calculated(*27*) the reaction path using *ab initio* methods and found that along the path the internuclear distance for the so-called spectator bond does indeed varies slowly and smoothly from its equilibrium value in ozone to that in molecular oxygen. More detailed studies of the potential surface exploring regions outside the reaction path and dynamics calculations are needed to clarify the validity of the spectator bond mechanism. An *ab initio* reduced dimensionality surface was developed(*41*) by Lauvergnat and Clary(LC) and used to calculate vibrationally selected rate constants. They also found values which are orders of magnitude smaller than the vibrational relaxation rates and therefore confirm the idea that the sharp increase observed for depletion rates must come from a different mechanism than chemical reaction leading to ozone formation. It is interesting to mention that the geometry of the saddle point predicted by the LC *ab initio* surface and our own reaction path calculations(*27*) is qualitatively similar to that of the VP surface and this has to be recognized as an achievement of the double many-body expansion methodology(*42*) since there was no *ab initio* information on the saddle point geometry used in the fitting procedure.

b) Other vibrational relaxation mechanisms

Our original (*13*) calculations for the vibrational relaxation rates were limited in two ways, first they only considered single quantum processes and second they were based on an *ab initio* surface which did not include the reactive region of the potential. It was reasonable to expect that the difference between theory and experiment for $v > 26$ could be related to these limitations.

The role of 2 → 1 vibrational transitions for the relaxation of $O_2(v)$ has been investigated (*48*) using a semiclassical wave packet method and using the VP potential. In accordance with our previous calculations(*13*) they find that the single quantum processes dominate up to $v = 25$ but the multiquantum process starts to compete for higher values and even dominates for $v = 30$ due to a reduction of the energy mismatch between reactants and products for this state. Taking into account the multiquantum process the total relaxation rate is still one order of magnitude smaller compared with the experimental depletion rates which shows that the dark channel must be due to other processes.

From our (*40*) reduced dimensionality time-dependent calculations of the reaction rate it became apparent that the saddle point region could have a strong influence on the vibrational relaxation since it was observed that wave packets which were inelastically scattered sampled that region of the potential. This effect was quantified by calculating the vibrational relaxation probabilities within the same reduced dimensionality approach and converting them into rates using an *ad hoc* procedure(*49,50*). The calculations showed, for the first time, a clear jump in the depletion rates due to enhancement of the vibrational relaxation rates through the saddle point region of the potential. Furthermore the calculations reproduced qualitatively the activated process behaviour found in experiments(*33*), ie, the temperature dependence of the critical value of v at which the rates show a dramatic increase. Quantitative differences remained both in the critical values of v and in the absolute values of the depletion rates both of which could be due to inaccuracy of the VP potential used in the calculations.

c) Evidence of non-adiabatic behaviour in highly vibrationally excited O_2 and O_4

Molecular oxygen is not only a stable open-shell species but presents very low-lying electronic states. For vibrational states above $v=5$ of the ground electronic state there are open channels for transfer into the lowest-lying electronic states and this already suggests the possible relevance of non-adiabatic effects in collisions of oxygen molecules. The possibility of having vibrational to electronic (V-E) energy transfer for highly vibrationally excited O_2 was briefly

Downloaded by NORTH CAROLINA STATE UNIV on September 14, 2012 | http://pubs.acs.org
Publication Date: August 14, 2002 | doi: 10.1021/bk-2002-0828.ch015

mentioned in our original paper on the rates of vibrational relaxation(*13*) and the topic in general has been the subject of many early theoretical studies(*51,52*).

In 1999 the Wodtke group obtained experimental evidence for electronic non-adiabaticity while doing high resolution spectroscopy for the isolated diatomic(*53*). Their main objective was to obtain very accurate molecular constants for the highly vibrationally excited states of $O_2(X^3\Sigma^-_g$, v = 26 - 31). The rotationally resolved spectra could be well reproduced using a Hamiltonian that included spin-spin and spin-rotation terms for all the vibrational states considered except for v=28 where the transitions between identical spin components showed clear evidence of a perturbing state which shifted the resonance peaks and introduced an additional peak. The perturbing state could be readily assigned as $O_2(b^1\Sigma^+_g$, v = 19) as it is well-known that spin-orbit coupling exists between the ground and second excited state of O_2 and for the vibrational states considered there is an energy mismatch between the two states of only a few cm^{-1}. Furthermore, inclusion of spin-orbit coupling through first order in the Hamiltonian reproduces the perturbed rotationally resolved spectrum. Using reliable (though incomplete) sets of values for the lower vibrational term energies(*54,55*) together with their own determination for the higher vibrational states they obtained RKR potentials for both ground and excited electronic state. The potentials cross around r = 2.45 Å at an energy of 40,463 ± 1000 cm^{-1} and a spin-orbit coupling of 200 ± 20 cm^{-1} has been estimated from a first-order perturbation theory analysis.

The presence of spin-orbit coupling in the isolated diatomic suggests that nonadiabatic effects could play a major role in the description of the collision dynamics for the O_4 system. It is important to emphasize that so far all dynamical calculations have relied on a single potential energy surface both for vibrational relaxation and for reactive processes.

Prompted by the new experimental findings we decided to study spin-orbit coupling effects for the collision system $O_2(v{>>}0)$ + $O_2(v=0)$ with the main objective of analyzing the influence of the intermolecular potential on the diatomic states which are coupled by the spin-orbit interaction(*56*). We considered a C_{2v} minimum energy path which corresponds to the equilibrium geometry of the $O_2(v{>>}0)$ ••• $O_2(v=0)$ van der Waals complex and constructed two dimensional surfaces by varying the internuclear distance of the vibrationally excited molecule(**r**) and the center of mass distance between them(**R**). The minimum for the van der Waals complex is of singlet multiplicity but there is a very low-lying triplet both of which correlate with the diatomic fragments in their electronic ground state and are degenerate asymptotically. There are six excited electronic states of triplet multiplicity which could be of relevance for nonadiabatic transitions. The spatial symmetry and parentage in terms of the diatomic fragments for the ground and excited states described above are:

Downloaded by NORTH CAROLINA STATE UNIV on September 14, 2012 | http://pubs.acs.org
Publication Date: August 14, 2002 | doi: 10.1021/bk-2002-0828.ch015

Downloaded by NORTH CAROLINA STATE UNIV on September 14, 2012 | http://pubs.acs.org
Publication Date: August 14, 2002 | doi: 10.1021/bk-2002-0828.ch015

$$X\,^3\Sigma_g^- + X\,^3\Sigma_g^-\,(\,X^1A_1 \text{ and } X^3A_1\,),\; X\,^3\Sigma_g^- + a\,^1\Delta_g\,(\,1^3A_1, 2^3A_1 \text{ and } X^3B_2, 1^3B_2\,),$$
$$X\,^3\Sigma_g^- + b\,^1\Sigma_g^+\,(\,2^3B_2\,, 3^3B_2)$$

Selection rules for the diatomic forbid spin-orbit coupling between the ground and first excited (a $^1\Delta_g$) electronic state so that for large values of **R** only the excited states which correlate with one fragment in the second excited state can be coupled to the ground singlet and triplet states through spin-orbit interactions. We have shown(*56*) that when the molecules are allowed to interact through the intermolecular potential there appear avoided crossings between the 1^3B_2 and 2^3B_2 states such that the lower state(1^3B_2) is now coupled through spin-orbit interactions with both ground singlet and triplet states(X^1A_1 and X^3A_1).

Compared with the isolated diatomic, spin-orbit transitions should occur at near-crossings of lower energy in the collision system $O_2(v{>>}0) + O_2(v{=}0)$ leading to V-E transfer:

$$O_2(X\,^3\Sigma_g^-, v{>>}0) + O_2(X\,^3\Sigma_g^-, v{=}0) \Rightarrow O_2(a^1\Delta_g, v{>>}0) + O_2(X\,^3\Sigma_g^-, v{=}0)$$
$$O_2(X\,^3\Sigma_g^-, v{>>}0) + O_2(X\,^3\Sigma_g^-, v{=}0) \Rightarrow O_2(b^1\Sigma_g^+, v{>>}0) + O_2(X\,^3\Sigma_g, v{=}0)$$

This finding gives further support to the possible relevance of nonadiabatic transitions in explaining the origin of the dark-channel observed in experiments. Furthermore this hypothesis can be tested in experiment since the electronically excited oxygen molecule formed from the vibration to electronic energy transfer could be detected spectroscopically. From the theoretical point of view we have started quantum scattering calculations on coupled potential energy surfaces to quantify the importance of V-E transfer.

Once we found evidence for spin-orbit coupling in the O_4 system within an inelastic C_{2v} approach it was natural to ask whether other minimum energy paths could show similar behaviour. We have calculated(*27*) the reaction path for the reactions leading to ozone formation and chemically bound tetraoxygen:

$$O_2 + O_2 \Rightarrow O_3 + O$$

$$O_2 + O_2 \Rightarrow O_4$$

Additionally we calculated the low-lying excited states and their spin-orbit coupling elements with the ground state at selected geometries of the reaction path. For the reaction that forms chemically bound O_4 we find no evidence of spin-orbit coupling effects, since there are no near-crossings of the relevant electronic states and furthermore the SO matrix elements are negligible.

The reaction forming ozone proved to be more interesting in this regard and we found that in the neighborhood of the saddle point region there appears both a true crossing between singlet and triplet states and appreciable SO matrix elements between them which would allow for V-E transfer. This mechanism could also be responsible or contribute to the dark channel observed in experiments and as noted earlier is subject to experimental verification via spectroscopy. From the theoretical point of view quantum scattering reduced dimensionality calculations on coupled surfaces are underway to make quantitative predictions on the importance of these processes.

Downloaded by NORTH CAROLINA STATE UNIV on September 14, 2012 | http://pubs.acs.org
Publication Date: August 14, 2002 | doi: 10.1021/bk-2002-0828.ch015

d) Unsolved questions and speculations

In the previous section we concentrated mainly on the possibility of vibrational to electronic energy transfer via spin-orbit coupling and its relevance to the unsolved question about the origin of the dark channel observed in experiments. Although this problem is still open, from the previous review sections we already know of different mechanisms that are contributing to the dark channel and what is still lacking is the quantitative determination of the rates for the different mechanisms proposed. In this final section I want to briefly mention other open problems related to the O_4 system.

In 1996 the Wodtke group measured vibrational, rotational and translational energy distributions for $O_2(v)$ coming from the reverse of the ozone forming reaction(R1)(*47*). To assist in the interpretation of results Schatz performed quasiclassical trajectories using the VP potential energy surface. Comparison between experiment and theory showed a large disagreement concerning the rotational and translational energy distributions, namely, experiment gave much colder distributions. Furthermore theory predicted that there should be one 'spectator bond' in the reaction such that one of the O_2 molecules formed is in its ground vibrational state. From conservation of energy theory predicts a very large rotational and traslational energy release. The authors considered that the most likely explanation for the observed differences should be a 'breakdown' of the spectator bond mechanism,ie, the VP surface incorrectly describes the reaction path. Much better agreement with experiment could be obtained assuming that both O_2 molecules emerge highly vibrationally excited($v=10-15$) but in their ground electronic states. *Ab initio* calculations of the reaction path(*27*) are consistent with the spectator bond model and this casts some doubt on the hypothesis of vibrational excitation on both molecules. Our work(*27,56*) on spin-orbit coupling effects in the O_4 system points out to another possible explanation for the discrepancy observed in the energy distribution: cold rotational and traslational distributions could also be obtained if one of the oxygen molecules is produced in a low-lying electronic state. This possibility has been mentioned(*47*) but we believe that in the light of our new results, additional experimental and theoretical work should be undertaken to clear this point.

In 1999 the Wodtke group(*57*) found a new mechanism which should be partially responsible for the dark channel observed in collisions of highly vibrationally excited O_2. They found that for $v \geq 23$ there are large multiquantum transitions($\Delta v = -9$) and for states v=28,30 a sizable fraction of the initial population decays through this multiquantum transition. No theoretical explanation of this puzzling and exciting result has been given so far. The formation of a collision complex which could be the chemically bound O_4 or a charge transfer complex(*57*) could be invoked but this is still speculative since no direct evidence of the relevance of such complexes, either theoretical or experimental, has been given yet.

Finally we would like to close this section mentioning an unsolved problem for the ozone molecule which is of interest in itself but also is directly related with the proper description of the reaction forming ozone(R1). In spite of its great practical importance and rich photochemistry there have been relatively few detailed experimental and theoretical papers describing the properties of the ground and low-lying excited states beyond the region of the equilibrium structures. The group of Peyerimhoff has performed *ab initio* calculations of the potential energy surfaces(*58,59*) which show a small barrier for the recombination process in the ground electronic state

$$O + O_2 \Rightarrow O_3 \qquad \text{(R2)}$$

Other recent theoretical work still predicts the presence of a barrier (*60,61*) but the level of calculation is not high enough to consider them final. From the point of view of experimental evidence the situation is not much better. In fact it has been pointed out(*62*) that even the bond dissociation energy is subject to uncertainties of the order of 10-15 %. The rate of reaction R2 has been measured as a function of temperature and close to 100 K it still increases with decreasing temperature(*63*) which of course can only be consistent with either a very small barrier or non at all. On the other hand from Raman scattering (*62*) there is evidence of vibrational levels of ozone above its dissociation limit. We have calculated the potential energy curve for dissociation(fixing the angle at its equilibrium value) at the CASMP2 level and found that, although there is a barrier at the CAS level, the inclusion of dynamical correlation removes the barrier. Although these are preliminary results they clearly point out to the need for accurate *ab initio* calculations to determine the existence or not of such a barrier. The proper dynamical modeling of a variety of processes involving ozone dissociation and recombination including the strange isotope effect by which stratospheric ozone is enriched in the heavy isotopes(*64,65*) will depend crucially on having a correct potential energy surface and we have started work in that direction.

Downloaded by NORTH CAROLINA STATE UNIV on September 14, 2012 | http://pubs.acs.org
Publication Date: August 14, 2002 | doi: 10.1021/bk-2002-0828.ch015

Acknowledgments

I would like to thank George Schatz and Russ Pack for many useful commentaries regarding non-adiabatic effects in the O_4 system and the strange isotope effect observed in ozone, respectively.

Downloaded by NORTH CAROLINA STATE UNIV on September 14, 2012 | http://pubs.acs.org
Publication Date: August 14, 2002 | doi: 10.1021/bk-2002-0828.ch015

References

1. Lewis, G.N. *J. Am. Chem. Soc.* **1924**, 46, 2027-2032.
2. Long, C.A.; Ewing, G.E. *Chem. Phys. Lett.* **1971**, 9, 225-229.
3. Long, C.A.; Ewing, G.E. *J. Chem. Phys.* **1973**, 58, 4824-4834.
4. Ewing, G.E. *Acc. Chem. Res.* **1975**, 8, 185-192.
5. Goodman, J. ; Brus, L.E. *J. Chem. Phys.* **1977**, 67, 4398-4407.
6. Orlando, J.J.; Tyndall, G.S.; Nickerson, K.E.; Calvert, J.G. *Geophys. Res. Lett.* **1991**, 96, 20755-20760.
7. Brown, L.; Vaida, V. *J. Phys. Chem.* **1996**, 100, 7849-7853.
8. Bussery, B.; Bacis, R.; Biennier, L.; Campargue, A.; Churassy, S.; Jost, R.; Kachanov, A.; Veyret, V. *Chem. Phys. Lett.* **1998**, 7, 1053-1056.
9. van der Avoird, A.; Wormer, P.E.S. *J. Chem. Phys.* **1984**, 81, 1929-1939.
10. van der Avoird, A.; Brocks, G. *J. Chem. Phys.* **1987**, 87, 5346.
11. Bussery, B.; Wormer, P.E.S. *J. Chem. Phys.* **1993**, 99, 1230.
12. Uhlik, F.; Slanina, Z.; Hinchliffe, A. *J. Mol. Struct.: THEOCHEM*, **1993**, 285, 273-276.
13. Hernández, R.; Toumi, R.; Clary, D.C. *J. Chem. Phys.* **1995**, 102, 9544-9556.
14. Minaev, B.F.; Nikolaev, V.D.; Agren, H. *Spectrosc. Lett.* **1996**, 29, 677-695.
15. Bussery, B.; Veyret, V. *J. Chem. Phys.* **1998**, 108, 3243-3248.
16. Aquilanti, V.; Ascenzi, D.; Bartolomei, M.; Cappelletti, D.; Cavalli, S.; de Castro Vitores, M.; Pirani, F. *Phys. Rev. Lett.* **1999**, 82, 69-72.
17. Aquilanti, V.; Ascenzi, D.; Bartolomei, M.; Cappelletti, D.; Cavalli, S.; de Castro Vitores, M.; Pirani, F. *J. Am. Chem. Soc.* **1999**, 121, 10794-10802.
18. Gorelli, F.A.; Ulivi, L.; Santoro, M.; Bini, R. *Phys. Rev. Lett.* **1999**, 83, 4093-4096.
19. Adamantides, V.; Neisius, D.; Verhaegen, G. *Chem. Phys.* **1980**, 48, 215.
20. Jubert, A.H.; Varetti, E.L. *An. Quim.* **1986**, 82, 227.
21. RØeggen, I; Nilssen, E.W. *Chem. Phys. Lett.* **1989**, 157, 409.
22. Hotokka, M.; Pyykkö, *Chem. Phys. Lett.* **1989**, 157, 416.
23. Seidl, E.T.; Schaeffer, H.F. *J. Chem. Phys.* **1992**, 96, 1176.
24. Raghavachari, K.; Trucks, G.W.; Pople, J.A.; Head-Gordon, M. *Chem. Phys. Lett.* **1989**, 157, 479.

25. Andersson, K.; Malmqvist, P.A.; Roos, B.O.; Sadlej, A.J.; Wolinski, K. *J. Phys. Chem.* **1990**, 94, 5483.

26. Andersson, K.; Malmqvist, P.A.; Roos, B.O. *J. Chem. Phys.* **1992**, 96, 1218.

27. Hernández-Lamoneda, R.; Ramírez-Solís, A. *J. Chem. Phys.* **2000**, 113, 4139-4145.

28. Dunn, K.M.; Scuseria, G.E.; Schaeffer, H.F. *J. Chem. Phys.* **1990**, 92, 6077.

29. Peterka, D.S.; Ahmed, M.; Suits, A.G.; Wilson, K.J.; Korkin,A.; Nooijen, M.; Bartlett, R.J. *J. Chem. Phys.* **1999**, 110,6095.

30. Yang, X.; Wodtke, A.M. *Int. Rev. Phys. Chem.* **1993**, 12, 123.

31. Rogaski, C.A.; Price, J.M.; Mack, J.A.; Wodtke, A.M. *Geophys. Res. Lett.* **1993**, 20, 2885.

32. Miller, R.L.; Suits, A.G.; Houston, P.L.; Toumi, R.; Mack, J.A.; Wodtke, A.M. *Science* **1994**, 265, 1831.

33. Rogaski, C.A.; Mack, J.A.; Wodtke, A.M. *Faraday Discuss.* **1995**, 100, 229.

34. Stranges, D.; Yang, X.M.; Chesko, J.D.; Suits, A.G. *J. Chem. Phys.* **1995**, 102, 6067.

35. Crutzen, P.J.; Grooβ, J.U.; Brühl, C.; Müller, R.; Russell III, J.M. *Science* **1995**, 268, 705.

36. Toumi, R.; Houston, P.L.; Wodtke, A.M. *J. Chem. Phys.* **1996**, 104, 775.

37. Price, J.M.; Mack, J.A.; Rogaski, C.A.; Wodtke, A.M. *Chem. Phys.* **1993**, 175, 83.

38. Summers, M.E.; Conway, R.R.; Siskind, D.E.; Stevens, M.H. Offermann, D; Riese, M.; Preusse, P.; Strobel, D.F.; Russell III, J.M. *Science* **1997**, 277, 1967.

39. Balakrishnan, N.; Billing, G.D. *Chem. Phys. Lett.* **1995**, 242, 68.

40. Hernández-Lamoneda, R.; Hernández, M.; Carmona-Novillo, E.; Campos-Martínez, J.; Echave, J.; Clary, D.C. *Chem. Phys. Lett.* **1997**, 276, 152.

41. Lauvergnat, D.M.; Clary, D.C. *J. Chem. Phys.* **1998**, 108, 3566.

42. Varandas, A.J.C.; Pais, A.A.C.C. In *Theoretical and Computational Models for Organic Chemistry*; Formosinho, S.J.; Czismadia, I.G.; Arnaut, L.C., Eds.; NATO ASI Ser. C; Kluwer: Dordrecht, 1991; Vol. 339, pp 55-78.

43. Szichman, H.A.; Varandas, A.J.C.; Baer, M. *Chem. Phys. Lett.* **1994**, 231, 253.

44. Szichman, H.A.; Varandas, A.J.C.; Baer, *J. Chem. Phys.* **1995**, 102, 3474.

45. Balakrishnan, N.; Billing, G.D. *J. Chem. Phys.* **1996**, 104, 9482.

46. Varandas, A.J.C.; Wang, W. *Chem. Phys.* **1997**, 215,167.

47. Mack, J.A.; Huang, Y.; Wodtke, A.M.; Schatz, G.C. *J. Chem. Phys.* **1996**, 105, 7495.

48. Balakrishnan, N.; Dalgarno, A.; Billing, G.D. *Chem. Phys. Lett.* **1998**, 288, 657.

49. Campos-Martínez,J.; Carmona-Novillo, E.; Echave, J.; Hernández, M.; Hernández-Lamoneda, R.; Palma, J. *Chem. Phys. Lett.* **1998**, 289, 150.

Downloaded by NORTH CAROLINA STATE UNIV on September 14, 2012 | http://pubs.acs.org
Publication Date: August 14, 2002 | doi: 10.1021/bk-2002-0828.ch015

50. Campos-Martínez,J.; Carmona-Novillo, E.; Echave, J.; Hernández, M.; Hernández-Lamoneda, R.; Palma, J. *Eur. Phys. J. D.* **1998**, 4, 159-168.

51. Freed, K.F. *Adv. Chem. Phys.* **1980**, 42, 207.

52. Freed, K.F. *Adv. Chem. Phys.* **1981**, 47, 291.

53. Jongma, R.T.; Shi, S.; Wodtke, A.M. *J. Chem. Phys.* **1999**, 111, 2588.

54. Slanger, T.; Cosby, P.C. *J. Phys. Chem.* **1988**, 92, 267-282.

55. Creek, D.M.; Nicholls, R.W. *Proc. Royal Soc.* **1975**, 341A, 517-536.

56. Hernández-Lamoneda, R.; Ramírez-Solís, A. *Chem. Phys. Lett.* **2000**, 321, 191-196.

57. Jongma, R.T.; Wodtke, A.M. *J. Chem. Phys.* **1999**, 111, 10957-10963.

58. Banichevich, A.; Peyerimhoff, S.D.; Grein, F. *Chem.Phys.Lett.* **1990**,173,1.

59. Banichevich, A.; Peyerimhoff, S.D.; Grein, F. *Chem. Phys.* **1993**, 178, 155.

60. Yamashita, K.; Morokuma, K.; LeQuere, F.; Leforestier, C. *Chem. Phys. Lett.* **1991**, 191, 515.

61. Atchity, G.J.; Ruedenberg, K. *Theor. Chem. Accounts* **1997**, 96, 176.

62. Chang, B.Y.; Kang, C.Y.; Kittrell, C.; Hsiao, C.W.; Johnson, B.R.; Glogover, S.G.; Kinsey, J.L. *J. Chem. Phys.* **1994**, 101, 1914.

63. Hippler, H.; Rahn, R.; Troe, J. *J. Chem. Phys.* **1990**, 93, 6560.

64. Thiemens, M.H. *Science* **1999**, 283, 341.

65. Mauersberger, K.; Erbacher, B.; Krankowsky, D.; Gunther, J.; Nickel, R. *Science* **1999**, 283, 370.

Downloaded by NORTH CAROLINA STATE UNIV on September 14, 2012 | http://pubs.acs.org
Publication Date: August 14, 2002 | doi: 10.1021/bk-2002-0828.ch015

Downloaded by UNIV MASSACHUSETTS AMHERST on September 14, 2012 | http://pubs.acs.org
Publication Date: August 14, 2002 | doi: 10.1021/bk-2002-0828.ch016

Chapter 16

Model Studies of Intersystem Crossing Effects in the O + H_2 Reaction

Mark R. Hoffmann[1] and George C. Schatz[2,3]

[1]Department of Chemistry, University of North Dakota, Box 9024,
Grand Forks, ND 58202–9024
[2]Theoretical Chemistry Group, Argonne National Laboratory, Argonne, IL 60439
[3]Department of Chemistry, Northwestern University, Evanston, IL 60208–3113

We use quantum scattering and trajectory surface hopping methods to examine the influence of intersystem crossing between the lowest energy triplet and singlet states on the $O(^3P) + H_2$ reaction dynamics. Several two-state reaction path models of the potential energy surfaces and spin-orbit coupling are studied. In these models, the triplet state curve shows a barrier along the reaction path and the singlet state a well such that the two states intersect at a location near the barrier top. Eleven choices of the parameters in the Hamiltonian are examined in which the effect of the triplet-singlet crossing location, the singlet well depth, and the size and coordinate dependence of the spin-orbit coupling are varied. The quantum calculations show that if the crossing occurs on the reagent side of the triplet barrier, and the spin-orbit coupling at that point is similar to what exists in the reagent O atom, then the low energy reactivity is dominated by intersystem crossing.

In Low-Lying Potential Energy Surfaces; Hoffmann, M., et al.;
ACS Symposium Series; American Chemical Society: Washington, DC, 2002.

This result is reasonably well described by surface hopping within the diabatic representation; the corresponding adiabatic representation results are less accurate below the adiabatic threshold, but more accurate above threshold. If the crossing occurs on the product side of the barrier, as actually occurs for the O + H_2 reaction, the influence of intersystem crossing is much smaller, though not completely. The influence of Stuckelberg interference effects on the state-resolved reaction probabilities is also studied.

Downloaded by UNIV MASSACHUSETTS AMHERST on September 14, 2012 | http://pubs.acs.org
Publication Date: August 14, 2002 | doi: 10.1021/bk-2002-0828.ch016

Although spin-orbit induced intersystem crossing is an old subject that has long been studied in photochemistry and photophysics, its influence on small molecule bimolecular reactions has received less attention. Such effects show up most commonly when the ground state of the reactants involves a triplet (or other high spin) potential surface (such as in the reaction of a triplet atom or molecule with a singlet molecule), while products correlate to both singlet and triplet states (such as is obtained from a doublet + doublet combination), thereby providing two pathways for reaction, a triplet spin-allowed path and a singlet spin-forbidden path. Often the singlet path involves the formation of a stable intermediate, while the triplet occurs over a barrier, so the reaction dynamics associated with these paths is quite different. In addition, the spin-forbidden path can in some cases take place over a lower barrier than the spin-allowed path, so the forbidden path could, in principle, dominate the dynamics.

There have been several experimental and/or theoretical studies during the past 10 years involving intersystem crossing effects in bimolecular reactions of O*(1-3)*, NH*(4)*, CH_2*(5-7)*, S*(8)* and CH*(9,10)*. Important spin-forbidden effects have been observed for reactions involving iodine*(1)*, however little is known about reactions involving lighter atoms where the allowed and forbidden pathways compete.

Recently, Hoffmann and Schatz*(11)* have developed a new level of treatment of spin-orbit effects in bimolecular reactions which enables a more sophisticated treatment of intersystem crossing dynamics than in the past. In this treatment high quality electronic structure methods are used to determine global surfaces for the reaction and spin-orbit matrix elements, and then trajectory surface hopping (TSH) methods are used to determine properties of the bimolecular collisions such as reactive cross sections and state distribution information. In an application of this theory to the O + H_2 reaction, the spin-orbit matrix elements were determined as a function of position, and then TSH calculations were done within a diabatic representation to determine cross sections. Intersystem crossing effects were found to be small for O + H_2 due to the fact that the crossing of the singlet and triplet surfaces occurs in the product region, making it hard to access geometries where hopping can occur. In addition the spin-orbit coupling is small, which means that the hopping probability is small. However the small fraction of trajectories that do undergo surface hopping have significantly different product state distributions than those which do not.

The Hoffmann-Schatz (HS) work raises some important questions in the description of nonadiabatic dynamics that go beyond the original work. HS found that for O + H_2 the triplet and singlet surfaces interact strongly in two places: where they cross near the barrier top, and where they become degenerate in the product region. The accuracy of TSH methods for this class of problems has not been described earlier, but HS found that unphysical results (excessively large cross sections) were obtained if TSH calculations were done in the adiabatic representation (a method that we denote TSH-A). Diabatic representation results (i.e., TSH-D) were more reasonable, but comparisons with quantum dynamics calculations were not performed, which means that the accuracy of the calculation is not known. In addition, the importance of interference in the coupled surface dynamics, something that would be imperfectly described using TSH-A or TSH-D, was not considered.

In this paper, we compare quantum scattering, TSH-A and TSH-D results for several two-state reaction path models which describe the O + H_2 reaction, and related reactions. Eleven model potentials have been considered, so as to determine the influence of triplet-singlet crossing location, the singlet well depth, and the size and coordinate dependence of the spin-orbit coupling.

Theory

In this section, we first describe the model Hamiltonians, and then the quantum and TSH nonadiabatic dynamics calculations that were performed.

Model Hamiltonians

The model Hamiltonians are designed to mimic the lowest energy triplet and singlet potential surfaces for O + H_2 along the minimum energy path of the triplet. As described by HS, the triplet state ($1^3A''$) has a collinear reaction path ($1^3\Pi$ symmetry) that correlates with $O(^3P)+H_2$ and $OH(^2\Pi)+H$ for reactant and product configurations, and with a linear O-H-H barrier (no wells) between these

Downloaded by UNIV MASSACHUSETTS AMHERST on September 14, 2012 | http://pubs.acs.org
Publication Date: August 14, 2002 | doi: 10.1021/bk-2002-0828.ch016

limits. The singlet state (1 $^1A'$) correlates with $O(^1D)+H_2$ and $OH(^2\Pi)+H$. It has a bent reaction path, and for C_{2v} geometries there is a deep intermediate well (with no barrier). To develop a reaction path model that has this behavior we take the triplet potential to be an asymmetrical Eckart barrier function of the type:

$$V_{11} = \frac{A}{1+e^{-ax}} + \frac{B}{[2\cosh\frac{1}{2}ax]^2} \qquad (1)$$

where x is the distance along the reaction path (not mass weighted) and the parameters A, B and a are given below. The singlet surface is also written as an Eckart function:

$$V_{22} = \Delta E + \frac{C}{1+e^{-b(x+f)}} + \frac{D}{[2\cosh\frac{1}{2}b(x+f)]^2} \qquad (2)$$

with parameters ΔE (the O atom singlet-triplet splitting), C, D, b and f, but here the parameters are chosen so that the potential exhibits a well rather than a barrier. The triplet-singlet coupling is assumed to be governed by a simple switching function of the type:

$$V_{21} = \frac{1}{4}s[1+\tanh g(x+h)] \qquad (3)$$

where s, g and h are additional parameters. In order to specify the 11 parameters in terms of physically meaningful quantities, we use the formulas in Eq. (4) below. With these definitions, the parameter C is no longer independent. Instead, the independent parameters are: A (exoergicity on the triplet surface), V_b (the triplet barrier), ΔE (defined above), a (triplet barrier width), b (singlet well width), g (determines how quickly the spin-orbit coupling is switched on as one moves from the reactants to the crossing point), w (singlet well depth),

Downloaded by UNIV MASSACHUSETTS AMHERST on September 14, 2012 | http://pubs.acs.org
Publication Date: August 14, 2002 | doi: 10.1021/bk-2002-0828.ch016

$$B = \frac{1}{2}(-v + \sqrt{v^2 - 4A^2}) \qquad v = 2A - 4V_b$$

$$C = A - \Delta E$$

$$D = \frac{1}{2}(-v' + \sqrt{v'^2 - 4C^2}) \qquad v' = 2C - 4(w - \Delta E)$$

f (determines the singlet-triplet crossing location, with x=0 corresponding to the triplet barrier location), s (magnitude of spin-orbit splitting) and h (determines where the spin-orbit coupling is turned on relative to the barrier at x=0). To simplify the parameters, we fix the first six parameters with the following values (modeled to mimic O + H_2 for slightly bent structures (where the triplet-singlet crossing is more accessible than for linear geometries) with roughly the right V_b and ΔE): A = 0.003187, V_b = 0.03187, ΔE = 0.06374, a = 1.5, b=1.5, g = 1.0. These values are in atomic units, and we will use these units throughout the paper. The remaining four parameters are given in Table 1 for the eleven models that we have considered. Figure 1 plots V_{11}, V_{22} and V_{21} as a function of x. Here is a summary of what each model does:

Model 1: Crossing is on the reagent side, coupling is turned on at the crossing point.
Model 2: Same as Model 1 except that the coupling is turned on after the crossing.
Model 3: Same as Model 1 except that the crossing point is moved to the product side of the barrier.
Model 4: Same as Model 3 except that the coupling is turned on after the crossing.
Model 5: Same as Model 2 except that the well depth is doubled.
Model 6: Same as Model 1 except that the well depth is doubled.
Model 7: Same as Model 1 except that the coupling is three times larger.
Model 8: Same as Model 2 except that the coupling is three times larger.
Model 9: Same as Model 2 except that the coupling is turned on further to the products.
Model 10: Same as Model 1 except that the crossing point and coupling are shifted further to the reactants.
Model 11: Same as 1 except that the crossing is right at the barrier top.

Quantum Scattering Calculations

Two-state quantum scattering calculations were done using a time-

Downloaded by UNIV MASSACHUSETTS AMHERST on September 14, 2012 | http://pubs.acs.org
Publication Date: August 14, 2002 | doi: 10.1021/bk-2002-0828.ch016

Downloaded by UNIV MASSACHUSETTS AMHERST on September 14, 2012 | http://pubs.acs.org
Publication Date: August 14, 2002 | doi: 10.1021/bk-2002-0828.ch016

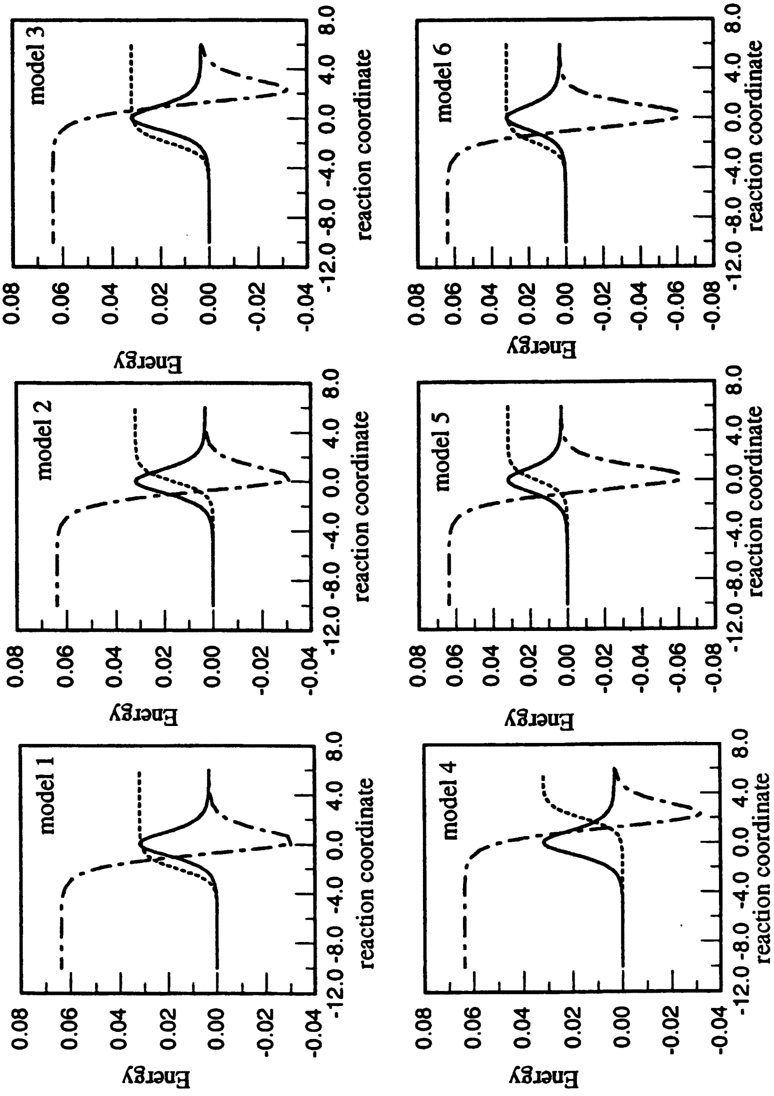

Downloaded by UNIV MASSACHUSETTS AMHERST on September 14, 2012 | http://pubs.acs.org
Publication Date: August 14, 2002 | doi: 10.1021/bk-2002-0828.ch016

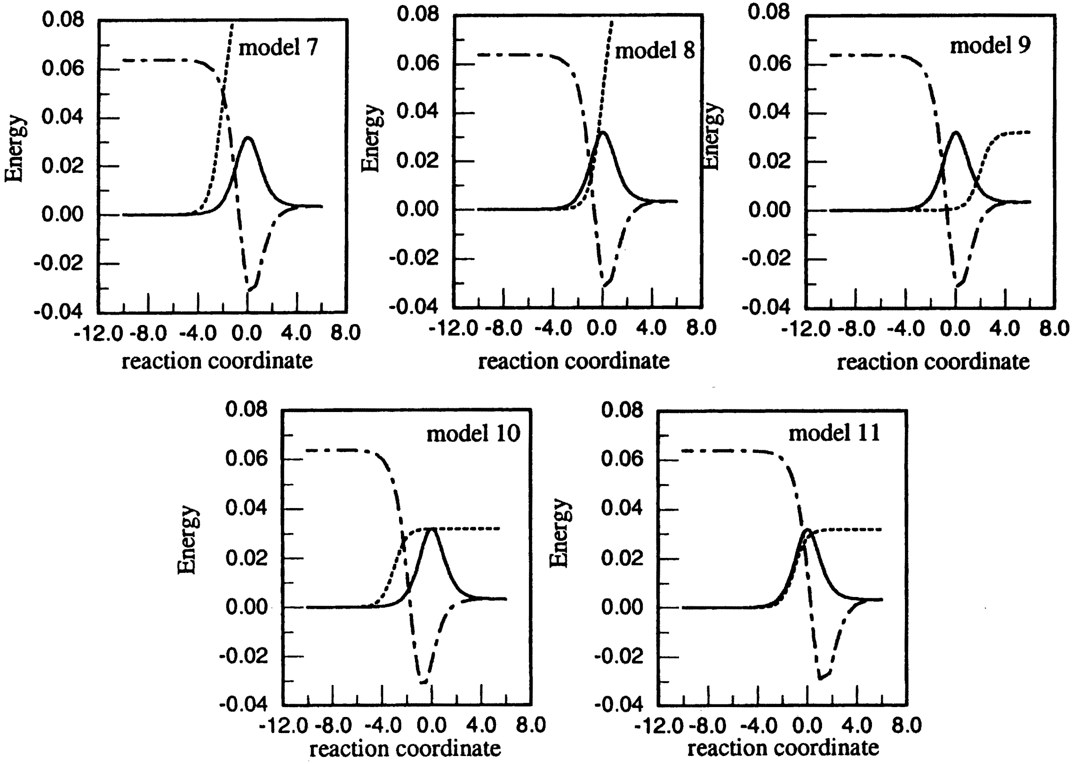

Figure 1. V_{11}, V_{22} *and* V_{21}*(the last multiplied by 100) as a function of x. The solid curve is* V_{11}*, dash-dot is* V_{22} *and dotted is* V_{21}*.*

Table 1. Parameters associated with the Model Hamiltonians

Model	*Well depth (w)*	*Crossing point shift(f)*	*Spin-orbit splitting(s)*	*Coupling shift (h)*
1	-0.0319	0.	0.4	2.0
2	-0.0319	0.	0.4	0.0
3	-0.0319	-2.	0.4	2.0
4	-0.0319	-2.	0.4	-2.0
5	-0.0637	0.	0.4	0.0
6	-0.0637	0.	0.4	2.0
7	-0.0319	0.	1.2	2.0
8	-0.0319	0.	1.2	0.0
9	-0.0319	0.	0.4	-2.0
10	-0.0319	1.	0.4	3.0
11	-0.0319	-1.	0.4	1.0

independent coupled channel method that is similar to a code that is described by Schatz *(12)*. In this code the Schrodinger equation for the two states is solved by sector propagation, integrating from x = -10 to x =6, using a step size of 0.01. The reduced mass in the calculation is 1AMU (1732 atomic units) which is approximately the mass of hydrogen. By propagating one set of independent solutions from negative x to positive x and then a second set from positive to negative, a complete set of linearly independent solutions is obtained, and then this is matched to proper asymptotic solutions to determine the scattering matrix and the reaction probabilities. Tests of convergence of these probabilities indicate that they are converged with respect to the integration parameters.

Trajectory Surface Hopping Calculations

TSH calculations were done using the fewest switches method *(13)*. Details are similar to work that was described earlier *(11)*, except that here we have considered calculations in both the diabatic and adiabatic representations. A time step of 1 atomic unit was used for all calculations, and 2000 trajectories were used to determine the reaction probabilities at each energy. Variation of the results with respect to the numerical parameters was within statistical uncertainty. We found the diabatic results to be significantly less sensitive to time step than the adiabatic results.

Downloaded by UNIV MASSACHUSETTS AMHERST on September 14, 2012 | http://pubs.acs.org
Publication Date: August 14, 2002 | doi: 10.1021/bk-2002-0828.ch016

Results

Figure 2 presents quantum reaction probabilities versus energy for each of the eleven models. These probabilities refer to the triplet (lower) initial state, and the two probabilities, labeled P_{11} and P_{12}, are for reaction to give the lower and upper final states, respectively. Note that the final states are defined in the adiabatic representation, and are roughly equal mixtures of singlet and triplet states that approximate the $^2\Pi_{3/2}$ and $^2\Pi_{1/2}$ states of OH. Linear and semilog plots are included for each model, so as to show both the below-barrier ($E<0.03187$) and above-barrier results. A summary of the results is as follows:

Model 1: This shows a large hump near E=0.022 which corresponds to the intersection energy between the two states in Fig. 1. At this energy each of the probabilities rises to about 0.01, then they drop to a minimum before rising at E=0.032 to values which oscillate around 0.5. The low energy hump is clearly an indication of a reaction that is dominated by intersystem crossing, while the high energy behavior is dominated by single surface dynamics, with Stuckelberg-like oscillations that probably arise from interference with the small reactive amplitude on the other surface.

Model 2: The coupling at the intersection is much smaller in this model than in Model 1, so the hump is much less important, and so are the oscillations at high energy.

Model 3: Here the crossing occurs in the product region, so even though the coupling is large at the crossing, the influence of surface hopping is much smaller, and no hump is seen. However the oscillations are still important, indicating that hopping occurs in the product region.

Model 4: The only coupling in this model is in the product region, so the results are completely dominated by single surface dynamics. However the two product states are equally probable, indicating that there is complete mixing of the final states.

Model 5: Here the deeper well causes the crossing to be in the reagent region, but the coupling is small. A hump is seen at E=0.017, but the probability at the peak is small.

Model 6: This is similar to Model 5 but now the coupling is larger, and the hump peaks at close to 0.01.

Model 7: The larger coupling, compared to Model 1, leads to much larger probabilities at the hump, close to 0.1, and larger oscillations at high energy. The larger coupling used in this model is designed to mimic intersystem crossing for second row atoms such as sulfur.

Model 8: Here the coupling is large as with Model 7, but it is not turned on near the crossing so the hump is now much smaller than for Model 7.

Downloaded by UNIV MASSACHUSETTS AMHERST on September 14, 2012 | http://pubs.acs.org
Publication Date: August 14, 2002 | doi: 10.1021/bk-2002-0828.ch016

Downloaded by UNIV MASSACHUSETTS AMHERST on September 14, 2012 | http://pubs.acs.org
Publication Date: August 14, 2002 | doi: 10.1021/bk-2002-0828.ch016

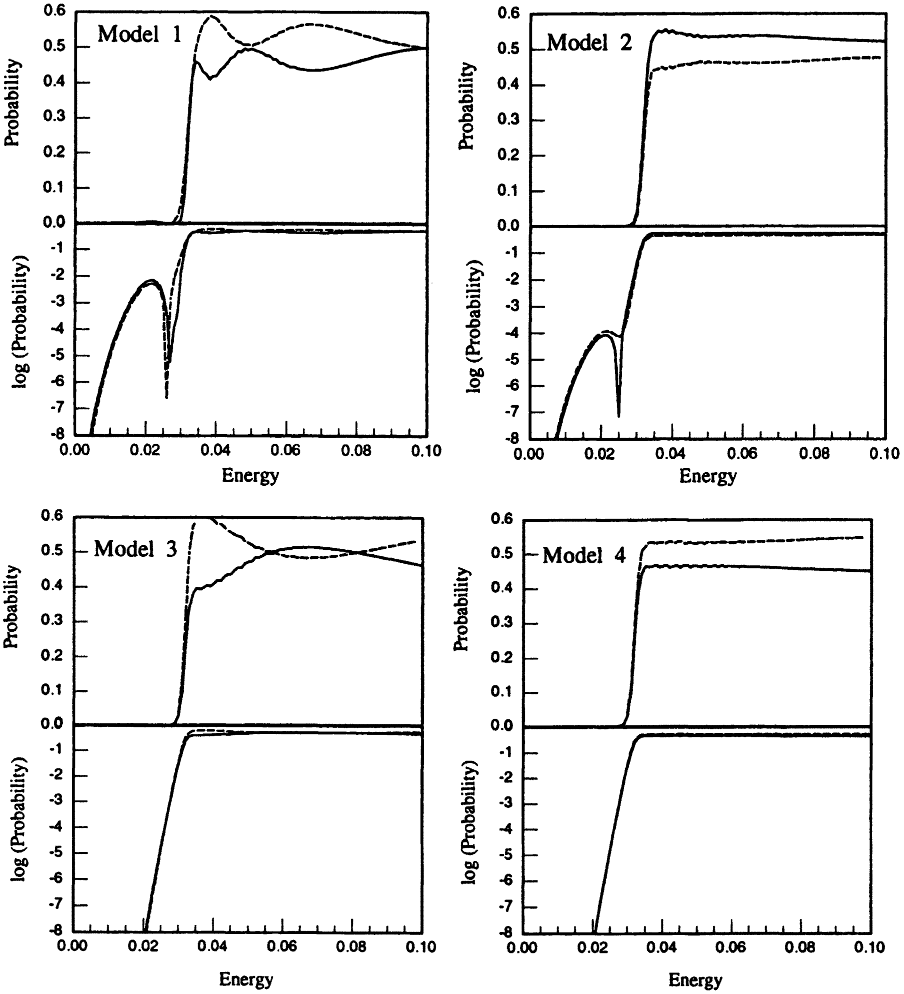

Figure 2. Quantum reaction probabilities P_{11} (solid) and P_{12}(dashed)

Downloaded by UNIV MASSACHUSETTS AMHERST on September 14, 2012 | http://pubs.acs.org
Publication Date: August 14, 2002 | doi: 10.1021/bk-2002-0828.ch016

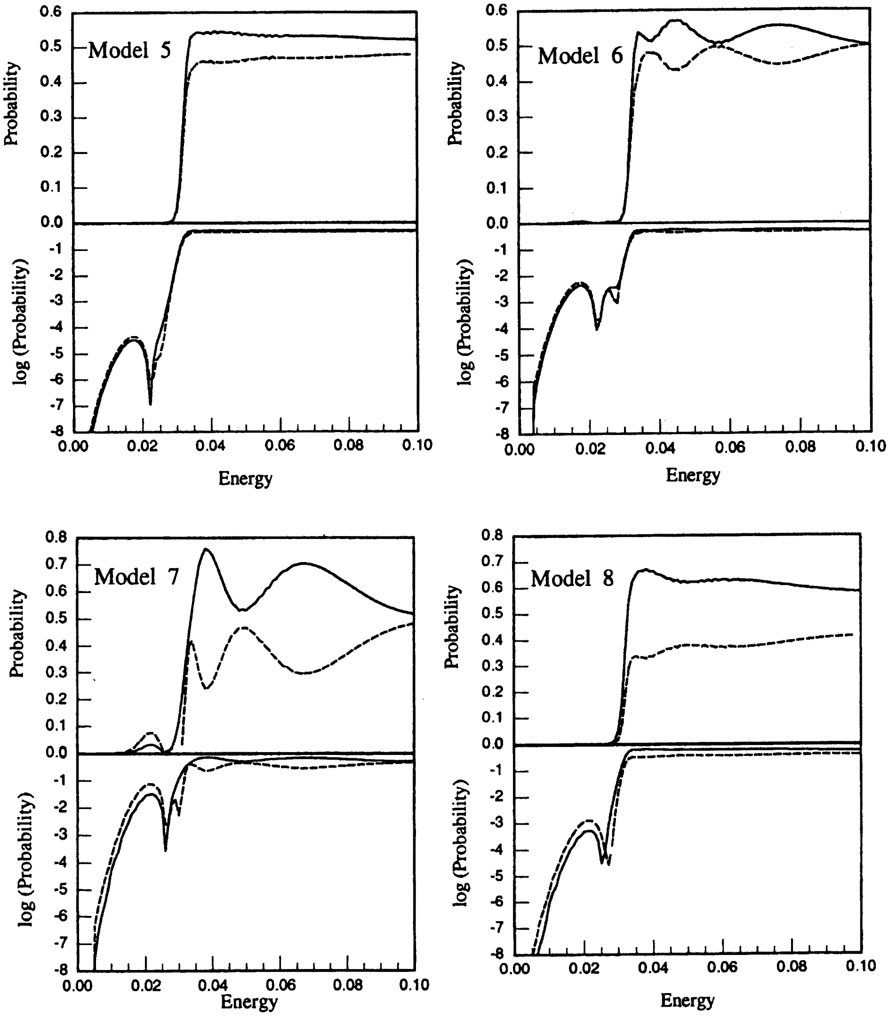

Figure 2. *Continued.*

Figure 2. ***Continued on next page.***

Downloaded by UNIV MASSACHUSETTS AMHERST on September 14, 2012 | http://pubs.acs.org
Publication Date: August 14, 2002 | doi: 10.1021/bk-2002-0828.ch016

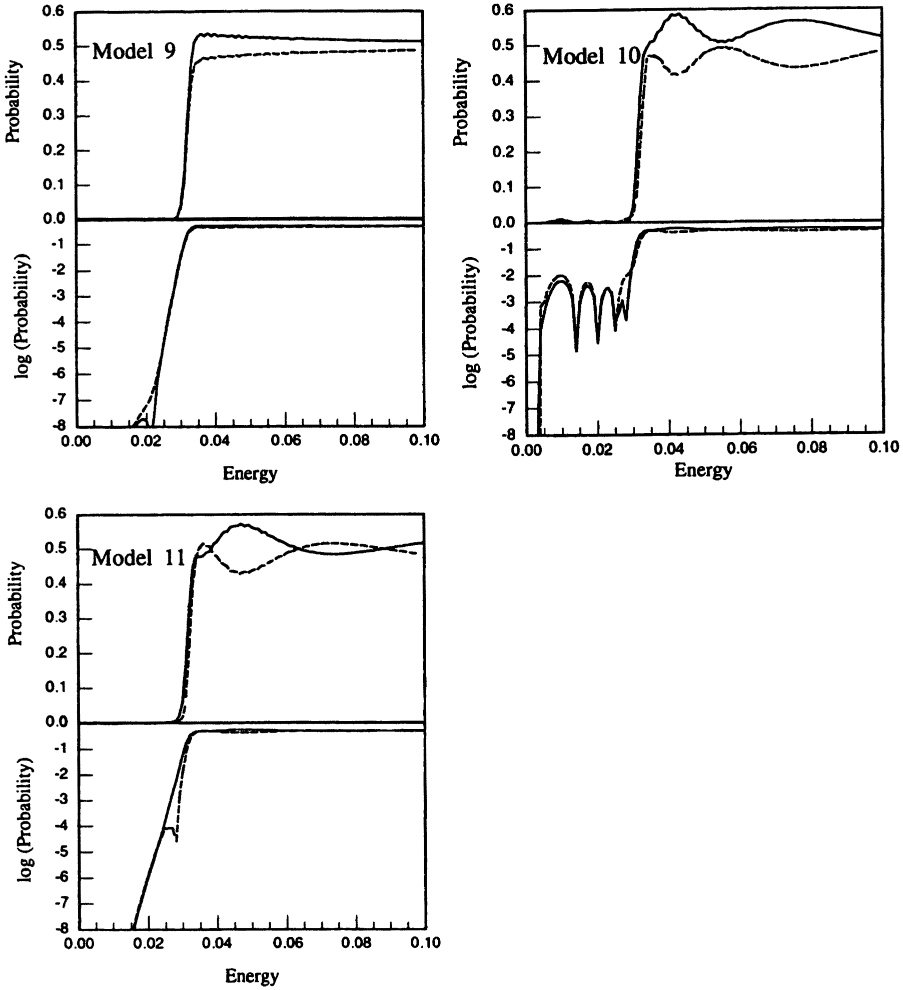

Figure 2. *Continued.*

Model 9: The coupling is so small at the crossing that the hump has almost disappeared and the results are close to those in Models 3 and 4.

Model 10: In this model, the crossing has been moved to roughly E = 0.01, and the first hump is seen at that energy, with a peak probability that is close to that for Model 1. Additional humps are seen below the barrier energy.

Model 11: This shows that when the crossing is at the barrier top, the hump from intersystem crossing is mixed up with the classical threshold.

Figure 3 summarizes results from the TSH-A and TSH-D calculations, along with the corresponding quantum results, all for Models 1 and 7. We chose these two models, as the crossing occurs before the barrier in these models, leading to significant nonadiabatic dynamics at energies below the barrier energy. Here we mainly focus on the behavior of the probabilities below the classical threshold. Above the threshold we find that the two TSH probabilities are unity, with the TSH-A probability mimicking the quantum results reasonably well, without, however describing the Stuckelberg oscillations, while the TSH-D probabilities predict that P_{11} is close to unity and P_{12} close to zero. The error in TSH-D here is due to the fact that the product asymptotic states, which are defined in the adiabatic representation, are not correctly described in the diabatic representation.

Figure 3 shows that at energies below the triplet barrier, the TSH-D probabilities have broad humps that are similar to the quantum results, except that the Stuckelberg interference oscillations are not correctly described. The problem with interference oscillations is to be expected, as the TSH model does not describe the coherence that would be associated with trajectories that react via the two pathways that are available. However the TSH-D results do predict approximately the correct peak probabilities, and the change in the probabilities that occurs in going from Model 1 to 7.

The TSH-A results, by contrast, are seriously in error. The total reaction probability jumps to unity at an energy of roughly 0.02, indicating that trajectories with a turning point exactly at the crossing point of the two surfaces react with a probability of close to unity, while those with higher or lower energies do not react at all. This poor behavior of the adiabatic results arises because although the surfaces are weakly coupled in the diabatic representation, they are strongly coupled in the adiabatic representation, and the TSH algorithm is unable to describe the coherence effects needed to describe this coupling accurately.

Conclusion

This paper has provided several important results pertaining to intersystem crossing effects in coupled singlet-triplet problems similar to O + H_2. First we

Downloaded by UNIV MASSACHUSETTS AMHERST on September 14, 2012 | http://pubs.acs.org
Publication Date: August 14, 2002 | doi: 10.1021/bk-2002-0828.ch016

Downloaded by UNIV MASSACHUSETTS AMHERST on September 14, 2012 | http://pubs.acs.org
Publication Date: August 14, 2002 | doi: 10.1021/bk-2002-0828.ch016

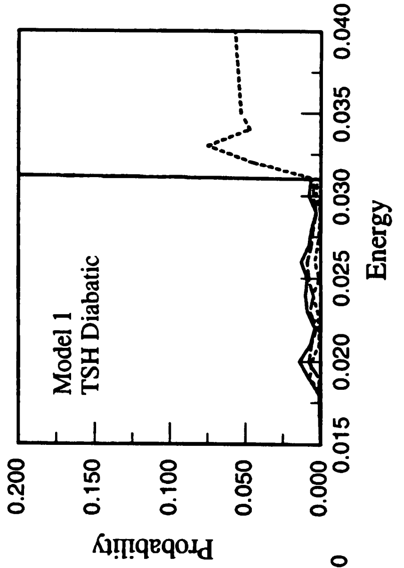

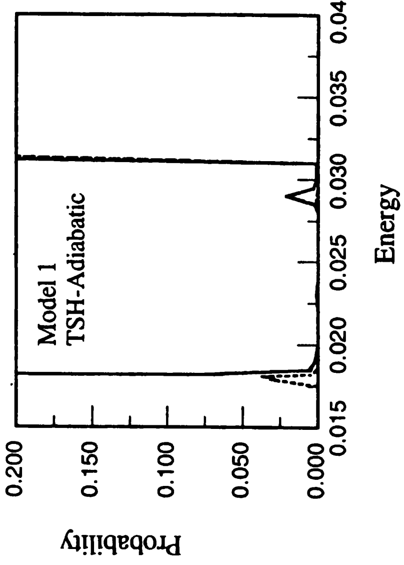

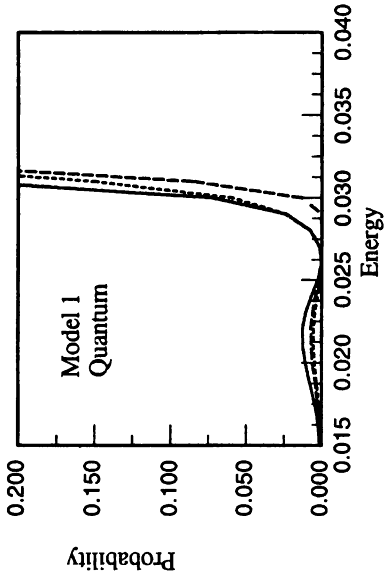

Downloaded by UNIV MASSACHUSETTS AMHERST on September 14, 2012 | http://pubs.acs.org
Publication Date: August 14, 2002 | doi: 10.1021/bk-2002-0828.ch016

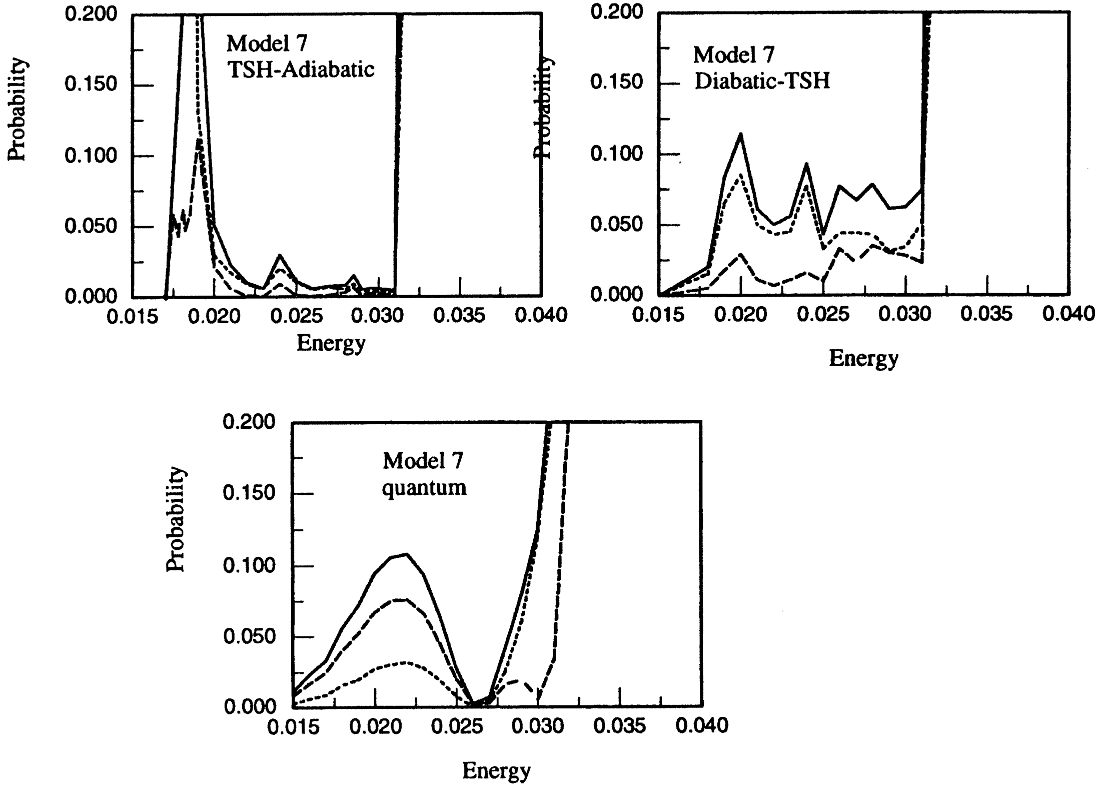

Figure 3. TSH-A, TSH-B and quantum probabilities for Model 1 (top) and 7 (bottom). In each figure the solid line is the total probability, the dashed one is P_{11} and the dotted one in P_{12}.

In Low-Lying Potential Energy Surfaces; Hoffmann, M., et al.;
ACS Symposium Series; American Chemical Society: Washington, DC, 2002.

used quantum scattering calculations to demonstrate that if the two states cross on the reagent side of the triplet barrier (as in models 1,2,5-10), then the low energy dynamics is dominated by reaction on the singlet state. The energy where this occurs is closely related to the energy of the crossing, and the size of the peak probability in this limit is determined by the size of the coupling at the crossing (compare models 1,2 and 9, or models 1 and 7, for example). Models for which the crossing occurs on the product side of the barrier (models 3,4) are dominated by adiabatic dynamics at energies below the barrier energy. Although this is a less interesting situation with respect to the importance of nonadiabatic dynamics, the models are still important, as the true potential surfaces and couplings for O + H_2 are closer to model 3 than to any of the other models considered here.

Additional results of this study were concerned with the use of TSH methods to describe intersystem crossing dynamics. We find that the TSH-D method is capable of determining reaction probabilities of reasonable accuracy for two models (1 and 7) where intersystem crossing is dominant, but TSH-A seriously overestimates these probabilities. This conclusion supports the interpretation of HS, who used TSH-D in preference to TSH-A in their full dimensionality calculations on O + H_2.

Finally, we see that Stuckelberg oscillations can occur as a result of interference between scattering on the two coupled surfaces. This effect is most likely exaggerated by the one dimensional model used here, and in all cases this plays a secondary role in determining the importance of intersystem crossing on the dynamics. TSH methods do not describe these effects correctly, so there is a need for higher quality semiclassical methods if one wants to describe fine details of the reaction dynamics.

Downloaded by UNIV MASSACHUSETTS AMHERST on September 14, 2012 | http://pubs.acs.org
Publication Date: August 14, 2002 | doi: 10.1021/bk-2002-0828.ch016

Acknowledgment

This work was supported was supported by the Office of Basic Energy Sciences, Division of Chemical Sciences, U.S. Department of Energy, under Contract No. W-31-109-ENG-38, and by AFOSR MURI grant F49620-01-1-0335.

References

1. M. Alagia, N. Balucani, L. Cartechini, P. Casavecchia, M. van Beek, G. G. Volpi, L. Bonnet, and J. C. Rayez, Faraday Discuss. (1999), **113**, 133-150.

2. N. Balucani, L. Beneventi, P. Casavecchia, D. Stranges, and G. G. Volpi, J. Chem. Phys. **94**, 8611 (1991).
3. R. Quandt, Z. Min, X. Wang and R. Bersohn, J. Phys. Chem. A **102**, 60 (1998); A. Misra, R. J. Berry and P. Marshall, J. Phys. Chem. A **101**, 7420 (1997).
4. J. Chen, E. K. Quinones, and P. J. Dagdigian, J. Chem. Phys. **90**, 7603 (1989).
5. U. Bley, M. Koch, F. Temps and H. G. Wagner, Ber. Bensen-Ges. Phys. Chem. **93**, 833 (1989).
6. U. Bley and F. Temps, J. Chem. Phys. **98**, 1058 (1993).
7. W. Gelbart and K. Freed, Chem. Phys. Lett. **18**, 470 (1973).
8. H. Shiina, A. Miyoshi and H. Matsui, J. Phys. Chem. A **102**, 3556 (1998).
9. M. R. Manaa and D. R. Yarkony, J. Chem. Phys. **95**, 1808 (1991).
10. T. Seideman and S. P. Walch, J. Chem. Phys. **101**, 3656 (1994).
11. M. R. Hoffmann and G. C. Schatz, J. Chem. Phys., **113**, 9456-9465, (2000).
12. G. C. Schatz, Chemical Reviews, **87**, 81-89 (1987)
13. J. C. Tully, *J. Chem. Phys.* **93**, 161(1990).

Downloaded by UNIV MASSACHUSETTS AMHERST on September 14, 2012 | http://pubs.acs.org
Publication Date: August 14, 2002 | doi: 10.1021/bk-2002-0828.ch016

Downloaded by STANFORD UNIV GREEN LIBR on September 14, 2012 | http://pubs.acs.org
Publication Date: August 14, 2002 | doi: 10.1021/bk-2002-0828.ch017

Chapter 17

The Challenge of High-Resolution Dynamics: Rotationally Mediated Unimolecular Dissociation of HOCl

Joel M. Bowman[1], Sergei Skokov[1,2], Shengli Zou[1], and Kirk Peterson[3]

[1]Department of Chemistry and Cherry L. Emerson Center for Scientific Computation, Emory University, Atlanta, GA 30322
[2]Current address: Intel Corporation, 2200 Mission College Boulevard, Santa Clara, CA 95052
[3]Department of Chemistry, Washington State University and Environmental Molecular Science Laboratory, Pacific Northwest National Laboratory, Richland, WA 99352

We review methods to calculate molecular resonances (also known as quasibound states), and illustrate them for the unimolecular dissociation of HOCl → Cl+OH, for which recent experiments have found dramatic fluctuations of the dissociation rate for HOCl($6\nu_{OH}$) with the rotational quantum numbers J and K. The calculations do capture the large fluctuations of the dissociation rate with respect to the HOCl total angular momentum, and a simple, general model is presented to rationalize these results. Calculated rates are also presented for HOCl($7\nu_{OH}$ and $8\nu_{OH}$) and compared with very recent experiments. Limited, new calculations of HO^{37}Cl dissociation show a dramatic isotope effect on the dissociation rate.

In Low-Lying Potential Energy Surfaces; Hoffmann, M., et al.;
ACS Symposium Series; American Chemical Society: Washington, DC, 2002.

Introduction

Unimolecular reactions are an important and ubiquitous process in chemistry. The textbook treatment of such reactions is based on a microcanonical, statistical theory such as RRK or RRKM theory (1). These theories apply to an energized molecule with energy in excess of say the dissociation energy of some fragment channel, or an isomerization process. Thus, these theories are not appropriate for a state-specific, unimolecular process, where the term state-specific refers to the energized molecule in a single quantum state. Such states are referred to as resonances. These metastable quantum states form the rigorous foundation of unimolecular rate theory, and this is the focus of this chapter. The relationship between these quantum states and statistical theories have been explored by a number of authors, and a recent, elegant approach to this relationship has been presented by Miller and co-workers (2), based on "random matrix" theory.

Experimentally, it is difficult to prepare a molecule in a specific quantum state from which a unimolecular process can occur, and this has only been achieved in rare cases. One very striking recent example of this are the beautiful experiments done by the Rizzo (3-6) and Sinha (7,8) groups on the unimolecular dissociation of HOCl (to form OH+Cl) prepared in high OH-overtone states with complete rotational resolution. The most extensive experiments done by these groups determined the unimolecular dissociation lifetimes for rotating HOCl($6\nu_{OH}$) as a function of J and K. In general, the lifetimes were determined to be of the order of hundreds of microseconds, depending on J and K, corresponding to a resonance width of the order of 10^{-4} cm^{-1}. Further the lifetime showed significant and intriguing fluctuations with J and K.

These experiments stimulated theoretical work by us (9-14), independently by Schinke and co-workers (15-17), and recently both groups (18) to rigorously model this unimolecular dissociation. *Ab initio*-based potential energy surfaces were constructed by these groups, and used in quantum dynamics calculations to obtain the real energies and widths of the HOCl resonances for OH-overtones. The results of our calculations and their interpretation will be reviewed below. However, before describing that work, we present a short overview of the theory and calculation of unimolecular resonances.

Short review of resonance theory and calculations

Resonances are eigenstates of a molecule that are not stationary in time, but which are nevertheless initially highly localized in space. The eigenenergies of resonances are complex, with the real part being the physical energy of the resonance and the imaginary part related simply to the width (see below). Generally the imaginary part is much smaller in magnitude than the real part. These complex energies form a discrete spectrum, and thus resonances share

Downloaded by STANFORD UNIV GREEN LIBR on September 14, 2012 | http://pubs.acs.org
Publication Date: August 14, 2002 | doi: 10.1021/bk-2002-0828.ch017

Downloaded by STANFORD UNIV GREEN LIBR on September 14, 2012 | http://pubs.acs.org
Publication Date: August 14, 2002 | doi: 10.1021/bk-2002-0828.ch017

some characteristics in common with true bound states, and for that reason they are also referred to as quasibound states. This picture of resonances applies to non-overlapping resonances, where non-overlappping refers to resonances where the real part of the resonance energies of adjacent resonances are separated by many times the magnitude of the imaginary part. If this criterion does not apply then some of the simple characteristics of resonances summarized below may not hold, and so we will restrict the discussion to non-overlapping resonances.

In the time-dependent picture, the resonance wavefunction is given by $\Psi(t) = \Psi(0) exp[-i(E - i\Gamma / 2)t$, where $E - i\Gamma/2$ is the complex energy eigenvalue of the resonance, mentioned above. $\Psi(0)$ is the resonance wave function at t = 0. Under "low resolution" $\Psi(0)$ looks like a bound state, but under "high resolution" this wavefunction actually has an oscillatory "tail" in the asymptotic region describing one or more dissociation channel. This split personality of resonances wavefunctions makes them fascinating to study, but also makes their calculations quite difficult, because they span a large region in configuration space. An example of a molecular resonance wavefunction that displays this behavior is shown in Fig. 1. As seen in this case, the "tail" is of much smaller magnitude than the main portion of the wavefunction which is located in the bound, strong interaction region of space.

The first rigorous calculations of molecular resonances were done using coupled channel scattering methods. This approach, while completely rigorous, is difficult and laborious, because it requires a search for the scattering energies that produce abrupt changes in the phase of the scattering matrix (19). Currently, L^2 methods that obtain resonance energies and wavefunctions directly are commonly used. These methods are like bound-state approaches, but differ from them in two essential ways. First, a basis in the dissociative degree(s) of freedom must extend to the non-interacting region. (This is not necessary for ordinary bound state calculations.) Second, a method must be introduced to accurately describe the exponential decay of the wavefunction in time. This can be done by explicitly propagating a wavepacket with a damping function that acts in the near asymptotic region, or by the analytic continuation of the Hamiltonian, H, to the complex plane. The latter approach has been used for a number of years by either the complex coordinate method (20), and more recently by the introduction of negative imaginary (absorbing) potentials in the near asymptotic region. It appears that the use of negative imaginary potentials for the explicit calculation of molecular resonances was first introduced by Jolicard and Leforestier (21). Since we use negative imaginary potentials in our calculations, we present some the details of their use next.

Negative imaginary potentials are introduced to deal with the problem of reflection of the wavefunction from the edges of a finite grid or L^2 basis (22). Thus, these potentials are only non-zero in the asymptotic region and within several deBroglie wavelengths of the end of the grid. For molecular resonances

Downloaded by STANFORD UNIV GREEN LIBR on September 14, 2012 | http://pubs.acs.org
Publication Date: August 14, 2002 | doi: 10.1021/bk-2002-0828.ch017

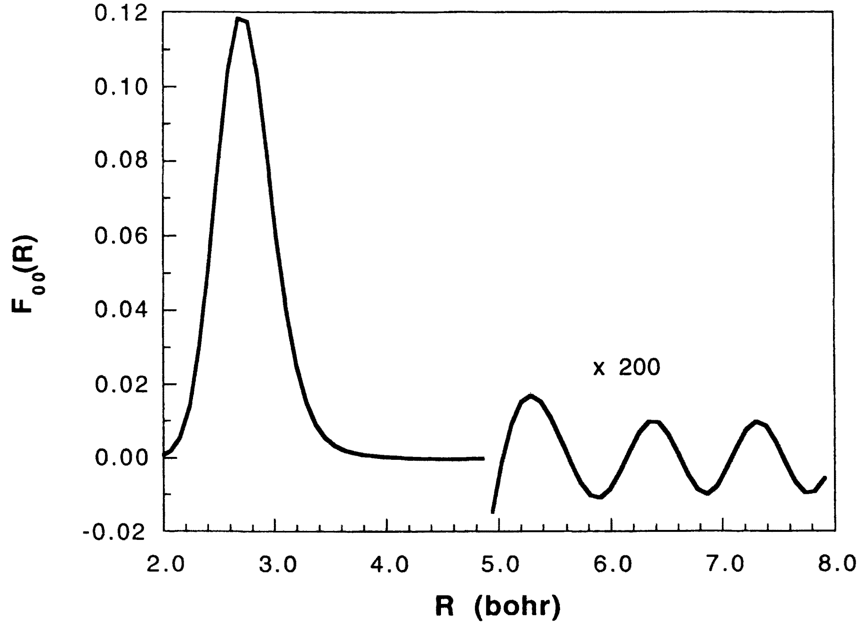

Fig.1 Radial part of resonance wavefunction clearly showing bound state charatcter in the strong interaction region and oscillatory, continuum character in the non-interacting region.

with a single fragmentation channel an often used form of the negative imaginary potential -iU(R) is

$$U(R)=\begin{cases} 0, & R<R_{min} \\ \lambda(\frac{R-R_{min}}{R_{max}-R_{min}})^{n}, R\geq R_{min} \end{cases}, \qquad (1)$$

where R is the distance between the centers of mass of the fragments. For a triatomic molecule that breaks up into an atom A and a diatomic BC, R is the distance between A and the center of mass of BC. Note that R_{min} denotes the boundary between the interacting and non-interacting region. Of course there is not a sharp boundary between these two regions, and so typically R_{min} is in the region where the interaction potential is say 10^{-4} times the real part of the resonance energy (or smaller). Also R_{min} is usually only several bohr from the end of the range in the coordinate R, denoted R_{max}. Negative imaginary potentials are also referred to as absorbing potentials, because the wavefunction decays in the region where they exist. In time-dependent propagation methods this decay of the wavefunction prevents unphysical reflection of the wave packet from the grid boundary. In time-independent methods, such as we describe the absorbing potential enforces the correct outgoing wave boundary condition of the wavefunction. This condition is not perfectly met for any absorbing potential, and some incoming wave component of the wavefunction is present (due to reflection). In practice the parameter λ in Eq. (1) is varied to minimize the incoming wave amplitude, as determined from a complex stabilization criterion (21). An example of this behavior will be given below.

To summarize the approach thus far, the eigenvalues (and optionally the bi-orthogonal set of eigenfunctions) of the complex Hamiltonian, $H_c(\lambda) \equiv H\text{-}iU(\lambda)$ are obtained over a range of the parameter λ. Stable eignevalues are associated with resonances. If eigenfunctions of H_c or even of H are obtained these can also be examined to determine if they have the expected properties of resonances, e.g., highly localized in the strong interaction region.

It is also possible using the L^2 approach to obtain the distribution of the internal states of the products of the unimolecular dissociation The rigorous, asymptotic (R goes to infinity) form of the resonance wavefunction for a triatomic molecule at the energy E_i, is given by

$$\psi \sim \sum_{vjm} S_{vjm} e^{ik_{vj}R} \left| vjm \right\rangle, \qquad (2)$$

where $\left| vjm \right\rangle$ is a given ro-vibrational state of the diatomic fragment, k_{vj} is the corresponding wavnumber, and S_{vjm} is the amplitude for the resonance to decay into that state. The asymptotic form of the complex L^2 eigenfunctions, given by Eq. (2), can be used directly to obtain the unknown amplitudes S_{vjm}. Even the real L^2 eignefunctions can be used to approximately obtain the S_{vjm}. In our computational approach, described in detail below, we do calculate the real L^2

Downloaded by STANFORD UNIV GREEN LIBR on September 14, 2012 | http://pubs.acs.org
Publication Date: August 14, 2002 | doi: 10.1021/bk-2002-0828.ch017

eigenfunctions of the real Hamiltonian, but generally do not obtain the complex ones. In this case the complex exponential in Eq. (2) is replaced by $sin(k_{vj}R)$ and the amplitudes S_{vjm} are real. The analysis to obtain the S_{vjm} is straightforward; the internal state $|vjm\rangle$ is projected onto the real L^2 eigenfunction representing the ith resonance, and then the resulting R-dependent amplitude is analysed in the asymptotic region to obtain the corresponding S_{vjm} (The wavefunction shown in Fig. 1 is actually the R-dependent amplitude of an L^2 resonance eigenfunction for zero.)

We now describe the details of the calculation of resonances of HOCl, the comparison with experiments reviewed above, and the interpretation of some of the results. The rigorous calculation of resonances requires an accurate, full dimensional potential energy surface. We briefly describe this crucial component of the dynamics calculations next.

Potential Energy Surface for HOCl

The *ab initio* electronic structure calculations were carried out with the MOLPRO suite of programs (23). Electron correlation effects were treated using highly correlated internally contracted multireference configuration interaction (icMRCI) wave functions (24,25). The reference function in the icMRCI calculations consisted of a full valence complete active space (CAS), i.e., 14 electrons in 9 orbitals. All single and double excitations with respect to this function were included in the final MRCI and the doubly external configurations were internally contracted. The core orbitals were not correlated (frozen core approximation). To approximately account for higher excitations, the multireference analog (26,27) of the Davidson correction (28) was also employed throughout (icMRCI+Q).

The basis sets used in the construction of the PES for HOCl were based on the correlation consistent basis sets of Dunning and co-workers (29-31), denoted cc-pV*n*Z with *n*=D, T, Q. As is now well known, calculations with the correlation consistent basis sets exhibit systematic convergence toward the apparent complete basis set (CBS) limit. The basis set convergence of the total energies has been modeled in this work by a simple extrapolation formula to obtain estimates of the energy in the CBS limit (32). For the present work, each of the points on the potential energy surface was calculated with three basis sets. These consisted of the cc-pVDZ, cc-pVTZ, and cc-pVQZ sets augmented with diffuse functions of *spd* symmetry for O and Cl and *sp* symmetry for H. The diffuse functions were taken from the standard aug-cc-pV*n*Z basis sets (30,31). In addition, in the present work the cc-pV*n*Z+diffuse *spd* basis sets were augmented with a single tight *d* function. The systematic behavior of these basis sets was then exploited by extrapolating each point on the PES using Eq.(1). The final result was an approximate CBS limit PES.

Downloaded by STANFORD UNIV GREEN LIBR on September 14, 2012 | http://pubs.acs.org
Publication Date: August 14, 2002 | doi: 10.1021/bk-2002-0828.ch017

Downloaded by STANFORD UNIV GREEN LIBR on September 14, 2012 | http://pubs.acs.org
Publication Date: August 14, 2002 | doi: 10.1021/bk-2002-0828.ch017

Several potential surfaces have been developed based on these calculations. The one used in the most recent resonance calculations was adjusted slightly (13) to give spectroscopically accurate agreement with experiment for vibrational energies. Another, global potential including the O(^{1}D)+HCl, ClO+H channels, as well as the HClO isomer, has also been developed based on the above *ab initio* calculations (33).

Finally note that the possible importance of electronically excited states was considered in these calculations. Conical intersections with excited states were found at the two linear geometries (9). However, these were all at energies 1 eV or greater above the dissociation energy of HOCl, and well above the energy of the dynamics calculations reveiwed below. In addition the resonances of relevance to experiment have no bending excitation and so do not sample the relevant linear geometries. Thus excited electronic states were not included in the dynamics calculations.

Computational details and results for HOCl resonances

The calculation of energies and widths of the resonances of HOCl was done using the complex L^2 method outlined in the previous section. In our particular implementation we used an efficient truncation/recoupling procedure (10,11) to obtain eigenvalues and eigenfunctions of the real Hamiltonian. The Hamiltonian for the HOCl dissociation is given in standard body-fixed Jacobi coordinates . For zero total angular momentum, J, it is:

$$\hat{H}^{J=0} = T_R + T_r + \frac{j_{op}^2}{2I(r,R)} + V(R,r,\gamma), \tag{3}$$

where R is the distance between Cl and the center of mass of OH and r is OH internuclear distance, and $\gamma$is the angle between the corresponding vectors **R** and **r**. T_R and T_r are radial kinetic energy operators for the variables R and r, j_{op}^2 is the square of the OH angular momentum, where the body-fixed z-axis is along the vector **R**, and V is the full potential.

For non-zero total angular momentum, J, and in particular for J in the range of the experiments on HOCl, i.e., J greater than 20, exact calculations are prohibitively expensive for us. But, based on limited exact calculations that we have done, and also on experiment, HOCl behaves as a nearly symmetric prolate top, with K (the projection quantum number of J on the a-axis) a nearly good quantum number. Thus, we used an approximate, "adiabatic" treatment of rotation that assumes K is a good quantum number (34). In this approximation, the Hamiltonian for any J and K is given by

$$\hat{H}^{JK} = \hat{H}^{J=0} + E^{JK}(R,r,\gamma),$$

where $\hat{H}^{J=0}$ is given by Eq. (3), and. E^{JK} is the symmetric top rotational energy given by

$$E^{JK}(R,r,\gamma)=\bar{B}(R,r,\gamma)J(J+1)+[A(R,r,\gamma)-\bar{B}(R,r,\gamma)]K^2.$$

This energy is obtained by determining the rotation constants in the principal axis system at each nuclear geometry. (Limited tests of this approximation for bound states of HOCl indicate that it is accurate to within several wavenumbers for ro-vibrational energies for J as large as 30 (35).)

The complex Hamiltonian for a given J and K is $\hat{H}^{JK}-iU$, where U is given by Eq. (1). Matrix elements of the complex Hamiltonian are obtained in the basis of real eigenfunctions of $\hat{H}^{JK}$, and thus they are given by

$$\left\langle \Psi_m^{JK} \middle| \hat{H}^{JK} \middle| \Psi_n^{JK} \right\rangle = E_m^{JK}\delta_{mn} - i\left\langle \Psi_m^{JK} \middle| U \middle| \Psi_n^{JK} \right\rangle,$$

where E_m^{JK} are the real energy eigenvalues of $\hat{H}^{JK}$. We experimented with values of 2 and 3 for n in Eq.(1) and also with the value of $R_{min.}$ and R_{max}. Because R_{min} must be large enough for the true interaction potential to be very small, matrix elements of $\left\langle \Psi_m^{JK} \middle| U \middle| \Psi_n^{JK} \right\rangle$ involving low-lying, localized bound states are negligible, and so those states were not used in the construction of the complex Hamiltonian. This results in a fairly small complex diagonalization problem (of the order of rougly 1000) relative to the real one (of the order of roughly 14 000). In the present calculations R_{min} was either 12.0 or 13.0 bohr and R_{max} was either 14.0 or14.5 bohr

The diagonalization of the complex Hamiltonian was repeated using different values of λ. For a resonance state, the complex energy should tend to constant when λ increases, and thus dE/dλ should be zero for resonance states over a fairly large range of λ. Thus a plot of the complex energy as λ varies should exhibit a cusp. This relationship is not satisfied exactly in numerical calculations, as illustrated in Fig. 2 for the $\nu_{OH} = 8$ (J = K = 0) resonance, where λ varies from 6561 to 50 625 cm^{-1}. As seen the complex energy is approximately stationary at the value (24176.62 cm^{-1}, -0.277 cm^{-1}). The imaginary part corresponds to a width of 0.55 cm^{-1}, in good agreement with the experimental estimate of 1 cm^{-1} (6).

Variation of 6ν_{OH} resonance width with total angular momentum

The variation of the resonance width with J and K for the fifth overtone of the OH-stretch that was seen experimentally (3-8) has also been found in calculations by us and by Schinke and co-workers . The widths are very small, i.e., of the order of 10^{-4} cm^{-1}, with a large variation with J and K, suggesting a

Downloaded by STANFORD UNIV GREEN LIBR on September 14, 2012 | http://pubs.acs.org
Publication Date: August 14, 2002 | doi: 10.1021/bk-2002-0828.ch017

Downloaded by STANFORD UNIV GREEN LIBR on September 14, 2012 | http://pubs.acs.org
Publication Date: August 14, 2002 | doi: 10.1021/bk-2002-0828.ch017

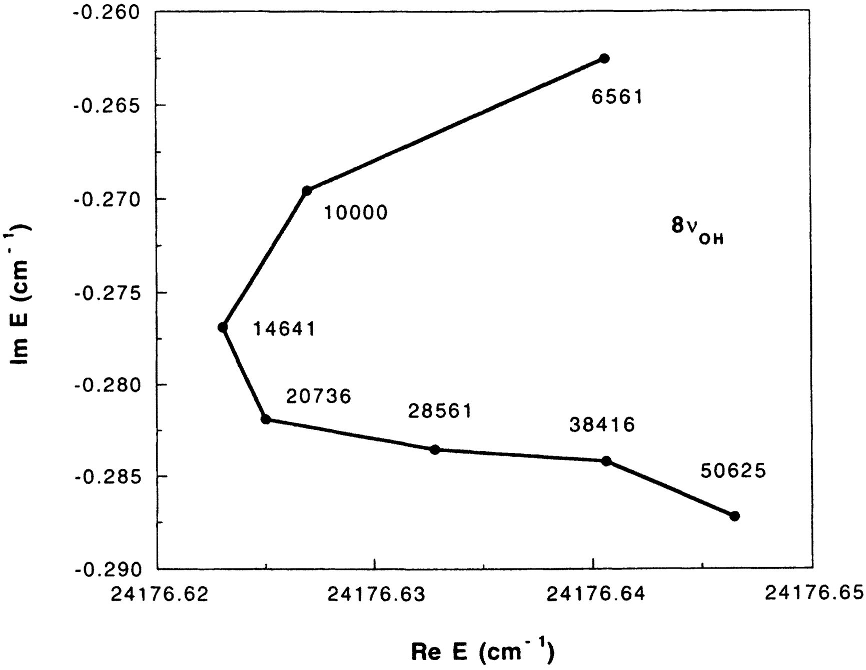

Fig.2 Plot of the complex energy of the $8\nu_{OH}$ resonance of HOCl as the strength of absorbing potential, λ (in cm^{-1}) varies, as indicated.

very non-statistical decay mechanism. Given that dissociation from the state $6\nu_{OH}$ (J, K) occurs just above the dissociation threshold energy, this result is not very surprising.

Previously (12), we gave a simplified explanation of this variation, based on a first-order perturbation theory argument, which we summarize here. The mixing of the state $6\nu_{OH}$ with dissociating states is mediated by rotation through a term given by $V/(E^{JK}_{6\nu_{OH}} - E^{JK}_{diss})$, where $E^{JK}_{6\nu_{OH}}$ and E^{JK}_{diss} are the energies of $6\nu_{OH}$ and dissociating states, respectively. Obviously, when these energies are equal the mixing is a maximum and the width will show a local increase. Assuming that the J and K-dependence of the ro-vibrational energy of molecular eigenstates is given by $E_i^{J=0} + \overline{B}_i J(J+1) + (A_i - \overline{B}_i)K^2$, where $E_i^{J=0}$ is the exact energy eigenvalue for J = K = 0, and $\overline{B}_i$ and A_i are the associated rotation constants, it is clear that the " diabatic crossings" with a bath of dissociative states occur at different values of J and K. This follows since dissociative states have large OCl-stretch excitation and thus a correspondingly small values of $\overline{B}$, compared to that of $6\nu_{OH}$, A schematic picture of these crossing is shown in Figure 3 for K = 0.. As seen, dissociateve states 'tune in' and 'tune out' of energy resonance with $6\nu_{OH}$ with J, resulting in large variations of the width. (Note the argument still applies for any value of K.)

The above picture of diabatic crossings is clearly oversimplified, because the "bath" of dissociative states are strongly interacting among themselves, and so the actual interactions among them and the $6\nu_{OH}$ state are quite complex with many avoided crossings as J and K vary. A more sophisticated model that captures this complexity was also developed by us previously (12). In brief, it consists of the following model complex Hamiltonian

$$H^J_{ij} = E^{J_0}_{ij}\delta_{ij} + \Delta\overline{B}[J(J+1) - J_0(J_0+1)]\delta_{ij} + V,$$

where $E^{J_0}_{ij}$ are complex eigenvalues for some reference value of J, denoted J_0, $\Delta\overline{B}_i$ is the difference in the rotation constant between the dissociative states and the $6\nu_{OH}$ state (which for simplicity we take to be a constant), and V_{ij} is the coupling between the states, which we also take to be a constant, V, for any pair of states. We took as the zero-order basis the $6\nu_{OH}$ state and 100 states with energies nearest to the $6\nu_{OH}$ energy for $J_0 = 24$ and K = 3 and diagonalized the complex Hamiltonian H^J. The constants $\Delta\overline{B}$ and V were varied to achieve semi-quantitative agreement with experiment and values for V = 0.05 cm^{-1} and $\Delta\overline{B} = 0.1$ cm^{-1} were obtained. This value for $\Delta\overline{B}$ is very much in accord with our calculation of $\overline{B}$-constants for the state $6\nu_{OH}$ and highly excited ClO-stretch states. The coupling constant of 0.05 cm^{-1} is also in good accord with the our analysis of rotation induced coupling for bound states of HOCl (35).

Downloaded by STANFORD UNIV GREEN LIBR on September 14, 2012 | http://pubs.acs.org
Publication Date: August 14, 2002 | doi: 10.1021/bk-2002-0828.ch017

Downloaded by STANFORD UNIV GREEN LIBR on September 14, 2012 | http://pubs.acs.org
Publication Date: August 14, 2002 | doi: 10.1021/bk-2002-0828.ch017

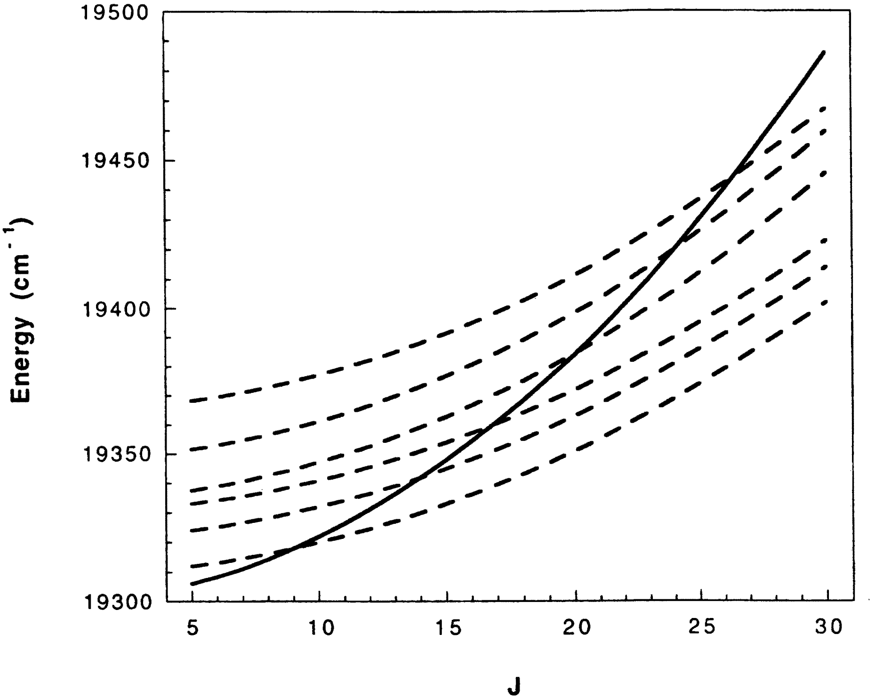

Fig.3 Schematic plot of the variation of the energies of state $6\nu_{OH}$ and dissociative states with J.

To conclude this section, we note that the above rotation-induced coupling mechanism suggests that the dissociation lifetime might be sensitive to isotope effects. We examined this in a very preliminary way for $HO^{37}Cl$, which is naturally present in the experiments, by repeating our calculations for this heavy isotope of Cl for $6\nu_{OH}$. The results, shown in Table I, are striking: the lifetime of $HO^{37}Cl$ is more than 10 times longer for the same values of J (and K = 0) than for $HO^{35}Cl$. This appears to be in qualitative agreement with preliminary observations of Sinha and co-workers, who had difficulty measuring the dissociation rate of $HO^{37}Cl(K=0)$ because of its apparently longer lifetime than $HO^{35}Cl$ (K=0) (36).

$7\nu_{OH}$ and $8\nu_{OH}$ resonances

The widths of the $7\nu_{OH}$ and $8\nu_{OH}$ resonances have recently been inferred by Callegari *et al.* (6), from line broadening measurements. As expected, the widths for these high overtones are much larger than for $6\nu_{OH}$, which is just above the dissociation threshold energy.

We recently reported calculations of these resonances for J = 0 (14). Tbe width for $8\nu_{OH}$ was plotted in Fig. 2 as a demonstration of the stability of the calculated results with respect to the strength of the absorbing potential. As noted, the stabilized value 0.55 cm^{-1} is in good agreement with the experimental estimate of 1 cm^{-1}. The width for $7\nu_{OH}$ was calculated to be 0.01 cm^{-1}, which is also in good agreement with experiment. Recent calculations of Schinke an co-workers obtain simililar values for these widths (18).

In addition to calculating the widths of these resonances, the distribution of OH states was also calculated using Eq. (2) and the methods describing how that equation is used. For the $7\nu_{OH}$ resonance only the ground vibrational state of OH is energetically open, and the OH rotational distribution is predicted to be inverted with a maximum N = 5. For the $8\nu_{OH}$ resonance, OH is predicted to be rotationally excited for both the ground and first excited vibrational states, with more rotational excitation for $v_{OH} = 0$ than $v_{OH} = 1$. Also, OH is predicted to be formed with a significant population in v = 1. The branching ratio v = 1: v = 0, summed over rotational states is roughly 1:2.

Summary and conclusions

We reviewed the theory and methods to calculated unimolecular resonances, and presented calculations for HOCl. The calculations were stimulated by high resolution experiments that determined the resonance lifetimes for precise rotational states of HOCl in high OH-stretch overtones. The calculations, which made use of a very high quality potential energy

Downloaded by STANFORD UNIV GREEN LIBR on September 14, 2012 | http://pubs.acs.org
Publication Date: August 14, 2002 | doi: 10.1021/bk-2002-0828.ch017

Downloaded by STANFORD UNIV GREEN LIBR on September 14, 2012 | http://pubs.acs.org
Publication Date: August 14, 2002 | doi: 10.1021/bk-2002-0828.ch017

Table I. Calculated widths (cm^{-1}) of HO^{35}Cl and HO^{37}C for indicated values of J for K = 0.

J	HO^{35}Cl	HO^{37}Cl
22	6.0e-06	7.6e-06
24	3.8e-05	8.0e-04
26	2.2e-04	6.8e-06
28	9.0e-03	1.1e-06
30	1.9e-03	8.0e-06

surface, were able to capture the marked variation of the widths of $6\nu_{OH}$ with total angular momentum. A simple model was also reviewed to rationalize this variation. Widths of the higher energy resonances $7\nu_{OH}$ and $8\nu_{OH}$ resonances of non-rotating HOCl were reported using the same potential energy surface. The calculated widths are approximately 0.01 and 0.6 cm^{-1}, respectively, in good agreement with recent experiments of Callegari *et al.* These widths are significantly larger than the one measured and calculated previously for $6\nu_{OH}$. The large increase of these widths is not unexpected and is presumably due to both an increase in the density of states, and coupling, with increasing energy. Finally, limited calculations of resonance widths were reported for HO^{37}Cl($6\nu_{OH}$,J,K) and found to significantly smaller than those for HO^{35}Cl.

Acknowledgments The Department of Energy (DE-FG02-97ER14782) is gratefully acknowledged for financial support. We thank Andreas Callegari and Thomas Rizzo for correspondence and for sending results of their experiments. We also thank Reinhard Schinke and Amit Sinha for helpful correspondance.

References

1. See for example, Baer, T.; Hase, W. L. *Unimolecular Reaction Dynamics*; Oxford, New York,1996;
2. Hernandez, R.; Miller, W. H.; Moore, C. B.; Polik, W. F. *J. Chem. Phys.* **1993**, *99* 950.
3. Callegari, A; Rebenstein, J; Muenter, J. S.; Jost, R.; Rizzo, T. R. *J. Chem. Phys.* **1999** *111* 123.

4. Callegari, A.; Rebenstein, J; Muenter, J. S.; Jost, R.; Rizzo, T. R. *J.Chem. Phys*. **2000** *112* 2569.
5. Callegari, A.; Rebenstein, J.; Jost, R.; Rizzo, T. R. *J. Chem. Phys.* **1999** *111* 7359.
6. Callegari, A.; Schmid, R.; Rebstein, J.; Theul, P.; Rizzo, T. R. *Phys. Chem. Chem. Phys.* in press.
7. Dutton, G.; Barnes, R. J.; Sinha, A. J. Chem. Phys. 1999 111 4976.
8. Barnes, R. J.; Dutton, G.; Sinha, A. J. Phys. Chem. A 1997 101 8374.
9. Skokov, S.; Bowman, J. M.; Peterson, K. A. *J. Chem. Phys.* **1998**, *109*, 2662.
10. Skokov, S.; Qi, J.; Bowman, J. M.; Yang, C.-Y; Gray, S. K.;. Peterson, K. A.; Mandelshtam, V. A. *J. Chem. Phys.* **1998**, *109*, 10273.
11. Skokov, S.; Bowman, J. M.; Mandelshtam, V. A *Phys. Chem. Chem. Phys.* **1999**, *1*, 1279.
12. Skokov, S.; Bowman, J. M. J. Chem. Phys. 1999 111 4933.
13. Skokov, S.; Peterson, K. A.; Bowman, J. M., Chem. Phys. Lett. 1999, 312, 494.
14. Zou, S.; Skokov, S.; Bowman, J. M. Chem. Phys. Lett. in press.
15. Hauschildt, J.; Wei§, J.; Schinke, R. Z. Phys. Chem, 2000, 214, 609
16. Wei§, J.; Hauschildt, J.; Grebenshchikov, S.; D ren, R.; Schinke, R.; Koput, J.; Stamatiadis, S.; Farantos, S. C. J. Chem. Phys. 2000, 112, 77.
17. Joyeux, M.; Sugny, D.; Lombardi, M.; Jost, R.; Schinke, R.; Skokov, S.; Bowman, J. M. J. Chem. Phys. 2000, 113, 9610.
18. Wei§, J.; Hauschildt, J.; Schinke, R.; Haan, O.; Skokov, S; Bowman, J. M.; Mandelshtam, V. A.; Peterson, K. A. " The unimolecular dissociation of the OH stretching states of HOCl: Comparison with experimental data", *J. Chem. Phys.* to be submitted.
19. See, for example, Gazdy, B.; Bowman, J.M.; Cho, S-W.; Wagner, A.F. J. Chem. Phys. **1991**, *94*, 4192.
20. *Resonances*; Truhlar, D. G., Ed.; American Chemical Society; Washington, DC, **1984**.
21. Jolicard, G.; Leforestier, C.; Austin, E. J. *J. Chem. Phys.* **1988**, *88* ,1026.
22. For a review, see Baer, M. in Adv. Coll. Dyn. and Mol. Vib., Vol IIa, Bowman, J. M., Ed.; JAI, Greenwich, CT, **1992**.
23. MOLPRO is a package of *ab initio* programs written by Werner; H.-J; Knowles P.J.; *et al.*
24. Werner, H.-J.; Knowles, P. J.; *J. Chem. Phys.* **1988**, *89*, 5803.
25. Knowles, P. J.; Werner, H.-J.; *Chem. Phys. Lett.* **1988**, *145*, 514.
26. Blomberg, M. R. A; Siegbahn, P. E. M. *J. Chem. Phys.* **1983**, *78*, 5682.
27. Simons, J. *J. Phys. Chem.* **1989**, *93*, 626.
28. Langhoff, S. R.; Davidson, E. R. *Int. J. Quantum Chem.* **1974**, *8*, 61.
29. Dunning, Jr.;T. H. *J. Chem. Phys.* **1989**, *90*, 1007.
30. Kendall, R. A.; Dunning, Jr.; T. H.; Harrison, R. J. *J. Chem. Phys.* **1992**, *96*, 6796.
31. Woon, D. E.; Dunning, Jr., T. H. *J. Chem. Phys.* **1993**, *98*, 1358.

Downloaded by STANFORD UNIV GREEN LIBR on September 14, 2012 | http://pubs.acs.org
Publication Date: August 14, 2002 | doi: 10.1021/bk-2002-0828.ch017

32. Peterson, K. A.; Woon, D. E.; Dunning, Jr., T. H. *J. Chem. Phys.* **1994**, *100*, 7410.
33. Bittererova, M.; Bowman, J. M.; Peterson, K. A *J. Chem. Phys.* **2000**, *113*, 6186.
34. Bowman, J. M. J. Phys. Chem.A 1998, 102, 3006.
35. Zou, S.; Skokov. S.; Bowman, J. M. *J. Phys. Chem.* **2001**, *105* 2423,
36. A. Sinha, private communication.

Downloaded by STANFORD UNIV GREEN LIBR on September 14, 2012 | http://pubs.acs.org
Publication Date: August 14, 2002 | doi: 10.1021/bk-2002-0828.ch017

Downloaded by UNIV MASSACHUSETTS AMHERST on September 14, 2012 | http://pubs.acs.org
Publication Date: August 14, 2002 | doi: 10.1021/bk-2002-0828.ch018

Chapter 18

The Electronic Adiabatic-to-Diabatic Transformation Matrix and the Irreducible Representation of the Rotation Group

Michael Baer

Department of Applied Physics, Soreq NRC, Yavne 81800, Israel

In this publication we consider the electronically multi-fold degeneracy with the aim of revealing the connection between the adiabatic-to-diabatic transformation matrices and Wigner's irreducible representation of the rotation group. To form the connection we constructed simplified models of two, three and four states, all (electronically) degenerate at a single point, and we employed the relevant non-adiabatic coupling matrices. We found that once these matrices are properly *quantized* (Baer, M. Chem. Phys. 259,123,2000) the adiabatic-to-diabatic transformation matrices and Wigner's $\mathbf{d}^j$–rotation matrices are related via a similarity transformation.

I. Introduction

During the last few years major efforts were made to understand the features of the non-adiabatic coupling terms (NACTs) and their role in the theory of molecular physics (*1-9*). The NACTs owe their existence to the Born-Oppenheimer (BO) assumption which says that the fast moving electrons can be treated separately from the (assumed) slowly moving nuclei (*10,11*). The BO treatment seems to be somewhat artificial and somewhat too mathematical but

In Low-Lying Potential Energy Surfaces; Hoffmann, M., et al.;
ACS Symposium Series; American Chemical Society: Washington, DC, 2002.

Downloaded by UNIV MASSACHUSETTS AMHERST on September 14, 2012 | http://pubs.acs.org
Publication Date: August 14, 2002 | doi: 10.1021/bk-2002-0828.ch018

nevertheless it justified itself in endless experiments in spectroscopy and scattering processes. Accepting the BO separation leads to an unavoidable encounter with these unique unresolved mathematical functions. The NACTs are characterized by two features: They are vectors (in contrast to potentials that are scalars) and they can become singular (in contrast to potentials which cannot). If arranged in matrices they acquire a third interesting feature, namely, the matrices are antisymmetric.

It could be that the NACTs, compared to potential energy surfaces, are less physical and more mathematical objects. This belief can, eventually, be justified if the unique feature of the NACTs namely their being singular were only rarely encountered in *ab-initio* treatments. In fact what happens is that singular NACTs are found all over configuration space (CS) (*9,12*), in large quantities, much more than ever anticipated. The fact that they are so numerous and are expected to play a dominant role in any study related to excited states calls for a better knowledge of these entities and a deeper understanding of their abilities.

The ordinary way to get acquainted with objects like the NACTs is to derive them from first principles, via *ab-initio* calculations (*13-16*), and probe their spatial structure - somewhat reminiscent of the way potential energy surfaces (PES) are studied. However, in contrast to PESs, this way is, by far, not enough. The fact that the NACTs are so frequently singular in addition to being vectors calls for more mathematics oriented approaches in order to understand their role in molecular physics. A very important methodology in this respect is to assume *ad-hoc* models and to look for the features these NACTs have to fulfill in order to be, indeed, appropriate for molecular systems (*17-23*). During the last decade we followed both courses but our main interest was pointing towards the physical-mathematical features of the NACTs (*17,18,20,24-26*). In this process we revealed the necessity of being able to form sub-Hilbert spaces (SHS) in the given region of interest in CS and the fact that the non-adiabatic coupling matrix (NACM) has to be *quantized* for this SHS if they are supposed to have physical significance (*20,25*). This *quantization* requirement enhanced the recognition that the NACMs are closely related, much more than anticipated, to the angular momentum operators. In the present article this approach is pursued. In particular we show, for special cases, that the adiabatic-to-diabatic transformation (ADT) matrix is closely related to Wigner's d^j rotation matrices that form the irreducible representation of the rotation group (*27,28*).

The model we consider for this purpose is a case of N surfaces all degenerate at one single point in CS where the NACM $\boldsymbol{\tau}(s)$ is of the following form (*20*):

$$\boldsymbol{\tau}(s) = g\mathbf{t}(s) \qquad (1)$$

Downloaded by UNIV MASSACHUSETTS AMHERST on September 14, 2012 | http://pubs.acs.org
Publication Date: August 14, 2002 | doi: 10.1021/bk-2002-0828.ch018

Here **g** is a NxN anti-symmetric constant matrix, **t**(s) is a vector and s is a point in CS. In what follows we consider integrals along contours. In particular we shall be interested in the integral:

$$\gamma(s) = \int_0^s d\mathbf{s}' \cdot \mathbf{t}(s') \tag{2}$$

carried out along Γ where both points, i.e. s=0 and s itself are on Γ. Here ds is the vectorial differential length along the contour and the dot stands for a scalar product. Next we introduce the angle α defined as the value of the above integral for a closed contour Γ. Thus:

$$\alpha = \oint_\Gamma d\mathbf{s} \cdot \mathbf{t}(s) \tag{3}$$

In what follows we shall be interested only in contours that surround the above mentioned point of degeneracy. Next it is assumed that for each chosen contour the elements of the **g**-matrix are arranged in such a way that the vector **t**(s) is guaranteed to be normalized as follows:

$$\alpha(\Gamma) = 2\pi \tag{4}$$

This implies that for each such a contour the **g**-matrix may have a different set of constant elements (although the elements of the τ(s)-matrix will be unchanged).

In the present article we derive conditions to be fulfilled by the **g**-matrix elements in order for the τ(s)-matrix to be a matrix of physical meaning. This we do in three steps: (a) first for the general case, next (b) for the τ(s)-matrix defined in Eq. (1), and finally (c) for the three special cases, namely: the two-degenerate case (N=2), the tri-degenerate case (N=3) and the tetra-degenerate case (N=4). Whereas the first two cases were already worked out by us on various occasions (*17,18,20*), the third case is not only new but also presents new interesting features different from the ones obtained in these first two studies.

II. Theoretical Background

In their treatment of the mixed systems of nuclei and electrons Born and Oppenheimer derived the Schroedinger equation (SE) for the nuclei which in present day notation can be written as (*20,25,29*):

$$-\frac{1}{2m}\left(\nabla + \tau\right)^2 \Psi + \left(\mathbf{u} - E\right)\Psi = 0 \tag{5}$$

where ∇ is the usual (mass-scaled) gradient operator, E is the total energy, Ψ is a column matrix which contains the nuclear functions $\{\psi_i;\ i=1,2\ldots\}$, $\mathbf{u}$ is a diagonal matrix which contains the adiabatic potentials and τ is a matrix which contains the above mentioned NACTs:

$$\tau_{ij} = \left\langle \zeta_i \middle| \nabla \zeta_j \right\rangle \tag{6}$$

This derivation holds for a complete Hilbert space but it can be shown to hold also for a SHS of finite dimension M (*20,25*) if and only if certain conditions are fulfilled (*26*).

From Eq. (5) it is noticed that τ, like the grad operator itself, is a momentum operator. With respect to that, a relevant question is: What happens if one integrates over τ along a closed contour Γ? In other words, is there any demand to be associated with the following differential $d\Lambda$:

$$d\Lambda = d\mathbf{s}\cdot\tau\ ? \tag{7}$$

The answer to this question is, as was found out recently (*17,18,20,25*), connected with the diabatic representation. Diabatic potentials can be formed in various ways but the more straightforward way is by employing a set of electronic eigenstates as calculated at one single point in configuration space (CS) (in this sense it can be said that diabatic potentials are a result of the BO treatment). From the way these potentials are calculated it can be seen that the diabatic potentials, just like adiabatic potentials, are single-valued in CS. Having single-valued potentials is an essential requirement because it is not possible to solve the relevant (nuclei) SE unless the potentials are single-valued.

The main drawback of forming the diabatic framework directly from the BO eigenfunctions (*29,30*), is that it does not yield the size of the minimal SHS required in order to obtain converged results for the nuclear (physical) observables. The only way to obtain the size of this reduced SHS is to calculate the NACTs and then to employ the line integral approach (to be discussed later) for this purpose (*24,29,31*).

In what follows we shall briefly describe another way of deriving the diabatic framework but which also yields this above mentioned missing information. It is based on eliminating the τ-matrix from Eq. (5). This is achieved by employing the adiabatic-to-diabatic transformation (ADT) matrix $\mathbf{A}$, which is derived as a solution of the following first order differential equation (*24*):

$$\nabla\mathbf{A} + \tau\mathbf{A} = \mathbf{0} \tag{8}$$

Downloaded by UNIV MASSACHUSETTS AMHERST on September 14, 2012 | http://pubs.acs.org
Publication Date: August 14, 2002 | doi: 10.1021/bk-2002-0828.ch018

Downloaded by UNIV MASSACHUSETTS AMHERST on September 14, 2012 | http://pubs.acs.org
Publication Date: August 14, 2002 | doi: 10.1021/bk-2002-0828.ch018

Once **A** is calculated, the diabatic potential matrix **W** follows from the expression:

$$\mathbf{W} = \mathbf{A}^{\dagger}\mathbf{u}\,\mathbf{A} \qquad (9)$$

where $\mathbf{A}^{\dagger}$is the complex conjugate matrix of **A**. It is important to emphasize that to derive the diabatic potentials this way is as valid as deriving them employing the 'direct' way. This does not mean that the two diabatic matrices are necessarily identical, but it means that they have to be related by a (constant) unitary transformation.

Before considering **W** we shall briefly discuss the conditions for Eq. (8) to have a solution. Being a first order differential equation, Eq. (8) is solved along a contour. The condition for the existence of a solution along this contour is fulfillment of the '**Curl**' condition (*20,24*). Thus if p and q are any two (Cartesian) coordinates then the '**Curl**' condition implies:

$$\frac{\partial}{\partial p}\tau_q - \frac{\partial}{\partial q}\tau_p = \left[\tau_q, \tau_p\right] \qquad (10)$$

This equation can also be written more compactly as:

$$Curl\,\tau = \left[\tau \mathrm{x} \tau\right] \qquad (11)$$

Let us now return to Eqs. (8) and (9). If this procedure is mathematically valid the diabatic potentials produced in this way have to have the same features as those obtained by any other valid procedure. So if a valid procedure leads to single-valued diabatic potentials the same has to apply for the present procedure as expressed by Eqs. (8) and (9). It is noticed that since the *adiabatic* potentials are single-valued by definition, the single-valuedness of **W** depends on the features of the **A**-matrix (see Eq. (9)). It is also obvious that if **A** is single-valued, the same applies to **W** (the sufficient condition for having a single-valued **A**-matrix is the fulfillment of the 'Curl' condition in the region of interest (*20,24*). However it turns out that **A** does not have to be single-valued in order to guarantee the single-valuedness of **W**. In fact it was proved (*20*) that the necessary condition for having single-valued diabatic potentials, along a given contour Γ, is that the τ-matrix fulfill a certain 'quantization' condition. This condition will be discussed next.

Assuming the '**Curl**' condition is fulfilled along Γ then Eq. (8) has a solution, which can be presented in the following way (*31,32*):

$$\mathbf{A}(s, s_0) = \wp \exp\left(-\int_{s_0}^{s} d\mathbf{s}\cdot\tau\right) \qquad (12)$$

where s and s_0 are two points on Γ and the symbol $\wp$ is introduced to indicate that this integral has to be carried out in a given order. In other words, $\wp$ is a path-ordering operator. In presenting $\mathbf{A}(s,s_0)$ in this way it is assumed that the boundary condition for the solution is the unit matrix.

Next we introduce a matrix $\mathbf{D}$ ($\equiv\mathbf{A}(s_0,s_0)$), hence termed the *topological* matrix, defined as (*17,18,20,25*):

$$\mathbf{D} = \wp \exp\left(-\oint_{\Gamma} d\mathbf{s}\cdot\boldsymbol{\tau}\right) \tag{13}$$

It can be proved (*20*) that *the necessary condition for having single-valued diabatic potentials* is that the **D**-matrix fulfill the following commutation relation:

$$[\mathbf{D},\mathbf{u}(s)] = 0 \tag{14}$$

at every point in the region of interest. Since **u**(s) is a diagonal matrix this condition can be satisfied if and only if the **D**-matrix is diagonal with numbers of norm 1, namely, numbers that are either (+1)s or (-1)s. In this sense Eq. (13) is a *quantization* condition. Thus it is indeed a quantization related to the (differential) expression in Eq. (7) but in a more complicated way. In particular the quantized expression is solely dependent on the $\boldsymbol{\tau}$-matrix and is related to a contour constructed by $\oint_{\Gamma} d\mathbf{s}$. The quantization refers to a certain closed contour but in fact, in order for **W** to be single-valued in a given region, Eq. (13) has to be fulfilled along any contour in this region (excluding singular points). It is important to emphasize that different (closed) contours may lead to different quantization conditions, namely, to different sets of (-1)s distributed along the diagonal and/or even to a different number of (-1)s. However it has to be emphasized that the possibly formed diabatic potentials will be the same, independent of the contours that were traced.

III. The Treatment of the Model NACM

For the model NACM as presented in Eq. (1) the **D**-matrix in Eq. (13) can be written as:

$$\mathbf{D} = \exp(-\mathbf{g}\alpha) \tag{15}$$

where α is defined in Eq. (3), or due to the normalization condition imposed on **t**(s) it can also be presented as:

$$\mathbf{D} = \exp(-2\mathbf{g}\pi) \tag{15'}$$

Downloaded by UNIV MASSACHUSETTS AMHERST on September 14, 2012 | http://pubs.acs.org
Publication Date: August 14, 2002 | doi: 10.1021/bk-2002-0828.ch018

Since is **g** a full matrix we still have to evaluate the exponential function. If **G** is the matrix that diagonalizes **g** and if λ_k; k=1,...,N are the corresponding eigenvalues then the D-matrix can be presented as:

$$\mathbf{D} = \mathbf{G}\, \mathbf{E}(\alpha)\, \mathbf{G}^{\dagger} = \mathbf{G}\, \mathbf{E}(2\pi))\, \mathbf{G}^{\dagger} \tag{16}$$

where the matrix E is a diagonal matrix with the elements:

$$E_{jk} = \delta_{jk} \exp(-\lambda_j \alpha) = \delta_{jk} \exp(-2\pi\lambda_j) \tag{17}$$

It might be important to remind the reader that the ADT matrix defined in Eq. (12) can be written in a similar form like Eqs (15) namely:

$$\mathbf{A} = \exp[-g\gamma(s)] \tag{18}$$

or also

$$\mathbf{A} = \mathbf{G}\, \mathbf{E}(\gamma(s))\, \mathbf{G}^{\dagger} \tag{18'}$$

where the **E**-matrix, is similar to the one defined in Eq. (17) except that γ replaces α:

$$E_{jk} = \delta_{jk} \exp(-\lambda_j \gamma(s)) \tag{19}$$

IV. The Treatment of Special Cases

For reasons of convenience and also in order to show the similarities between our various ADT matrices and the Wigner's $\mathbf{d}^j$-matrices we assume the **g**-matrix to have non-zero elements along the two tri-diagonals only (this, comment is not relevant for the two-surface case). Thus we assume for **g** the following structure:

$$g_{jk} = \delta_{jk-1}\, g_j \quad \text{and} \quad g_{jk} = -\delta_{jk+1}\, g_j \tag{20}$$

We shall refer to three special cases, namely, the two-state degeneracy, the tri-state degeneracy and the tetra-state degeneracy. The first two cases were already discussed before and will be mentioned here just for the sake of completeness, but we shall elaborate on the tetra-surface case (N=4) which is presented here for the first time.

Downloaded by UNIV MASSACHUSETTS AMHERST on September 14, 2012 | http://pubs.acs.org
Publication Date: August 14, 2002 | doi: 10.1021/bk-2002-0828.ch018

Downloaded by UNIV MASSACHUSETTS AMHERST on September 14, 2012 | http://pubs.acs.org
Publication Date: August 14, 2002 | doi: 10.1021/bk-2002-0828.ch018

IV.1 The Two-State Degeneracy

The g-matrix in this case is given in the form:

$$\mathbf{g} = \begin{pmatrix} 0 & g_1 \\ -g_1 & 0 \end{pmatrix} \tag{21a}$$

The matrix **G** that diagonalizes g is:

$$\mathbf{G} = \frac{g_1}{\sqrt{2}} \begin{pmatrix} 1 & 1 \\ i & -i \end{pmatrix} \tag{21b}$$

and the corresponding eigenvalues are $\lambda_{1,2} = \pm i g_1$. Substituting Eq. (21b) in Eq. (16) where in Eq. (17) the two λ's are replaced by ± g_1 yields the following **D**-matrix:

$$\mathbf{D} = \begin{pmatrix} \cos(2\pi g_1) & -\sin(2\pi g_1) \\ \sin(2\pi g_1) & \cos(2\pi g_1) \end{pmatrix} \tag{22}$$

Since **D** has to be a diagonal matrix the allowed values for g_1 are:

$$g_1 = n/2 \tag{23}$$

where n is an integer. In case n is an odd integer we encounter the Jahn-Teller *(33-35)* model and in case it is an even integer we have the Renner-Teller model *(36,37)*.

From Eqs. (18), (19) and (23) we get for the ADT matrix:

$$\mathbf{A} = \begin{pmatrix} \cos(\gamma/2) & -\sin(\gamma/2) \\ \sin(\gamma/2) & \cos(\gamma/2) \end{pmatrix} \tag{24}$$

where γ is given in Eq. (3) and is defined in the [0,2π] interval.

IV.2 The Tri-Fold Degeneracy Case

The g-matrix is given in the form:

$$\mathbf{g}=\begin{pmatrix} 0 & g_1 & 0 \\ -g_1 & 0 & g_2 \\ 0 & -g_2 & 0 \end{pmatrix} \tag{25}$$

For this matrix we get the following eigenvalues:

$$\lambda_{1,2}=\pm i\omega\,,\quad \lambda_3=0\,;\quad where\ \omega=\sqrt{g_1^2+g_2^2} \tag{26a}$$

and the corresponding matrix, **G**, that diagonalizes it:

$$\mathbf{G}=\frac{1}{\omega\sqrt{2}}\begin{pmatrix} g_1 & g_1 & g_2\sqrt{2} \\ i\omega & -i\omega & 0 \\ -g_2 & -g_2 & g_1\sqrt{2} \end{pmatrix} \tag{26b}$$

Substituting Eq. (26b) in Eq. (16) where in Eq. (17) the three λ's are replaced by Eq. (26a) yields the following **D**-matrix:

$$\mathbf{D}=\omega^{-2}\begin{pmatrix} g_2^2+g_1^2C & g_1\omega S & g_1g_2(1-C) \\ g_1\omega S & \omega^2C & -g_2\omega S \\ g_1g_2(1-C) & g_2\omega S & g_1^2+g_2^2C \end{pmatrix} \tag{27}$$

where:

$$\mathrm{C}=\cos(2\pi\omega)\quad\text{and}\quad \mathrm{S}=\sin(2\pi\omega) \tag{28}$$

Since the **D**-matrix has to be diagonal this requirement can be fulfilled if and only if (*17,18*)

Downloaded by UNIV MASSACHUSETTS AMHERST on September 14, 2012 | http://pubs.acs.org
Publication Date: August 14, 2002 | doi: 10.1021/bk-2002-0828.ch018

Downloaded by UNIV MASSACHUSETTS AMHERST on September 14, 2012 | http://pubs.acs.org
Publication Date: August 14, 2002 | doi: 10.1021/bk-2002-0828.ch018

$$\omega = n \tag{29}$$

where n is an integer (see also Eq. (26a)). Substituting Eqs. (28) and (29) in Eq. (27) shows that the diagonal of the **D**-matrix contains only (+1)s, which implies that the **D**-matrix is, in fact, a unit matrix.

From Eqs. (18), (19) and (29) we get for the ADT matrix (assuming n=1):

$$A(\gamma) = \begin{pmatrix} g_2^2 + g_1^2 C(\gamma) & g_1 S(\gamma) & g_1 g_2 (1 - C(\gamma)) \\ g_1 S(\gamma) & C(\gamma) & -g_2 S(\gamma) \\ g_1 g_2 (1 - C(\gamma)) & g_2 S(\gamma) & g_1^2 + g_2^2 C(\gamma) \end{pmatrix} \tag{30}$$

where we recall that:

$$\sqrt{g_1^2 + g_2^2} = 1 \tag{31}$$

and

$$C(\gamma) = \cos(\gamma) \quad \text{and} \quad S(\gamma) = \sin(\gamma) \tag{32}$$

Here γ is given in Eq. (3), where we recall that it is defined along the $[0, 2\pi]$ interval.

IV.3 The Tetra-fold Degeneracy Case

The **g**-matrix for this case is:

$$\mathbf{g} = \begin{pmatrix} 0 & g_1 & 0 & 0 \\ -g_1 & 0 & g_2 & 0 \\ 0 & -g_2 & 0 & g_3 \\ 0 & 0 & -g_3 & 0 \end{pmatrix} \tag{33}$$

For this matrix we get the corresponding eigenvalues:

Downloaded by UNIV MASSACHUSETTS AMHERST on September 14, 2012 | http://pubs.acs.org
Publication Date: August 14, 2002 | doi: 10.1021/bk-2002-0828.ch018

$$\begin{aligned}\lambda_{1,2} &= \pm ip \\ \lambda_{3,4} &= \pm iq\end{aligned} \tag{33a}$$

where p and q are:

$$\begin{aligned} p &= \frac{1}{\sqrt{2}}\left(\omega^2 + \sqrt{\omega^4 - 4\left(g_1 g_3\right)^2}\right)^{(1/2)} \\ q &= \frac{1}{\sqrt{2}}\left(\omega^2 - \sqrt{\omega^4 - 4\left(g_1 g_3\right)^2}\right)^{(1/2)} \end{aligned} \tag{35}$$

and

$$\omega = \sqrt{\left(g_1^2 + g_2^2 + g_3^2\right)} \tag{36}$$

It is seen that both p and q are real functions and that p>q.

The corresponding matrix, **G**, that diagonalizes the matrix τ is:

$$\mathbf{G} = \frac{1}{\sigma\sqrt{2}}\begin{pmatrix} \lambda_q\sigma & \lambda_q\sigma & -\lambda_p\sigma & -\lambda_p\sigma \\ -ip\lambda_q & ip\lambda_q & iq\lambda_p & -iq\lambda_p \\ \lambda_p\sigma & \lambda_p\sigma & \lambda_q\sigma & \lambda_q\sigma \\ -iq\lambda_p & iq\lambda_p & -ip\lambda_q & ip\lambda_q \end{pmatrix} \tag{34b}$$

where σ stands for g_1 and λp and λq are defined as:

$$\lambda_p = \sqrt{\frac{p^2 - \sigma^2}{p^2 - q^2}}; \quad \lambda_q = \sqrt{\frac{\sigma^2 - q^2}{p^2 - q^2}} \tag{37}$$

Substituting Eq. (34b) in Eq. (16) where, in Eq. (17), the four λ's are replaced by Eqs. (34a), yields the following **D**-matrix:

$$
\begin{array}{lll}
D_{11} = \lambda_q^2 C_p + \lambda_p^2 C_q; & D_{12} = (p\lambda_q^2 S_p + q\lambda_p^2 S_q)/\sigma & \\
D_{13} = -\lambda_p\, \lambda_q (C_p - C_q); & D_{14} = \lambda_p\, \lambda_q (-qS_p + pS_q)/\sigma & \\
D_{22} = (p^2\lambda_q^2 C_p + q^2\lambda_p^2 C_q)/\sigma^2; & D_{23} = \lambda_p\, \lambda_q\, (pS_p - qS_q)/\sigma & \\
D_{24} = pq\lambda_p\, \lambda_q (C_p - C_q)/\sigma^2; & D_{33} = (\lambda_p^2 C_p + \lambda_q^2 C_q & \\
D_{34} = -(q\lambda_p^2 S_p + p\lambda_q^2 S_q)/\sigma; & D_{44} = (q^2\lambda_p^2 C_p + p^2\lambda_q^2 C_q)/\sigma^2 & \\
D_{21} = -D_{12}; \qquad D_{31} = D_{13}; & & D_{32} = -D_{23}; \\
D_{41} = -D_{14}; \qquad D_{42} = D_{24}; & & D_{43} = -D_{34}
\end{array}
\tag{38}
$$

where:

$$C_p = \cos(2\pi p); \qquad S_p = \sin(2\pi p) \tag{39a}$$

$$C_q = \cos(2\pi q); \qquad S_q = \sin(2\pi q) \tag{39b}$$

The conditions for the **D**-matrix to become diagonal is that p and q fulfill the following conditions:

$$p = n \tag{40a}$$

and

$$q = \ell \tag{40b}$$

where n (>1) and ℓ defined in the range n>ℓ≥0, are allowed to be either integers or half integers but m=n-ℓ can only attain integer values. The difference between the case where n and ℓ are integers and the case where both are half integers is as follows: Going through the expressions in Eq. (38) it is noticed that in the first case all diagonal elements of **D** are (+1) (so that **D** is, in fact, the unit matrix) and in the second case we get that all four diagonal elements are (-1) (so that **D** is, in fact, the minus 4x4 unit matrix).

Since p and q are directly related to the g_j, j=1,2,3 (see Eqs. (35) and (36)) the two conditions in Eqs. (40) imply 'quantization' conditions for the values of the **g**-matrix elements.

It is interesting to note that this is the first time that in the present framework the quantization is formed by *two* quantum numbers: a quantum number n to be termed the principal quantum number and a quantum number ℓ, to be termed the secondary quantum number. This case is reminiscent of the two quantum numbers that characterize the hydrogen atom or the three dimensional harmonic oscillator.

To obtain the ADT we again employ Eqs. (38), where p and q are replaced by n and ℓ respectively and C_p, S_p, C_q and S_q in Eqs. (40) are replaced by:

Downloaded by UNIV MASSACHUSETTS AMHERST on September 14, 2012 | http://pubs.acs.org
Publication Date: August 14, 2002 | doi: 10.1021/bk-2002-0828.ch018

$$C_p = \cos(\gamma p); \qquad S_p = \sin(\gamma p) \tag{41a}$$

$$C_q = \cos(\gamma q); \qquad S_q = \sin(\gamma q) \tag{41b}$$

respectively. Here, as in the previous cases, γ is defined in Eq. (2) and attain values in the interval $[0,2\pi]$.

V. The Adiabatic-to-Diabatic Transformation Matrix and the Wigner Rotation Matrix

The explicit elements of the Wigner's three dimensional rotation matrix $\mathbf{D}^j(\theta)$ are written as (28):

$$D^j_{m'm}(\theta) = \left\langle jm' \middle| R(k,\theta) \middle| jm \right\rangle = e^{-i(m'\alpha+m\gamma)} \left\langle jm' \middle| e^{-i\beta J_y} \middle| jm \right\rangle \tag{42}$$

where $R(k,\theta)$ is the ordinary angular momentum operator in the limit $\theta \to 0$, m and m' are the components of the total angular momentum operator J along the z and the z' axes, respectively, α, β and γ are the corresponding three Euler angles and $| jm\rangle$ is an eigenfunction of the Hamiltonian, of $\mathbf{J}^2$ and of $\mathbf{J}_z$. As a result Eq. (42) will be written as:

$$D^j_{m'm}(\theta) = e^{-i(m'\alpha+m\gamma)} d^j_{m'm}(\beta) \tag{43}$$

It is noticed that if we are interested in finding a relation between the ADT matrix and Wigner's rotation matrices we should concentrate on the $\mathbf{d}^j$-matrix. However before going into a detailed comparison between the two types of matrices it could be of interest to consider the elements of the $\mathbf{J}_y$-matrix, which is responsible for the formation of the $\mathbf{d}^j$ -matrix. Employing Eqs (2.18) and (2.28) of Ref. *28* it can be shown that:

$$\left\langle jm \middle| \mathbf{J}_y \middle| jm+k \right\rangle = \delta_{1k} \frac{1}{2i} \sqrt{(j+m+1)(j-m)} \tag{44a}$$

$$\left\langle jm+k \middle| \mathbf{J}_y \middle| jm \right\rangle = -\delta_{1k} \frac{1}{2i} \sqrt{(j-m+1)(j+m)} \tag{44b}$$

Downloaded by UNIV MASSACHUSETTS AMHERST on September 14, 2012 | http://pubs.acs.org
Publication Date: August 14, 2002 | doi: 10.1021/bk-2002-0828.ch018

Downloaded by UNIV MASSACHUSETTS AMHERST on September 14, 2012 | http://pubs.acs.org
Publication Date: August 14, 2002 | doi: 10.1021/bk-2002-0828.ch018

Now defining $\tilde{\mathbf{J}}_{\mathbf{y}}$ -as:

$$\tilde{\mathbf{J}}_{\mathbf{y}} = i\mathbf{J}_{\mathbf{y}} \tag{45}$$

it is seen that the $\tilde{\mathbf{J}}_{\mathbf{y}}$ -matrix is an antisymmetric matrix just like the **g**-NACM (compare Eq. (20) with Eqs. (44) and (45)). Moreover since the $\mathbf{d}^{\mathbf{j}}$ -matrix can be defined as:

$$\mathbf{d}^{\mathbf{j}}(\beta)= \exp(-i\beta Jy) = \exp(\beta\, \tilde{\mathbf{J}}_{\mathbf{y}}) \tag{46}$$

it is expected that the $\mathbf{d}^{\mathbf{j}}$-matrices belong to the same group as the ADT matrices if the angle β is identified with the phase γ (see Eq. (18)). Next we inspect the three above studied cases:

(1) For the two-state case (i.e. j=1/2), the $\tilde{\mathbf{J}}_{\mathbf{y}}$ -matrix is of the form:

$$\tilde{\mathbf{J}}_{\mathbf{y}} = \frac{1}{2}\begin{pmatrix} 0 & 1 \\ -1 & 0 \end{pmatrix} \tag{47}$$

thus the value of the corresponding g_1 in Eq. (21a) is (1/2) which is its value if in Eq. (23) we assume n=1 (i.e., the Jahn-Teller case).

(2) For the tri-state case (i.e., j=1), the $\tilde{\mathbf{J}}_{\mathbf{y}}$ -matrix is of the form:

$$\tilde{\mathbf{J}}_{\mathbf{y}} = \frac{1}{2}\begin{pmatrix} 0 & \sqrt{2} & 0 \\ -\sqrt{2} & 0 & \sqrt{2} \\ 0 & -\sqrt{2} & 0 \end{pmatrix} \tag{48}$$

Comparing Eqs. (48) and (25) it is noticed that the $\tilde{\mathbf{J}}_{\mathbf{y}}$ -matrix and the g-matrix become identical when

$$g_1 = g_2 = \sqrt{2}/2 \Rightarrow \omega = 1 \tag{49}$$

From Eq. (28) it is noticed that the integer n has to be equal to 1. For this case it is easy to see that **A**(γ) in Eq. (29) becomes identical to $\mathbf{d}^1(\gamma)$, given in Ref. 28.

(3) For the tetra-state case (i.e. j=3/2), the $\tilde{\mathbf{J}}_y$ -matrix is of the form:

$$\tilde{\mathbf{J}}_y = \frac{1}{2}\begin{pmatrix} 0 & \sqrt{3} & 0 & 0 \\ -\sqrt{3} & 0 & 2 & 0 \\ 0 & -2 & 0 & \sqrt{3} \\ 0 & 0 & -\sqrt{3} & 0 \end{pmatrix} \tag{50}$$

Comparing Eqs. (50) and (33) it is noticed that the $\tilde{\mathbf{J}}_y$ -matrix and the g-matrix become identical when

$$g_1 = g_3 = \sqrt{3}/2; \quad g_2 = 1 \tag{51}$$

Employing Eqs. (35) and (36) it can be seen that for this choice the two numbers p and q become:

$$\mathrm{p} = \mathrm{n} = 3/2 \quad \text{and} \quad \mathrm{q} = \ell = 1/2 \tag{52}$$

These possibilities were discussed in the paragraph that follows Eqs. (40). Since Wigner's rotation matrix for this case i.e., $\mathbf{d}^{3/2}(\gamma)$, is usually not given in the text books, it is presented here for the sake of completeness:

$$\mathbf{d}^{\frac{3}{2}}(\gamma) = \begin{pmatrix} C^3 & -\sqrt{3}C^2S & -\sqrt{3}S^2C & S^3 \\ \sqrt{3}C^2S & C(1-3S^2) & -S(1-3C^2) & -\sqrt{3}S^2C \\ -\sqrt{3}S^2C & S(1-3C^2) & C(1-3S^2) & -\sqrt{3}C^2S \\ -S^3 & -\sqrt{3}S^2C & \sqrt{3}C^2S & C^3 \end{pmatrix} \tag{53}$$

where C=cos(γ/2) and S=sin(γ/2).

Downloaded by UNIV MASSACHUSETTS AMHERST on September 14, 2012 | http://pubs.acs.org
Publication Date: August 14, 2002 | doi: 10.1021/bk-2002-0828.ch018

VI. Discussion and Summary

In this publication we considered multi-fold degeneracy with the aim of revealing the connection between the ADT matrices and the irreducible representation of the rotation group. To form the connection we constructed simplified models of two, three and four states, all degenerate at a single point and employed a general but relevant NACMs. This type of models (except the two-state model) may not exist in real chemical systems and if they do they are far from being common. Nevertheless we think that such a study, which also leads to some interesting results, can expose realistic situations which may exist but could not be predicted otherwise.

We know already that the NACMs have to be *quantized* not only because the electronic *ab-initio* programs produce them as such (when calculated for the relevant SHS) *(1-10,38)* but in order to guarantee that the relevant diabatic potentials are singlevalued. In other words this kind of NACM is the only one that will lead to ADT matrices which guarantee *physically correct* diabatic potentials. We showed that the $\tilde{\mathbf{J}}_y$-matrix ($\tilde{\mathbf{J}}_y$ -= i$\mathbf{J}_y$ where $\mathbf{J}_y$ is the y-component of the total angular momentum), which is responsible for the formation of the irreducible group of the rotation matrices, is an antisymmetric matrix just like the NACM. In fact we showed more than that. We found (at least for the 2x2, the 3x3 and the 4x4 matrices) that all relevant NACMs have eigenvalues that turn out to be *identical* to those of the relevant $\tilde{\mathbf{J}}_y$-matrices. Thus, in both cases the eigenvalues of the 2x2 matrices are (1/2,-1/2), those of the 3x3 matrices are (1,0,-1) and those of the 4x4 matrices are (3/2,1/2, -1/2 – 3/2). Assuming that this situation applies for any dimension NxN, this means that all quantized **g**-matrices of the type presented in Eq. (1) and all the $\tilde{\mathbf{J}}_y$-matrices are *similar*, namely, related via an orthogonal transformation. It is straightforward to show that, because of this fact, the same relation holds between the ADT matricx (generated by the NACMs) and Wigner's $\mathbf{d}^j$–rotation matricx namely, they too are related via a similarity transformation.

VI. References

1. Yarkony, D.R. *J. Chem. Phys.* **1996**, *105*, 10456.
2. Chaban, G.; Gordon, M. S.; Yarkony, D.R. *J. Phys. Chem.* **1997,** *101A*, 7953.
3. Yarkony, D.R. *J. Phys. Chem.* **1997** *101*, 4263.

Downloaded by UNIV MASSACHUSETTS AMHERST on September 14, 2012 | http://pubs.acs.org
Publication Date: August 14, 2002 | doi: 10.1021/bk-2002-0828.ch018

4. Yarkony, D.R. *Acc. Chem. Res.* **1998,** *31*, 511.
5. Xu, Z.R.; Baer, M.; Varandas, A.J.C. *J. Chem. Phys.* **2000,** *112*, 2746.
6. Mebel, A.M., Baer, M.; Lin, S.H. *J. Chem. Phys.***2000,** *112,* 10703.
7. Mebel, A.M.; Baer, M.; Rozenbaum, V.M.; Lin, S.H. *Chem. Phys. Lett.* **2001,** *336,* 135
8. Mebel, A.M.; Baer, M.; Lin, S.H. *J. Chem. Phys.*, **2001**, *114*, 5109.
9. Mebel, A.M.; Baer, M.; Yahalom, A.; Englman, R. *J. Chem. Phys.* (in press).
10. Born, M.; Oppenheimer, J.R. *Ann. Phys.(Leipzig),* **1927,** *84*, 457.
11. Born, M.; Huang, K. *Dynamical Theory of Crystal Lattices*, Oxford University: New York, NY, 1954.
12. Haas, Y.; Klessinger, M.; Zilberg, S., Eds.: *Conical Intersections in Photochemistry, Spectroscopy and Chemical Dynamics* (special issue), *Chem Phys.* **2000,** *259,* 121-352.
13. Krishnan, R.; Frisch, M.; Pople, J.A. *J. Chem. Phys.* **1980,** *72,* 4244.
14. Werner, H.-J.; Knowles, P.J. *J. Chem. Phys.* **1985,** *82,* 5033.
15. Saxe, P.; Lengsfield, B.H.; Yarkony, D.R. *Chem. Phys. Lett.*, **1985,** *113*, 159.
16. MOLPRO is a package of *ab initio* programs written by H.-J. Werner and P. J. Knowles, with contributions by J. Almlöf, et. al.
17. Baer, M.; Alijah, A.. *Chem. Phys. Lett.*, **2000,** *319*, 489.
18. Baer, M. *J. Phys. Chem. A,* **2000**, *104*, 3181..
19. Alijah, A.; Baer, M. *J. Phys. Chem. A*, **2000**, *104*, 389.
20. Baer, M. *Chem. Phys.*, **2000,** *259*, 123.
21. Adhikari, S.; Billing, G.D. *J. Chem. Phys.***1999,** *111*, 40.
22. Baer, R.; Charutz, D.; Kosloff, R.; Baer, M. *J. Chem. Phys.* **1996,** *105*, 141.
23. Baer, M. *Chem. Phys. Lett.*, **1975,** *35*, 112.
24. Baer, M.; Lin, S.H.; Alijah, A.; Adhikari, S.; Billing, G.D. *Phys. Rev. A*, **2000,** 62, 032506-1.
25. Baer, M. *Chem. Phys. Lett.* **2000,** *329*, 450.
26. Baer, M. and Englman, R.; *Chem. Phys. Lett.* **2001,** *335*, 85.
27. Wigner, E.P. *Gruppentheorie*; Friedrich Vieweg und Sohn: Braunschweig, Germany, 1931.
28. Rose, M.E. *Elementary Theory of Angular Momentum*; John Wiley & Sons, Inc., New York, NY, 1957; Chapter IV.
29. Pacher, T.; Cederbaum, L.S.; Köppel, H. *Adv. Chem. Phys.* **1993,** *84*, 293.
30. Sidis, V., in Baer, M.; Ng, C.Y., Eds.: *State-to-State Ion Molecule Reaction Dynamics*, (Adv. Chem. Phys. Vol. 82), 1992, Vol. II, p. 73.
31. Baer, M. *Molec. Phys.* **1980,** *40*, 1011.

Downloaded by UNIV MASSACHUSETTS AMHERST on September 14, 2012 | http://pubs.acs.org
Publication Date: August 14, 2002 | doi: 10.1021/bk-2002-0828.ch018

32. Cohen-Tannoudji, C.; Diu, B.; Laloe, F. *Quantum Mechanics,* Herman: Paris, 1977.
33. Jahn, H.A.; Teller, E. *Proc. R. Soc. London, Ser. A*, **1937**, *161*, 220.
34. Englman, R., *The Jahn-Teller Effect in Molecules and Crystals*, Wiley (Interscience): New York, NY, 1972.
35. Baer, M.; Englman, R. *Molec. Phys.* **1992,** *75*, 293.
36. Renner, R. *Z. Phys.* **1934,** *92* 172.
37. Zwanziger, J.W.; Grant, E.R. *J. Chem. Phys* **1987**, *87*, 2954.
38. Baer, M.; Mebel, A.M. *Int. J. Quant. Chem.* (in press).

Downloaded by UNIV MASSACHUSETTS AMHERST on September 14, 2012 | http://pubs.acs.org
Publication Date: August 14, 2002 | doi: 10.1021/bk-2002-0828.ch018

Chapter 19

Spectroscopic Determination of Potential Energy Surfaces for the Out-of-Plane Ring Vibrations of Indan and Related Molecules in Their S_0 and S_1 (Π, Π*) States

J. Laane[1], Z. Arp[1], S. Sakurai[1], K. Morris[1], N. Meinander[1], T. Klots[2],
E. Bondoc[1], K. Haller[1], and J. Choo[1]

[1]Department of Chemistry, Texas A&M University, College Station, TX 77843
[2]SC Johnson Polymer, 8310 16th Street, Sturtevant, WI 53177

Downloaded by STANFORD UNIV GREEN LIBR on September 14, 2012 | http://pubs.acs.org
Publication Date: August 14, 2002 | doi: 10.1021/bk-2002-0828.ch019

The laser induced fluorescence excitation spectra of jet-cooled indan and related moelcules along with their ultraviolet absorption spectra have been used to study their $S_1(\pi,\pi^*)$ excited states. Far-infrared, Raman, and dispersed fluorescence were utilized to obtain the vibrational data for the S ground states. This allowed the potential energy surfaces (PESs) of these molecules to be determined in terms of the ring-puckering and ring-flapping coordinates for both states. These PESs provide barriers to planarity and conformational structures for these bicyclic molecules. Phthalan has a barrier of 35 cm^{-1} in S_0 but no barrier for S_1. Coumaran has an S_0 barrier of 279 cm^{-1}, while 1,3-benzodioxole has barriers of 171 and 264 cm^{-1} for S_0 and S_1, respectively, due to the anomeric effect. The barriers for indan are 1077 cm^{-1} for S_0 and 698 cm^{-1} for S_0. *Ab initio* calculations in general provide good barrier values for the ground state.

In Low-Lying Potential Energy Surfaces; Hoffmann, M., et al.;
ACS Symposium Series; American Chemical Society: Washington, DC, 2002.

Introduction

Conformational changes in molecules often proceed along vibrational pathways. In selected cases these pathways can be represented by one- or two-dimensional vibrational potential energy surfaces (PESs). In our laboratory we have for many years investigated the PESs of cyclic and bicyclic molecules in their electronic ground states using far-infrared and Raman spectroscopy.[1-5] In recent years we have also used fluorescence spectra of jet-cooled molecules and ultra-violet absorption spectra to determine the PESs in electronic excited states.[3-5] In the present paper we present our results for the ground (S_0) and excited [$S_1(\pi,\pi^*)$] electronic states of several molecules in the indan family which are shown in Scheme I.

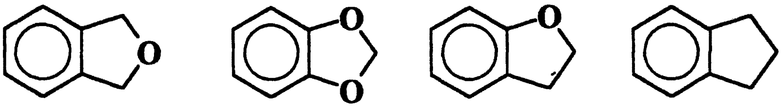

PHT **BZD** **COU** **IND**

Scheme I.

Each of these molecules possesses three low-frequency out-of-plane vibrations involving the five-membered ring and these are shown in Figure 1 for indan.

Each of these vibrations has a vibrational frequency below 300 cm^{-1}. As we shall see, these molecules are often puckered so that the ring-puckering vibration υ_P can be used to represent the conformational changes when the molecule converts from one puckered structure to the other. During the process the molecule passes through the higher energy planar configuration. These molecules may also have energy minima corresponding to a small amount of flapping, but this is generally much less than the puckering. However, since both υ_P and υ_F are of large-amplitude, have low frequencies, and have the same symmetry, these vibrations interact very strongly and a two-dimensional analysis is desirable for analyzing the conformational processes. Since the ring twisting is of a different symmetry species (A_2), interactions with these motion can typically be neglected.

We employ several spectroscopic methods to determine the vibrational quantum states for both the electronic ground and excited states. The transitions

Downloaded by STANFORD UNIV GREEN LIBR on September 14, 2012 | http://pubs.acs.org
Publication Date: August 14, 2002 | doi: 10.1021/bk-2002-0828.ch019

Downloaded by STANFORD UNIV GREEN LIBR on September 14, 2012 | http://pubs.acs.org
Publication Date: August 14, 2002 | doi: 10.1021/bk-2002-0828.ch019

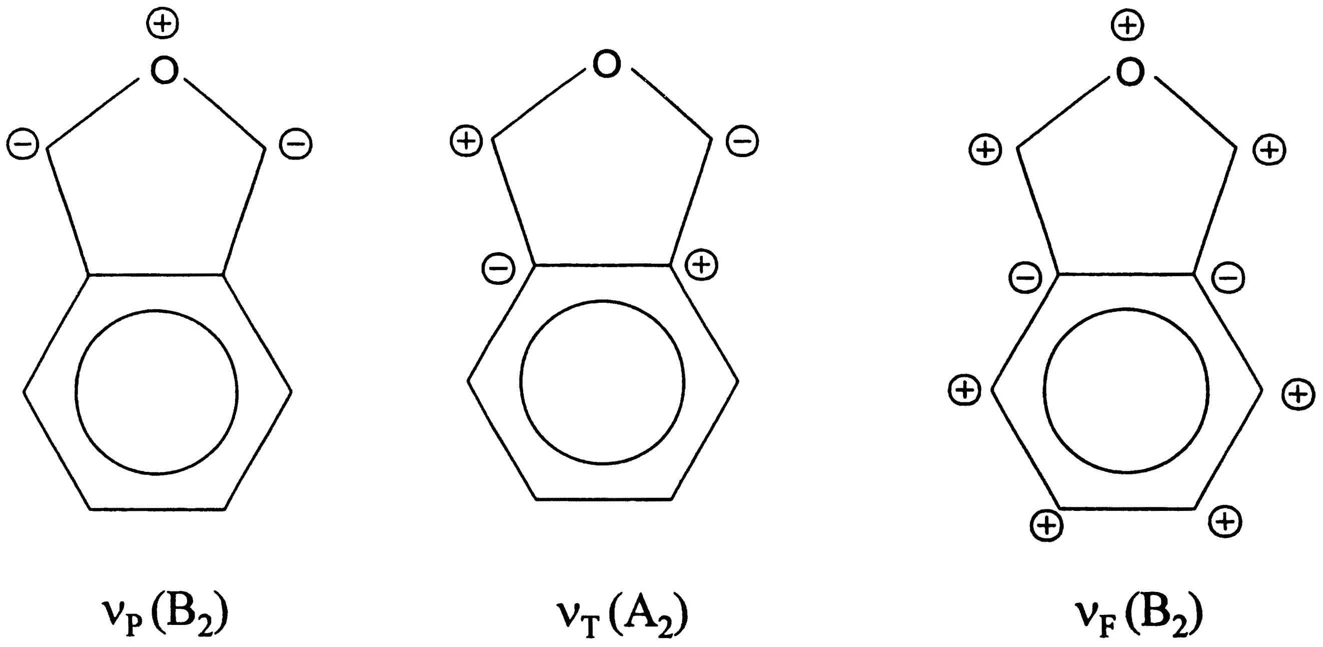

Figure 1. Out-of-plane ring vibrations of indan. + indicates motion out of the page (xz plane); - indicates motion into the page.

Downloaded by STANFORD UNIV GREEN LIBR on September 14, 2012 | http://pubs.acs.org
Publication Date: August 14, 2002 | doi: 10.1021/bk-2002-0828.ch019

involved are shown in Figure 2 for the ring-puckering states of phthalan (PHT). Far-infrared absorption spectra can be used to study the single ($\Delta v_P = 1$) and triple (and sometimes double) quantum jumps of the ring-puckering vibrations in S_0 along with transitions involving the ring-flapping quantum states of the right symmetry (A_1 or B_2 for indan). In the vapor-phase Raman spectra, recorded for samples which have been heated to increase their vapor pressure, the totally symmetric transitions are almost always the only ones observed and these involve $\Delta v_P = 2$. Laser induced fluorescence (LIF) of molecules cooled in a supersonic jet provides an excellent method for determining the vibronic levels in the S_1 electronic excited state. By tuning the laser through the ultraviolet region, fluorescence excitation spectra (FES) are produced whenever the laser frequency matches the energy difference between the ground state and a vibronic level. The selection rule for these transitions is typically $\Delta v_P = 0,2,4...$ The LIF can also be used to produce single vibrational level fluorescence (SVLF) by examining the frequencies of the emitted fluorescence. These transitions from a specific vibronic level terminate on S_0 vibrational levels and generally also require that $\Delta v_P = 0,2,4....$ The SVLF data is helpful in confirming the ground state (S_0) assignments. Ultraviolet absorption data are also invaluable in complementing the LIF data. These are recorded at room temperature and follow the same selection rules as LIF but many more transition frequencies can be observed since many of the S_0 vibrational quantum states are significantly populated. Without the LIF spectra, the ultraviolet absorption spectra are too complex to be interpreted correctly. Together with the simpler LIF spectra, however, the ultraviolet data can be used to determine many additional vibronic levels in the S_1 excited state. The experimental methods for collecting spectra have been described elsewhere.[1-5,12-14]

Theory

Figure 3 shows the definition of the puckering (x) and flapping (τ) vibrational coordinates for the indan family of molecules. Atoms 1 to 5 are part of the five-membered ring, atoms 4 and 5 are common to both rings, and the benzene ring on the left is assumed to be rigid. The angle bisector model,[1-5] where CH_2 and CCC angles have common bisectors, has been assumed. The methods for computing the coordinate dependent reduced masses and cross terms for these motions have been described.[6-11] For the two-dimensional computation, the Hamiltonian in terms of x and τ is

$$\begin{aligned}\mathcal{H}(x,\tau) = & -\hbar^2/2\ [\partial/\partial x(g_{44}(x,\tau))\partial/\partial x + \partial/\partial\tau(g_{55}(x,\tau))\partial/\partial\tau \\ & + \partial/\partial x(g_{45}(x,\tau))\partial/\partial\tau\ \partial/\partial\tau(g_{45}(x,\tau))\partial/\partial x] + V(x,\tau)\end{aligned} \qquad (1)$$

Downloaded by STANFORD UNIV GREEN LIBR on September 14, 2012 | http://pubs.acs.org
Publication Date: August 14, 2002 | doi: 10.1021/bk-2002-0828.ch019

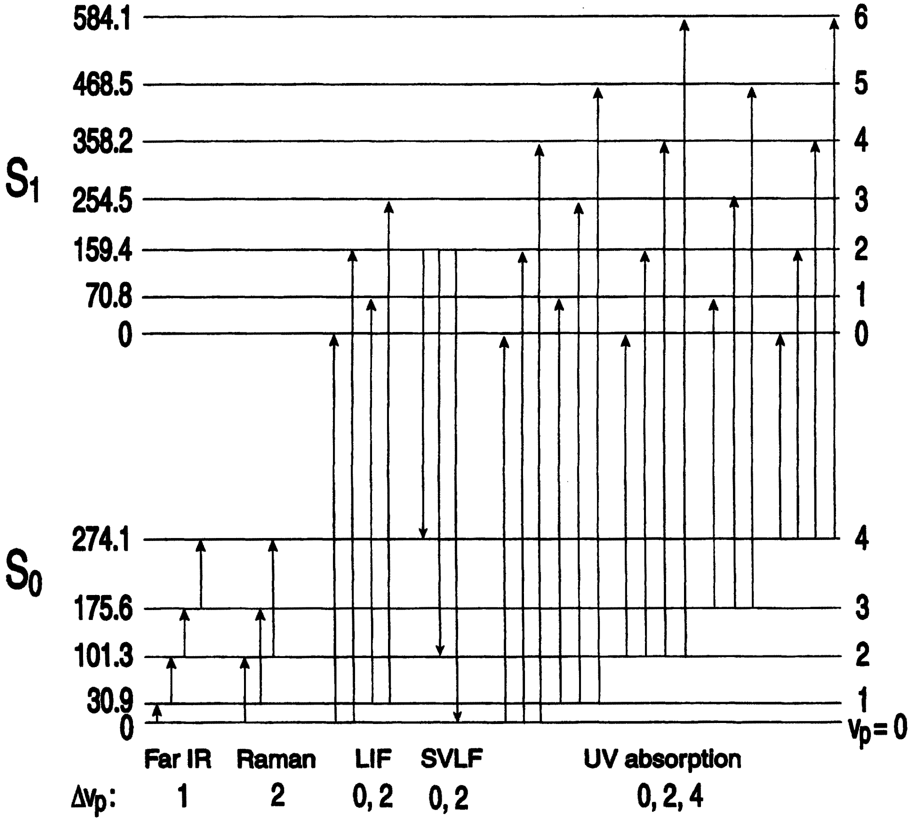
S_1
584.1
468.5
358.2
254.5
159.4
70.8
0
6
5
4
3
2
1
0
S_0
274.1
175.6
101.3
30.9
0
4
3
2
1
$v_p = 0$
Far IR
Raman
LIF
SVLF
UV absorption
Δv_p:
1
2
0, 2
0, 2
0, 2, 4

Figure 2. Spectroscopic transitions for the ground and excited states of phthalan (PHT) and related molecules in the indan family.

Downloaded by STANFORD UNIV GREEN LIBR on September 14, 2012 | http://pubs.acs.org
Publication Date: August 14, 2002 | doi: 10.1021/bk-2002-0828.ch019

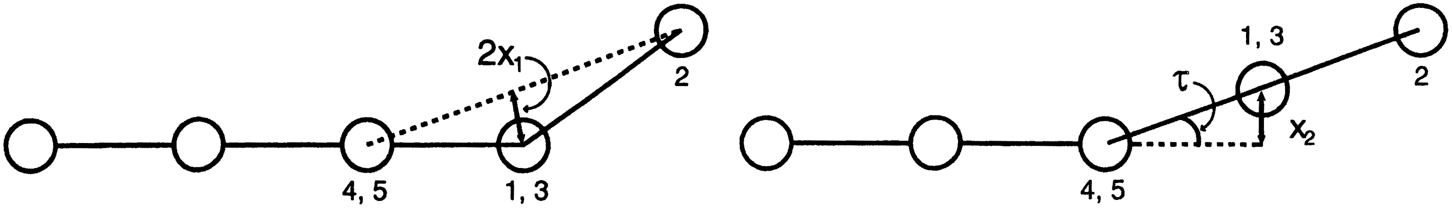

Figure 3. Definition for the puckering (x) and flapping (τ) vibrational coordinates.

where g_{44} and g_{55} are the kinetic energy expressions (reciprocal reduced masses) for the ring-puckering and ring-flapping, respectively. The g_{45} expression is the kinetic interaction term. The kinetic energy expressions are coordinate dependent since the reduced mass changes with the amount of puckering and flapping. Figure 4 shows g_{45} as a function of both x and τ, for 1,3-benzodioxole and the coordinate dependence can be seen to be substantial. The potential energy generally has the form

$$V(x,\tau) = a_1x^4 + b_1x^2 + a_2\tau^4 + b_2\tau^2 + cx^2\tau^2 \qquad (2)$$

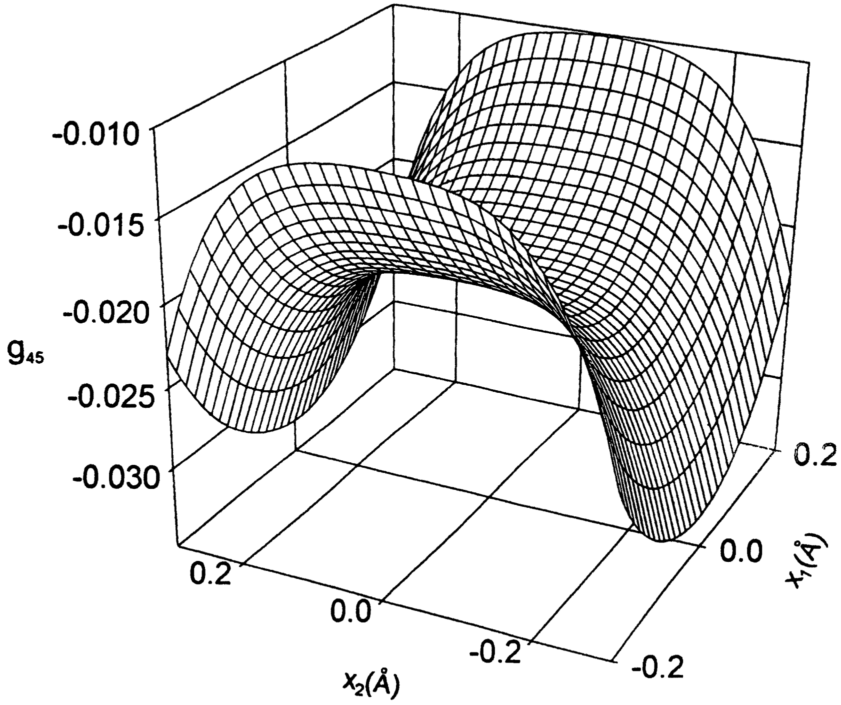

Figure 4. Kinetic energy function for the cross term (g_{45}) of 1,3-benzodioxole in terms of x and τ.

Downloaded by STANFORD UNIV GREEN LIBR on September 14, 2012 | http://pubs.acs.org
Publication Date: August 14, 2002 | doi: 10.1021/bk-2002-0828.ch019

Results and Discussion

The far-infrared spectrum of coumaran (COU),[15] which is shown in Figure 5, very nicely demonstrates how the spectroscopic data is utilized to determine the quantum states for the puckering and flapping vibrations. In the figure the puckering transitions are labeled. Most of these are for the flapping vibrational ground state ($v_F = 0$), but those with primes are for the transitions with $v_F = 1$. In the flapping excited state, the puckering frequencies are shifted considerably (127.8 → 133.4, 3.2 →2.7, 37.0 →32.5 cm^{-1}, etc.). This reflects a moderately large interaction between υ_P and υ_F. Nonetheless, a one-dimensional potential energy function [ignoring the kinetic and potential energy interactions in Eqs. (1) and (2)] of the form

$$V(cm^{-1}) = 7.92 \times 10^5 x^4 - 2.99 \times 10^4 x^2 \qquad (3)$$

where x is in Å, nicely reproduces the observed spectral frequencies. Figure 6 shows this function along with the observed transitions. The barrier to planarity

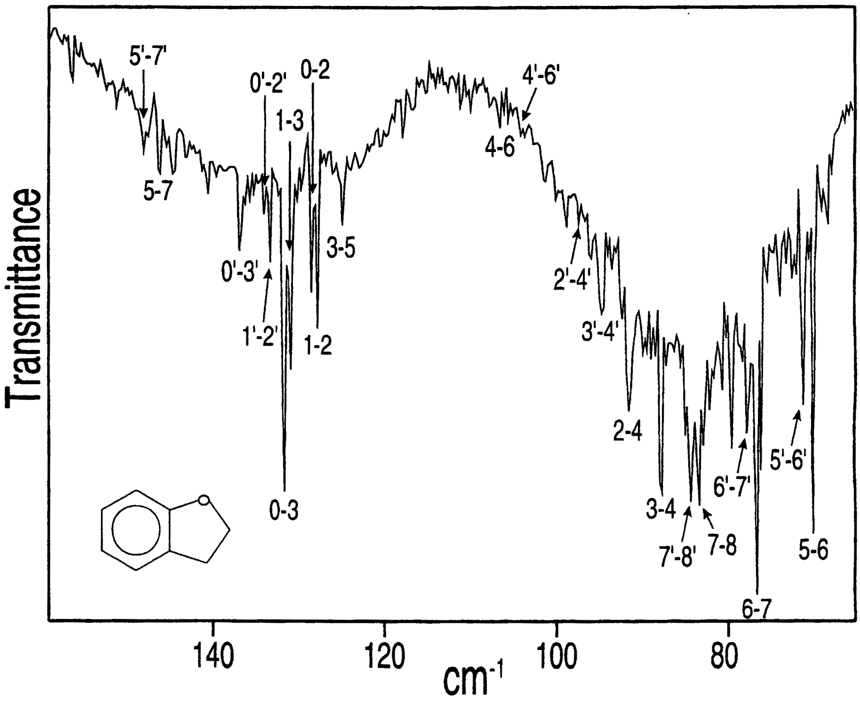

Figure 5. Far-infrared spectrum of coumaran.

Downloaded by STANFORD UNIV GREEN LIBR on September 14, 2012 | http://pubs.acs.org
Publication Date: August 14, 2002 | doi: 10.1021/bk-2002-0828.ch019

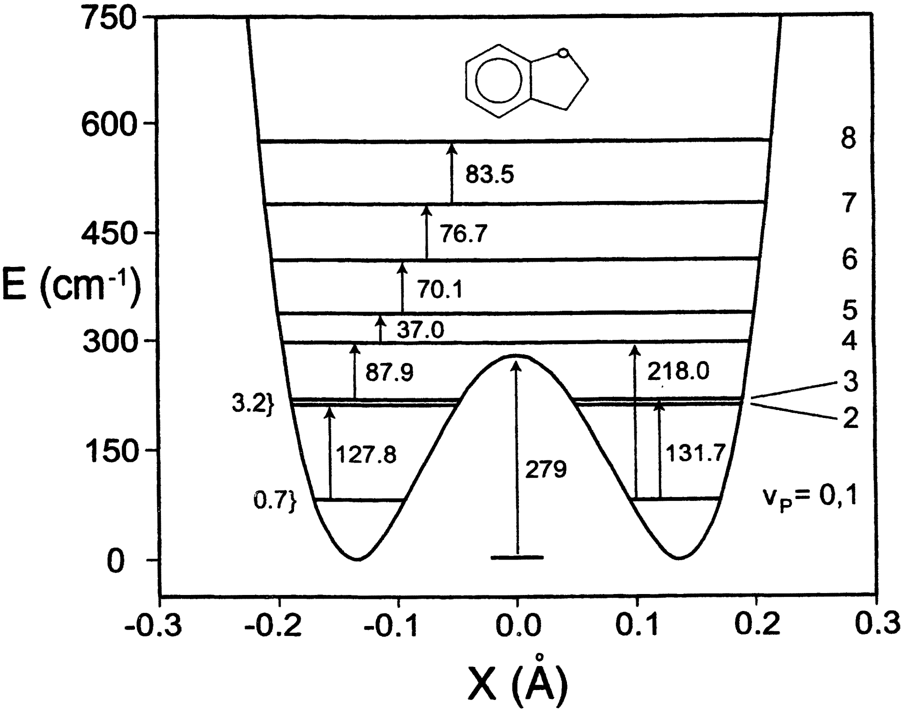

Figure 6. One-dimensional potential energy function for the ring-puckering of coumaran.

is 279 cm^{-1} (0.80 kcal/mole) and the energy minima correspond to x = ± 0.14 Å or dihedral angles of ± 30°. The more complex two-dimensional analysis accounts for the puckering/flapping interaction but results in essentially the same barrier and dihedral angles.[15] Studies of coumaran in its $S_1(\pi,\pi^*)$ are underway but have been complicated by apparent dimer formation.

The far-infrared spectrum of phthalan (PHT)[16] is quite irregular and can not be fitted well using a one-dimensional potential energy function. It has three low-frequency bands between 30 and 35 cm^{-1}, a large group of bands between 65 and 80 cm^{-1}, and another large group of bands between 90 and 110 cm^{-1}. Many hot bands involving the ring-flapping excited states v_F = 1 and 2 states are also present between 210 and 235 cm^{-1}. While the puckering levels change only somewhat in the v_F = 1 and 2 states, the irregular pattern (74.3, 98.5, 93.2, 100.6) can not at all be accounted for without the utilization of the two-dimensional model [Eqs. (1) and (2)] that includes a large kinetic energy interaction through the g_{45} term. However, use of this two-dimensional PES results in an excellent fit to the experimental data and shows that a tiny barrier to planarity of 35 cm^{-1} is present.[17] This is less than the zero-point energy. The $S_1(\pi,\pi^*)$ excited state of

Downloaded by STANFORD UNIV GREEN LIBR on September 14, 2012 | http://pubs.acs.org
Publication Date: August 14, 2002 | doi: 10.1021/bk-2002-0828.ch019

phthalan was also studied using FES and ultraviolet absorption spectroscopy. Figure 7 shows the π and π* orbitals of phthalan correlated to those of benzene. The S_1 state arises from the $B_2 \rightarrow B_1$ electronic transition at 37,034.2 cm^{-1}. The S_1 energies of the vibronic levels (Figure 2 shows some of the levels) were used to obtain the PES for the excited state, and this has the form

$$V\ (cm^{-1}) = 7.96 \times 10^5 x^4 + 4.09 \times 10^3 \tau^2 + 1.44 \times 10^5 x^2 \tau^2. \qquad (4)$$

This surface, unlike the ground state, has no barrier to planarity and is stiffer along the puckering coordinate. This is shown in Figure 8 where the one-dimensional slices of the two-dimensional surfaces for the S_0 and S_1 states are compared (τ has been set to zero). The puckering energy levels for the S_1 state for

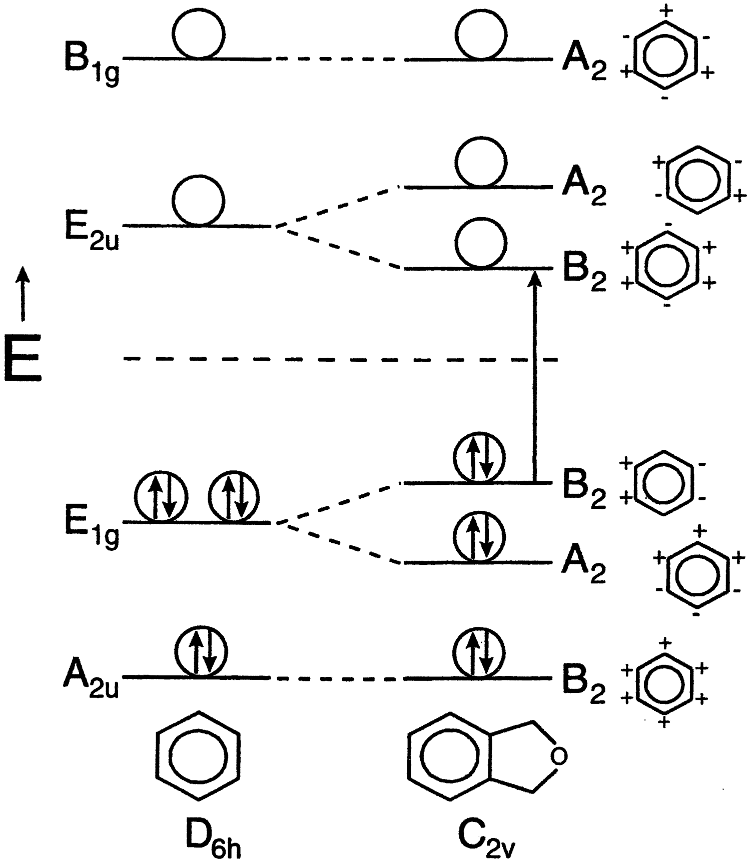

Figure 7. Molecular orbitals for phthalan and the electronic transition producing the $S_1(\pi, \pi^*)$ state. The correlation to benzene orbitals is shown.

Downloaded by STANFORD UNIV GREEN LIBR on September 14, 2012 | http://pubs.acs.org
Publication Date: August 14, 2002 | doi: 10.1021/bk-2002-0828.ch019

Downloaded by STANFORD UNIV GREEN LIBR on September 14, 2012 | http://pubs.acs.org
Publication Date: August 14, 2002 | doi: 10.1021/bk-2002-0828.ch019

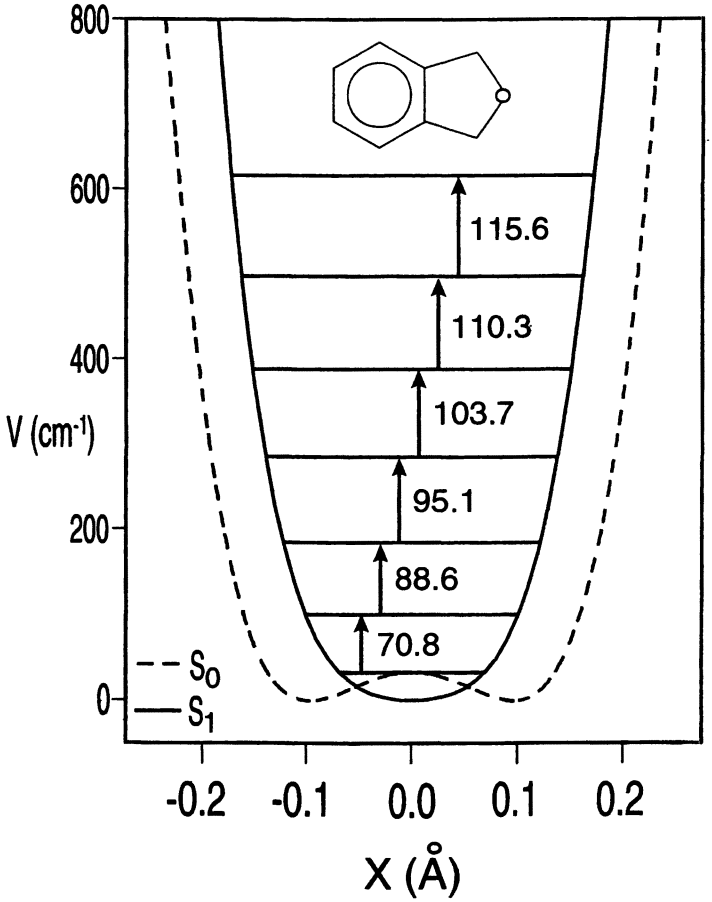

Figure 8. Potential energy along the ring-puckering coordinate fo the ground (S_0) and excited states $S_1(\pi, \pi^*)$] of phthalan.

$v_F = 0$ are also shown. The PES along the flapping coordinate has the expected decrease in stiffness reflecting the decreased π bonding of the benzene ring. The results for both the ground and excited electronic states demonstrate that he kinetic energy interaction plays a major role in determining the nature of the puckering levels. The potential energy interaction term is not significant for the S_0 state but increases in magnitude for $S_1(\pi,\pi^*)$.

Of this group of molecules, the investigation of 1,3-benzodioxole (BZD) proved to be the most interesting due to the presence of the anomeric effect resulting from the -O-CH_2-O- configuration. Previously we have studied 1,3-dioxole,[18] $OCH_2OCH{=}CH_2$, and showed that his molecule was puckered with a barrier to planarity of 325 cm^{-1} arising from the anomeric effect. The far-infrared

In Low-Lying Potential Energy Surfaces; Hoffmann, M., et al.;
ACS Symposium Series; American Chemical Society: Washington, DC, 2002.

spectrum of BZD[19] is very rich and was analyzed with a two-dimensional PES which has a barrier to planarity of 164 cm^{-1}. Its FES and uv absorption spectra[20] are shown in Figure 9 while the vibrational quantum states for the puckering are presented in Figure 10. All the data can be fit very well with separate PESs for the two states. The S_0 surface, with a barrier to planarity of 164 cm^{-1}, and minima at puckering and flapping angles of ± 24° and ∓ 3°, respectively, is shown in Figure 11. The non-planarity clearly arises from the anomeric effect which is generally attributed to orbital interactions between n and σ^* orbitals. Figure 12 shows that this interaction for BZD is most effective when the the five-membered ring is puckered. The BZD barrier of 164 cm^{-1}, however, is less than expected based on the 1,3-dioxole results (325 cm^{-1} barrier). This suggests that the benzene ring π orbitals are competing to interact with the non-bonded orbitals on the oxygen atoms, thereby decreasing the anomeric effect. If this is the case, then the disruption of the π bonding on the benzene ring by a $\pi \rightarrow \pi^*$ transition should decrease the suppression of the anomeric effect and the barrier in the $S_1(\pi,\pi^*)$ state should increase. This is indeed the case as the barrier in the excited state is

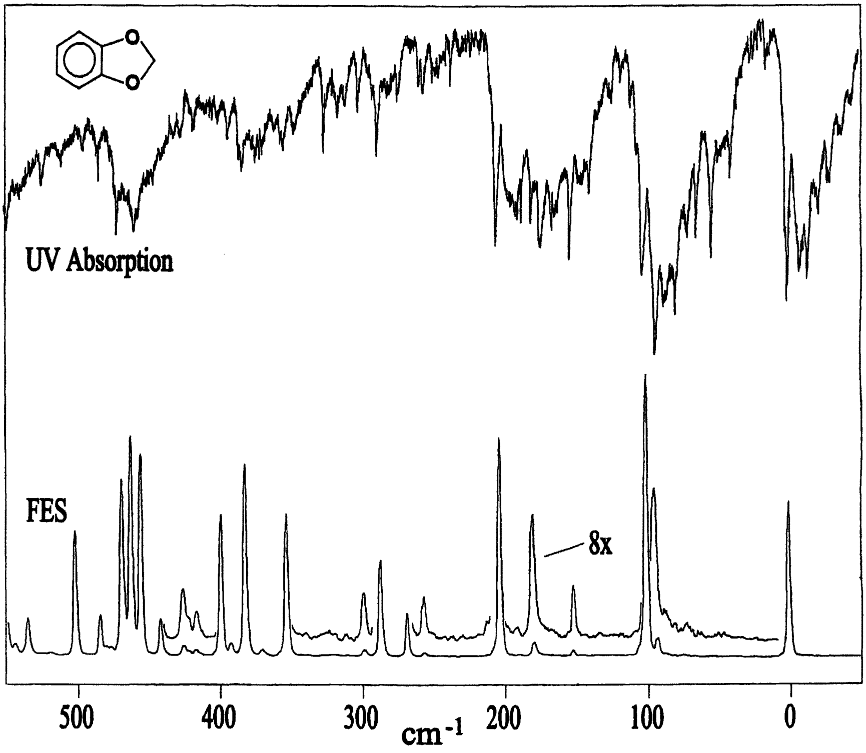

Figure 9. Fluorescence excitation spectra (jet-cooled) and ultraviolet absorption spectra of 1,3-benzodioxole.

Downloaded by STANFORD UNIV GREEN LIBR on September 14, 2012 | http://pubs.acs.org
Publication Date: August 14, 2002 | doi: 10.1021/bk-2002-0828.ch019

Downloaded by STANFORD UNIV GREEN LIBR on September 14, 2012 | http://pubs.acs.org
Publication Date: August 14, 2002 | doi: 10.1021/bk-2002-0828.ch019

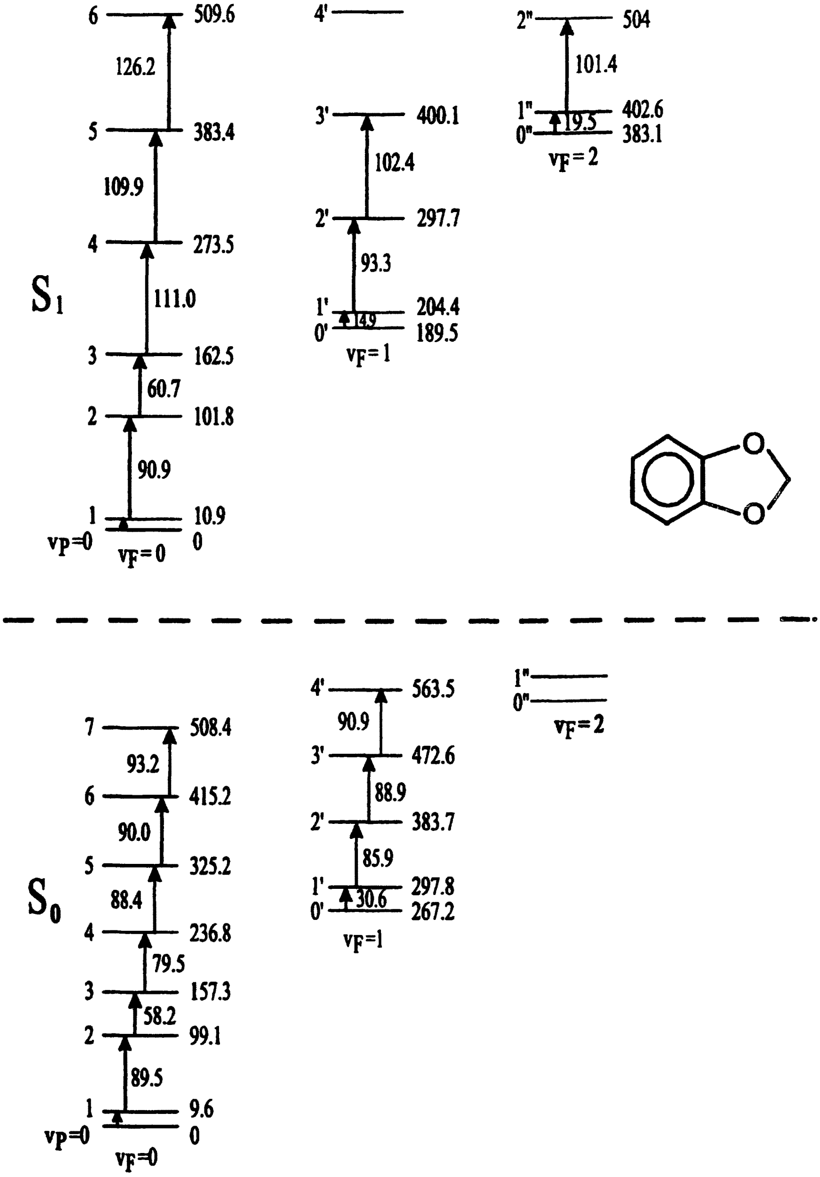
S1
6 509.6
126.2
5 383.4
109.9
4 273.5
111.0
3 162.5
60.7
2 101.8
90.9
1 10.9
vP=0 vF=0 0
4'
3' 400.1
102.4
2' 297.7
93.3
1' 204.4
14.9
0' 189.5
vF=1
2" 504
101.4
1" 402.6
19.5
0" 383.1
vF=2
O
O
S0
7 508.4
93.2
6 415.2
90.0
5 325.2
88.4
4 236.8
79.5
3 157.3
58.2
2 99.1
89.5
1 9.6
vP=0 0
vF=0
4' 563.5
90.9
3' 472.6
88.9
2' 383.7
85.9
1' 297.8
30.6
0' 267.2
vF=1
1"
0"
vF=2

Figure 10. Ring-puckering quantum states of 1,3-benzodioxole in different flapping and electronic states.

Downloaded by STANFORD UNIV GREEN LIBR on September 14, 2012 | http://pubs.acs.org
Publication Date: August 14, 2002 | doi: 10.1021/bk-2002-0828.ch019

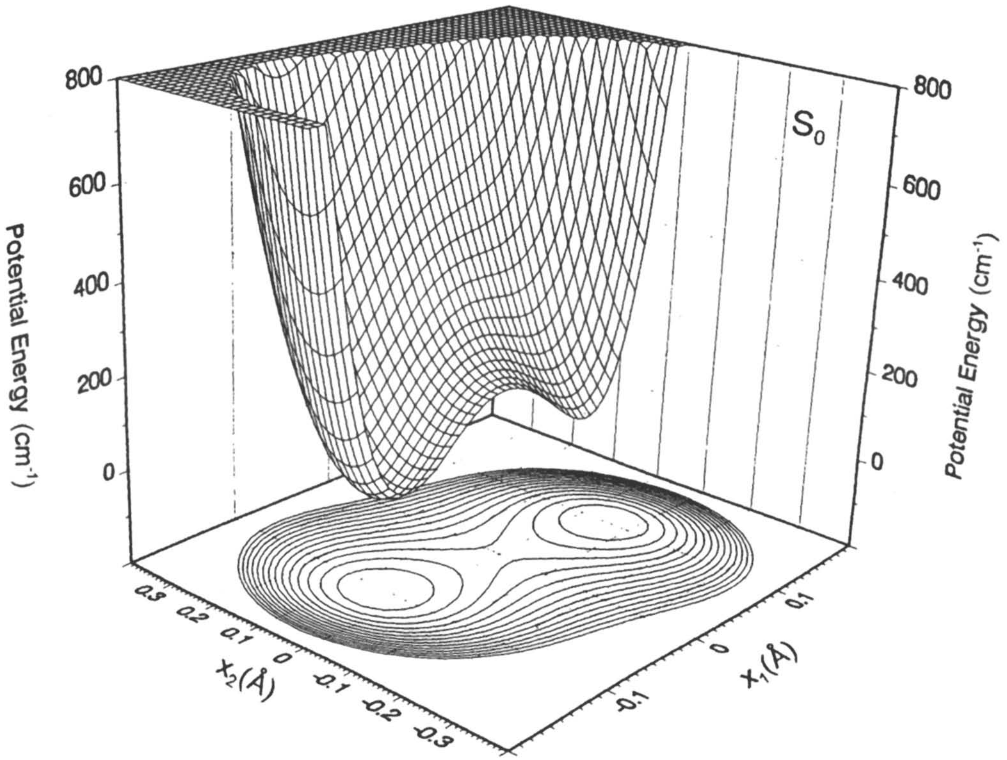

Figure 11. Two-dimensional potential energy surface of 1,3-benzodioxole in its S_0 state.

In Low-Lying Potential Energy Surfaces; Hoffmann, M., et al.;
ACS Symposium Series; American Chemical Society: Washington, DC, 2002.

Downloaded by STANFORD UNIV GREEN LIBR on September 14, 2012 | http://pubs.acs.org
Publication Date: August 14, 2002 | doi: 10.1021/bk-2002-0828.ch019

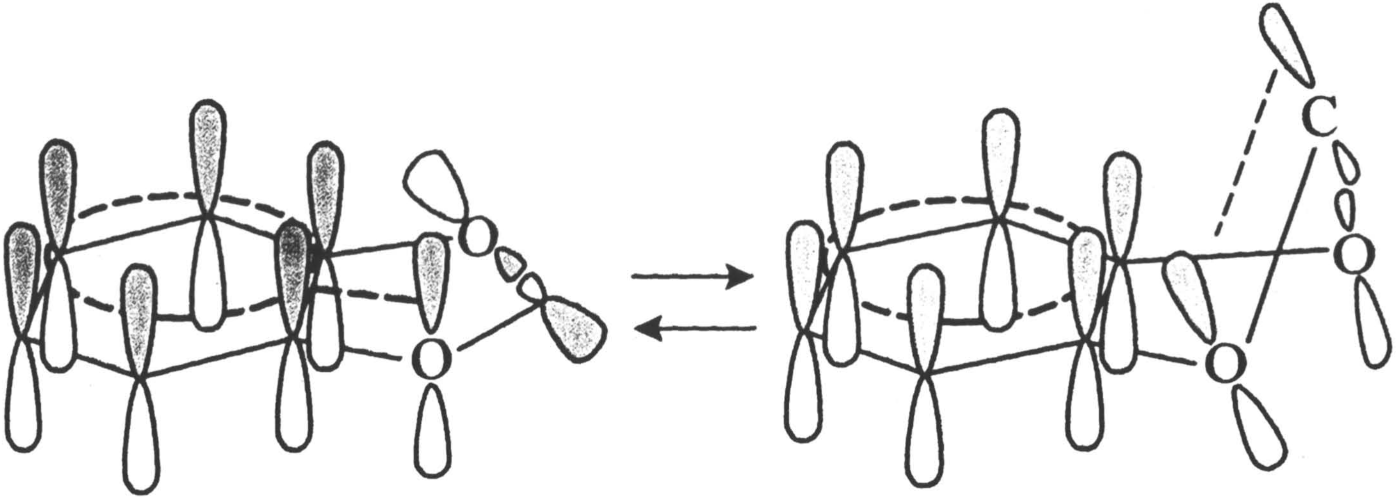

Figure 12. The n-σ^* anomeric interaction for 1,3-benzodioxole. The planar structure (left) has no interaction but puckering (right) allows overlap to occur.

nearly doubled to 264 cm^{-1}. This value is much more in line with the 1,3-dioxole result where there is not competition from benzene ring orbital interactions with the oxygen non-bonded orbitals. Thus, the $\pi \rightarrow \pi^*$ transition clearly decreases the suppression of the anomeric effect.

The parent molecule in this group of molecules is indan. Its far-infrared spectrum shows a group of closely spaced bands originating at 143 cm^{-1} arising from the ring-puckering while bands near 250 cm^{-1} are due to the ring-flapping. The ring-twisting can be seen in the vapor-phase Raman spectrum at 178 cm^{-1}. Without additional information, however, the assignment of the levels is not unambiguous. Figure 13 shows the FES and ultraviolet absorption spectra of indan. The ring-puckering, twisting, and flapping bands can be observed at 116, 137, and 176 cm^{-1} for the $S_1(\pi,\pi^*)$ state, all at lower values reflecting the reduced rigidity of the molecule. Figure 14 shows the dispersed (SVLF) spectra resulting from excitation of the 0_0^0 band. This along with the dispersed spectra from the other vibronic quantum states in S_1 not only provide energy level data for the S_0 ground state, but also help with the assignment of the excited state. Vibronic levels associated with puckering levels in S_1 tend to give rise to fluorescence transitions to puckering levels in S_0, twisting vibronic states fluoresce to twisting S_0 levels, and flapping vibronic states to flapping S_0 levels. This type of analysis then is invaluable for making both the S_0 and $S_1(\pi,\pi^*)$ energy level assignments. Figure 15 presents the one-dimensional potential energy functions for the ring-puckering for both electronic states based on the experimental data. The barrier for the ground state is 1077 cm^{-1}; this drops to 698 cm^{-1} for the excited state. For indan, as for coumaran, the barrier arises from $-CH_2-CH_2-$ torsional interactions which tend to bend the five-membered ring into a non-planar conformation. Since there are three of these interactions as opposed to two for coumaran, the barrier is considerably higher in the ground state.

Ab initio calculations were also carried out to compare predicted barrier heights with experimental values. The results are summarized in Table 1. The agreement for the ground state is remarkably good except for indan where the computed barrier is too low. For excited state calculations the computational methodology is not as well established and the calculated values are less satisfactory.

Conclusions

The spectroscopic methods described here provide a powerful way for accurately determining PESs for both ground and excited electronic states. The work on the indan family of molecules provided a number of unusual results.

Downloaded by STANFORD UNIV GREEN LIBR on September 14, 2012 | http://pubs.acs.org
Publication Date: August 14, 2002 | doi: 10.1021/bk-2002-0828.ch019

Downloaded by STANFORD UNIV GREEN LIBR on September 14, 2012 | http://pubs.acs.org
Publication Date: August 14, 2002 | doi: 10.1021/bk-2002-0828.ch019

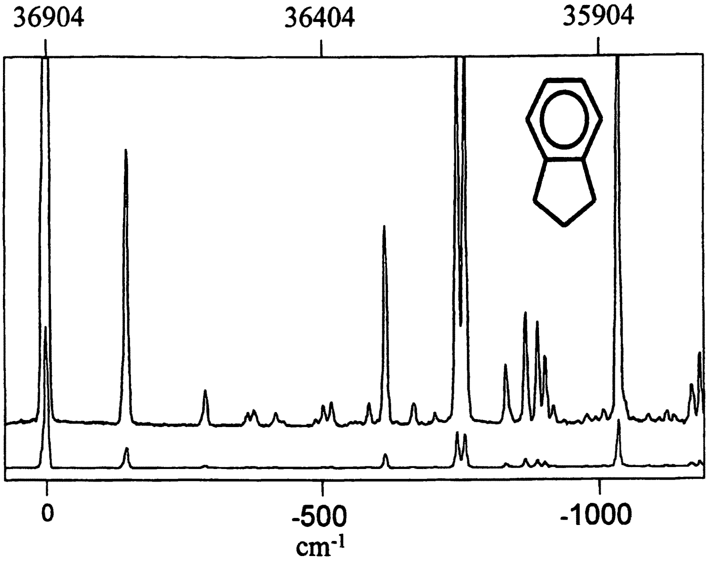

Figure 13. Fluorescence excitation and ultraviolet absorption spectra of indan.

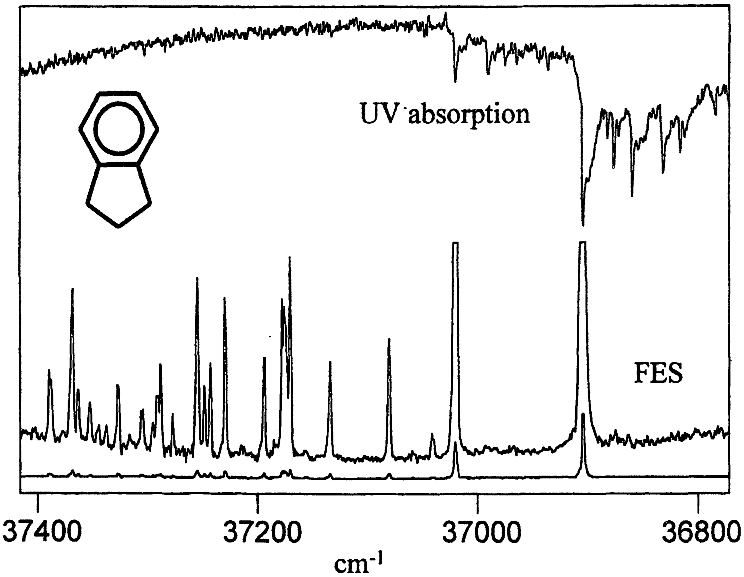

Figure 14. Dispersed fluorescence (SVLF) spectra of jet-cooled indan.

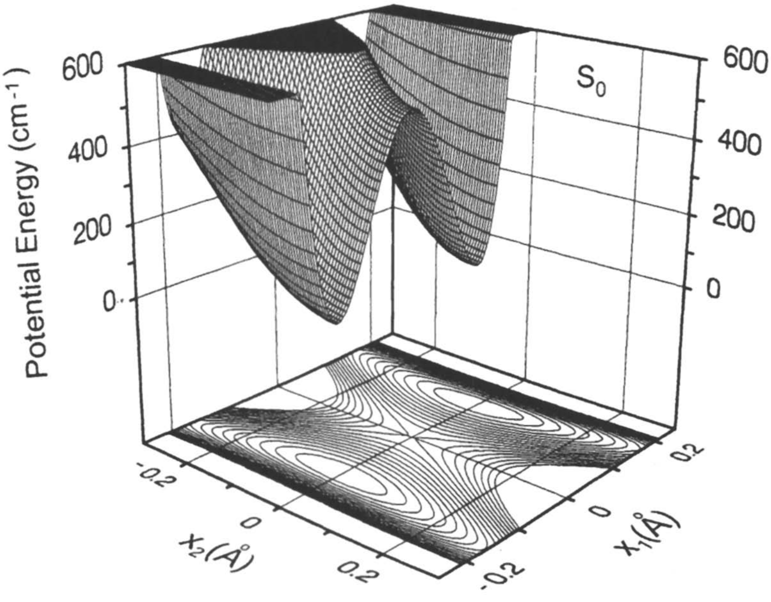

Figure 15. One-dimensional potential energy functions for the ring-puckering of indan in its ground and excited electronic states.

Table I. Comparison of Experimental and *Ab Initio* Barriers (cm^{-1}) for Molecules in the Indan Family

	Ground State		$S_1(\pi,\pi^*)$ Excited State	
Molecule	Exp.	*Ab Initio*^{b}	Exp.	*Ab Initio*
PHT	35	91	0	0
BZD	164	171	264	369
COU	279	258	----	---
IND	488	662	441	841

Ground: MP2/6-31G* basis set
Excited: CIS/6-311+G(2s.p)//CIS/6-31+G* basis set

Downloaded by STANFORD UNIV GREEN LIBR on September 14, 2012 | http://pubs.acs.org
Publication Date: August 14, 2002 | doi: 10.1021/bk-2002-0828.ch019

Phthalan has a low but unexpected barrier to planarity in S_0 which disappears as the five-membered ring becomes more rigid in the excited state. 1,2-Benzodioxole is non-planar in S_0 due to the anomeric effect. In S_1 the anomeric effect and barrier increase as suppression by interactions with the benzene ring is decreased. Indan has a much higher barrier to planarity than the similar cyclopentene. This barrier decreases in S_1. *Ab initio* calculations do a remarkably good job in predicting barriers for the electronic ground sate (less so for indan), but the methodology for excited state calculations is not as well established.

Downloaded by STANFORD UNIV GREEN LIBR on September 14, 2012 | http://pubs.acs.org
Publication Date: August 14, 2002 | doi: 10.1021/bk-2002-0828.ch019

Acknowledgements

The authors wish to thank the National Science Foundation, the Texas Advanced Research Program, and the Robert A. Welch Foundation for financial assistance.

References

1. Laane, J. *Pure & Appl. Chem.* 1987, *59*, 1307.
2. Laane, J. In *Structures and Conformations of Non-Rigid Molecules*, J. Laane, M. Dakkouri, B. van der Veken, and H. Oberhammer, Eds., Amersterdam, 1993; Chapter 4.
3. Laane, J. *Annu. Rev. Phys. Chem.* 1994, *45*, 179.
4. Laane, J. *Int. Rev. Phys. Chem.* 1999, *18*, 301.
5. Laane, J. *J. Phys. Chem,,* 2000, *104*, 7715.
6. Malloy, T. B. *J. Mol. Spectrosc.*, 1972, *44*, 504.
7. Laane, J.; Harthcock, M. A.; Killough, P. M.; Bauman, L. E.; Cooke, J. M. *J. Mol. Spectrosc.*, 1982, *91,* 286.
8. Harthcock, M. A.; Laane, J. *J. Mol. Spectrosc.*, 1982, *91,* 300.
9. Schmude, R. W.; Harthcock, M. A.; Kelly, M. B.; Laane, J. *J. Mol. Spectrosc.*, 1987, *124,* 369.
10. Tecklenburg, M. M.; Laane, J. *J. Mol. Spectrosc.*, 1989, *137*, 65.
11. Strube, M. M.; Laane, J. *J. Mol. Spectrosc.*, 1988, *129,* 126.
12. Cheatham, C. M.; Huang, M.-H.; Laane, J. *J. Mol. Struct.*, 1996, *377,* 93.
13. Cheatham, C. M.; Huang, M.-H.; Meinander, N.; Kelly, M. B.; Haller, K.; Chiang, W.-Y.; Laane, J. *J. Mol. Struct.*, 1996, *377,* 81.
14. Morris, K. Ph.D. Thesis, Texas A&M University, 1999; Morris, K.; Laane, J. to be published.

15. Bondoc, E.; Klots, T.; Laane J. *J. Phys. Chem.*, 2000, *104*, 275.
16. Klots, T.; Sakurai, S.; Laane, J. *J. Chem. Phys.*, 1998, *108*, 3531.
17. Sakurai, S.; Meinander, N.; Laane, J. *J. Chem. Phys.*, **1998,** *108*, 3537.
18. Cortez, E.; Verastegui, R.; Villarreal, J. R.; Laane, J. *J. Amer. Chem. Soc.*, 1993, *115*, 12132.
19. Sakurai, S.; Meinander, N.; Morris, K.; Laane, J., *J. Amer. Chem. Soc.*, **1999,** *121*, 50.
20. Laane, J..; Bondoc, E.; Sakurai, S.; Morris, K.; Meinander, N.; Choo, J. *J. Amer. Chem. Soc.*, **2000,** *122*, 2628.

Downloaded by STANFORD UNIV GREEN LIBR on September 14, 2012 | http://pubs.acs.org
Publication Date: August 14, 2002 | doi: 10.1021/bk-2002-0828.ch019

Downloaded by UNIV MASSACHUSETTS AMHERST on September 14, 2012 | http://pubs.acs.org
Publication Date: August 14, 2002 | doi: 10.1021/bk-2002-0828.ch020

Chapter 20

Semiclassical Time Evolution in the Forward–Backward Stationary-Phase Limit

Nancy Makri[1] and Jiushu Shao[2,3]

**Departments of [1]Chemistry and Physics and [2]Chemistry, University of Illinois,
601 South Goodwin Avenue, Urbana, IL 61801
[3]Current address: State Key Laboratory of Molecular Reaction Dynamics, Institute of Chemistry, Chinese Academy of Sciences, Beijing 100080, China**

Several versions of the time-dependent semiclassical approximation have recently become available as practical tools for calculating dynamical quantities of large molecular systems. These methods are based on the forward-backward idea that combines the quantum evolution in opposite directions of time into a single, consecutive propagation. The forward-backward semiclassical propagator is not highly oscillatory and is thus suitable for numerical evaluation by Monte Carlo methods. The present article reviews a forward-backward phase space formulation of the Heisenberg operator that also eliminates the semiclassical prefactor, leading to a practical tool for calculating observables and time correlation functions.

In Low-Lying Potential Energy Surfaces; Hoffmann, M., et al.;
ACS Symposium Series; American Chemical Society: Washington, DC, 2002.

The last two decades have witnessed spectacular advances in the theoretical description of low-energy electronic states. The Born-Oppenheimer approximation is usually sufficiently accurate in this regime, allowing separation of the problem into (a) the electronic structure calculation, which yields a potential surface on which the nuclear motion takes place, and (b) simulation of the nuclear dynamics on this surface. Essentially every available tool of quantum mechanics has been employed in the development of electronic structure methods, and reliable calculations can now be performed in systems with tens of atoms. Similarly, a host of quantum and classical mechanical ideas have been used to describe the dynamics of the atomic nuclei, although progress in this direction has been hampered by some serious difficulties. Currently, simulations of time-dependent properties in polyatomic molecules, clusters, or condensed phases employ a variety of approximations, which are largely built around variational, perturbation, quantum-classical or semiclassical ideas. While approximate techniques have proven extremely valuable in many situations, their regime of applicability is limited. Perhaps more importantly, checking the accuracy of the results is usually completely impractical, and thus reliability becomes a significant concern.

The fundamental obstacle in the numerical solution of the Schrödinger equation is storage of the multidimensional wavefunction, which occupies a volume that grows exponentially with the number of particles. This limitation is circumvented in the path integral formulation, where quantum mechanical transition amplitudes are expressed as sums over paths with complex-valued phases (1,2). Because of the rapid oscillation of the phase, however, numerical evaluation of the real-time path integral by means of stochastic methods is plagued by severe numerical instabilities (3,4). Moreover, explicit summation over all paths is far from feasible, as their number (if space and time are discretized) increases exponentially with the number of degrees of freedom and the total propagation time. The same phase cancellation problem is encountered in the semiclassical approximation (5,6). In this, the propagator is expressed as a sum of complex-valued amplitudes, but here the summation is restricted to paths that satisfy the classical equations of motion. Significant advances, most notably the formulation of initial value representations (7-16) and the development of filtering procedures (17-22), have enabled calculations in several models and chemical systems (23-35) Further progress has been made recently with the development (36-48) and application (49-54) of forward-backward semiclassical methods. The latter exploit the structure of observables, which involve a pair of time evolution operators that propagate in opposite directions. By combining the two propagators into a single forward-backward step the action integral that gives rise to the semiclassical phase becomes small, leading to a smooth integrand amenable to Monte Carlo methods.

Downloaded by UNIV MASSACHUSETTS AMHERST on September 14, 2012 | http://pubs.acs.org
Publication Date: August 14, 2002 | doi: 10.1021/bk-2002-0828.ch020

Downloaded by UNIV MASSACHUSETTS AMHERST on September 14, 2012 | http://pubs.acs.org
Publication Date: August 14, 2002 | doi: 10.1021/bk-2002-0828.ch020

A practical forward-backward semiclassical dynamics (FBSD) methodology is reviewed in this Chapter. This uses a derivative identity to bring a Heisenberg operator into a form suitable for application of the forward-backward semiclassical approximation. The result is an attractive expression in which the semiclassical prefactor is eliminated and which can also be brought into the form of a quasiclassical average. Combined with suitable representations of the initial density, this version of FBSD provides an efficient tool for following time-dependent observables or correlation functions, offering an accurate description of the dynamics in polyatomic systems.

The Semiclassical Propagator

For a system of n degrees of freedom, the time-dependent semiclassical approximation to the quantum mechanical propagator between two coordinate points takes the form (5,6):

$$\left\langle \mathbf{x}_2 \middle| U(t) \middle| \mathbf{x}_1 \right\rangle_{\mathrm{SC}} = \sum_{\substack{\text{classical} \\ \text{paths } \mathbf{x}_k(t')}} D_{\mathrm{VV}}(\mathbf{x}_1, \mathbf{x}_2) e^{iS[\mathbf{x}_k(t')]/\hbar} e^{-i\mu\pi/2} \tag{1}$$

Here D_{VV} is the semiclassical prefactor given by one of the elements of the stability matrix,

$$D_{\mathrm{VV}} = (2\pi i\hbar)^{-\frac{n}{2}} \left(\det \left| \frac{\partial^2 S}{\partial \mathbf{x}_1 \partial \mathbf{x}_2} \right| \right)^{-\frac{1}{2}} \tag{2}$$

and μ is the Maslov index (55) which supplies the proper phase by keeping track of focusing characteristics of the classical trajectories. The sum in Eq. (1) arises because there are in general multiple solutions to the boundary value problem specified by the endpoint constraints imposed on the classical paths.

Eq. (1) represents the stationary phase approximation to the full quantum mechanical propagator, which in Feynman's path integral formulation takes the form of a sum over all paths. This can be seen directly by realizing that the stationary phase condition amounts precisely to Hamilton's principle, and inclusion of quantum fluctuations within a tube of size $\hbar$ around classical trajectories gives rise to the semiclassical prefactor.

In practical applications, the propagator is usually integrated with respect to both endpoints. Miller has shown (8) that a change of integration variables brings a semiclassical expression in the form of an intial value representation,

Downloaded by UNIV MASSACHUSETTS AMHERST on September 14, 2012 | http://pubs.acs.org
Publication Date: August 14, 2002 | doi: 10.1021/bk-2002-0828.ch020

where relevant classical trajectories are specified by their initial position and momentum, such that one does not need to identify solutions to a double-ended boundary value problem. The optimal initial value representation is in phase space. Herman and Kluk have shown (10,11) that the semiclassical evolution operator can also be brought into the form

$$U(t)=(2\pi\hbar)^{-n}\int d\mathbf{x}_0\int d\mathbf{p}_0\ D_{\mathrm{HK}}(\mathbf{x}_0,\mathbf{p}_0)e^{iS(\mathbf{x}_0,\mathbf{p}_0)/\hbar}\left|g(\mathbf{x}_f,\mathbf{p}_f)\right\rangle\left\langle g(\mathbf{x}_0,\mathbf{p}_0)\right| \quad (3)$$

Here $\mathbf{x}_f,\mathbf{p}_f$ stand for the final coordinate and momentum of a classical trajectory with initial conditions $\mathbf{x}_0,\mathbf{p}_0$ and the coherent state wavefunction is defined as

$$\left\langle\mathbf{x}\middle|g(\mathbf{x}_0,\mathbf{p}_0)\right\rangle=\left(\frac{2}{\pi}\right)^{\frac{n}{4}}(\det\mathbf{\Gamma})^{1/4}\exp\left[-(\mathbf{x}-\mathbf{x}_0)^{\mathrm{T}}\cdot\mathbf{\Gamma}\cdot(\mathbf{x}-\mathbf{x}_0)+\frac{i}{\hbar}\mathbf{p}_0\cdot(\mathbf{x}-\mathbf{x}_0)\right] \quad (4)$$

Finally, the coherent state prefactor is given by the expression

$$D_{\mathrm{HK}}(x_0,p_0)=\sqrt{\det\frac{1}{2}\left(\frac{\partial\mathbf{x}_f}{\partial\mathbf{x}_0}+\frac{\partial\mathbf{p}_f}{\partial\mathbf{p}_0}-2i\hbar\mathbf{\Gamma}\cdot\frac{\partial\mathbf{x}_f}{\partial\mathbf{p}_0}-\frac{1}{2i\hbar}\mathbf{\Gamma}^{-1}\cdot\frac{\partial\mathbf{p}_f}{\partial\mathbf{x}_0}\right)} \quad (5)$$

Other phase space representations are also possible (12,13).

While the above advances bring semiclassical expressions in desirable forms, allowing determination of trajectories from their initial conditions, serious problems arise when these expressions are applied to many-body systems. To obtain observables, it is necessary to evaluate the multidimensional phase space integrals that arise via Monte Carlo methods. This is an extremely demanding task because the integrand is a highly oscillatory function of the integration variables. It is well known that Monte Carlo methods fail to converge in such situations (3,4).

Fortunately, progress can be made because the Heisenberg operator involved in the evolution of time correlation functions or the quantum mechanical density matrix involves not only the forward time evolution operator but also its inverse. It is well understood that a dramatic phase cancellation takes place between these two propagation steps upon integration, and this cancellation is entirely responsible for the failure of Monte Carlo methods. To remedy this situation, Makri and Thompson proposed a forward-backward semiclassical approximation (36) in which the time evolution operator and its inverse are combined into a single semiclassical treatment. This procedure is equivalent to a stationary phase evaluation of the integral between the two propagators. The success of the idea lies in the fact that the relevant trajectories are integrated along a forward-backward time contour and thus the net action tends to be small, leading to a well-behaved integrand.

Originally, FBSD was formulated in the context of the influence functional (2) entering the path integral representation of quantum dynamical quantities, for which the forward-backward approximation is unique (36,38). Miller and coworkers (37,40,43,47,48), as well as our group (39,41,42,44-46) have extended FBSD to time correlation functions. The presence of an arbitrary operator between the forward and backward propagators leads to several distinct versions of FBSD. In the following section we review the derivative form of FBSD obtained by Shao and Makri for general correlation functions (41,42). As trajectories are nearly continuous at the midpoint in time, it is possible (47) to bring the FBSD expression in a form where the semiclassical prefactor is eliminated, and also in the form of a quasiclassical average. These simplifications result from the neglect of quantum interference. While other versions are superior in terms of accuracy, the simplicity and dramatic efficiency attained by the derivative version of FBSD make it presently the method of choice for simulating processes in large clusters or in solution where dephasing interactions are a natural source of decoherence and thus FBSD can be quantitative.

Downloaded by UNIV MASSACHUSETTS AMHERST on September 14, 2012 | http://pubs.acs.org
Publication Date: August 14, 2002 | doi: 10.1021/bk-2002-0828.ch020

Forward-Backward Semiclassical Dynamics Without Prefactors

Systems of many atoms are usually characterized in terms of ensemble-averaged quantities, such as correlation functions or the reduced density matrix. Consider, for concreteness, a correlation function of the type

$$C(t) = \mathrm{Tr}\left(\rho(0) A e^{iHt/\hbar} B e^{-iHt/\hbar}\right) = \mathrm{Tr}\left(\rho(0) A B(t)\right) \tag{1}$$

where $\rho(0)$ is the equilibrium density matrix and A, B are arbitrary operators. The Heisenberg operator $B(t)$ contains two propagators in opposite times and this structure can be exploited to reduce the severity of the sign problem.

A particularly practical expression is obtained by expressing $B(t)$ in the form of a derivative, namely

$$B(t) = -i\frac{\partial}{\partial\mu}\left[e^{iHt/\hbar} e^{i\mu B} e^{iHt/\hbar}\right]_{\mu=0}. \tag{2}$$

Downloaded by UNIV MASSACHUSETTS AMHERST on September 14, 2012 | http://pubs.acs.org
Publication Date: August 14, 2002 | doi: 10.1021/bk-2002-0828.ch020

The product of three exponential operators in this expression can be interpreted as propagation under the time-dependent Hamiltonian (37)

$$\tilde{H}(t') = H - \hbar\mu B\delta(t'-t). \tag{3}$$

Thus, $B(t)$ is approximated by a single semiclassical propagator for the time-dependent Hamiltonian of Eq. (3). The last term of this Hamiltonian imposes discontinuous jumps of the coordinates and momenta of a classical trajectory at the end of the forward propagation time t:

$$\delta\mathbf{x}_t = -\hbar\mu\nabla_{\mathbf{p}_t} B(\mathbf{x}_t,\mathbf{p}_t), \qquad \delta\mathbf{p}_t = \hbar\mu\nabla_{\mathbf{x}_t} B(\mathbf{x}_t,\mathbf{p}_t) \tag{4}$$

$$\delta S = \mathbf{p}_t \cdot \delta\mathbf{x}_t + \hbar\mu B(\mathbf{x}_t,\mathbf{p}_t) \tag{5}$$

Inserting the Herman-Kluk representation of Eq. (2) into the correlation function, we showed in References (41) and (42) that the correlation function can be brought into the form

$$C(t) = -i(2\pi\hbar)^{-n}\int d\mathbf{x}_0 \int d\mathbf{p}_0 \frac{\partial}{\partial\mu}\Big[e^{iS(\mathbf{x}_0,\mathbf{p}_0)/\hbar}\big\langle g(\mathbf{x}_0,\mathbf{p}_0)\big|\rho(0)A\big|g(\mathbf{x}_f,\mathbf{p}_f)\big\rangle\Big]\Big|_{\mu=0} \tag{6}$$

In this, the semiclassical coherent state prefactor has been eliminated. To compensate for its absence, the position, momentum and action jumps arising from the infinitesimal evolution with $\tilde{H}$ have been rescaled. Thus, the trajectories must incur the following increments at time t:

$$\delta\mathbf{q}_t = -\frac{1}{2}\hbar\mu\nabla_{\mathbf{p}_t} B(\mathbf{q}_t,\mathbf{p}_t), \qquad \delta\mathbf{p}_t = \frac{1}{2}\hbar\mu\nabla_{\mathbf{q}_t} B(\mathbf{q}_t,\mathbf{p}_t)$$

$$\delta S = \hbar\mu B(\mathbf{q}_t,\mathbf{p}_t) + \mathbf{p}_t \cdot \delta\mathbf{q}_t. \tag{7}$$

Miller and coworkers have shown (47) that the derivative in the prefactor-free FBSD expression can also be eliminated. Below we generalize their result to a general operator depending on coordinates and/or momenta and a multidimensional Hamiltonian. For this purpose, we rewrite the semiclassical Heisenberg operator as the sum of three terms,

$$B(t) = (2\pi\hbar)^{-n}\int d\mathbf{x}_0 \int d\mathbf{p}_0 (B_1 + B_2 + B_3)\big|g(\mathbf{x}_0,\mathbf{p}_0)\big\rangle\big\langle g(\mathbf{x}_0,\mathbf{p}_0)\big|, \tag{8}$$

Downloaded by UNIV MASSACHUSETTS AMHERST on September 14, 2012 | http://pubs.acs.org
Publication Date: August 14, 2002 | doi: 10.1021/bk-2002-0828.ch020

where B_1, B_2, and B_3 are contributions from the prefactor, the action and the final state respectively, which assume the explicit forms:

$$B_1 = i(\mathbf{x}-\mathbf{x}_0)\cdot\mathbf{\Gamma}\cdot\left.\frac{\partial\mathbf{x}_f}{\partial\mu}\right|_{\mu=0} - \frac{1}{2\hbar}(\mathbf{x}-\mathbf{x}_0)\cdot\left.\frac{\partial\mathbf{p}_f}{\partial\mu}\right|_{\mu=0}, \tag{9}$$

$$B_2 = B(\mathbf{x}_t,\mathbf{p}_t) + \frac{1}{\hbar}\mathbf{p}_0\cdot\left.\frac{\partial\mathbf{x}_f}{\partial\mu}\right|_{\mu=0}, \tag{10}$$

$$B_3 = -2i(\mathbf{x}-\mathbf{x}_0)\cdot\mathbf{\Gamma}\cdot\left.\frac{\partial\mathbf{x}_f}{\partial\mu}\right|_{\mu=0} + \frac{1}{\hbar}(\mathbf{x}-\mathbf{x}_0)\cdot\left.\frac{\partial\mathbf{p}_f}{\partial\mu}\right|_{\mu=0} - \frac{1}{\hbar}\mathbf{p}_0\cdot\left.\frac{\partial\mathbf{x}_f}{\partial\mu}\right|_{\mu=0}. \tag{11}$$

Summing up these contributions yields

$$\begin{aligned} B(t) = (2\pi\hbar)^{-n}\int d\mathbf{x}_0\int d\mathbf{p}_0 \Bigg(& B(\mathbf{x}_t,\mathbf{p}_t) - i(\mathbf{x}-\mathbf{x}_0)\cdot\mathbf{\Gamma}\cdot\left.\frac{\partial\mathbf{x}_f}{\partial\mu}\right|_{\mu=0} \\ & + \frac{1}{2\hbar}(\mathbf{x}-\mathbf{x}_0)\cdot\left.\frac{\partial\mathbf{p}_f}{\partial\mu}\right|_{\mu=0}\Bigg) G(\mathbf{x}_0,\mathbf{p}_0), \end{aligned} \tag{12}$$

where $G(\mathbf{x}_0,\mathbf{p}_0) = |g(\mathbf{x}_0,\mathbf{p}_0)\rangle\langle g(\mathbf{x}_0,\mathbf{p}_0)|$ denotes the coherent state projection operator. Note that $\partial\mathbf{x}_f/\partial\mu = -\hbar\nabla_{\mathbf{p}_0}B(\mathbf{x}_t,\mathbf{p}_t)$ and $\partial\mathbf{p}_f/\partial\mu = \hbar\nabla_{\mathbf{x}_0}B(\mathbf{x}_t,\mathbf{p}_t)$ at $\mu = 0$. Using the relations

$$\nabla_{\mathbf{x}_0}G(\mathbf{x}_0,\mathbf{p}_0) = 2\mathbf{\Gamma}\cdot\left[(\mathbf{x}-\mathbf{x}_0)G(\mathbf{x}_0,\mathbf{p}_0) + G(\mathbf{x}_0,\mathbf{p}_0)(\mathbf{x}-\mathbf{x}_0)\right] \tag{13}$$

and

$$\nabla_{\mathbf{p}_0}G(\mathbf{x}_0,\mathbf{p}_0) = \frac{i}{\hbar}\left[\mathbf{x}G(\mathbf{x}_0,\mathbf{p}_0) - G(\mathbf{x}_0,\mathbf{p}_0)\mathbf{x}\right] \tag{14}$$

and integrating by parts, the above expression can be simplified as

$$\begin{aligned} B(t) = (2\pi\hbar)^{-n}\int d\mathbf{x}_0\int d\mathbf{p}_0 B(\mathbf{x}_t,\mathbf{p}_t)\Big(& [1+\tfrac{1}{2}n]G(\mathbf{x}_0,\mathbf{p}_0) \\ & - 2(\mathbf{x}-\mathbf{x}_0)\cdot\mathbf{\Gamma}\cdot G(\mathbf{x}_0,\mathbf{p}_0)(\mathbf{x}-\mathbf{x}_0)\Big) \end{aligned} \tag{15}$$

Substitution of this result into Eq. (1) leads to the following expression for the correlation function:

$$\begin{aligned} C(t) = (2\pi\hbar)^{-n} \int d\mathbf{x}_0 \int d\mathbf{p}_0 \Big([1+\tfrac{1}{2}n] \Big\langle g_{\mathbf{x}_0,\mathbf{p}_0} \Big| \rho_0 A \Big| g_{\mathbf{x}_0,\mathbf{p}_0} \Big\rangle \\ -2 \Big\langle g_{\mathbf{x}_0,\mathbf{p}_0} \Big| (\mathbf{x}-\mathbf{x}_0)\rho_0 A \cdot (\mathbf{x}-\mathbf{x}_0) \cdot \boldsymbol{\Gamma} \cdot \Big| g_{\mathbf{x}_0,\mathbf{p}_0} \Big\rangle \Big) B(\mathbf{x}_t,\mathbf{p}_t) \end{aligned} \tag{16}$$

Equations (6), (15) and (16) can be viewed as the stationary phase approximation to the conventional semiclassical representation of the Heisenberg operator or the correlation function in which each evolution operator is expressed as a separate Herman-Kluk propagator. The additional stationary phase approximation implicit in these prefactor-free expressions imposes continuity of the trajectories at time *t* (i.e., the discontinuities in Eq. (7) are infinitesimal), eliminating possible cross terms corresponding to distinct forward and backward trajectories. The consequence of this is loss of interference. Indeed, Eq. (16) has the structure of a quasiclassical trajectory average similar to the Wigner formalism (32,56,57) Combined with an accurate treatment of the factors involving the initial density, these expressions provide a rigorous, yet practical way of including quantum effects in classical trajectory simulations. Since the only dynamical quantity entering Eq. (16) is a function of the position and momentum along a classical trajectory, it is a simple matter to evaluate this expression using accurate force fields employed in standard molecular dynamics calculations or obtaining the forces through "on the fly" *ab initio* electronic structure calculations.

Coherent State Density Matrix

Implementation of the FBSD schemes requires knowledge of the initial density matrix in the coherent state representation. Usually, the initial density corresponds either to the ground vibrational state of a polyatomic molecule or a Boltzmann distribution. Below we describe ways of obtaining the coherent state matrix element through closed form expressions or in terms of an imaginary time path integral evaluated along the same Monte Carlo random walk which samples the trajectory initial conditions.

Gaussian Initial State

When the system is initially at zero temperature the harmonic approximation about the potential minimum is often satisfactory. Since the corresponding

Downloaded by UNIV MASSACHUSETTS AMHERST on September 14, 2012 | http://pubs.acs.org
Publication Date: August 14, 2002 | doi: 10.1021/bk-2002-0828.ch020

Downloaded by UNIV MASSACHUSETTS AMHERST on September 14, 2012 | http://pubs.acs.org
Publication Date: August 14, 2002 | doi: 10.1021/bk-2002-0828.ch020

wavefunction is a product of Gaussians in the normal mode representation, the coherent state matrix element involves evaluating a Gaussian integral. For instance, if the initial density operator has the form

$$\rho_0 = |\Phi_0\rangle\langle\Phi_0|$$

where

$$\Phi_0(x) = \left(\frac{2\alpha}{\pi}\right)^{\frac{1}{4}} \exp\left[-\alpha(x-\lambda)^2\right],$$

then one finds

$$\langle g(x_0,p_0)|\rho(0)|g(x_0,p_0)\rangle = 2\frac{\sqrt{\alpha\gamma}}{\alpha+\gamma} \times\exp\left(-\frac{2\alpha\gamma}{\alpha+\gamma}(x_0-\lambda)^2 - \frac{1}{2\hbar^2(\alpha+\gamma)}p_0^2\right) \tag{17}$$

and

$$\langle g(x_0,p_0)|(x-x_0)\rho(0)(x-x_0)|g(x_0,p_0)\rangle = \left[\left(\frac{\alpha}{\alpha+\gamma}\right)^2(\lambda-x_0)^2 + \frac{p_0^2}{4\hbar^2(\alpha+\gamma)^2}\right]\langle g(x_0,p_0)|\rho(0)|g(x_0,p_0)\rangle \cdot \tag{18}$$

The multidimensional generalization of these equations is straightforward. Expectation values are readily obtained from Eq. (15) and these expressions. Similarly, if the operator A is given by a low-order polynomial, the coherent state transform of $\rho_0 A$ can be evaluated analytically.

Finite Temperature

When the initial condition is given by the Boltzmann operator, the coherent state matrix element generally cannot be calculated exactly. The most accurate and general procedure in such cases is its path integral representation (58). Thus, the coherent state representation of a Boltzmann-weighted operator is written in the form

$$\left\langle g_{\mathbf{x}_0,\mathbf{p}_0}\middle| e^{-\beta H} A \middle| g_{\mathbf{x}_0,\mathbf{p}_0}\right\rangle = \int d\mathbf{x}_1 \cdots \int d\mathbf{x}_{N+1} \left\langle g_{\mathbf{x}_0,\mathbf{p}_0}\middle| e^{-\Delta\beta H_0/2}\middle|\mathbf{x}_1\right\rangle e^{-\Delta\beta V(\mathbf{x}_1)}$$
$$\times\left\langle \mathbf{x}_1\middle| e^{-\Delta\beta H_0}\middle|\mathbf{x}_2\right\rangle \ldots e^{-\Delta\beta V(\mathbf{x}_N)}\left\langle \mathbf{x}_N\middle| e^{-\Delta\beta H_0/2}\middle|\mathbf{x}_{N+1}\right\rangle \tag{19}$$
$$\times A(\mathbf{x}_{N+1})\left\langle \mathbf{x}_{N+1}\middle| g_{\mathbf{x}_0,\mathbf{p}_0}\right\rangle$$

and

$$\left\langle g_{\mathbf{x}_0,\mathbf{p}_0}\middle|(\mathbf{x}-\mathbf{x}_0)\cdot e^{-\beta H} A(\mathbf{x}-\mathbf{x}_0)\middle| g_{\mathbf{x}_0,\mathbf{p}_0}\right\rangle = \int d\mathbf{x}_1 \cdots \int d\mathbf{x}_{N+1}$$
$$\times\left\langle g_{\mathbf{x}_0,\mathbf{p}_0}\middle|(\mathbf{x}-\mathbf{x}_0) e^{-\Delta\beta H_0/2}\middle|\mathbf{x}_1\right\rangle e^{-\Delta\beta V(\mathbf{x}_1)}$$
$$\times\left\langle \mathbf{x}_1\middle| e^{-\Delta\beta H_0}\middle|\mathbf{x}_2\right\rangle \ldots e^{-\Delta\beta V(\mathbf{x}_N)}\left\langle \mathbf{x}_N\middle| e^{-\beta H_0/2}\middle|\mathbf{x}_{N+1}\right\rangle \tag{20}$$
$$\times A(\mathbf{x}_{N+1})\cdot(\mathbf{x}_{N+1}-\mathbf{x}_0)\left\langle \mathbf{x}_{N+1}\middle| g_{\mathbf{x}_0,\mathbf{p}_0}\right\rangle$$

The various coherent state matrix elements are easily evaluated analytically. Jezek and Makri have described a Monte Carlo procedure for calculating the FBSD expression for a correlation function in conjunction with a path integral treatment of the Boltzmann operator (45). If the operator A has a simple form, for example, if it is a linear function of position or momentum, the last integral in the above equations can also be performed analytically.

Numerical Examples

The performance of the prefactor-free FBSD expressions, Equations (6) or (15), is clearly illustrated in several numerical examples. The first involves the average position in a model of an initially displaced quartic oscillator described by the Hamiltonian (41)

$$H = \frac{p^2}{2m} + \frac{1}{2}m\omega^2 x^2 - bx^3 + bx^4 \tag{21}$$

with $m = 1$, $b = 0.1$ and $\omega = \sqrt{2}$, coupled to a bath of 30 harmonic degrees of freedom at zero temperature. As seen from Figure 1, for zero coupling FBSD reproduces the first several oscillations qualitatively but dephases faster than the exact result and fails to capture the revivals of the correlation function, unlike the full semiclassical treatment that produces very accurate results for this system. Weak system-bath coupling, whose strength is commonly characterized by the dimensionless Kondo parameter ξ (59), introduces dissipation that leads to

Downloaded by UNIV MASSACHUSETTS AMHERST on September 14, 2012 | http://pubs.acs.org
Publication Date: August 14, 2002 | doi: 10.1021/bk-2002-0828.ch020

considerable quenching of the oscillations, and FBSD follows closely the exact results obtained via iterative evaluation of the path integral (60-62) as displayed in Figure 2.

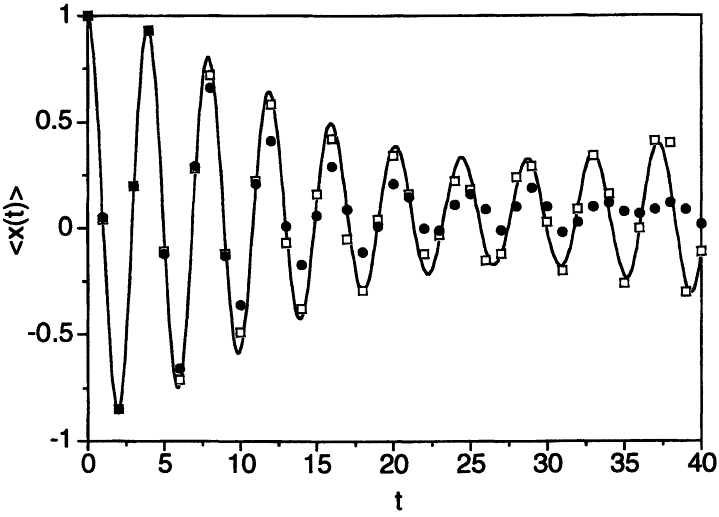

Figure 1. Average position for a one-dimensional quartic oscillator. Solid line: exact results obtained via the split propagator method. Solid circles: FBSD. Hollow squares: full semiclassical calculation.

Figures 3 and 4 show numerical results obtained by Jezek and Makri (45) for the position correlation function of the same one-dimensional quartic oscillator at two temperatures such that $\hbar\omega\beta = \sqrt{2}/10$ or $3\sqrt{2}$. The Boltzmann operator was discretized using up to $N = 6$ path integral slices. The effects of potential anharmonicity are seen as dephasing of the correlation function, which becomes more significant as the temperature is increased. At the higher temperature the FBSD-path integral results are practically exact. At lower temperatures the FBSD results are still accurate during the first few oscillation periods but tend to overestimate somewhat the dephasing rate. Note that in both cases the overall magnitude and oscillation frequency of the real and imaginary parts of the correlation function obtained from the FBSD-path integral calculation are in good agreement with the exact results. By contrast, the purely classical calcula-

Downloaded by UNIV MASSACHUSETTS AMHERST on September 14, 2012 | http://pubs.acs.org
Publication Date: August 14, 2002 | doi: 10.1021/bk-2002-0828.ch020

tion is accurate only at high temperature, and significant discrepancies from the exact results are observed away from that limit. As expected, the classical approximation cannot reproduce the correct magnitude of the correlation function at low temperatures, and the classical oscillation period is larger than that predicted by the quantum mechanical calculation, a consequence of the neglect of zero point energy in the classical treatment. Even more importantly, the classical method can only yield real-valued results and thus fails to provide any information about the imaginary part of the correlation function. The latter is as sizable as the real part at low temperatures and plays an important role in determining the shapes of absorption spectra. The FBSD methodology with a path integral treatment of the Boltzmann factor does not suffer from the above artifacts of the classical approximation and thus provides a reasonably accurate, yet practical alternative to a full quantum calculation.

Shao and Makri have used FBSD to calculate correlation functions of various normal modes in clusters of two and four water molecules. The largest of these clusters has 30 active degrees of freedom and the calculation involves a 60-dimensional integral which was evaluated with only 2,500 sampling points per integration variable (42). Typical results are shown in Figure 5.

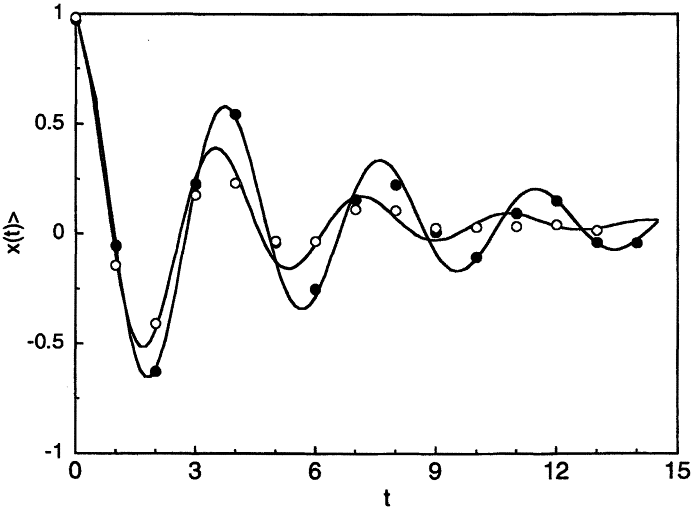

Figure 2. Average position of a quartic oscillator coupled to a bath of 30 harmonic degrees of freedom at zero temperature. The markers show the results of FBSD. Filled circles: $\xi = 0.25$. Hollow circles: $\xi = 0.50$. The lines show the exact results.

Downloaded by UNIV MASSACHUSETTS AMHERST on September 14, 2012 | http://pubs.acs.org
Publication Date: August 14, 2002 | doi: 10.1021/bk-2002-0828.ch020

Downloaded by UNIV MASSACHUSETTS AMHERST on September 14, 2012 | http://pubs.acs.org
Publication Date: August 14, 2002 | doi: 10.1021/bk-2002-0828.ch020

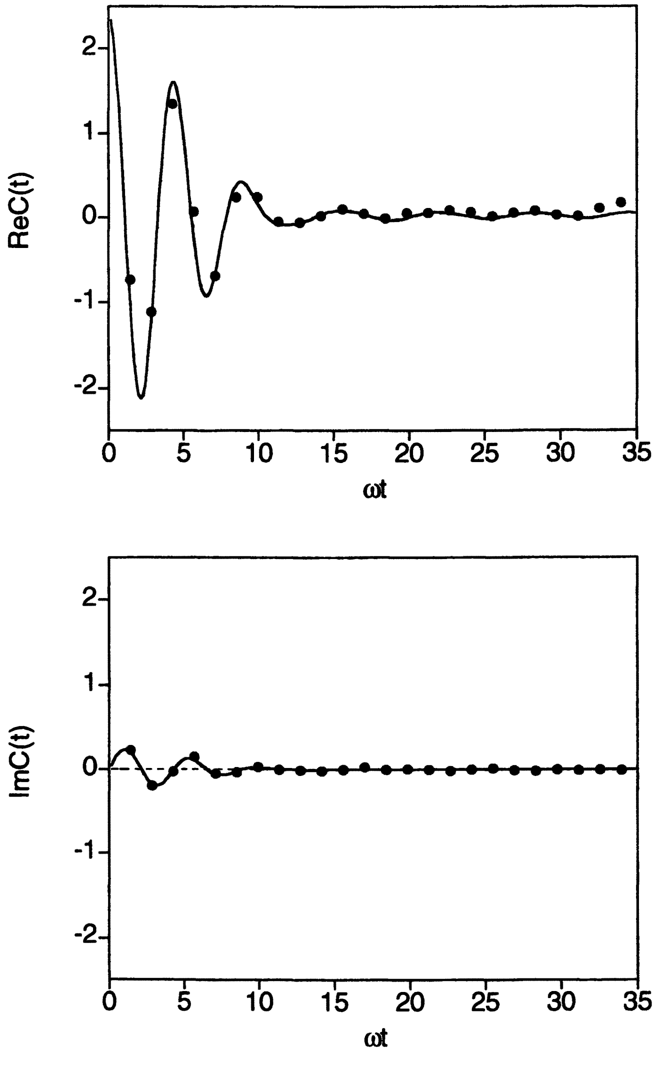

Figure 3. Real and imaginary parts of the position correlation function for the quartic oscillator described in this section at a high temperature, $\hbar\omega\beta = \sqrt{2}/10$. Solid lines: exact quantum mechanical results. Markers: FBSD-path integral results with $N = 1$ and 10,000 Monte Carlo points per integration variable. Dashed lines: classical results.

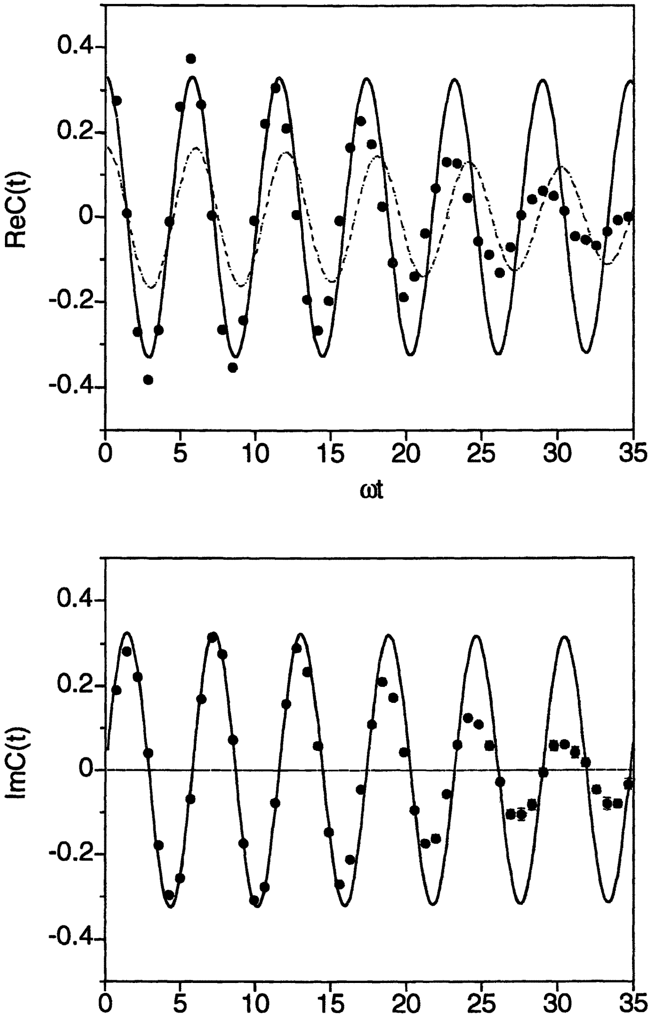

Figure 4. Real and imaginary parts of the position correlation function for the quartic oscillator described in this section at a high temperature, $\hbar\omega\beta = 3\sqrt{2}$. Solid lines: exact quantum mechanical results. Markers: FBSD-path integral results with $N = 6$ and 10,000 Monte Carlo points per integration variable. Dashed lines: classical results.

Downloaded by UNIV MASSACHUSETTS AMHERST on September 14, 2012 | http://pubs.acs.org
Publication Date: August 14, 2002 | doi: 10.1021/bk-2002-0828.ch020

Downloaded by UNIV MASSACHUSETTS AMHERST on September 14, 2012 | http://pubs.acs.org
Publication Date: August 14, 2002 | doi: 10.1021/bk-2002-0828.ch020

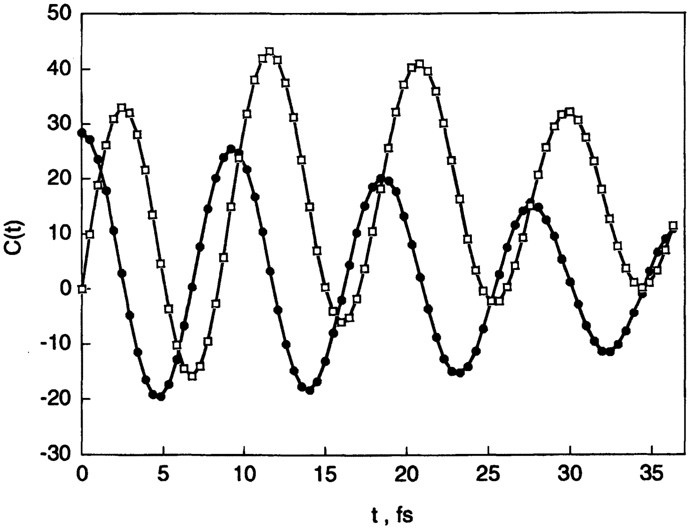

Figure 5. Correlation function of the O-H stretching normal mode of the water tetramer at zero temperature. The real and imaginary parts are shown as solid circles and hollow squares, respectively.

Concluding Remarks

Forward-backward semiclassical methods are emerging as a powerful numerical tool in quantum dynamics. The forward-backward implementation of the time-dependent semiclassical approximation circumvents the sign problem by shifting the troublesome cancellation of oscillatory terms to a cancellation between actions. Although this step tends to wipe out quantum interference, various versions of FBSD can be very successful in describing the dynamics of polyatomic systems at finite temperature where long-lasting coherences are naturally suppressed. Combined with a path integral treatment of the Boltzmann operator, FBSD can properly account for initial conditions, including zero point effects and frequency shifts, and captures quantitatively the imaginary parts of time correlation functions.

Apart from combining efficiency and reasonable accuracy, an appealing feature of the present FBSD scheme reviewed in this Chapter is its simplicity and ease of implementation. It is thus expected that FBSD and its forthcoming extensions will soon become the method of choice for large-scale simulations on molecules, clusters, and condensed phase systems.

Downloaded by UNIV MASSACHUSETTS AMHERST on September 14, 2012 | http://pubs.acs.org
Publication Date: August 14, 2002 | doi: 10.1021/bk-2002-0828.ch020

Acknowledgments

This work has been supported by the National Science Foundation under Award No. NSF CHE-9877050.

References

(1) Feynman, R. P. *Rev. Mod. Phys.* **1948**, *20*, 367.
(2) Feynman, R. P.; F. L. Vernon, J. *Ann. Phys.* **1963**, *24*, 118.
(3) Doll, J. D.; Freeman, D. L. *Adv. Chem. Phys.* **1988**, *73*, 289.
(4) Makri, N. *Comp. Phys. Comm.* **1991**, *63*, 389.
(5) Van Vleck, J. H. *Proc. Nat. Acad. U.S. Sci.* **1928**, *14*, 178.
(6) Morette, C. *Phys. Rev.* **1952**, *81*, 848.
(7) Marcus, R. A. *J. Chem. Phys.* **1972**, *56*, 3548.
(8) Miller, W. H. *Adv. Chem. Phys.* **1974**, *25*, 69.
(9) Heller, E. J. *J. Chem. Phys.* **1991**, *94*, 2723.
(10) Herman, M. F.; Kluk, E. *Chem. Phys.* **1984**, *91*, 27.
(11) Kluk, E.; Herman, M. F.; Davis, H. L. *J. Chem. Phys.* **1986**, *84*, 326.
(12) Campolieti, G.; Brumer, P. *Phys. Rev. A* **1994**, *50*, 997.
(13) Wilkie, J.; Brumer, P. *Phys. Rev. A* **2001**, *61*, 064101.
(14) Kay, K. G. *J. Chem. Phys.* **1994**, *100*, 4377.
(15) Kay, K. G. *J. Chem. Phys.* **1994**, *100*, 4432.
(16) Kay, K. *J. Chem. Phys.* **1997**, *107*, 2313.
(17) Filinov, V. S. *Nucl. Phys. B* **1986**, *271*, 717.
(18) Makri, N.; Miller, W. H. *Chem. Phys. Lett.* **1987**, *139*, 10.
(19) Walton, A. R.; Manolopoulos, D. E. *Mol. Phys.* **1996**, *84*, 961.
(20) Brewer, M. L.; Hulme, J. S.; Manolopoulos, D. E. *J. Chem. Phys.* **1997**, *106*, 4832.
(21) McQuarrie, B. R.; Brumer, P. *Chem. Phys. Lett.* **2000**, *319*, 27.
(22) Wang, H.; Manolopoulos, D. E.; Miller, W. H. *J. Chem. Phys.* **2001**, *115*, 6317.
(23) Tomsovic, S.; Heller, E. J. *Phys. Rev. Lett.* **1991**, *67*, 664.

(24) Sepulveda, M. A.; Tomsovic, S.; Heller, E. J. *Phys. Rev. Lett.* **1992**, *69*, 402.

(25) Sepulveda, M. A.; Grossmann, F. *Adv. Chem. Phys.* **1996**, *XCVI*, 191.

(26) Grossmann, F. *Phys. Rev. A* **1999**, *60*, 1791.

(27) Herman, M. F. *J. Chem. Phys.* **1987**, *87*, 4779.

(28) Herman, M. F. *Ann. Rev. Phys. Chem.* **1994**, *45*, 83.

(29) Sun, X.; Miller, W. H. *J. Chem. Phys.* **1997**, *106*, 916.

(30) Garashchuk, S.; Grossmann, F.; Tannor, D. *J. Chem. Soc. Faraday Trans.* **1997**, *93*, 781.

(31) Sun, X.; Miller, W. H. *J. Chem. Phys.* **1998**, *108*, 8870.

(32) Wang, H.; Sun, X.; Miller, W. H. *J. Chem. Phys.* **1998**, *108*, 9726.

(33) Sun, X.; Wang, H.; Miller, W. H. *J. Chem. Phys.* **1998**, *109*, 4190.

(34) Herman, M. F.; Coker, D. F. *J. Chem. Phys.* **1999**, *111*, 1801.

(35) Coronado, E. A.; Batista, V. S.; Miller, W. H. *J. Chem. Phys.* **2000**, *112*, 5566.

(36) Makri, N.; Thompson, K. *Chem. Phys. Lett.* **1998**, *291*, 101.

(37) Miller, W. H. *Faraday Discuss.* **1998**, *110*, 1.

(38) Thompson, K.; Makri, N. *J. Chem. Phys.* **1999**, *110*, 1343.

(39) Thompson, K.; Makri, N. *Phys. Rev. E* **1999**, *59*, R4729.

(40) Sun, X.; Miller, W. H. *J. Chem. Phys.* **1999**, *110*, 6635.

(41) Shao, J.; Makri, N. *J. Phys. Chem.* **1999**, *103*, 7753.

(42) Shao, J.; Makri, N. *J. Phys. Chem.* **1999**, *103*, 9479.

(43) Wang, H.; Thoss, M.; Miller, W. H. *J. Chem. Phys.* **2000**, *112*, 47.

(44) Shao, J.; Makri, N. *J. Chem. Phys.* **2000**, *113*, 3681.

(45) Jezek , E.; Makri, N. *J. Phys. Chem.* **2001**, *105*, 2851.

(46) Makri, N. Forward-backward semiclassical dynamics. In *Fluctuating paths and fields*; Janke, W., Pelster, A., Schmidt, H.-J., Bachmann, M., Eds.; World Scientific: Singapore, 2001.

(47) Wang, H.; Thoss, M.; Sorge, K. L.; Gelabert, R.; Gimenez, X.; Miller, W. H. *J. Chem. Phys.* **2001**, *114*, 2562.

(48) Thoss, M.; Wang, H.; Miller, W. H. *J. Chem. Phys.* **2001**, *114*, 9220.

(49) Batista, V.; Zanni, M. T.; Greenblatt, J.; Neumark, D. M.; Miller, W. H *J. Chem. Phys.* **1999**, *110*, 3736.

(50) Skinner, D. E.; Miller, W. H. *J. Chem. Phys.* **1999**, *111*, 10787.

(51) Thoss, M.; Miller, W. H.; Stock, G. *J. Chem. Phys.* **2000**, *112*, 10282.

(52) Miller, W. H. *J. Phys. Chem.* **2001**, *105*, 2942.

(53) Gelabert, R.; Giménez, X.; Thoss, M.; Wang, H.; Miller, W. H. **2001**, *114*, 2572.

(54) Ovchinnikov, M.; Apkarian, V. A.; Voth, G. A. *J. Chem. Phys.* **2001**, *114*, 7130.

(55) Maslov, V. P.; Fedoriouk, M. V. *Semiclassical approximation in quantum mechanics*; Reidel: Boston, 1981.

Downloaded by UNIV MASSACHUSETTS AMHERST on September 14, 2012 | http://pubs.acs.org
Publication Date: August 14, 2002 | doi: 10.1021/bk-2002-0828.ch020

(56) Wigner, E. J. *Chem. Phys.* **1937**, *5*, 720.

(57) Heller, E. J. *J. Chem. Phys.* **1976**, *65*, 1289.

(58) Feynman, R. P. *Statistical Mechanics*; Addison-Wesley: Redwood City, 1972.

(59) Leggett, A. J.; Chakravarty, S.; Dorsey, A. T.; Fisher, M. P. A.; Garg, A.; Zwerger, M. *Rev. Mod. Phys.* **1987**, *59*, 1.

(60) Makri, N.; Makarov, D. E. *J. Chem. Phys.* **1995**, *102*, 4600.

(61) Makri, N.; Makarov, D. E. *J. Chem. Phys.* **1995**, *102*, 4611.

(62) Makri, N. *J. Math. Phys.* **1995**, *36*, 2430.

Downloaded by UNIV MASSACHUSETTS AMHERST on September 14, 2012 | http://pubs.acs.org
Publication Date: August 14, 2002 | doi: 10.1021/bk-2002-0828.ch020

In Low-Lying Potential Energy Surfaces; Hoffmann, M., et al.;
ACS Symposium Series; American Chemical Society: Washington, DC, 2002.

Downloaded by STANFORD UNIV GREEN LIBR on September 14, 2012 | http://pubs.acs.org
Publication Date: August 14, 2002 | doi: 10.1021/bk-2002-0828.ch021

Chapter 21

Development and Application of an Ab Initio Methane–Water Potential for the Study of Phase Equilibria of Methane Hydrates

Zhitao Cao, Brian J. Anderson, Jefferson W. Tester, and Bernhardt L. Trout*

Department of Chemical Engineering and Energy Laboratory, Massachusetts Institute of Technology, Room 66–556, 77 Massachusetts Avenue, Cambridge, MA 02139

An *ab initio* potential for the methane-water bimolecular system has been developed for use in modeling methane hydrates and in order to evaluate currently used statistical thermodynamic models. In this paper, an introduction to gas hydrates is first given, and the problem with the Lennard-Jones and Devonshire (LJD) approximation, typically used for modeling hydrates, is described. Second, the methodologies for generating the *ab initio* potential energy surface are described and results discussed. Third, computed phase equilibrium data for methane hydrates using the obtained *ab initio* potential are presented and compared to experimental data. Finally, results regarding the issue of the reference state for the statistical thermodynamic model, including analysis and determination of reference state properties via *ab initio* calculations, are given.

In Low-Lying Potential Energy Surfaces; Hoffmann, M., et al.;
ACS Symposium Series; American Chemical Society: Washington, DC, 2002.

Introduction

Natural gas clathrate-hydrates (called gas hydrates) are systems of polyhedral cells formed by hydrogen-bonded water molecules. These form nonstiochiometric inclusion compounds consisting of a three-dimensional host lattice of water molecules, in which guest molecules, such as methane and/or carbon dioxide, are encaged. An illustration of the empty lattice structure of Structure I hydrates is shown in Figure 1. The development of production and transmission operations for conventional natural gas hydrates depends on the ability to model and make quantitative predictions of methane hydrate behavior. Since the late 50's, the van der Waals and Platteeuw statistical mechanical model with the Lennard-Jones and Devonshire (LJD) spherical cell potential approximation (*1,2*) has been the basis of most modeling efforts. However, our studies, as well as other previous work, have demonstrated the inadequacy of the LJD approximation (*3,4*). Moreover, such inadequacy has long been surmised based on the fact that potential parameters computed from gas-hydrate phase data using the LJD approximation do not match those computed from other experimental data (*4-6*). Thus, present methods can be used to fit experimental data, but cannot be generalized to make accurate predictions. Proper determination of the form of the intermolecular interaction potential is necessary both to compute equilibria thermodynamic properties and to perform classical simulations of kinetic phenomena such as formation and dissociation. Experimental techniques, however, cannot be used easily to determine the physical interaction potential. Our objective is therefore to use methods of computational chemistry to develop an accurate and robust multi-dimensional potential between guest and host molecules and then apply it to phase equilibria and kinetics studies.

The Lennard-Jones 6-12 and Kihara potentials are commonly chosen to represent average interactions between the lattice (water) and guest molecules (methane, ethane, etc.). The parameters in these potentials are often determined by mixing the potentials for pure component water and pure component guest molecules. Lennard-Jones parameters for liquid hydrocarbons have been optimized to reproduce experimental densities and heats of vaporization with an accuracy of approximately 5% in what is termed the OPLS model (*7*). A popular model for water is the TIP3P model, which has, on the oxygen and hydrogen atoms, three point charges to represent the dipole and Lennard-Jones parameters centered on the oxygen atom. TIP3P has been parameterized to reproduce liquid water properties very well (*8*). However, using a simple mixing rule, the TIP3P model for water and the OPLS model for hydrocarbons failed to give a reasonable Langmuir constant, a key term in the van der Waals and Platteeuw statistical model, for several hydrates (*3,9,10*).

Downloaded by STANFORD UNIV GREEN LIBR on September 14, 2012 | http://pubs.acs.org
Publication Date: August 14, 2002 | doi: 10.1021/bk-2002-0828.ch021

Downloaded by STANFORD UNIV GREEN LIBR on September 14, 2012 | http://pubs.acs.org
Publication Date: August 14, 2002 | doi: 10.1021/bk-2002-0828.ch021

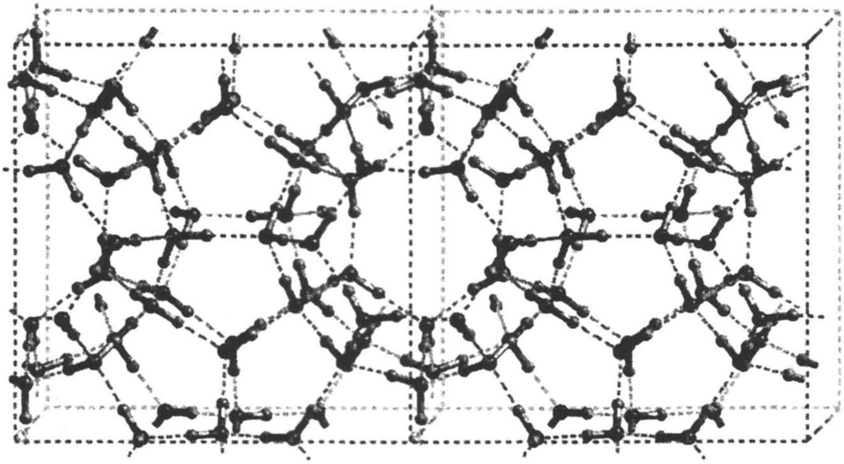

Figure 1. Ball and stick model of Structure I clathrate with two unit cells (SOURCE: Adapted with permission from refrence 20. Copyright 2001 American Institute of Physics)

Recent work by Bazant and Trout has uncovered the possibility of extracting a spherically averaged cell potential directly from experimental data that can be used to represent the interaction energy between a guest molecule and the surrounding cage (*11*). This method, which involves an analytical "inversion" based on the van der Waals and Platteeuw statistical model together with the LJD approximation, is simpler and more meaningful than the empirical fitting of Kihara potentials. Bazant and Trout showed the adherence of the extracted cell potentials of cyclopropane and ethane Structure I hydrates to the ideal van't Hoff temperature dependence. Additional work by Anderson et al. expanded the cell potential method to include the Structure II hydrates of cyclopropane, propane, and isobutane and showed that these cell potentials can be used to predict independently the phase behavior of hydrates containing mixtures of guest molecules (*12*).

Our approach, an alternative approach to fitting experimental data, is to compute the potential directly from first-principles or *ab initio* methods. Such an approach would provide a direct route to determine the intermolecular potential, which can then be validated independently using experimental data.

Downloaded by STANFORD UNIV GREEN LIBR on September 14, 2012 | http://pubs.acs.org
Publication Date: August 14, 2002 | doi: 10.1021/bk-2002-0828.ch021

Ab initio Calculations

Methodology

Several research groups have investigated the accuracy and efficiency of *ab initio* calculations in characterizing methane-water interactions. In Monte Carlo (MC) studies of aqueous solutions of methane, Owichi and Scheraga (*13*) and Swaminathan (*14*) used an intermolecular potential energy based on *ab initio* calculations. Novoa et al. (*15*) performed *ab initio* calculations on methane-water at the self-consistent-field molecular orbital (SCF-MO) and MP2 levels with various quality basis sets, including a near Hartree-Fock Limit (NHFL) case. Szczesniak et al. (*16*) then explored more configurations between methane and water using fourth-order Møller-Plesset perturbation theory with the basis set, 6-31++G(2d,2p). Both of the previous studies showed that diffuse functions are necessary to remove the basis set superposition error (BSSE). Novoa et al. (*17*) continued to perform a numerical test of evaluating interaction energy using very large basis sets for $H_2O\cdots HF$ and $CH_4\cdots H_2O$ at the MP2 level. They suggested that the counterpoise (CP) method provides reasonable estimates of the interaction energy when the basis set is large enough. The qualified adequate basis sets resulting from their study consist of Near Hartree-Fock Limit (NHFL) (4d3f, 4p3d), 6-31++G(4d3f,4p3d), and cc-pVQZ.

In our study, accuracy and computational intensity of various methods and basis sets were compared, and the best approach was carefully selected. Using a moderately accurate method, 18,000 points on the 6-dimensional potential energy hypersurface between methane and water were computed. About 100 points on this hypersurface were computed with a highly accurate method, and using these points, a correction method was developed for the entire 18,000 points on the hypersurface. The computed multi-dimensional interaction energies were then averaged to construct a robust spherically symmetric radial potential for use in computations involving methane hydrates.

The potential energy hypersurface was computed as a pair potential between the carbon on methane (C) and the oxygen on water (O), choosing the C-O distance as the interaction distance r. The center of mass distance was not chosen because the crystallographic structural data (*18,19*) of clathrate hydrates directly gives the position of the oxygen atom within the lattice. Six dimensions, the three dimensions characterizing the relative positions of CH_4 and H_2O and the three Euler angles of CH_4, were sampled on the potential energy hypersurface. The full MP2 method was found to describe electronic correlation accurately, but a very large basis set, cc-pVQZ, with counterpoise correction was necessary to compute accurate energies of interaction by minimizing BSSE. Because MP2/cc-pVQZ calculations are quite compute-intensive, even for this small system, CH_4-H_2O, MP2/6-31++G(2d,2p) calculations were performed to compute energies of all 18,000 points. The correction method developed uses the results of ~100 MP2/cc-pVQZ calculations in order to achieve nearly MP2/cc-pVQZ accuracy for all 18,000 points. We expect ~0.1-0.2 kcal/mol accuracy via this approach.

The geometries of the hydrocarbon guest (i.e. methane) and water molecule host were fixed in the calculations with each molecule optimized separately at the MP2/6-31++G(2d,2p) level. The optimized geometries of water and hydrocarbons compare favorably with the experimental data (*20*). The choice of orientations between the guest molecule and the host water molecule was made based on possible orientations in the actual clathrate structure. By inspecting the ball and stick model of a Structure I clathrate hydrate with two adjacent unit cells, shown in Figure 1 (methane forms a Structure I clathrate hydrate (*9*)), the relative orientations between the guest and water molecule mainly fall into the two types characterized by the plane containing the water molecule as shown in Figure 2. The position of the guest molecule is moved in a coordinate system (similar to a spherical coordinate system) where the water oxygen is the origin. The rigid body of the guest molecule is further rotated using the three classical Euler angles (α, β, γ) (*21*). The six-dimensional grid is illustrated in Figure 3, where r, ξ and φ are the coordinates used to define the position of methane carbon with the water oxygen as the origin. The ξ and φ coordinates were used instead of the spherical coordinates, θ and ϕ, in this study for generation of the

Downloaded by STANFORD UNIV GREEN LIBR on September 14, 2012 | http://pubs.acs.org
Publication Date: August 14, 2002 | doi: 10.1021/bk-2002-0828.ch021

Downloaded by STANFORD UNIV GREEN LIBR on September 14, 2012 | http://pubs.acs.org
Publication Date: August 14, 2002 | doi: 10.1021/bk-2002-0828.ch021

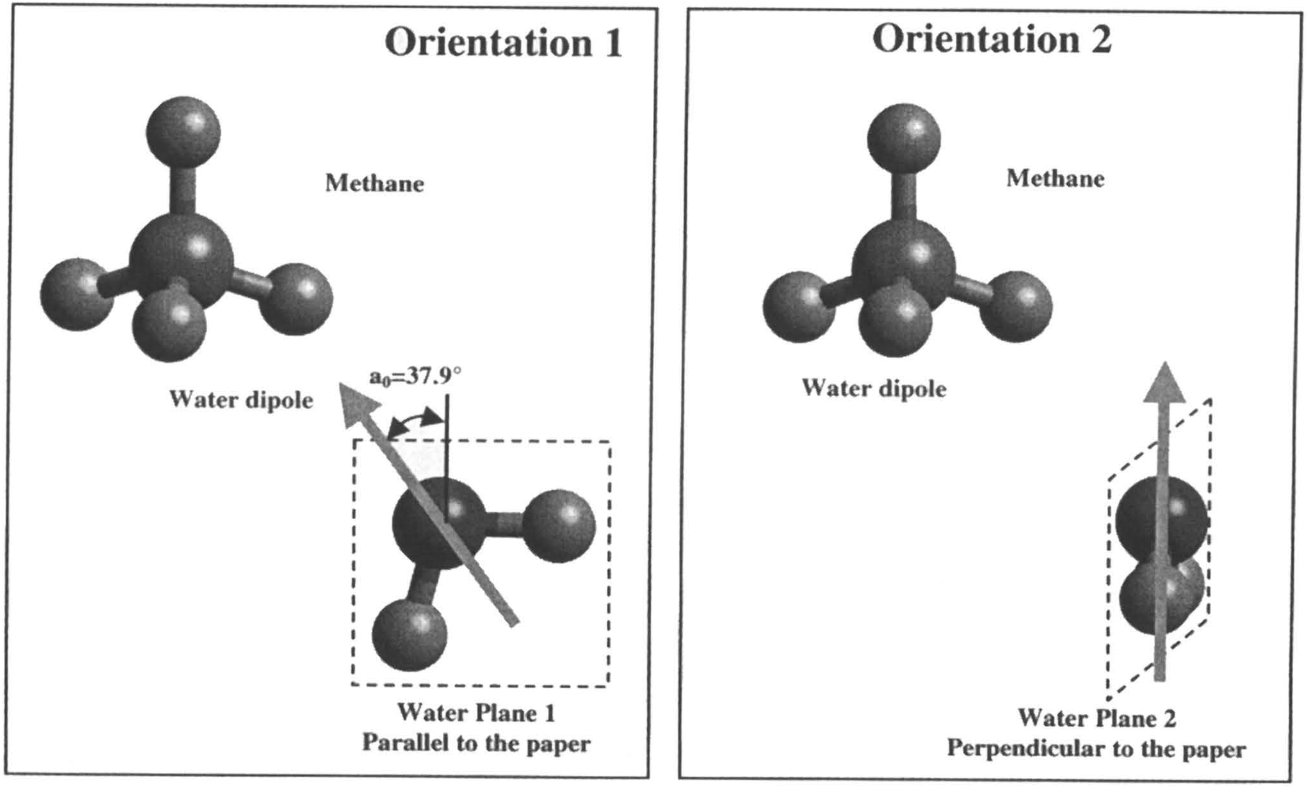
Orientation 1
Methane
Water dipole
a_0=37.9°
Water Plane 1
Parallel to the paper
Orientation 2
Methane
Water dipole
Water Plane 2
Perpendicular to the paper

Figure 2. Two characteristic water plane orientations in the methane-water clathrate viewed from the center of cavity (SOURCE: Adapted with permission from refrence 20. Copyright 2001 American Institute of Physics)

Downloaded by STANFORD UNIV GREEN LIBR on September 14, 2012 | http://pubs.acs.org
Publication Date: August 14, 2002 | doi: 10.1021/bk-2002-0828.ch021

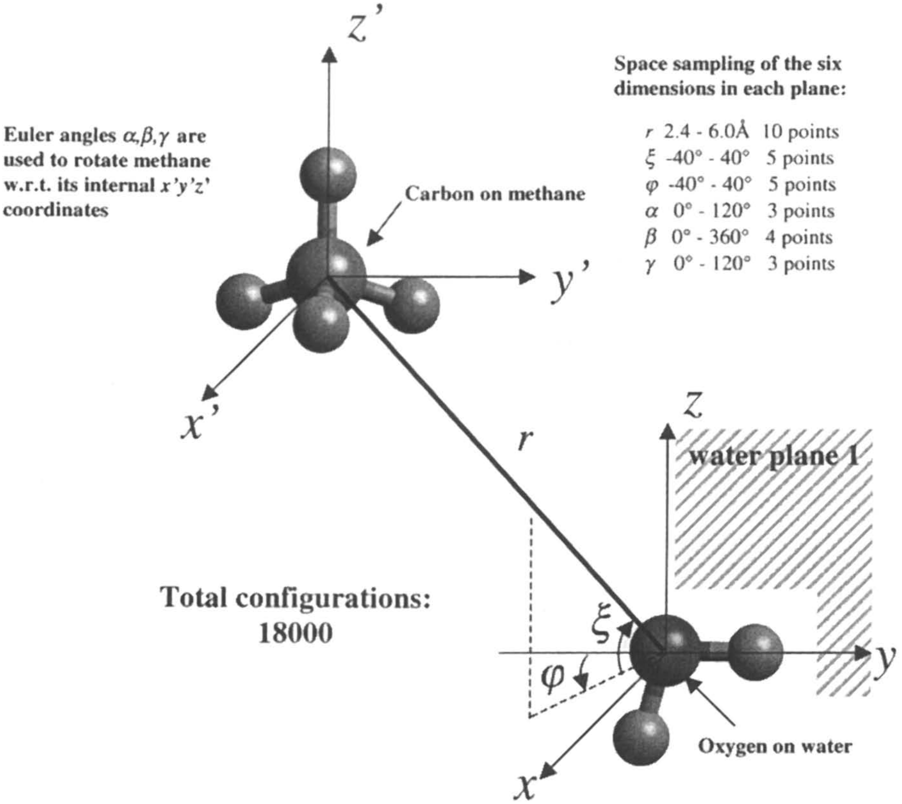
z'
Euler angles α,β,γ are used to rotate methane w.r.t. its internal x'y'z' coordinates
Carbon on methane
y'
x'
r
z
water plane 1
Total configurations: 18000
ξ
φ
y
Oxygen on water
x

Space sampling of the six dimensions in each plane:

r	2.4 - 6.0Å	10 points
ξ	-40° - 40°	5 points
φ	-40° - 40°	5 points
α	0° - 120°	3 points
β	0° - 360°	4 points
γ	0° - 120°	3 points

Figure 3. The six dimensions (r, ξ, φ, α, β, γ) used to define the orientation between a methane guest and water host molecule (SOURCE: Adapted with permission from refrence 20. Copyright 2001 American Institute of Physics)

18,000 different input files for use in Gaussian 94 (*22*). Ten points from 2.4-6.0 Å are sampled in the radial dimension, considering the constraints of the clathrate cage. Five equally spaced points from –40° to 40° were considered to be sufficient for methane-water phase space sampling for ξ and φ. Three points, 0°, 40° and 80°, were sampled for α and γ and four points, 0°, 90°, 180° and 270°, were used in sampling β.

The interaction energy between methane and water can then be expressed as

$$\Delta E_{cp} = E_{mw} - E_{m,cp} - E_{w,cp} \tag{1}$$

where ΔE_{cp} is the interaction energy, or binding energy, computed with the counterpoise method, E_{mw} is the total energy of the methane-water complex system at a specific configuration, and $E_{m,cp}$ and $E_{w,cp}$ are the counterpoise-corrected energies of the methane and water molecules. For each radial position, there are two different water planes and $5 \times 5 \times 3 \times 4 \times 3 = 900$ orientations of the methane molecule. In order to combine the $900 \times 2 = 1800$ interaction energies to obtain one angle-averaged energy at each specific interatomic distance between guest and host molecules, Boltzmann-weighted averages were performed at the temperature of interest.

Molecular orbital theories (*ab initio* methods (*23*)) were chosen and validated in this study to characterize the interaction energies between methane and water, while electron density functional theories (*24*) were tested, but found to be inadequate (see below). Four different *ab initio* methods were used in the validation: MP2 (*25,26*), MP4(SDTQ) (*27*), QCISD(T) (*28*) and CCSD(T) (*29*). Three different DFT methods, BLYP (*30,31*), B3LYP (*32*) and BPW91 (*33*), were used and the results compared with the *ab initio* methods. In addition, for each of the above methods, the effect of the size of different basis sets was investigated; specifically, 6-31++G(2d,2p), cc-pVDZ, cc-pVTZ and cc-pVQZ were used. 6-31++G(2d,2p) was chosen, because it was reported to yield reasonable results compared with that at near the basis set limit on this system (*17*). The others were chosen in order to observe the effect of systematically increasing the size of the basis set. Gaussian 94 (*22*) was used for all the above calculations.

The "Binding Energy Difference" for use in our correction method is given by

$$\delta E_{BED} = \Delta E_{Method/cc\text{-}pVQZ} - \Delta E_{MP2/6\text{-}31{+}{+}G(2d,2p)} \tag{2}$$

Downloaded by STANFORD UNIV GREEN LIBR on September 14, 2012 | http://pubs.acs.org
Publication Date: August 14, 2002 | doi: 10.1021/bk-2002-0828.ch021

Although the binding energies calculated at the MP2 level are slightly higher than those calculated using the other three methods, the MP2 method was still selected for the calculations due to the computational time issue and the fact that the binding energy difference is no more than 0.05 kcal/mol.

The correction method that we have developed achieves binding energy results nearly as accurate as MP2/cc-pVQZ from predominantly MP2/6-31++G(2d,2p) computations. The correction method provides a functional form that gives results proportional to the correction for basis set at any orientation of H_2O-CH_4 pair. The numerical value given by this functional form is referred to as the "basis set correction factor". In the correction method, the binding energy difference, or energy correction, between binding energies computed with MP2/cc-pVQZ and MP2/6-31++G(2d,2p) is

$$\delta E_{BED} = C_i \Phi_{mw} \tag{3}$$

where δE_{BED} is the binding energy difference, C_i is a proportionality constant determined via a modified factorial design, and Φ_{mw} is the form of the "basis set correction factor". The functional form for Φ_{mw} was chosen as the form of the interaction between a polarizable methane molecule and a water molecule with a permanent dipole moment (*34*). Note that any convenient mathematical form could be chosen as long as it adequately describes the numerical "basis set correction factor".

From classical electromagnetic field theory (*34,35*), Eq. 4 is the functional form selected to represent Φ_{mw}.

$$\Phi_{mw} = \frac{1}{8\pi\varepsilon_0 r_{mw}^3}\left[(\boldsymbol{\mu}_m \cdot \boldsymbol{\mu}_w) - 3(\boldsymbol{\mu}_m \cdot \mathbf{r}_{mw})(\boldsymbol{\mu}_w \cdot \mathbf{r}_{mw})/r_{mw}^2\right] \tag{4}$$

where $\boldsymbol{\mu}$ is the dipole moment vector, m and w indicate methane and water respectively, $\mathbf{r}_{mw}$ is the vector of carbon on methane with respect to oxygen on water as origin, and r_{mw} is its length. Details of the derivation and choice of Eq. 4 is can be found in Ref. 20.

In our study, the polarizability tensor of methane calculated from Gaussian 94 (*22*) is isotropic within the numerical accuracy of the calculation. Therefore the formula and calculations could be simplified. However, for most guest molecules in clathrate hydrates that are not as symmetric as methane, this derivation gives a general approach to characterize the induced dipole-dipole interaction.

The next step was to determine the proportional factor C_i in Eq. 3, and test the chosen form of the "basis set correction factor". The C_i's were determined from a number of MP2/cc-pVQZ runs selected from a modified experimental

Downloaded by STANFORD UNIV GREEN LIBR on September 14, 2012 | http://pubs.acs.org
Publication Date: August 14, 2002 | doi: 10.1021/bk-2002-0828.ch021

fractional factorial design (*36*). The main objective of the experiments (the selected MP2/cc-pVQZ runs) is to assess the effects of distance and five angles on the "basis set correction factor". A simple efficient filter was used to screen the factors with the minimum number of runs needed to fully explore the six-dimensional methane-water hypersurface (*20*).

In order to develop a spherically symmetric radial potential, a Boltzmann-weighted average was taken at each radial point to integrate out effectively the 5 other degrees of freedom. The average interaction energies at each interatomic distance r are

$$\left\langle E_{cp}(r)\right\rangle = \frac{\sum_{i=1}^{1800} \Delta E_{cp}(r)\exp(-\Delta E_{cp}(r)/kT)}{\sum_{i=1}^{1800} \exp(-\Delta E_{cp}(r)/kT)} \tag{5}$$

where k is the Boltzmann constant and T is the absolute temperature. Thus, a particular value of T must be used to perform the average. Note the potential profile calculated by Eq. 5 is based on C-O distance. In order to compare with experimental data, the averaged center-of-mass distance was also calculated.

Experimental dissociation pressure-temperature data that exist for hydrates typically range between 260 K and 300 K (*37*). Over this temperature range, the effective energy profile does change significantly. For comparison in this study, the melting point of ice, 273.15 K, was chosen for use in Eq. 5. The resulting potential profile is compared below with experimental data and other simple potential forms.

Results and discussions

In order to evaluate the choice of basis set, we chose to perform calculations using several different basis sets on the optimized (minimum energy) H_2O-CH_4 structure. The binding energies computed using these six basis sets are plotted in Figure 4. Figure 4 shows that the binding energy calculated with the cc-pV*Z series monotonically increases (except the one calculated using the AUG-cc-pVQZ basis set), and the one computed with cc-pVQZ approaches the asymptotic value within 0.1 kcal/mol. It would be preferable to use the AUG-cc-pVQZ basis set, but this would have led to a substantial increase in computational time, already quite large. Binding energies computed using several different methods to treat electron correlation are presented in Table I.

From the above studies, we can come to several conclusions. As expected, the three DFT methods predict binding interactions between methane and water

Downloaded by STANFORD UNIV GREEN LIBR on September 14, 2012 | http://pubs.acs.org
Publication Date: August 14, 2002 | doi: 10.1021/bk-2002-0828.ch021

Downloaded by STANFORD UNIV GREEN LIBR on September 14, 2012 | http://pubs.acs.org
Publication Date: August 14, 2002 | doi: 10.1021/bk-2002-0828.ch021

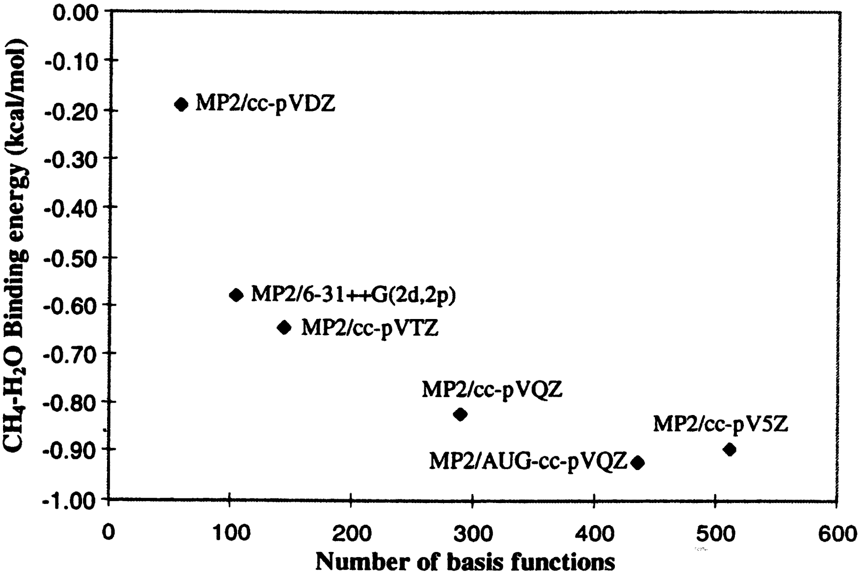

Figure 4. The effect of size of the basis set on estimated binding energy of optimized $CH_4\cdots H_2O$ complex (SOURCE: Adapted with permission from refrence 20. Copyright 2001 American Institute of Physics)

Downloaded by STANFORD UNIV GREEN LIBR on September 14, 2012 | http://pubs.acs.org
Publication Date: August 14, 2002 | doi: 10.1021/bk-2002-0828.ch021

TABLE I. Binding energies (kcal/mol) calculated at cc-pVQZ with counterpoise (CP) and without counterpoise (no CP) method

		r = 3.0 Å (a)		r = 3.8 Å (b)		r = 3.509 Å (c)	
calculation method		repulsive (CP)	repulsive (no CP)	attractive (CP)	attractive (no CP)	optimized (CP)	optimized (no CP)
Ab initio methods	MP2	1.6180	1.1715	-0.1765	-0.3553	-0.8235	-1.0112
	MP4SDTQ	1.5407	1.1029	-0.2019	-0.3771	-0.8563	-1.0439
	QCISD(T)	1.5543	1.1449	-0.1992	-0.3628	-0.8485	-1.0246
	CCSD(T)	1.5611	1.1550	-0.1974	-0.3596	-0.8446	-1.0189
DFT methods	BLYP	2.8344	2.3063	0.3158	0.0697	0.0797	-0.1914
	B3LYP	2.4370	2.0350	0.1837	-0.0046	-0.1931	-0.3843
	BPW91	3.5565	3.1260	0.6069	0.4028	0.4906	0.2669

that are much weaker than those predicted from *ab initio* methods. The counterpoise method is definitely needed to calculate accurately the binding energy between methane and water. When the basis set is increased from cc-pVDZ to cc-pVQZ, the deviations of binding energies calculated with CP and without CP decrease. Among the *ab initio* methods examined, the predicted $CH_4 \cdots H_2O$ binding energies are within a few hundredths of a kcal/mol for all correlation methods tested. This agreement validates the MP2 method as quantitatively adequate to characterize the interaction between methane and water in the gas phase. The correction method we used to refine the results from the 18,000 points calculated using MP2/6-31++G(2d,2p) is very efficient and successful. Our model gives good predictions (high R^2 values from 0.97 to 0.99) of energy corrections (*20*), considering that it takes into account six dimensional effects on binding energies.

Using Eq. 5, the profile of averaged interaction energies at different distances with and without the six-dimensional correction is completed and the entire numerical potential can be found at http://troutgroup.mit.edu/clathrate/methane/potential.html. The corrected interaction potential in the repulsive region was even softer than the MP2/6-31++G(2d,2p) potential. The corrected potential was then adapted to a center-of-mass basis. Both potential profiles, in terms of C-O and center-of-mass distance, as well as the uncorrected potential are compared with the Kihara potential in Figure 5. The Kihara potential parameters were fitted from experimental second virial coefficient data (*4,9,38*). In the attractive region, when the distance between the carbon on methane and oxygen on water is at or above the minimum (r > 3.7 Å), our potential profile matches the experimental second virial coefficient potential very well. However, the *ab initio* potential is much softer than the experimental potential in the repulsive region. We believe that our potential is more accurate than the experimental potential in the repulsive region because the relationship (*38*) between the intermolecular potential (the Kihara potential form) and second virial coefficient data is accurate to the second order, that is, only when the gas density is low, or when the distance between molecules is sufficiently large. This explains the excellent agreement in the region where the distance is greater than the potential minimum. Second virial coefficient data, however, is not expected to be accurate at small distances. The Boltzmann-averaged center-of-mass distance at the potential well of the averaged *ab initio* potential is 3.76 Å (the corresponding C-O distance is 3.71 Å) while the experimental value for the averaged center-of-mass distance between methane and water at ground state from far infrared vibration-rotation-tunneling (VRT) spectroscopy is 3.70 Å (*39*), another validation of our method. Additional details can be found in Ref. 20.

Downloaded by STANFORD UNIV GREEN LIBR on September 14, 2012 | http://pubs.acs.org
Publication Date: August 14, 2002 | doi: 10.1021/bk-2002-0828.ch021

Downloaded by STANFORD UNIV GREEN LIBR on September 14, 2012 | http://pubs.acs.org
Publication Date: August 14, 2002 | doi: 10.1021/bk-2002-0828.ch021

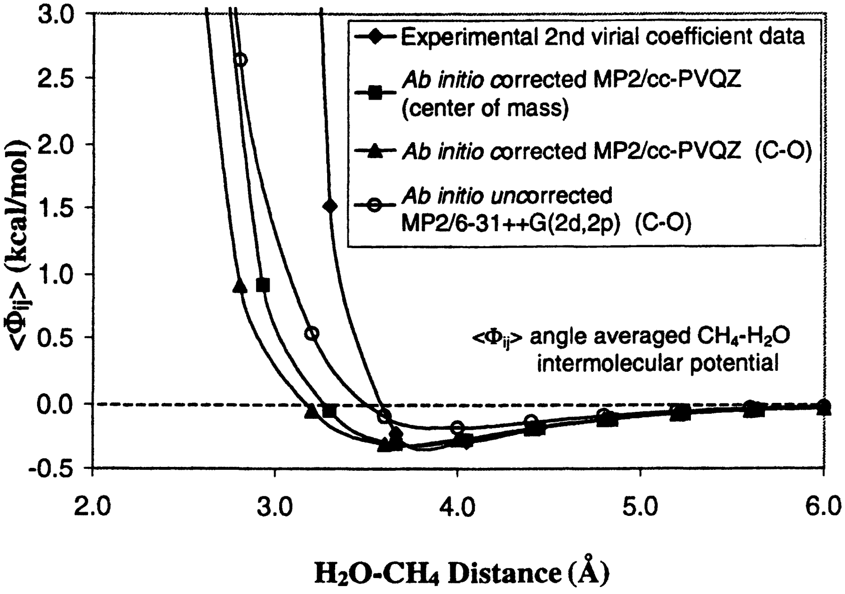

Figure 5. Ab initio potentials (C-H_2O (center-of-mass) and C-O distance) compared with experimental potential (in the Kihara form based on C-H_2O distance) obtained from second virial coefficients

Application to hydrate phase equilibria calculations

The most important test of our bimolecular potential is its use in statistical thermodynamic models for the prediction of phase equilibria. Monovariant, three-phase pressure-temperature measurements and invariant point determinations of various gas hydrates are available and are typically used to fit parameters in molecular computations. The key component needed for phase equilibrium calculations is a model of the intermolecular potential between guest and host molecules for use in the configurational integral. Lennard-Jones and Kihara potentials are usually selected to fit the experimental dissociation pressure-temperature data using the LJD approximation (*2,4,6*). Although this approach is able to reproduce the experimental data well, the fitted parameters do not have any physical connection to the properties of the molecules involved.

In the statistical model developed by van der Waals and Platteeuw (*2*), the difference in chemical potential between a clathrate and empty host lattice is expressed as

$$\Delta\mu^{\beta-H} = RT\sum_i \nu_i \ln(1+\sum_J C_{Ji}\hat{f}_J) = RT\sum_i \nu_i \ln(1-\sum_J y_{Ji}) \tag{6}$$

where ν_i is the number of type *i* cavities per water molecule, $\hat{f}_J$ is the fugacity of guest molecule *J* which is usually calculated from a suitable equation of state (EOS) such as Peng-Robinson EOS (*40*), and y_{Ji} is the fractional occupation probability of guest *J* in cavity *i* (y_{Ji} is related to the mole fraction of the guest molecule in the water clathrate), given by an expression similar to the Langmuir isotherm

$$y_{Ji} = \frac{C_{Ji}\hat{f}_J}{1+\sum_i C_{Ji}\hat{f}_J} \tag{7}$$

C_{Ji} is the Langmuir constant of guest molecule *J* in cage *i*, defined as

$$C_{Ji} \equiv \frac{Z_{Ji}}{kT} \tag{8}$$

where Z_{Ji} is the six-dimensional configurational integral, which depends on the interaction potential between guest and host molecules

Downloaded by STANFORD UNIV GREEN LIBR on September 14, 2012 | http://pubs.acs.org
Publication Date: August 14, 2002 | doi: 10.1021/bk-2002-0828.ch021

$$Z_{Ji} \equiv \frac{1}{8\pi^2}\int_V \exp(-\Phi_{Ji}(r,\theta,\phi,\alpha,\beta,\gamma)/kT)r^2 \sin\theta\, dr\, d\theta\, d\phi\, d\alpha\, d\beta\, d\gamma \qquad (9)$$

With this thermodynamic model, we treat the clathrate as a two-component system. Thus, the phase equilibrium of clathrate hydrates can be described by

$$\begin{aligned} \mu_w^H &= \mu_w^{L \text{ or } \alpha} \\ \mu_w^{\beta-H} &= \mu_w^{\beta} - \mu_w^{H} = \mu_w^{\beta} - \mu_w^{L \text{ or } \alpha} = \Delta\mu_w^{\beta-L \text{ or } \alpha} \end{aligned} \qquad (10)$$

where μ_w^β is the chemical potential of the hypothetical empty hydrate lattice in which no cages are occupied by guest molecules, μ_w^H is the chemical potential of water in the hydrate phase, and $\mu_w^{L \text{ or } \alpha}$ is the chemical potential of water in the solid ice phase (α) or liquid aqueous phase (L) depending on whether the temperature is below 273.15 K or not. Following the convention proposed by Holder (*41*), the chemical potential difference between the water in the hypothetical empty lattice and the water in the hydrate phase can be expressed as

$$\frac{\Delta\mu_w^{\beta-L \text{ or } \alpha}(T,P)}{kT} = \frac{\Delta\mu_w^{\beta-\alpha}(T_0,0)}{kT_0} - \int_{T_0}^{T}\left[\frac{\Delta H_w^{\beta-L \text{ or } \alpha}}{kT^2}\right]_P dT + \int_0^P\left[\frac{\Delta V_w^{\beta-L \text{ or } \alpha}}{kT}\right]_T dP - \ln a_w^L \qquad (11)$$

where $\Delta\mu_w^{\beta-\alpha}(T_0,0)$ is the reference chemical potential difference at the reference temperature, T_0, usually taken to be 273.15 K, and zero pressure. Once reference state values for $\Delta\mu_w^0 \equiv \Delta\mu_w^{\beta-\alpha}(T_0,0)$, $\Delta H_w^0 \equiv \Delta H_w^{\beta-\alpha}(T_0)$, $\Delta C_p^{\beta-L \text{ or } \alpha}(T_0)$ and $\Delta V_w^{\beta-L \text{ or } \alpha}(T_0)$ are specified, $\Delta\mu^{\beta-H}(T,P)$ can be computed at a T and P of interest using Eqs. 10-11 (*9*).

Our study used two basic approaches to model or predict phase equilibria for methane hydrates. In Approach 1, potential forms were employed to fit the experimental data with and without the LJD approximation. In Approach 2, the intermolecular potential obtained from first principles (*20*) was incorporated in phase equilibrium computations.

In Approach 1, experimental equilibrium three-phase dissociation pressure data compiled by Sloan (*37*), consisting of 97 points for the methane-water system from 148.8 to 320.1 K, were used in the parameter optimization. Although the fits were satisfactory, the intermolecular parameters fitted from the experimental data did not have much physical meaning (*9*). We also found that none of the simple potentials, including Lennard-Jones 12-6, Kihara, and optimized potential from liquid simulation (OPLS), were able to predict both

Downloaded by STANFORD UNIV GREEN LIBR on September 14, 2012 | http://pubs.acs.org
Publication Date: August 14, 2002 | doi: 10.1021/bk-2002-0828.ch021

cage occupancies and potential-distance profiles correctly when compared with experimental data (see Ref. 9 for more detail). Therefore, Approach 2 was explored to test its capability to characterize both microscopic (intermolecular potential profile) and macroscopic (dissociation pressure and occupancies) properties correctly. Based on the simple clathrate system – methane hydrates, the *ab initio* potential, developed in the previous section, was implemented to predict the phase diagram.

In Approach 2, the algorithm proposed by Parrish and Prausnitz (*42*) was used in an iterative manner to obtain the converged pressure that satisfies the van der Waals and Platteeuw model, in order to predict the three-phase (L_w(liquid water)-H(hydrate)-V(methane gas)) hydrate equilibrium pressure at any given temperature. In our calculation, the Peng-Robinson EOS is used to calculate the fugacity of methane. All the reference thermodynamic properties used are those listed in Table II, and the convergence criterion is either a relative error of less than 1% for large dissociation pressures (> 1 bar) or an absolute error of less than 0.05 bar for small dissociation pressures (< 1 bar). In all *ab initio* calculations in this study, the averaged potential profiles were computed point by point with all the intermediate values obtained via a cubic spline interpolation at a given temperature (*43*). To make sure that the spline fit works well outside the fitted distance, five additional highly accurate calculations using MP2/cc-pVQZ were performed at distances from 7.0 Å to 11.0 Å and the interaction energies at larger distances from 13.0 Å to 18.0 Å were set to be zero so that the spine-fitted profile approaches zero at very large distances, as expected.

A wide temperature range from 148.8 to 320.1 K (*37*) was included in the phase equilibrium prediction and compared with experimental values in Figure 6 in both linear and logarithmic scales. In Figure 6, the phase diagram calculated using the fitted molecular parameters within the LJD approximation, a potential derived from 2^{nd} virial coefficient data and our five-shell integration method are also plotted. The predicted phase diagram using the 2^{nd} virial coefficient potential gives poor agreement with experiment, possibly because it fails to capture the interaction in the repulsive region, but also possibly because of the failures of the LJD approximation. It is obvious that the LJD and five-shell integration(*9*) methods match the experimental data very well since they were fitted (separately) to the *P-T* phase diagram, but the *ab initio* potential, with no adjustable parameters, gives equally excellent agreement. In addition, below 200 K and above 310 K, the *ab initio* potential gives the best prediction of dissociation pressure as shown in Figure 6(a) and 6(b). The *ab initio* potential, different from any fitted potential with an analytical form, characterizes the interaction between guest and host molecules in a physically meaningful manner and provides an accurate prediction of macroscopic gas hydrate phase equilibria.

Downloaded by STANFORD UNIV GREEN LIBR on September 14, 2012 | http://pubs.acs.org
Publication Date: August 14, 2002 | doi: 10.1021/bk-2002-0828.ch021

TABLE II: Thermodynamic reference properties - Structure I water clathrate

Chemical potential difference ($T_0 = 273.15$ K, $P_0 = 0$ atm)	
$\Delta\mu_w^0$	$1263\ \mathrm{J \cdot mol^{-1}}$
Enthalpy difference (T_0, P_0)	
ΔH_w^0	$1389\ \mathrm{J \cdot mol^{-1}}$
Latent Heat (T_0, P_0)	
$\Delta H_w^{\alpha-L}$	$-6009.5\ \mathrm{J \cdot mol^{-1}}$
Volume differences	
$\Delta V_w^{\beta-\alpha}$	$3.0 \times 10^{-6}\ \mathrm{m^3 \cdot mol^{-1}}$
$\Delta V_w^{L-\alpha}$	$-1.598 \times 10^{-6}\ \mathrm{m^3 \cdot mol^{-1}}$
Heat capacity differences	
	$T > T_0$
$\Delta C_p^{\beta-L}$	$-38.12\ \mathrm{J \cdot mol^{-1} \cdot K^{-1}}$
$\Delta b^{\beta-L}$	$0.141\ \mathrm{J \cdot mol^{-1} \cdot K^{-2}}$
	$T < T_0$
$\Delta C_p^{\beta-\alpha}$	$0.565\ \mathrm{J \cdot mol^{-1} \cdot K^{-1}}$
$\Delta b^{\beta-\alpha}$	$0.002\ \mathrm{J \cdot mol^{-1} \cdot K^{-2}}$

TABLE III: Comparison of cage occupancies of methane hydrates in both small and large cages

T (K)	Experimental value[44]		Fitted 5-shell integration (Kihara Potential)		*Ab initio* potential	
	y_1	y_2	y_1	y_2	y_1	y_2
273.65	0.920	0.971	0.709	0.983	0.961	0.957
274.65	0.899	0.972	0.710	0.983	0.961	0.957
275.65	0.869	0.974	0.728	0.984	0.964	0.961
276.65	0.866	0.973	0.738	0.985	0.965	0.963

Downloaded by STANFORD UNIV GREEN LIBR on September 14, 2012 | http://pubs.acs.org
Publication Date: August 14, 2002 | doi: 10.1021/bk-2002-0828.ch021

Downloaded by STANFORD UNIV GREEN LIBR on September 14, 2012 | http://pubs.acs.org
Publication Date: August 14, 2002 | doi: 10.1021/bk-2002-0828.ch021

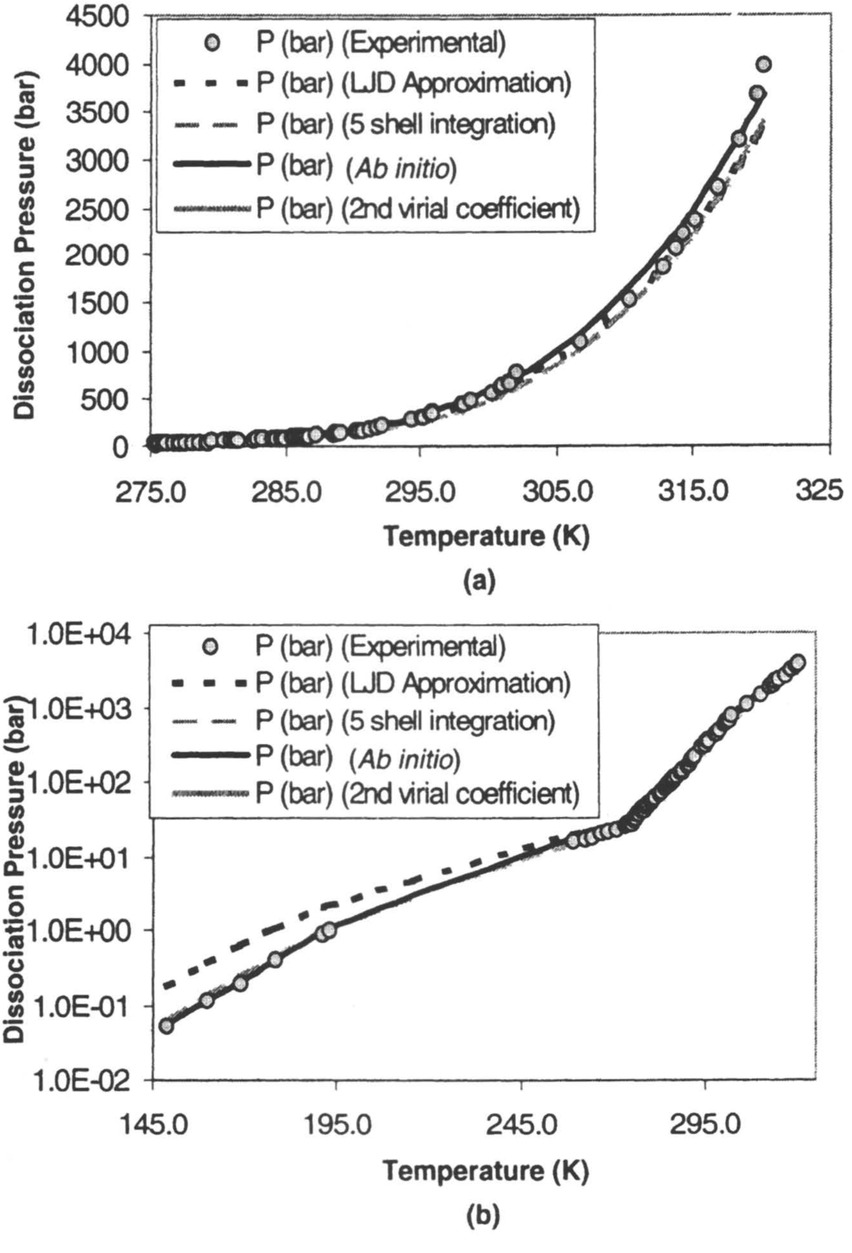

Figure 6: Experimental and predicted methane hydrate phase diagrams computed using different potentials. (6(a) is a linear plot, with temperature below 250 K not shown. 6(b) is a log-linear plot, with entire temperature range shown.) (SOURCE: Adapted with permission from refrence 9. Copyright 2001 American Chemical Society)

Downloaded by STANFORD UNIV GREEN LIBR on September 14, 2012 | http://pubs.acs.org
Publication Date: August 14, 2002 | doi: 10.1021/bk-2002-0828.ch021

The *ab initio* potential was also used to predict the occupancies of both cages in methane hydrates with results listed in Table III. Experimental cage occupancies of methane hydrates were extracted indirectly from Raman spectroscopic data as reported by Sum et al. (*44*). The occupancy extraction method used in that study is model dependent and is subject to possible systematic errors. Because only the relative occupancy between large and small cages is calculated from the deconvolution of two highly overlapping bands, a small deviation of the ratio could introduce a large error in the resulting occupancies. Furthermore, because the ratio of occupancies is close to 1.0, these errors may actually lead to incorrect interpretation of occupancy trends between the two cavities. We also note that at temperatures closer to the ice point, our *ab initio* potential yields occupancies that are much more sensitive to variations in temperature. Further analysis will be presented in future work.

Although the *ab initio* potential cannot be represented exactly by an analytical expression, the exp-6 potential provides the best representation at any specific temperature in both the attractive and repulsive regions and thus was selected in our sensitivity analysis (*9*). The expression for the exp-6 potential can be represented as

$$\Phi_{ij}(r) = \frac{\varepsilon}{\alpha - 6}\left\{6\exp\left[\alpha\left(1 - \frac{r}{r^*}\right)\right] - \alpha\left(\frac{r^*}{r}\right)^6\right\} \tag{12}$$

where r is the distance between the two molecules, α is the stiffness parameter as a measurement of repulsive interaction, ε is the depth of the potential well, and r^* is the distance parameter that gives the position of the minimum of the potential. The two parameters, ε and α were varied independently to investigate their effect on phase equilibrium predictions of methane hydrates. In our sensitivity analysis, the variation of ε/k and α from their base values were 5.0 K and 0.5 Å. Each variation shifts the predicted pressure-temperature curves by a factor of approximately 1.5 (see Ref. 9 for more detail). This indicates that the phase equilibrium prediction is extremely sensitive to both ε and α. The shape and curvature of the potential profile is even more sensitive to ε than to α. This shows again the superior advantage of our temperature dependent *ab initio* potential over simple potential forms fitted to experimental data.

Issue of the reference state

The statistical thermodynamic model for hydrate equilibria developed by van der Waals and Platteeuw in 1959 (*2*) was generalized by Parrish and Prausnitz for prediction of hydrate dissociation pressures (*42*). The method of

Downloaded by STANFORD UNIV GREEN LIBR on September 14, 2012 | http://pubs.acs.org
Publication Date: August 14, 2002 | doi: 10.1021/bk-2002-0828.ch021

phase equilibria prediction was further simplified by Holder at al. (*41*) in 1980 to eliminate the need for the reference hydrate by introducing a universal set of reference properties for each type of structure. This established the methodology for most of the later thermodynamic and equilibrium calculations of gas hydrates (*6*).

It is very important to obtain accurate values of the reference properties because they are the most critical inputs to the statistical model. Several investigators have determined values of two of the thermodynamic reference parameters, namely $\Delta\mu_w^0$ and ΔH_w^0. Table IV lists some of the values that have been determined using various calculation and experimental techniques. Although they seem to agree with each other to some extent, the variation remains large enough to affect the prediction of the model significantly.

Independent studies by Dharmawardhana et al. (*45,46*) and Holder et. al (*47*), Handa and Tse (*48*), and Sloan (*6*) have obtained the three different sets of reference parameters that are considered the most accurate. With current available data in the literature, it is still unclear which set of reference parameters should be used in phase equilibria studies, given their apparent numerical discrepancies. In addition, the sensitivity of the effect on the prediction of phase equilibria from different values of reference properties has not been studied quantitatively before.

The relationship in Eqs. 10-11 can be expanded and used to fit the reference properties. Holder et al. (*47*) integrated and rearranged Eqs. 10-11 in the following form

$$Y = \frac{\Delta\mu_w^0}{RT_0} + \frac{\Delta H_w^0 + \Delta H_w^{\alpha-L}(T_0)}{R}\left[\frac{1}{T} - \frac{1}{T_0}\right] \tag{13}$$

where Y is a function of the experimental conditions (T, P, composition) and other parameters, namely $\Delta\mu_w^{\beta-H}(T,P)$, $\Delta b^{\beta-L \text{ or } \alpha}$, $\Delta C_p^{\beta-L \text{ or } \alpha}(T_0)$ and $\Delta V_w^{\beta-L \text{ or } \alpha}(T_0)$. A plot of the experimental value of Y vs. $(1/T\text{-}1/T_0)$ should yield a straight line whose intercept and slope will give us the values of $\Delta\mu_w^0$ and ΔH_w^0. This analysis was based on the experimental *s*I cyclopropane data obtained by Dharmawardhana et al. (*45,46*).

Another independent study was performed by Handa and Tse (*48*). The empty lattice of clathrate hydrates, which serves as a hypothetical reference state, is unstable and has never been synthesized in the laboratory. Xenon forms *s*I hydrates and the fugacity of xenon is 1.467 bar for the hydrate-ice-gas equilibrium at 273.15 K. In the case of small and spherical monatomic species like xenon, this experimental condition of xenon hydrates is very close to that of the empty lattice (T_0=273.15 K, P_0=0 bar). Therefore, Eq. 6 was used to estimate $\Delta\mu_w^0$ since the two fractional occupation probabilities in both cages can be determined from ^{129}Xe NMR and calorimetric study (*49*). This is reasonable because the error introduced by the pressure difference, 1.47 bar, is extremely small compared with other terms in Eq. 11, as found in our calculations (*50*).

The same fitting approach used by Holder et. al (*47*) can be applied to determine the reference properties from the *ab initio* pair potential. The only difference is that the experimental compositional measurements, y_{Ji}, are not needed in this case to evaluate $\Delta\mu^{\beta-H}$ in Eq. 6 because they can be calculated directly from the numerical integration of the Langmuir constants C_{Ji}. The only experimental data needed for this approach is the readily available methane hydrate *P-T* phase equilibrium data. This gives us the great advantage of using nearly 100 data points in the fitting procedure and the elimination of the uncertainty introduced by the composition measurements that are hard to perform accurately in practice over a wide temperature range.

Via this approach, we were able to obtain the reference properties directly from the *ab initio* potential and methane hydrate *P-T* equilibrium. Without the need of the composition data, we incorporated 97 data points for the methane-water system (*37*) in our fitting procedure. The result is shown in Figure 7. The fitted reference properties ($\Delta\mu_w^0 = 1236$ J/mol, $\Delta H_w^0 = 1703$ J/mol) are within the range of the previous studies as listed in Table IV. The ΔH_w^0 value is on the high end of the experimental values, but the hydrate system is much more sensitive to $\Delta\mu_w^0$ than it is to ΔH_w^0 (*50*). The line fit had a highly linear correlation (R^2=0.996), and we obtained a 95% confidence deviation of only 8 J/mol for $\Delta\mu_w^0$ from the regression analysis. This is promising because the regression analysis using the *ab initio* method is now free from the experimental uncertainties related to difficult composition measurements. The good linear relationship that results from using the *ab initio* method confirms, to some extent, that the van der Waals and Platteeuw model works well for the methane-water system with the empty lattice as the reference state.

Conclusions

We have developed a six-dimensional methane-water pair potential for use in computing properties of methane hydrates. This potential was developed from *ab initio* calculations, using a new method for correcting from energies of interaction computed using small basis sets to those computed using large ones. The potential was validated using second virial coefficient data, spectroscopic data, and methane hydrate phase data. It was used to compute thermodynamic reference data with fewer assumptions than used hitherto.

Downloaded by STANFORD UNIV GREEN LIBR on September 14, 2012 | http://pubs.acs.org
Publication Date: August 14, 2002 | doi: 10.1021/bk-2002-0828.ch021

Downloaded by STANFORD UNIV GREEN LIBR on September 14, 2012 | http://pubs.acs.org
Publication Date: August 14, 2002 | doi: 10.1021/bk-2002-0828.ch021

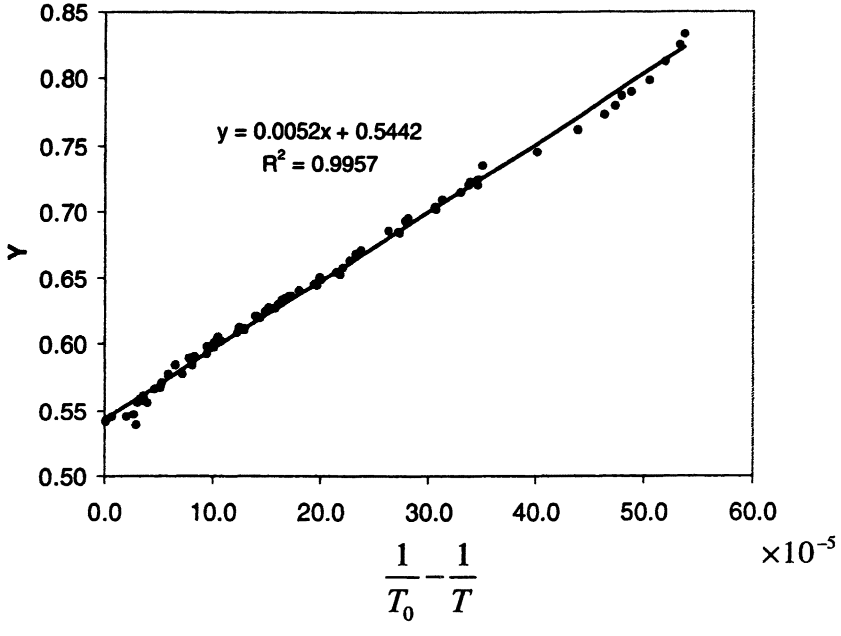

Figure 7: Linear fit of ab initio methane hydrate data for evaluation of Structure I empty lattice reference parameters

Downloaded by STANFORD UNIV GREEN LIBR on September 14, 2012 | http://pubs.acs.org
Publication Date: August 14, 2002 | doi: 10.1021/bk-2002-0828.ch021

TABLE IV: Differences in thermodynamic properties between ice and the empty hydrate lattice (adapted from Sloan, 1998[6])

Structure I		Structure II		Reference
$\Delta\mu_w^0$ J/mol	ΔH_w^0 J/mol	$\Delta\mu_w^0$ J/mol	ΔH_w^0 J/mol	
699	0	820	0	van der Waals and Platteeuw (1959)
		366-537		Barrer and Ruzicka (1962)
		833		Scortland and Robinson (1964)
1255.2	753	795	837	Child (1964)
1264	1150		808	Parrish and Prausnitz (1972)
1155	381		0	Holder (1976)
1297	1389	937	1025	Dharmawardhana, Parrish and Sloan (1980)
1299	1861			Holder, Malekar, and Sloan (1984)
1120	931	1714	1400	John, Papadopoulos, and Holder (1985)
1297				Davidson, Handa, and Ripmeester (1986)
1287	931	1068	764	Handa and Tse (1986)

Acknowledgements

We would like to thank the Idaho National Engineering and Environmental Laboratory for partial support of this work.

References

Downloaded by STANFORD UNIV GREEN LIBR on September 14, 2012 | http://pubs.acs.org
Publication Date: August 14, 2002 | doi: 10.1021/bk-2002-0828.ch021

(1) Fowler, R. H.; Guggenheim, E. A. *Statistical Thermodynamics*; Cambridge University Press: , 1952.

(2) van der Waals, J. H.; Platteeuw, J. C. *Adv. Chem. Phys.* **1959**, *2*, 1.

(3) Sparks, K. A.; Tester, J. W.; Cao, Z.; Trout, B. L. *J. Phys. Chem. B* **1999**, *103*, 6300.

(4) John, V. T.; Papadopoulos, K. D.; Holder, G. D. *AIChE Journal* **1985**, *31*, 252.

(5) John, V. T.; Holder, G. D. *J. Phys. Chem.* **1985**, *89*, 3279.

(6) Sloan, E. D., Jr. *Clathrate hydrates of natural gases - 2nd ed., rev. and expanded*; Marcel Dekker, Inc.: Monticello, 1998.

(7) Jorgensen, W. L.; Madura, J. D.; Swenson, C. J. *J. Am. Chem. Soc.* **1984**, *106*, 6638.

(8) Sun, Y.; Kollman, P. A. *Journal of computational chemistry* **1995**, *16*, 1164-1169.

(9) Cao, Z.; Tester, J. W.; Sparks, K. A.; Trout, B. L. *J. Phys. Chem. B* **2001**, 105, 10950.

(10) Sparks, K. A. *MIT Chemical Engineering Department, PhD Thesis* **1991**.

(11) Bazant, M. Z.; Trout, B. L. *Physica A* **2001**, 300, 139.

(12) Anderson, B. J.; Cao, Z.; Bazant, M.; Tester, J. W.; Trout, B. L. *to be submitted* **2001**.

(13) Owicki, J. C.; Scheraga, H. A. *J. Am. Chem. Soc.* **1977**, *99*, 7413.

(14) Swaminathan, S.; Harrison, S. W.; Beveridge, D. L. *J. Am. Chem. Soc.* **1978**, *100*, 5705.

(15) Novoa, J. J.; Tarron, B.; Whangbo, M.-H.; Williams, J. M. *J. Chem. Phys.* **1991**, *95*, 5179.

(16) Szczesniak, M. M.; Chalasinski, G.; Cybulski, S. M.; Cieplak, P. *J. Chem. Phys.* **1993**, *98*, 3078.

(17) Novoa, J. J.; Planas, M.; Rovira, M. C. *Chem. Phys. lett.* **1996**, *251*, 33.

(18) McMullan, R. K.; Jeffrey, G. A. *J. Chem. Phys.* **1965**, *42*, 2725.

(19) Mak, T. C. W.; McMullan, R. K. *J. Chem. Phys.* **1965**, *42*, 2732.

(20) Cao, Z.; Tester, J. W.; Trout, B. L. *J. Chem. Phys.* **2001**, *115*, 2550.

(21) Goldstein, H. *Classical mechanics*, 2nd Edition ed.; Addison-Wesley Publishing Company: Reading, Massachusetts, 1980.

(22) Frish, M. J.; Trucks, G. W.; Schlegel, H. B.; Gill, P. M. W.; Johnson, B. G.; Robb, M. A.; Cheeseman, J. R.; Keith, T. A.; Petersson, G. A.; Montgomery, J. A.; Raghavachari, K.; Al-Laham, M. A.; Zakrzewski, V. G.; Ortiz, J. V.; Foresman, J. B.; Cioslowski, J.; Stefanov, B. B.; Nanayakkara, A.; Challacombe, M.; Peng, C. Y.; Ayala, P. Y.; Chen, W.; Wong, M. W.; Andres, J. L.; Replogle, E. S.; Gomperts, R.; Martin, R. L.; Fox, D. J.; Binkley, J. S.; Defrees, D. J.; Baker, J.; Stewart, J. P.; Head-Gordon, M.; Gonzalez, C.; Pople, J. A. *Gaussian 94*; Gaussian, Inc.: Pittsburgh PA, 1995.

(23) Szabo, A.; Ostlund, N. S. *Modern Quantum Chemistry: Introduction to Advanced Electronic Structure Theory*; McGraw-Hill, Inc.: New York, 1989.

(24) Parr, R. G.; Yang, W. *Desnsity-Functional theory of Atoms and Molecules*; Oxford University Press: New York, 1989.

(25) Møller, C.; Plesset, M. S. *Phys. Rev.* **1934**, *46*, 618.

(26) Frisch, M. J.; M., H.-G.; Pople, J. A. *Phys. Lett.* **1990**, *166*, 281.

(27) Krishnan, R.; Pople, J. A. *J. Quant. Chem.* **1978**, *14*, 91.

(28) Pople, J. A.; Head-Gordon, M.; Raghavachari, K. *J. Chem. Phys.* **1987**, *87*, 5968.

(29) Pople, J. A.; Krishnan, R.; Schlegel, H. B.; Binkley, J. S. *Int. J. Quant. Chem.* **1978**, *XIV*, 545.

(30) Becke, A. D. *Phys. Rev. A* **1988**, *38*, 3098.

(31) Lee, C.; Yang, W.; Parr, R. G. *Physical review B* **1988**, *37*, 785.

(32) Becke, A. D. *J. Chem. Phys.* **1993**, *98*, 5648.

(33) Perdew, J. P.; Wang, Y. *Physical review B* **1992**, *45*, 13244.

(34) Hirschfelder, J. O.; Curtiss, C. F.; Bird, R. B. *Molecular theory of gases and liquids*; John Wiley &Sons, Inc.: New York, 1964.

(35) Plonsey, R.; Collin, R. E. *Principles and applications of electromagnetic fields*; McGraw-Hill Book Company, Inc.: New York, 1961.

(36) Hicks, C. R.; Turner, K. V., Jr. *Fundamental concepts in the design of experiments*, 5th Edition ed.; Oxford Univeristy Press, Inc.: New York, 1999.

(37) Sloan, E. D. *Clathrate hydrate of natural gases*; Marcel Dekker Inc.: New York, 1990.

(38) Tee, L. S.; Gotoh, S.; Stewart, W. E. *Ind. Eng. chem. Fund.* **1966**, *5*, 363.

(39) Dore, L.; Cohen, R. C.; Schmuttenmaer, C. A.; Busarow, K. L.; Elrod, M. J.; Loeser, J. G.; Saykally, R. J. *J. Chem. Phys.* **1994**, *100*, 863.

(40) Peng, D.-Y.; Robinson, D. B. *Ind. Eng. Chem. Fundam.* **1976**, *15*, 59.

(41) Holder, G. D.; Corbin, G.; Papadopoulos, K. D. *Ind. Eng. Chem. Fundam.* **1980**, *19*, 282.

(42) Parrish, W. R.; Prausnitz, J. M. *Ind. Eng. Chem. Process Des. Develop.* **1972**, *11*, 26.

Downloaded by STANFORD UNIV GREEN LIBR on September 14, 2012 | http://pubs.acs.org
Publication Date: August 14, 2002 | doi: 10.1021/bk-2002-0828.ch021

(43) Press, W. H.; Flannery, B. P.; Teukolsky, S. A.; Vetterling, W. T. *Numerical recipes: the art of scientific computing (Fortran version)*; Cambridge University Press: Cambridge, 1989.

(44) Sum, A. K.; Burruss, R. C.; Sloan, E. D. *J. Phys. Chem.* **1997**, *101*, 7371.

(45) Dharmawardhana, P. B.; Parrish, W. R.; Sloan, E. D. *Ind. Eng. Chem. fundam.* **1980**, *19*, 410.

(46) Dharmawardhana, P. B.; Parrish, W. R.; Sloan, E. D. *Ind. Eng. Chem. Fundam.* **1981**, *20*, 306.

(47) Holder, G. D.; Malekar, S. T.; Sloan, E. D. *Ind. Eng. Chem. Fundam.* **1984**, *23*, 123.

(48) Handa, P. Y.; Tse, J. S. *J. Phys. Chem.* **1986,** *90*, 5917.

(49) Davidson, D. W.; Handa, Y. P.; Ripmeester, J. A. *J. Phys. Chem.* **1986,** *90*, 6549.

(50) Cao, Z.; Trout, B. L.; Tester, J. W. *J. Phys. Chem. B (to be submitted)* **2002**.

Downloaded by STANFORD UNIV GREEN LIBR on September 14, 2012 | http://pubs.acs.org
Publication Date: August 14, 2002 | doi: 10.1021/bk-2002-0828.ch021

Author Index

Anderson, Brian J., 418
Arp, Z., 380
Baer, Michael, 361
Boatz, J. A., 221
Bondoc, E., 380
Bowman, Joel M., 346
Byrd, Edward F. C., 93
Cao, Zhitao, 418
Casida, Mark E., 199
Chattopadhyay, Sudip, 109
Chaudhuri, Rajat K., 154
Choo, J., 380
Dyall, Kenneth G., 1
Fedorov, Dmitri G., 276
Field, R. W., 238
Freed, Karl F., 154
Ghosh, Pradipta, 109
Gordon, Mark S., 276
Gwaltney, Steven R., 93
Haller, K., 380
Harrison, J. F., 238
Head-Gordon, Martin, 93
Hinde, R. J., 221
Hoffmann, Mark R., 1, 176, 329
Jarrold, C. C., 238
Khait, Yuriy G., 176
Klots, T., 380
Kowalski, Karol, 31
Kucharski, Stanislaw A., 31
Laane, J. 380
Lamoneda, Ramón Hernández, 314
Langhoff, P. W., 221
Li, Xiangzhu, 10
Mahapatra, Uttam Sinha, 109
Makri, Nancy, 400
Meinander, N. 380
Miller, Charles E., 260
Morris, K., 380
Mukherjee, Debashis, 109
Nanbu, Shinkoh, 300
Nooijen, Marcel, 65
Paldus, Josef, 10
Peterson, Kirk, 346
Piecuch, Piotr, 31
Pimienta, Ian S. O., 31
Potts, Davin M., 154
Sakurai, S., 380
Schatz, George C., 329
Shao, Jiushu, 400
Sheehy, J. A., 221
Skokov, Sergei, 346
Suzuki, Toshinori, 300
Tester, Jefferson W., 418
Trout, Bernhardt L., 418
Van Voorhis, Troy
Wladyslawski, Mark, 65
Zou, Shengli, 346

Downloaded by 217.66.152.144 on September 14, 2012 | http://pubs.acs.org
Publication Date: August 14, 2002 | doi: 10.1021/bk-2002-0828.ix001

Subject Index

A

Ab initio calculations
  advantage of density functional theory (DFT) over *ab initio* methods, 200
  characterization of bromine monoxide, 267*t*
  characterization of chlorine monoxide, 265*t*
  characterization of fluorine monoxide, 263*t*
  characterization of iodine monoxide, 269*t*
  comparing experimental and *ab initio* barriers of indan family, 397*t*
  comparison of all one-electron excitation energies of C_2H_4 with good *ab initio* calculations, 210*f*
  computations of molecular properties, 11
  methodology of *ab initio* calculations for methane hydrates, 421–427
  potential predicting cage occupancies of methane hydrates, 435*t*
  reduced dimensionality surface for vibrationally selected rate constants, 319
  See also Halogen monoxides; Methane hydrates
Absorbing potentials, molecular resonances, 348, 350
ACES II, electronic structure programs, 71–72
Adiabatic local density approximation (ALDA), lowest level, 205
Adiabatic-to-diabatic transformation matrix and rotation matrix
  Curl condition, 365
  multi-fold degeneracy, 376
  non-adiabatic coupling terms (NACTs), 361–362
  quantizing non-adiabatic coupling matrix (NACM), 362, 376
  tetra-fold degeneracy case, 370–373
  theoretical background, 363–366
  treatment of model NACM, 366–367
  treatment of special cases, 367–373
  tri-fold degeneracy case, 369–370
  two-state degeneracy, 368
  Wigner rotation matrix, 373–375
Allene
  $^1A_1$, $^1A_2$, $^1B_1$, and $^1B_2$ states, 155–156
  C_3H_4 torsional potential energy curves, 171*f*
  comparing IVO–CASCI and effective valence shell Hamiltonian (H^v) vertical excitation energies (VEE), 172*t*
  comparing IVO–CASCI and H^v VIPs using bases of increasing size, 168*t*
  comparing VIPs by IVO–CASCI and H^v methods with MRSDCI method and experiments, 165*t*
  computational details, 161–163
  equilibrium geometry parameters for, and twisted, 164*t*
  excitation energies and oscillator strengths from IVO–CASCI and H^v vs. experiment and MRSDCI, 170*t*
  excited states of C_3H_4, 166, 169, 173
  excited states of $C_3H_4^+$, 163, 166
  first optical spectrum, 155

In Low-Lying Potential Energy Surfaces; Hoffmann, M., et al.;
ACS Symposium Series; American Chemical Society: Washington, DC, 2002.

Downloaded by 217.66.152.21 on September 14, 2012 | http://pubs.acs.org
Publication Date: August 14, 2002 | doi: 10.1021/bk-2002-0828.ix002

generation of improved virtual orbitals (IVO), 159–161
H^v method, 156
interest for photoelectron and optical spectra, 154–155
IVO–CASCI method, 156
molecular point group, 154
photoelectron spectrum (PES), 155
subset of neutral allene Hartree–Fock (HF) molecular orbitals and energies, 164*t*
theory of H^v method, 157–159
torsional potential energy curves for positive ion, 167*f*
vertical ionization potentials (VIPs) as function of reference space for production of X^2E, X^4E, A^2E ion states, 165*t*

Amplitude-correcting methods
  average deviations of calculated from experimental frequencies of N_2 molecule by CCSD, 4R- and 8R-reduced multi-reference (RMR) CCSD methods, 17*t*
  coupled-cluster CCSD methods, 13
  RMR CCSD version, 15–18
  vibrational levels of HF with CCSD and 4R-RMR CCSD methods, 16*t*
  vibrational term values for N_2 molecule and deviations from experimental values, 17*t*

Anions
  calcium and zinc fluorides, 244, 246–247
  comparing energy separations for CaF and ZnF and their anions, 247*f*
  comparing energy separations for CaO and ZnO and their anions, 256*f*

Atmosphere, chemical composition, 317

Atomic-interaction-based theory, chemical bonding, 222

B

Bending dissociation
  non-adiabatic, as orbital unlocking, 309, 312
  non-adiabatic transition in bending coordinate, 308–309
  See also OCS

1,3-Benzodioxole (BZD)
  anomeric effect, 390–391, 395
  comparing experimental and *ab initio* barriers, 397*t*
  electronic states, 381
  fluorescence excitation spectra and ultraviolet absorption spectra, 391*f*
  kinetic energy function for cross term, 386*f*
  n–σ* anomeric interaction, 394*f*
  ring-puckering quantum states in different flapping and electronic states, 392*f*
  two-dimensional potential energy surface in S_0 state, 393*f*
  See also Potential energy surfaces (PESs), spectroscopic determination

BH, completely renormalized CCSD(T), CR–CCSD(TQ), and CR–CCSDT(Q), 50–51

Bimolecular reactions, spin-orbit effects, 330–331

Binding energies. *See* Methane hydrates

Binding energy difference, 425–426

Bond breaking. *See* Coupled cluster (CC) methods for bond-breaking

Bonding, chemical. *See* Spectral theory of chemical bonding

Bromine monoxide (BrO)
  ab initio characterization, 267*t*
  comparing RKR and multi-reference configuration interaction (MRCI) potential, 266*f*
  RKR potentials, 265

Downloaded by 217.66.152.21 on September 14, 2012 | http://pubs.acs.org
Publication Date: August 14, 2002 | doi: 10.1021/bk-2002-0828.ix002

  RKR potentials and vibrational levels, 266*f*
  See also Halogen monoxides

C

C$_2$ molecule
  equation of motion CCSD (EOMCCSD) for excited states, 56–57
  excited states, 54–55
  ground-state potential energy surfaces (PESs), 51–52
  potential energy curves for CH$^+$ ion, 57*f*
  vertical excitation energies, 54*t*
Cage occupancies. *See* Methane hydrates
Calcium
  atomic characteristics, 240
  selected energy levels, 240*f*
Calcium fluoride (CaF)
  anions, 244, 246–247
  cations, 247–248
  comparison of CaF and ZnF and their anions, 247*f*
  dipole moments, 245*t*
  excited electronic states, 238
  generalized Morse potentials, 246*f*
  ionization energies and electron affinities, 245*t*
  neutrals, 241, 244
  population analysis, 242*t*
  spectroscopic properties, 243*t*
  technical details, 239
  theoretical work, 239
Calcium oxide (CaO)
  anions, 253, 255
  cations, 255
  comparison of CaO and ZnO and their anions, 256*f*
  dipole moments, 245*t*, 252–253
  excited electronic states, 238
  generalized Morse potentials, 250*f*, 257*f*
  ionization energies and electron affinities, 245*t*
  Mulliken populations, 252
  neutrals, 248–253
  population analysis, 249*t*
  spectroscopic properties, 251*t*, 254*t*
  technical details, 239
  theoretical work, 239
Carbon dioxide (CO$_2$), Walsh diagram and schematic molecular orbitals, 307*f*
Carbon monoxide, ionization potential, 209*t*
CASPT2 functionality, GAUSSIAN software, 1–2
Cations
  calcium and zinc fluorides, 247–248
  calcium and zinc oxides, 255
CH$_2$O molecule, ionization potential, 209*t*
Chemical bonding. *See* Spectral theory of chemical bonding
Chlorine monoxide (ClO)
  ab initio characterization, 265*t*
  comparing RKR and CCI+Q potential, 264*f*
  RKR potentials, 263
  RKR potentials and vibrational levels, 264*f*
  See also Halogen monoxides
Clathrate hydrate. *See* Methane hydrates
Clebsch–Gordan coefficients
  relations, 293, 295
  spin-orbit coupling calculations, 279–280
Coherent state density matrix
  finite temperature, 408–409
  Gaussian initial state, 407–408
  See also Forward-backward semiclassical dynamics (FBSD)
Complete active space (CAS), dividing electron correlations into

Downloaded by 217.66.152.21 on September 14, 2012 | http://pubs.acs.org
Publication Date: August 14, 2002 | doi: 10.1021/bk-2002-0828.ix002

  nondynamical and dynamical effects, 94–95
Completely renormalized (CR) methods
  CCSDT(Q) approach, 45
  CCSD(TQ) methods, 44–45
  coupled-cluster CCSD(T) and CCSD[T] methods, 43–44
  ground-state potential energy surfaces (PESs) for H_2O, BH, F_2, and N_2 systems, 50–51
  See also Method of moments of coupled-cluster (MMCC) equations
Configuration interaction (CI) and coupled-cluster (CC) approaches
  accounting for dynamic and nondynamic correlations, 12
  multifaceted complementarity, 11
  requirement for nondegeneracy, 11
  See also Coupled-cluster (CC) methods
Configuration interaction (CI) methods
  ab initio computations of molecular properties, 11
  arbitrary CI wavefunction symmetry labeling, 290–293
  energy, 18–19
  single reference (SR) version, 11
  study of ground and excited states potential energy surfaces, 176–177
  See also Table-configuration interaction (CI) method
Configuration state functions (CSFs)
  computational speed in spin-orbit calculations, 287–288
  electronic structure of OCS, 305
  use of genealogical CSFs in table-CI method, 177–180
  See also Table-configuration interaction (CI) method
Correlation function, forward-backward semiclassical dynamics (FBSD), 404, 407
Coumaran (COU)
  comparing experimental and *ab initio* barriers, 397*t*
  electronic states, 381
  far-infrared spectrum, 387*f*
  one-dimensional potential energy function for ring-puckering, 388*f*
  quantum states for puckering and flapping vibrations, 387–388
  See also Potential energy surfaces (PESs), spectroscopic determination
Coupled channel scattering methods, molecular resonances, 348
Coupled-cluster (CC) methods
  ab initio computations of molecular properties, 11
  accounting for dynamic correlation, 12
  amplitude-correcting methods, 13
  CCSD (singles and doubles), 11, 32
  effect of higher than pair clusters (primarily in triples) (CCSD(T)), 12–13
  energy, 18–19
  energy-correcting methods, 14
  energy formula, 13
  externally corrected (EC) CCSD, 13
  generalized Bloch equations (DGB method), 15
  intermediate Hamiltonian approach (IH), 112
  method of moments (MM) CC approach, 14
  overcoming shortcomings of CCSD method, 12
  reduced multi-reference (RMR) CCSD, 14
  renormalized versions (RCCSD(T)), 14
  state specific or state selective (SS) approaches, 11, 13, 14–15
  valence optimized orbital (VOO) CCSD, 14

Downloaded by 217.66.152.21 on September 14, 2012 | http://pubs.acs.org
Publication Date: August 14, 2002 | doi: 10.1021/bk-2002-0828.ix002

- wavefunctions as external source, 13–14
- *See also* Configuration interaction (CI) and coupled-cluster (CC) approaches; Method of moments of coupled-cluster (MMCC) equations; State-specific multi-reference coupled-cluster (SS–MRCC) methods

Coupled cluster (CC) methods for bond-breaking
- calculations of triple bond dissociation of N_2 in STO-3G basis, using full CI (FCI), conventional coupled cluster doubles (CCD), variational CCD (VCCD), and quadratic CCD (QCCD), 99*f*
- CCD wave functions, 95–97
- deviations from FCI for water double dissociation, 106*t*
- difficulty of CCD energy functional, 97–100
- double bond dissociation of water using perfect pairing (PP), imperfect pairing (IP), and restricted pairing local correlation models, 102*f*
- double zeta (DZ) basis for double dissociation of water, 96*f*
- energy deviations from FCI for N_2, 106*t*
- expanding energy to second order, 104
- extended coupled cluster (ECC) theory, 98
- imperfect pairing (IP) operator, 101
- improving reference CCD energy, 102–106
- perfect pairing (PP) operator, 100–101
- performance of second order corrections without using active spaces, 105–106
- perturbatively correcting QCCD model, 105
- QCCD for double bond-breaking, 99
- QCCD for triple bond-breaking, 100
- QCCD method, 98
- restricted pairing (GVB–RCC) model, 101–102
- second order energy expression, 104–105
- similarity-transformed Hamiltonian, 103
- simplicity of CCD wave function, 100–102
- VCCD calculations, 94
- VCCD, CCD, and FCI calculations on double dissociation of water, 96*f*

Coupled cluster doubles (CCD). *See* Coupled cluster (CC) methods for bond-breaking

D

Density functional theory, time-dependent (TDDFT)
- adiabatic local density approximation (ALDA), 205
- advantage of DFT over *ab initio* methods, 200
- charge transfer correction (CTC), 208
- comparison of all one-electron excitation energies of C_2H_4 with good *ab initio* calculations, 210*f*
- configuration interaction singles (CIS), 205
- correlation between various exchange, exchange-correlation methods, and older and more explored (OEP) for C_2H_4, 213*f*
- correlation graph between various x-only method and OEP for C_2H_4, 213*f*
- exchange-correlation energy, 203

Downloaded by 217.66.152.21 on September 14, 2012 | http://pubs.acs.org
Publication Date: August 14, 2002 | doi: 10.1021/bk-2002-0828.ix002

exchange-correlation kernel, 203
exchange-correlation potential, 203
excitation energies for C_2H_4, 211*t*
excited states in DFT, 201–205
fundamental tool in quantum chemistry, 200
generalized gradient approximations (GGAs), 202–203
H_2 ground and excited state surfaces, 207*f*
Jacob's jungle gym for TDDFT, 202*f*, 205
Kohn–Sham formulation, 201
ladder-by-ladder analysis, 205–215
local density approximation (LDA) by homogeneous electron gas (HEG), 201–202
older and more explored (OEP) fourth level of ladder, 202
problems with exchange-correlation energy, 205–208
problems with exchange-correlation kernel, 212, 214–215
problems with exchange-correlation potential, 208–212
Δself-consistent field (ΔSCF) approach, 203–204
solving problem of unknown functional, 200
stability of Kohn–Sham wave function with respect to symmetry-breaking, 206
strength of ΔSCF approach, 204
symmetry breaking in ground state, 206, 208
Tamm–Dancoff approximation (TDA), 208
TDDFT theory, 204–205
TDLDA results for N_2, 206*t*
time-dependent Hartree–Fock (TDHF), 205
time-dependent local density approximation (TDLDA), 205
traditional, 201–203
variational collapse of ethylene π excitation energies above TDLDA ionization threshold, 210*f*
Diabatic crossings, dissociation, 355, 356*f*
DIP–EOM–CCSD. *See* Double ionization potential equation-of-motion coupled cluster singles and doubles (DIP–EOM–CCSD)
Dipole moments
  calcium and zinc fluorides, 245*t*
  calcium and zinc oxides, 245*t*, 252–253
DIP–STEOM–CCSD. *See* Double ionization potential similarity transformed equation-of-motion coupled cluster singles and doubles (DIP–STEOM–CCSD)
Dissociation. *See* Unimolecular dissociation of HOCl
Double group symmetry
  comparing point and double group selection rules, 286–287
  spin-orbit coupling, 282–286
Double ionization potential equation-of-motion coupled-cluster singles and doubles (DIP–EOM–CCSD)
  method, 68
  optimization of NO_3^+ cation ground state geometry, 88
  See also Nitrogen trioxide radical (NO_3)
Double ionization potential similarity transformed equation-of-motion coupled-cluster singles and doubles (DIP–STEOM–CCSD)
  character of lowest DIP–STEOM–CCSD NO_3^+ states, 76*t*
  conical intersections of surfaces in C_{2v} symmetry, 87*t*
  method, 67–68
  optimization of NO_3^+ cation ground state geometry, 88
  optimization of NO_3^+ excited states, 88–89

Downloaded by 217.66.152.21 on September 14, 2012 | http://pubs.acs.org
Publication Date: August 14, 2002 | doi: 10.1021/bk-2002-0828.ix002

optimized geometries and adiabatic ionization potentials (IPs) for NO_3^+ excited state, 79*t*
  optimized geometries of NO_3^+ cation excited states, 82–83
  See also Nitrogen trioxide radical (NO_3)
Double-zeta (DZ) model
  double dissociation of water, 96*f*
  HF molecule, 23–24
  N_2, 24–27
  potential energy curves for double-zeta (CA) HF, N_2, and C_2 molecules and cc-pVDZ F_2 molecule, 49*f*
Dynamical electron correlation, vs. nondynamical, 2–3
Dynamic and nondynamic correlations
  amplitude-correcting methods, 15–18
  average deviations of calculated from experimental frequencies of N_2 molecule with CCSD, 4R- and 8R-reduced multi-reference (RMR) CCSD methods, 17*t*
  complete active space (CAS) methods, 94–95
  configuration interaction (CI) and coupled cluster (CC) method types, 11–12
  energy-correcting methods, 18–27
  examples of energy-correcting methods, 23–27
  HF molecule, 23–24
  N_2 molecule, 24–27
  theory of energy-correcting methods, 18–23
  vibrational levels of HF using CCSD and 4R-RMR CCSD methods, 16*t*
  vibrational term values for N_2 and deviation from experimental values, 17*t*
Dynamics, semiclassical. *See* Forward-backward semiclassical dynamics (FBSD)

E

Eckart functions. *See* Intersystem crossing effects in O + H_2 reaction
Effective valence shell Hamiltonian (H^v) method
  theory, 157–159
  vertical ionization and excitation energies, 156–157
Electron affinities
  calcium and zinc fluorides, 245*t*
  calcium and zinc oxides, 245*t*
Electronic structure
  dynamical vs. nondynamical electron correlation, 2–3
  incentive to retain simplicity of single reference theories, 94
  multiple potential energy surfaces (PESs), 3–4
  nonadiabatic coupling matrix elements, 4–6
  nondynamical correlation, 6
  OCS, 305–308
  static correlation, 6
  See also O_4 system
Electronic structure programs, ACES II, 71–72
Electron pair-bond
  calculations, 231*t*
  See also Spectral theory of chemical bonding
Electron repulsion integrals. *See* Table-configuration interaction (CI) method
Energies
  comparing calcium and zinc fluorides and their anions, 247*f*
  NO_3^+ cation excited states, 84*t*, 85*f*
Energy-correcting methods
  examples, 23–27
  HF molecule, 23–24
  N_2 molecule, 24–27
  theory, 18–23

Downloaded by 217.66.152.21 on September 14, 2012 | http://pubs.acs.org
Publication Date: August 14, 2002 | doi: 10.1021/bk-2002-0828.ix002

Epstein–Nesbet (EN) type perturbation theory, unperturbed Hamiltonian, 20
Equation-of-motion coupled-cluster singles and doubles (EOM–CCSD), 69–70
Equation of motion (EOM), dynamic vs. nondynamic correlation, 3
Equilibrium geometry
  cation NO_3^+ ground state, 77*t*
  NO_3 neutral ground state, 72*t*
Ethylene, C_2H_4
  comparing all one-electron excitation energies of, with good *ab initio* calculations, 210*f*
  correlation graph between various exchange, exchange-correlation methods, and OEP (older and more explored fourth level), 213*f*
  correlation graph between various x-only method and OEP, 213*f*
  describing excited states, 209, 211–212
  excitation energies, 211*t*
  Hartree–Fock orbitals, 211
  ionization potential, 209*t*
  orbital energies, 212, 213*f*
  variational collapse of π excitation energies above time-dependent local density approximation (TDLDA), 210*f*
  See also Density functional theory, time-dependent (TDDFT)
Exchange-correlation energy, density functionals, 203
Exchange-correlation kernel, second derivative, 203
Exchange-correlation potential, effect on charge density, 203
Excitation energies, comparing IVO–CASCI and H^v methods with experiment, 169, 170*t*
Excited states
  anions of calcium and zinc fluorides, 244, 246–247
  anions of calcium and zinc oxides, 253, 255
  calcium and zinc fluorides, 238
  calcium and zinc oxides, 238, 250–253
  cations of calcium and zinc fluorides, 247–248
  cations of calcium and zinc oxides, 255
  See also Calcium fluoride (CaF); Calcium oxide (CaO); Zinc fluoride (ZnF); Zinc oxide (ZnO)
Excited-state theory, method of moments of coupled-cluster (MMCC), 37–41
Extended coupled cluster (ECC), theory, 98
Externally corrected (ec), coupled-cluster CCSD methods, 13

F

Flapping vibrations
  definition of coordinates, 385*f*
  theory, 383, 386
  See also Potential energy surfaces (PESs), spectroscopic determination
Fluorescence excitation spectra (FES), 383
Fluoride F_2, completely renormalized CCSD(T), CR–CCSD(TQ), and CR–CCSDT(Q), 50–51
Fluorides. *See* Calcium fluoride (CaF); Zinc fluoride (ZnF)
Fluorine monoxide (FO)
  ab initio characterization, 263*t*
  comparing RKR and *ab initio* potentials, 262*f*
  RKR potentials, 261, 263
  RKR potentials and vibrational levels, 262*f*
  See also Halogen monoxides

Downloaded by 217.66.152.21 on September 14, 2012 | http://pubs.acs.org
Publication Date: August 14, 2002 | doi: 10.1021/bk-2002-0828.ix002

Downloaded by 217.66.152.21 on September 14, 2012 | http://pubs.acs.org
Publication Date: August 14, 2002 | doi: 10.1021/bk-2002-0828.ix002

Forward-backward semiclassical dynamics (FBSD)
  advantages of tool, 414–415
  average position for one-dimensional quartic oscillator, 410*f*
  average position of quartic oscillator coupled to bath of 30 harmonic degrees of freedom at zero temperature, 411*f*
  coherent state density matrix, 407–409
  coherent state prefactor, 403
  coherent state wavefunction, 403
  correlation function, 404, 407
  correlation function of O–H stretching normal mode of water tetramer at zero temperature, 414*f*
  correlation functions of various normal modes in clusters of two and four water molecules, 411, 414*f*
  FBSD without prefactors, 404–407
  finite temperature, 408–409
  Gaussian initial state, 407–408
  numerical examples, 409–411
  position correlation function of one-dimensional quartic oscillator at two temperatures, 412*f*, 413*f*
  quartic oscillator, 409–411
  semiclassical Heisenberg operator, 405–406
  semiclassical prefactor, 402
  semiclassical propagator, 402–404
  time-dependent Hamiltonian, 405

G

Gas hydrates
  illustration of empty lattice structure, 420*f*
  systems of polyhedral cells, 419
  See also Methane hydrates
GAUSSIAN software, CASPT2 functionality, 1–2
Genealogical configuration state functions. *See* Table-configuration interaction (CI) method
Generalized gradient approximations (GGAs), level of approximation, 202–203
Geometry
  arrangement of atoms in rectangular Li_4, 135*f*
  cation NO_3^+ excited state, 79*t*
  cation NO_3^+ ground state, 77*t*
  NO_3^+ cation excited states, 84*t*, 85*f*
  NO_3 neutral ground state, 72*t*
  optimization of NO_3^+ cation ground state, 88
  parameters for allene and twisted allene, 163, 164*t*
  rectangular, of Li_4 model, 134, 137
  trapezoidal, of H_4 model, 137, 142, 144
  See also Nitrogen trioxide radical (NO_3)
Ground states
  anions of calcium and zinc fluorides, 244, 246–247
  anions of calcium and zinc oxides, 253, 255
  calcium and zinc fluorides, 241
  calcium and zinc oxides, 248–250
  cations of calcium and zinc oxides, 255
  See also Calcium fluoride (CaF); Calcium oxide (CaO); Zinc fluoride (ZnF); Zinc oxide (ZnO)
Ground-state theory, method of moments of coupled-cluster (MMCC), 34–37

H

H_4 model
  benchmark for judging performance of multi-reference formulation, 137

  correlation energies of ground state vs. standard multi-reference (MR) techniques, 144*t*
  description, 137, 142
  energies of 2^1A_1 state, 146*t*
  potential energy surface of ground state, 143*f*
  potential energy surface of some low-lying states, 145*f*
  robustness of formalisms, 142, 144
  trapezoidal geometry, 137, 142, 144
Halogen monoxides
  ab initio characterization of BrO X ($^2\Pi$), 267*t*
  ab initio characterization of ClO X ($^2\Pi$), 265*t*
  ab initio characterization of FO X($^2\Pi$), 263*t*
  ab initio characterization of IO X ($^2\Pi$), 269*t*
  axial and non-axial quadrupole coupling parameters (eQqs), 272–273
  BrO, 265
  BrO $X_1(^2\Pi_{3/2})$ and $X_2(^2\Pi_{1/2})$ RKR potentials and vibrational levels, 266*f*
  chemical bonding, 261
  ClO, 263
  ClO $X_1(^2\Pi_{3/2})$ and $X_2(^2\Pi_{1/2})$ RKR potentials and vibrational levels, 264*f*
  comparing RKR and CCI+Q potential for ClO X ($^2\Pi$), 264*f*
  comparing RKR and MRCI potential for BrO X ($^2\Pi_{eff}$), 266*f*
  comparison of FO RKR $^2\Pi$ potential with *ab initio* potentials, 262*f*
  deriving RKR potentials, 261
  expectation values, 271, 272*t*
  fine structure splittings, 269–270
  FO, 261, 263
  FO $^2\Pi_{3/2}$ and $^2\Pi_{1/2}$ RKR potentials and vibrational levels, 262*f*
  IO, 267, 269
  IO $X_1(^2\Pi_{3/2})$ and $X_2(^2\Pi_{1/2})$ RKR potentials and vibrational levels, 268*f*
  magnetic hyperfine structure and quadrupole coupling parameters, 271
  multi-reference configuration interaction (MRCI) methods for BrO and IO, 270
  probability of finding spin inducing electron at halogen nucleus, 271–272
  relativistic effects, 269–273
  RKR and MRDCI potentials for IO X ($^2\Pi$), 268*f*
  spectroscopic quality potential energy surface, 260–261
  structural and relativistic contributions to eQqs, 273*t*
Hamiltonian matrix elements
  algorithm for constructing, 180
  configuration-driven algorithm, 177
  See also Table-configuration interaction (CI) method
Hellmann–Feynman theorem, electronic charge predictions, 232
HOCl. *See* Unimolecular dissociation of HOCl
Hoffmann–Schatz (HS), spin-orbit effects in bimolecular reactions, 330–331
Hydrates. *See* Methane hydrates
Hydrogen fluoride (HF)
  double-zeta (DZ) model, 23–24
  ground-state potential energy surfaces (PESs), 49–50
  potential energy curve and vibrational term values, 52–53
  selected vibrational term values and dissociation energies, 52*t*
  total full configuration interaction (FCI) energies and energy differences for DZ model, 24*t*

Downloaded by 217.66.152.21 on September 14, 2012 | http://pubs.acs.org
Publication Date: August 14, 2002 | doi: 10.1021/bk-2002-0828.ix002

See also Method of moments of coupled-cluster (MMCC) equations
Hydrogen (H_2) molecule
  eigenvalues for metric matrix, 229*f*
  electron pair-bond calculations, 231*t*
  energies and expectation values for lowest-lying states, 230, 232
  ground and excited state surfaces, 207*f*
  lowest-lying attractive and repulsive states of electron pair bond, 226–227
  lowest-lying singlet and triplet states, 235–236
  one-electron charge distribution in plane of two nuclei for ground state, 233*f*
  potential energy curves, 234*f*
  spectral energies for atomic hydrogen, 228*t*
  See also H_4 model; Spectral theory of chemical bonding

I

Improved virtual orbitals (IVO)
  generation, 159–161
  IVO–CASCI (complete active space configuration interaction) method, 156–157
  vertical ionization and excitation energies by IVO–CASCI, 156–157
  See also Allene
Indan
  comparing experimental and *ab initio* barriers, 397*t*
  dispersed fluorescence spectra of jet-cooled, 396*f*
  electronic states, 381
  far-infrared spectrum, 395
  fluorescence excitation and ultraviolet absorption spectra, 396*f*
  one-dimensional potential energy function for ring-puckering in ground and excited states, 397*f*
  See also Potential energy surfaces (PESs), spectroscopic determination
Inorganic oxides. *See* Halogen monoxides
Intersystem crossing effects in O + H_2 reaction
  Eckart functions, V_{11}, V_{22}, and V_{21}, 332
  Hoffmann–Schatz (HS) work, 330–331
  model Hamiltonians, 331–333
  model results, 337, 341
  parameters for model Hamiltonians, 336*t*
  plots of V_{11}, V_{22}, and V_{21} as function of distance along reaction path, 334*f*, 335*f*
  quantum reaction probabilities versus energy for each model, 338*f*, 339*f*, 340*f*
  quantum scattering calculations, 333, 336
  spin-orbit effects in bimolecular reactions, 330–331
  spin-orbit induced intersystem crossing, 330
  theory, 331–336
  trajectory surface hopping (TSH) methods, 330–331
  TSH calculations, 336
  TSH calculations with corresponding quantum results, 342*f*, 343*f*
Intruder states, appearance, 4
Iodine monoxide (IO)
  ab initio characterization, 269*t*
  RKR and MRD–CI potentials, 268*f*
  RKR potentials, 267, 269
  RKR potentials and vibrational levels, 268*f*
  See also Halogen monoxides
Ionization energies

Downloaded by 217.66.152.21 on September 14, 2012 | http://pubs.acs.org
Publication Date: August 14, 2002 | doi: 10.1021/bk-2002-0828.ix002

- calcium and zinc fluorides, 245*t*
- calcium and zinc oxides, 245*t*
- neutral NO_3 vertical, 74–77

Ionization potentials (IPs), cation NO_3^+ excited state, 79*t*

Isotope effects, dissociation lifetime, 357, 358*t*

J

Jacob's ladder
- density functional approximation, 201–202, 205
- *See also* Density functional theory, time-dependent (TDDFT)

Jahn–Teller distortion
- difference in magnitude for excited states NO_3^+, 85*f*, 86
- potential energy surface for D_{3h} degenerate electronic state (NO_3^+), 80

K

Kihara potential
- comparing corrected and uncorrected interaction potentials with, 430, 431*f*
- interactions between lattice and guests, 419
- *See also* Methane hydrates

Kohn–Sham formulation
- density functional theory (DFT), 201
- stability of wave function with respect to symmetry breaking, 206

L

L^2 approach
- unimolecular dissociation, 350–351
- *See also* Unimolecular dissociation of HOCl

Laser induced fluorescence (LIF), method for determining vibronic levels, 383

Lennard–Jones 6-12 potential, interactions between lattice and guests, 419

Lennard–Jones and Devonshire (LJD), spherical cell potential approximation, 419

Li_4 model
- arrangement of Li atoms in rectangular, 135*f*
- difference energy plot of ground state vs. full CI (FCI) values, 136*f*
- PES of some low-lying $^1A_1$ states of rectangular model, 138*f*
- PES of some low-lying $^1A_2$ states of rectangular model, 139*f*
- PES of some low-lying $^1B_1$ states of rectangular model, 140*f*
- PES of some low-lying $^1B_2$ states of rectangular model, 141*f*
- plot of CSF energies of rectangular model, 135*f*
- rectangular geometry, 134, 137

Linear coefficients. *See* Table-configuration interaction (CI) method

Local density approximation (LDA), exchange-correlation energy density, 201–202

Low-energy electronic states, theoretical advances, 401

M

Many-electron basis functions (MEBFs), assumption, 3–4

Methane hydrates
- *ab initio* potential predicting cage occupancies, 435*t*
- accuracy and efficiency of *ab initio* calculations, 421

Downloaded by 217.66.152.21 on September 14, 2012 | http://pubs.acs.org
Publication Date: August 14, 2002 | doi: 10.1021/bk-2002-0828.ix002

application to hydrate phase equilibria calculations, 432–437
approaches to model or predict phase equilibria for, 433–434
ball and stick model of clathrate hydrate with two adjacent unit cells, 423*f*
binding energies calculated at cc-pVQZ with and without counterpoise method, 429*t*
binding energies of H_2O–CH_4 structure using six basis sets, 428*f*
binding energy difference, 425–426
cage occupancies from Raman spectroscopic data, 437
comparing corrected and uncorrected interaction potentials with Kihara potential, 430, 431*f*
determining proportional factor and testing form of basis set correction factor, 426–427
determining reference properties from *ab initio* pair potential, 439, 440*f*
developing spherically symmetric radial potential, 427
empty lattice of clathrate hydrates, 438–439
fitted reference properties, 441*t*
geometries of methane and water molecule, 422, 425
interaction energy between methane and water, 425
issue of reference state, 437–439
methodology of *ab initio* calculations, 421–427
molecular orbital theories, 425
Peng–Robinson equation of state (EOS), 432, 434
phase diagram using phase equilibrium prediction and experimental values, 436*f*
potential energy hypersurface, 422
predictions by density functional theory (DFT) and *ab initio* methods, 427, 430
reference thermodynamic properties, 435*t*
six-dimensional grid, 424*f*
treating clathrate as two-component system, 433
van der Waals and Platteeuw model, 434
Method of moments (MM), coupled-cluster CC method, 14
Method of moments of coupled-cluster (MMCC) equations
active-space single-reference (SRCC) methods and equation of motion (EOMCC) extensions, 33
applicability of ground-state SSRC approaches, 33–34
approximate MMCC methods: MMCC(m_A,m_B) and renormalized CC schemes, 41–48
attempts to remove failing of perturbative CC approximations at large internuclear separations, 32–33
C_2 molecule, 51–52
completely renormalized CCSD(T) methods, 43–44
completely renormalized CCSDT(Q) approach, 45
completely renormalized CCSD(TQ) methods, 44–45
completely renormalized (CR)–CCSD(T), CR–CCSD(TQ), and CR–CCSDT(Q) for H_2O, BH, F_2, and N_2, 50–51
energy expressions for MMCC(m_A,m_B) approximations, 41–42
EOMCC-related approach completing with noniterative MMCC, 58
excited-state MMCC(m_A,m_B) methods: MMCC(2,3), 46–48

Downloaded by 217.66.152.21 on September 14, 2012 | http://pubs.acs.org
Publication Date: August 14, 2002 | doi: 10.1021/bk-2002-0828.ix002

Downloaded by 217.66.152.21 on September 14, 2012 | http://pubs.acs.org
Publication Date: August 14, 2002 | doi: 10.1021/bk-2002-0828.ix002

  excited-state PESs, 53–59
  excited states of C_2, 56–57
  excited-state theory, 37–41
  extension of existing SRCC methods, 32
  general formalism, 34–41
  general nature of MMCC theory, 45–46, 59–60
  ground-state MMCC(m_A,m_B) methods and renormalized CCSD(T), CCSD(TQ), and CCSDT(Q) schemes, 42–46
  ground-state potential energy surfaces (PESs) involving bond breaking, 48–53
  ground-state theory, 34–37
  HF molecule, 49–50, 52–53
  MMCC(2,3), MMCC(2,4), and MMCC(3,4) approximations, 43
  N_2 molecule, 51
  N_2 molecule vs. H_2O, 55–56
  performance of noniterative MMCC(2,3) approximation, 59
  potential energy curves for CH^+ ion, 57*f*
  potential energy curves for double-zeta (CA) HF, N_2, and C_2 molecules and cc-pVDZ F_2 molecule, 49*f*
  selected vibrational term values and dissociation energies of HF molecule, 52*t*
  vertical excitation energies of H_2O, N_2, and C_2, 54*t*
Model Hamiltonians. *See* Intersystem crossing effects in O + H_2 reaction
Monoxides. *See* Halogen monoxides
Morse potentials
  CaF and CaF^-, 246*f*
  CaO, 250*f*
  CaO and CaO^-, 257*f*
  ZnF and ZnF^-, 246*f*
  ZnO, 252*f*
  ZnO and ZnO^-, 257*f*
Multi-configuration self-consistent (MCSCF), nondynamical electron correlation, 3, 6
Multiple potential energy surfaces (PESs). *See* Potential energy surfaces (PESs)
Multi-reference configuration interaction (MRCI), performance for BrO and IO, 270
Multi-reference configuration interaction method (MR–CISD)
  categorizing alternatives, 2–3
  nondynamic and dynamic electron correlation, 2
Multi-reference coupled-cluster linear response theory (MR–CCLRT)
  algorithmic considerations, 131–132
  performance for low-lying potential energy surface (PES) of Li_4 model, 138*f*, 139*f*, 140*f*, 141*f*
  See also State-specific multi-reference coupled-cluster (SS–MRCC) methods
Multi-reference coupled electron-pair approximation linear response theory (MR–CEPALRT)
  algorithmic considerations, 131–132
  potential energy surface (PES) for low-lying states of H_4 model, 144, 145*f*
  See also State-specific multi-reference coupled-cluster (SS–MRCC) methods
Multi-reference perturbation theory (MRPT), dynamic vs. nondynamic correlation, 3

N

N_2O, shapes of HOMO and LUMO as function of θ, 311*f*
Natural gas clathrate-hydrates
  illustration of empty lattice structure, 420*f*

Downloaded by 217.66.152.21 on September 14, 2012 | http://pubs.acs.org
Publication Date: August 14, 2002 | doi: 10.1021/bk-2002-0828.ix002

  Lennard–Jones 6-12 and Kihara potentials, 419
  Lennard–Jones and Devonshire (LJD) spherical cell potential approximation, 419
  systems of polyhedral cells, 419
  See also Methane hydrates
Negative imaginary potentials, molecular resonances, 348, 350
Nitrogen N_2 molecule
  completely renormalized CCSD(T), CR–CCSD(TQ), and CR–CCSDT(Q), 50–51
  double-zeta (DZ) model, 24–27
  energy deviations from full configuration interaction (FCI), 106*t*
  excited states, 54–55
  ground-state potential energy surfaces (PESs), 51
  ionization potential, 209*t*
  time-dependent local density approximation (TDLDA), 205, 206*t*
  total FCI energies and energy differences for DZ model, 25*t*
  triple bond dissociation, 99*f*
  vertical excitation energies, 54*t*
  See also Coupled cluster (CC) methods for bond-breaking; Method of moments of coupled-cluster (MMCC) equations
Nitrogen trioxide radical (NO_3)
  ACES II electronic structure programs, 71–72
  atmospheric chemistry, 66
  avoiding symmetry breaking problem of orbitals, 67
  cation contributing to sharp lower energy peaks, 76–77
  cation NO_3^+ ground state $^1A_1'$ equilibrium geometry and vibrational frequencies, 77*t*
  character of lowest double ionization potential similarity transformed equation-of-motion coupled-cluster singles and doubles (DIP–STEOM–CCSD) NO_3^+ states, 76*t*
  configuration interaction (CI) theory for straightforward diagonalization approach, 69
  cross section of potential energy surface for D_{3h} degenerate electronic state, 80*f*
  difference in magnitude of Jahn–Teller effect for excited states, 85*f*, 86
  DIP–EOM–CCSD (double ionization potential equation-of-motion coupled-cluster singles and doubles) method, 68
  DIP–EOM–CCSD for states of NO_3^+ cation, 70–71
  DIP–STEOM–CCSD method, 67–68
  DIP–STEOM–CCSD/TZ2P conical intersections of surfaces in C_{2v} symmetry, 87*t*
  DIP–STEOM–CCSD/TZ2P optimized geometries and adiabatic electronic ionization potentials (IPs) for $^1E''$ state, 79*t*
  DIP–STEOM–CCSD/TZ2P optimized geometries of three excited states, 82–83
  energy diagram of uppermost restricted Hartree–Fock (RHF) orbitals of $NO_3^{\cdot}$, 69*f*
  EOM–CCSD method for excitation energies, electron affinities, ionization potentials of closed-shell systems, 69–70
  experimental photoelectron spectrum, 75*f*
  experimental study measuring HeI photoelectron (PE) spectrum, 66
  first photoionization study of neutral system, 66
  Fock space multi-reference coupled-cluster (FSMRCC), 67

Downloaded by 217.66.152.21 on September 14, 2012 | http://pubs.acs.org
Publication Date: August 14, 2002 | doi: 10.1021/bk-2002-0828.ix002

  graph of DIP–STEOM–CCSD/TZ2P relative energies of components of $^{3}E''$, $^{3}E'$, and $^{3}A_2'$ states at each optimized geometry, 85*f*
  harmonic vibrational frequencies at minimum and transition state stationary points, 81*t*
  Jahn–Teller distortion, 80
  neutral ground state $^{2}A_2'$ equilibrium geometry and vibrational frequencies, 72*t*
  neutral vertical ionization energies, 74–77
  NO_3^+ cation excited states $^{3}E''$, $^{3}E'$, and $^{3}A_2'$, 82–88
  NO_3^+ cation ground state $^{1}A_1'$, 77–78
  NO_3^+ cation excited state $^{1}E''$, 79–82
  NO_3 neutral ground state $^{2}A_2'$, 72–73
  optimization of $^{3}E''$, $^{3}E'$, and $^{3}A_2'$ states in DIP–STEOM–CCSD, 88–89
  quasi-restricted Hartree–Fock coupled-cluster (QRHF CC), 67
  relative energies of five components of states at each optimized geometries, 84*t*
  relative ionization potentials (IPs), 75
  RHF CCSD(T) geometry optimization of cation ground state, 78
  single point calculations at RHF CCSD(T)/TZ2P optimized C_{2v} geometry, 78
  STEOM–CCSD method for excitation energies, double electron attachments, and double ionization potentials of closed-shell systems, 70
  symmetrically correct wavefunctions for ground state, 67
  symmetry breaking problem for neutral and cation ground states, 66–67
  theoretical and computational details, 68–72
  vertical ionization energies, 74*t*
  vertical ionization spectrum by DIP–STEOM–CCSD and DIP–EOM–CCSD methods, 88
Non-adiabatic coupling matrix (NACM)
  model, 362–363
  quantizing for sub-Hilbert space (SHS), 362, 376
  treatment of model, 366–367
  See also Adiabatic-to-diabatic transformation matrix and rotation matrix
Non-adiabatic coupling terms (NACTs)
  comparison to potential energy surfaces, 362
  features and role in molecular physics, 361–362
  See also Adiabatic-to-diabatic transformation matrix and rotation matrix
Nondynamical electron correlation
  describing potential energy surfaces (PESs), 6
  versus dynamical, 2–3

O

$O + H_2$ reaction. *See* Intersystem crossing effects in $O + H_2$ reaction
O_4 system
  ab initio reduced dimensionality surface for vibrationally selected rate constants, 319
  CASMP2 method, 316
  CCSD(T) method, 316
  chemical composition of atmosphere, 317
  chemically bound complex, 316
  combined experimental and theoretical study of products energy distribution for reverse ozone forming reaction, 319

  condensed phases of oxygen, 315
  evidence for spin-orbit coupling, 322
  evidence of non-adiabatic behavior in highly vibrationally excited O_2 and O_4, 320–323
  experimental determination of self-relaxation rates of molecular oxygen, 317–318
  formation of oxygen rings, 316
  internuclear distance for spectator bond, 319
  ozone forming reaction, 322–323
  potential energy surface, 318–319
  spin-orbit coupling effects for collision system, 321–322
  spin-orbit transitions, 322
  study of highly vibrationally excited molecules, 317
  theoretical studies on ozone forming reaction (R1), 318–319
  unsolved questions and speculations, 323–324
  van der Waals complex, 315
  vibrational, rotational, and translational energy distributions for O_2 from reverse ozone forming reaction, 323
  vibrational relaxation mechanisms, 320

OCS
  bending potential around point of largest non-adiabatic coupling along reaction coordinate, 311*f*
  bimodal speed distribution of S, 303
  bond angles of triatomic molecules, 306–307
  CASSCF calculations, 305
  configuration state functions (CSFs), 305
  2D imaging of $S(^1D_2)$ in photodissociation of, 302–303
  electronic structure, 305–308
  inverse Abel transforms of $S(^1D_2)$ images at 223, 235, and 248 nm, 304*f*
  non-adiabatic bending dissociation as orbital unlocking, 309, 312
  non-adiabatic transition in bending coordinate, 308–309
  photodissociation, 301
  picture of molecular orbitals (MOs) along reaction coordinate, 310*f*
  resonance-enhanced multiphoton ionization (REMPI), 301
  section of potential energy surfaces for R and θ coordinates, 305*f*, 306*f*, 311*f*
  shapes of HOMO and LUMO of N_2O as function of θ, 311*f*
  two-dimensional photofragment imaging, 301–302
  Walsh diagram for isovalent CO_2, 307*f*

Orbital unlocking, non-adiabatic bending dissociation, 309, 312

Oscillator strengths, comparing IVO–CASCI and H^v methods with experiment, 169, 170*t*

Oxides. *See* Calcium oxide (CaO); Halogen monoxides; Zinc oxide (ZnO)

Oxygen, molecular
  evidence of non-adiabatic behavior in highly vibrationally excited, 320–321
  experimental determination of self-relaxation rates, 317–318
  mechanism for dark channel in collisions of highly vibrationally excited O_2, 324
  vibrational, rotational, and translational energy distributions for O_2 from reverse ozone forming reaction, 323
  vibrational relaxation mechanism, 320
  See also O_4 system; Ozone, O_3

Ozone, O_3
  reaction forming, 322–323
  theoretical studies on ozone forming reaction, 318–319

Downloaded by 217.66.152.21 on September 14, 2012 | http://pubs.acs.org
Publication Date: August 14, 2002 | doi: 10.1021/bk-2002-0828.ix002

  unsolved problem, 324
  vibrational, rotational, and translational energy distributions for O_2 from reverse ozone forming reaction, 323
  See also O_4 system

P

Pauli–Breit Hamiltonian
  Hermitian character, 281–282
  spin-orbit coupling, 277–278
  See also Symmetry in spin-orbit coupling
Peng–Robinson equation of state (EOS), 432, 434
Phase equilibria. *See* Methane hydrates
Photochemistry. *See* Density functional theory, time-dependent (TDDFT)
Photodissociation
  inverse Abel transforms of $S(^1D_2)$ images at 223, 235, and 248 nm, 304*f*
  OCS, 301
  two-dimensional imaging of $S(^1D_2)$ of OCS, 302–303
Photoelectron spectrum, nitrogen trioxide, 75*f*
Photofragment imaging, two-dimensional, 301–302
Phthalan (PHT)
  comparing experimental and *ab initio* barriers, 397*t*
  electronic states, 381
  electronic transition producing $S_1(\pi,\pi^*)$ state, 389*f*
  far-infrared spectrum, 388–389
  molecular orbitals, 389*f*
  potential energy along ring-puckering coordinate for ground and excited states, 390*f*
  spectroscopic transitions for ground and excited states, 384*f*
  See also Potential energy surfaces (PESs), spectroscopic determination
Point group symmetry
  comparing point and double group selection rules, 286–287
  spin-orbit coupling, 286
Potential energy curves
  torsional, for positive allene ion, 166, 167*f*
  torsional, of C_3H_4, 169, 171*f*
Potential energy surfaces (PESs)
  accuracy and effort of calculation vs. reliability for multiple, 4–5
  development of methods including relativistic effects, 5
  excited-state PESs, 53–59
  extension of single-reference coupled-cluster (SRCC) methods, 32
  ground-state, involving bond breaking, 48–53
  HF molecule, 49–50
  HOCl, 351–352
  linear response theory based on state-specific multi-reference coupled cluster formalism (MR–CCLRT), 125–128
  linear response theory based on state-specific multi-reference coupled electron-pair approximation (MR–CEPALRT), 128–130
  multiple, 3–4
  N_2 molecule vs. H_2O, excited states, 55–56
  nondynamical correlation, 6
  nuclear motion, 300–301
  potential energy curves for CH^+ ion, 57*f*
  potential energy curves for double-zeta (DZ) HF, N_2, and C_2 molecules and cc-pVDZ F_2 molecule, 49*f*

Downloaded by 217.66.152.21 on September 14, 2012 | http://pubs.acs.org
Publication Date: August 14, 2002 | doi: 10.1021/bk-2002-0828.ix002

problems of using multi-reference coupled-cluster (MRCC) theories, 111–112
progress of theoretic study, 1–2
rigorous approaches, 5–6
sections of OCS along R and θ coordinates, 305*f*, 306*f*, 311*f*
spectroscopic quality, 260–261
spin-orbit effects, 5
vertical excitation energies of H_2O, N_2, and C_2, 54*t*
See also Halogen monoxides; Method of moments of coupled-cluster (MMCC) equations; Potential energy surfaces (PESs), spectroscopic determination; State-specific multi-reference coupled-cluster (SS–MRCC) methods

Potential energy surfaces (PESs), spectroscopic determination
comparison of experimental and *ab initio* barriers for molecules in indan family, 397*t*
conformational changes along vibrational pathways, 381
definition for puckering and flapping vibrational coordinates, 385*f*
determining quantum states for puckering and flapping vibrations, 387–388
dispersed fluorescence spectra of jet-cooled indan, 396*f*
electronic states of molecules in indan family, 381
far-infrared spectrum of coumaran, 387*f*
far-infrared spectrum of phthalan (PHT), 388–389
fluorescence excitation and ultraviolet absorption spectra of indan, 396*f*
fluorescence excitation spectra and ultraviolet absorption spectra of 1,3-benzodioxole (BZD), 391*f*
fluorescence excitation spectra (FES), 383
indan, parent molecule, 395
investigation of BZD, 390–391, 395
kinetic energy function for cross term of BZD, 386*f*
laser induced fluorescence (LIF), 383
molecular orbitals for PHT and electronic transition producing $S_1(\pi,\pi^*)$ state, 389*f*
n–σ* anomeric interaction for BZD, 394*f*
one-dimensional potential energy function for ring-puckering of coumaran, 388*f*
one-dimensional potential energy functions for ring-puckering of indan in ground and excited states, 397*f*
out-of-plane vibrations of indan, 382*f*
PES along flapping coordinate, 389–390
potential energy along ring-puckering coordinate for ground and excited states $S_1(\pi,\pi^*)$ of PHT, 390*f*
ring-puckering quantum states of BZD in different flapping and electronic states, 392*f*
single vibrational level fluorescence (SVLF), 383
spectroscopic methods for determining vibrational quantum states, 381, 383
spectroscopic transitions for ground and excited states of PHT and related molecules, 384*f*
theory, 383, 386
two-dimensional PES of BZD in S_0 state, 393*f*
vibrational frequency below 300 cm^{-1}, 381

1,2-Propadiene. *See* Allene

Puckering vibrations
definition of coordinates, 385*f*

Downloaded by 217.66.152.21 on September 14, 2012 | http://pubs.acs.org
Publication Date: August 14, 2002 | doi: 10.1021/bk-2002-0828.ix002

theory, 383, 386
See also Potential energy surfaces (PESs), spectroscopic determination

Q

Quadratic coupled cluster doubles (QCCD)
double bond-breaking, 99
method, 98
triple bond-breaking, 100
Quantum scattering
calculations, 333, 336
quantum reaction probabilities versus energy for models, 338*f*, 339*f*, 340*f*
trajectory surface hopping (TSH) and quantum results for models, 341, 342*f*, 343*f*
See also Intersystem crossing effects in O + H_2 reaction
Quartic oscillator
average position for one-dimensional, 410*f*
average position of, coupled to bath of 30 harmonic degrees of freedom at zero temperature, 411*f*
example using forward-backward semiclassical dynamics (FBSD), 409–411
position correlation function of one-dimensional, at two temperatures, 412*f*, 413*f*
Quasi-degenerate perturbation theory (QDPT)
dynamic vs. nondynamic correlation, 3
theory, 132–133

R

Rectangular geometry, Li_4 model, 134, 137
Reduced multi-reference coupled-cluster (RMRCC) approaches
coupled-cluster CCSD method, 14
molecular potential energy surfaces, 32
successes of RMRCC singles and doubles (RMRCCSD) approach, 32–33
Relativistic effects, potential energy surfaces (PESs), 5
Renormalized versions, coupled-cluster CCSD methods, 14
Resonance-enhanced multiphoton ionization (REMPI), photofragment imaging, 301
Resonance theory
resonance wavefunction, 348, 349*f*
review, 347–351
See also Unimolecular dissociation of HOCl
Ring-puckering. *See* Potential energy surfaces (PESs), spectroscopic determination
RKR potentials. *See* Halogen monoxides

S

Schrödinger equation, obstacle in numerical solution, 401
Self-consistent field (SCF)
density functional theory (DFT), 203–204
strength of approach, 204
Semiclassical dynamics
forward-backward, without prefactors, 404–407
quantum mechanics, 402–404
See also Forward-backward semiclassical dynamics (FBSD)
Similarity transformed equation-of-motion coupled-cluster singles and doubles (STEOM–CCSD) method, 70

Downloaded by 217.66.152.21 on September 14, 2012 | http://pubs.acs.org
Publication Date: August 14, 2002 | doi: 10.1021/bk-2002-0828.ix002

Downloaded by 217.66.152.21 on September 14, 2012 | http://pubs.acs.org
Publication Date: August 14, 2002 | doi: 10.1021/bk-2002-0828.ix002

Similarity transform equation of motion (STEOM), dynamic vs. nondynamic correlation, 3
Single-reference coupled-cluster (SRCC) methods
  active-space, 33
  applicability of ground-state SRCC approaches, 33–34
  extension to quasidegenerate and excited states, 32
  linear response theory (SR–CCLRT), 125–128
  See also Method of moments of coupled-cluster (MMCC) equations
Single reference electronic structure methods, simplicity, 94
Single vibrational level fluorescence (SVLF), laser induced fluorescence (LIF), 383
Spectral theory of chemical bonding
  antisymmetric subspace, 225–226
  application of formalism to lowest-lying singlet and triplet states of H_2, 235–236
  computational applications, 226–235
  eigenvalues of metric matrix S for H_2, 227, 229*f*, 230
  electronic charge predictions, 232
  electron pair-bond calculations, 231*t*
  energies and expectation values for lowest-lying states in H_2, 230, 232
  lowest-lying attractive and repulsive states of electron pair bond (H_2), 226–227
  many-electron Hamiltonian operator, 224
  one-electron charge distribution in plane of two nuclei for ground state, 233*f*
  potential energy curves in H_2 from recursive development, 234*f*
  predictions of chemical structure and reactions, 222
  rate of convergence with increasing angular momentum, 232
  recursive projection procedure, 225–226, 232, 235
  role of symmetric group, 222–223
  spectral energies for atomic hydrogen, 228*t*
  theoretical approach, 223
  theoretical formalism, 223–225
Spectroscopic properties
  calcium and zinc fluorides, 253*t*
  calcium and zinc oxides, 251*t*
Spin-orbit coupling
  effects for collision system $O_2 + O_2$, 321–322
  O_4 system, 322
  See also Symmetry in spin-orbit coupling
Spin-orbit effects
  bimolecular reactions, 330–331
  potential energy surfaces (PESs), 5
State-averaged multiconfiguration self-consistent (SA–MCSCF), nondynamical electron correlation, 6
State-reference coupled-cluster (SRCC)
  accuracy at SD or SD(T) truncation levels, 110
  multi-reference (MR) generalization, 111
  theory, 110
  treating quasi-degeneracy, 110–111
  See also State-specific multi-reference coupled-cluster (SS–MRCC) methods
State-specific multi-reference coupled-cluster (SS–MRCC) methods
  algorithmic considerations, 131–132
  approximate versions, 117–124
  Baker–Campbell–Hausdorff formula, 116

correlation energies for ground state of H_4 model vs. standard MR techniques, 144*t*
difference energy plot of ground state of Li_4 model vs. full CI (FCI), 136*f*
energies of 2^1A_1 state of H_4 model, 146*t*
Epstein–Nesbet (EN) partitioning, 119–120
expressions for Rayleigh–Schrödinger (RS) and Brillouin–Wigner (BW) based SS–MRPT, 118
formalism, 112–113
geometrical arrangement of atoms in rectangular Li4, 135*f*
H_4 model: trapezoidal geometry, 137, 142, 144
Li_4 model: rectangular geometry, 134, 137
linear response theory based on SS–MRCC formalism (MR–CCLRT), 125–128
linear response theory based on SS–MRCEPA formalisms (MR–CEPALRT), 128–130
MR configuration interaction (MRCI) equation, 124
numerical implementation, 131–132
PES of ground state of H_4 model, 143*f*
PES of some low-lying $^1A_1$ states of Li_4 model, 138*f*
PES of some low-lying $^1A_2$ states of Li_4 model, 139*f*
PES of some low-lying $^1B_1$ states of Li_4 model, 140*f*
PES of some low-lying $^1B_2$ states of Li_4 model, 141*f*
PES of some low-lying states of H_4 model, 145*f*
plot of CSF energies of Li_4 model, 135*f*
problems in use of MRCC for studying potential energy surfaces (PESs), 111–112
quasi-degenerate perturbation theory (MC–QDPT), 132–133
SRCC theory, 110
SS formalism, 116–117
SS MR coupled electron-pair approximation (SS–MRCEPA) formalisms, 122–124
SS–MR perturbation theories (SS–MRPT), 117–122
state-universal MRCC (SU–MRCC) theory, 114–115
strength of MR-based method, 111
testing robustness of formalisms for H_4 model, 142, 144
theories of excited state PES via linear response approach, 125–130
theory, 113–117

State-specific multi-reference coupled electron-pair approximation (SS–MRCEPA)
  algorithmic considerations, 131
  approximations, 122–123
  energies for 2^1A_1 state of H_4 model, 146*t*
  energies for ground state of H_4 model, 142, 144*t*
  energy and cluster amplitude finding equations, 123
  ground state PES for H_4 model, 142, 143*f*
  linear response theories, 128–130
  MR configuration interaction (MRCI) equation, 124

State-specific multi-reference perturbation theories (SS–MRPT)
  algorithmic considerations, 131
  energy denominators in Rayleigh–Schrödinger (RS) and Brillouin–Wigner (BW) versions, 121
  Epstein–Nesbet (EN) partitioning, 119–120

Downloaded by 217.66.152.21 on September 14, 2012 | http://pubs.acs.org
Publication Date: August 14, 2002 | doi: 10.1021/bk-2002-0828.ix002

Downloaded by 217.66.152.21 on September 14, 2012 | http://pubs.acs.org
Publication Date: August 14, 2002 | doi: 10.1021/bk-2002-0828.ix002

- expressions for RS and BW versions, 118
- Hamiltonian, 117–118
- perturbed energy, 120
- pseudo-effective operator, 121–122
- size-extensivity of perturbative formalisms, 118–120
- unperturbed energy, 120

State specific (SS)
- approaches, 11
- coupled-cluster CCSD methods, 13
- generalized Bloch equations (DGB method), 14–15

State-universal multi-reference coupled-cluster (SU–MRCC), theory, 114–115

Symmetry in spin-orbit coupling
- arbitrary configuration interaction (CI) wavefunction symmetry labeling, 290–293
- Clebsch–Gordan coefficient relations, 279–280, 293, 295
- comparison of point and double group selection rules, 286–287
- computational speed-up, 287–288
- detailed structure of H_{so} matrix, 295–296
- double group symmetry, 282–286
- efficient spin-orbit (SO) coupling calculation, 277
- general SO matrix element, 277
- Hermitian character of H_{so}, 281–282
- Hermiticity and time reversal, 280–281
- Hso matrix for different multiplicities, 296*t*
- Hso matrix for equal multiplicities, 296*t*
- improving conventional scalar calculations, 276–277
- Pauli–Breit Hamiltonian SO coupling, H_{so}, 277–278
- phases and determinants, 294*t*
- point group symmetry, 286
- relativistic spin-dependent correction, 277–278
- scalability of SOC code, 289*f*
- states represented by real valued wavefunctions, 280–281
- time-reversal symmetry, 282
- Wigner–Eckart theorem, 278–280
- Wigner functions, 290

T

Table-configuration interaction (CI) method
- algorithm constructing Hamiltonian matrix elements, 180
- analysis of ΔK=1 cases, 185–190
- analysis of ΔK=2 case, 182–185
- analysis of pairs of configurations with same number of open shells, 190–196
- analysis of relationships between pairs of configurations, 180–196
- case of same configuration, 195–196
- case of spin-free Hamiltonian, 178–179
- configuration-driven algorithm, 177
- electron repulsion integrals and linear coefficients for ΔK=0, P=1 case, 191*t*
- electron repulsion integrals and linear coefficients for ΔK=1, P=1 case, 186*t*
- electron repulsion integrals and linear coefficients for ΔK=2 case, 183*t*
- ΔK=0, P=1 case, 190–192
- ΔK=0, P=2 case, 192–193
- ΔK=0, P=3 case, 193–195
- ΔK=1, P=1 case, 185–187
- ΔK=1, P=2 case, 187–188
- ΔK=1, P=3 case, 188–190
- ΔK describing pairs of configurations, 180

Downloaded by 217.66.152.21 on September 14, 2012 | http://pubs.acs.org
Publication Date: August 14, 2002 | doi: 10.1021/bk-2002-0828.ix002

- parameters P labeling types of molecular integral, 180
- possible non-vanishing relationships between random pairs of configurations, 181*t*
- requirement for effective implementation, 185
- use of genealogical CSFs, 177–180

Tamm–Dancoff approximation (TDA), excitation energy equation, 208

Time-dependent local density approximation (TDLDA), lowest level, 205

Torsional potential energy curves
- allene, 169, 171*f*
- positive allene ion, 166, 167*f*

Trajectory surface hopping (TSH)
- calculations, 336
- methods, 330–331
- *See also* Intersystem crossing effects in O + H_2 reaction

Trapezoidal geometry, H_4 model, 137, 142, 144

U

Unimolecular dissociation of HOCl
- absorbing potentials, 350
- calculation of energies and widths of resonances by L^2 method, 352
- complex coordinate method, 348
- computational details and results for HOCl resonances, 352–357
- coupled channel scattering methods, 348
- diabatic crossings, 355, 356*f*
- diagonalization of complex Hamiltonian, 353, 354*f*
- dissociation lifetime and isotope effects, 357, 358*t*
- experimental work, 347
- Hamiltonian for any total angular momentum, J and quantum number, K, 352–353
- L^2 approach, 350–351
- negative imaginary potentials, 348, 350
- potential energy surface for HOCl, 351–352
- resonance wavefunction, 348, 349*f*
- review of resonance theory and calculations, 347–351
- variation of $6\nu_{OH}$ resonance width with J, 353, 355, 357
- $7\nu_{OH}$ and $8\nu_{OH}$ resonances, 357

Unrestricted Hartree–Fock (UHF), dissociation limit, 12

V

Valence optimized orbital (VOO), coupled-cluster CCSD method, 14

van der Waals complex, O_4 system, 315

Variational coupled cluster doubles (VCCD)
- double bond dissociation of water, 95, 96*f*
- triple bond dissociation, 99*f*, 100

Vertical excitation energies (VEE), comparing methods for allene, 169, 172*t*, 173

Vertical ionization energies, neutral nitrogen trioxide, 74–77

Vertical ionization potentials (VIPs)
- allene as function of reference space, 165*t*
- allene by methods and experiment, 165*t*
- comparing VIPs by IVO–CASCI and H^v methods using bases of increasing size, 166, 168*t*

Vibrational frequencies
- cation NO_3^+ ground state, 77–78

  minimum and transition state stationary points for excited states (NO_3^+), 81–82
  neutral NO_3 ground state, 72–73
  See also Nitrogen trioxide radical (NO_3)
Vibrations. *See* Potential energy surfaces (PESs), spectroscopic determination

W

Water
  completely renormalized CCSD(T), CR–CCSD(TQ), and CR–CCSDT(Q), 50–51
  correlation function of O–H stretching normal mode of tetramer at zero temperature, 414*f*
  correlation function of various normal modes in clusters of two or four, 411, 414*f*
  double bond dissociation using perfect pairing (PP), imperfect pairing (IP), and restricted pairing models, 102*f*
  double zeta (DZ) basis for double dissociation of, 96*f*
  energy deviations from full CI (FCI) for double dissociation, 106*t*
  excited states, 54–55
  variational CCD (VCCD), conventional CCD, and full CI (FCI) calculations on double dissociation of, 96*f*
  vertical excitation energies, 54*t*
  See also Coupled cluster (CC) methods for bond-breaking; Methane hydrates
Wigner–Eckart theorem
  functions, 290
  spin-orbit coupling calculations, 278–280
  See also Symmetry in spin-orbit coupling
Wigner rotation matrix
  calculation, 373–375
  See also Adiabatic-to-diabatic transformation matrix and rotation matrix

Z

Zinc
  atomic characteristics, 240
  selected energy levels, 240*f*
Zinc fluoride (ZnF)
  anions, 244, 246–247
  cations, 247–248
  comparison of CaF and ZnF and their anions, 247*f*
  dipole moments, 245*t*
  excited electronic states, 238
  generalized Morse potentials, 246*f*
  ionization energies and electron affinities, 245*t*
  neutrals, 241, 244
  population analysis, 242*t*
  spectroscopic properties, 243*t*
  technical details, 239
  theoretical work, 239
Zinc oxide (ZnO)
  anions, 253, 255
  cations, 255
  comparison of CaO and ZnO and their anions, 256*f*
  dipole moments, 245*t*, 252–253
  excited electronic states, 238
  generalized Morse potentials, 252*f*, 257*f*
  ionization energies and electron affinities, 245*t*
  Mulliken populations, 252
  neutrals, 248–253
  population analysis, 249*t*
  spectroscopic properties, 251*t*, 254*t*
  technical details, 239
  theoretical work, 239

Downloaded by 217.66.152.21 on September 14, 2012 | http://pubs.acs.org
Publication Date: August 14, 2002 | doi: 10.1021/bk-2002-0828.ix002